Synthesis and Application of Functionalised Carbohydrates for Targeted Protein Degradation and Bacterial Glycan Recognition

Caitlin Eileen Shepperson

A thesis submitted in fulfillment of the requirements for the degree of

Doctor of Philosophy

School of Chemistry

University of Sydney

2026

This is to certify that to the best of my knowledge; the content of this thesis is my own work unless specified otherwise. No generative AI tools were used as part of the research project or to write sections of this thesis. This research was supported by an Australian Government Program Offset Scholarship.

This thesis has not been submitted for any other degree or other purposes.

Caitlin E Shepperson

January 2026

Attribution Statement and Originality Statement

This thesis is a summary of the work carried out in the School of Chemistry at The University of Sydney under the supervision of Prof. Richard J. Payne, Dr Leo Corcilius, and Dr Elizabeth Cairns, between April 2021 and September 2025.

In this thesis, I designed compound libraries, synthetic routes, and carried out synthesis and characterisation on all compounds, with the exception for where amide coupling conditions were required. This is a result of an allergy to the coupling reagents used for these processes. Pharmacological and other work was performed by persons as follows.

In chapter 2, amide couplings were performed by Dr Leo Corcilius or Dr Eric Sparkes. Peptides sequences BL-07, BL-08, BD-12, BD-16, BD-20, BD-21, BL-24, and BD-26 were synthesised are purified by Mr Beiyuan Cui. Biophysical characterisation of compounds was performed by Dr Jessica Zhong. Pharmacological data were obtained by Dr Elizabeth Cairns (Lambert Initiative, The University of Sydney), and Dr Monica Patel under the guidance of Prof. Michelle Glass from the University of Otago, New Zealand

In chapter 4, amide couplings were performed by Dr Leo Corcilius. In chapters 4 and 5, binding evaluation of compounds was obtained by Dr Niccolay Madiedo with Prof. Ethan Goddard-Borger at the Walter and Eliza Hall Institute, Melbourne, Australia.

As supervisor (Richard J. Payne) and auxiliary supervisor (Dr Leo Corcilius) for the candidature upon which this thesis is based, we can confirm that the author attribution statements above are correct.

Richard J. Payne

January 2026

[Redaction]

Leo Corcilius

January 2026

Caitlin E Shepperson

January 2026

Table of Contents

Abstract ..... *xi*

Abbreviations ..... *xiii*

Proteinogenic Amino Acids ..... *xx*

Acknowledgements ..... *xxi*

Chapter 1: Introduction *1*

1.1 Overview of carbohydrates **1**

1.1.1 Definition and Classification of Carbohydrates 1

1.1.2 Structural diversity of carbohydrates 2

1.2 Biological Roles and Functions of Carbohydrates **6**

1.2.1 Structural Roles 6

1.2.2 Cell-Cell Communication and Recognition 8

1.2.3 Protein Folding, Stability, and Half-Life 10

1.3 Therapeutic potential of carbohydrates **12**

1.3.1 Carbohydrate-based drugs 12

1.3.2 Glycosides and glycoconjugates 14

1.3.3 Glycan antigens in immunotherapy 18

1.4 Synthetic Challenges and Opportunities in Carbohydrate Chemistry **23**

1.5 Thesis Overview **24**

Chapter 2: CB_1 targeting LYTACs and ASGPR peptides *26*

2.1 Introduction **26**

2.1.1 The liver 26

2.1.2 Liver Disease 26

2.1.3 Current treatments for Liver Disease 28

2.1.4 Role of cannabinoid receptor 1 (CB_1) in metabolic and liver function 30

2.1.5 Targeting CB_1 in treatment of liver disease 32

2.1.6 Receptor degradation of CB_1 in hepatocytes 33

2.1.7 Targeted protein degradation 35

2.2 Chapter Aims 36

2.3 Results and Discussion 37

2.3.1 Synthetic Design of LYTACs 37

2.3.2 Synthesis of Rimonabant-type acceptor 40

2.3.2.1 Piperidine functionalisation 40

2.3.2.2 Attempted methyl functionalisation 47

2.3.3 Synthesis of tri-GalNAc ASGPR ligand 49

2.3.4 Assembly of CB_1 LYTAC candidates 51

2.4 Assessment of CB_1 ligand interactions 52

2.4.1 Binding characterisation of CB_1 LYTACs 52

2.4.2 Functional characterisation 55

2.5 The use of RaPID mRNA display to identify macrocylic peptide binders of ASGPR ... 60

2.5.1 Peptides as ligands 60

2.5.2 Identification of RaPID hits 63

2.5.3 Synthesis of RaPID hits 66

2.5.4 Biological Assessment of RaPID peptides 71

2.5.5 Identification of RaPID hits incorporating β-Ser-GalNAc 74

2.5.6 Synthesis of Fmoc-β-Ser-GalNAc$(OAc)_3$-OH building block: 74

2.5.7 Synthesis of cyclic glycopeptide RaPID hits incorporating β-Ser-GalNAc 76

2.5.8 Biological Assessment of GalNAc containing RaPID peptides 78

2.6 Conclusion and Future Work 80

Chapter 3: Bacterial Glycans and Recognition 82

3.1 Background on Bacteria 82

3.1.1 Structure and Classification of Bacteria 83

3.2 Treatment of Bacterial Infections 89

3.2.1 Cell wall synthesis inhibitors 90

3.2.2 Protein synthesis inhibitors 91

3.2.3 Nucleic acid synthesis inhibitors 91

3.2.4 Antimetabolites 91

3.3 Antibiotic resistance 92

3.3.1 Mechanisms of Antibiotic Resistance 94

3.3.2 Antibody-based therapies for targeting Gram-negative bacteria 95

Chapter 4: Synthesis of Pseudaminic Acid Analogues for Binding Studies and Methodological Improvements 100

4.1 Pseudaminic Acid 100

4.1.1 Pse anomeric nomenclature 103

4.2 Summary of Prior anti-Pse mAb Generation Work in the Payne Group 103

4.2.1 Limitations of Existing Tools for Pse Detection 104

4.2.2 Hapten Design and Synthesis of Pse Glycopeptides 105

4.2.3 Generation and Characterisation of Monoclonal Antibodies 106

4.2.4 Insight into Pan-Specificity *via* Structural Biology 106

4.2.5 Enrichment and Glycoproteomic Mapping of Pse-Modifications 108

4.2.6 Therapeutic Potential of Anti-Pse mAbs 108

4.2.7 Probing Substrate Flexibility of mAb 109

4.3 Chemical Synthesis of Pseudaminic Acids 109

4.3.1 Synthetic Route by Knirel and coworkers 110

4.3.2 Synthetic route by Ito and coworkers 111

4.3.3 Synthetic Routes utilising sialic acid (Neu5Ac) 113

4.3.4 Synthetic route by Kiefel, Payne, and co-workers 114

4.3.5 Synthetic routes by Crich and co-workers 116

4.3.6 Crich's 2022 synthesis 119

4.3.7 Synthesis by Li and co-workers 120

4.4 Stereocontrol of Chemical Pseudaminylation 122

4.5 Chapter Aims 128

4.6 Results and Discussion 129

4.6.1 Synthetic Methodology 129

4.6.2 Limitations of Current Synthesis 130

4.7 Synthesis of Pseudaminic acid analogues 135

4.7.1 Preparation of aldehyde 135

4.7.2 Aldol-type reaction of Garner's aldehyde 136

4.7.3 Li's route to *syn*-aldol product 142

4.7.4 Strategies for the installation of the C1 – C3 fragment 144

4.7.5 Attempted late-stage installation of Azide 149

4.7.6 Azide installation on linear substrate 152

4.7.7 Final synthesis of Pse variants 158

4.8 Binding Studies of Synthesised N7-variable Pseudaminylated Methyl Glycosides (performed with Professor Ethan Goddard-Borger, Walter and Eliza Hall Institute) 160

4.9 Conclusions and Future Work 163

Chapter 5: Total Synthesis of Legionaminic Acid 165

5.1 Background on Legionaminic Acid 165

5.1.1 Identification of Legionaminic Acid 165

5.1.2 Leg and analogues in bacteria 165

5.1.3 Anomeric nomenclature 167

5.2 Previous Syntheses 167

5.2.1 Synthetic Route by Knirel and co-workers 168

5.2.2 Synthetic Route by Seeberger and co-workers 169

5.2.3 Synthetic Routes by Crich and co-workers 172

5.3 Chapter Aims 177

5.4 Results and Discussion 178

5.4.1 Selection of Synthesis 178

5.5 Synthesis of Legionaminic acid donor 184

5.5.1 Glycosidation of donor 186

5.6 Binding Evaluation of Synthesised legionaminic acid glycoside (performed with Professor Ethan Goddard-Borger, Walter and Eliza Hall Institute) 190

5.7 Conclusions and Future Work 191

Chapter 6: Experimental 193

6.1 General Experimental Materials 193

6.1.1 Solution-Phase Chemistry Materials 193

6.1.2 Solid-Phase Chemistry Materials 193

6.2 General Experimental Methods 194

6.2.1 Nuclear Magnetic Resonance Spectroscopy 194

6.2.2 Mass Spectrometry 194

6.2.3 Infrared (IR) Absorption Spectrometry 195

6.2.4 Optical Rotation 195

6.2.5 Preparative Reversed-Phase HPLC 195

6.2.6 Preparative Reversed-Phase Mass-Directed HPLC 195

6.2.7 Analytical Reversed-Phase HPLC 196

6.3 General Solution Phase Procedures 197

6.3.1 *N*-nitrosylation of piperidinylmethanols 197

6.3.2 Reduction and Boc protection on *N*-nitrosylated piperidinylmethanols 197

6.3.3 Acrylation of *tert*-butyl ((hydroxymethyl)piperidinyl)carbamates 197

6.3.4 Simultaneous *N*-Boc and *tert*-butyl ester deprotection 198

6.3.5 Amide Couplings with Rimonabant-NHS ester 198

6.3.6 Benzyloxycarbonyl/ azide hydrogenolysis 199

6.3.7 Amide coupling of tri-GalNAc to PEG linkers 199

6.3.8 Deacetylation of tri-GalNAc conjugates 199

6.3.9 Amide coupling of tri-GalNAc-linker moiety to isomeric rimonabant structures 199

6.3.10 Preparation of α-MeO-Pse N7 variants 200

6.4 General Peptide Synthesis Procedures 201

6.4.1 Automated Solid-Phase Peptide Synthesis at 40 °C 201

6.4.2 Automated Solid-Phase Peptide Synthesis at 75 °C 201

6.4.3 Modified Automated SPPS for Coupling Chloroacetic Acid 201

6.4.4 Modified Automated SPPS for Coupling Speciality Amino Acids 202

6.4.5 Manual SPPS for Coupling Fmoc-Ser(β-GalNAc$(OAc)_3$)-OH 202

6.4.6 Manual SPPS for Coupling Chloroacetic Acid 202

6.4.7 Simultaneous Resin Cleavage and Global Side Chain Deprotection 203

6.4.8 Cyclisation of Chloroacetyl-Cysteinyl Peptides A 203

6.4.9 Cyclisation of Chloroacetyl-Cysteinyl Peptides B 203

6.4.10 Neopentyl deprotection in ligation buffer 203

6.4.11 Deacetylation of GalNAc incorporated peptides 203

6.5 Experimental Data for Chapter 2 205

6.5.1 Synthesis of Modified Rimonabant Scaffolds 205

6.5.2 Synthesis of tri-GalNAc ASGPR binder 213

6.5.3 Synthesis of tri-GalNAc linker intermediates 216

6.5.4 Synthesis of final rimonabant-based bifunctional molecules 220

6.5.5 Synthesis of Cyclic Peptides 244

6.5.6 Synthesis of Fmoc-Ser(*O*-β-D-GalNAc(OAc)$_3$)-OH 260

6.5.7 Synthesis of Cyclic Peptides incorporating GalNAc 266

6.6 Experimental data for Chapter 4 277

6.6.1 Synthesis of psuedaminic acid intermediates 277

6.6.2 Synthesis of final Pse N7 variants 291

6.7 Experimental Data for Chapter 5 293

6.8 Pharmacological and Binding Methods 306

6.8.1 CB_1 Radioligand Binding Assay 306

6.8.2 *in vitro* Cannabinoid Receptor Functional Activity Assays 307

6.8.3 RaPID mRNA display selection with/ without reprogramming against ASGPR1 308

6.8.4 Production of biotinylated 1E8 Fab' 310

6.8.5 Surface plasmon resonance (SPR) 311

References 312

Appendix I: Exemplar NMR Data 353

Appendix II: Raw data for CB_1 Activity Assays 429

Abstract

Carbohydrates are structurally diverse biomolecules that have essential roles in metabolism, structural organisation, cell signalling, immune recognition, and host-pathogen interactions. The highly specific interactions of carbohydrates with glycan-binding proteins make them attractive targets for investigating biological function as well as development of novel therapeutics. This thesis explores the application of functionalised glycans in two areas of chemical biology, namely targeted protein degradation in liver disease, and glycan recognition in Gram-negative bacterial infections.

Chapter 1 provides background on carbohydrates and their roles in biological systems. Chapter 2 focuses on the design and synthesis of liver-directed lysosome-targeting chimeras (LYTACs) to investigate selective and tissue-specific degradation of cannabinoid receptor 1 (CB_1). CB_1 is a G protein-coupled receptor (GPCR) involved in both metabolic dysfunction-associated liver disease (MASLD) and alcoholic liver disease (ALD). A library of bifunctional conjugates was synthesised by linking rimonabant, a high-affinity and selective CB_1 antagonist, to "tri-GalNAc" motifs designed to engage the asialoglycoprotein receptor (ASGPR) and mediate receptor degradation. These molecules allowed exploration of a novel therapeutic strategy for achieving selective receptor degradation, with the goal of minimising the central nervous system (CNS) effects associated with classical CB_1 antagonists. Additionally, two series of cyclic peptides identified as ASGPR binders discovered using random non-standard peptide integrated discovery (RaPID) mRNA display were synthesised. These peptides incorporated non-canonical amino acids in a unique effort to generate high-affinity cyclic peptide ASGPR ligands.

Chapter 3 provides a detailed overview of bacteria, focussing on bacterial surface glycans, including nonulosonic acids such as pseudaminic acid (Pse) and legionaminic acid (Leg), and their role in host-pathogen interactions and antimicrobial resistance. Chapter 4 describes the synthesis of stereochemically defined pseudaminic acid derivatives to investigate antibody-binding specificity, in addition to efforts to optimise

the synthetic methodology. Similarly, Chapter 5 outlines the total synthesis of a legionaminic acid glycoside to further probe antibody specificity across different nonulosonic acids.

Abbreviations

2-AG	2-arachidonoylglycerol
3_RHb	(*R*)-3-hydroxybutanoyl
5-HT	serotonin
7TM	seven transmembrane
AA	amino acid
Ac	acetyl
Ac_2O	acetic anhydride
ACC1	acetyl-CoA carboxylase 1
Aci	acetaminic acid
AcOH	acetic acid
AdSH	1-adamantane thiol
AEA	anandamide
AIBN	azobisisobutyronitrile
ALD	alcoholic liver disease
Alloc	allyloxycarbonyl
Alt	altrose
AMR	antimicrobial resistance
app	apparent
ASGPR	asialoglycoprotein receptor
BAIB	(diacetoxyiodo)benzene
BBB	blood-brain barrier
Bn	benzyl
Boc	*tert*-butoxycarbonyl
Boc_2O	di-*tert*-butyl dicarbonate
BSA	*N,O*-bis(trimethylsilyl)acetamide
Bu_2SnO	dibutyltin oxide
Bz	benzoyl
cAMP	Cyclic adenosine monophosphate
CB_1	cannabinoid receptor 1
CB_2	cannabinoid receptor 2
Cbz	carbobenzyloxy
CbzCl	benzyl chloroformate

CCW	counterclockwise
cDNA	complementary DNA
CDR	complementarity-determining region
CI-M6PR	cation-independent mannose-6-phosphate receptor
ClAc	chloroacetyl
CNS	central nervous system
CPS	capsular polysaccharide
CPT1	carnitine palmitoyltransferase 1
CRC	concentration response curve
CRD	carbohydrate recognition domains
Ctx	centuximab
CV	column volumes
CW	clockwise
DAG	diacylglycerol
DAGL	diacylglycerol lipase
DBCO	dibenzocyclooctyne
DBU	1,8-diazabicyclo[5.4.0]undec-7-ene
DCC	*N,N'*-dicyclohexylcarbodiimide
DCE	1,2-dichloroethane
DIC	*N*,*N*'-diisopropylcarbodiimide
DIPEA	*N,N*-diisopropylethylamine
DMF	*N*,*N*-dimethylformamide
DMP	Dess–Martin periodinane
DMSO	dimethyl sulfoxide
DNA	deoxyribose nucleic acid
DNP	dinitrophenol
E+	electrophile
EC_{50}	effective concentration producing 50% of the maximal response
EC_{80}	effective concentration producing 80% of the maximal response
ECM	extracellular matrix
EDA	ethylenediamine
EGFR	epidermal growth factor receptor

eq	equivalents
ELISA	enzyme-linked immunosorbent assay
EPO	erythropoietin
EPS	extracellular polymeric substances
ESBL	extended spectrum β-lactamase
ESI	electrospray ionisation
EtOH	ethanol
FAS	fatty acid synthase
FDA	Food and Drug Administration
FLIPR	fluorescent imaging plate reader
Fmoc	9-fluorenylmethyloxycarbonyl
FT-MS	fourier transform mass spectrometry
GAG	glycosaminoglycan
Gal	galactose
GalNAc	*N*-acetyl galactosamine
Gc	glycoamido
Gdn	guanidinium
GIRK	G protein-activated inwardly rectifying K^+ channels
GlcNAc	*N*-acetyl glucosamine
GLP-1RAs	glucagon-like peptide-1 receptor agonsits
GPCR	G protein-coupled receptor
GPI	glycosylphosphatidylinositol
GRK	G protein-coupled receptor kinases
h	hours
HATU	*O*-(7-azabenzotriazol-1-yl)-*N*,*N*,*N*',*N*'-tetramethyluronium hexafluorophosphate
HCC	hepatocellular carcinoma
HEPES	4-(2-Hydroxyethyl)-1-piperazineethanesulfonic acid
HF	high fat
HILIC	hydrophilic interaction liquid chromatography
HOBt	1-hydroxybenzotriazole
HOSu	*N*-hydroxysuccinimide
HPLC	high-performance liquid chromatography
IC_{50}	half maximal inhibitory concentration

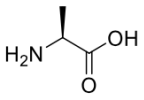
IgG	immunoglobulin G
***i*Pr**	isopropyl
***i*PrNEt$_2$**	*N*,*N*-diisopropylethylamine
***i*Pr$_3$SiH**	triisopropylsilane
IRC	ion-exchange resin, cationic
K_D	dissociation constant
KLH	keyhole limpet hemocyanin
LC-MS	liquid chromatography-mass spectrometry
LDA	lithium diisopropylamide
Leg	legionaminic acid
Lev	levulinate
LG	leaving group
LiHMDS	lithium bis(trimethylsilyl)amide
LiOTf	lithium trifluoromethanesulfonate
LPS	lipopolysaccharides
LYTAC	lysosome-targeting chimera
M6Pn	mannose-6-phosphonate
mAbs	monoclonal antibodies
MASLD	metabolic dysfunction-associated liver disease
MDR	multidrug-resistant
Me	methyl
MeI	methyl iodide
MeOD	deuterated methanol
MeOH	methanol
MeCN	acetonitrile
min	minutes
mGluR	metabotropic glutamate receptor
MoDE-As	molecular degraders of extracellular proteins through the asialoglycoprotein receptor
MS	mass spectrometry
mRNA	messenger RNA
Mtb	*Mycobacterium tuberculosis*
MVB	multivesicular body
N.B.	No binding

NALFD	non-alcoholic fatty liver disease
NaOMe	sodium methoxide
NAPE	*N*-arachidonoyl phophatidylethanol
NAPR-PLD	NAPE-referring phospholipase D
NASH	non-alcoholic steatohepatitis
NBS	*N*-bromosuccinimide
NEt_3	triethylamine
Neu	neuraminic acid
NGP	neighbouring group participation
NHS	*N*-hydroxysuccinimide
NMM	*N*-methylmorpholine
NMR	nuclear magnetic resonance
NulO	nonulosonic acid
OXYMA	ethyl (hydroxyimino)cyanoacetate
PCR	polymerase chain reaction
PEG	polyethylene glycol
Ph	phenyl
PKA	protein kinase A
PNS	peripheral nervous system
POI	protein of interest
PPTS	pyridinium *p*-toluenesulfonate
PROTAC	proteolysis-targeting chimera
Pse	pseudaminic acid
py	pyridine
q	quartet
quin.	quintet
RaPID	random non-standard peptide integrated discovery
RNA	ribonucleic acid
RND	resistance-nodulation-division
RP-HPLC	reverse-phase high-performance liquid chromatography
rRNA	ribosomal RNA
rt	room temperature
RU	response units
SAR	structure-activity relationship

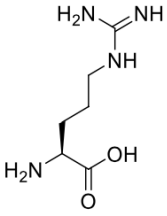
SCRAs	synthetic cannabinoid receptor agonists
S_N1	nucleophilic substitution, unimolecular
S_N2	nucleophilic substitution, bimolecular
SPPS	solid-phase peptide synthesis
SPR	surface plasmon resonance
SREPB-1c	sterol regulatory element binding protein 1c
sTn	sialyl-Tn
Su	succinimide
sY	sulfotyrosine
TACA	tumour-associated carbohydrate antigen
TB	tuberculosis
TBAB	tetra-*n*-butylammonium bromide
TBAF	tetrabutylammonium fluoride
TBDPS	*tert*-butyldiphenylsilyl
TBS	*tert*-butyldimethylsilyl
***t*Bu**	*tert*-butyl
Temp	temperature
TEMPO	2,2,6,6-tetramethylpiperidine-1-oxyl
TES	triethylsilyl
Tf	trifluoromethanesulfonyl
Tf_2O	trifluoromethanesulfonyl anhydride
TFA	trifluoroacetic acid
TfN_3	trifluoromethanesulfonyl azide
TfOH	trifluoromethanesulfonic acid
TGA	Therapeutic Goods Administration
THC	Δ^9-tetrahydrocannabinol
THF	tetrahydrofuran
TLC	thin-layer chromatography
TMS	trimethylsilyl
TMSOTf	trimethylsilyl trifluoromethanesulfonate
Tn	Thomsen–nouvelle antigen
Tol	p-tolyl
TPD	targeted protein degradation
Tris	2,4,6-triisopropylbenzenesulfonyl

tRNA	transfer RNA
Troc	2,2,2-trichloroethoxycarbonyl
TTMS	tris(trimethylsilyl)silane
UDP	uridine diphosphate
UPLC	ultra-performance liquid chromatography
UPS	ubiquitin-proteasome system
UTI	urinary tract infection
WT	wild type

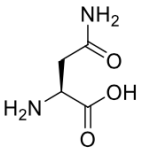
Proteinogenic Amino Acids



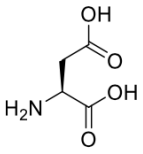
Alanine
Ala, A



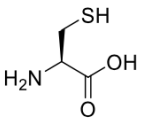
Arginine
Arg, R



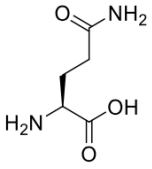
Asparagine
Asn, N



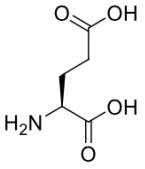
Aspartic acid
Asp, D



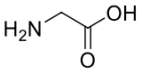
Cysteine
Cys, C



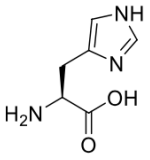
Glutamine
Gln, Q



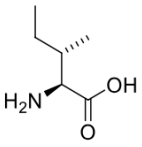
Glutamic acid
Glu, E



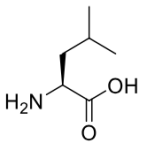
Glycine
Gly, G



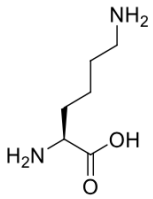
Histidine
His, H



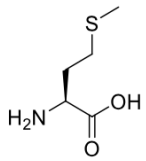
Isoleucine
Ile, I



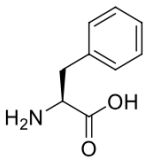
Leucine
Leu, L



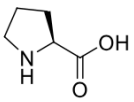
Lysine
Lys, K



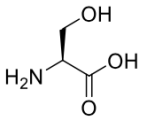
Methionine
Met, M



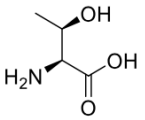
Phenylalanine
Phe, F



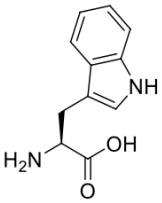
Proline
Pro, P



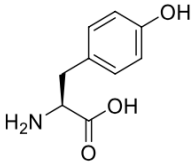
Serine
Ser, S



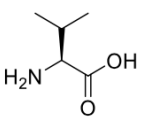
Threonine
Thr, T



Tryptophan
Trp, W



Tyrosine
Tyr, Y



Valine
Val, V

Acknowledgements

I would firstly like to thank my primary supervisor Prof. Richard Payne his support throughout my PhD. Your unyielding energy and passion for science has built an incredible environment to work in, and I feel extremely fortunate to have been able to do my PhD in such a group. You had no obligation to take me on at the end of my first year, but you did, and you stuck with me through it all, despite the concussions, allergic reactions, needle-stick injuries, fire, and extensions; for that I am truly thankful. Thank you for putting me on projects that you knew would push me and for not letting me just go through the motions. I do think my opinion on peptides has changed slightly since 2019; however, I think we can firmly establish that carbohydrates are where it's at.

To my secondary supervisor Dr. Leo Corcilius, thank you for your mentorship throughout the past four years. Thank you for teaching me how to do chemistry, be patient, write a HIRAC, analyse NMR, and read labels on bottles. I am particularly grateful for every amide coupling you did for me, and for helping me to set up a safe space to work. Thank you for being both my mentor and my friend, and for making every day and late night in the lab richer and more enjoyable.

I would also like to thank Dr. Elizabeth Cairns, also my secondary supervisor, for her support throughout my PhD. Liz, thank you for teaching me about how to do and understand pharmacology properly. You have worked very hard for me throughout my PhD, helping me to get the results I need, and pushing me to become a better scientist.

I would like to thank all of our collaborators for different projects: Dr Niccolay Madiedo Soler and Prof. Ethan Goddard-Borger at the Walter and Eliza Hall Institute; Dr Jessica Zhong at the University of Sydney; and Dr Monica Patel and Prof. Michelle Glass at the University of Otago. I would also like to acknowledge Barry and Joy Lambert, Lamberton and Agnes Campbell prizes, PhD completion scholarship, and Sydney Uni EAP for the financial support during my studies. I am very grateful to Dr Adam Ametovski, Dr Richard Kevin, and Ms Cheryl Handford for their support whilst working at the BMC. Thank you to Dr Arthur Tang for his assistance with my PhD, both as a Post Doc and Lab manager.

Thank you to the additional people who read sections of my thesis: Eric, Jessica, Kat, and my brother, Oscar. To everyone in the Payne group, thank you for making coming into the lab each day such a joy. Anthony, Toby, and Sarah, thanks for always being up for a chat or a coffee. Dan, Max, and Kat, thank you for being so knowledgeable and great to talk to. Pat, I definitely owe you thanks for every digestive I stole from your desk (and maybe for every time you taught me how to prep).

To Eric, you have really been there from day 1 in the dungeon to now in the beautiful level 5 lab. Thank you for your skill, drive, relentlessness in doing things properly, ability to put up with me and my driving, for introducing me to nandos, and for your friendship.

Ben, Andy, Ann – I would not be the chemist I am today without the three of you. Thank you for giving seventeen-year-old me a chance and giving me that call back. Through all the doubts I had about my ability throughout both my undergraduate and DPhil, and as I said in my part ii, thank you for never once doubting my ability to succeed in absolutely anything I wanted to. To Omar and Ned, I have no doubt that I wouldn't enjoy organic chemistry nearly as much as I do now if I hadn't sat through all those tutorials (and pre- and post- tutorial debriefs) with the two of you. I learnt as much as I did from you two as I did pouring over books in the library, and I am so very thankful.

To my church and community group for being my rock throughout it all. Thank you also to Prof. Peter Gill for both your mentorship and for giving me the best advice I've ever received. Moose: I know you can't read this but thank you for being the best thesis writing buddy ever, for stamping your paws on my laptop keys when you had had enough of me writing, and for forcing me, day in day out, whatever the weather, to go and spend time outside. To Oscar, thank you for helping me with all things peptide, and for encouraging me with your drive, creativity, and curiosity.

Thank you to Mum and Dad, who despite being across an ocean are never more than a phone call away (even if it's just to show me the dogs). To Mum, thank you for exemplifying how to be kind, successful, hard-working, and passionate. To Dad, thank you for showing me what a life of loving chemistry and science looks like, and for being a

pillar of support for women in science more than anyone else I know. To you both; I am forever grateful for every opportunity you've provided me in my life to learn and grow.

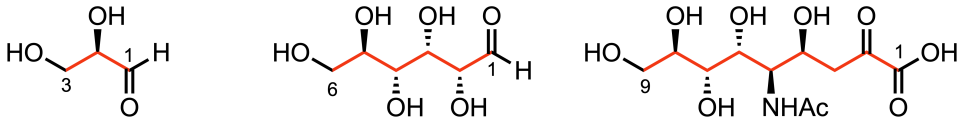
To my lovely Jackson, you have been so patient (probably too patient) in waiting for me to finish my PhD, sacrificing your own career opportunities for me to have "just one more month". Thank you for your exemplification of how to be patient, humble, kind, thoughtful, and hard-working, many of which I am still learning how to do myself. You have unwavering support for me and everything I want to do in life, believing in me more than anyone else that I can do it all – be an athlete training every day, read 52 books in a year, play piano at church, go to book club and community group – all whilst being a full-time PhD student and owning a dog. I can confidently say that I wouldn't have been able to achieve half of the things I have achieved in the past four years without you by my side, and I am so blessed to be able to do life with you.

Chapter 1: Introduction

1.1 Overview of carbohydrates

1.1.1 Definition and Classification of Carbohydrates

Carbohydrates are organic compounds composed primarily of carbon, hydrogen, and oxygen. In their simplest structural form, carbohydrates exist as monosaccharides, which are small, hydrophilic molecules bearing multiple alcohol functional groups and either an aldehyde (aldoses) or ketone (ketoses). Monosaccharides generally contain between three and nine carbon atoms, with the most well-known class being the hexoses, which contain six carbon atoms (Figure 1.1).[1]



Glyceraldehyde (1.1) **Glucose (1.2)** **Sialic acid (1.3)**

Figure 1.1. Examples of common carbohydrates with varying carbon chain lengths: Aldoses glyceraldehyde (**1.1**) and glucose (**1.2**), and ketose sialic acid (Neu5Ac, **1.3**). All structures are depicted in their D-configuration, with the carbon backbone highlighted in red and the initial and terminal carbons numbered for reference.

As monosaccharides contain both carbonyl and alcohol functional groups, they can form cyclic hemi-acetals and hemi-ketals if chain length permits. In aqueous solution, monosaccharides exist in equilibrium between their open chain and cyclic forms. For monosaccharides containing five or more carbons, the position of the equilibrium lies strongly in favour of the cyclic form, forming stable five- or six-membered rings that are known as furanoses and pyranoses, respectively (Figure 1.2). Although this cyclisation results in some loss of conformational entropy, the enthalpically favourable strain-reducing conformations and additional C-O bond render pyranose and furanose forms more stable than their open chain forms.[2]

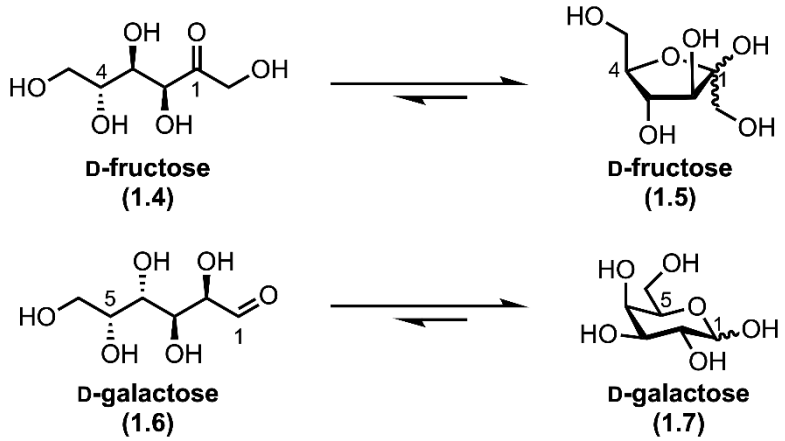


Figure 1.2. Equilibrium between linear and cyclised/lactol forms of carbohydrates: the ketose D-fructose in equilibrium between its linear (**1.4**) and furanose forms (**1.5**), and the aldose D-galactose in equilibrium between its linear (**1.6**) and pyranose (**1.7**) forms. Although the furanose form is depicted here, it should be noted that D-fructose exists predominantly as the β-pyranose in aqueous solution (~70%).

Although only the furanose form is depicted here, it should be noted that D-fructose exists predominantly as the β-pyranose form in aqueous solution (~70%)

1.1.2 Structural diversity of carbohydrates

Monosaccharides are chiral molecules that contain multiple stereogenic centres and are primarily found as D-enantiomers (although L-enantiomers are more common for some monosaccharides). The D/L designation is usually determined by comparison to glyceraldehyde: in the Fischer projection, if the hydroxyl group of the highest-numbered stereogenic centre is on the right, the sugar is classified as D, and if it is on the left, as L (Figure 1.3). Although distinct from *R*/*S* nomenclature, the D/L configuration commonly correlates with *R* at the highest stereogenic centre for D-sugars and *S* for L-sugars.

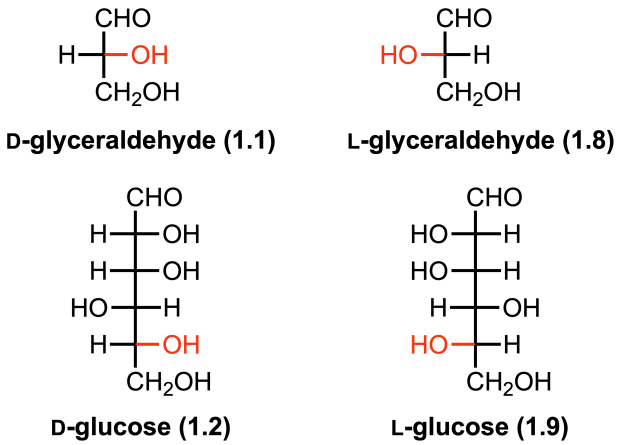


Figure 1.3. D- (**1.1**) and L- (**1.8**) glyceraldehyde as reference molecules for stereochemical assignment, and their application to D- (**1.2**) and L- (**1.9**). The D/L designation is determined by the orientation of the hydroxyl group on the highest-numbered stereogenic centre in the Fischer projection, shown in red: right = D, left = L.

The stereochemical diversity of carbohydrates is a defining feature that often underpins their biological specificity. For example, the stereospecificity of the human glucose-transport system allows only D-glucose and not its enantiomer, L-glucose, to cross the blood-brain barrier and enter the brain.[3] Furthermore, even inversion at a single stereocentre, such as C2 in D-glucose provides a sugar with different biological function (i.e. D-mannose) that is not a substrate for the transporter.[4]

Additional structural diversity can be introduced by chemical modification of the parent saccharide units. Examples include deoxy-sugars (e.g. 2-deoxy-D-ribose (**1.10**)), amino-sugars (e.g. *N*-acetyl-D-galactosamine (GalNAc) (**1.11**)), and acidic sugars (e.g. D-glucuronic acid (**1.12**)) (Figure 1.4), as well as *O*-sulfation, phosphorylation and acetylation of the alcohol functional groups.

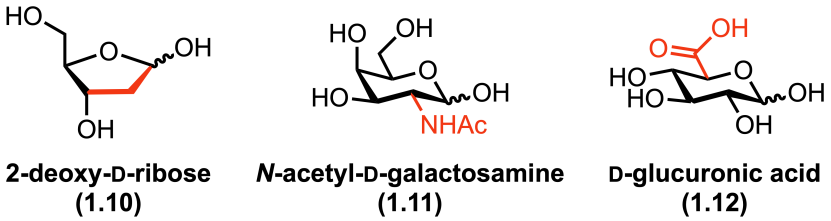


Figure 1.4. Common modifications of parent saccharide units: deoxy, amino, and acidic sugars.

The monosaccharides described above can be linked to other molecules *via* a glycosidic bond, a covalent bond formed between the anomeric carbon of a sugar and typically an

alcohol on another molecule to generate an acetal linkage. Glycosides have two possible configurations at the anomeric carbon, referred to as α and β, shown for D-glucose (Figure 1.5).[5] The α (**1.13**) and β (**1.14**) descriptors refer to the configuration of the anomeric substituent relative to the penultimate stereogenic carbon. For typical pyranosides in which C5 is the penultimate stereogenic carbon, β has the anomeric substituent *syn* to the exocyclic CH_2OH substituent and α has it *anti*.

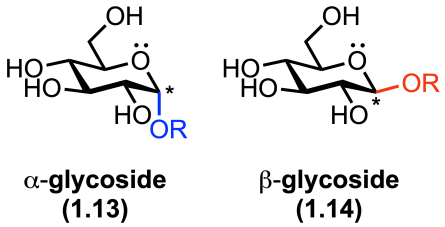


Figure 1.5. α and β glycosides of D-glucose showing the configuration of the anomeric substituent. The anomeric carbon is indicated by *.

Many of the synthetic methods for glycosylation can result in mixtures of α and β anomers by virtue of proceeding through an S_N1-type mechanism (e.g. Fischer glycosylation, Figure 1.6).[6] It is worth noting that there are many stereoselective methods for chemical glycosylation that will be discussed in later chapters. An alternative means of accessing glycosides is through enzymatic glycosylations. These enzymes use activated glycosyl donors such as nucleotide diphosphate sugars as substrates (e.g. UDP-glucose) and proceed in a highly stereoselective manner. Depending on the enzyme, the reaction may proceed through a retaining or inverting mechanism, arriving at a single anomer by virtue of tightly controlled transition states in the enzyme active site.[7]

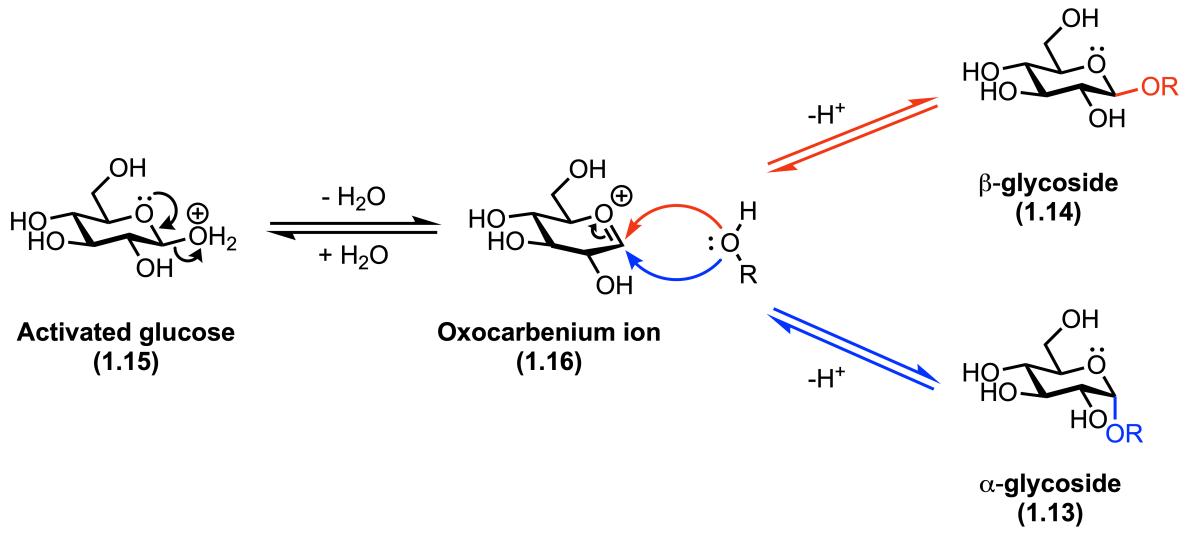


Figure 1.6. Mechanism for Fischer glycosidation of D-glucose in which protonated D-glucose (**1.15**) dehydrates to an oxocarbenium ion (**1.16**), which can be attacked at either face by the alcohol, providing a mixture of β-D-glycoside (**1.14**) and α-D-glycoside (**1.13**).

Monosaccharides can also condense with each other to form disaccharides, oligosaccharides and polysaccharides, hereafter referred to as glycans. Glycans encompass an enormous degree of structural diversity by virtue of the ability to form both branched and unbranched structures, with variable monosaccharide composition and sequence, as well as variation of the stereochemistry and regiochemistry of each glycosidic linkage. Additionally, since glycan biosynthesis is not under templated control (unlike protein synthesis), they are often produced as heterogeneous mixtures with composition dependent on the local expression of glycosyltransferase enzymes. This complex structural diversity is the foundation of a highly sophisticated biological "glycocode", that is only just beginning to be understood.[8] This intricate glycocode, referring to the structural information encoded by glycans, is interpreted by glycan-binding proteins such as lectins,[9,10] antibodies,[11] and glycosyltransferases,[12] and is responsible for essential biological processes such as cell-cell communication,[13] immune recognition,[14] and host-pathogen interactions.[15] Understanding how this molecular information translates to function is a crucial step towards harnessing biological carbohydrate signalling mechanisms for the development of new medicines and biotechnologies.

1.2 Biological Roles and Functions of Carbohydrates

In addition to the well-known energy storage functions of carbohydrates (e.g. starch and glycogen), they also serve diverse roles in structure, cell signalling, protein stability, and host–pathogen recognition in both eukaryotes and prokaryotes—functions that are equally exploited by pathogens to support their own survival and infection strategies.[16]

1.2.1 Structural Roles

Carbohydrates play key structural roles, contributing to both cellular architecture and extracellular matrix identity. Polysaccharides are generally responsible for these structural functions, as they are able to form hydrated gels, rigid barriers, or flexible coatings dependent on their composition and location.[17] For example, the membranes of both eukaryotic and prokaryotic cells are typically coated by the glycocalyx, a dense layer of glycans made up of glycolipids, glycoproteins, and proteoglycans (Figure 1.7). This carbohydrate-rich layer acts as both a protective barrier and signalling interface, facilitating cell-adhesion, cell-cell recognition and immune modulation as well as conferring mechanical resilience.[18,19]

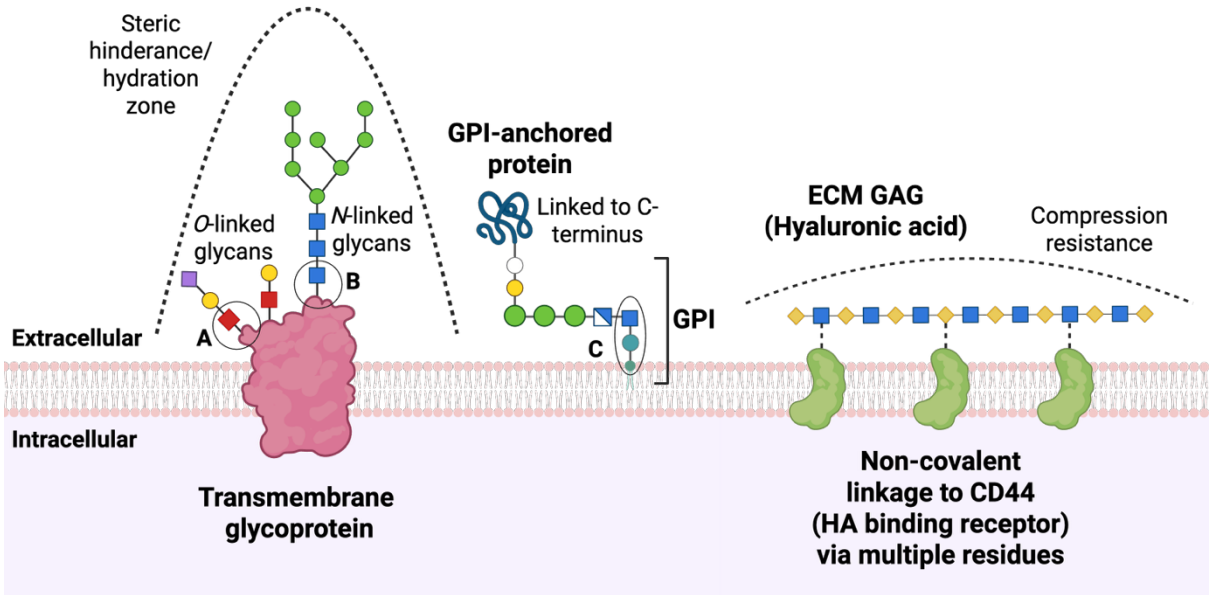


Figure 1.7. Representative structural glycoconjugates found in the glycocalyx at the eukaryotic cell surface. **A**, **B** and **C** refer to linkage types depicted in Figure 1.7. Figure made with biorender.com.

Within the glycocalyx, transmembrane glycoproteins span the lipid bilayer and have extracellular domains decorated with *N*-linked and/or *O*-linked glycans. *N*-linked glycans are branched oligosaccharides initiated through an *N*-glycosidic linkage to the side chain of asparagine (Asn) residues (**1.18**), and *O*-linked glycans are more variable in structure and initiate through an *O*-glycosidic linkage, typically to serine (Ser) and threonine (Thr) (**1.17**) (Figure 1.8A and B).[20] Transmembrane glycoproteins are bulky and hydrophilic, extending out from the membrane into the highly hydrated extracellular matrix (ECM) and spanning up to 50 nm. This creates steric hindrance, controlling the accessibility of membrane-bound ligands and receptors, regulating intracellular spacing, and acting as a selective barrier to pathogens or extracellular enzymes.[21,22] Additionally, some proteins can be attached to the cell surface *via* glycosylphosphatidylinositol (GPI) anchors (**1.19**) (Figure 1.8C). These GPI-anchored proteins contribute to membrane organisation, curvature, and signal clustering.[23]

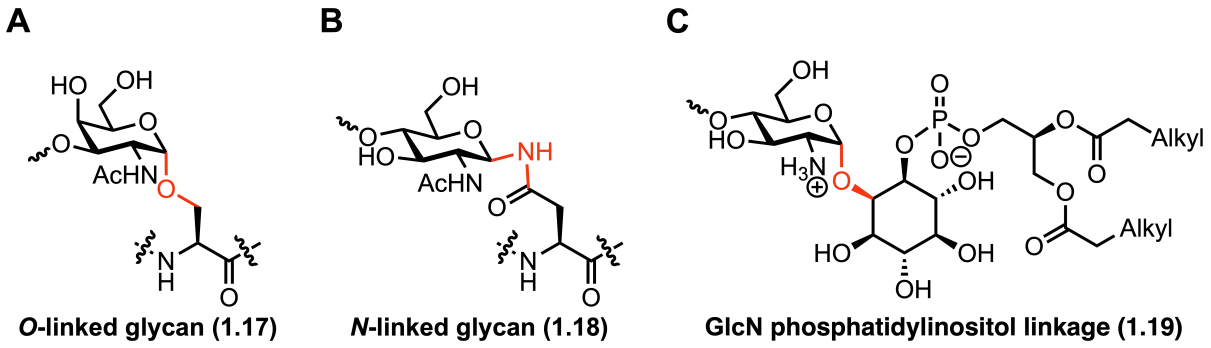


Figure 1.8. Representative protein–glycan and glycan–lipid linkages. (**A**) *O*-linked glycan, where GalNAc attaches to the hydroxyl group of serine or threonine. (**B**) *N*-linked glycan, where GlcNAc to the side-chain nitrogen of asparagine. (**C**) GlcNAc phosphatidylinositol linkage, illustrating the α1–6 linkage of GlcN to inositol in glycosylphosphatidylinositol (GPI) anchors, connecting proteins to membrane lipids.

In the glycocalyx, ECM polysaccharides commonly occur as proteoglycans, structures in which a core protein is decorated with glycosaminoglycan (GAG) chains such as sulfated structures heparan sulfate and chondroitin sulfate which can exist freely within the extracellular space or be indirectly associated with the cell surface. These molecules are key structural and signalling components of the glycocalyx, linking cells to the ECM while modulating growth factor distribution, chemokine gradients and cellular responses to mechanical forces.[24] Non-sulfated GAGs include hyaluronic acid, a major ECM glycosaminoglycan (GAG) which can be non-covalently linked to membrane proteins. It

forms highly hydrated polymer networks due to its extended, linear conformation and high number of negatively charged carboxylate groups.[24] The negative charges attract a large volume of water molecules and generate osmotic swelling pressure, enabling the matrix to resist compression and maintain tissue elasticity.[25]

In prokaryotes like bacteria, surface carbohydrates including capsular polysaccharides (CPS), O-antigens of lipopolysaccharides (LPS), and flagellin glycosylation play key roles in both host-pathogen interactions and as structural components.[26] These glycans can form dense outer layers that provide structural stability, osmotic protection, and environmental resilience, acting as a protective shell against stress, desiccation, and bacteriophage predation.[27,28] Additionally, the viscous and charged nature of these polysaccharide coats limits the diffusion of antimicrobial peptides, forming a structural "stealth" layer which enables immune evasion.[29] These carbohydrate-mediated recognition strategies are not unique to bacteria, with viruses also exploiting glycan binding to assist with infection. Recently, the spike protein of the original SARS-CoV-2 strain were shown to contain a sialic acid binding site, directly engaging sialylated host glycans as auxiliary binding partners. This increased non-specific adhesion and host engagement, facilitating entry into host cells and contributing to virulence.[30]

1.2.2 Cell-Cell Communication and Recognition

Cells commonly utilise glycoproteins and glycolipids on the cell-surface as identity markers, facilitating interactions with other cells and molecules. Lectins - carbohydrate-binding proteins that recognise and bind to specific glycans - are key to this process. A notable group of lectins are selectins, which are glycoproteins embedded in the membrane of both endothelial cells and some immune cells. E- and P-selectins on the endothelium bind to specific sialylated and fucosylated sites on leukocytes, resulting in adhesion and migration of leukocytes to the endothelial cell surface.[31] Simultaneously, L-selectins on the surface of immune cells bind to carbohydrate ligands on other immune cells, supporting adhesion and initiating migration of immune cells to the site of infection or injury.[32]

Sialic acid (**1.3**), the primary nonulosonic acid found in eukaryotes, plays an essential role in self-recognition and immune evasion. Sialic acid residues are often found at the outermost position of glycan chains attached to glycoproteins and glycolipids, where they can be recognised by lectins known as siglecs (sialic acid binding lectins). Siglecs present on the surface of immune cells allow modulation of immune responses via the recognition of endogenous sialylated glycans. This recognition typically leads to an inhibitory signal that suppresses immune activation and prevents immune cells from attacking normal, healthy cells.[33,34] Conversely, the removal of terminal sialic acids by sialidases exposes underlying galactose or *N*-acetylgalactosamine residues. This loss alters glycoprotein stability and circulation time, marking glycoproteins as 'aged' or damaged. For example, desialylated glycans are recognised by the lectin 'asialoglycoprotein receptor' (ASGPR), which is expressed primarily on hepatocytes in the liver and binds to terminal GalNAc residues (Figure 1.9).[35] ASGPR is a heterooligomeric complex that contains three carbohydrate recognition domains (CRDs). These CRD's cooperatively bind terminal GalNAc residues that would otherwise be bound to sialic acid in normal healthy glycans.[36] Once bound to ASGPR, the glycoprotein is internalised and endocytosed, followed by degradation in the acid environment of the lysosome, whilst the ASGPR escapes the endosome and is recycled back to the cell surface for further use. This process allows for removal of unnecessary and damaged molecules from the blood stream, in addition to clearing pathogens or infected cells that have altered their surface glycosylation to avoid immune recognition.[37] The ability of ASGPR to act as a protein degrader has made it a key target in therapeutic strategies for applications in the liver, as it offers potential to both degrade unwanted extracellular proteins and deliver drugs into the cell.[38]

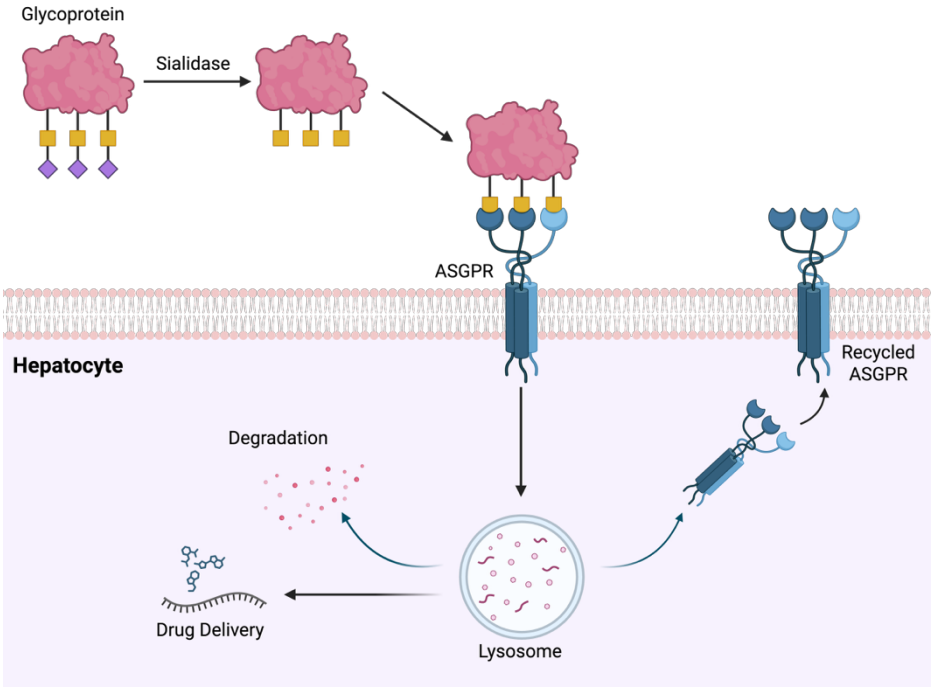


Figure 1.9. Mechanism of ASGPR-mediated glycoprotein clearance and liver-targeted delivery. Desialylated glycoproteins containing exposed GalNAc residues (yellow squares) are recognised by the asialoglycoprotein receptor (ASGPR). Prior to recognition, terminal sialic acid residues (purple diamonds) are removed by sialidases, revealing the underlying GalNAc moieties. Binding of GalNAc to ASGPR results in receptor-mediated endocytosis and trafficking to the lysosome for degradation, while the receptor is recycled back to the plasma membrane. Although binding to all three carbohydrate recognition domains (CRDs) of the ASGPR heterooligomer is not strictly required, multivalent ligands that occupy multiple sites show significantly enhanced avidity and internalisation efficiency. This natural clearance mechanism is exploited for liver-specific drug delivery using GalNAc-conjugated therapeutics.[39] Figure made with biorender.com.

Given the importance of capping sialic acid residues as 'self' markers, many pathogens, such as bacteria *Campylobacter jejuni* and *Helicobacter pylori*, have evolved to incorporate sialylated glycans on their surfaces.[40] This allows the pathogens to 'camouflage' themselves, preventing recognition by immune cells that would typically target them as foreign invaders. On the molecular level, the siglecs that recognise 'self'-sialylated structures cannot distinguish between host and pathogen, thereby facilitating the immune evasion of the pathogen.[41]

1.2.3 Protein Folding, Stability, and Half-Life

Glycosylation is also involved in protein folding and conformation, often through interactions with chaperone proteins, specialised proteins that help newly synthesised

polypeptides obtain the correct three-dimensional structure.[42] Post-translational modifications (PTMs), such as *N*-linked glycosylation of asparagine residues and *O*-linked glycosylation of serine and threonine residues, allow for recognition and binding by chaperone proteins, ensuring correct protein folding.[43] If a protein is misfolded, attached glycans can signal the protein to be refolded or degraded, allowing only properly folded proteins to function in the cell. In addition to interactions with chaperones, glycosylation stabilises the tertiary structure. The highly polar and hydrophilic nature of glycans helps to prevent exposure of hydrophobic regions of the protein, reducing the chance of aggregation and denaturation and increasing solubility in aqueous environments.[44] Carbohydrates can also introduce flexibility and plasticity into the protein structure. Branched glycans can provide steric hinderance that lets proteins adopt the required conformations for biological activity.[22]

ASGPR, as highlighted in section 1.2.2, is a key modulator in the clearance of glycoproteins. In addition to the glycosylation pattern of a protein playing a role in protein degradation, it can also influence its half-life by determining the rate at which is it recognised by ASGPR and other clearance receptors.[45] Glycoproteins that are heavily sialylated are able to evade ASGPR recognition and have longer circulating half-lives, as opposed to proteins which readily undergo desialylation and are rapidly cleared.[46] This dynamic regulation of glycoprotein half-life is key to maintaining proper protein turnover and cellular homeostasis. The implication of this regulation also extends to drug design, allowing control of the therapeutic window and stability of therapeutic proteins.

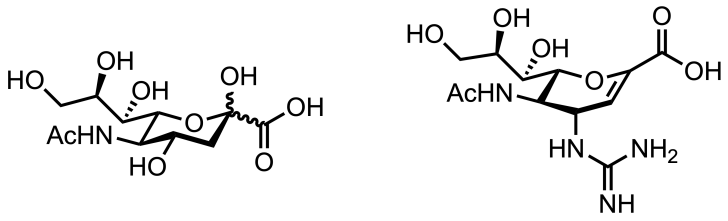
1.3 Therapeutic potential of carbohydrates

The diverse roles and functions of carbohydrates, including those in structure, cell signalling, immune recognition, and protein stability, highlight their importance in both normal physiology and disease. These essential biological functions make both carbohydrates and their receptors attractive targets for therapeutic interventions. The high degree of specificity between carbohydrates and carbohydrate-recognising proteins can in theory be leveraged to create highly targeted therapies with reduced off-target effects compared to small molecule drugs. For this reason, carbohydrate-based drugs and therapies are increasingly significant targets in drug discovery and development.[47]

1.3.1 Carbohydrate-based drugs

Carbohydrate-based drugs include both naturally occurring and synthetic glycans.[48] The ubiquity of monosaccharides in the human body, however, poses challenges in the use of carbohydrate as drugs; pure carbohydrates, particularly unmodified monosaccharides, can disrupt regular biological functions or elicit unwanted immune responses. Modified carbohydrates and carbohydrate mimics can circumvent these issues, and a range of these molecules are used for treatment of a variety of diseases.

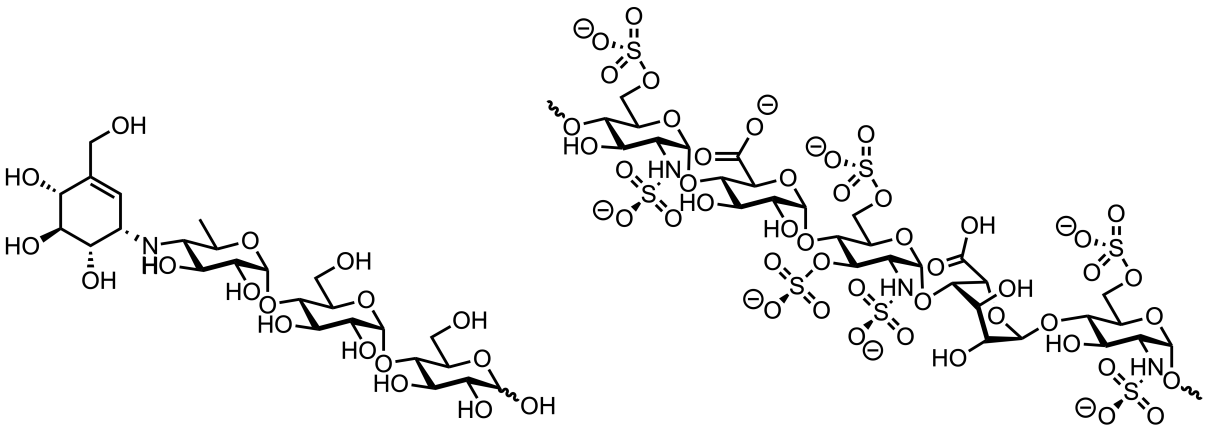
Many carbohydrate-based drugs act by mimicking the functions of monosaccharides. One example is zanamivir (**1.20**), a synthetic analogue of sialic acid (**1.3**) that acts as an inhibitor of neuraminidase, a sialidase enzyme (Figure 1.10).[49] Zanamivir binds tightly to the active site of influenza neuraminidase, prevents cleavage of terminal sialic acids from host glycoconjugates, thereby blocking release of new virions from infected cells. As a result, newly formed influenza virions remain attached to the host cell surface instead of detaching and spreading to infect neighbouring cells, halting viral propagation.



Sialic acid (1.3) **Zanamivir (1.20)**

Figure 1.10. Chemical structures of sialic acid (**1.3**) and Zanamivir (**1.20**).

Oligosaccharides and polysaccharides are also used as drugs to treat a range of conditions. However, due to their hydrophilicity they often have poor bioavailability following oral administration.[50] Additionally, acidic gastric pH and digestive enzymes can cleave glycosidic bonds, rendering orally administered drugs inactive. Therefore, many oligosaccharide and polysaccharide drugs are used to treat gastrointestinal tract diseases, where less absorption is necessary, or are required to be administered intravenously. Examples include, acarbose (**1.21**),[51,52,53] an orally administered anti-diabetic oligosaccharide, and heparin (**1.22**),[54,55,] an intravenously administered native sulfated GAG used as an anticoagulant (Figure 1.11).



Acarbose (1.21) **Heparin (Antithrombin binding region) (1.22)**

Figure 1.11. Structures of Acarbose (**1.21**), an anti-diabetic oligosaccharide, and Heparin (**1.22**), a sulfated GAG used for anticoagulation.

Despite several carbohydrate-based drugs having achieved clinical success, their widespread application is limited by a range of challenges.[48] These include poor oral bioavailability, lability of glycosidic linkages resulting in degradation, undesirable immune responses, and difficulties in achieving selective targeting. These limitations

have shifted development away from purely carbohydrate-based drugs towards carbohydrate-drug conjugates, in which carbohydrate moieties are covalently attached to non-carbohydrate pharmacophores, resulting in improved stability, solubility, bioavailability, and target specificity.[56]

1.3.2 Glycosides and glycoconjugates

Carbohydrate-drug conjugates can contain a wide range of pharmacophores, including small molecules, peptides, and proteins.[57] In most cases, the carbohydrate moiety is not the main pharmacophore, instead facilitating targeting, or improving the binding of the main pharmacophore. Small molecule glycosides (Figure 1.12) are typically natural products, such as the anticancer agent doxorubicin (**1.23**), in which the protonated aminoglycoside acts to stabilise an intercalated DNA complex through interactions with the phosphate backbone.[58] Heterocyclic glycosides are also scaffolds in natural products and synthetic drugs.[59] In the case of D-glucose primaquine (**1.24**), the *N*-linked glucosyl moiety acts as a pro-drug, releasing the quinoline in a controlled manner through enzymatic deglycosylation.[60] In doing so, the glycan improves water solubility while modulating plasma levels and improving tissue targeting.[61] Fluorophore-glycan conjugates, such as Cy5-conjugated galactose (**1.25**), are used as imaging agents.[62] In the case of **1.25**, the galactose moiety exploits bacterial galactose transport/binding systems to facilitate uptake of the fluorophore and thereby enable bacterial imaging.

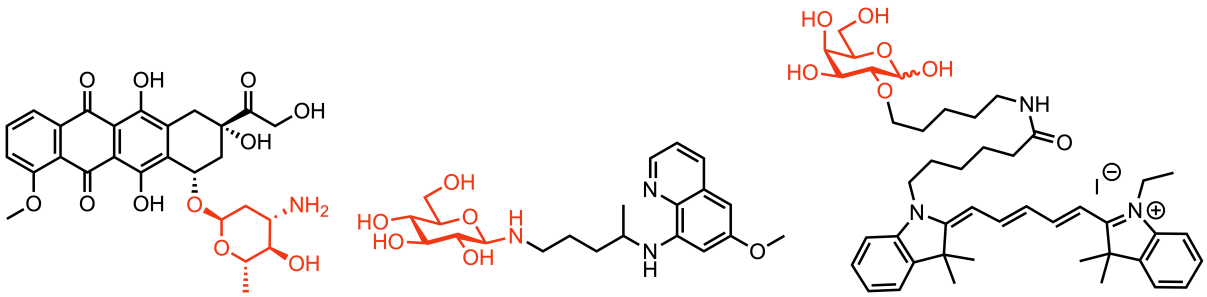
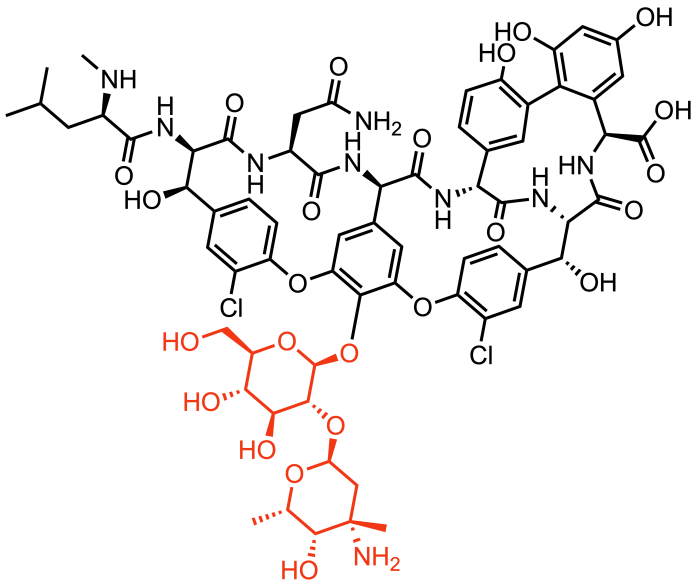


Figure 1.12. Structures of common carbohydrate small-molecules conjugates, including doxorubicin (**1.23**), D-glucose primaquine (**1.24**), and Cy5-conjugated galactose (**1.25**). The carbohydrate moieties in each of the conjugates are highlighted in red.

Peptides and proteins are another class of scaffolds that are commonly natively glycosylated or conjugated to carbohydrates. Glycosylation plays a similar role to that in small-molecule conjugates, in addition to modulating biological activity and extending serum-half life. Examples include glycopeptide antibiotics such as vancomycin (**1.26**) and glycoproteins such as erythropoietin (EPO), a heavily glycosylated hormone (Figure 1.13).



Vancomycin (1.26)

Figure 1.13. Structure of vancomycin (**1.26**), a glycopeptide antibiotic. The carbohydrate moiety is highlighted in red.

In vancomycin, the disaccharide moiety is essential for activity: aglycone vancomycin being 10-100x less active than natural vancomycin in antibacterial assays.[63] The sugars enhance binding the D-Ala-D-Ala terminus of the peptidoglycan. This improves solubility and protects the peptide core from degradation.[64] EPO is heavily glycosylated with oligosaccharide chains, containing both *N*-linked and *O*-linked glycans; native EPO is ~40% carbohydrate by mass after glycosylation,[65] and are critical for stability and circulation. Terminal sialic acids on oligosaccharide chains prevent ASGPR-mediated clearance,[66] while proper glycosylation supports folding, reduces aggregation, and increases bioavailability.[67]

Targeted protein degradation conjugates

While carbohydrate-drug conjugates primarily improve pharmacokinetic, solubility, and tissue targeting *via* engagement with endogenous sugar-recognition pathways, innovations in the field have focused on utilising the cell's degradative machinery to eliminate disease-causing proteins entirely.

Two types of carbohydrate-directed protein degraders have been developed, both utilising the machinery of ASGPR (Section 1.2.2) and lysosomal degradation. Lysosomes are responsible for degrading a range of substrates, including long-lived proteins, insoluble protein aggregates, and cell-surface receptors, breaking them down into components that can be recycled or discarded.[68]

The first lysosome-targeting chimeras (LYTACs) were reported by Bertozzi and co-workers in 2020. By utilising glycopolypeptides decorated with mannose-6-phosphonate (M6Pn), the cation-independent mannose-6-phosphate receptor (CI-M6PR) could be engaged, a natural pathway for lysosomal trafficking.[69] This early work indicated that synthetic glycans could be exploited to direct extracellular and membrane proteins to the lysosome for degradation.

In 2021, both Bertozzi and co-workers[70] and Spiegel and co-workers[71] developed bifunctional molecules targeting ASGPR for lysosomal degradation. Bertozzi's group introduced GalNAc-based LYTACs by conjugating antibodies to high-affinity tri-antennary GalNAc ligands, while Spiegel developed molecular degraders of extracellular proteins through ASGPR (MoDE-As), fully synthetic bifunctional molecules containing a GalNAc ligand covalently attached to a small-molecule binder. Both LYTACs and MoDE-As are capable of degrading membrane bound and extracellular proteins of interest (POI) (Figure 1.14).

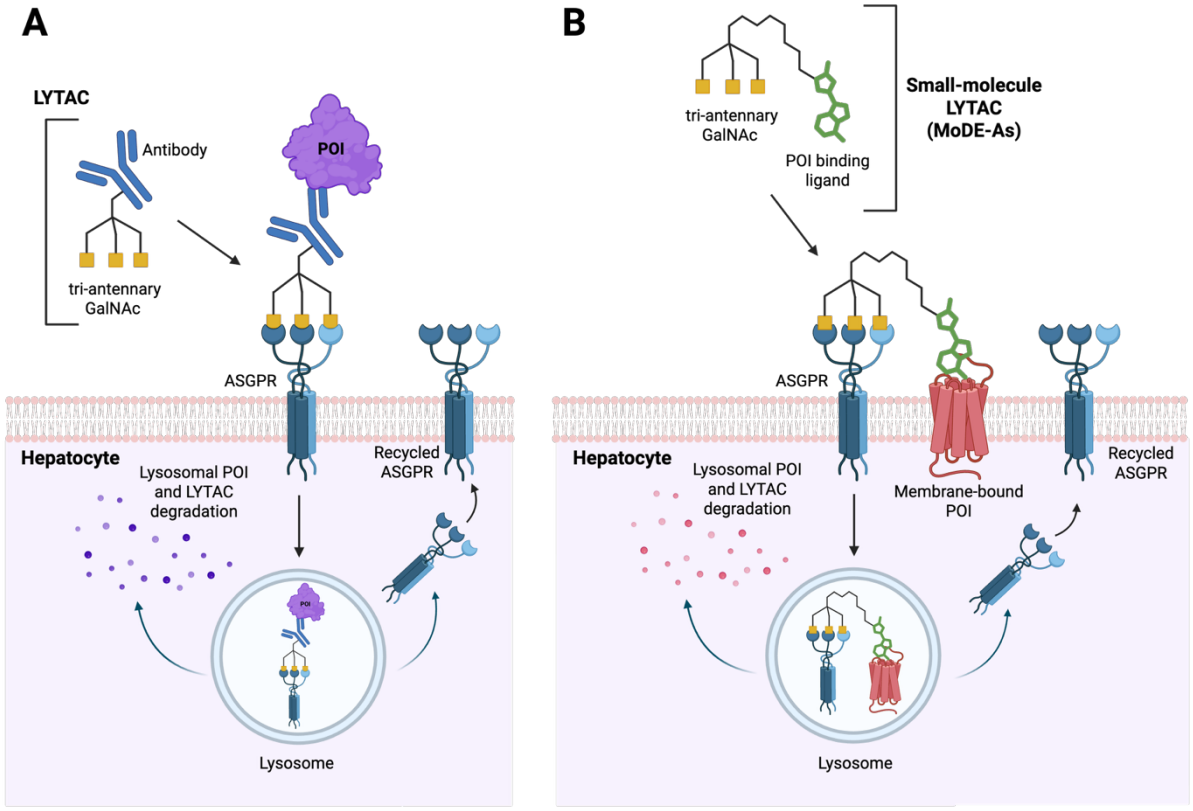


Figure 1.14. Mechanisms of ASGPR-mediated targeted protein degradation by LYTACs and MoDE-As. **(A)** Antibody-based LYTACs are bifunctional molecules composed of an antibody used to target a POI (extracellular shown), and a conjugated tri-GalNAc ligand that engages ASGPR on hepatocytes. The ternary complex is internalised through receptor-mediated endocytosis, in which the POI with the antibody-tri-GalNAc LYTAC is transferred to the lysosome for degradation, and ASGPR is recycled back to the cell surface. **(B)** MoDE-As are small bifunctional molecules that combine a POI-binding ligand and a tri-GalNAc motif for ASGPR engagement. The resulting complex undergoes the same pathway of endocytosis and lysosomal degradation of the POI and degrader, with ASGPR dissociating and recycling to the cell surface.

Both GalNAc-based LYTACs and MoDE-As achieved efficient and hepatocyte-specific degradation of extracellular and membrane proteins, including clinically relevant targets such as epidermal growth factor receptor (EGFR).[70] Encouragingly, no evidence of *in vivo* hepatic toxicity was observed. These conjugates highlight how carbohydrates can serve as essential targeting elements in protein degradation conjugates, expanding the scope of protein degradation to extracellular and membrane-associated proteins.[72]

While carbohydrate-drug conjugates such as LYTACs and MoDE-As demonstrate how sugars can be harnessed to direct therapeutic degradation of proteins, disease-associated glycans can also be incorporated into vaccines as antigens to stimulate or modulate immune responses.

1.3.3 Glycan antigens in immunotherapy

Carbohydrates are crucial for immune recognition, enabling the immune system to detect pathogens or abnormal host cells. Aberrant glycosylation is a trait of many cancers, resulting in the presentation of tumour-associated carbohydrate antigens (TACAs) on the cell surface.[73] Similarly, microbial capsular polysaccharides and viral glycans act as potent immune triggers.[74] These glycan signatures can be leveraged to develop new immunotherapeutic agents, including carbohydrate-based vaccines, monoclonal antibodies, and engineered immune cells such as CAR-T cells directed against TACAs.[75]

Tumour-associated carbohydrate antigens (TACAs)

TACAs on the cell surface are key markers for malignant transformation. These include truncated O-glycans on mucosal transmembrane mucin glycoproteins such as α-GalNAc-*O*-Ser/Thr (Tn, **1.27**), and sialyl-Tn (sTn, **1.28**), in addition to more complex structures such as Galβ1-4(Fucα1-3)GlcNAc (Lewis^x, **1.29**) on both cell membrane glycolipids and glycoproteins (Figure 1.15).[76,77] TACAs tend to be heavily overexpressed in certain types of cancer, while being minimally expressed on healthy tissues.[78] The prevalence of TACAs on cancer cells arises from disruption of normal glycosylation machinery; misregulation, and in some cases mutation,[79] of key glycosyltransferases prevents the full elongation or premature capping of glycan chains.[80] Tumours can also re-express embryonic glycan antigens that are normally silenced in adult tissues.[81] Their restricted distribution and unique glycan epitopes have made them attractive as therapeutic targets, with several candidates evaluated in preclinical and clinical trials.

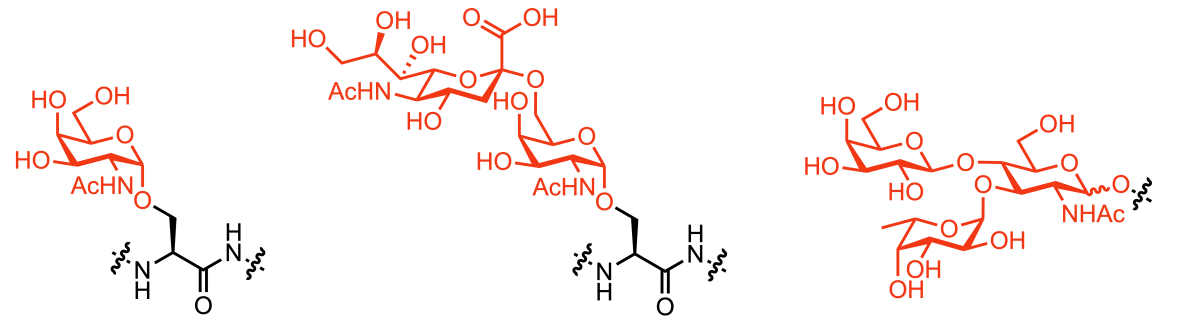


Figure 1.15. Structures of common TACAs, including Tn (**1.27**), sTn (**1.28**), and Lewis^x (**1.29**).

Clinical vaccine strategies have relied on synthetic glycans, such as Sialyl-Tn (**1.28**) in the vaccine Theratope,[82] conjugated to carrier proteins that enhance immunogenicity. By promoting antibody production against the glycan epitope, these conjugates stimulate B-cell and T-cell responses, effectively training the immune system to recognise and attack cells that contain the same carbohydrates structures.[83] Despite vaccines such as Theratope advancing to clinical trials, they have shown limited clinical success due to poor immunogenicity and tumour heterogeneity.

A more promising form of treatment utilising TACAs are monoclonal antibodies (mAbs). Derived from animals immunised with synthetic glycan-protein conjugates which are subsequently humanised to reduce immunogenicity, these antibodies recognise specific carbohydrate epitopes.[84] One such example is disialoganglioside GD2 (recognised by dinutuximab), the only TACA to date with an approved antibody therapy.[85] Monoclonal antibody therapies illustrate that carbohydrates can act as the molecular determinants of immunogenicity, providing the targets for antibody design even when the final therapeutic is a protein.

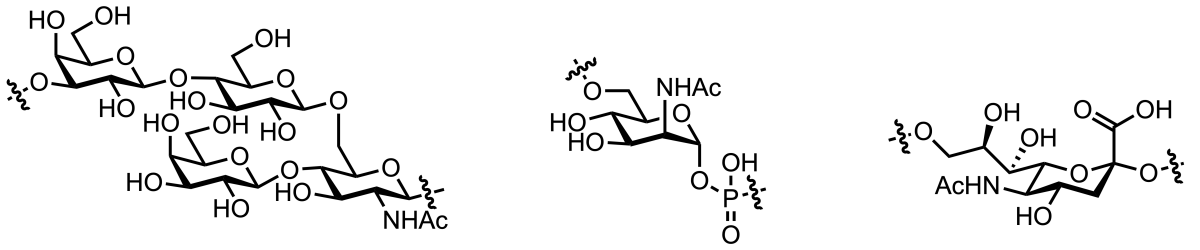
Despite some success in developing TACA targeting therapeutics, challenges arise due to the similarity between human glycans and tumour-associated ones. This results in therapeutics potentially suffering from poor immunogenicity and autoimmunity issues.[86]

Bacterial glycan antigens

Compared with tumour-associated carbohydrate antigens, bacterial surface glycans consist of more distinct epitopes, thus making them better immunogens and more

attractive vaccine targets[87] (See Chapter 3 for a more detailed introduction to bacterial carbohydrates). Capsular polysaccharides, lipopolysaccharide O-antigens, and other glycan structures displayed by pathogenic bacteria often have no close analogues in mammalian cells, resulting in increased immunogenicity.[88] Consequently, vaccines targeting specific glycan antigens on bacterial surfaces have had a number of successes in the clinic.

Examples of vaccines targeting bacterial carbohydrates include the Meningococcal, Pneumococcal, and Typhoid vaccines, which have been highly successful in reducing disease instances and mortality worldwide. The first generation of vaccines against *Streptococcus pneumonia* and *Neisseria meningitidis* used capsular polysaccharide-based vaccines to generate an immune response.[89] These vaccines used purified capsular polysaccharides from several distinct serogroups of the respective bacteria. Serogroups are classifications based on the chemical structure, specifically the sugar composition and linkages, of the capsular polysaccharide that surround the bacterial cell. Different strains can express different serotypes, necessitating the development of multi-polysaccharide vaccines that include a selection of the most common and virulent CPS antigens (Figure 1.16).[90] For example, the pneumococcal (*S. pneumonia*) vaccine contains serotypes such as serotype 14, a branched tetrasaccharide repeating unit **1.30**,[91] alongside more structurally complex serotypes such as serotype 19A and serotype 18C, whose branched heteropolymers and ribitol phosphate motifs exemplify the incredible diversity of capsular polysaccharides.[92,93] In meningococcus (*N. meningitidis)*, serogroup A is composed of (α1→6)-linked *N*-acetylmannosamine-1-phosphate (**1.31**),[94] while serogroups C, Y and W contain sialylated homopolymers or heteropolymers (e.g. α2→9 *N*-acetylneuraminic acid in serogroup C (**1.32**)).[95] These unique carbohydrate epitopes elicit antibodies that recognise the saccharide structures and promote opsonophagocytic clearance, in which immune cells recognise the opsonised polysaccharide surface and allow for bacterial destruction.[96]



***S. pneumoniae* type 14 (1.30)** ***N. meningitidis* type A (1.31)** ***N. meningitidis* type C (1.32)**

Figure 1.16. Virulent serotypes found in the CPS of pathogenic bacteria such as *S. pneumoniae* and *N. meningitidis*.

The main drawback of using capsular polysaccharides as antigens is that they are T-independent antigens, activating B cells directly through their repetitive carbohydrate epitopes. This results in only short-lived antibody responses without immunological memory.[97] This limitation of 'polysaccharide only' vaccines stimulated the development of conjugate vaccines in which capsular polysaccharides are covalently linked to carrier proteins. The presence of T-cell epitopes in the carrier protein triggers the recruitment of T-cells, which creates a more durable and long-lasting immunity.[98] The success of conjugate capsular polysaccharide vaccines is exemplified by the *Neisseria meningitidis* serogroup C (MenC) vaccine (e.g. Menjugate, NeisVac-C, Meningitec) in which MenC disease dropped by over 90% among vaccinated age groups within a few years, with herd immunity protecting unvaccinated individuals. In contrast, MenC polysaccharide-only vaccines have failed to generate herd immunity or long-term protection.[99]

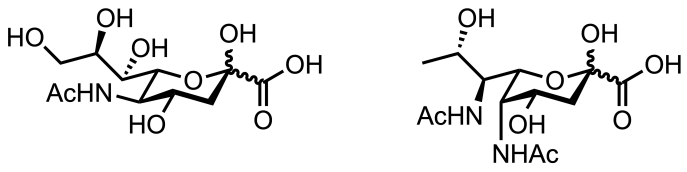
An alternate strategy to targeting bacterial capsular glycans is the direct use of monoclonal antibodies. Unlike vaccines, which require generation of an immune response from the host, and can be ineffective in infants or immunocompromised people, monoclonal antibodies provide immediate protection via the administration of pre-formed and high-affinity antibodies.[100] Monoclonal antibodies (mAbs) against bacterial glycans usually target capsular polysaccharides or O-antigens,[101] where repeating epitopes such as α2→9 *N*-acetylneuraminic acid as seen in *Neisseria meningitidis* vaccines can provide opportunities for multivalent binding. These mAbs are able to successfully mimic the protection offered by vaccine-induced polyclonal antibodies in addition to the benefit of rapid protection.[102] Although conjugate vaccines

offer strong population-level protection against CPS, mAbs are valuable for situations requiring immediate protection in compromised individuals.

Recent work led by Tang *et al.* in the Payne research group (discussed in detail in Chapter 4) highlights the potential to expand beyond traditional capsule- and O-antigen-directed mAbs. In this work, a bacterial nonulosonic acid (nine-carbon sugar) analogue of sialic acid, pseudaminic acid (Pse, **1.33**, Figure 1.17), was chemically synthesised and incorporated into bacterial flagellin-derived glycopeptides with both α- and β-configuration. This allowed generation of the first pan-specific mAbs able to recognise this unique sugar across diverse contexts, including capsular polysaccharides, lipooliogsaccharides, and flagellar glycoproteins. The ability to target flagellar glycosylation is significant as flagellar pseudaminylation is essential for motility and virulence in pathogens such as *Campylobacter jejuni* and *Helicobacter pylori*.

Complementary work by Yang *et al.*[103] built on this concept using a different strategy. Chemically synthesised Pse derivatives were conjugated directly to carrier proteins and used as immunogens in mice, followed by hybridoma screening. This resulted in identification of the monoclonal antibody Pse-MAB1, which showed strong and selective recognition of Pse displayed on the surface of *Acinetobacter baumannii*.

These studies demonstrate how synthetic carbohydrate chemistry can be utilised to generate antibodies against nonulosonic acid motifs. Unlike classical mAbs, which are restricted to a single serogroup capsule, these Pse-specific antibodies recognise the sugar scaffold itself, enabling cross-reactivity between multiple bacterial species and glycosylation sites, from CPS to flagellar glycoproteins. This has the potential to significantly broaden the scope of anti-glycan immunotherapy.



Sialic acid (1.3) **Pse5Ac7Ac (1.33)**

Figure 1.17. Structures of Sialic acid (**1.3**), and Pseudaminic acid (**1.33**) in its most common form, Pse5Ac7Ac.

1.4 Synthetic Challenges and Opportunities in Carbohydrate Chemistry

Carbohydrate chemistry is distinct from nucleic acid or peptide chemistry in terms of its unique set of synthetic challenges. The large number of possible linkage types, combined with subtle stereoelectronic effects dictating glycosidic bond formation, necessitates judicious choice of protecting groups, nucleophile ('glycosyl acceptor')-electrophile ('glycosyl donor') combinations and reaction conditions. The complexity of glycans has traditionally slowed progress in the field, however it has also necessitated the development of innovative methodologies. These include strategies such as automated glycan assembly,[104] one-pot glycosylation strategies,[105] and orthogonal protecting group methodologies,[106] all now central to modern synthetic carbohydrate chemistry.

Once overlooked compared to nucleic acids and proteins, carbohydrate chemistry was often thought to be too complex and insignificant to study throughout much of the 20th century. However, the rewards of being able to manipulate, synthesise, and understand complex carbohydrates are far-reaching and certainly outweigh the challenges that are sometimes encountered in carbohydrate chemistry.[107] The ability to synthesise complex glycans has allowed for the development of carbohydrate-based vaccines, such as the pneumococcal conjugate vaccines, which have saved millions of lives worldwide by preventing pathogenic bacterial infections.[108] Likewise, the synthesis of rare monosaccharides has provided tools to study pathogens, allowing for improvements in diagnostics and therapeutics. Glycoengineering, specifically the tuning of glycosylation patterns, has vastly improved the pharmacokinetics of proteins like EPO, by increasing circulation half-life, potency, and reducing immunogenicity.[66]

The opportunities in carbohydrate chemistry continue to expand as new functions, methodologies, and applications are understood. A key focus is the effort to decipher the so-called "glycocode", the idea that glycan structures, encode biological information in their sequences, branching, and modifications. However, unlike the genetic code which is linear, glycan "languages" are complex and impacted by both enzymatic and environmental factors. The ability to synthesise glycans is key to be able to probe and interpret this code, allowing for advancing our understanding of immune recognition,

pathogen infection, and cell-cell communication. This has the potential to transform carbohydrate chemistry from a synthetic challenge to a powerful tool for medicine, allowing for the creation of vaccines, glycoengineered therapeutics, and innovative strategies to target infection and disease.

1.5 Thesis Overview

Carbohydrates perform a plethora of complex roles in biology, far from acting as simple energy storage and structural molecules. Information-rich, structurally complex, and functionally diverse, carbohydrates are attractive targets in chemical biology and therapeutic development. This thesis explores the application of carbohydrate chemistry and modern chemical biology tools to tackle two key disease types, namely liver disease, and Gram-negative bacterial infections. A summary of each chapter is provided below:

- **Chapter 2** describes the design and synthesis of liver-targeted lysosome-targeting chimeras (LYTACs) for the selective degradation of cannabinoid receptor 1 (CB_1). Combining a modified Rimonabant (high affinity, selective CB_1 antagonist) ligand with a triantennary GalNAc motif that engages the asialoglycoprotein receptor (ASGPR), this works develops a therapeutic strategy for the degradation of a therapeutically relevant G protein-coupled receptor (GPCR) implicated in both alcoholic liver disease (ALD) and metabolic dysfunction-associated liver disease (MASLD). Additionally, a series of peptides identified from a RaPID screen targeting ASGPR, some containing reprogrammed residues such as GalNAc-β-Ser, were synthesised and screened for binding affinity against ASGPR.
- **Chapter 3** provides a detailed introduction to bacteria, including cell structure, disease-relevant bacteria and bacterial glycans, and details the role of these glycans in host-pathogen interaction. This chapter also introduces mechanisms of antibiotic action, the rise of antimicrobial resistance, and the current and future developments of treatments for bacterial infection.
- **Chapter 4** describes the stereoselective synthesis of pseudaminic acid (Pse) analogues for screening for their ability to bind to the Pse-specific monoclonal

antibody developed by the Payne group. This chapter also focusses on improving the methodology for the synthesis of Pse, with the aim of circumventing the issues observed on the previously reported synthesis and creating a common glycan intermediate that can be modified to produce other nonulosonic acids.

- **Chapter 5** details the synthesis of a bacterial legionaminic acid (Leg) glycan derivative, which was also used to probe the specificity of the Pse-targeting antibody, and is currently being used in the production of a Leg-specific antibody.

Chapter 2: CB_1 targeting LYTACs and ASGPR peptides

2.1 Introduction

2.1.1 The liver

The liver is the largest internal organ in the human body[109] and is essential to the body's physiological functions.[110] The main function of the liver is to control detoxification, metabolism, and the production of proteins and bile.[111] Many of these functions occur in hepatocytes, the parenchymal cells of the liver, which constitute 80% of the total liver volume.[112,113] Hepatocytes are involved in glucose homeostasis through storage and release of glycogen, which is important in regulating the concentrations of glucose in the bloodstream.[114] Hepatocytes also participate in the detoxification of exogenous substances and endogenous waste products, protecting the body from poisoning and liver damage.[115] In addition to this, hepatocytes are responsible for bile production, which is essential for the emulsification and absorption of dietary lipids and lipid-soluble vitamins.[116] Without adequate bile production, lipids cannot be effectively emulsified and absorbed, leading to malabsorption, nutritional deficiencies, and digestive complications.

2.1.2 Liver Disease

Liver disease affects over 1.5 billion people worldwide[117], with up to 40% of the population in Western countries experiencing some form of disease of the organ.[118] Each year, over one million deaths are attributed to liver disease globally, and the cost to Australia exceeds over five billion dollars annually.[119] Liver disease has various causes, including viral hepatitis, dietary factors, alcohol consumption, and genetic predisposition.[120] If left untreated, liver diseases can result in cirrhosis, a condition characterised by severe scarring of the liver that is currently irreversible and often necessitates liver transplantation. For patients with end-stage liver disease, lack of a liver transplant results in continued liver deterioration, resulting in complications such as bleeding, portal hypertension, and multi-organ failure, which are life-threatening.

Even when transplantation is possible, donor organ shortages, long waiting lists, and the need for lifelong immunosuppression mean it is neither a timely nor definitive cure. Liver disease is progressive, with the effects of the disease often taking years to be felt, partly due to the remarkable ability of the liver to regenerate and repair itself,[121] especially in the early stages of damage.

Two major types of liver disease, metabolic dysfunction-associated liver disease (MASLD) (previously known as non-alcoholic fatty liver disease,[122] NAFLD) and alcoholic liver disease (ALD), collectively account for more than 60% of liver diseases.[123] MASLD is primarily associated with metabolic syndrome and its risk-factors such as obesity, while ALD is a result of prolonged excessive alcohol intake. Despite their distinct causes, both diseases share a similar pathological progression.[124] They both begin with steatosis, the accumulation of triglycerides in lipid droplets within hepatocytes making up greater than 5% of liver weight.[125,126] Steatosis can cause inflammation and oxidative stress, damaging liver cells. Fibrosis results as a wound-healing response to repeated liver injury, leading to the accumulation of ECM proteins, particularly collagen, within hepatocytes.[127] Healthy liver tissue can be replaced by scar tissue, reducing liver function.[128] Without intervention at this stage, both diseases can progress irreversibly. [129] As fibrosis progresses, ECM deposition disrupts liver architecture, eventually resulting in cirrhosis. Cirrhosis is characterised by severe scarring, significantly impairing liver function.[130] Consequently, cirrhosis can lead to complications such as liver failure and hepatocellular carcinoma, the most common type of liver cancer.[131,132] In advanced stages, liver cancer compromises vital liver functions, and this loss of function is a major contributor to mortality (Figure 2.1).

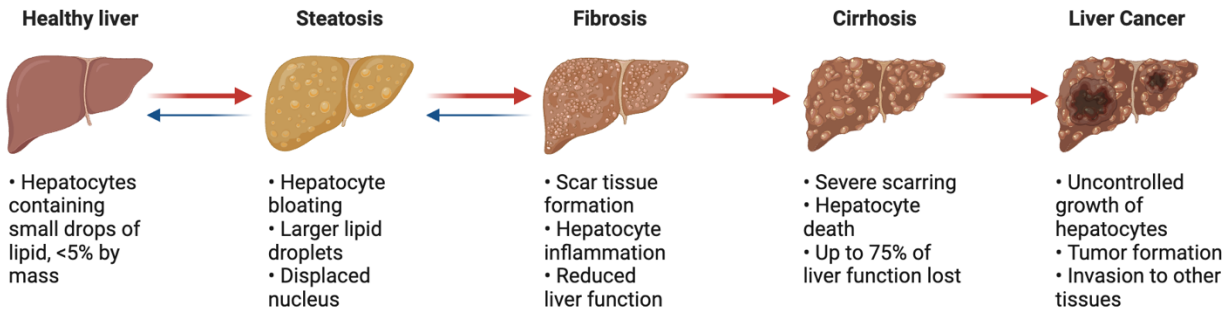


Figure 2.1: General progression of fatty liver diseases. Figure made with biorender.com.[126,131,133,134]

2.1.3 Current treatments for Liver Disease

The current primary treatment for both ALD and MASLD is lifestyle change. For ALD, this involves abstinence from alcohol[135], and for MASLD, this includes weight loss, dietary changes, and exercise.[136] Sustained weight loss of ≥7–10% has been associated with improvements in hepatic steatosis, inflammation, and in some cases, fibrosis.[137] Similarly, complete discontinuation of alcohol consumption has shown to significantly improve survival and disease progression in ALD, even in patients with advanced liver injury.[138] However, only 10% of patients achieve successful lifestyle modification at one year, with fewer than half of those patients retaining weight loss after five years.[139] Similarly, in ALD, only 37% of patients report abstinence upon receival of a formal diagnosis. Among those who subsequently entered alcohol-use treatment, including counselling and/or pharmacological treatments, approximately 60% achieved abstinence, although less than 58% maintain abstinence for at least one year.[137] While lifestyle and behavioural interventions are often the first line of management, their limited success rates necessitate consideration of pharmacological therapies (Figure 2.2). These approaches, however, carry their own drawbacks or constraints.

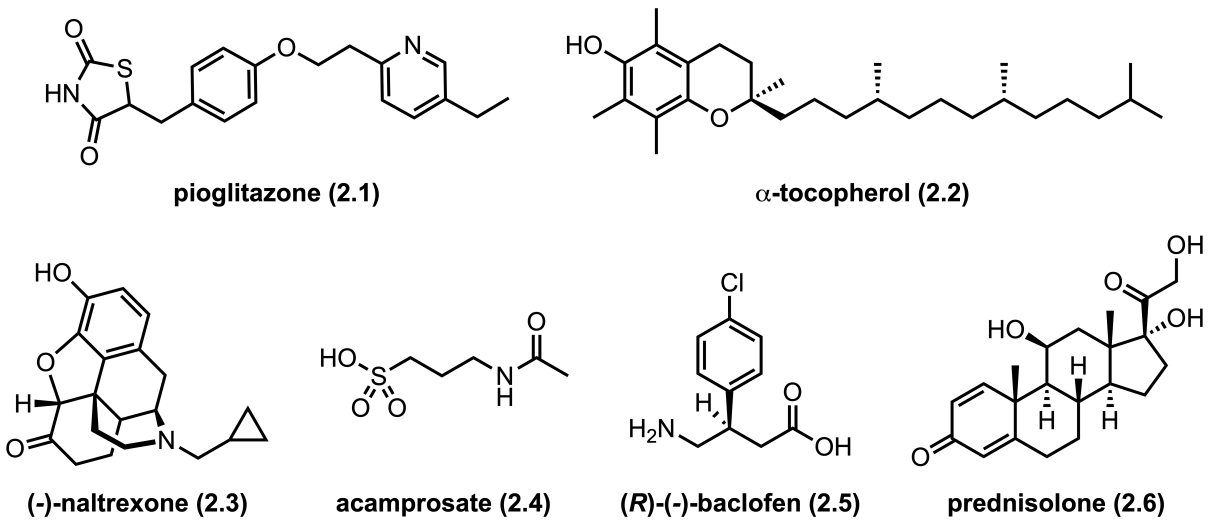


Figure 2.2. Common pharmaceutics and supplements employed in treatment of MASLD (pioglitazone, vitamin E α-tocopherol) and ALD (naltrexone, acamprosate, baclofen, prednisolone).

No medication specifically for the treatment of MASLD is currently approved in Australia;[140] however, a range of interventions are being trialled, including non-specific approaches such as vitamin E supplementation, in addition to the off-label use of

existing pharmaceuticals. In the liver, insulin normally suppresses glucose production and promotes glycogen and lipid synthesis; insulin resistance disrupts this balance, resulting in continued glucose production while lipid synthesis continues, resulting in hepatic fat accumulation. Insulin sensitisers, such as pioglitazone (**2.1**)[141,142], have been shown to improve hepatic steatosis and inflammation by restoring insulin responsiveness in muscle and adipose tissues, lowering the metabolic load on the liver and reducing hepatic lipid accumulation. However, concerns about long-term safety, including lack of definitive evidence linking histological improvements to clinical benefit[143,144] have limited the use of insulin sensitisers in formal approval and treatment of MASLD. Antioxidants, including vitamin E (α-tocopherol isoform, **2.2**),[145,146] have been investigated in MASLD to counteract oxidative stress that is thought to cause hepatocellular injury. While some clinical trials suggest histological improvement, vitamin E is a dietary supplement as opposed to a registered medicine, and as such its use represents a non-approved therapeutic approach rather than an off-label drug. More recently, glucagon-like peptide-1 receptor agonists (GLP-1RAs), such as semaglutide, the active compound in the well-known drug Ozempic®, have been shown to be beneficial by improving insulin resistance, promoting weight loss, and reducing hepatic fat content, and are currently being assessed in late-phase trials for metabolic dysfunction-associated steatohepatitis.[147,148]

For ALD, pharmacological therapy is largely focussed on managing alcohol dependence and associated complications. Pharmaceuticals such as naltrexone[149,150] (**2.3**), acamprosate[151,152,153] (**2.4**), and baclofen[154,155,156,157] (**2.5**) aid alcohol abstinence[158,159] through neurochemical modes of action. While these medications have been efficacious in supporting alcohol abstinence in patients with ALD, one of their major limitations is that these agents mainly act on the central nervous system (CNS), with no evidence that they directly modulate hepatic inflammation or fibrosis.[160] Their use is limited to reducing alcohol intake, which may slow disease progression; however, they do not address the underlying hepatic injury, and are unable to reverse hepatic inflammation, fibrosis, or steatosis. In severe alcoholic hepatitis, corticosteroids (typically prednisolone, **2.6**) may offer a short-term (28 days) survival benefit in patients without contraindications.[161,162] However, they have not been shown to improve long-term outcomes and are not used in

chronic management of ALD.[163] Resultingly, in cases involving progressive fibrosis or cirrhosis, management shifts towards treating complications of portal hypertension, and where appropriate, liver transplantation.[164]

Despite the use of several pharmacological approaches for both ALD and MASLD, none are truly disease-modifying or curative, highlighting the urgent need for novel therapeutic strategies.

2.1.4 Role of cannabinoid receptor 1 (CB_1) in metabolic and liver function

A potential target for the treatment of liver disease is the endocannabinoid system, particularly cannabinoid receptor 1 (CB_1). CB_1 is G protein-coupled receptor (GPCR) that is highly expressed in the central nervous system (CNS), where its activation by Δ^9-tetrahydrocannabinol (THC, **2.7**) is responsible for producing the well-known intoxicating effect associated with *Cannabis sativa* consumption (Figure 2.3). However, CB_1 is also expressed in peripheral tissues, including the liver.[165]

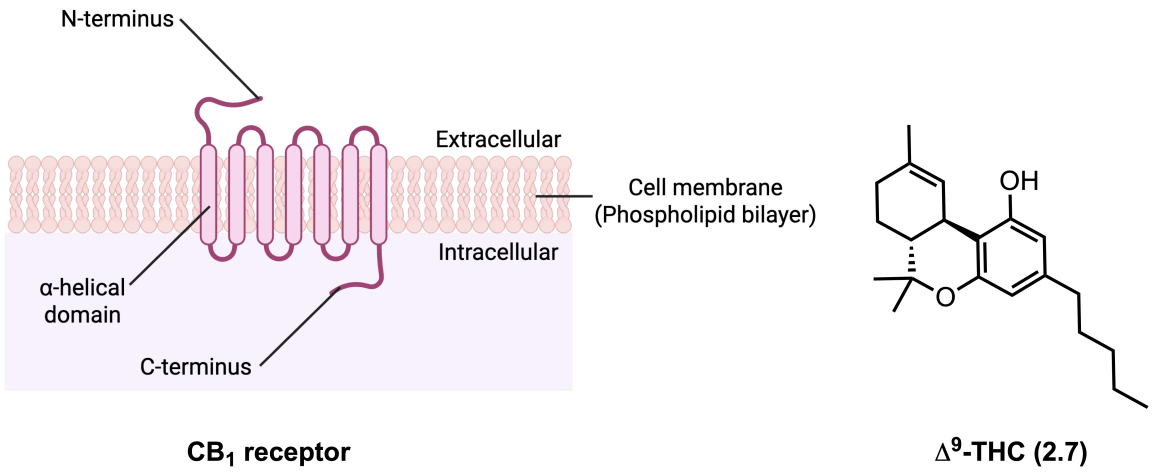


Figure 2.3. Structure of the CB_1 receptor and Δ^9-tetrahydrocannabinol (THC). The CB_1 receptor is a class A G protein-coupled receptor (GPCR) embedded in the cell membrane. It consists of seven transmembrane α-helical domains, and an extracellular N-terminus and intracellular C-terminus. Shown alongside is Δ^9-THC (2.7), the primary psychoactive phytocannabinoid, which acts as a partial agonist of CB_1. Figure made with biorender.com.[166,167]

In disease states such as obesity, MASLD, and ALD, CB_1 expression is significantly upregulated in hepatocytes.[168,169] CB_1 signalling influences hepatic lipid metabolism under normal conditions, its upregulation in disease states exaggerates these effects,

promoting fatty acid synthesis from carbohydrate precursors while also reducing fatty acid oxidation. This increase in CB_1-driven lipid accumulation is thought to contribute to hepatic steatosis and may play a role in the progression to steatohepatitis (Figure 2.4).[170]

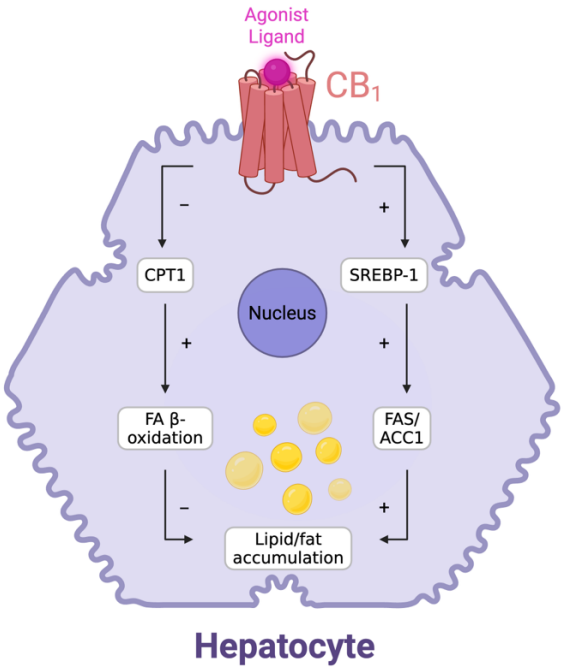
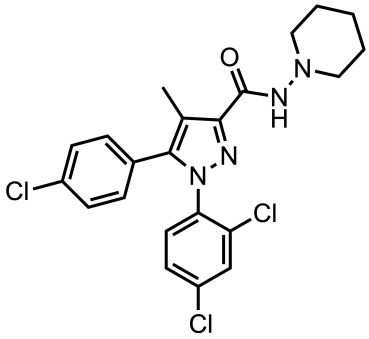


Figure 2.4. CB_1 signalling in a hepatocyte. Activation of CB_1 by agonists reduces cyclic adenosine monophosphate (cAMP), inhibiting protein kinase A (PKA) activity. This decreases phosphorylation of regulatory proteins that normally suppress lipogenesis, increasing the activity of sterol regulatory element binding protein-1 (SREBP-1). Activated SREBP-1 upregulates key enzymes including fatty acid synthase (FAS) and acetyl-CoA carboxylase 1 (ACC1), enzymes that are responsible for *de novo* lipogenesis and triglyceride synthesis. In parallel, CB_1 signalling downregulates carnitine palmitoyltransferase 1 (CPT1), an enzyme involved in mitochondrial β-oxidation, reducing fatty acid breakdown. Collectively, this combined effect of increased lipogenesis and reduced fatty oxidation results in lipid accumulation within hepatocytes.[169,171,172,173]

These proposed mechanisms suggest that CB_1 acts as a key mediator of hepatic lipid accumulation, linking its upregulation to the development of steatosis in liver diseases. Animal studies have confirmed this role, showing CB_1 upregulated in the livers of mice fed a high-fat (HF) diet[168,174] or low-fat ethanol (EtOH) diet.[169] In both cases, mice lacking CB_1 globally ($CB_1^{-/-}$) or hepatocyte-specifically ($LCB_1^{-/-}$) were resistant to diet-induced steatosis. In comparison, wild-type (WT) controls developed significant lipid accumulation. These findings collectively establish hepatocyte CB_1 signalling as a key mediator of metabolic and ethanol-induced steatosis in mice.

Given this putative role, CB_1 has been investigated as a potential target in the treatment of liver diseases.[174,175,169] One therapeutic strategy is to effect CB_1 blockade in the liver. Rimonabant (**2.8**),[176] a CB_1 selective antagonist (with inverse-agonist properties shown in the CNS) is a valuable tool to determine the viability of CB_1 as a therapeutic target (Figure 2.5).



Rimonabant (2.8)

Figure 2.5. Rimonabant (**2.8**), a CB_1 selective antagonist.

The positive effect of CB_1 blockade is supported by preclinical studies: treatment of obese rats with rimonabant (**2.8**) led to a marked reversal of steatosis.[175] Similarly, in ethanol-fed mice, rimonabant significantly reduced visible fat accumulation in hepatocytes.[169] Together, these results show that pharmacological CB_1 inhibition in rodents can prevent or reverse hepatic steatosis, strengthening its potential as a therapeutic target in MASLD and ALD.

2.1.5 Targeting CB_1 in treatment of liver disease

The CB_1 antagonist rimonabant (**2.8**) was formerly approved in Europe as an anti-obesity medication.[177] Although rimonabant achieved sustained weight loss of 5-10% weight over one year,[178] it was subsequently withdrawn from the market after two years due to serious psychiatric side effects, including depression, suicidal ideation, and reported suicides.[179–181]

As mentioned previously, CB_1 is highly expressed in the CNS, specifically in basal ganglia, hippocampus, cerebellum, amygdala, and cerebral cortex; regions associated with motor control, memory, coordination, emotion, and cognition (Figure 2.6).[182]

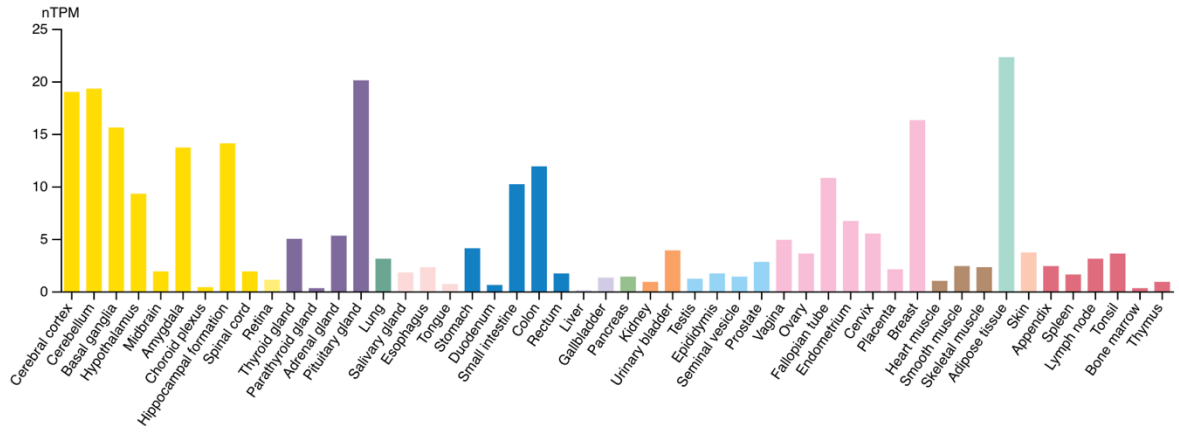


Figure 2.6. Relative expression of CB_1 mRNA across human tissues, highlighting high expression of CB_1 in the CNS (yellow). nTPM = (number of transcripts per million), with organs being group by colour. Figure from reference.[165]

In the CNS, CB_1 is primarily located on presynaptic nerve terminals, where it regulates synaptic transmission by altering neurotransmitter release.[183] Through balancing excitatory[184,185] glutamatergic and inhibitory[186] GABAergic signalling,[187] CB_1 maintains the dynamic equilibrium required for normal brain activity. Blocking CB_1 in the CNS, for example with rimonabant which is able to cross the blood-brain barrier (BBB)[188], has been associated with core depressive features such as mood dysregulation, low motivation, anhedonia and lower stress resilience[189], potentially through modulation of serotonergic signalling.

Exploring novel approaches for CB_1 antagonism is crucial to harness its therapeutic potential in liver disease while circumventing the central side effects.

2.1.6 Receptor degradation of CB_1 in hepatocytes

One potential method of avoiding the psychiatric side effects associated with central CB_1 modulation is to restrict CB_1 antagonism to the periphery. Peripherally restricted CB_1 inverse agonists, such as JD5037 (**2.9**) and AM6545 (**2.10**), were developed primarily as anti-obesity agents and for metabolic dysfunction (Figure 2.7). Despite being effective in preclinical models, translation to clinical cases was limited. It was difficult to completely exclude the drugs from the CNS, particularly in disease states where BBB integrity is compromised, and even minimal central penetration can trigger anxiety- or depression-like effects. Additionally, CB_1 has essential physiological functions in the periphery,

including appetite regulation,[190] contribution to cardiovascular homeostasis,[191] and reproductive processes.[192] These additional roles of CB_1 in the periphery mean that broad peripheral antagonism may result in undesirable on-target effects outside the liver. These limitations require a more selective strategy.

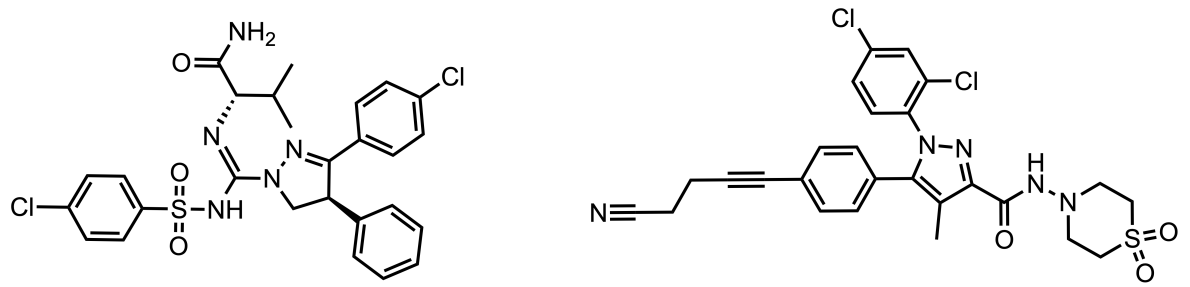


Figure 2.7. Peripherally restricted CB_1 antagonists JD5037 (**2.9**) and AM6545 (**2.10**). Both compounds were designed to restrict CNS penetration while retaining CB_1 activity.

While peripherally restricted CB_1 inverse agonists are a logical approach, receptor degradation affords a novel strategy that eliminates CB_1 signalling entirely, including constitutive activity. This provides a more durable and complete suppression of CB_1 signalling, including constitutive activity, while also allowing for cell- and organ-specific targeting. This approach would allow selective removal of CB_1 receptors in hepatocytes, where upregulation contributes to steatosis, without impacting the important roles of CB_1 in other peripheral tissues or the brain.

Receptor degradation refers to the breakdown of receptors, either following their removal from the cell surface or from intracellular components. Receptors undergo degradation for a variety of reasons, including termination of signalling following ligand binding, regulation of receptor abundance after sustained activation, recycling or clearance of damaged receptors, and general homeostatic control of receptor turnover.[193] There are two main types of protein degradation: proteasomal degradation and lysosomal degradation.[194] Proteasomes are generally responsible for elimination of short-lived proteins and soluble misfolded proteins, occurring in the cytoplasm or nucleus of the cell.[195] In contrast, lysosomes are responsible for degradation of range of substrates, including long-lived proteins, insoluble protein aggregates, and cell-surface receptors.[68]

2.1.7 Targeted protein degradation

Targeted protein degradation (TPD) is therapeutic strategy that leverages the cell's endogenous degradation machinery to selectively eliminate proteins of interest (POI).[68] These can include enzymes, receptors, transcription factors, and scaffolding proteins, many of which can often be challenging to modulate with small-molecule inhibitors. Unlike classical small-molecule inhibitors, TPD can achieve a more prolonged suppression of signalling by removing the protein entirely, including in contexts where ongoing transcription and translation can continue to replenish the target protein. For example, degradation of the androgen receptor in prostate cancer and the estrogen receptor in breast cancer have demonstrated durable suppression of the signalling pathway.[196,197] In addition to this durability, TPD can be tissue-specific, offering an extra layer of precision that allows for selective degradation in relevant cell types and therefore reduces side effects. The most established class of TPD molecules are proteolysis-targeting chimeras (PROTACs). PROTACs are bifunctional small molecules that can simultaneously recruit an E3 ubiquitin ligase and a POI, resulting in ubiquitination of the target and subsequent degradation *via* the proteasome.[198]

A more recently emerging class of TPD is through lysosomal degradation, through a class of molecules called lysosomal targeting chimeras (LYTACs). LYTACs are heterobifunctional molecules that are capable of degrading proteins of interest (POI), utilising the machinery of ASGPR to degrade extracellular and membrane-associated proteins.[69] As ASGPR is highly and almost exclusively expressed on hepatocytes, it is an attractive target for liver-specific therapeutic strategies. Both Bertozzi's[70] and Spiegel's[71] strategies allow for use of ASGPR on hepatocytes for degradation of either circulating extracellular or membrane proteins. However, where antibody-based LYTACs are limited by the structure and properties of the antibody scaffold, small-molecule degraders provide greater flexibility, allowing independent alteration of the ligand that engages that target protein. This is particularly relevant for CB_1, as available antibodies have frequently shown limited efficacy and consistency,[199] meaning that small molecules offer a more reliable route for selective degradation of this receptor.

2.2 Chapter Aims

This aim of this chapter was to investigate liver-specific CB_1 degradation as a novel therapeutic strategy. Targeted receptor degradation has potential to allow for more sustained suppression of signalling than classical inhibition, while hepatocyte-specific delivery *via* ASGPR provides a way to avoid global CB_1 loss. To explore this concept, bifunctional molecules were designed that couple a high-affinity CB_1 ligand linked to a hepatocyte-targeting motif, with a view to facilitating selective receptor removal within the liver. Through TPD methodology, the goal was to evaluate whether this strategy could provide a viable approach for the development of potential drug candidates. In parallel to the work on the CB_1 degraders, alternative ligands for ASGPR to the traditionally used 'tri-GalNAc' ligand were also investigated, including cyclic peptides identified from random non-standard peptide integrated discovery (RaPID) screens.

2.3 Results and Discussion

2.3.1 Synthetic Design of LYTACs

A series of lysosomal targeting chimeras (LYTACs) targeting CB_1 and ASGPR were first designed. The bifunctional LYTACs were proposed comprising three covalently linked domains: a CB_1 binding motif, a polyethylene glycol (PEG) spacer, and the ASGPR binder.

Selection of CB_1 motif

The CB_1 binding motif needed to exhibit high selectivity for CB_1 to ensure that degradation was limited to CB_1-expressing cells, minimising off-target effects. Additionally, the chosen ligand needed to offer suitable sites for linker attachment, avoiding disruption of the ligand's affinity for CB_1 and providing synthetically accessible routes to modification.

Rimonabant was selected as the CB_1 targeting ligand of choice due to its high affinity for CB_1 (pK_i = 8.75), over cannabinoid receptor 2 (CB_2), the second principal cannabinoid receptor in the endocannabinoid system (pK_i = 6.29).[200] CB_2 is frequently bound off-target by CB_1 ligands; CB_2 plays key roles in immune regulation which are important to avoid to prevent unwanted immunomodulatory effects.[201] Additionally, the crystal structures of structurally similar antagonist AM6538 (**2.10**) to CB_1 facilitated rational selection of a range of positions for viable linker attachment (Figure 2.8A).[202] Rimonabant (**2.8**) bears the same pyrazole core as AM6538, differing in the aryl substituents, with AM6538 bearing an alkynyl nitrate in place of the chlorine substituent seen in rimonabant (Figure 2.8B). This allowed for the binding conformation of the crystal structure to be used to dock rimonabant (Figure 2.8C/D).

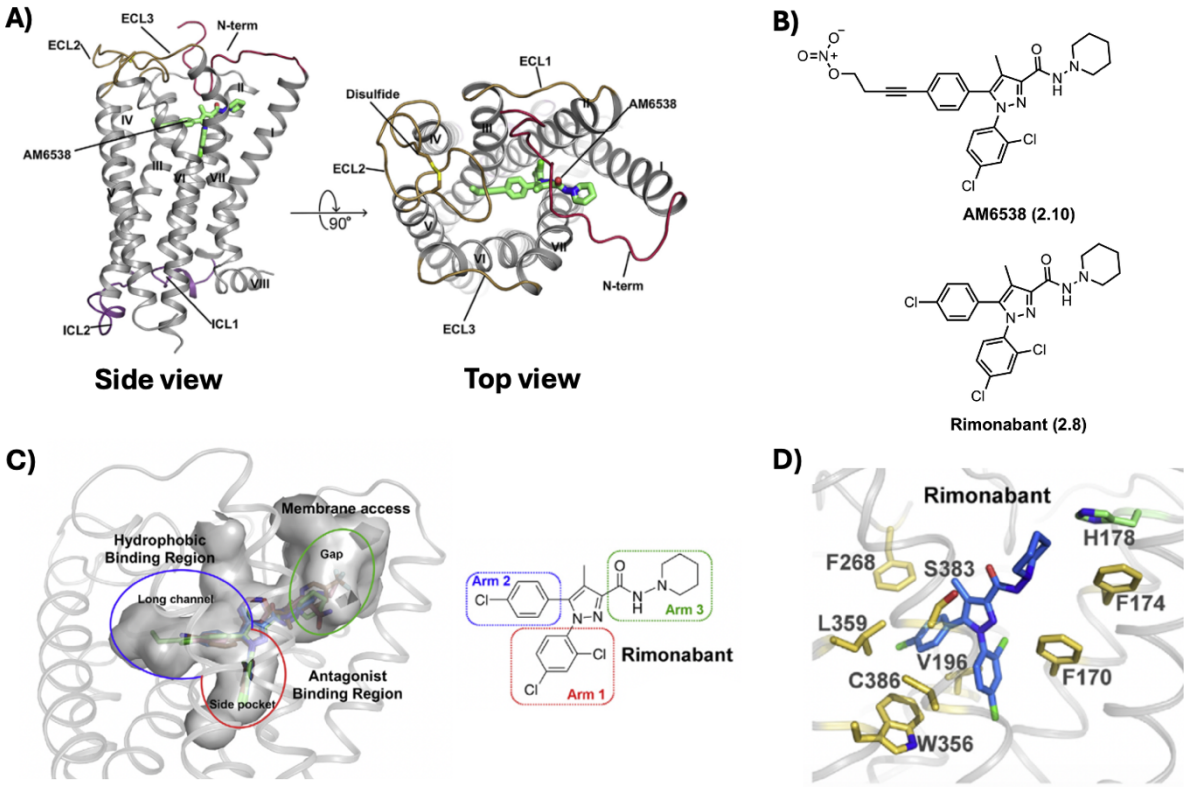


Figure 2.8. **A)** Crystal structure of CB_1-AM6538 complex, shown from both side view and top view. The receptor is shown in grey, and the ligand AM6538 is shown with green sticks. **B)** Structures of AM6538 (**2.10**) and rimonabant (**2.8**), showing their structural similarity. **C)** Docking of rimonabant in the CB_1 crystal structure. CB_1 binding pocket with rimonabant (blue sticks) are shown in the grey surface representation. The red/blue/green rectangles show how the arms in the molecule are positioned in the CB_1 binding pocket. **D)** Predicted binding mode of rimonabant (blue sticks) with CB_1. The interacting residues are shown with yellow sticks.[202] Figure reproduced with permission from Hua *et al.*, Cell, 2016.

Virtual docking showed that rimonabant bound in a similar conformation to AM6538, enabling identification of potential modification and linker attachment positions. The four regions selected were: the 4-methyl group of the pyrazole ring, and the three positions of the piperidine ring (Figure 2.9). This was based on their orientation in the receptor and accessibility to the cell surface.[202]

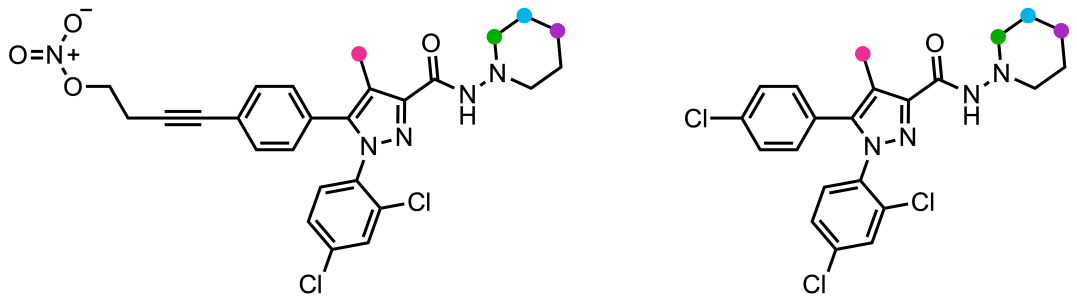


Figure 2.9. Structures of AM6538 and Rimonabant, highlighting four potential sites for modification and linker attachment.

Selection of linkers and ASGPR binder

Polyethylene glycol (PEG) linkers of varying lengths were proposed for attachment at each position identified, allowing for structure-activity relationships (SAR) to be established. The tri-GalNAc ligand (**2.11**) developed by Bertozzi was selected as the ASGPR ligand[70] (Figure 2.10).

As in Spiegel's work, **2.11** did not require bioorthogonal conjugation to the POI ligand.[71] The presence of a free amine functionality on **2.11** allows for a straightforward amide coupling with linkers bearing a carboxylic acid functionality. Amide bonds can be formed under relatively mild and reliable conditions that are compatible with most functional groups. PEG linkers were chosen due to their hydrophilicity, flexibility, low immunogenicity, and ability to improve aqueous solubility compared to simple alkyl chains.[203] Additionally, the conformational flexibility and spacing provided by PEG linkers would help to minimise steric interaction between the CB_1 binding pocket and the attached tri-GalNAc. It was envisaged that optimisation of both linker length and position would facilitate successful engagement with both the CB_1 receptor and ASGPR.

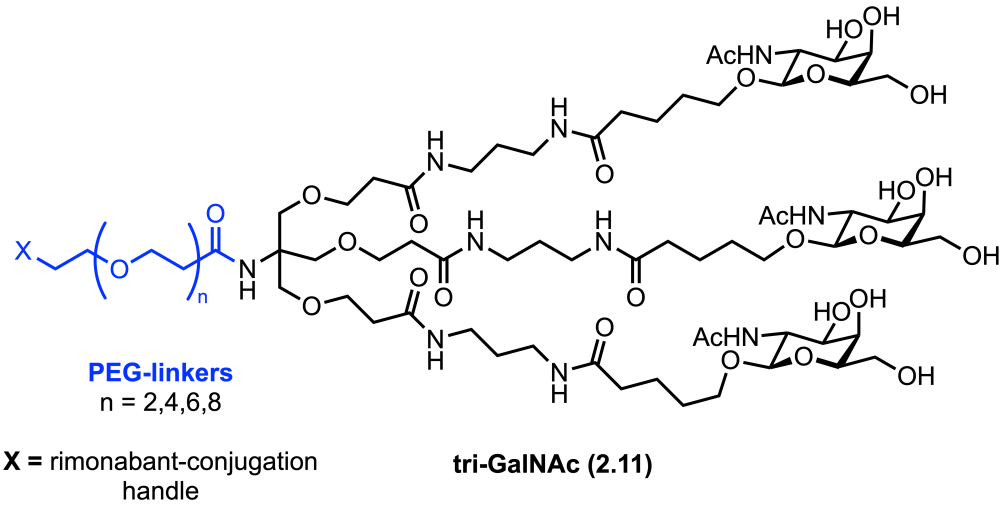


Figure 2.10. Structure of tri-GalNAc ASGPR binder (**2.11**) coupled to PEG linkers of various lengths.

PEG linkers of varying lengths (PEG-2, PEG-4, PEG-6, and PEG-8) each terminating in a carboxylic acid group, were chosen as the spacer moieties for conjugating the tri-GalNAc to the CB_1 ligand rimonabant. These lengths were chosen to explore a range of linker lengths that could balance simultaneous engagement of CB_1 and ASGPR without having excessive flexibility, which results in an entropic penalty that can reduce degradation efficiency. The identity of the functional group, X, at the rimonabant-conjugating end of the linker was dependent on the synthetic feasibility of introducing a compatible handle onto the rimonabant scaffold.

2.3.2 Synthesis of Rimonabant-type acceptor

2.3.2.1 Piperidine functionalisation

For LYTACs based on functionalisation on the piperidine ring of rimonabant, retrosynthesis of rimonabant linker-triGalNAc LYTAC (**2.12**) identified commercially available rimonabant acid (**2.13**) and substituted piperidin-1-amine (**2.14**) as precursors. Piperidin-1-amine **2.14** could be prepared from the three regioisomers of piperidinylmethanol (**2.15, 2.16,** and **2.17**), with the R group of **2.14** to be determined by synthetic tunability of the piperidinylmethanols (Figure 2.11).

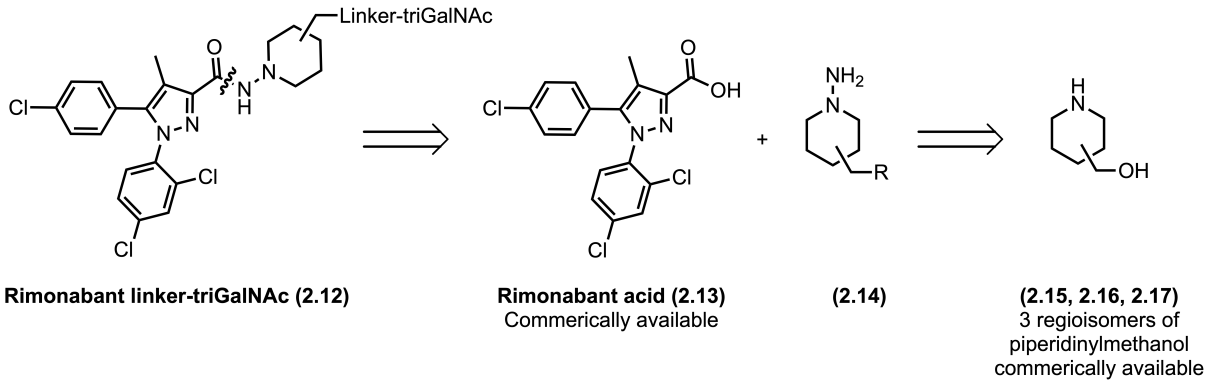


Figure 2.11. Retrosynthesis of rimonabant-linked linker-triGalNAc.

In order to convert piperidin-2 (**2.15**), -3 (**2.16**), and -4 (**2.17**) ylmethanols into the desired substituted 1-amino variants, their racemates were first converted to their respective 1-nitroso variants (**2.18**, **2.19**, and **2.20**) by treatment with sodium nitrite and acetic acid (AcOH) in water (Figure 2.12). The presence of the N-nitroso group was identified through LC-MS analysis.

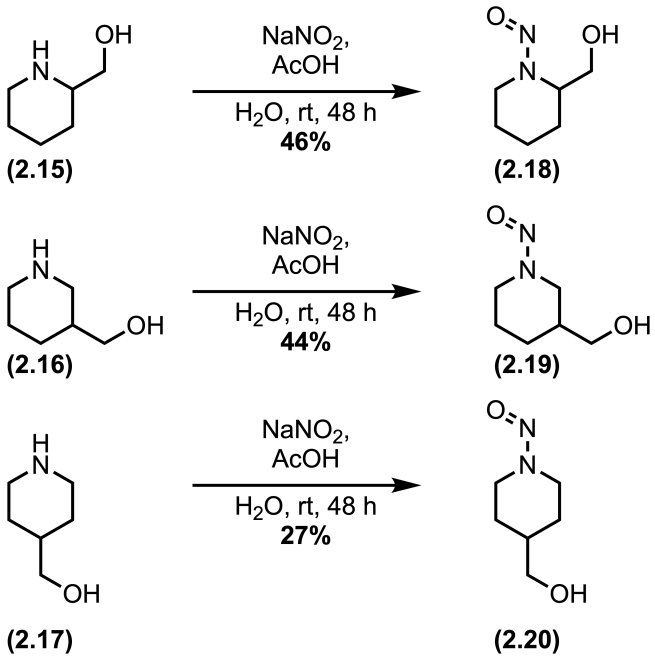


Figure 2.12. *N*-nitrosation reaction of three regioisomers of piperidinylmethanols **2.15**, **2.16**, and **2.17**.

The 1-nitroso variants were then subjected to reduction to produce hydrazine variants (Figure 2.13). Reduction of *N*-nitroso compounds to hydrazines typically employ reducing metal, catalytic hydrogenation, or hydride reductions, with optimal conditions being highly substrate-dependent.

A variety of reduction conditions were trialled using (1-nitrosopiperidin-2-yl)methanol (**2.18**), as this regioisomer was the highest yielding from the *N*-nitrosation reactions (Table 2.1).

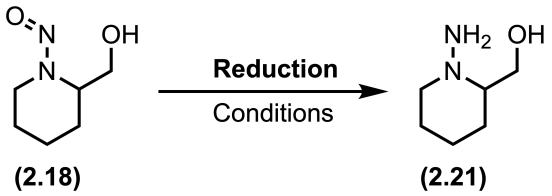


Figure 2.13. Reduction of (1-nitrosopiperidin-2-yl)methanol (**2.18**) to (1-aminopiperidin-2-yl)methanol (**2.21**).

Table 2.1. Conditions and results of *N*-nitroso reductions.

Conditions	Result
Zn (10 eq), AcOH, rt, 24 h	No conversion
Zn (10 eq), AcOH, reflux, 24 h	No conversion
Zn (3 eq), Pd/C (3 eq), H_2O, reflux, 24 h	No conversion
Fe (4 eq), NH_4Cl (1 eq), H_2O, reflux, 24 h	No conversion
$LiAlH_4$ (2 eq), THF, reflux, 24 h	No conversion
$LiAlH_4$ (5 eq), THF, reflux, 48 h	No conversion
Zn (6 eq), 10 M HCl, rt, <10 min	**2.15** observed on LC-MS
Zn (4 eq), AcOH (15 eq), MeOH, rt, 6 h	**2.15** + **2.21** observed on LC-MS
Zn (6 eq), 4 M HCl, rt, <2 min	**2.21** observed on LC-MS (~40%)

The reduction conditions required significant optimisation, with the substrate sensitive to the reducing metal, acid, and solvent used. The optimal conditions were identified as zinc (6 eq) and 4 M HCl at room temperature. The concentration of acid was of particular note, as 10 M HCl was found to produce piperidin-2-ylmethanol **2.15**.

Following reduction, aminopiperidinyl alcohols **2.21**, **2.22**, and **2.23**, were immediately subjected to *tert*-butoxycarbonyl (Boc) protection, producing their respective *N*-Boc-aminopiperidinyl alcohols (**2.24**, **2.25**, and **2.26**) (Figure 2.14). This step facilitated easier purification of the aminopiperidinyl alcohols and prepared the substrate for selective functionalisation of the hydroxyl group in subsequent steps.

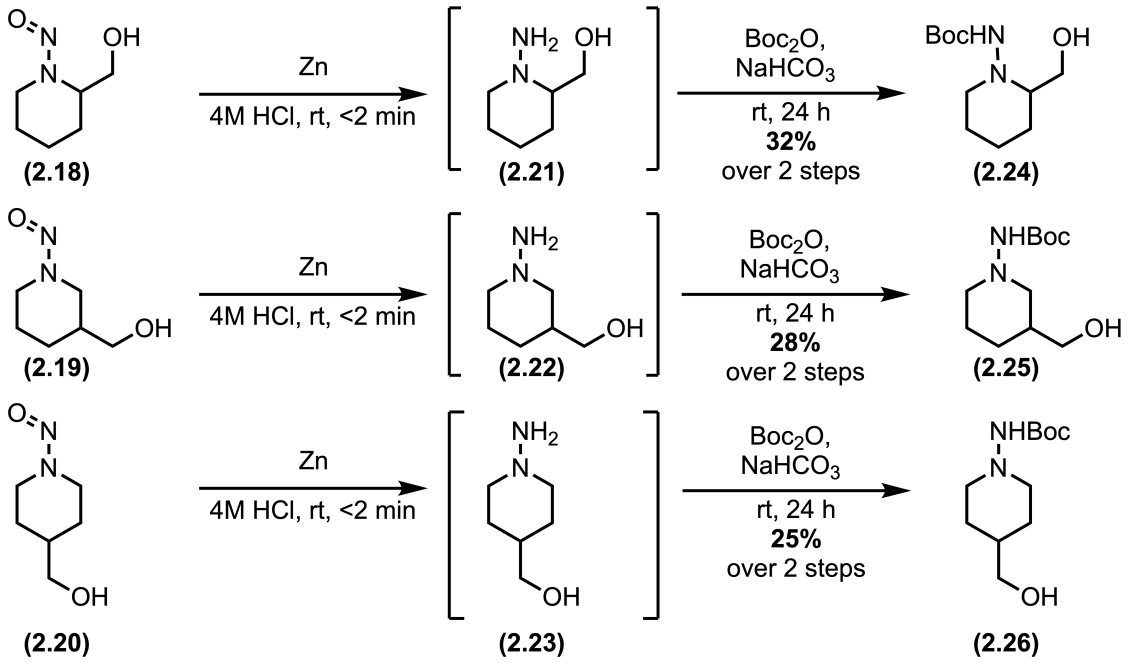


Figure 2.14. Reduction and Boc-protection of *N*-nitroso alcohols to produce **2.24**, **2.25**, and **2.26.**

The yields were notably low, owing to the formation of three undesired products: **2.15**, Boc-protected **2.15**, and **2.21**, the product of incomplete Boc protection, were observed on thin-layer chromatography (TLC) for **2.18**, and analogous undesired products for **2.19** and **2.20**. However, it was decided that further optimisation of the reaction conditions at this stage was unnecessary with clean material already in hand.

Having synthesised *N*-Boc-aminopiperidinyl alcohols, it was envisioned that the desired linker could be introduced *via* an S_N2 reaction between the alcohol and a primary alkyl halide. The 3-substituted regioisomer (**2.25**) was selected for the initial trials, as opposed to the 2-substituted regioisomer (**2.24**), due to the potential for **2.24** to introduce undesirable steric hinderance that could hinder S_N2 reactions. Commercially available bromo PEG4 *tert*-butyl ester (**2.27**) was trialled as the electrophile, due to its intermediate chain length relative to the full series of PEG linkers (Figure 2.15), and its ability to produce a carboxylic acid upon acid-mediated deprotection. Polar aprotic solvent *N*,*N*-dimethylformamide (DMF) was used, along with three equivalents of sodium hydride at room temperature.

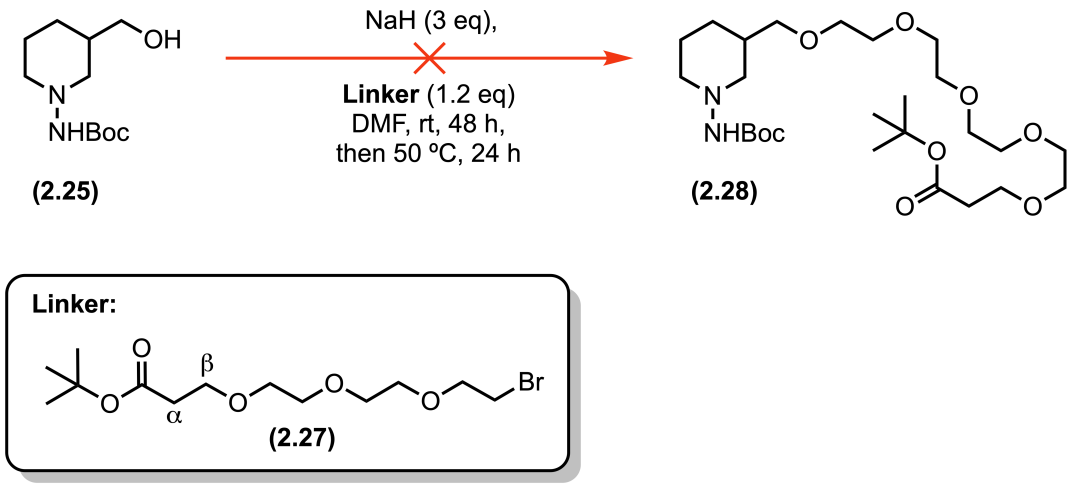


Figure 2.15. Attempted S_N2 reaction between *N*-Boc-(1-aminopiperidin-3-yl)methanol (**2.25**) and linker (**2.27**). No reaction was observed.

After 48 h, no reaction was observed, and the reaction was heated to 50 °C for a subsequent 24 h. After a total 72 h, no conversion of starting material (**2.25**) to desired product (**2.28**) was observed. This was attributed to either insufficient deprotonation of the alcohol or competing enolate formation.

An alternative strategy using a stronger base, sodium hydride (NaH), and modified electrophile was trialled (Figure 2.16). The 4-substituted regioisomer (**2.26**) was used to further rule out any impeding steric effects. Alcohol **2.26** was first subjected to deprotonation with NaH in anhydrous DMF at 0 °C, followed by addition of commercially available bromide linker **2.29**. Notably, linker **2.29** possesses a less acidic α proton than that seen in linker **2.27** due to adjacent electron donating oxygen atom. After addition of linker, the reaction was either kept at 0 °C for 6 h or warmed to rt and stirred for 6 h.

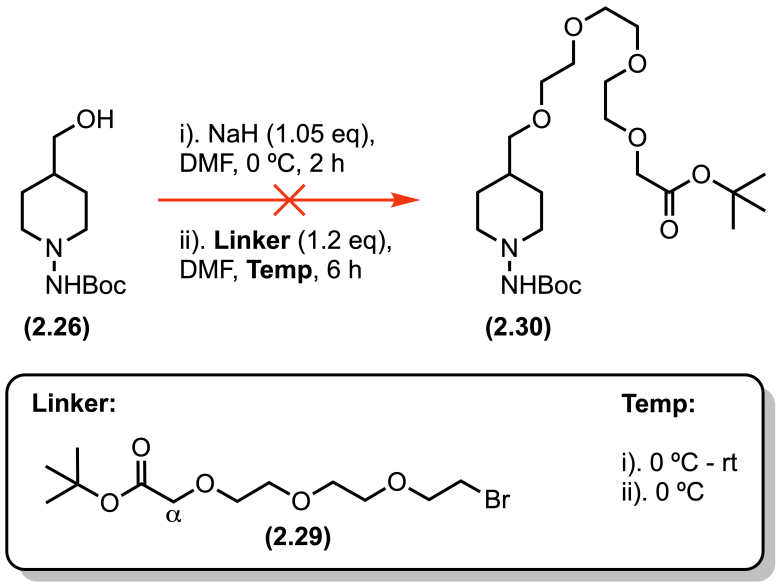


Figure 2.16. Attempted formation of **2.30** *via* S_N2 reaction between *N*-Boc-(1-aminopiperidin-4-yl)methanol (**2.26**) and linker **2.29**. No reaction was observed.

No consumption of starting material was observed. Due to the inability to directly alkylate alcohols **2.25** and **2.26** with PEG bromides to form ether linkages, a strategy involving conversion of **2.26** into a moiety that would allow an amide coupling with a linker was proposed. Amide couplings are mild and often reliable, often offering more substrate combability than S_N2 reactions. Towards this end, alcohol **2.26** was subjected to conjugate addition with *tert*-butyl acrylate and aqueous NaOH in THF (Figure 2.17). Michael addition between the alcohol and α,β-unsaturated carbonyl of *tert*-butyl acrylate was observed, albeit in low yield due to sluggish reactivity.

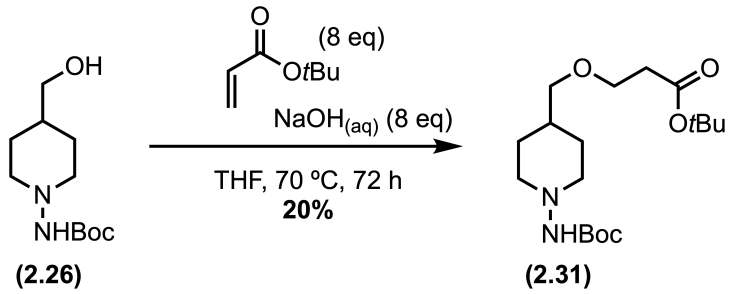


Figure 2.17. Michael addition of alcohol **2.26** to *tert*-butyl acrylate, forming desired product **2.31** in 20% yield.

Pleasingly, conducting the reaction in CH_2Cl_2 in the presence of a phase transfer catalyst tetra-*n*-butylammonium bromide (TBAB) improved the rate of reaction significantly,

allowing the reaction to occur at room temperature, and reducing the number of equivalents of acrylate and NaOH required. The TBAB-promoted acrylation reactions were carried out for the three regioisomers, producing **2.32**, **2.33**, and **2.31** in 70%, 75%, and 80% yields respectively (Figure 2.18).

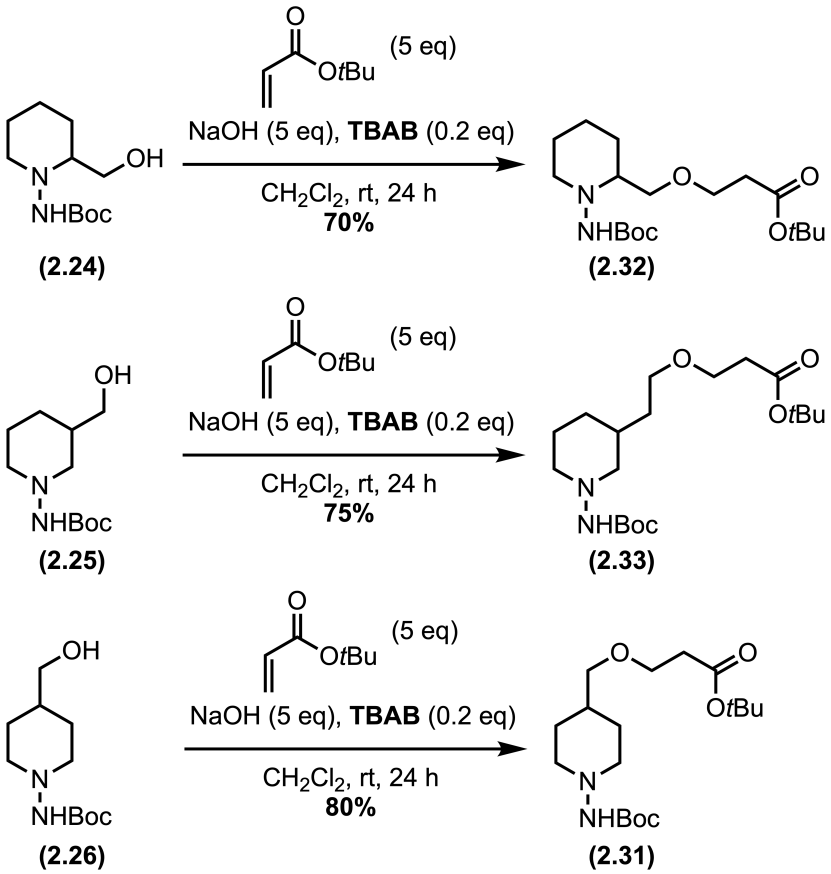


Figure 2.18. Acrylation reactions of *N*-Boc-aminopiperidinyl alcohols, producing desired ethers **2.32**, **2.33**, and **2.31** in high yields.

To facilitate coupling of the aminopiperidinyl moieties to the rimonabant scaffold, 5-(4-chlorophenyl)-1-(2,4-dichlorophenyl)-4-methyl-1H-pyrazole-3-carboxylic acid (rimonabant acid, **2.13**) was converted into its *N*-hydroxysuccinimidyl ester (**2.34**) using *N*-hydroxysuccinimide (HOSu) and *N,N'*-dicyclohexylcarbodiimide (DCC) (Figure 2.19). This would serve as a common active ester intermediate for amidation of the three aminopiperidines.

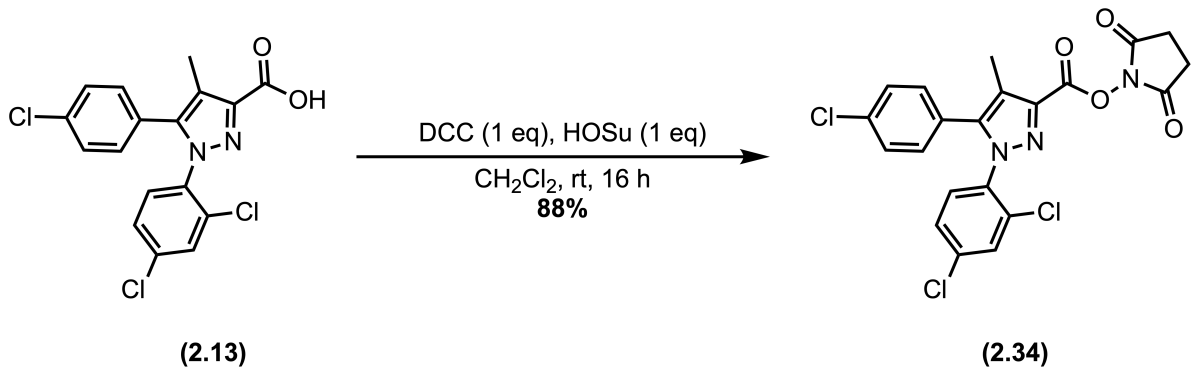


Figure 2.19. Quantitative conversion of rimonabant acid (**2.13**) to succinimide Rim-OSu (**2.34**).

The Boc-aminopiperidine *tert*-butyl esters **2.32**, **2.33**, and **2.31**, were subjected to simultaneous Boc and *tert*-butyl deprotection providing the respective organic hydrazines **2.35**, **2.36**, and **2.37** (Figure 2.20). Rim-OSu (**2.34**) was next added to a solution of each hydrazine and *N*,*N*-diisopropylethylamime (*i*Pr_2NEt) in DMF, producing the rimonabant derivatives **2.38**, **2.39**, and **2.40** as their bis(trifluoroacetate) salts in moderate yields after C18 flash purification with trifluoroacetic acid (TFA) buffer.

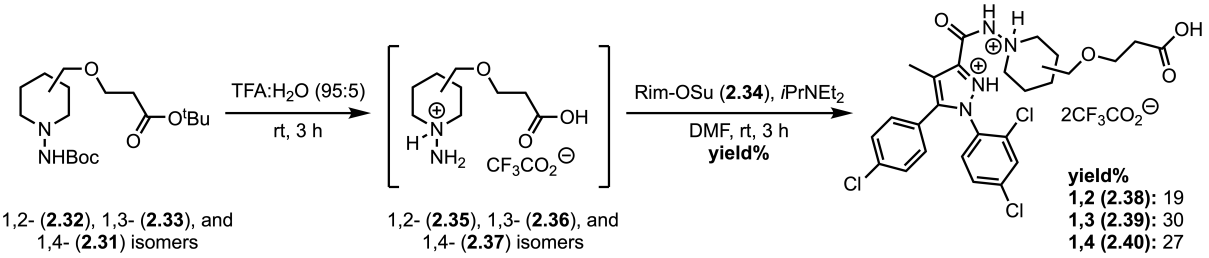


Figure 2.20. Assembly of rimonabant derivatives **2.38**, **2.39**, and **2.40**.

2.3.2.2 Attempted methyl functionalisation

With the piperidine ring of rimonabant functionalised and ready for amide coupling with a linker, the modification of the methyl group on the pyrazole ring was investigated. It was proposed that radical allylic bromination could produce a reactive alkyl bromide, able to undergo an S_N2 reaction with either a thiol or alcohol linker.

Allylic bromination was first trialled using *N*-bromosuccinimide (NBS) and azobisisobutyronitrile (AIBN) on a variety of substrates, including rimonabant (**2.8**), rimonabant hydrochloride (**2.41**), rimonabant acid (**2.13**), and rimonabant methyl ester (**2.42**) (Figure 2.21).

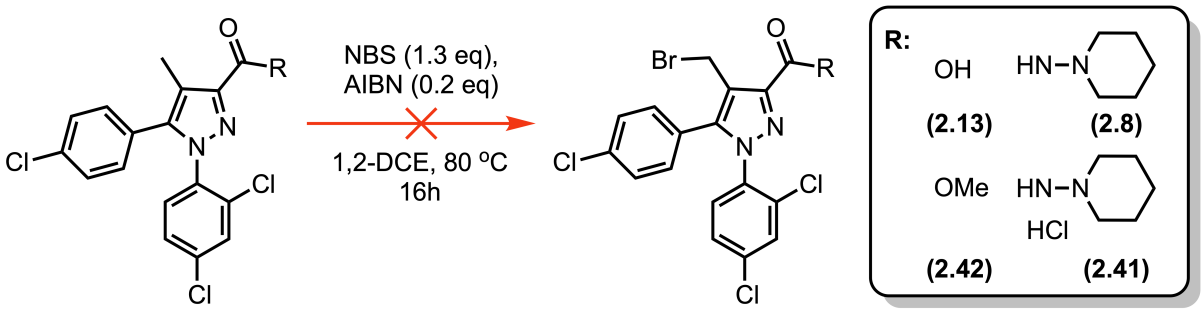


Figure 2.21. Attempted allylic bromination of the 4-methyl position on the pyrazole, using NBS and AIBN on a variety of substrates.

None of the substrates trialled resulted in observable formation of the corresponding bromide. As an alternative approach, a Riley oxidation was undertaken to generate an allylic alcohol, with the rationale that this would allow Michael addition to an acrylate as was previously demonstrated for the piperidinyl methanol analogues (Figure 2.22). The reaction was trialled on the same substrates using selenium dioxide (SeO_2), 1,4-dioxane under reflux, and monitored for progression over 24 h.

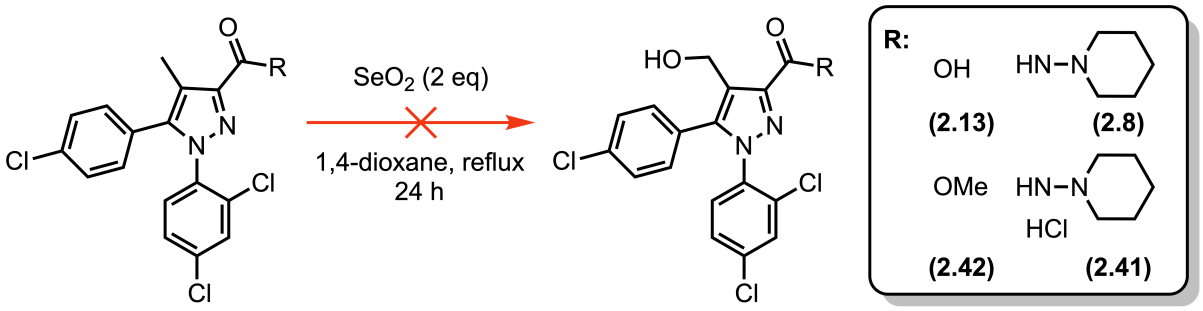


Figure 2.22. Attempted Riley oxidation to generate respective allylic alcohols.

As was observed with the bromination, none of the substrates trialled resulted in conversion to the corresponding allylic alcohol. Given the recalcitrant reactivity of the allylic position, it was decided to advance with the piperidinyl methanol analogues as a proof of concept before attempting more allylic modifications.

2.3.3 Synthesis of tri-GalNAc ASGPR ligand

Next, a peracetylated tri-GalNAc ligand[204] was assembled using commercially available materials, standard amide coupling chemistry and protecting group manipulations (Figure 2.23). Specifically, commercially available tri-*tert*-butyl ester amine (**2.43**) was protected using benzyl chloroformate (Cbz-Cl) in the presence of aqueous sodium bicarbonate ($NaHCO_3$), yielding a carbobenzyloxy (Cbz)-protected amine (**2.44**). This was subjected to acidolytic *tert*-butyl ester deprotection producing tri-carboxylic acid (**2.45**), which was amide coupled with *N*-Boc-1,3-propanediamine using *O*-(7-Azabenzotriazol-1-yl)-*N*,*N*,*N*',*N*'-tetramethyluronium hexafluorophosphate (HATU) and *N*-methylmorpholine (NMM) to produce desired **2.46**. Compound **2.46** underwent further acid-mediated Boc-deprotection to produce a tri-amine which was coupled to a commercially available peracetylated β-GalNAc pentanoic acid derivative to produce peracetylated and Cbz protected tri-GalNAc derivative (**2.47**). Following hydrogenolysis of the benzyl carbamate, the peracetylated tri-GalNAc ligand was afforded as the free amine derivative (NH_2-tri-GalNAc-OAc, **2.48**), which was used without further purification.

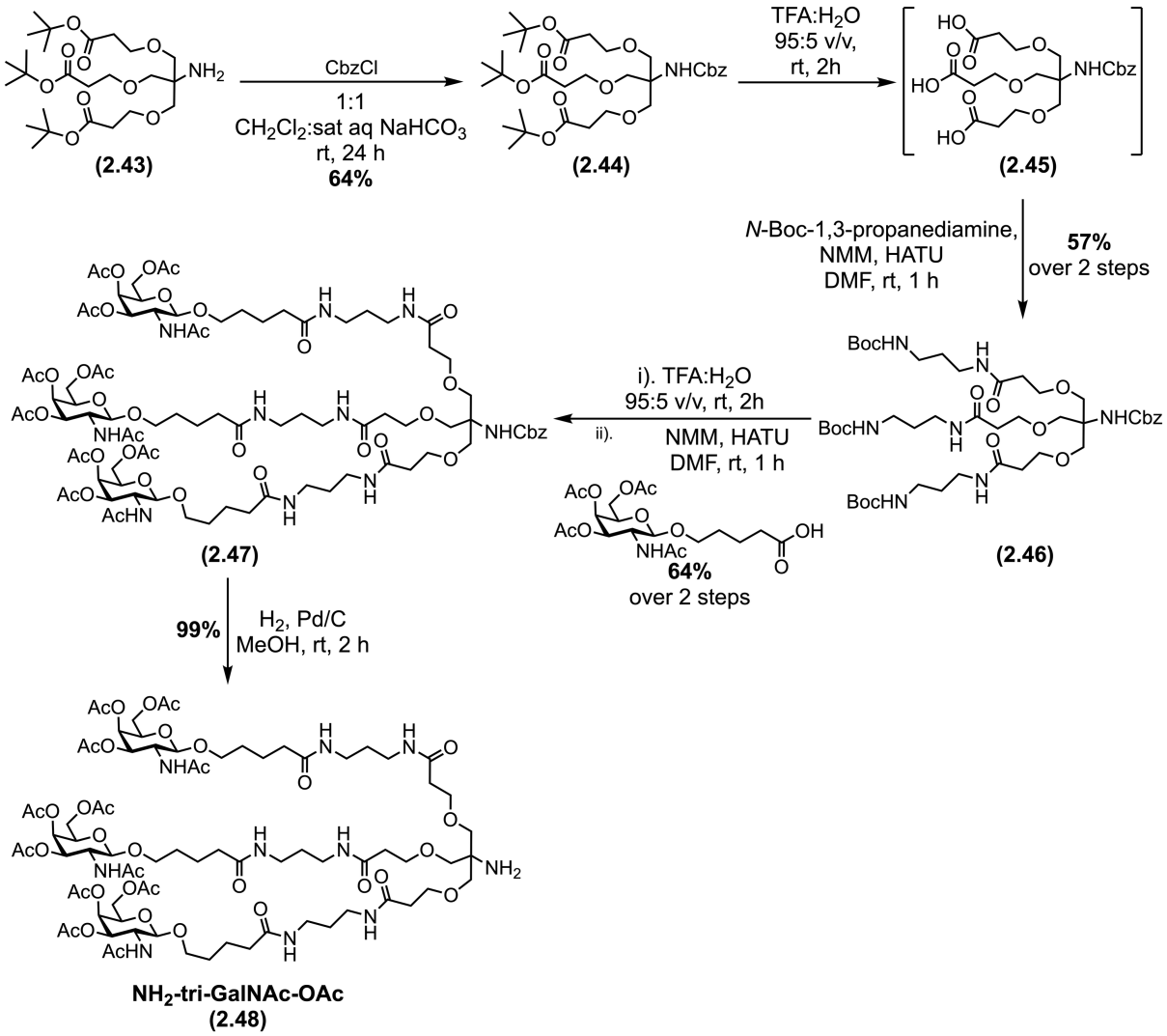


Figure 2.23. Synthesis of NH_2-tri-GalNAc-OAc (**2.48**) from tri-*tert*-butyl ester amine (**2.43**), *via* a series of protections, deprotections, and amide couplings.*

Next the peracetylated tri-GalNAc free amine (**2.48**) was elongated with PEG spacers (Figure 2.24). This involved HATU and NMM-mediated amide coupling with PEG acids **2.49**, **2.50, 2.51**, and **2.52** (PEG2, 4, 6 and 8), that were functionalised with either a Cbz or azido group on the other end, to produce PEG derivatives **2.53**, **2.54**, **2.55**, and **2.56**. The choice of a Cbz deprotection or azide reduction to an amine simply came down to substrate availability since both could be converted easily through hydrogenolysis. Accordingly, deacetylation with catalytic NaOH in MeOH,[205] followed by hydrogenolysis of the Cbz or azide produced free amines **2.57**, **2.58**, **2.59**, **2.60** ready for attachment of rimonabant derivatives.

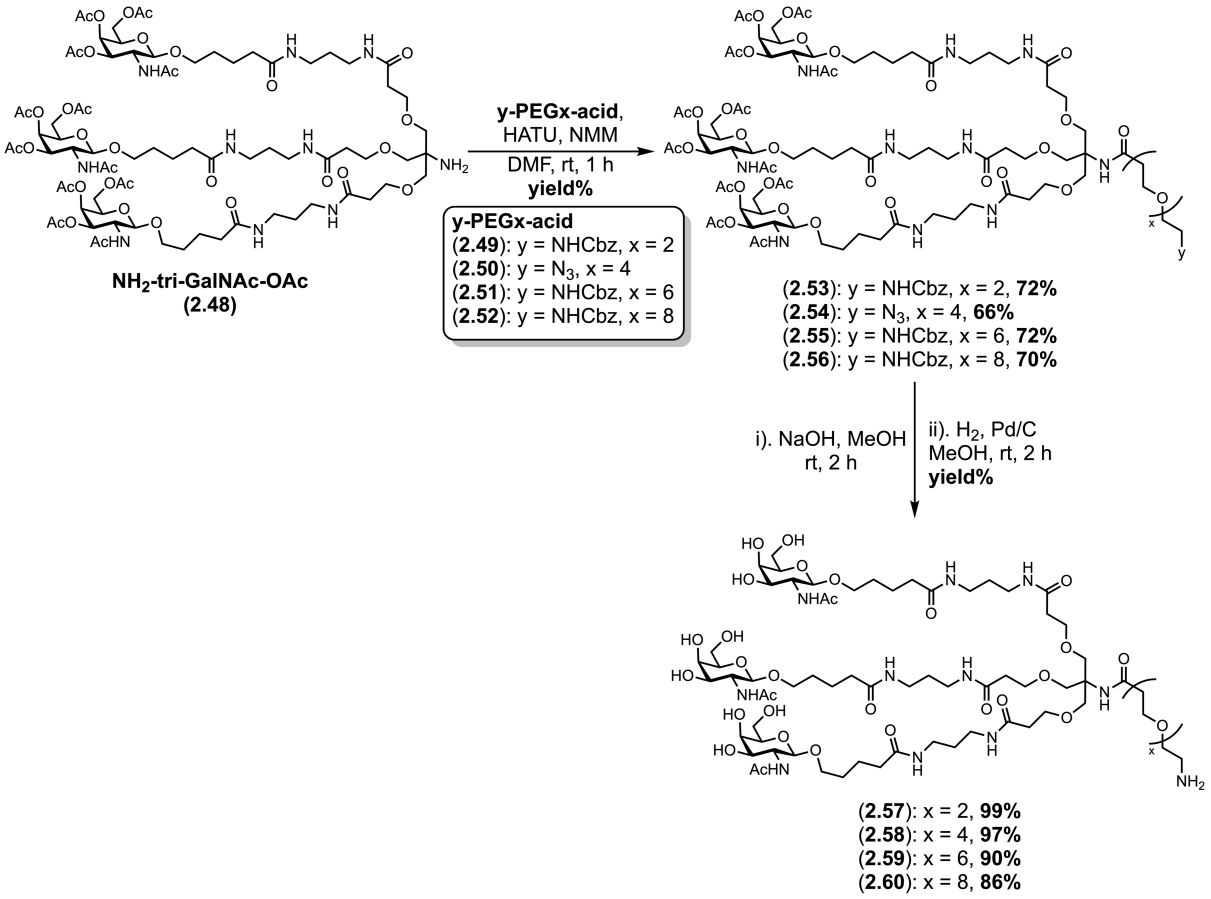


Figure 2.24. Linker attachment to tri-GalNAc, followed by deacetylation and hydrogenolysis to provide free amines **2.57**, **2.58**, **2.59**, and **2.60**.

2.3.4 Assembly of CB_1 LYTAC candidates

The amines (**2.57**, **2.58**, **2.59**, **2.60**) were next subjected to amide couplings with the three regioisomeric rimonabant carboxylic acids (**2.38**, **2.39**, and **2.40**). Identical conditions of HATU and NMM in DMF were used as before, producing 12 final LYTAC candidates in 58 to 82% yields after C18 flash purification (Figure 2.25).

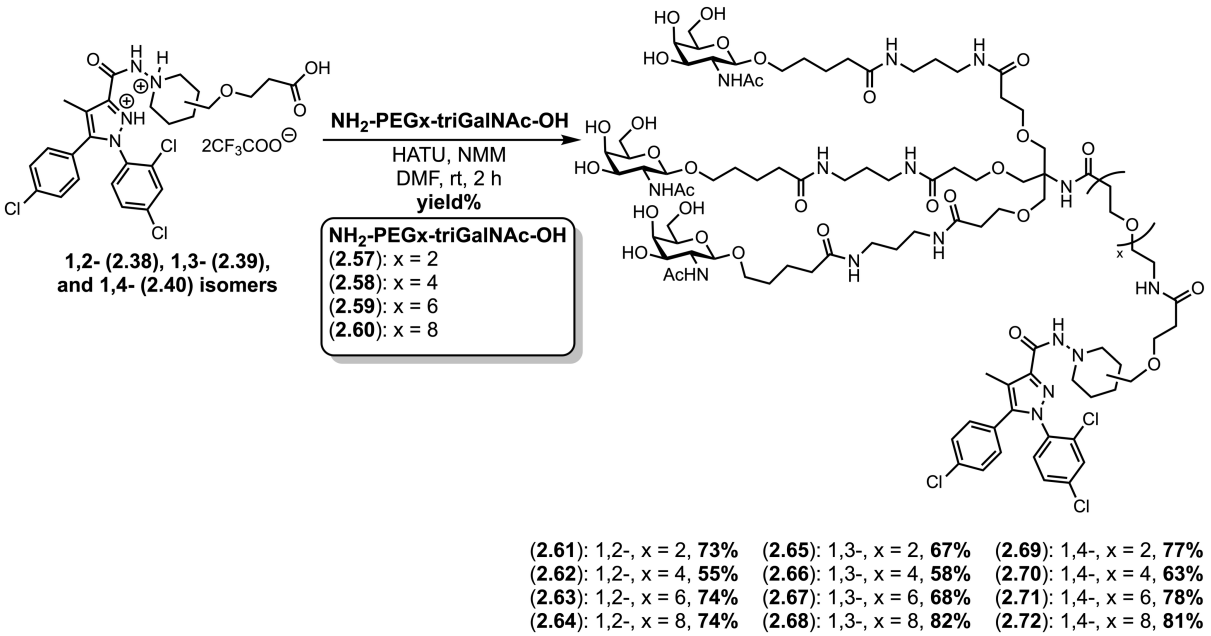


Figure 2.25. Synthesis of twelve final LYTACs; each of the four PEG-linkers were amide coupled to the three regioisomers of rimonabant acceptor.

The twelve synthetic LYTACs were first assessed for retention of CB_1 binding affinity before embarking on functional characterisation.

2.4 Assessment of CB_1 ligand interactions

2.4.1 Binding characterisation of CB_1 LYTACs

(All aspects of the binding assay were performed by Dr Monica Patel in collaboration with Prof Michelle Glass, University of Otago, New Zealand)

Receptor binding describes the interaction between a ligand and its target protein, such as CB_1. The affinity of this interaction reflects how tightly the ligand binds and can be estimated by measuring the ability of test compounds to compete with a known radioligand for receptor binding. In competition assays, the degree to which a test compound displaces radioligand binding is a relative indicator of binding affinity.

To obtain a preliminary indication of CB_1 binding, the twelve compounds were screened at two concentrations (10 μM and 100 nM) in a radioligand competition assay using [^{3}H]CP55,940 (tritium-labelled synthetic cannabinoid agonist CP55,940) as the probe.

Across the twelve LYTACs tested, displacement of [^{3}H]CP55,940 was limited, indicating poor binding to CB_1 (Figure 2.26). Alhough none achieved full displacement at 10 μM, some partial displacement of [^{3}H]CP55,940 was observed (Figure 2.26). The compound with the highest displacement at 10 μM was LYTAC-1,4-PEG 8 (**2.72**) displacing 36.6% (63.4 ± 6.9% vehicle, n = 3) of tracer binding, with compounds LYTAC-1,3-PEG 4 (**2.66**), LYTAC-1,4-PEG 4 (**2.70**) and LYTAC-1,4-PEG 6 (**2.71**) showing intermediate effects (26-34% displacement). Compounds LYTAC-1,3-PEG 6 (**2.67**), LYTAC-1,3-PEG 8 (**2.68**), and LYTAC-1,4-PEG 2 (**2.69**) showed minimal effects, displacing less than 20% of the radioligand, whilst all LYTAC-1,2 compounds (**2.61**, **2.62**, **2.63**, and **2.64**) and LYTAC-1,3-PEG 2 (**2.65**) did not show displacement distinguishable from the vehicle. At a concentration of 100 nM, displacement was negligible for nearly all compounds.

The limited displacement observed, even at 10 μM, suggests that the LYTACs bind CB_1 only weakly: at equilibrium, a low-affinity ligand cannot effectively compete with the radioligand, resulting in, at equilibrium, only a proportion of receptors being occupied. As only two concentrations were screened, accurate binding cannot be determined. However, the limited displacement observed suggests that these LYTACs are unlikely to be high-affinity CB_1 ligands.

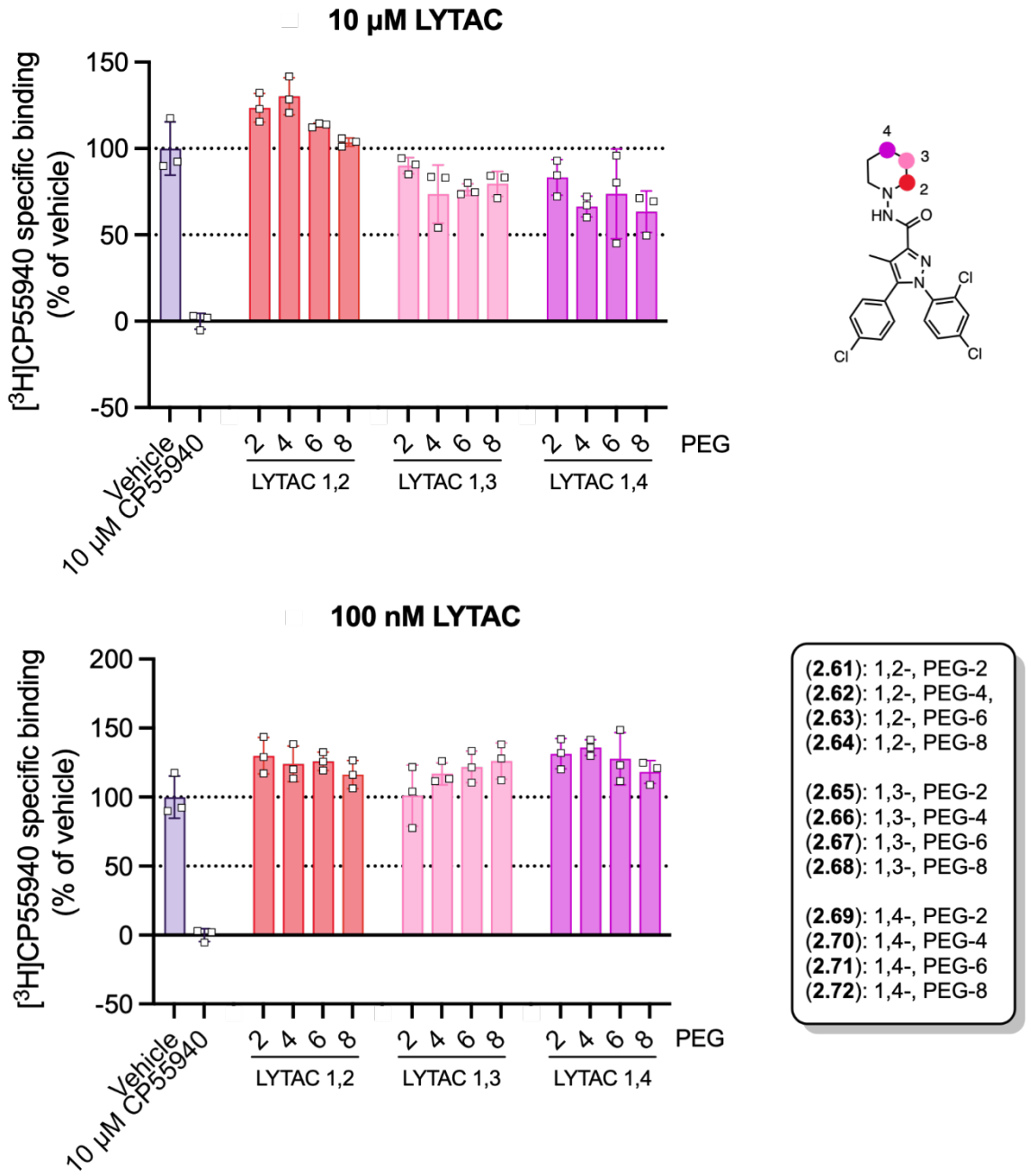


Figure 2.26. CB_1 radioligand displacement binding assay. Binding of [^{3}H]CP55,940 to recombinant CB_1 receptors was measured in the presence of LYTACs (**2.61**-**2.72**) at 10 µM and 100 nM. Vehicle and 10 mM unlabelled CP55,940 were used as negative and positive controls, respectively. Several compounds showed partial displacement at 10 µM, while minimal effect was observed at 100 nM. Data are normalised to the vehicle response (100%) and are represented as the as mean ± SEM (n = 3).

The binding data revealed clear structure-activity relationships based on both the attachment point of the linker on the rimonabant and the length of the PEG chain. LYTACs modified at the 4-position of the piperidine ring (**2.69**, **2.70**, **2.71**, and **2.72**) consistently showed higher displacement than analogues with linkers attached at the 2 or 3 position.

This suggests that the 1,4- position is the least sterically hindered position on the piperidine ring within the CB_1 receptor binding pocket. As attachment of the linker gets closer to the pyrazole core, displacement dropped substantially. This is likely due to unfavourable steric or polar interactions that interfere with receptor engagement, disrupting the optimal binding conformation of rimonabant.

Additionally, LYTACs incorporating longer PEG linker lengths (PEG 8; **2.64**, **2.68**, and **2.72**) showed consistently more displacement than the shorter chains lengths (PEG2; **2.61**, **2.65**, and **2.69**), which may suggest higher affinity for the receptor. This might suggest that a certain minimum linker length is necessary for the conjugated tri-GalNAc to extend beyond the CB_1 binding pocket and access the extracellular space, where it can engage ASGPR. Short linkers such as PEG2 may restrict flexibility, either by positioning the tri-GalNAc too close to the CB_1 protein, creating steric clashes, or by positioning it too close to rimonabant, restricting the ligand's ability to reach the binding pocket.

2.4.2 Functional characterisation

Receptor engagement is the key parameter for LYTACs, as functional modulation is of limited consequence once the receptor is degraded. However, functional assays were performed alongside binding evaluations to corroborate that the compounds interact with CB_1 in line with receptor engagement.

A FLIPR (Fluorescent Imaging Plate Reader)-based membrane-potential assay was used to measure changes in membrane potential as an indirect measure of ion movement across the cell membrane. When CB_1 is activated in an AtT20 cell, downstream signalling results in the opening of potassium channels, leading to K^+ efflux and membrane hyperpolarisation, which can be detected as a change in fluorescence. Opposingly, CB_1 inhibitors block this signal, retaining baseline fluorescence when an agonist is applied.

To screen the LYTACs, 10 μM of ligands were added to the wells prior to addition of the agonist. When the agonist was added (1 μM CP55,940), if the LYTAC is an antagonist, it would block the agonist activity by inhibiting or reducing the potassium signal, leading to a reduction in fluorescence. The degree of signal reduction was used to measure the

%response of that seen for the EC_{80} concentration of CP55,940. Lower percentages indicate stronger antagonist activity. The compounds were screened four times each, with an average percent response of EC_{80} CP55,940 shown Figure 2.27B.

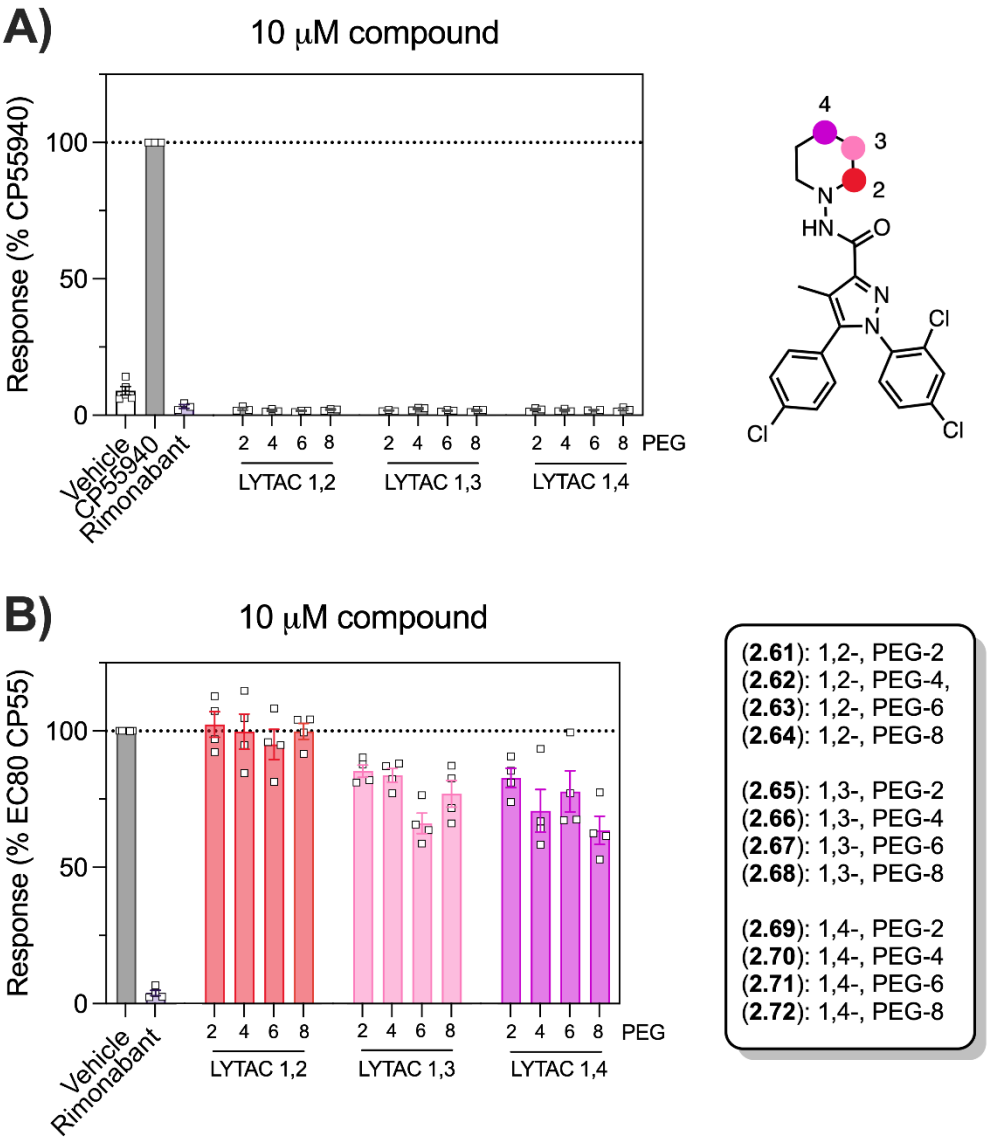


Figure 2.27. Agonist and antagonist activity of CB_1 LYTACs with varying point of linker attachment and linker length. Compounds were screened at 10 μM in both agonist (A) and antagonist modes (B). Data are normalised to the CP55,940 response (100%) and expressed as mean ± SEM (n = 4).

The data showed that the linker attached at the 1,4-position generally reduced the CP55,940 signal more than those at the 1,2- or 1,3- positions when screened at the same concentration. This trend is exemplified in the PEG-8 linker group, showing a decrease in CP55,940 signal and thus an increase in antagonist activity from PEG-8 1,2- (99.8 ± 3.0%,

n = 4), 1,3- (76.9 ± 4.9%, n = 4) and 1,4- (63.5 ± 5.1%, n = 4). Additionally, longer linkers (e.g., linker length PEG-8) showed more inhibition at 10 μM. PEG-8 attachments had consistently better displacement than PEG-2 attachments, with improvements in inhibition between PEG-8 and PEG-2 of 1,2- (2.5%), 1,3- (8.3%), and 1,4- (19.2%). Although showing some antagonist activity, the ability to decrease CP55,940 signal was low compared to rimonabant (3.9 ± 1.0%, n = 4 at 10 μM), consistent with rimonabant's low-nanomolar affinity.[176] However, similar to rimonabant, none of the LYTACs displayed any agonist activity at CB_1, indicating that the LYTACs retained the intended antagonist profile at CB_1 without inducing unwanted agonist activity.

Concentration–response curves (CRCs) were generated to further investigate the antagonist activity of the LYTACs. The data showed that attachment of the linker at the 1,4-position generally produced stronger antagonism than at the 1,2- or 1,3-positions, consistent with the earlier single-point screening. Rimonabant produced the expected inhibitory profile with an apparent half maximal inhibitory concentration (IC_{50}) in the low-nanomolar range when tested against an effective concentration producing 80% of the maximal response (EC_{80}) of CP55,940, consistent with its established high affinity for CB_1. By contrast, the PEG-8 LYTACs (1,2- (**2.64**), 1,3- (**2.68**) and 1,4- (**2.72**) substituted) showed only shallow inhibition curves, with incomplete maximal responses and no clear IC_{50} values within the concentrations tested (Figure 2.28A). These data reinforce that while linker position and length may modestly influence activity, the current LYTAC designs exhibit only weak antagonism relative to rimonabant. Within the 1,4-substituted series, antagonist activity increased notably with linker length (Figure 2.28B). PEG-2 (**2.69**) and PEG-4 (**2.70**) LYTACs resulted in low reduction in CP55,940 signalling, PEG-6 (**2.71**) showed a slight downward trend, and PEG-8 (**2.72**) gave the greatest inhibition but still failed to reach full suppression. In all cases, the curves were shallow, with IC_{50} values >10 μM, reinforcing that even at higher concentrations these LYTACs act only as weak antagonists relative to rimonabant.

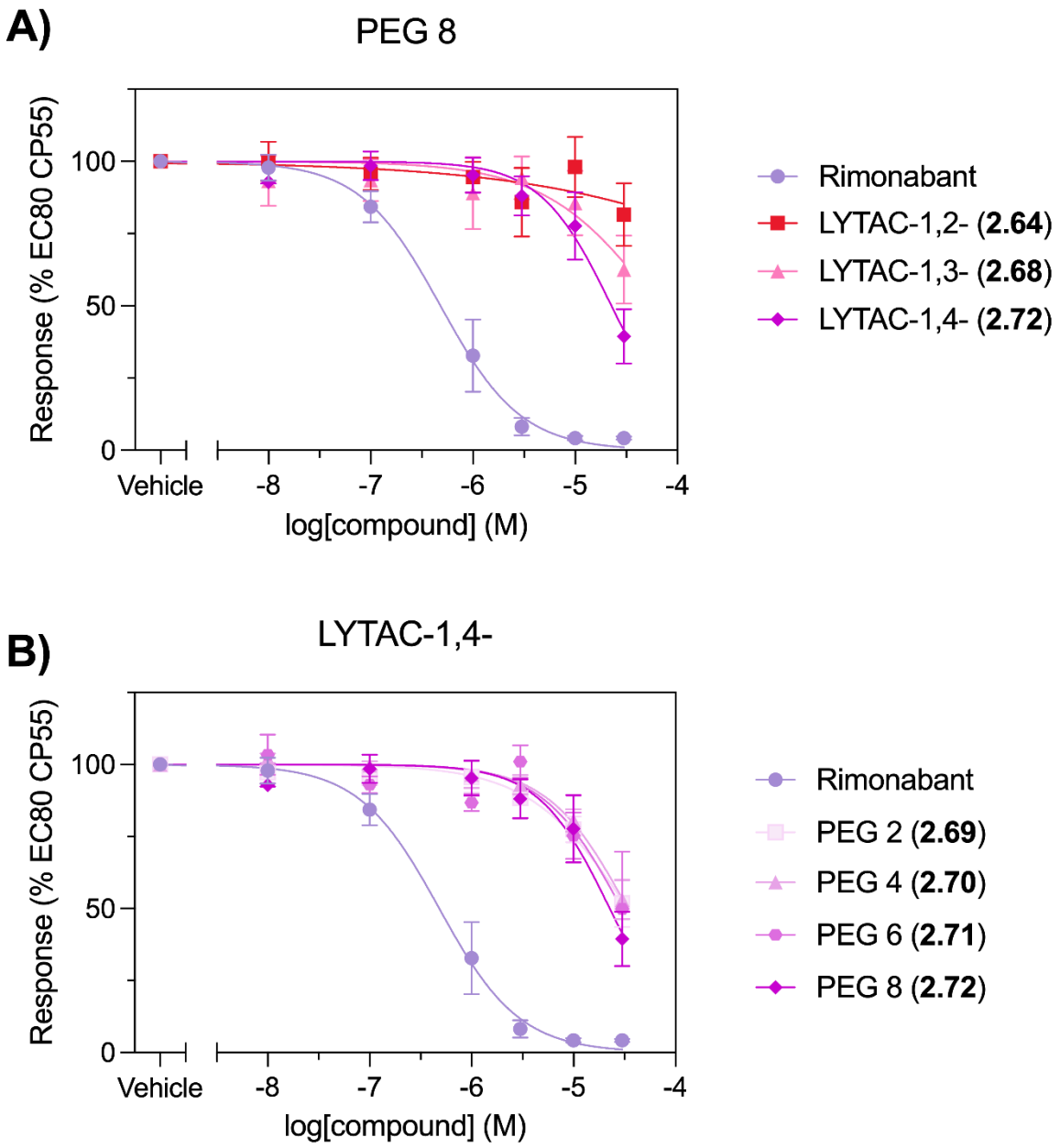


Figure 2.28. Functional activity of CB_1-targeting LYTACs in a FLIPR assay. A) CRCs for rimonabant and PEG8-linked LYTACs with varying substitution patterns measuring inhibition of CP55,940-stimulated CB_1 signalling. **B)** Comparison of LYTAC-1,4 derivatives containing PEG linkers of different lengths (PEG 2, PEG 4, PEG 6, PEG 8). Data are normalised to the EC_{80} response of CP55,940 (100%) and expressed as mean ± SEM (n = 4).

Consistent with the binding data, the functional data showed clear SAR. LYTACs modified at the 4- position of the piperidine ring (**2.69**, **2.70**, **2.71**, and **2.72**) exhibited higher antagonist displacement than those modified at the 2- or 3- positions. Additionally, longer linkers (e.g. PEG 8) showed slightly improved displacement relative to shorter linkers, supporting the conclusion that extended linkers more effectively

position the tri-GalNAc moiety beyond the CB_1 binding site. Together, both binding and functional data indicate the 4-position of the piperidine ring as the least sterically hindered site for linker attachment and show the importance of sufficient linker length for reaching the extracellular space.

The binding and functional assays provided similar insights; both interactions were weak, indicating that the structures screened were not optimal. Both showed a higher importance of linker position as opposed to linker length, favouring the 1,4 series. Across the 1,4 series, the longest linker (PEG 8, **2.72**) was shown to be both more efficacious in ligand displacement and antagonist activity than in the shorter linkers (PEG 2, **2.69**) in both screens. This suggests that while the current structures lack interaction, optimal linker positioning in addition to sufficient length is key for effective CB_1 engagement.

Despite the LYTACs produced showing some binding affinity and antagonist potency for CB_1, these results suggested that the addition of the linker and tri-GalNAc moiety as trialled here were suboptimal for binding and antagonist function, likely due to linker length, geometry, or attachment vector. While lack of function is not a restrictive feature on these molecules being used for TPD, binding affinity is a critical parameter for TPD strategies as it is indicative of target engagement. It was envisioned that longer linkers attached at the 4-position would be explored in future studies, with the goal of minimising steric clashes between the tri-GalNAc moiety and the CB_1 receptor surface.

At the same time as the work above was being performed, development of alternative ASGPR binders began, due to inherent limitations and challenges with synthesis and application of the tri-GalNAc ASGPR ligand used in the above LYTAC candidates. While tri-GalNAc enabled selective targeting of hepatocytes, its synthesis proved challenging, and the acidic lysosomal environment led to rapid degradation of the molecule, preventing it from functioning catalytically. To overcome these drawbacks, additional strategies were explored. Cyclic peptides present a particularly attractive option: they are easier to synthesise, can achieve high binding selectivity, and often display improved proteolytic stability compared to linear peptides or small molecules. To identify novel cyclic peptide binders of ASGPR, RaPID mRNA display technology, using genetic code reprogramming, was employed.

2.5 The use of RaPID mRNA display to identify macrocylic peptide binders of ASGPR

2.5.1 Peptides as ligands

Amino acids are covalently linked together by amide bonds between the carboxyl group of one amino acid and the amino group of the next to form peptides. The unique properties of the twenty-two proteinogenic amino acids can allow for the precise design of peptides.[206] Specifically, these designs can allow for high target specificity and reduced off-target effects which are commonly observed with small molecules, resulting in peptides often being considered a safer molecule class.[207]

Peptides can be either linear or cyclic. Linear peptides are composed of amino acids joined in a straight chain, having a free amino (N-terminal) and carboxyl (C-terminal) end. They are more flexible than cyclic peptides due to greater conformational freedom, making them more susceptible to enzymatic degradation. Additionally, their conformational diversity results in a higher entropic penalty upon binding, making binding less favourable compared to that of cyclic peptides. In cyclic peptides, the amino acid chain forms a loop, constrained head-to-tail, side chain to terminus, or side chain to side chain, often lacking an N- and C-terminus (Figure 2.29). Due to their comparatively constrained structure, they can shield peptide bonds from enzymatic attack, making them more resistant to enzymatic degradation.[208] The conformational restraint of cyclic peptides reduces their entropic penalty, resulting in more favourable binding.[209] Pre-organisation of the peptide also can allow for stronger and more selective binding, due to a defined orientation of functional groups.

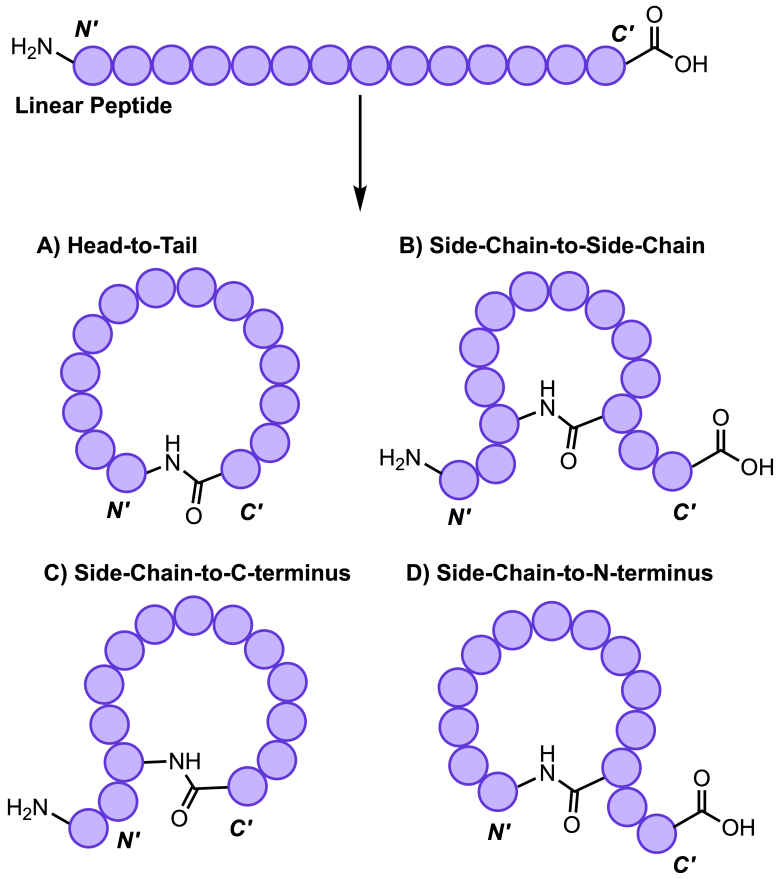


Figure 2.29. Common modes of cyclisation of linear peptides. (A) head-to-tail (amide bond between N- and C-termini); **B)** side-chain-to-side-chain; **C)** side-chain-to-C-terminus; **D)** side-chain-to-N-terminus.

Novel macrocyclic peptides[210] – defined as cyclic peptides containing twelve or more atoms within the ring – can be discovered using Random non-standard Peptide Integrated Discovery (RaPID) messenger ribonucleic acid (mRNA) display, a technology capable of identifying molecules with high affinity and specificity for a given target (Figure 2.30).[211]

RaPID is an *in vitro* selection technique that combines mRNA display[212] with the ability to incorporate non-standard (including unnatural) amino acids into macrocyclic peptides. Classical mRNA display involves using a large (10^{12} – 10^{13}) DNA library, each sequence consisting of 100-150 nucleotides. This library is transcribed into mRNA, and each mRNA molecule is then ligated to a synthetic DNA-puromycin linker at the 3' end via a phosphodiester bond. Puromycin is an aminonucleoside antibiotic that inhibits protein synthesis by mimicking the 3' end of aminoacylated transfer RNA (tRNAs). These mRNA-puromycin linkages are subject to *in vitro* ribosomal translation, initiating translation at

the start codon and catalysing amide bond formation between adjacent amino acids to form the peptide chain according to the mRNA template. This chain elongation of the peptide continues until the ribosome reaches the 3' end of the mRNA, where it encounters the puromycin moiety. The puromycin accepts the C-terminal residue of the growing peptide, resulting in a covalent peptide-puromycin-mRNA fragment, a key feature that enables sequencing and identification of high affinity peptides. These fragments are incubated with a target molecule such as a protein, receptor, or antigen, allowing for the selective retention of high-affinity binders, while non-binders are washed away. These bound fragments are then reverse transcribed into complementary DNA, which is amplified to regenerate the library for additional rounds of selection. This iterative process allows for the select identification of peptides with high affinity and specificity for the target.[213]

RaPID mRNA display, although operating similarly to classical mRNA display, offers unique advantages.[211] DNA library design can include initiator codons for non-standard amino acids, such as chloroacetylated amino acids, as well as a cysteine codon downstream to enable macrocyclization. Transcription and puromycin linker attachment occur similarly to classical mRNA display. However, tRNA charging, the process of attaching an amino acid to its corresponding tRNA, occurs *via* "[207]flexizymes", ribozymes that charge tRNAs with non-standard amino acids such as sulfotyrosine (sY, **2.73**), D-amino acids, and β-serine GalNAc.[214] This allows for translation to incorporate non-standard amino acids into the peptide chain. The chloroacetyl group reacts with a downstream cysteine to form a stable thioether macrocycle, resulting in a macrocyclic peptide. As in classical mRNA display, the puromycin accepts the C-terminal residue of the growing peptide, resulting in a covalent peptide-puromycin-mRNA fragment. Incubation with a target, washing, reverse transcription and amplification occur as with classical display. The advantages of RaPID over classical mRNA display include the expansion of chemical diversity by incorporation of non-canonical amino acids and generation of more stable macrocyclic peptides.

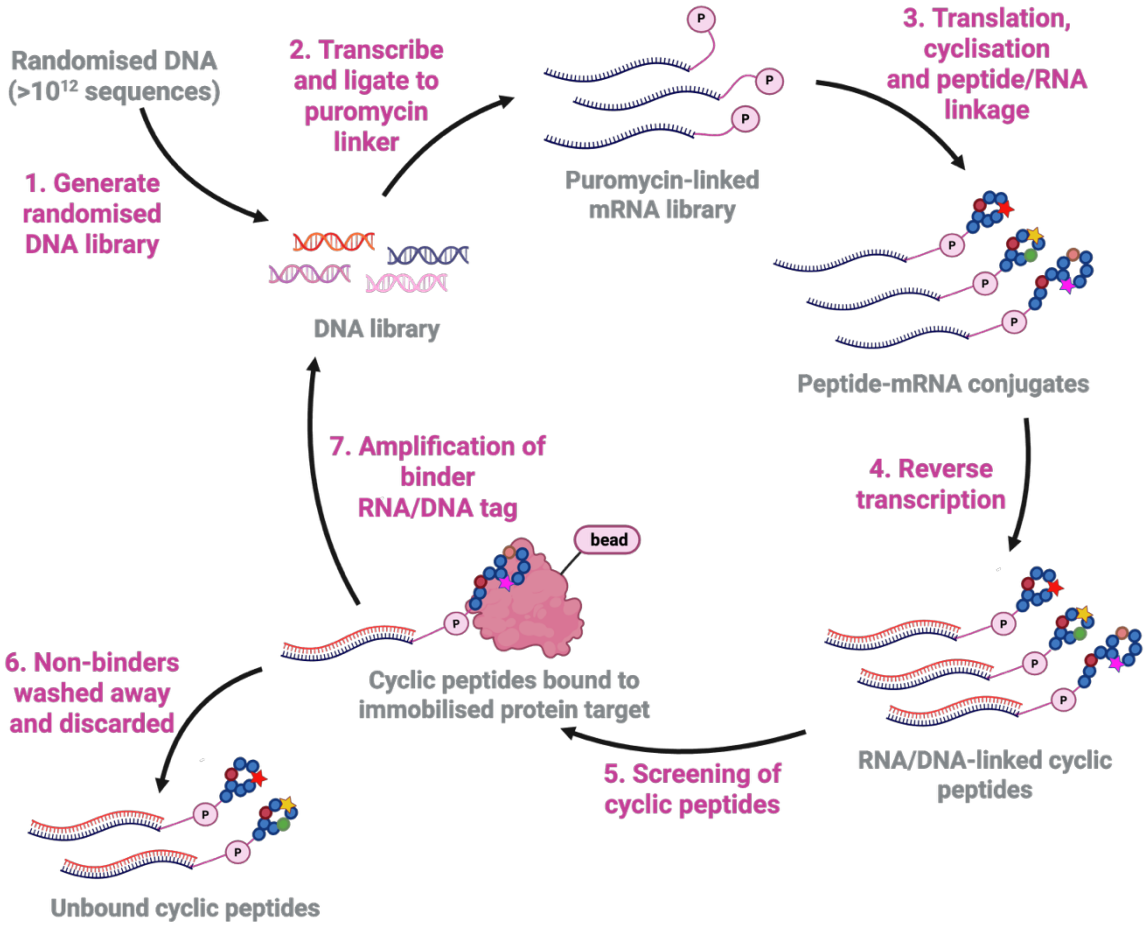


Figure 2.30. RaPID (Random nonstandard Peptides Integrated Discovery) system. A randomised DNA library is transcribed, linked to puromycin, and translated to generate cyclic peptide–mRNA conjugates. After reverse transcription, cyclic peptides are screened against an immobilised protein target; non-binders are discarded, and bound sequences are recovered and amplified for iterative selection. Figure made with biorender.com.

2.5.2 Identification of RaPID hits

(All aspects of the RaPID screen were performed by Dr Jessica Zhong, Payne Research Group, The University of Sydney)

Two series of RaPID selections, with or without genetic code reprogramming of sY were performed to identify macrocyclic peptide binders of ASGPR.[211] All selections began from semi-random DNA libraries, which were transcribed into mRNA and ligated to a synthetic DNA-puromycin linker at the 3' end. These linkages were subjected to *in vitro* ribosomal translation, resulting in a covalently linked peptide-puromycin-mRNA conjugate. The

mRNA was then reverse transcribed to form a complementary DNA (cDNA) -mRNA complex, that stabilises the conjugate and prevents RNase-mediated degradation.

Cyclisation results from genetic code reprogramming of the tRNA recognising the start codon from N-terminal formyl-methionine to *N*-chloroacetyl-L-tyrosine (L- screen), or *N*-chloroacetyl-D-tyrosine (D- screen). Formation of the macrocyclic peptide occurs following translation; S_N2 reaction of a nucleophilic thiol from a downstream cysteine residue occurs rapidly with the introduced electrophilic chloroacetyl group. Genetic code reprogramming was also used to incorporate sY at defined positions throughout the peptide. Following translation and repeated counter-selections to remove peptides that bound non-specifically to the immobilisation matrix, the peptide-puromycin-mRNA library was panned against biotinylated recombinant ASGPR immobilised on streptavidin-coated beads. Unbound or weakly bound peptides were washed away, allowing the remaining bound peptide-mRNA conjugates to be enriched. The associated cDNA was recovered, and polymerase chain reaction (PCR)-amplified. The resulting double stranded DNA was used as the template for subsequent rounds of selection (seven total rounds), progressively enriching the library for peptides with high specificity and affinity for ASGPR. The top ten enriched peptides from the L-screen and D-screen (Table 2.2) are reported below. It is of note that a mixture of sequences both with and without sY residues were obtained; the incorporation of sY via genetic code reprogramming does not eliminate the ability to obtain residues lacking a sY, yet interestingly, a little under half of the top ten residues identified contained a sY residue. A second sequencing of the first RaPID screen was also completed, and any additional peptides identified from this were included in the selected peptides listed in Table 2.3.

Table 2.2. Top ten peptides identified from L- and D-selections in sY reprogrammed screen. **X** = sY, 1 = ClAc, y = D-tyrosine. Enrichment data reported as a % of total peptides identified from RaPID.

L-Tyr top 10 peptides from the 7th round		
Enrichment	**Name**	**Sequence**
29.499	AL-01	1YRILIKYTVYFLKLKC
10.177	AL-02	1YTWELPSWYLEHYFPTC
8.850	AL-03	1YSAXLYRVNEKVYLVC
4.130	AL-04	1YRILIKYTVYILKLKC
3.835	AL-05	1YRILIKYTVYYLKLKC
2.507	AL-06	1YSAXLYRVNDKVYLVC
1.032	AL-07	1YGIRIYFXNSKYXIVC
0.885	AL-08	1YPHRLIWSYLVPLLRC
0.885	AL-09	1YRILIKYTVYFXKLKC
0.737	AL-10	1YLYRVNEKVYLVC

D-Tyr top 10 peptides from the 7th round		
Enrichment	**Name**	**Sequence**
5.957	AD-01	1yFLCSXHAAIWHXXC
5.106	AD-02	1yKSYLWKTKFINEC
4.681	AD-03	1yILWCHXTRCYLLKC
3.830	AD-04	1yITCLNTYVESFC
2.553	AD-05	1yTWELPSWYLEHYFTTC
2.553	AD-06	1yXCYXXAWTFHYNAQVC
2.553	AD-07	1yLCXXXTWFWHRLLRC
2.128	AD-08	1yQVIFIXKHRPHIYWC
2.128	AD-09	1yFTILNRNRHSYLVYLC
1.702	AD-10	1yRCIIIRQAKFLYPAC

Table 2.3. Combined top thirty peptides identified from L- and D- selections in sY reprogrammed screen. **X** = sY, 1 = ClAc, y = D-tyrosine. Enrichment data reported as a % of total peptides identified from RaPID.

L-Tyr top peptides		
Enrichment	**Name**	**Sequence**
31.395	BL-01	1YLFVYRSRTYLAC
3.530	BL-04	1YSFWLPQWYKTHYC
0.976	BL-06	1YRALLYRVNEKVYLVC
29.236	BL-07	1YRILIKYTVYFLKLKC
1.453	BL-08	1YSALLYRVNEKVYLVC
0.295	BL-09	1YQVLLRSRFVFC
1.363	BL-10	1YIWYKSNAWYLQINC
0.752	BL-22	1YLWREGNAVYLVC
0.752	BL-23	1YRAXLYRVNEKVYLVC
0.334	BL-24	1YRALRYVRRSVFLILLC

D-Tyr top peptides		
Enrichment	**Name**	**Sequence**
35.608	BD-12	1yTWELPSWYLEHYFTTC
25.569	BD-13	1ySFWVPQWYKTHYC
1.333	BD-14	1yTYIYRNTIFIVQC
0.627	BD-15	1yITCLNTYVESFC
0.314	BD-16	1yRILIKYTVYFLKLKC
11.451	BD-17	1ySALLYRVNEKVYLVC
0.471	BD-18	1yKSYLWKTKFINEC
0.426	BD-19	1yIWYKSNAWYLQINC
0.314	BD-20	1yKIFFASYRNNKITSWC
0.95	BD-21	1yANLLYHHNGRLYLWC
4.009	BD-26	1yTWELPSWYLEHYFPTC
1.794	BD-27	1yXLCLXXNYWGTWATC
1.603	BD-28	1yKFLIYRTSAFRIXLKC
0.883	BD-30	1yLIFRXNYPRIIVIHAC

2.5.3 Synthesis of RaPID hits

The peptides were synthesised using 9-fluorenylmethyloxycarbonyl (Fmoc) solid-phase peptide synthesis (SPPS) (Figure 2.31). For the synthesis of the peptides described herein, an Fmoc-Rink-amide linker was employed. Functionalisation of the polystyrene resin with Fmoc-Rink-amide facilitates the synthesis of C-terminally amidated peptides. The resin is designed for Fmoc-SPPS, where the Fmoc group is removed under basic conditions during the initial deprotection step, allowing the incoming Fmoc-protected C-terminal amino acid to be coupled to the N-terminal free amine of the resin-bound elongated peptide. Iterative cycles of Fmoc-removal, coupling, and capping, which ensures any unreacted amine groups that did not couple will not participate in further chain growth, resulted in elongation of the hit peptide sequences yielding the desired peptides in moderate yields. Following coupling of the N-terminal L- or D- tyrosine and subsequent deprotection, chloroacetic acid was coupled. Upon complete elongation the linear peptides were removed from the resin with concomitant global deprotection *via* an $A_{AL}1$-type cleavage with a TFA/water mixture, together with triisopropylsilane (iPr$_3$SiH) as a cation scavenger.

The resultant peptides were treated with a solution of iPr$_2$EtN in DMSO (5:95, *v/v*), promoting cyclisation *via* an intramolecular S_N2 reaction between the cysteine thiol and the chloroacetyl moiety yielding the desired thioether macrocyclic peptides. The peptides were then purified by reverse-phase high-performance liquid chromatography (RP-HPLC).

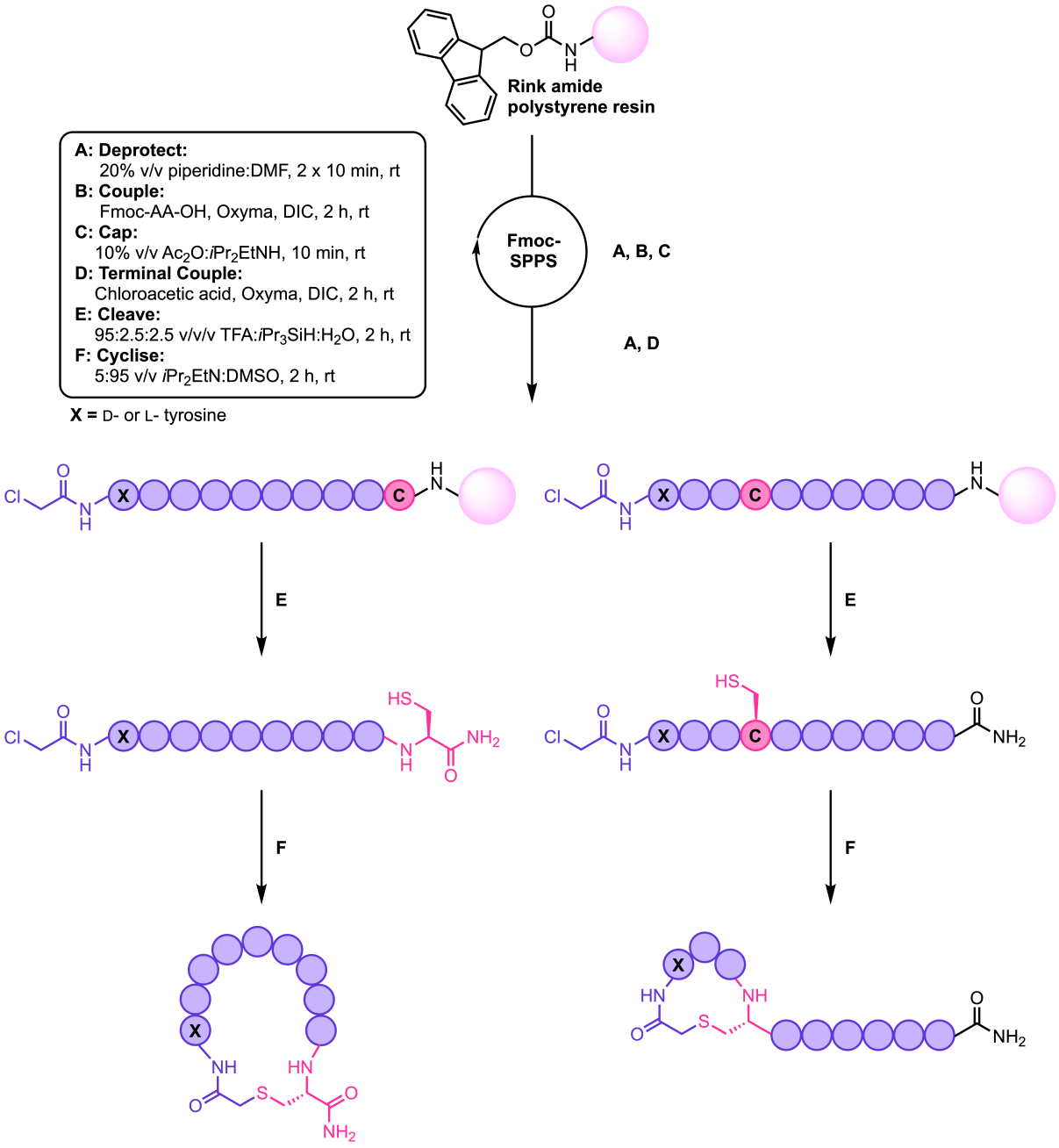


Figure 2.31. Synthesis of cyclic peptides *via* Fmoc-SPPS followed by cleavage and cyclisation steps. Synthesis of cyclic peptides bearing both a C-terminal cysteine and internal cysteine are shown.

For peptides that contained sY residues, a neopentyl protected sY building block (**2.73**), compatible with Fmoc-SPPS was incorporated into Fmoc-SPPS. This was prepared as outlined in Figure 2.32.

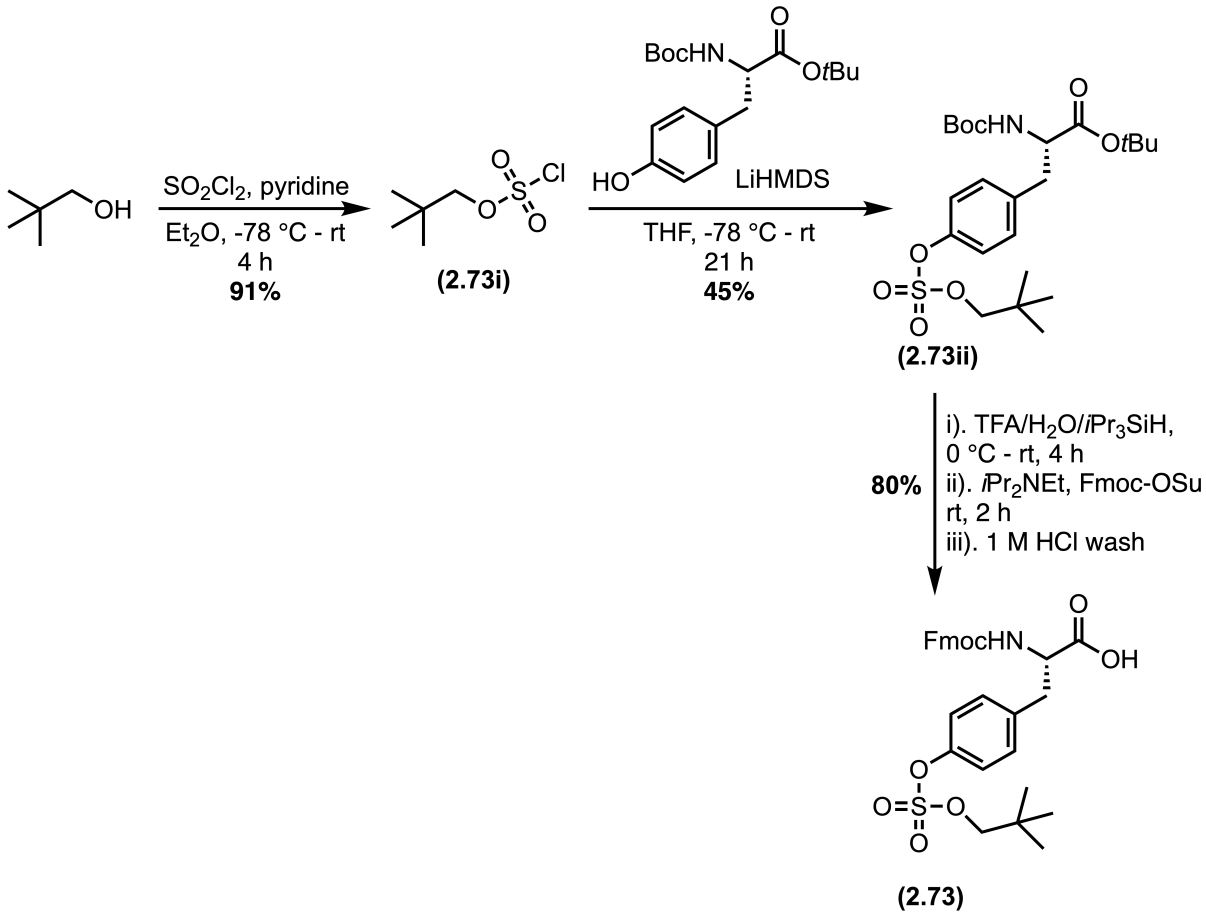


Figure 2.32. Synthesis of neopentyl protected sulfotyrosine (**2.73**) from Fmoc-Tyr-O*t*Bu.

The peptides were synthesised analogously to the route described in Figure 2.31. Following cyclisation, the peptides were purified by RP-HPLC and subjected to neopentyl deprotection conditions to unmask the negatively charged sY residues on the macrocycle (Figure 2.33).

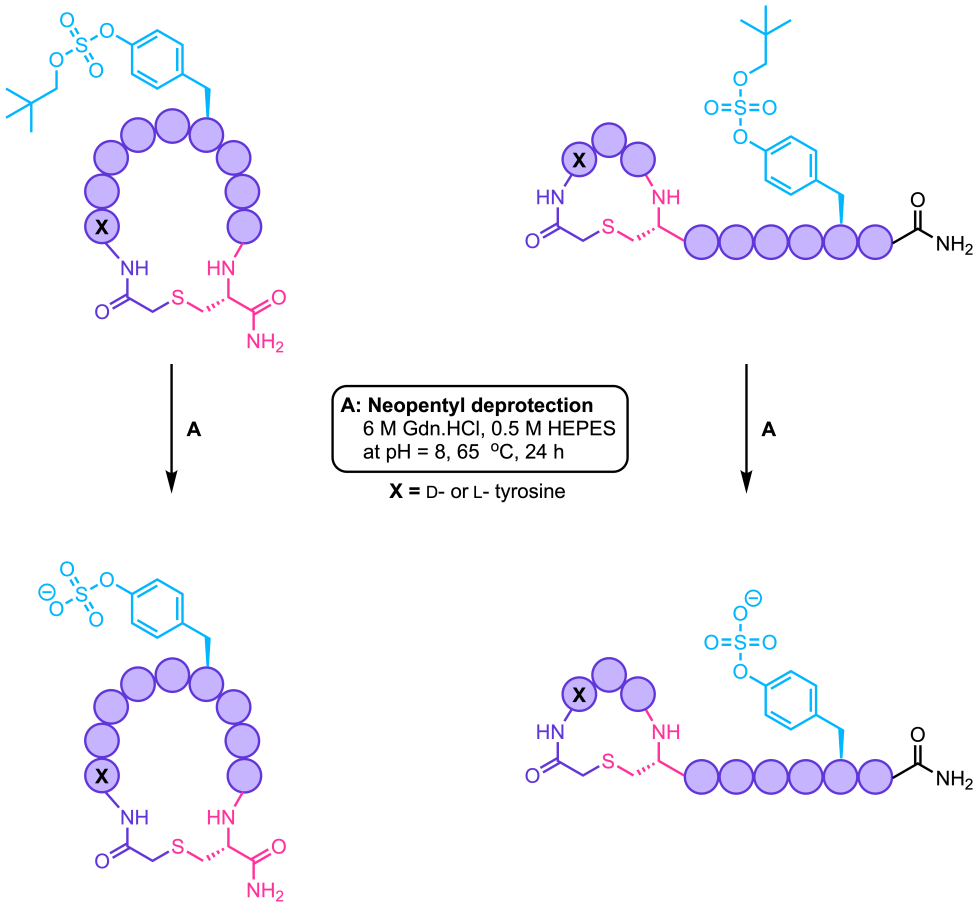


Figure 2.33. Neopentyl deprotection of sulfated tyrosine residues.

Twenty-five of the peptides were successfully synthesised with yields ranging from 1 to 23% (Table 2.4). Figure 2.34 shows the chemical structure of three of the peptides synthesised, highlighting a peptide cyclised from a terminal cysteine (**2.88**), an example of cyclisation with a terminal internal cysteine (**2.79**), and a peptide containing a sY residue (**2.75**).

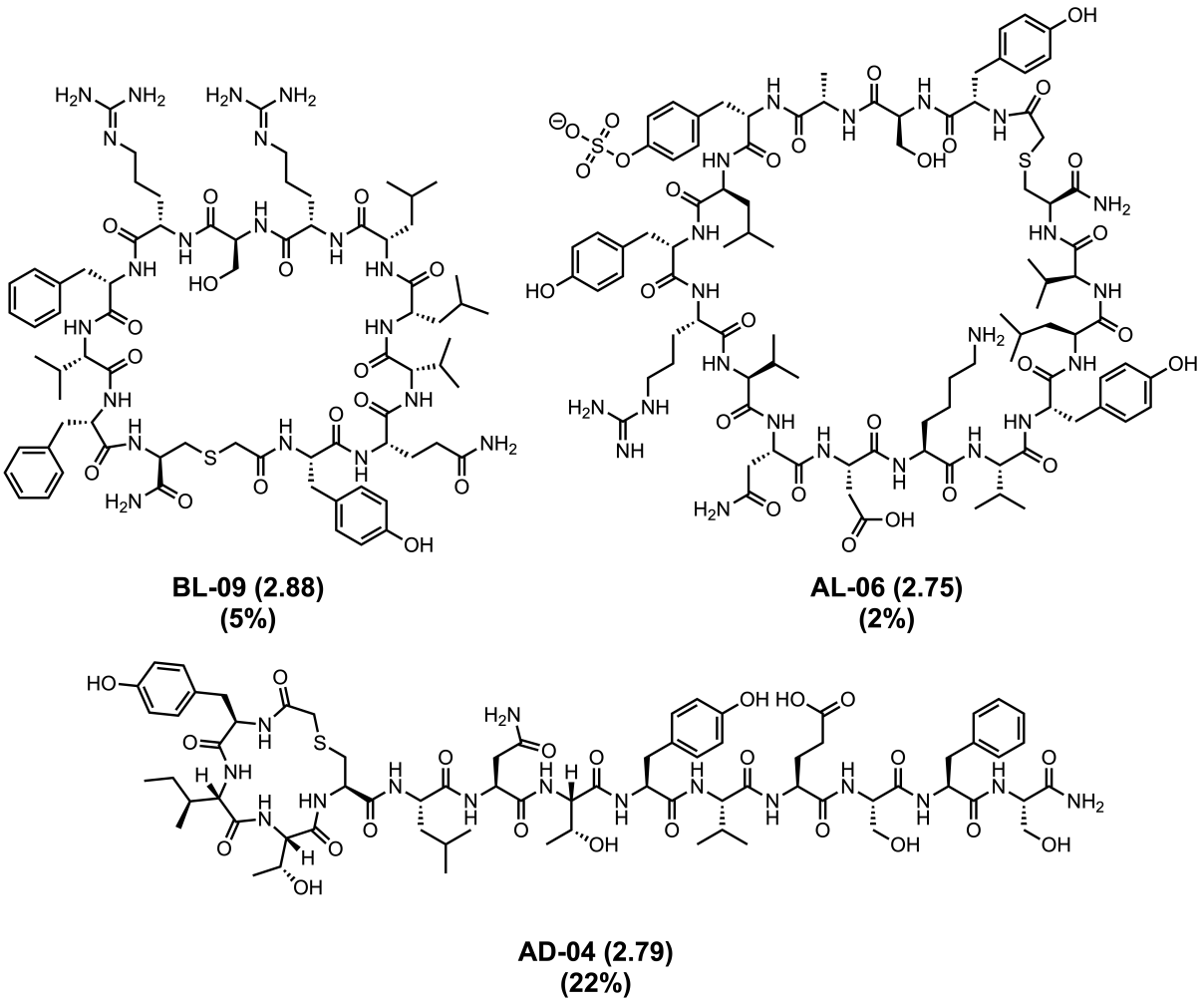


Figure 2.34. Structures of three of the peptides synthesised. BL-09 (**2.88**) shows a peptide cyclised from a terminal cysteine, AL-06 (**2.75**) highlights a peptide containing a sY residue, and AD-04 (**2.79**) is an example of cyclisation with an internal cysteine residue.

Table 2.4. Sequences and yields for the peptides synthesised from both screen A and screen B. 1 = ClAc, **X** = sY, y = D-tyrosine. NB: that the yields quoted are based upon the resin loading of the first amino acid and are therefore over 24-38 synthetic steps.

Peptide	Sequence	Yield (%)
AL-02 (**2.74**)	1YTWELPSWYLEHYFPTC	11
AL-06 (**2.75**)	1YSA**X**LYRVNDKVYLVC	2
AL-08 (**2.76**)	1PHRLIWSYLVPLLRC	11
AL-10 (**2.77**)	1YLYRVNEKVYLVC	12
AD-02 (**2.78**)	1yKSYLWKTKFINEC	23
AD-04 (**2.79**)	1yITCLNTYVESFS	22
AD-05 (**2.80**)	1yTWELPSWYLEHYFTTC	3
AD-08 (**2.81**)	1yQVIFI**X**KHRPHIYWC	3
AD-09 (**2.82**)	1yFTILNRNRHSYLVYLC	4
AD-10 (**2.83**)	1yRCIIIRQAKFLYPAS	5
BL-01 (**2.84**)	1YLFVYRSRTYLAC	10
BL-04 (**2.85**)	1YSFWLPQWYKTHYC	7
BL-07*(**2.86**)	1YRILIKYTVYFLKLKC	2
BL-08* (**2.87**)	1YSALLYRVNEKVYLVC	2
BL-09 (**2.88**)	1YQVLLRSRFVFC	5
BD-12* (**2.89**)	1yTWELPSWYLEHYFTTC	1
BD-13 (**2.90**)	1ySFWVPQWYKTHYC	7
BD-14 (**2.91**)	1yTYIYRNTIFIVQC	6
BD-16* (**2.92**)	1yRILIKYTVYFLKLKC	1
BD-17 (**2.93**)	1ySALLYRVNEKVYLVC	2
BD-20* (**2.94**)	1yKIFFASYRNNKITSWC	1
BD-21* (**2.95**)	1yANLLYHHNGRLYLWC	2
BL-22 (**2.96**)	1YLWREGNAVYLVC	10
BL-24* (**2.97**)	1YRA**X**LRYVRRSVFLILLC	1
BD-26* (**2.98**)	1yTWELPSWYLEHYFPTC	2

2.5.4 Biological Assessment of RaPID peptides

The binding of the selected peptides to ASGPR was evaluated using surface plasmon resonance (SPR, Biacore). Biotinylated-ASGPR was first immobilised on the sensor

surface, with the peptides flowed over at increasing concentrations to monitor real-time association and dissociation events. This allowed for determination of affinity constants, as outlined in Table 2.5.

Across the hits, the majority of peptides did not display measurable binding affinities; responses were either too weak for reliable fitting or indistinguishable from background. Several peptides did show detectable affinity; however, these interactions were not strong, falling in the low-to-mid micromolar range. The best binder was BL-09 (**2.88**), with a dissociation constant (K_D) of 5.19 μM, followed closely by BD-20 (**2.94**, 5.67 μM), and BD-21 (**2.95**, 7.80 μM). Despite being the best binders of the set, they still fall short of the nanomolar affinities generally considered desirable for receptor targeting. Other peptides, such as BD-13 (**2.90**, 17.8 μM), showed weak binding, while sequences BL-04 (**2.85**), BD-12 (**2.89**), BL-17 (**2.93**), and BD-22 (**2.96**) produced very weak affinities (>30 μM).

The poor success of this library may reflect the specificity of ASGPR, which is optimised to recognise terminal galactose or GalNAc residues. Without carbohydrate structures, peptide-receptor interactions rely on weak, opportunistic binding. Additionally, ASGPR typically engages multivalent glycoproteins, in which several sugar residues bind simultaneously across multiple receptor subunits. These multivalent interactions produce an avidity effect, in which multiple weak sugar-receptor interactions combine to create overall strong binding. The peptides screened likely only have a single point of contact and cannot benefit from avidity. A combination of these factors likely explain why binding was restricted to the low micromolar range. Resultingly, subsequent peptide synthesis was directed towards GalNAc-incorporated RaPID peptide libraries, which were developed by the Payne group. Incorporation of carbohydrate moieties allows exploitation of ASGPR's natural glycan preference, potentially providing ligands with improved affinity and more biologically relevant interactions.

Table 2.5. Steady state affinities measured for peptides against ASGPR. N.B. = no binding measured at 10 μM, 1 = ClAc, **X** = sY, y = D-tyrosine.

Peptide	Sequence	Steady state affinity
AL-02 (**2.74**)	1YTWELPSWYLEHYFPTC	N.B.
AL-06 (**2.75**)	1YSA**X**LYRVNDKVYLVC	N.B.
AL-08 (**2.76**)	1PHRLIWSYLVPLLRC	N.B.
AL-10 (**2.77**)	1YLYRVNEKVYLVC	N.B.
AD-02 (**2.78**)	1yKSYLWKTKFINEC	N.B.
AD-04 (**2.79**)	1yITCLNTYVESFS	N.B.
AD-05 (**2.80**)	1yTWELPSWYLEHYFTTC	N.B.
AD-08 (**2.81**)	1yQVIFI**X**KHRPHIYWC	N.B.
AD-09 (**2.82**)	1yFTILNRNRHSYLVYLC	N.B.
AD-10 (**2.83**)	1yRCIIIRQAKFLYPAS	N.B.
BL-01 (**2.84**)	1YLFVYRSRTYLAC	N.B.
BL-04 (**2.85**)	1YSFWLPQWYKTHYC	>30 μM
BL-07*(**2.86**)	1RILIKYTVYFLKLKC	N.B.
BL-08* (**2.87**)	1SALLYRVNEKVYLVC	N.B.
BL-09 (**2.88**)	1YQVLLRSRFVFC	5.19 μM
BD-12* (**2.89**)	1yTWELPSWYLEHYFTTC	>30 μM
BD-13 (**2.90**)	1ySFWVPQWYKTHYC	17.8 μM
BD-14 (**2.91**)	1yTYIYRNTIFIVQC	N.B.
BD-16* (**2.92**)	1yRILIKYTVYFLKLKC	N.B.
BD-17 (**2.93**)	1ySALLYRVNEKVYLVC	>30 μM
BD-20* (**2.94**)	1yKIFFASYRNNKITSWC	5.67 μM
BD-21* (**2.95**)	1yANLLYHHNGRLYLWC	7.80 μM
BL-22 (**2.96**)	1YLWREGNAVYLVC	>30 μM
BL-24* (**2.97**)	1YRA**X**LRYVRRSVFLILLC	N.B.
BD-26* (**2.98**)	1yTWELPSWYLEHYFPTC	N.B.

*= peptides synthesised in parallel by Mr. Beiyuan Cui.

2.5.5 Identification of RaPID hits incorporating β-Ser-GalNAc

(All aspects of the RaPID screen were performed by Dr Jessica Zhong, Payne Research Group, The University of Sydney)

RaPID selections were performed similarly to those discussed in 2.5.2. Genetic code reprogramming was used to incorporate the synthetic dipeptide *N*-chloroacetyl-Ser(β-GalNAc)-Phe at the N-terminus of all peptide sequenecs in the library, as ASGPR typically recognises β-linked Gal and GalNAc.[45] Peptides were selected based on enrichment data and family groupings, outlined in Table 2.6.

Table 2.6. β-Ser-GalNAc incorporated peptides identified by RaPID, with respective enrichments. 1 = ClAc, 2 = β-Ser-GalNAc.

Enrichment	Name	Sequence
49.426	Gal-01	12FALNYYPLWYRKHYLKC
0.148	Gal-02	12FALSYYPLWYRKHYLKC
0.869	Gal-03	12FIPLWYTLYYDSNAC
0.410	Gal-05	12FNSINRYPQWYIVNYLC
0.099	Gal-06	12FNWELPSWYLEHYFTTC
0.182	Gal-08	12FTLNYYPLWYRKHYLKC
0.159	Gal-11	12FYQIDHTDLWRIIFSRC
0.091	Gal-12	12FYWHPSWYRKHYLKC
0.074	Gal-15	12FDDEKDYGPSSC
0.211	Gal-16	12FALNYFPLWYRKHYLKC
0.074	Gal-18	12FVIWYRKHYLKC

2.5.6 Synthesis of Fmoc-β-Ser-GalNAc$(OAc)_3$-OH building block:

Before embarking on the synthesis of the most enriched glycopeptides from the RaPID mRNA selection, peracetylated-β-Ser-GalNAc building block (**2.99**) first required synthesis for direct incorporation in Fmoc-SPPS of the targets. (Figure 2.35). To this end, galactosamine hydrochloride (**2.100**) was first subjected to a *N*-Troc protection, followed by peracetylation of the alcohols to provide **2.101**. The *N*-Troc protection is essential, as

the amine cannot be acetylated prior to glycosidation due to the neighbouring group participation (NGP) of the *N*-acetyl group at the 2 position, forming a stable oxazoline and preventing glycosidation without harsh conditions that could damage the donor or acceptor.[215] The anomeric alcohol of **2.101** was selectively deacetylated using acetic acid and ethylenediamine (EDA).[216] The anomeric acetate is activated by the neighbouring ring oxygen through the exo-anomeric effect. The exocyclic oxygen of the C1-*O*-acetyl group can back donate into the σ* orbital of the C1-O ring bond. This n→σ* interaction increases the electrophilicity of the *O*-acetyl carbonyl carbon, making the anomeric acetate uniquely susceptible to nucleophilic attack *via* aminolysis. Under the mild and buffered conditions of EDA·AcOH, the nucleophile attacks the acetyl carbonyl, removing the Ac group and revealing the hemiacetal. As the other *O*-acetates on the sugar lack this increased electrophilicity, they react much more slowly, giving selective deacetylation at C1. The α-trichloroacetimidate (**2.102**) was formed selectively from reaction with trichloroacetonitrile and 1,8-diazabicyclo[5.4.0]undec-7-ene (DBU). The exclusive formation of the α-trichloroacetimidate arises from the reversibility of imidate formation and the stereoelectronic stabilisation present in the α-isomer. In the β-imidate, poor orbital alignment precludes effective anomeric stabilisation from the n(O-ring)→σ* of C1-O(exocyclic). Resultingly, the N-H of the imidate is more acidic, allowing for elimination back to an alcohol in a strong base such as DBU. This equatorial alcohol is in equilibrium with its axial counterpart, which reacts to form an α-imidate. Contrastingly, the α-imidate has antiperiplanar orbital alignment with the lone pairs on the ring oxygen, allowing anomeric stabilisation. This results in increased electron density on the acetimidate oxygen, rendering the N-H less acidic and making elimination less favourable, resulting in the α anomer as the major product.[217]

Glycosidation of trichloroacetimidate **2.102** was performed using Fmoc-Ser-O*t*Bu and Lewis acid catalyst TMSOTf, resulting in exclusive β-glycoside (**2.103**) formation. Activation of trichloroacetimidate donors with TMSOTf generate an oxocarbenium ion intermediate, reacting in and S_N1-like manner. Selectivity arises from neighbouring-group participation from the C2 Troc groups, forming a transient 1,2-oxazoline intermediate that blocks the α-face and directs attack to provide the β-glycoside. Stereoselectivity is further reinforced by the departing trichloroacetimidate anion

shielding the α-face of the intermediate, biasing nucleophilic attack from the opposite side to form predominantly the β-glycoside. Troc deprotection was performed using zinc in acetic anhydride, proceeding *via* reductive cleavage of a C-Cl bond to liberate the free amine which is trapped as the *N*-acetyl (**2.104**) by acetic anhydride. The final step of the synthesis was *tert*-butyl removal to reveal to free acid (**2.99**), ready for coupling to the peptide fragment. It should be noted that the *O*-acetyl groups were left protected to prevent any cross reactivity with the peptide fragment prior to coupling and cyclisation. Overall, the glycosylamino acid building block was synthesised in five steps from D-galactosamine with an overall yield of 40% and in >1 g quantity.

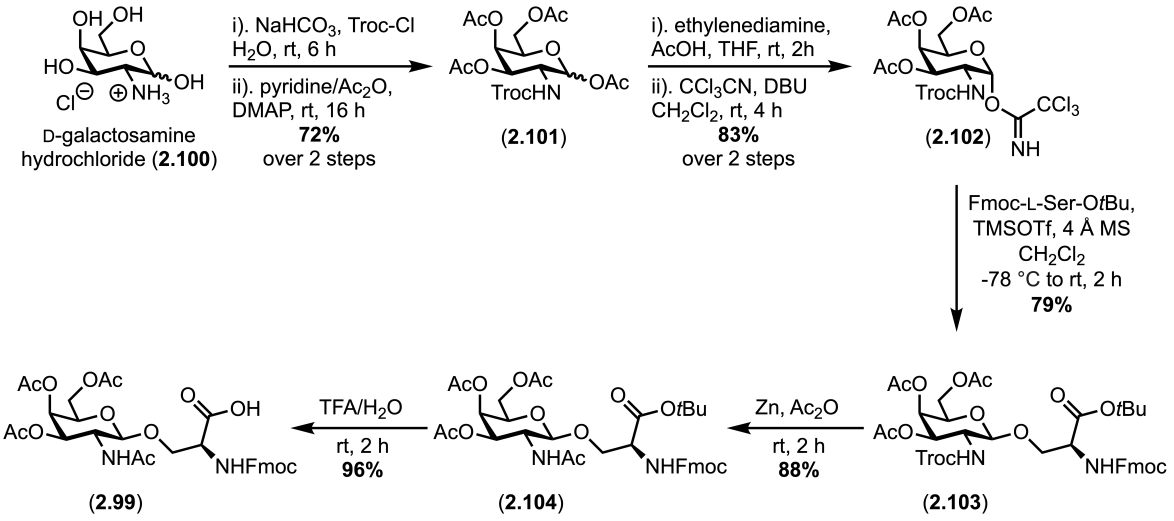


Figure 2.35. Synthesis of peracetylated β-Ser-GalNAc (**2.99**) from galactosamine hydrochloride (**2.100**).

2.5.7 Synthesis of cyclic glycopeptide RaPID hits incorporating β-Ser-GalNAc

For each of the target glycopeptides, the peptide sequences from Phe to the C-terminus (e.g. FALNYYPLWYRKHYLKC for Gal-01) were first synthesised using automated Fmoc-SPPS on Rink amide resin as outlined in Figure 2.31. Following elongation to the penultimate Phe residue, β-Ser-GalNAc was manually coupled to the peptide fragments. Due to standard SPPS conditions resulting in epimerisation or elimination of the glycan,[218] and the precious nature of the synthetic glycosyl amino acid (*vide infra*), the residue was coupled by hand, followed by the addition of chloroacetic acid. The elongated peptides were next Fmoc deprotected, followed by treatment with a solution of Fmoc-Ser(β-GalNAc(OAc)$_3$)-OH (**2.99**), HATU, 1-hydroxybenzotriazole (HOBt), and

2,4,6-trimethylpyridine in DMF.[218] The resin-bound GalNAc-containing glycopeptide fragment was next subjected to a further round of Fmoc removal and then treated with a solution of chloroacetic acid, Oxyma, and DIC in DMF to couple on the C-terminal chloroacetyl residue. These conditions were used due to standard SPPS conditions (HATU, HOBt) resulting in epimerisation or elimination of the glycan.[218]

The resin was then subjected to resin cleavage and global side chain deprotection with TFA/*i*Pr_3SiH/H_2O, precipitated, and cyclised with *i*Pr_2NEt in $MeCN/H_2O$. The cyclisation was completed in $MeCN/H_2O$ as opposed to DMSO to facilitate direct lyophilisation so deacetylation of the peracetylated-GalNAc could be completed without prior purification. The lyophilised peptide was dissolved in MeOH, and NaOH was added until the pH was 10 to deacetylate the peptide. The use of NaOH in MeOH allowed for simple quenching with acetic acid, and evaporation of MeOH to provide the crude cyclic glycopeptides ready for RP-HPLC purification. The cyclic glycopeptides were purified *via* RP-HPLC, with yields between 0.3 and 4% based on initial resin loading, as outlined in Table 2.7. It is worth noting that the yields were notably lower than the peptides lacking the GalNAc residue, in part due to some β-elimination observed upon deacetylation.

Table 2.7. β-Ser-GalNAc incorporated peptides identified by RaPID, with respective yields. 1 = ClAc, 2 = β-Ser-GalNAc.

Name	Sequence	Yield (%)
Gal-01 (**2.105**)	12FALNYYPLWYRKHYLKC	1
Gal-02 (**2.106**)	12FALSYYPLWYRKHYLKC	2
Gal-03 (**2.107**)	12FIPLWYTLYYDSNAC	2
Gal-05 (**2.108**)	12FNSINRYPQWYIVNYLC	0.4
Gal-06 (**2.109**)	12FNWELPSWYLEHYFTTC	4
Gal-08 (**2.110**)	12FTLNYYPLWYRKHYLKC	2
Gal-11 (**2.111**)	12FYQIDHTDLWRIIFSRC	0.3
Gal-12 (**2.112**)	12FYWHPSWYRKHYLKC	1
Gal-15 (**2.113**)	12FDDEKDYGPSSC	3
Gal-16 (**2.114**)	12FALNYFPLWYRKHYLKC	2
Gal-18 (**2.115**)	12FVIWYRKHYLKC	1

2.5.8 Biological Assessment of GalNAc containing RaPID peptides

As in section 2.5.4, the binding of the selected peptides to ASGPR was evaluated using SPR. Peptide concentrations were quantified by measuring absorbance at 280 nm on a NanoDrop spectrophotometer, using each peptide's calculated extinction coefficient to convert absorbance to concentration prior to screening. Affinity constants are outlined in Table 2.8.

As with the non-glycosylated libraries screened, the majority of peptides did not display measurable binding. Gal-01 (**2.105**), the most enriched peptide, and Gal-02 (**2.106**) only showed weak binding. Only peptide Gal-11 (**2.111**) (Figure 2.36) showed detectable affinity, with a dissociation constant (K_D) of 4.3 ± 1 μM. However, the peptide still did not reach the desired nanomolar affinity for receptor targeting. All other peptides showed no binding at 10 μM.

Table 2.8. Sequences and binding affinities for β-Ser-GalNAc containing peptides. N.B. = no binding measured at a concentration of 10 μM, 1 = ClAc, 2 = β-Ser-GalNAc.

Name	Sequence	Steady state affinity
Gal-01 (**2.105**)	12FALNYYPLWYRKHYLKC	>30 μM
Gal-02 (**2.106**)	12FALSYYPLWYRKHYLKC	>30 μM
Gal-03 (**2.107**)	12FIPLWYTLYYDSNAC	N.B.
Gal-05 (**2.108**)	12FNSINRYPQWYIVNYLC	N.B.
Gal-06 (**2.109**)	12FNWELPSWYLEHYFTTC	N.B.
Gal-08 (**2.110**)	12FTLNYYPLWYRKHYLKC	N.B.
Gal-11 (**2.111**)	12FYQIDHTDLWRIIFSRC	1.1 μM
Gal-12 (**2.112**)	12FYWHPSWYRKHYLKC	N.B.
Gal-15 (**2.113**)	12FDDEKDYGPSSC	N.B.
Gal-16 (**2.114**)	12FALNYFPLWYRKHYLKC	N.B.
Gal-18 (**2.115**)	12FVIWYRKHYLKC	N.B.

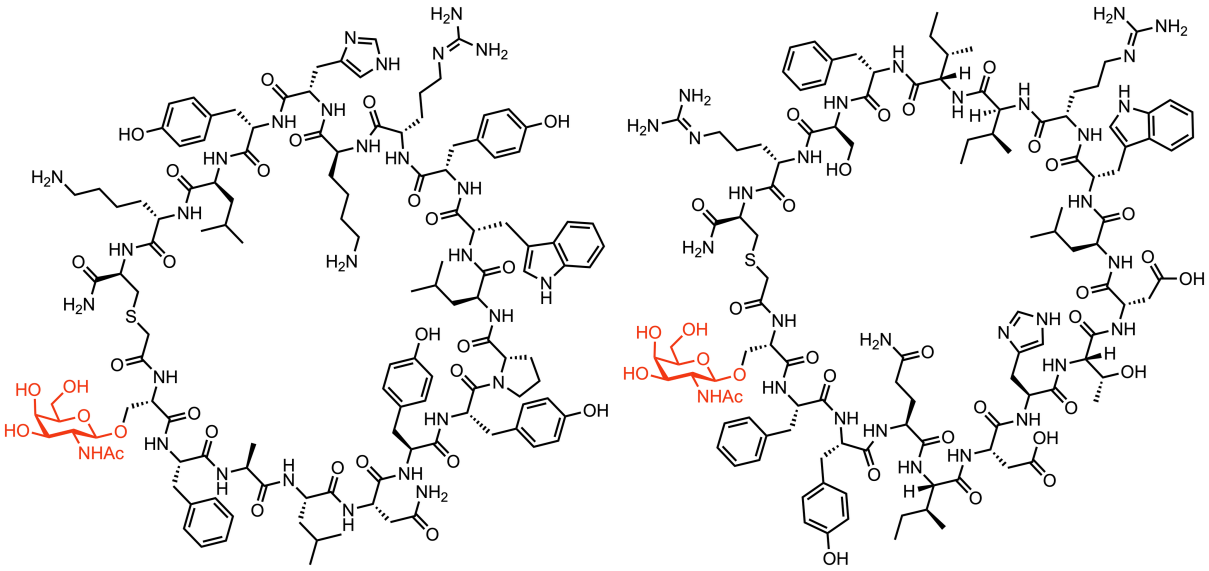


Figure 2.36. Chemical structures of peptides Gal-01 (**2.105**), the most enriched, and Gal-11 (**2.111**), the highest affinity binder. The GalNAc moiety is shown in red.

These results are consistent with a single GalNAc residue being an inherently weak ligand Recognition by ASGPR is dependent on Ca^{2+} coordination of the 3-equatorial and 4-axial hydroxyl group motif of GalNAc within the carbohydrate recognition domain (CRD).[219] It is possible that in most of the cyclised peptides, the sugar was buried in the peptide scaffold or projected at an unfavourable angle, resulting in poor interaction with the binding pocket. It is plausible that Gal-11 presents its GalNAc in a more solvent-exposed conformation, allowing for CRD recognition and resulting in measurable binding. In Gal-11, the resides surrounding the GalNAc are relatively permissive. Polar, medium-sized residues like Tyr, Gln, and Asp (which are near GalNAc in Gal-11) likely do not pack as tightly around a glycosylated serine as bulky hydrophobic residues or Pro/Trp pairs do. In comparison, peptides in which Pro, Trp/Tyr pairs are present near the GalNAc can restrict how the Ser can project, either from hydrophobic collapse around the sugar or by sterically caging it.

As neither series of peptides showed nanomolar binding affinity, further identification of potential peptidic or glycopeptidic ASGPR binders needs to be completed, focussing on both valency and presentation of GalNAc. To improve affinity, screens could be conducted using incorporation of two or more GalNAc residues into each macrocycle or

using short linkers to project the sugars from the peptide surface. Once higher-affinity peptides are discovered, they will provide access to an alternative ASGPR binder for incorporation into novel degraders, including the CB_1 targeting LYTACs described in this thesis.

2.6 Conclusion and Future Work

This chapter described the synthesis of potential lysosome-targeting chimeras (LYTACs) as a novel strategy for CB_1 degradation in hepatocytes for treatment of liver diseases. Specifically, a library of rimonabant-derived CB_1 ligands conjugated to ASGPR binder tri-GalNAc *via* PEG linkers were successfully synthesised and screened for receptor binding and biological activity. Clear structure-activity relationships were elucidated, with the 4-position of the piperidine ring being identified as the site linker binding that retained the most affinity for CB_1. Additionally, longer PEG linkers were shown to improve both binding affinity and functional antagonism. Despite showing some measurable CB_1 activity, these conjugates were much less potent relative to rimonabant, highlighting the steric and conformational challenges of bifunctional molecules. These findings provide proof of concept that ASGPR-mediated degradation of CB_1 is synthetically achievable and biologically possible, allowing for future investigation into a liver-specific therapeutic approach to liver disease.

In parallel, macrocyclic peptides identified through RaPID mRNA display were investigated as alternate ligands to tri-GalNAc for ASGPR. Peptides offer advantages over tri-GalNAc, with easier synthesis, enhanced lysosomal stability, and the potential for higher selectivity. Two series of peptides were synthesised, some containing non-canonical amino acids in the RaPID screen. These included sulfotyrosine and β-Ser-GalNAc. The highest affinity peptide, Gal-11, displayed micromolar affinity for ASGPR.

Future work will seek to build on these results by aiming to improve both halves of the bifunctional design. For the CB_1-targeting functionality, optimisation should focus on exploring extended linkers (such as PEG-12, 24, and 36), additional modification points on rimonabant, variable attachment functionality (i.e. linear ether vs amide), or alternative high-affinity CB_1 binders. For ASGPR targeting, further identification of

peptides by RaPID mRNA display could be conducted. These screens could include incorporation of multiple glycan residues to increase avidity for the receptor or increasing spacing of glycan from peptide surface to increase exposure. Additionally, the bulky and hydrophobic Phe residue could be switched out and the screen performed with a smaller and more polar GalNAc containing dipeptide instead.

Taken together, the findings described in this chapter demonstrate both the feasibility of engineering CB_1-targeting LYTACs for liver-specific degradation and expand the range of ASGPR ligands through peptide discovery. This work lays the foundation for both therapeutic targeting of CB_1 in liver disease and the broader application of novel peptide ligands as ASGPR binders.

Chapter 3: Bacterial Glycans and Recognition

3.1 Background on Bacteria

Bacteria are microscopic, single-cell organisms that are classed as prokaryotes. As such, they lack a true nucleus and membrane-bound organelles. Having emerged over 3 billion years ago, bacteria are among the earliest lifeforms and have come to inhabit nearly every environment on earth, including soil, water, extreme environments, as well as within and on living organisms, including plants, animals, and humans. This ubiquity, combined with their ability to reproduce and adapt rapidly, makes them among the most resilient life forms. While the majority of bacterial species are either harmless or beneficial to humans, some are pathogenic and responsible for diseases.[220]

Infection with pathogenic bacteria can lead to severe symptoms and death without treatment.[221] Bacterial infections result in over 7 million deaths annually and, as such, pathogenic bacteria represent one of the greatest threats to public health. Tuberculosis (TB), caused by *Mycobacterium tuberculosis* (*Mtb*), is the deadliest bacterial disease.[221] In 2023, an estimated 10.8 million people were infected with *Mtb*, with 1.3 million deaths resulting from TB.[221] A range of other bacterial species are responsible for life-threatening infections across both community and hospital-acquired settings. The most significant of these are listed in Table 3.1.

Table 3.1. Common bacterial species and their related diseases.[222,223]

Bacterium	Related Disease
Escherichia coli (*E. coli*)[224]	Urinary tract infections (UTIs), biliary infections, gastroenteritis (toxigenic strains), neonatal meningitis, sepsis
Salmonella species[225]	Gastroenteritis, typhoid fever, sepsis
Neisseria gonorrhoeae[226]	Urethritis, cervicitis, pelvic inflammatory disease
Campylobacter species (e.g. *C. jejuni*)[227]	Gastroenteritis, Guillain-Barré syndrome (immune mediated)
Legionella pneumophila[228]	Legionnaires' disease, Pontiac fever

Enterococcus faecium[229]	Endocarditis, UTIs, sepsis, intra-abdominal infections
Staphylococcus aureus[230]	Skin and soft tissue infection, pneumonia, sepsis, infective endocarditis, septic arthritis, surgical site infections
Klebsiella pneumoniae[231]	Pneumonia, UTIs, sepsis, liver abscess
Acinetobacter baumannii (A. baumannii)[232]	Ventilator-associated pneumonia, wound infections, sepsis
Pseudomonas aeruginosa[233]	Hospital-acquired pneumonia, wound infections, UTIs, chronic lung infections

These pathogens are variable not only in the diseases they cause, but also in the underlying structural features on and within the bacterial cell. These features strongly influence the interaction of bacteria with their host in addition to their susceptibility to treatment.

3.1.1 Structure and Classification of Bacteria

Bacteria exhibit diverse structural architectures that influence their survival, pathogenicity, and response to antimicrobials. Unlike eukaryotes, they generally contain a relatively simple internal structure but are enclosed by protective surface layers that vary between species (Figure 3.1). For instance, many bacteria are surrounded by a capsule (similar to the glycocalyx) composed of CPS, which shields the cell from immune detection, desiccation, and killing by antimicrobial peptides and phagocytes.[26] The ability of the capsule to mask underlying surface antigens protects the cell against host immunity and is a major determinant of virulence.[234]

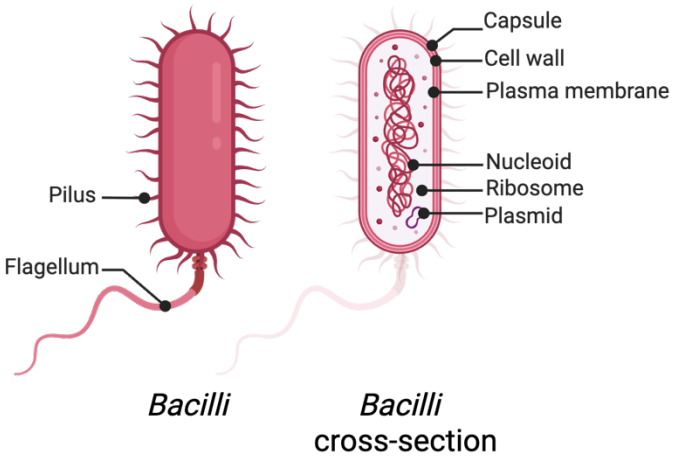


Figure 3.1. Structure of a *Bacillus*-shaped bacterium. Schematic representation of a rod-shaped bacterium showing common structural features. Not all bacteria possess every feature shown: capsules and flagella are variably present across species, and some bacteria lack a cell wall altogether. Figure made with biorender.com.

Beneath the capsule (when present) is the cell wall, a more rigid structure made of peptidoglycan that provides mechanical strength and helps to maintain the cell's shape.[235] However, some bacteria lack a cell wall altogether, instead relying on other structural adaptations for survival. Inside the cell wall (or directly beneath the capsule in wall-less species) is the plasma membrane, which controls the movement of substances in and out of the cell. Beneath these outer layers is the cytoplasmic region, containing essential components such as the nucleoid, where the bacterial chromosome is located, ribosomes for protein synthesis, plasmids, and circular DNA molecules which carry genes encoding for enzymes that can inactivate antibiotics.[236]

Externally, bacteria can have pili and flagella. Pili are hair-like appendages found on the surface of many bacteria. Pili are composed of peptides and, in some bacteria, can be glycosylated.[237] They facilitate adhesion to surfaces and can mediate transfer of plasmid DNA from one bacterium to another. Pili are often antigenic; however, some bacteria can change which pilin proteins are displayed to avoid immune detection.[238] Flagella are long, whip-like protein filaments that are attached to the cell membrane via a rotary motor complex, and behave like helical propellers that provide motility.[239] The ability of the motor to reverse the direction of rotation confers motility through a process known as 'run and tumble' (Figure 3.2).[240] Specifically, counterclockwise (CCW) motion projects

the cell forward (aka 'run'), and clockwise (CW) motion causes the bacterium to tumble in a random direction. In the presence of a favourable stimulus such as glucose, the flagella rotate counterclockwise, allowing longer runs and fewer tumbles in the direction of the attractant. With a repellent such as low pH, bacteria increase tumbling frequency to reorientate and escape the unfavourable stimulus.[241]

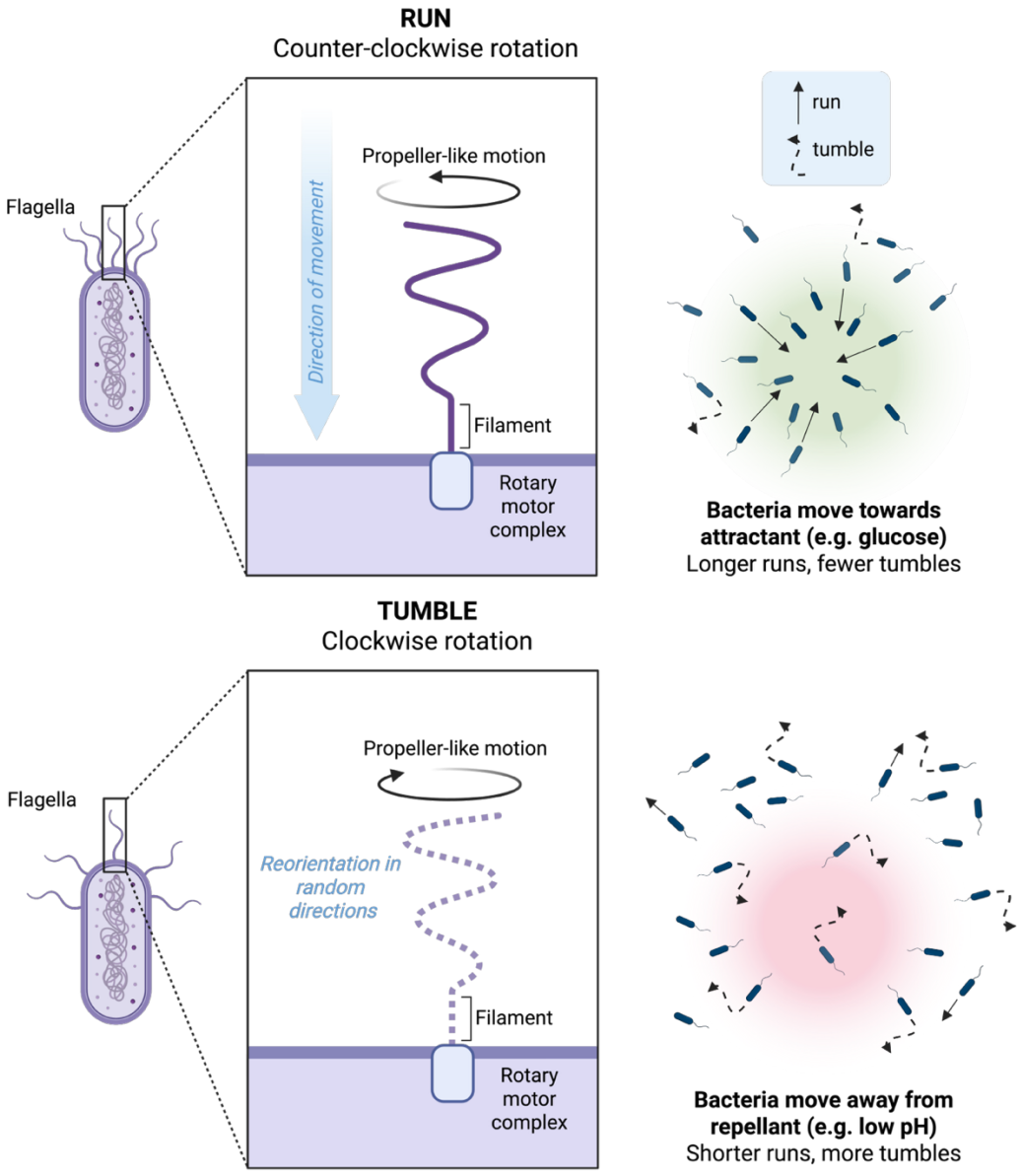
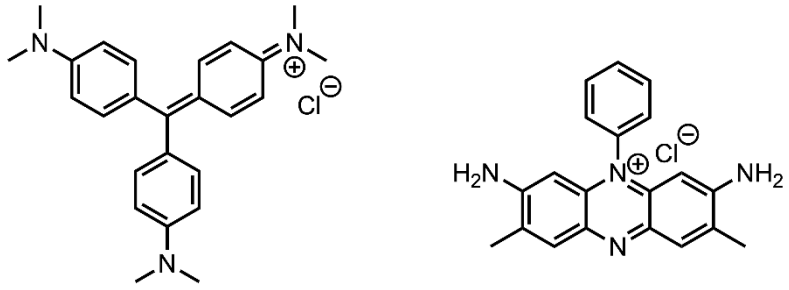


Figure 3.2. Flagellar motility and chemotaxis. Counterclockwise (CCW) rotation bundles the flagella, creating a smooth forward motion, known as a "run". Clockwise (CW) rotation disrupts this bundle, causing the bacterium to "tumble" and reorientate. In the presence of an attractant such as glucose, bacteria undergo longer runs with fewer tumbles, promoting movement towards the attractant. When exposed to a repellent such as low pH, tumbling frequency increases, resulting in shorter runs and more tumbles, reorientating the bacteria away from the repellent. Figure made with biorender.com.

In addition to their roles in motility, flagella also contribute to surface adhesion, biofilm formation, and secretion of effector molecules that modulate host processes.[242] In certain species, flagellins are glycosylated with unique glycans that are important for correct flagellar function.[243]

Bacteria are broadly classed into three groups relating to their shapes: spherical shapes being *cocci*, rod shapes being *bacilli*, and spiral shapes being *spirochetes*.[244] Additionally, bacteria can be classed into two distinctive classes, Gram-negative and Gram-positive. This distinction is based on differences in bacterial cell wall structure, revealed by a staining technique known as the Gram stain.[245] Developed in 1884 by Danish bacteriologist Hans Christian Gram, the Gram stain results in bacteria either retaining a crystal violet-iodine complex dye (**3.1**) and appearing purple, whilst others do not and instead take up a pink counterstain, Safranin (**3.2**) (Figure 3.3).



Crystal Violet (3.1)
Stains Gram-positive bacteria purple

Safranin (3.2)
Stains Gram-negative bacteria pink

Figure 3.3. Structures of cationic dyes Crystal Violet and Safranin, used in the Gram stain technique used to classify bacterial cells based on their cell wall structure.

The difference in staining observed in the Gram stain procedure is due to fundamental differences in bacterial cell wall architecture.[246] Gram-positive bacteria are characterised by a thick, multilayered peptidoglycan matrix, which constitutes the main structural component of the cell wall.[247] This dense polymeric network traps the crystal violet dye during the staining process, resulting in the cells being a deep purple under light microscopy (Figure 3.4). Gram-negative bacteria are distinguished by a more complex, multilayered cell surface that significantly differ from the simpler structure of the Gram-positive bacteria.[248] Their cell surface consists of three main components: the inner cytoplasmic membrane, a thin peptidoglycan layer, and a unique outer membrane

(Figure 3.4). During the decolourisation step, the outer membrane is dissolved by the solvent (commonly acetone or ethanol) and the peptidoglycan layer is too thin to retain the violet-iodine complex dye. Once the outer membrane is gone, application of Safranin, a smaller dye, occurs without resistance.[249]

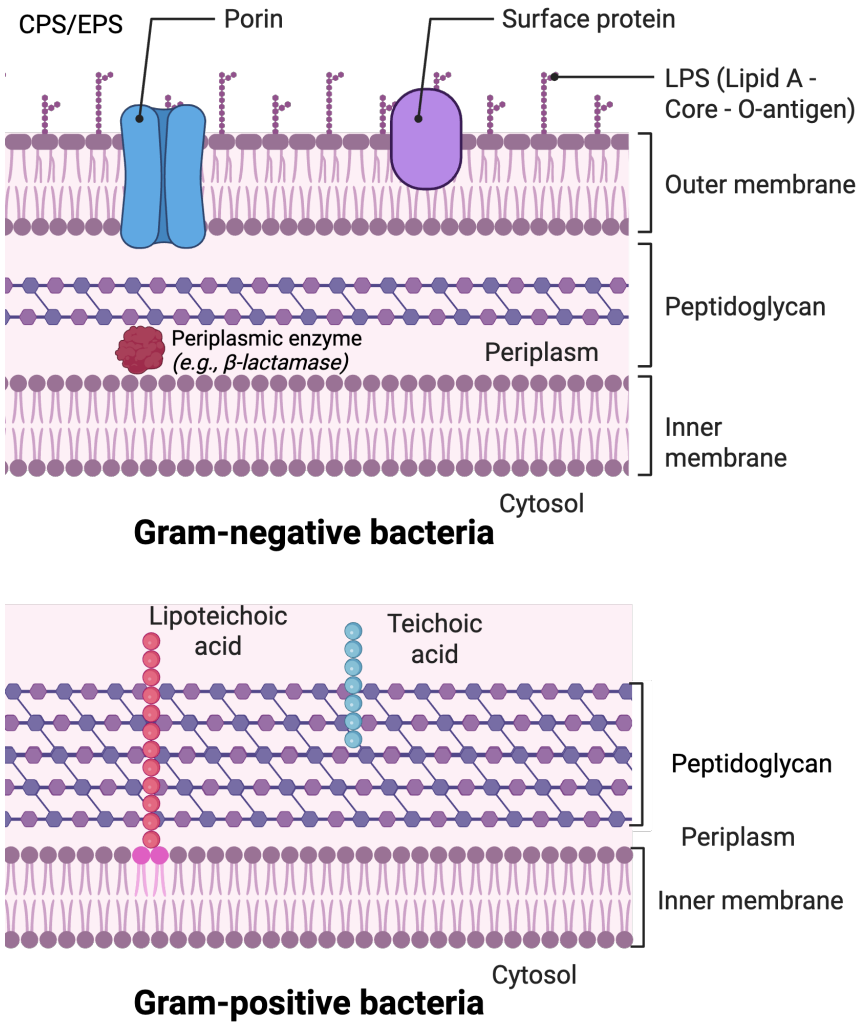


Figure 3.4. Gram-negative bacteria (left) consist of an inner membrane, a thin peptidoglycan layer, and an outer membrane rich in lipopolysaccharides (LPS), capsular polysaccharides (CPS), and/or extracellular polymeric substances (EPS). The outer membrane contains porins and surface proteins, allowing selective permeability and immune evasion. A defined periplasmic space contains enzymes such as β-lactamases, which contribute to antibiotic resistance. Gram-positive bacteria (right) lack an outer membrane but have a thick, multilayered peptidoglycan wall embedded with teichoic and lipoteichoic acids, contributing to cell wall structure and host immune interactions. Gram-positive bacteria contain a much smaller periplasm and do not house periplasmic enzymes.[250] Figure made with biorender.com.

These structural differences in the cell surface layers not only influence staining properties but also impact pathogenicity, immune recognition, antibiotic susceptibility,

and drug permeability, making Gram classification a clinically and biologically significant distinction. The outer membrane is a key feature of Gram-negative bacteria. It contains LPS molecules in its outer layer, playing critical roles in immune evasion and virulence. LPS extend into the extracellular space, contributing to structural integrity by stabilising the membrane and creating a permeability barrier.[251,252] The O-antigen, consisting of long repeating glycan units, extends outward and acts as an immune shield by masking other antigens from host recognition. Additionally, O-antigens are extensively structurally diverse across serotypes, allowing for bacteria to evade immune memory.[253] These features result in the LPS being both essential for virulence and are also highly immunogenic due to their repetitive carbohydrate motifs. The outer membrane acts as a selective permeability barrier, limiting the entry of hydrophobic compounds, including many antibiotics.[254] Porin proteins embedded in the outer membrane allow for passive diffusion of small hydrophilic molecules, while active efflux pumps can expel a wide range of antimicrobial agents.[255] Additionally, the periplasmic space of Gram-negative bacteria concentrates β-lactamase enzymes, allowing efficient inactivation of β-lactam antibiotics as they diffuse through the cell envelope. In Gram-positive bacteria, β-lactamases produced are secreted extracellularly, diluting their activity, with resistance in these bacteria more commonly resulting from structural modification of the bacterial cell wall.[256]

Many of the most life threatening bacterial pathogens, including *E. coli*, *Salmonella*, *Campylobacter*, *Klebsiella*, *Acinetobacte*r, and *Pseudamonas*, are Gram-negative species.[257] In contrast, only a smaller subset including *Staphylococcus* and *Enterococcus* are Gram-positive. This disparity is also reflected in the disproportionate number of challenging to treat infections attributed to Gram-negative bacteria in both community and hospital-acquired (nosocomial) infections. The structural features of Gram-negative bacteria, notably their protective outer membrane, porin-mediated selective permeability, and the existence of periplasmic enzymes, makes them less susceptible to many antibiotic classes.[258] Additionally, Gram-negative pathogens commonly acquire additional resistance mechanisms *via* mobile genetic elements such as plasmids and integrons which allows them to resist last-line therapies and

predominate nosocomial infections, making effective treatment methods critically important and increasingly complex.[259]

3.2 Treatment of Bacterial Infections

The most common and effective treatment for both Gram-positive and Gram-negative bacterial infections are antibiotics—medications that kill or inhibit the growth of bacteria.[260] Penicillin G (**3.3**), identified by Alexander Fleming in 1928 from *Pencillium notatum* (a type of mould), was the first antibiotic to be discovered.[261] Belonging to the β-lactam class of antibiotics, Penicillin G is mainly active against Gram-positive bacteria. Streptomycin (**3.4**), identified in 1943 from *Streptomyces griseus* (a soil-dwelling actinobacterium), is a natural aminoglycoside antibiotic and the first antibiotic active against Gram-negative bacteria and *M. tuberculosis*.[262]

Over the following decades, the discovery and development of antibiotics expanded rapidly, with a range of distinct classes identified from both natural and synthetic sources (Figure 3.5). These antibiotics exert their effects through multiple pathways targeting essential bacterial processes including cell wall synthesis, protein synthesis, and nucleic acid replication.[260] Despite advances in antibacterial discovery and design, Gram-negative bacteria remain challenging to treat due to their complex cell envelope and acquired resistance mechanisms.

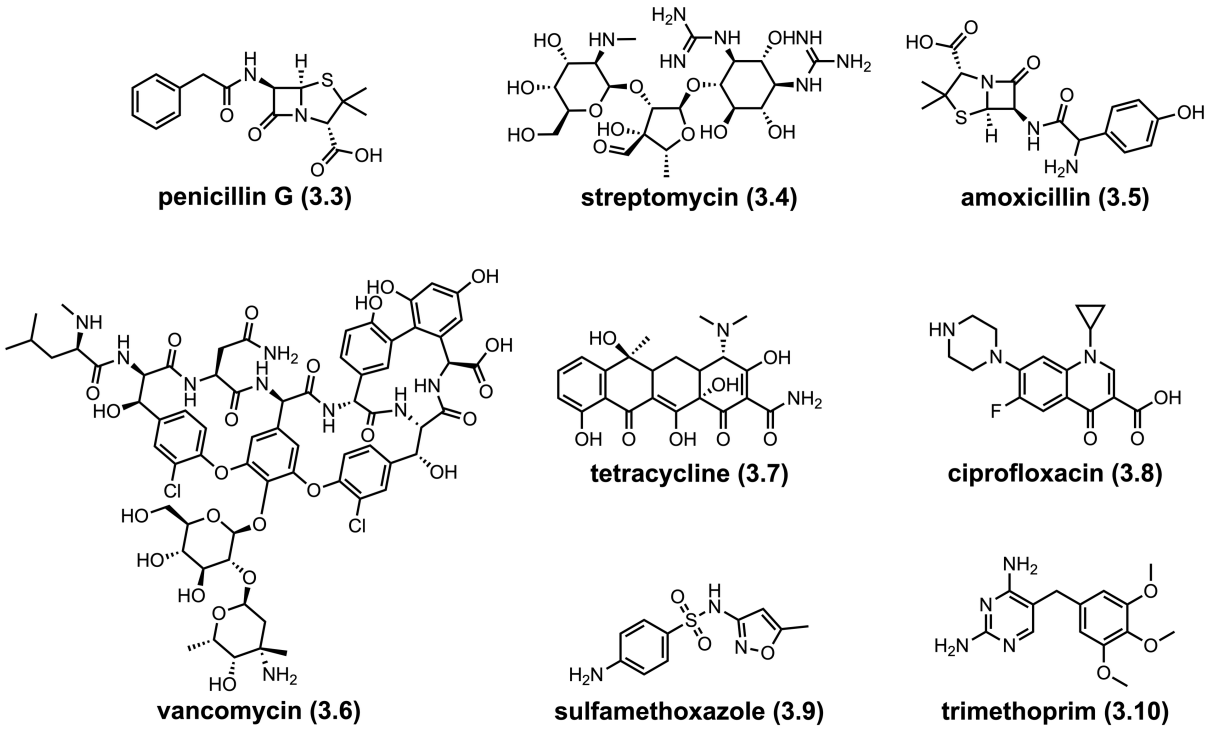


Figure 3.5. Common antibiotics used in treatment of Gram-positive and/or Gram-negative bacterial infections.

3.2.1 Cell wall synthesis inhibitors

Inhibition of bacterial cell wall synthesis is one of the most well-established mechanisms of antibiotics[263] and include β-lactams (penicillin (**3.3**), amoxicillin (**3.5**)), and glycopeptides (vancomycin (**3.6**)).[264] β-lactam antibiotics such as penicillins and cephalosporins inhibit transpeptidase enzymes, also known as penicillin-binding proteins,[265] which are responsible for cross-linking peptidoglycan strands to rigidify the cell wall.[266] Inhibition of transpeptidase prevents cross-linking and results in a weakened peptidoglycan network, ultimately leading to osmotic lysis and cell death. Cell wall synthesis inhibitors are generally most effective against Gram-positive bacteria, as the absence of an outer membrane leaves their thick peptidoglycan layer directly accessible.[267] Resistance in Gram-positive species is usually mediated by structural alterations in penicillin-binding proteins, whereas Gram-negative bacteria can inactivate β-lactam antibiotics before they reach their target through periplasmic β-lactamases.[268]

3.2.2 Protein synthesis inhibitors

Another common mechanism of action of antibacterials is through inhibition of bacterial protein synthesis by targeting the unique features of prokaryotic ribosomes.[269] Several antibiotic classes inhibit bacterial protein synthesis by binding to bacterial ribosomal RNA (rRNA). This can cause codon misreading and mistranslation, or block tRNA binding and prevent peptide chain elongation, ultimately leading to suppression of growth or cell death. These include antibiotics such as aminoglycosides (e.g. streptomycin (**3.4**)) and tetracyclines (e.g. tetracycline (**3.7**)) that can be used to treat Gram-negative infections.[270] However, their uptake is often restricted by the outer membrane which restricts the diffusion of many hydrophilic molecules and drugs with a high molecular weight. In addition, efflux pumps can actively remove aminoglycosides before they can reach their ribosomal targets, while modifying enzymes can chemically inactivate the drugs, making them ineffective on their bacterial targets.[271] Although these drug resistance mechanisms are also found in Gram-positive bacteria, their impact is more significant in Gram-negative bacteria where they can act with the outer membrane to create a powerful multilayered resistance mechanism.

3.2.3 Nucleic acid synthesis inhibitors

In addition to targeting protein synthesis, many antibiotics interfere with bacterial nucleic acid synthesis, either by inhibiting DNA replication or RNA transcription, key processes for bacterial growth and cell division. Antibiotics such as fluoroquinolones (e.g. ciprofloxacin (**3.8**)) bind non-covalently and inhibit bacterial enzymes responsible for relieving DNA supercoiling during replication, resulting in DNA double-strand breaks, stalling replication and ultimately leading to cell death.[272] These are active against many Gram-negative pathogens; however, resistance frequently develops *via* mutations in target genes and efflux pump overexpression, restricting their use.[273]

3.2.4 Antimetabolites

Antimetabolite antibiotics act by imitating or inhibiting key metabolites involved in DNA or RNA synthesis. These include folate metabolism inhibitors which block the bacterial

synthesis of folate, a key cofactor used in nucleotide synthesis.[274] In bacteria, folate is synthesised internally, unlike eukaryotes who must obtain it from their diet. Antibiotics of this class include sulfonamides (e.g. sulfamethoxazole (**3.9**)) and trimethoprim (**3.10**)), which both inhibit enzymes involved in the folate cycle, depleting folate and preventing the synthesis of DNA and RNA precursors, leading to bacterial cell death.[275] These therapeutics retain some activity against Gram-negative bacteria, however, resistance is widespread due to plasmid-borne alternative enzymes and efflux mechanisms.[276]

While multiple classes of antibiotics have been successful in controlling bacterial infections, their effectiveness is undermined by the emergence of resistant strains. This has resulted in once-curable infections, particularly those caused by Gram-negative bacteria, becoming persistent clinical challenges.

3.3 Antibiotic resistance

Antibiotic resistance is the ability of bacteria to resist the effects of drugs that once killed them or inhibited their growth. The first report of antibiotic resistance occurred shortly after the widespread use of Penicillin began, when in 1940 Fleming himself reported the emergence of penicillin-resistant strains of *Staphylococcus aureus*.[277] This indicated that bacteria could adapt and develop mechanisms to counteract the drug's effects.

Antibiotic resistance has emerged as one of the greatest global health threats of the 21st century.[278] The ability of bacteria to evolve and develop resistance to once effective drugs is occurring at an alarming rate, with the risk of entering a post-antibiotic era where common infections could once again become deadly.[279] Antibiotic resistance is currently attributed to an estimated 700,000 deaths annually,[280] with up to 4.95 million deaths reported as having some association with antimicrobial resistance (AMR).[281] Projections suggest up to 10 million AMR associated deaths per year by 2050, surpassing cancer as a leading cause of mortality.[281] Resistance is rising across a broad range of bacterial pathogens, as outlined in Figure 3.6.[221] These include both community-acquired and nosocomial (hospital-acquired) infection. Of particular importance are the ESKAPE pathogens, a group of six highly virulent, multidrug-resistant bacteria - *Enterococcus faecium*, *Staphylococcus aureus*, *Klebsiella pneumoniae*, *Acinetobacter baumannii*,

Pseudomonas aeruginosa and *Enterobacter* spp. Because the emergence of multidrug resistance is coupled with high mortality and limited treatment options, ESKAPE pathogens are a high priority for new treatment strategies.

Factors driving antibiotic resistance include the overuse and misuse of antibiotics in both humans and animals, poor infection control measures, and the lack of development of novel antibiotic classes. Gram-negative bacteria are of particular concern, showing resistance to last-report drugs such as carbapenems (penicillin-binding protein inhibitors).[282]

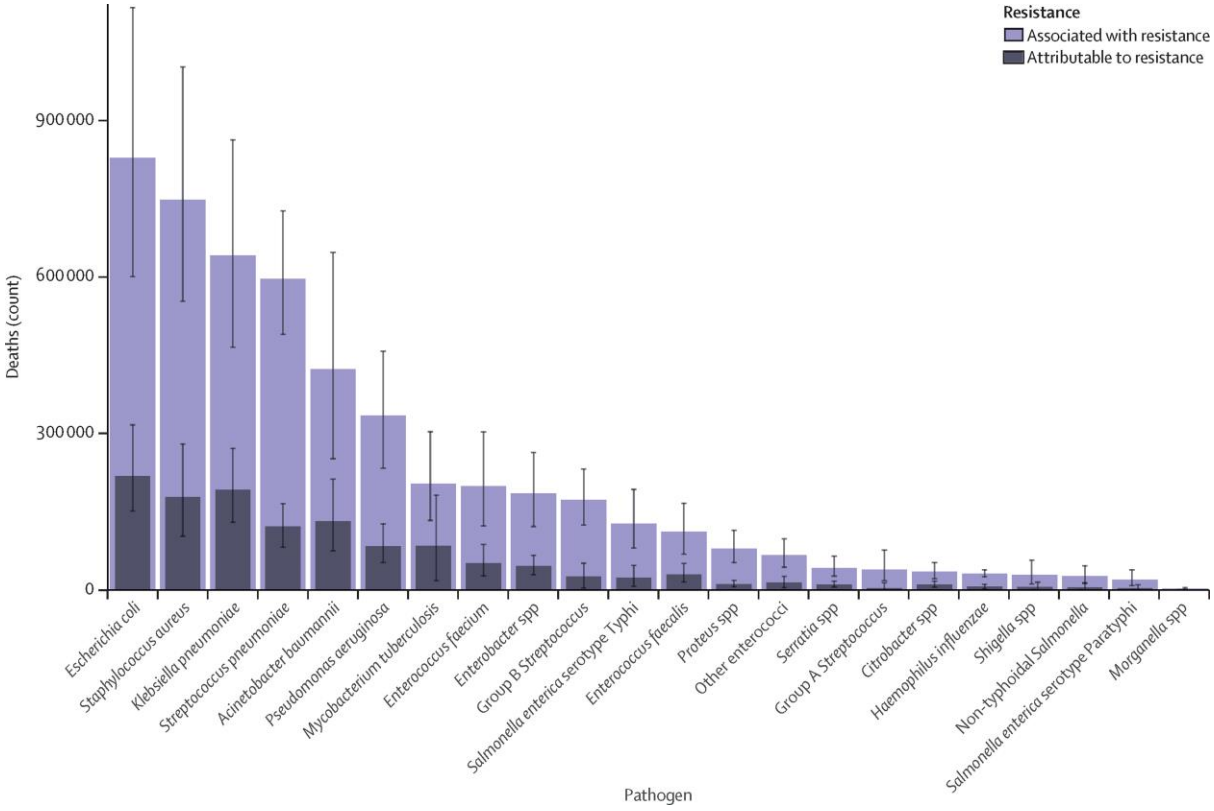


Figure 3.6. Estimated global death counts attributable and associated with bacterial antimicrobial resistance infections in 2019. (Reprinted with permission from Elsevier. Murray, C. J. L.; Ikuta, K. S.; Sharara, F.; Swetschinski, L.; Robles Aguilar, G., *et al.*, *The Lancet* 2022, *399* (10325), 629-655. Copyright 2022).[281]

Bacterial strains are increasingly acquiring resistance to multiple classes of antibiotics, leaving fewer effective treatment options. As such, it is paramount that novel therapeutic strategies be investigated.

3.3.1 Mechanisms of Antibiotic Resistance

Bacteria have evolved a wide range of mechanisms to resist the effects of antibiotics (Figure 3.7). These strategies are broadly classed into four groups: enzymatic inactivation of the drug, modification of the drug target, alteration of permeability and active efflux, and metabolic bypass.[283,284] Bacterial pathogens can also employ multiple resistance mechanisms simultaneously, creating higher levels of resistance, thus making treatment more challenging. As highlighted previously, Gram-negative pathogens pose significant challenges due to their unique resistance mechanisms.

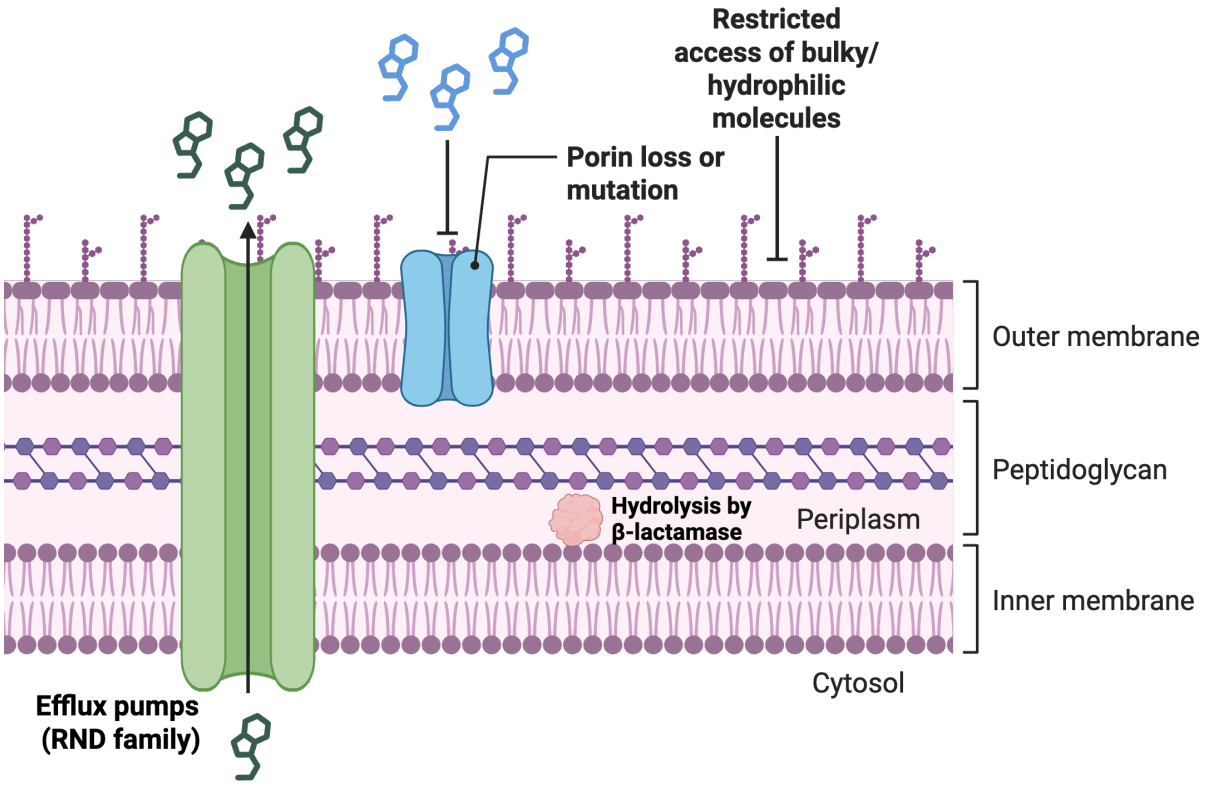


Figure 3.7. Resistance mechanisms of Gram-negative bacteria. Figure made with biorender.com.

The most significant feature of Gram-negative resistance is their cell envelope architecture. The outer membrane acts a permeability barrier, restricting entry of hydrophilic and bulky molecules such as many protein and nucleic acid synthesis inhibitors.[285] Porins normally allow hydrophilic molecules to diffuse across the outer membrane, however porin loss or mutation can restrict entry thereby resulting in resistance, restricting the ability of antibiotics to access the internal cell machinery.[286]

Even when drugs can pass through this barrier, they can often be expelled by efflux pumps such as those from the resistance-nodulation-division (RND) family, tripartite systems spanning both membranes that are unique to Gram-negative bacteria and can expel a broad spectrum of structurally unrelated drugs back out of the cell.[287,288] Additionally, the presence of β-lactamases, extended spectrum β-lactamases (ESBLs), and carbapenems, inactivate β-lactam antibiotics, while aminoglycoside-modifying enzymes impair binding of this drug class to ribosomes.[289]

These defence mechanisms act cooperatively, mutually reinforcing each other to make Gram-negative bacteria particularly resilient and leaving limited treatment options. The relatively limited scope of bacterial processes that these antibiotics target, e.g. the cell wall, protein, or nucleic acid synthesis, have driven interest in exploration of alternative antibiotic classes. One promising alternative to small molecule antibiotics is the use of antibody-based therapies. Importantly, antibodies targeting bacteria offer high specificity, the ability to neutralise virulence factors, and the potential to recruit host immune mechanisms to eliminate a given pathogen.[290]

3.3.2 Antibody-based therapies for targeting Gram-negative bacteria

Although antibody-based therapies have been developed for both Gram-positive and Gram-negative bacteria, they are of particular interest as a treatment for Gram-negative infections due to the structural barriers that restrict antibiotic penetration and the occurrence of multidrug resistance. The use of mAbs against bacterial pathogens was first achieved in targeting the capsular polysaccharides of *S. pneumoniae* and *N. meningitidis* to improve upon the drawbacks of polysaccharide and conjugate vaccines.[291,292] Unlike vaccines, which take time to generate immunity and are not as effective in outbreaks or immunocompromised populations, mAbs can provide instant treatment. Additionally, mAbs offer a novel strategy to treating drug-resistant bacterial infections, particularly in situations where vaccines are ineffective or impractical.

Antibody-based therapies are an intrinsically different strategy to conventional antibiotics. Instead of inhibiting essential bacterial processes such as cell wall and protein synthesis, antibodies utilise extracellular and surface-exposed structures to

interfere with bacterial virulence factors including adhesion, motility, and toxin delivery, whilst simultaneously recruiting host immune responses.[293] Specifically, lipopolysaccharides (LPS), capsular polysaccharides (CPS), flagella, and the pili/fimbriae have unique roles in bacterial virulence, and each offer a potential point of intervention.[294,295] These surface structures are particularly attractive to antibodies as they are highly exposed and immunogenic (Figure 3.8).

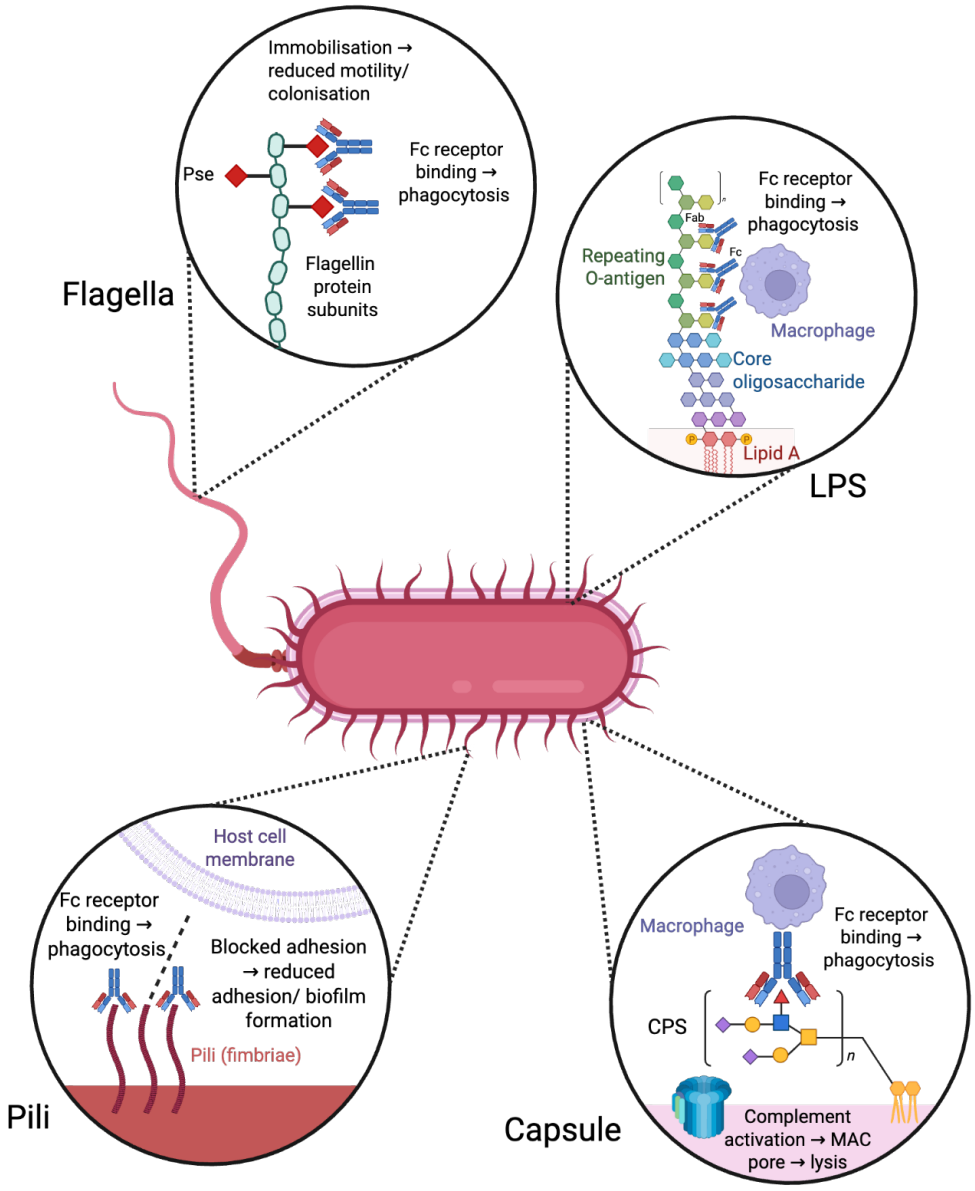


Figure 3.8. Antibody-based targeting of major Gram-negative surface structures. Monoclonal antibodies can bind to (i) flagella, blocking motility and recognising glycosylated epitopes such as pseudaminic acid (Pse); (ii) LPS, coating *O*-antigens to promote immune clearance; (iii) pili (fimbriae), disrupting adhesion and biofilm formation; and (iv) CPS, reducing capsule protection and enabling complement- and Fc-mediated immune clearance. Figure made with biorender.com.

The repetitive glycan motifs of LPS *O*-antigens provide a source of abundant and accessible biding sites. This makes them strong immune triggers, allowing antibodies to coat the bacterial surface for recognition and clearance, turning a structure normally used for protection into a point of weakness.[296,297] CPS, normally serving to shield the cell from host defences, lose their protective function once bound by antibodies, allowing coating of the bacterial cell with immune proteins that promote phagocytic uptake as well as pore formation that causes bacterial lysis.[298,299] Antibody binding to flagella can immobilise the bacterium, preventing colonisation whilst also facilitating uptake by immune cells.[300] Additionally, flagellin glycosylation is a trait of several Gram-negative pathogens, decorated with unique glycans such as nonulosonic acids. These glycans are not only unique bacterial epitopes but are essential for flagellar assembly, stability, and motility, playing roles in colonisation and virulence.[301] This role as both functional requirements and unique antigens makes glycosylated flagella particularly attractive antibody targets. Likewise, pili and fimbriae are surface-exposed appendages that are key for adhesion and biofilm formation. Fimbriae are typically shorter structures specialised for adhesion, whereas pili are longer filaments that can also mediate functions such as DNA transfer. Antibody targeting of these structures can therefore block the ability of the bacterium to attach to host cells and reduce biofilm stability.[302]

Because antibodies act on virulence-associated biomolecules rather than proteins involved in essential processes in bacteria, the selective pressure they enforce differ. While evasion is possible, it often results in reduced bacterial pathogenicity.[303] Resultingly, antibodies can reduce bacterial pathogenicity without applying the same evolutionary pressures that steer resistance toward broad-spectrum antibiotics.

Classical antibody approaches such as those used against *S. pneumoniae* and *N. meningitidis* focused on CPS and *O*-antigens as targets. This involves the use of polysaccharides derived directly from bacteria as antigens. However, these molecules are inherently heterogenous, containing mixtures of chains with variable lengths and modifications. This results in the antigenic polysaccharides being hard to control batch-to-batch and potentially containing impurities, in addition to resulting in ambiguity regarding which part of the polysaccharide the antibody recognises.[304–306] Seeberger and

colleagues were able to advance this classical technique by moving from heterogenous, purified polysaccharides to chemically defined oligosaccharides derived from O-antigens and CPS (Figure 3.9).[307,308] These short and structurally uniform oligosaccharides provide reproducibility and the ability to map exactly which part of the polysaccharide structure is necessary for antibody recognition. Importantly, this work also showed that short oligosaccharide motifs, when presented multivalently, can produce sufficient and protective antibody responses.

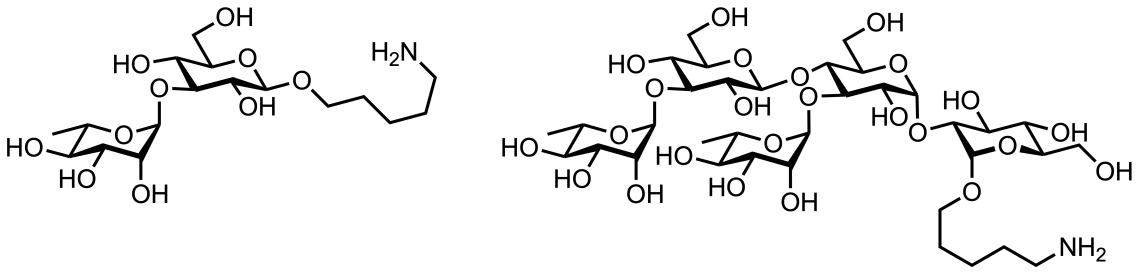


Figure 3.9. Synthetic oligosaccharides developed by Seeberger and colleagues, derived from *Clostridium difficile* polysaccharide 1 (PS-1). **3.11** represents the minimal epitope of PS-1, while **3.12** correspond to the full repeating unit. Both were synthesised with an aminopentyl aglycon to allow for conjugation to carrier proteins.

Drawbacks of polysaccharide-binding antibodies include their lack of serotype diversity, capsular shielding, and biofilm architecture which can limit breadth and potency. Serotype diversity can result in an antibody raised against one capsular or O-antigenic structure failing to recognise others, as was seen in early pneumococcal antibody strategies where protection was limited to only a small number of serotypes, resulting in multivalent vaccines being required.[309,310] Capsular shielding prevents antibodies from efficiently accessing their targets, a limitation observed in attempts to develop mAbs against *K. pneumoniae*, where the thick capsule reduced the efficacy in preclinical and early-phase trials.[311] Biofilm architecture creates physical and immunological barriers that restrict antibody penetration. For example, mAbs screened against *P. aeruginosa* infections (such as Panobucumab, an anti-O11 LPS immunoglobin trialled in pneumonia) failed to demonstrate consistent clinical benefit.[312] Biofilm formation is a key feature of *P. aeruginosa* infections, likely contributing, in addition to serotype restriction, to the lack of success of these antibodies.[313]

These challenges have driven the search for alternative bacterial glycans that are strongly immunogenic and broadly applicable, reducing risk of serotype restriction. Beyond traditional glycans seen in CPS and LPS, nonulosonic acids such as pseudaminic acid (Pse) and legionaminic acid (Leg) have become recognised as particularly attractive targets. These nine-carbon, acidic, sialic acid-like sugars are found primarily in Gram-negative bacteria, decorating capsules, lipooligosaccharides, and flagellar proteins.[314,315] Crucially, they are absent in eukaryotes, providing unique epitopes that can be targeted therapeutically without the risk of cross-reactivity with the host.

Discussed in detail in section 4.2, Tang *et al*. recently developed synthetic Pse-containing glycopeptides (derived from flagellin proteins) that were used to generate the first pan-specific mAbs capable of recognising Pse across diverse bacterial contexts, including flagellar glycosylation in *C. jejuni* and *H. pylori*.[316] This work is unique in that it produced mAbs that could overcome the serotype restriction of capsule-directed antibodies, instead recognising a scaffold present across multiple pathogens.

Building on the work of Tang *et al*. the following chapters focus on the development of synthetic analogues of two nonulosonic acids, Pse and Leg. In Chapter 4, a library of Pse derivatives was generated to screen against the pan-specific mAb and define its specificity and the structural features required for recognition. Chapter 5 adopts a parallel approach with Leg, with the goal of developing analogous Leg-specific mAbs in the future. Together, the goal of the work described in the chapters that follow is to create synthetic analogue libraries as tools for determining antibody specificity, and for guiding the design of new anti-glycan antibodies to recognise these nonulosonic acid motifs across diverse bacterial contexts.

Chapter 4: Synthesis of Pseudaminic Acid Analogues for Binding Studies and Methodological Improvements

4.1 Pseudaminic Acid

Pseudaminic acid (Pse) is a member of the nonulosonic acid (NulO) family of carbohydrates, a group of structurally diverse nine-carbon α-keto acid sugars found in both eukaryotic and prokaryotic organisms. First identified in 1984 by Knirel *et al.*,[317] Pse was isolated from the lipopolysaccharides (LPS) of *Pseudomonas aeruginosa* (serotypes O5 and O10a) and *Shigella boydii* (serotype 7). Although Pse was not isolated in its free form, its structure was determined through NMR analysis of oligosaccharides derived from the parent LPS. These compounds were characterised as derivatives of 5,7-diamino-3,5,7,9-tetradeoxynon-2-ulosonic acid, later identified specifically as 5-*N*-acetyl-7-*N*-[(*R*)-3-hydroxybutanoyl]pseudaminic acid (Pse5Ac7(3_RHb), **4.1**). Among the various derivatives identified to date, 5,7-diacetamidopseudaminic acid (Pse5Ac7Ac, **4.2**) is the most commonly found form across bacterial species (Figure 4.1).

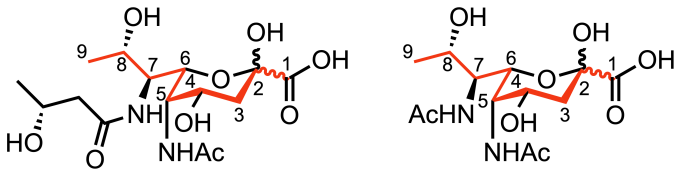


Figure 4.1. Structures of Pse5Ac7(3RHb) and Pse5Ac7Ac, the most common variant of pseudaminic acid. The nine-carbon backbone common to nonulosonic acids is highlighted in red and numbered.

Pse bears close resemblance to the widely studied eukaryotic nonulosonic acid, sialic acid (aka neuraminic acid or Neu); both share a nine-carbon backbone terminating in a carboxylic acid at C1 and a *N*-substituent at C5. In the case of sialic acid, the *N*-substituent is usually acetamido (Neu5Ac, **4.3**) or glycolamido (Neu5Gc).[318] However, Pse differs distinctly in its stereochemistry and functional substitution. Pse contains amino groups at both C5 and C7, making it a 5,7-diamino derivative, found with a variety of *N*-substitutions at these two positions (Figure 4.2). These modifications, coupled with

its distinct stereochemistry, distinguish Pse from other NulOs, making it a potentially useful biomarker for infection.

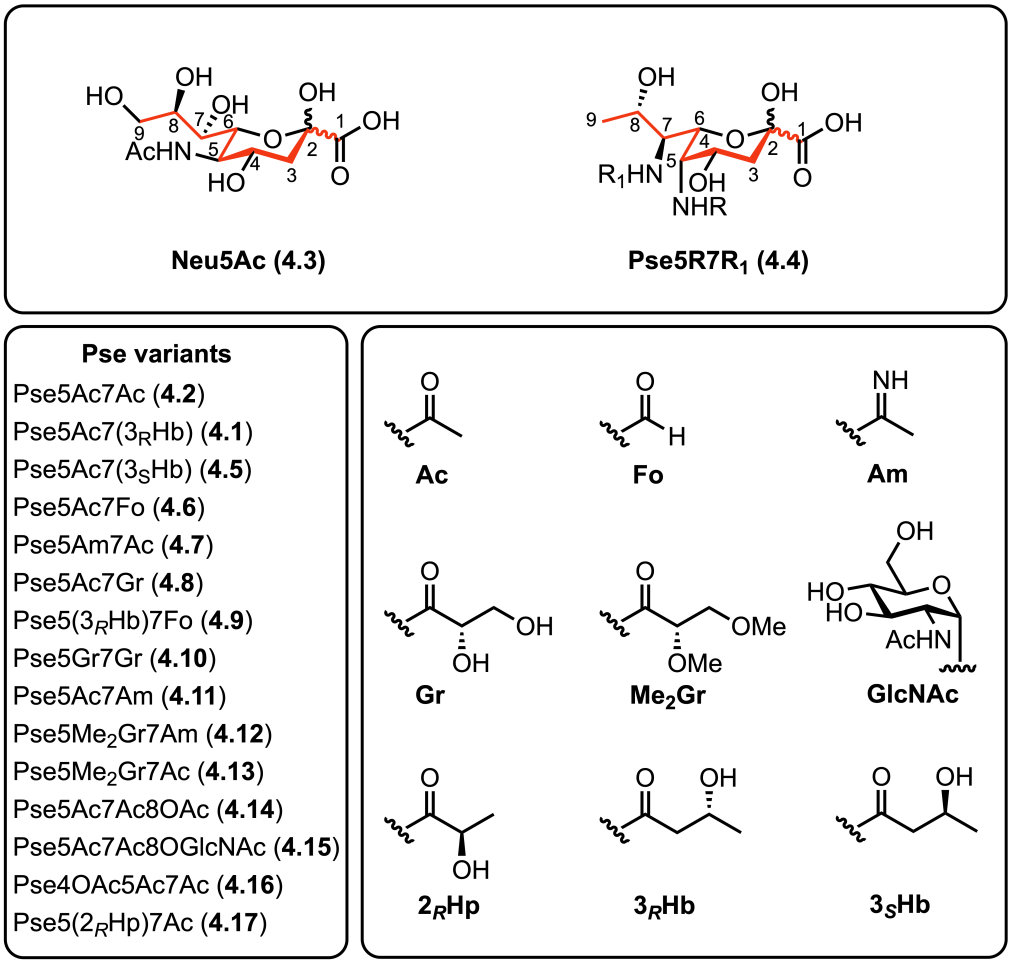


Figure 4.2. List and structure of pseudaminic acid (Pse) variants.

While sialic acids are found across a large range of organisms, pseudaminic acid (Pse), is only found in bacteria, primarily in Gram-negative bacteria.[319] Pseudaminic acid and its derivatives have since been found to decorate a wide variety of bacterial surface structures, including lipooligosaccharides, capsular polysaccharides, and most notably, flagellin proteins. Glycosylation of flagellin by Pse has been reported in several Gram-negative bacteria, particularly those associated with host interactions or pathogenesis, including *Campylobacter jejuni*, *Helicobacter pylori*, and *Acinetobacter baumannii* (Table 4.1).

Table 4.1. Pathogenic and opportunistic bacteria reported to express pseudaminic acid-linked glycans.

Pse derivative	Family	Bacterial species/strain	Antigen
Pse5Ac7Ac (**4.2**)	Enterobacteriaceae	*Escherichia coli* O136[319]	LPS
		Proteus vulgaris O39[319]	
		Enterobacter cloacae K7[320],	
	Campylobacteraceae	*Campylobacter jejuni* 81-176,	Flagellum
		Campylobacter coli VC167[319]	
	Pseudoalteromonadaceae	*Pseudoalteromonas atlantica* T9,	LPS
		IAM 14165[319]	
	Helicobacteraceae	*Helicobacter pylori* 1061[319]	Flagellum
	Aeromonadaceae	*Aeromonas caviae* UU51[319]	Flagellum
	Flavobacteriaceae	Cellulophaga fucicola[319]	LPS
	Vibrionaceae	*Vibrio vulnificus* 27562[319]	LPS
	Moraxellaceae	*Acinetobacter baumannii*	CPS
		Multiple strains including*:*	
		52-249[323], A74[324], ACICU[325],	
		NIPH67[328], NIPH329[322],	
		Acinetobacter	EPS
	Enterobacterales (other)	*Caulobacter crescentus*	Flagellum
		Piscirickettsia salmonis[319]	LPS
		Psychrobacter arcticus 273-4[331]	CPS
		Rhizobium spp. NGR234[319]	
		Sinorhizobium meliloti Rm41[332]	
Pse5Ac7(3_RHb) (**4.1**)	Pseudomonadaceae	*Pseudomonas aeruginosa* O10a,	LPS
		Pseudomonas chlororaphis UCM	
		B-106[333]	
	Enterobacteriaceae	*Shigella boydii* type 7[319]	LPS
		Plesiomonas shigelloides O36[334]	
		Escherichia coli O165[335]	
	Rhizobiaceae	*Sinorhizobium fredii* HH103[319]	CPS
	Moraxellaceae	*Acinetobacter*	CPS
		Acinetobacter	
Pse5Ac7(3_SHb) (**4.5**)	Rhizobiaceae	*Sinorhizobium fredii* HH103[337]	CPS
Pse5Ac7Fo (**4.6**)	Pseudomonadaceae	Pseudomonas aeruginosa O7a,	LPS
		O7a, 7d (immunotype 6)[319]	
	Pseudoalteromonadaceae	*Pseudoalteromonas*	LPS
Pse5Am7Ac (**4.7**)	Vibrionaceae	*Vibrio cholera O*:2[319]	LPS
	Campylobacteraceae	*Campylobacter jejuni* 81-176[319],	Flagellum
		Campylobacter coli VC167[319]	
Pse5Ac7Gr (**4.8**)	Vibrionaceae	*Vibrio vulnificus* 27562[319]	LPS
Pse5(3_RHb)7Fo (**4.9**)	Pseudomonadaceae	*Pseudomonas aeruginosa* O7a,	LPS
		Pseudomonas	Pilus
Pse5Gr7Gr (**4.10**)	Campylobacteraceae	*Campylobacter jejuni* 81-176[319]	Flagellum
Pse5Ac7Am (**4.11**)	Campylobacteraceae	*Campylobacter jejuni* 11168[319]	Flagellum

Pse5Me$_2$Gr7Am (**4.12**)	Campylobacteraceae	*Campylobacter jejuni* 11168[319]	Flagellum
Pse5Me$_2$Gr7Ac (**4.13**)	Campylobacteraceae	*Campylobacter jejuni* 11168[319]	Flagellum
Pse5Ac7Ac8OAc (**4.14**)	Campylobacteraceae	*Campylobacter jejuni* 81-176[337]	Flagellum
Pse5Am7Ac8OGlnAc (**4.15**)	Campylobacteraceae	*Campylobacter jejuni* 81-176[337]	Flagellum
Pse4OAc5Ac7Ac (**4.16**)	Pseudomonadaceae	*Pseudomonas aeruginosa* O10a, 10b[337]	LPS
Pse5(2$_R$Hp)7Ac (**4.17**)	Moraxellaceae	*Psychrobacter marincola KMM*	CPS

In these organisms, Pse plays key roles in motility, biofilm formation, immune evasion, and virulence.[319,340] The presence and variation of Pse structures contribute to antigenic diversity and immune modulation, making these molecules a focus for diagnostic development.[341]

4.1.1 Pse anomeric nomenclature

In Pse, the anomeric nomenclature is opposite of that in sialic acids due to the inverted configuration at the highest number stereogenic centre, the C8 carbon. The axial glycosidic linkage in Pse is assigned as α, and the equatorial as β (Figure 4.3).

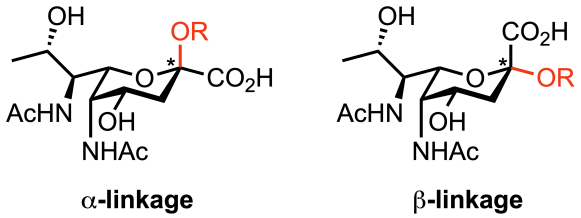


Figure 4.3. α and β glycosidic linkages of Pse. Glycosidic linkages are highlighted in red, and the anomeric carbon is identified by *.

4.2 Summary of Prior anti-Pse mAb Generation Work in the Payne Group

The following sections outline the unpublished work by Tang *et al.* as a collaboration between the University of Sydney, the Walter and Elisa Hall Institute, the University of Melbourne, the University of Western Australia and the University of Hong Kong. In this

work Tang *et al.*[316] generated multiple pan-specific mAbs that recognise Pse in a range of glycan and peptide linkages. To generate these mAbs, α- and β-linked Pse glycopeptides were first chemically synthesised based on known glycosylation sites in *Helicobacter pylori* (*H. pylori*) flagellin proteins. These synthetic glycopeptides enabled the determination of the native anomeric configuration of Pse to serine and threonine residues in the flagellin glycoproteins in *H. pylori*, which was confirmed to be α-linked through comparative LC-MS and fragmentation analyses. Hybridoma technology was used to generate mAbs that displayed broad specificity, recognising both anomers of Pse and its C8 epimer, and facilitated enrichment of Pse-modified glycopeptides from *H. pylori*, *Campylobacter jejuni* (*C. jejuni*), and *Acinetobacter baumannii* (*A. baumannii*). Structural studies identified key interactions responsible for Pse recognition and showed that the antibody has the potential to accommodate variability at the N7 and C8 positions. These mAbs not only uncovered new Pse-modified protein targets but also showed strong therapeutic potential by clearing multidrug-resistant *A. baumannii* infections in mice.

4.2.1 Limitations of Existing Tools for Pse Detection

Detection of pseudaminic acid (Pse) on bacteria has largely relied on metabolic labelling strategies.[342,343] These methods have enabled the detection of highly abundant Pse-decorated substrates such as flagellins. However, they lack the specificity and sensitivity needed to detect lower-abundance targets and less accessible sites, or to define exact glycosylation sites. Chemical labelling is also restricted by structural diversity and cellular accessibility of the labelled Pse. Consequently, modification-specific affinity reagents, such as mAbs offer a more versatile approach.

Despite polyclonal antibodies and engineered phage-derived proteins with affinity for Pse having been reported,[329,344,345] these proteins have not significantly advanced the mapping of Pse-dependent glycosylation or enabled discovery of new Pse-modified substrates. The development of high-affinity mAbs that can recognise a range of Pse variants would be a valuable tool for exploring bacterial pseudaminylation and its biological implications.

4.2.2 Hapten Design and Synthesis of Pse Glycopeptides

The generation of mAbs required the synthesis of defined Pse-modified glycopeptides from *H. pylori* flagellin proteins (FlaA, FlaB, and FlgE) (Figure 4.4). *O*-pseudaminylation sites at serine and threonine residues were initially identified using tandem LC-MS/MS. Synthetic tryptic glycopeptides containing either α- and β-linked Pse were prepared *via* solid-phase peptide synthesis, incorporating glycosylated serine building blocks made from thioglycoside donors (Figure 4.4). Comparative analysis *via* LC-MS/MS enabled the assignment of the native Pse anomeric configuration in *H. pylori* as α-linked, based on the co-elution and fragmentation profiles of the synthetic tryptic glycopeptide standards (Figure 4.5).

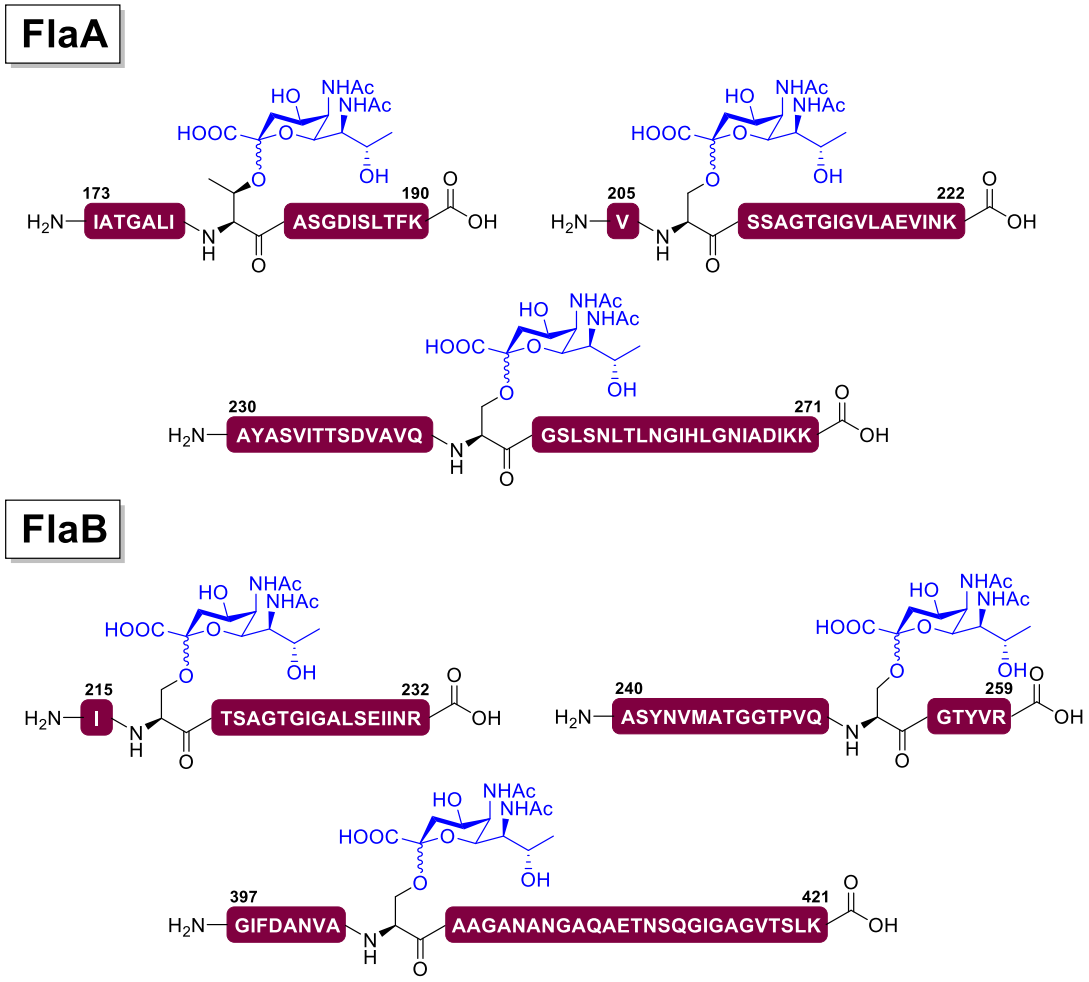


Figure 4.4. Tryptic glycopeptide fragments from *H. pylori* flagellin proteins (FlaA and FlaB), in which the anomeric configuration of Pse was unknown. A range of these fragments were synthesised by Tang as both α and β anomers.

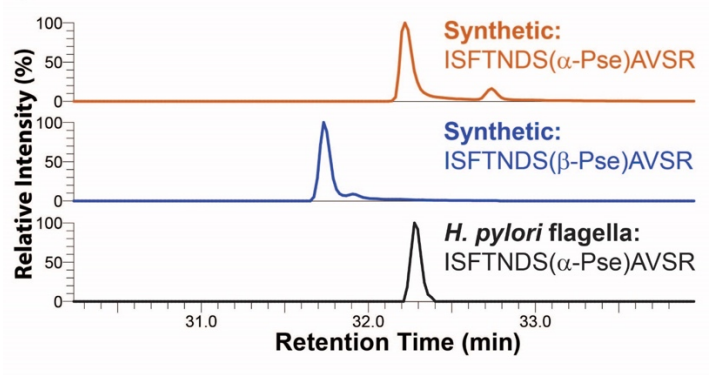


Figure 4.5. Comparative LC–MS/MS chromatograms of synthetic glycopeptide standards and native *H. pylori* flagellar glycopeptides. Synthetic ISFTNDS(α-Pse)AVSR (orange) and ISFTNDS(β-Pse)AVSR (blue) were analysed alongside the native tryptic glycopeptide isolated from *H. pylori* flagella (black). Elution and matched fragmentation profiles of the native material with the α-linked synthetic standard enabled assignment of the natural Pse anomeric configuration as α-linked.

4.2.3 Generation and Characterisation of Monoclonal Antibodies

The synthetic α-Pse glycopeptides were conjugated to carrier proteins – either Keyhole Limpet Hemocyanin (KLH) or Bovine Serum Albumin (BSA) - and administered to mice to generate hybridoma lines producing Pse-reactive mAbs. High-throughput Enzyme-Linked Immunosorbent Assay (ELISA) screening identified clones with high specificity for Pse in glycopeptide and native glycoprotein contexts. A subset of nine clones were isolated, with several sharing highly similar heavy and light chain regions. Of these, three mAbs (1E8, 3E11, 6D2) were selected for further development based on affinity, specificity, and sequence diversity. Of these, 1E8 possessed the highest affinity (K_D = 69 nM) for the α-Pse glycopeptides.

Interestingly, these antibodies also showed broad specificity, recognising both α- and β-configured Pse, as well as its C8 epimer (8ePse), on both glycopeptides and full glycoconjugates.

4.2.4 Insight into Pan-Specificity *via* Structural Biology

High-resolution X-ray crystallography of the Fab (fragment antigen-binding) of mAb 1E8 in complex with a synthetic serinyl-Pse ligand elucidated key structural features responsible for the broad recognition ability of the mAb. Antigen binding was mediated by conserved complementarity-determining region (CDR) loops that bind to the pyranose

ring and key functional groups on Pse, while tolerating variation at the anomeric centre and aglycone. Importantly, modelling indicated that bulky substitutions at N5 or O4, such as the hydroxybutyryl group found in some *Pseudomonas* strains, may disrupt binding, whereas modifications at N7 or C8 could be well tolerated by virtue of an open groove in the N7 direction, and the C8 hydroxyl group being solvent exposed (Figure 4.6).

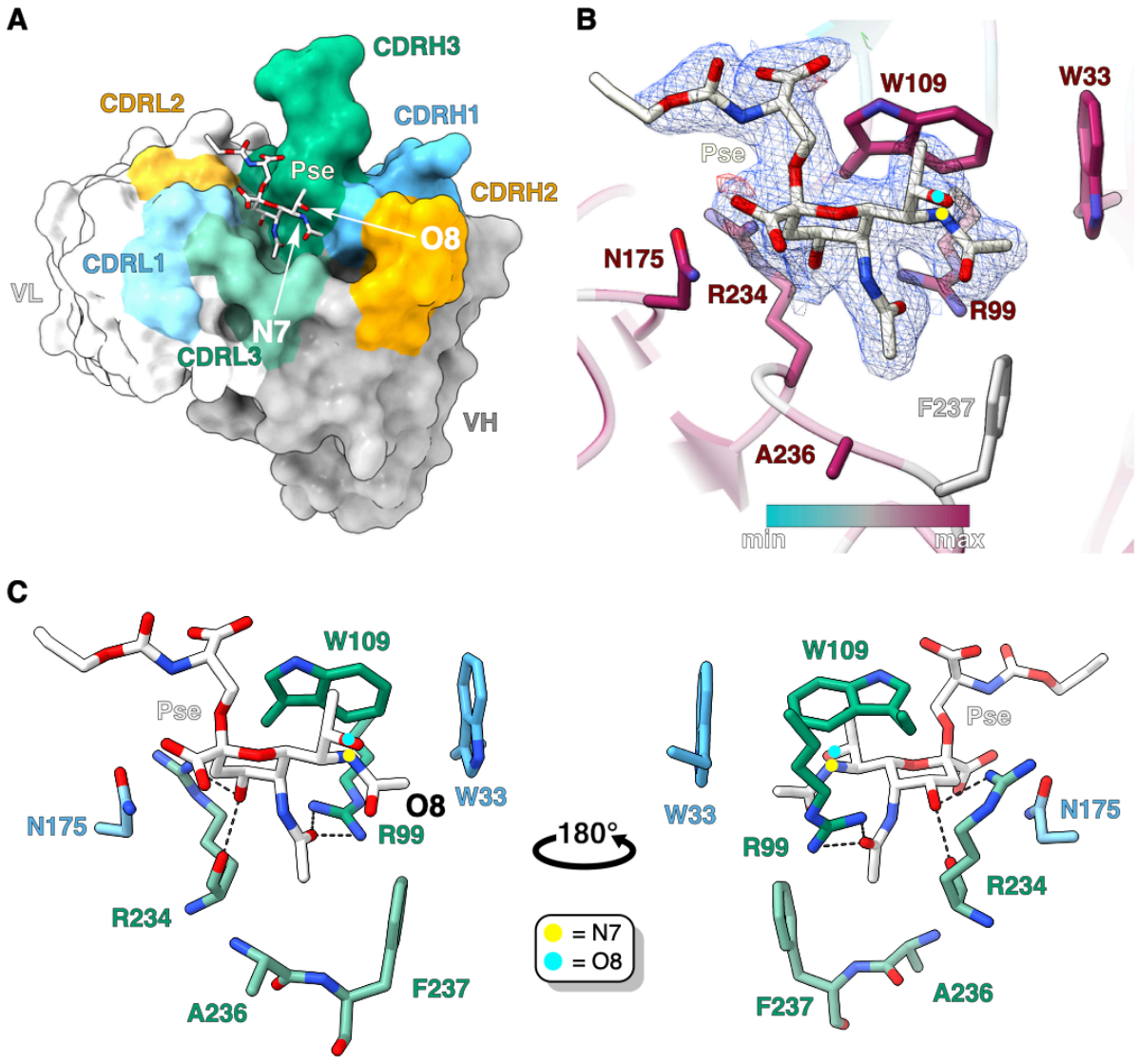


Figure 4.6. Insight into recognition of Pse5Ac7Ac by mAb 1E8 through X-ray crystallography. (A) serinyl-Pse (white sticks) bound to 1E8 in the antigen binding site. N7 and O8 positions are highlighted by white arrows. (B) Structure of serinyl-Pse bound to mAb 1E8b, shown with a Fo-Fc omit map contoured at 1.5σ around the ligand. Residues surrounding the Pse are colour-coded by sequence conservation across the nine unique monoclonal antibodies sequenced in this study (maroon: highly conserved; teal: poorly conserved). (C) Key interactions between Pse and 1E8 within the binding site. N7 (yellow) and O8 (turquoise) are highlighted by dots in (B) and (C).

4.2.5 Enrichment and Glycoproteomic Mapping of Pse-Modifications

The mAbs were next applied to immunoprecipitate Pse-modified glycopeptides from bacterial lysates. Using mass spectrometry-based glycoproteomics, the antibodies enabled the identification of known and novel Pse-modified proteins in *H. pylori*, *C. jejuni*, and *A. baumannii*. In addition to established targets such as FlaA and FlaB, newly discovered pseudaminylated proteins included DnaK, glucose-6-phosphate isomerase, and regulatory proteins in *H. pylori*, as well as several components of the motility and secretion machinery in *C. jejuni*.

In *A. baumannii*, the mAbs enabled the enrichment of glycopeptides bearing both simple Pse residues and extended Pse-containing glycans from capsular polysaccharides. This also allowed recognition of α-Pse and β-8ePse terminal residues in branching glycan motifs, supporting the broad utility of these mAbs.

4.2.6 Therapeutic Potential of Anti-Pse mAbs

As the antibodies were highly specific and easily accessible, they were also evaluated for therapeutic utility against multidrug-resistant (MDR) *A. baumannii*. The mAb 1E8 provided significant protection in a murine post-infection model. Mice treated with mAb 1E8 following systemic *A. baumannii* infection exhibited full survival and complete bacterial clearance from the bloodstream, whereas control animals reached their humane endpoint in less than 24 h (Figure 4.7).

These results show the potential of Pse-specific mAbs as passive immunotherapeutics against clinically relevant Gram-negative pathogens and emphasise the value of targeting common bacterial nonulosonic acid epitopes as an effective antibacterial strategy.

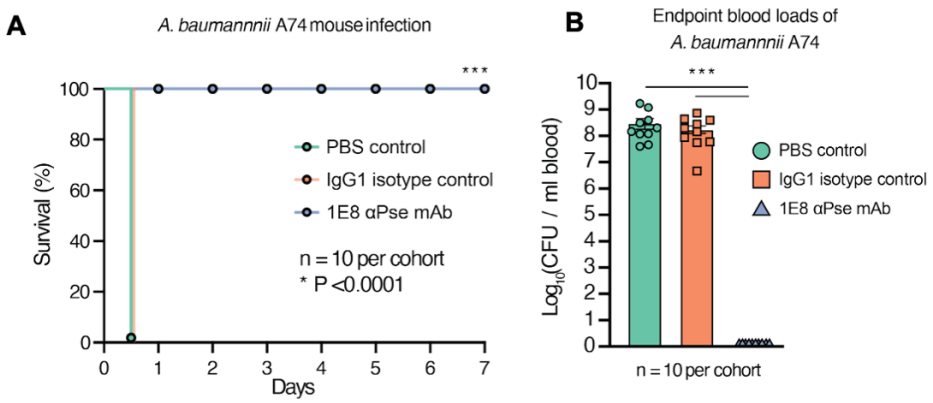


Figure 4.7. Use of Pse mAb 1E8 to treat *A. baumannii* infection in a murine model. **A)** Kaplan–Meier survival curve of mice infected with *A. baumannii* A74 followed by injection of either Pse mAb 1E8 (n = 20), mouse IgG1 isotype control (n =10), or PBS (n = 10). **B)** Bacterial loads (t = 18 h) in blood.

4.2.7 Probing Substrate Flexibility of mAb

Given the significance of the mAb generated in the above work as a molecular biology tool and therapeutic, it is important to further characterise its substrate specificity. In particular, the flexible N7 binding pocket observed in the crystal structure suggests that it might recognise several native Pse derivatives in addition to Pse5Ac7Ac and its 8-epimer [e.g. Pse5Ac7$_R$Hb (**4.1**) and Pse5Ac7Fo (**4.6**)]. Probing this possibility would rely on access to pure pseudaminic acid derivatives and their pseudaminosides, which was a key aim of the research described in this chapter. However, a limitation of the current work is a lengthy chemical synthesis of the parent pseuadaminoside (Pse5Ac7Ac) and its peptide derivatives (*vide infra*). Therefore, a secondary aim of the work described in this chapter was the development of a more robust synthetic route to access pseudaminosides. Current strategies for the synthesis of pseudaminosides, including those used in the generation of the mAb, are outlined in the sections below.

4.3 Chemical Synthesis of Pseudaminic Acids

Despite their prevalence in bacterial systems, pseudaminic acids (Pse) are difficult to obtain in their free form from natural sources and in synthetically useful quantities.[346] As a result, access to Pse currently relies on either chemoenzymatic[347] or purely chemical syntheses.[348] However, chemical synthesis poses significant challenges due to the high number of stereogenic centres and structural dissimilarity with readily available sugars.

Multiple strategies have been applied for the chemical synthesis of the most common derivative Pse5Ac7Ac (Figure 4.8). In one approach, the use of the amino acid L-*allo*-threonine[349] (**4.18**) as a starting material enables the early installation of the correct stereochemistry at the C7 and C8 positions. Another commonly employed method utilises Neu5Ac[350,351] (**4.3**), which already contains the nine-carbon backbone found in Pse but requires a number of stereogenic centre inversions. Additionally, several convergent approaches have been reported that integrate features of both strategies, starting from smaller carbohydrate precursors such as GlcNAc[352] (**4.19**), UDP-GlcNAc[347] (**4.20**), or 3,4-di-*O*-benzoyl-L-rhamnopyranose[353] (**4.21**).

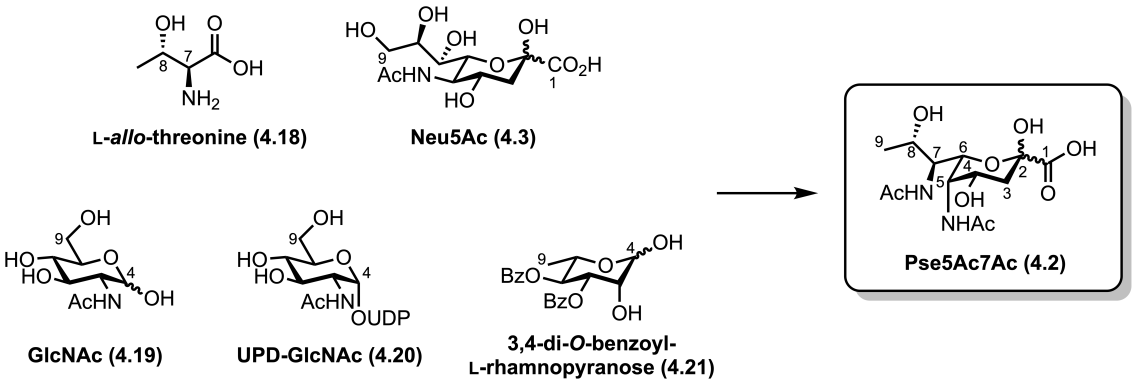


Figure 4.8. Previously utilised starting materials in approaches towards the synthesis of Pse5Ac7Ac.

The following section outlines several of the key reported strategies for the synthesis of Pse.

4.3.1 Synthetic Route by Knirel and coworkers

Seventeen years after the initial discovery[317] of the Pse family in the lipopolysaccharides of *Pseudomonas aeruginosa* and *Shigella boydii*, Knirel and co-workers developed a synthesis[353] of nine stereoisomers of 5,7-diacetamido-3,5,7,9-tetradeoxynon-2-ulosonic acid. These isomers were constructed from a range of readily available pyranose precursors, with the objective of confirming the stereochemistry of naturally occurring members of the Pse family. The absolute configurations of the synthetic compounds were determined by NMR comparison of Pse derivatives isolated from bacterial sources. The pathway originating from 3,4-di-*O*-benzoyl-L-rhamnopyranose (**4.21**) provided the stereoisomer consistent with natural Pse (Figure 4.9). This was achieved through a series

of protecting group manipulations, hydroxyl inversions, and substitutions to obtain **4.22**. The final step of the synthesis was a Knoevenagel condensation and decarboxylation to provide **4.2** with an overall 0.7% yield over 19 steps.

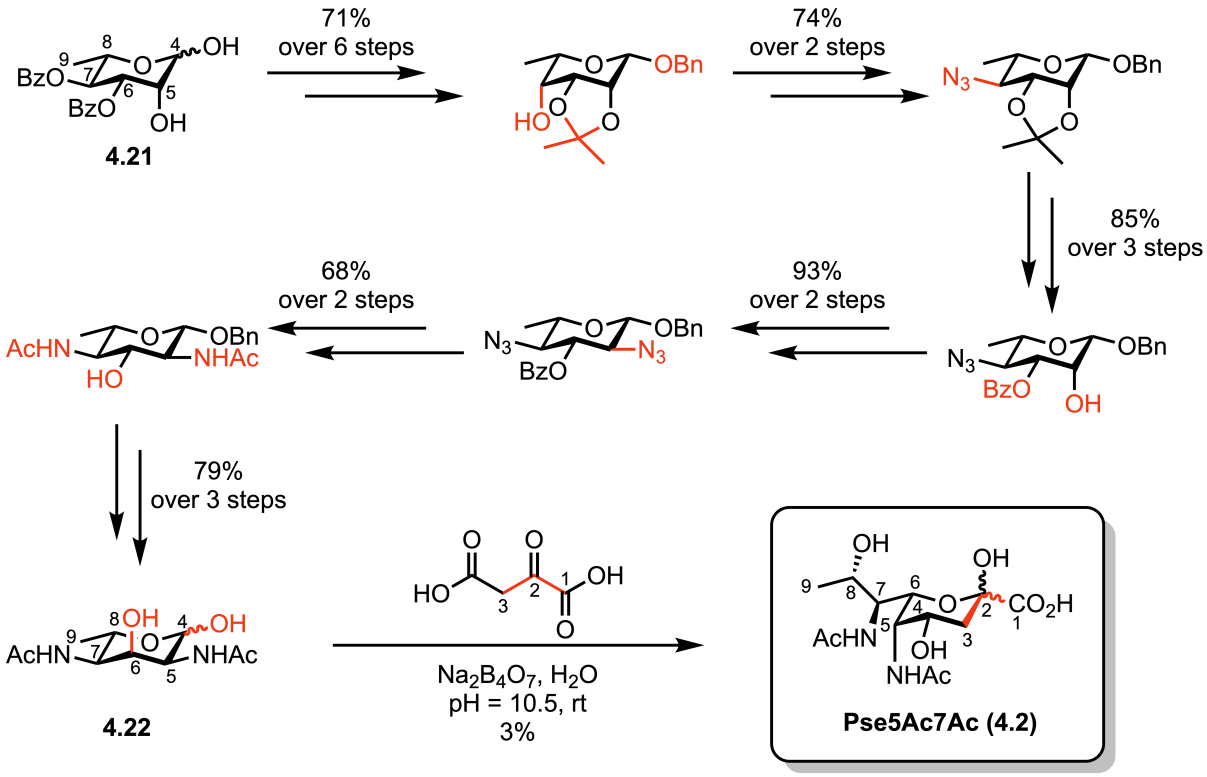


Figure 4.9. Total synthesis of Pse5Ac7Ac (**4.2**) by Knirel and co-workers. Key transformations are highlighted in red.

Although this synthetic route provides access to Pse5Ac7Ac in fewer steps than some subsequent procedures, it was ultimately deemed unsuitable for use due to several limitations. The final transformation proceeds with low yield and results in the formation of numerous side products. In addition, the overall synthesis is reliant on the use of toxic and environmentally hazardous reagents, including dibutyltin oxide (Bu_2SnO) and benzene, which further detract from its practicality and scalability.

4.3.2 Synthetic route by Ito and coworkers

In 2011, Ito and coworkers[352] utilised inexpensive *N*-acetylglucosamine (GlcNAc, **4.19**) as the starting material for the total synthesis of Pse5Ac7Ac. Their approach was to mimic the biosynthetic pathway,[347] employing 6-deoxy-AltdiNAc (**4.23**) as a key intermediate (Figure 4.10).

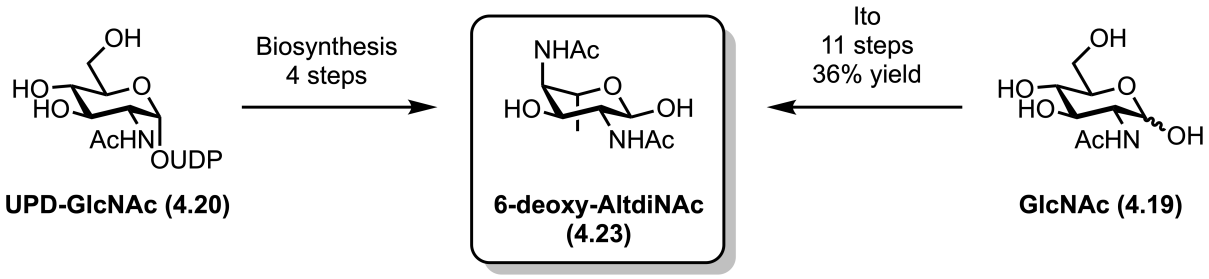


Figure 4.10. Synthesis of 6-deoxy-AltidiNAc (**4.23**), key intermediate in biosynthesis of Pse5Ac7Ac from UDP-GlcNAc (**4.20**) and Ito's biosynthetic synthesis from GlcNAc (**4.19**). 6-deoxy-AltidiNAc (**4.23**) shown in the $^4C_1$ conformation for clarity of conversion from **4.20** and **4.19**.

In the Ito synthesis, 6-deoxy-AltdiNAc (**4.23**) can be converted efficiently (77%) to **4.24** (*erythro*) and **4.25** (*threo*) through the irreversible In-mediated Barbier reaction under slightly acidic conditions (Figure 4.11). The *erythro* (**4.24**) and *threo* (**4.25**) isomers were then subjected to ozonolysis to provide the 2-keto moiety and allow spontaneous cyclisation to the hemiketal. Pse5Ac7Ac (**4.2**) was provided following ethyl ester hydrolysis of the hemiketal *erythro* isomer in a 5.4% overall yield (21 steps).

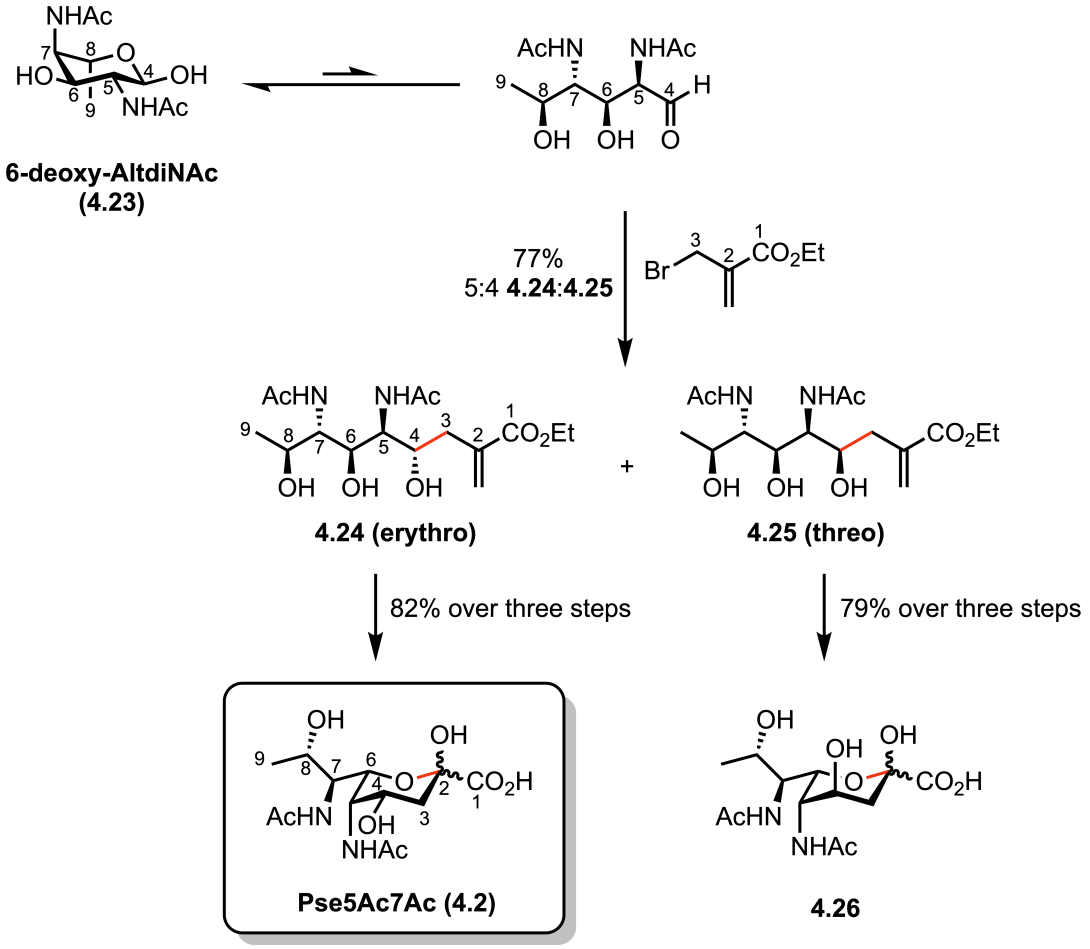


Figure 4.11. Ito's synthesis of Pse5Ac7Ac (**4.2**) from 6-deoxy-AltdiNAc (**4.23**). 4epi-Pse5Ac7Ac (**4.26**) can also be accessed *via* this route.

Although Ito's synthesis from GlcNAc provided an improved overall yield relative to the work of Knirel and co-workers, it presented two major limitations. First, the use of GlcNAc as a starting material precludes modification of the N5 position with other acyl groups. Second, the synthesis suffered from poor stereocontrol in the Barbier reaction (5:4 ratio of **4.24**:**4.5**) despite extensive optimisation efforts, including the use of Lewis acids and chiral ligands. As a result, this route was considered unsuitable for the production of large quantities of Pse donor.

However, several transformations developed in Ito's synthesis – notably the Barbier reaction and ozonolysis – have been strategically valuable and were subsequently incorporated into later synthetic efforts.[349]

4.3.3 Synthetic Routes utilising sialic acid (Neu5Ac)

Several synthetic routes have been developed from commercially available Neu5Ac, which inherently possesses the nine-carbon backbone characteristic of nonulosonic acids. These routes typically focus on the sequential, stereospecific modification of the existing stereocentres in Neu5Ac, minimising the need for stereochemistry-setting C-C bond formation reactions. The key features differentiating Pse5Ac7Ac (**4.2**) from Neu5Ac (**4.3**) include the lack of C9 terminal alcohol, the inversion of C8 stereochemistry, the *N*-acetyl group at C7 as opposed to the alcohol, and the inversion of configuration of the *N*-acetyl group at C5 (Figure 4.12).

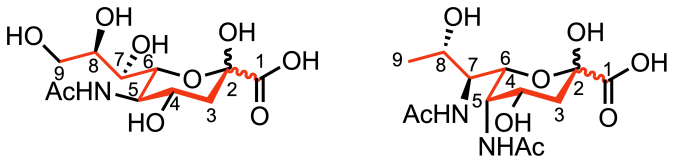


Figure 4.12. Structures of Neu5Ac (**4.3**) and Pse5Ac7Ac (**4.2**). The nine-carbon backbone characteristic of nonulosonic acids is highlighted in red.

Representative examples of pseudaminic acid syntheses originating from Neu5Ac are outlined in the sections that follow.

4.3.4 Synthetic route by Kiefel, Payne, and co-workers

The synthesis of Pse5Ac7Ac from Neu5Ac was reported by Kiefel, Payne and co-workers in 2016.[354] The synthesis utilised a stereoretentive Zbiral deamination[355] on the peracetylated methyl ester, methyl glycoside **4.27** to replace the C5-acetamido group with an acyloxy group (Figure 4.13). Buda and Crich[355] conducted mechanistic studies providing insight into the origin of the stereoretention observed in the Zbiral deamination. The deamination and subsequent substitution go through **4.28** to form diazonium ion **4.29**, liberating nitrogen gas to form carbenium ion **4.30**. While substitutions at carbenium centres typically result in racemisation, the high degree of stereoretention observed here implies a mechanism involving neighbouring group participation (NGP).

Through trials of variations of substituents at C4 and C7, Buda and Crich were able to establish that the carbenium ion **4.30** is in equilibrium with bicyclic oxonium ion **4.31**, resulting in the high degree of retention of configuration. Subsequent nucleophilic attack at the bridgehead carbon results in inversion of configuration (overall retention from **4.27**) to provide C5 equatorial acetate **4.32**. Importantly, the position of this equilibrium was found to be highly sensitive to the electronic nature of the alcohol substituents. In the presence of multiple inductively electron withdrawing groups - as is in the case in intermediate **4.30** - the carbenium ion is destabilised sufficiently to shift the equilibrium to the bicyclic oxonium ion **4.31**. Comparatively, in systems lacking such electron-withdrawing substituents, the carbenium ion is sufficiently stable to dominate the equilibrium, resulting in partial loss of stereochemical integrity. This mechanistic insight imposes a limitation on the timing of the Zbiral deamination within the synthetic sequence, which is ideally performed at an early stage – specifically when the sialic acid framework remains peracetylated. Consequently, this constrains the ability to retain the more stable *N*-acetyl functionality throughout the synthesis.

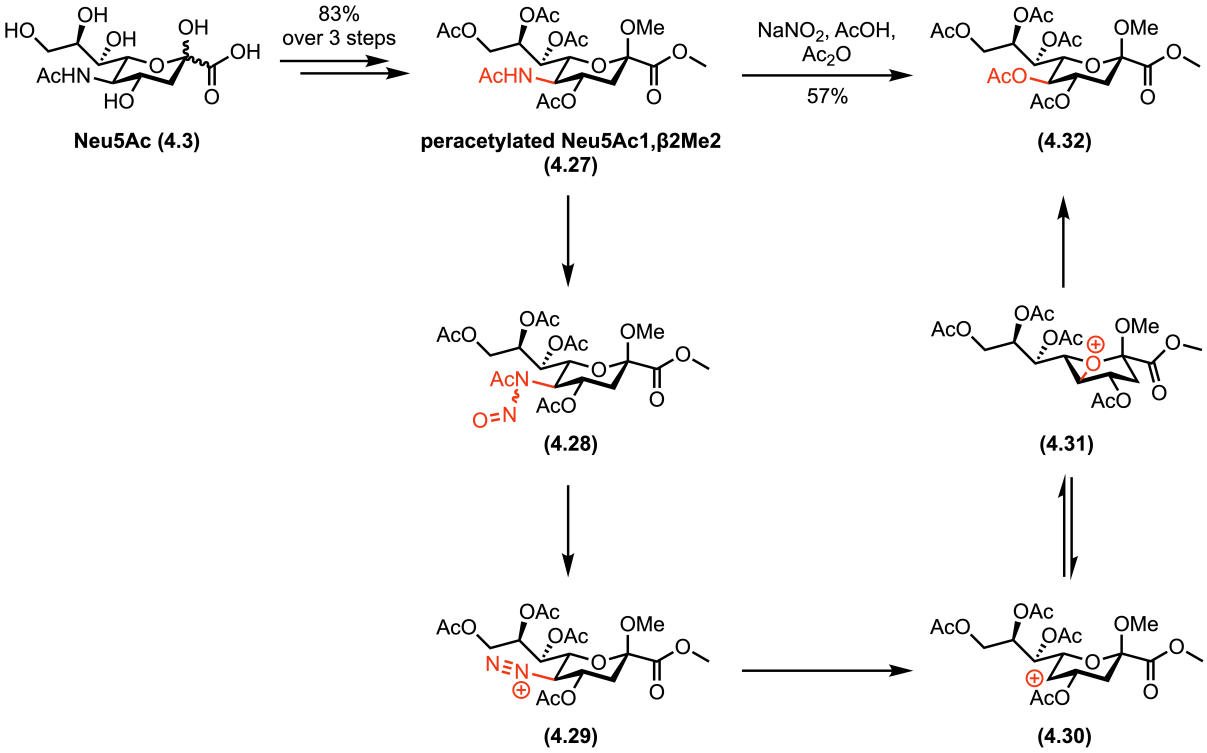


Figure 4.13: Zbiral deamination and substitution, highlighting key intermediates including equilibrium between carbenium ion **4.30** and bicyclic oxonium ion **4.31**.

Following further protecting group manipulations, **4.33** was produced, allowing for simultaneous stereochemical inversion at C5 and C7 via a bimolecular nucleophilic substitution (S_N2) with sodium azide to produce **4.34**. The subsequent nine steps involved conversion of **4.34** to **4.35** through a series of protecting group manipulations, an alcohol inversion at C8, and simultaneous azide-reduction. Intermediate **4.35** was then subjected to deoxygenation at C9 *via* an Appel reaction and subsequent hydrodeiodination using Pearlman's catalyst to afford the Pse glycoside. The final step of this route was a global ester hydrolysis to provide the desired Pse5Ac7Ac **4.2** (Figure 4.14).

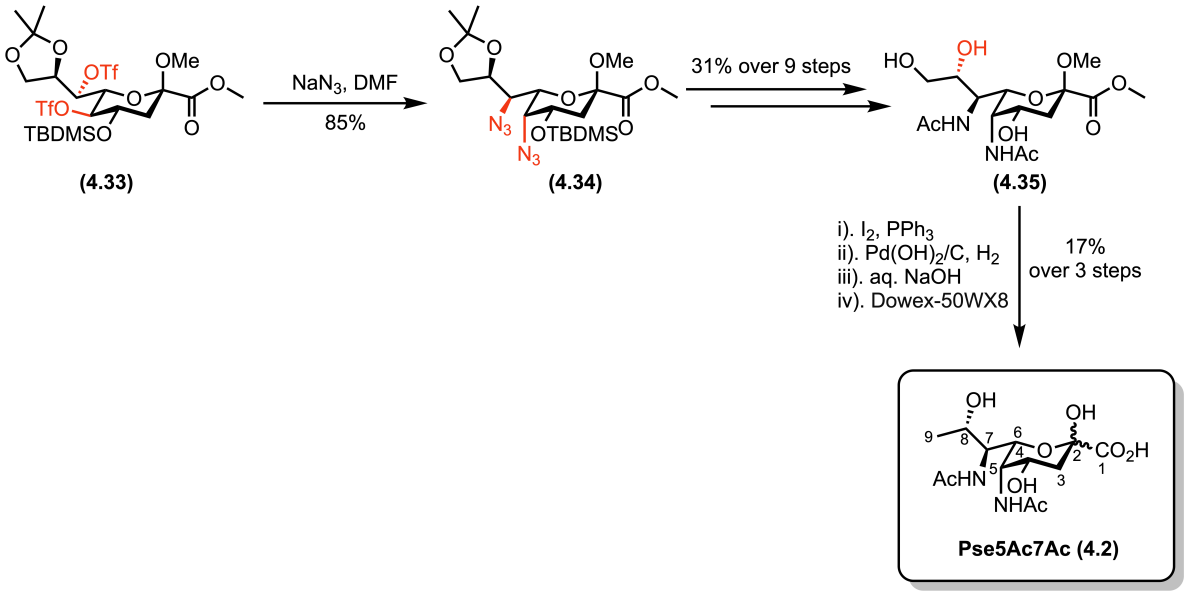


Figure 4.14. Key synthetic steps in Kiefel and Payne's route.

While this synthetic route is notable for circumventing the need for carbon-carbon bond formation steps, it presents several limitations. Although regioselective reduction of azides at N5 and N7 has been demonstrated,[351] potentially enabling the installation of structural variants at these sites, Liu[349] has shown that the presence of an azide at C5 is critical for achieving high glycosylation selectivity. Consequently, strategies that involve retaining azide functionality through to the glycosylation stage are incompatible with the late-stage deoxygenation at C9, which relies on iodination and reductive conditions. In addition to this, the final three transformations in this synthesis proceeded in low yield, presenting a barrier to scalability.

4.3.5 Synthetic routes by Crich and co-workers

Crich and co-workers have reported total chemical syntheses of Pse glycosyl donors in both 2018[350] and 2022.[351] As has been reported by Li and co-workers (*vide infra*), both of Crich's syntheses utilised a Pse thioglycoside donor as a key intermediate. Thioglycosides are readily activated at low temperatures and allow for the stereoselective synthesis of Pse glycosides, making them efficient glycosyl donors.

Crich's 2018 synthesis

Crich's 2018 synthesis trialled both late-stage and intermediate-stage oxidative deamination. Both routes involved fully protecting and thioglycosidating Neu5Ac (**4.23**), providing peracetylated Neu5Ac adamantyl thioglycoside **4.36** in three steps, followed by protecting group manipulations to provide common intermediate **4.37** over three steps (Figure 4.15).

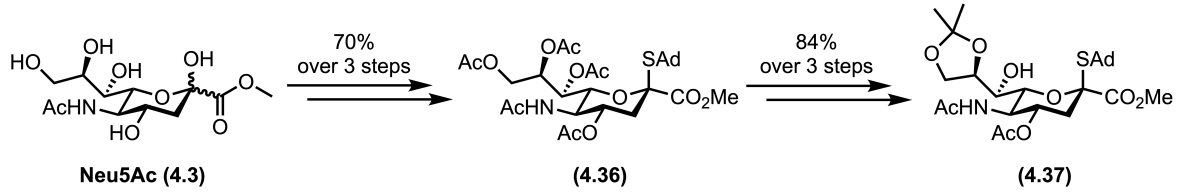


Figure 4.15. Crich's synthesis of common intermediate **4.37**.

Initially, **4.37** was subject to further protecting group manipulations, stereochemical inversion at C8, and deoxygenation at C9 to obtain **4.38** (Figure 4.16). Thioglycoside **4.38** was subjected to a late-stage oxidative deamination with substitution by levulinic acid to provide intermediate **4.39**, followed by selective removal of the levulinyl group with buffered hydrazine, and isolation of **4.40**. However, this conversion provided no stereoselectivity (1:1 mixture of stereoisomers) resulting in a 38% yield of **4.40**. This was attributed to the lack of C-O bond at C9, which decreases the overall inductive electron-withdrawing effect of the side chain. As a result, there is less stereoelectronic assistance from the ring oxygen, and more carbenium ion character at the 5-position. Additionally, the OTBS group at C7 is only weakly electron-withdrawing, further reducing the side chain's overall inductive effect in comparison to the peracetylated Neu5Ac analogue (see Figure 4.13). The low yield and poor selectivity resulted in Crich adopting a sequence in which the deamination reaction was conducted before deoxygenation at C9.

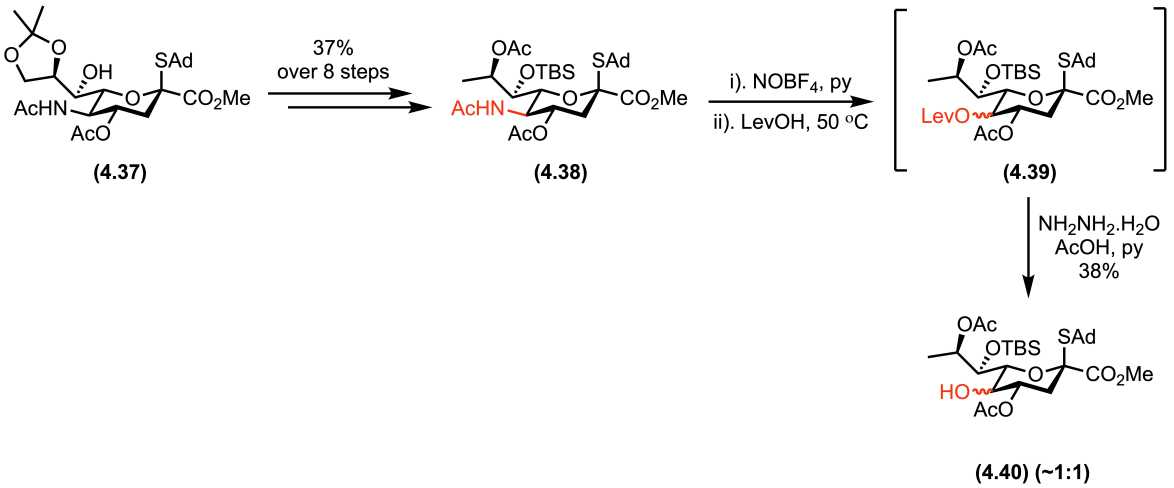


Figure 4.16. Crich's first attempted route for synthetising Pse donor, highlighting late-stage oxidative deamination at C5. Key transformations are highlighted in red.

Crich and co-workers then proceeded to take common intermediate **4.37** and protect the alcohol on C7 with a slightly more electron withdrawing O-Nap group to produce **4.41**. This intermediate was then subjected to a Zbiral oxidative deamination resulting in overall substitution of a levulinate ester (Lev) with retention of configuration at C5, producing **4.42**. The presence of the additional C9 C-O bond and *O*-Nap ether at C7 proved to be critical for the retention of configuration. However, a competing elimination reaction also led to formation of an unproductive alkene byproduct **4.43** (21%) (Figure 4.17).

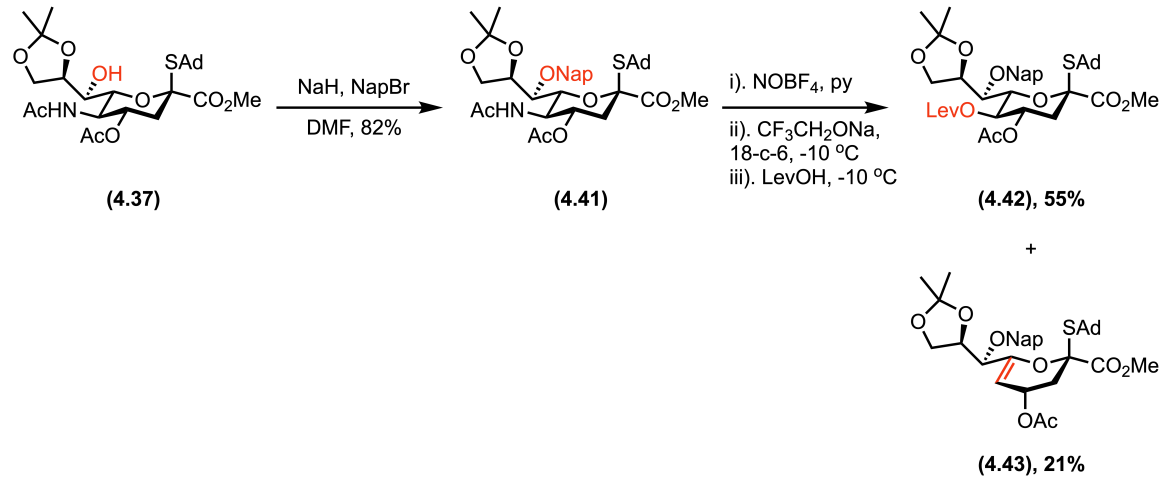


Figure 4.17. Crich's second route for synthesis of Pse donor, highlighting early-stage oxidative deamination and substitution at C5.

Intermediate **4.42** then underwent a series of further transformations, including protecting group manipulations, inversion at C8, deoxygenation at C9, and S_N2 azide displacement at C5 and C7 to provide bis-azido thioglycoside donor **4.44**. Donor **4.44** was glycosidated with benzyl alcohol to provide glycosidated intermediate **4.45** as the β-anomer, which was transformed into Pse5Ac7Ac (**4.2**) in another three steps (Figure 4.18). The overall yield for this strategy was 5% over 20 steps.

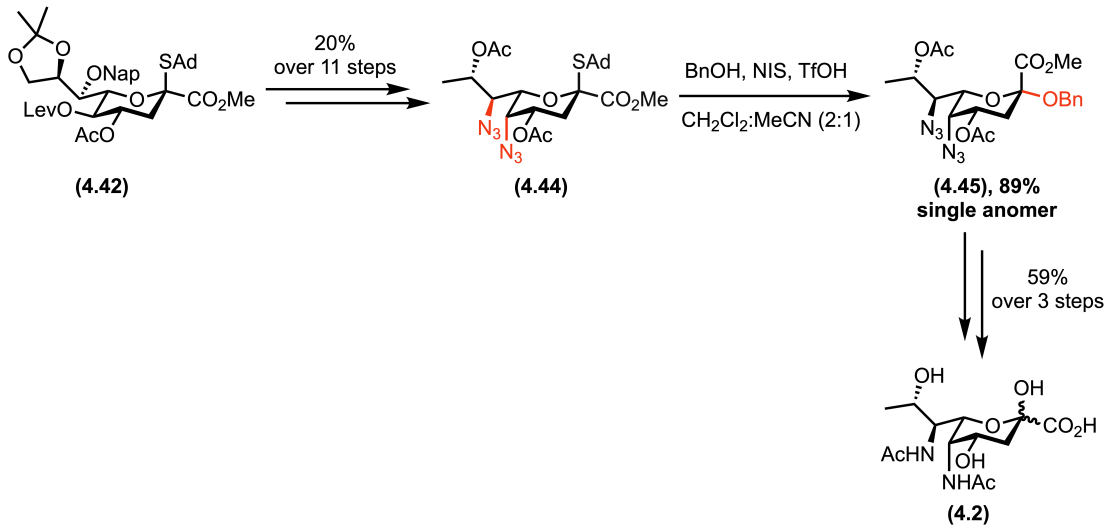


Figure 4.18. Glycosidation of adamantyl thioglycoside Pse donor **4.44** to provide exclusively β-benzyl alcohol glycoside **4.45**, followed by formation of desired Pse5Ac7Ac **4.2**.

4.3.6 Crich's 2022 synthesis

Crich's 2022 synthesis also utilised early thioglycoside installation and Zbiral oxidative deamination. Uniquely, this synthesis employed $NaIO_4$-mediated oxidative cleavage, resulting in an aldehyde terminus at C7 of **4.47** following cleavage of **4.46**, which was converted in situ to sulfinamide **4.48** through condensation with (*S*)-Ellman's reagent. Sulfinamide **4.48** was underwent SmI_2-mediated reductive addition of acetaldehyde to provide sulfonamide **4.49** along with aminal **4.50**. Removal of Ellman's auxiliary, diazotisation, regioselective deacetylation, triflation of C5 alcohol and subsequent S_N2 displacement with sodium azide provided Pse donor **4.44** in a 4% overall yield over five less steps that Crich's 2018 synthesis. In addition, Crich and co-workers were able to demonstrate regioselective conversion of C7 azide to NHCbz *via* amine **4.51**, providing a Pse donor **4.52** with orthogonal amine protecting groups (Figure 4.19).

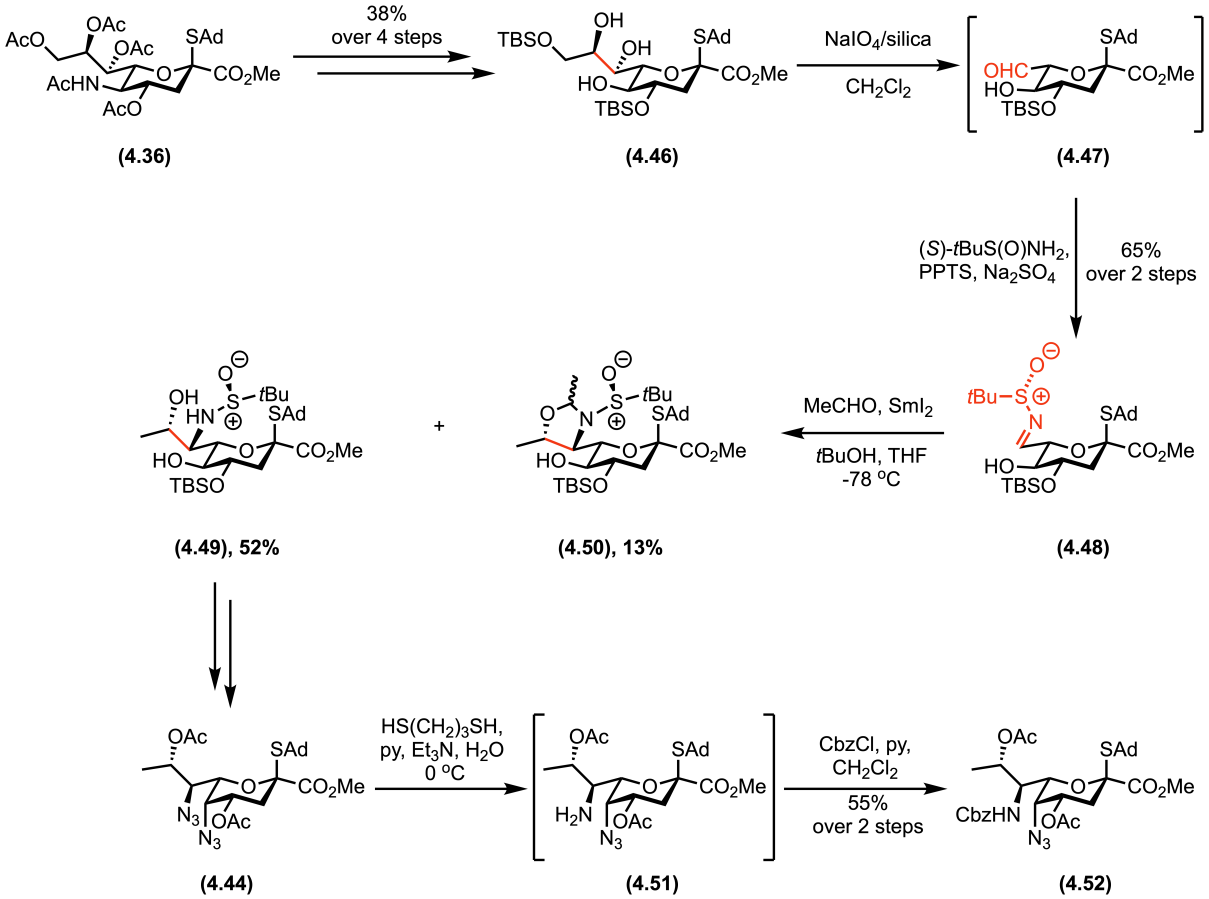


Figure 4.19. Crich's 2022 synthesis of Pse donor **4.52** with orthogonal amine protecting groups, highlighting key oxidative cleavage and SmI_2 mediated addition.

4.3.7 Synthesis by Li and co-workers

Li and co-workers reported the total chemical synthesis of Pse5Ac7Ac (**4.2**) in 2017.[349] Unlike the other syntheses described, their strategy employed inexpensive and commercially available amino acid L-threonine as the starting material. In analogy with the Crich syntheses, Li and co-workers targeted a thioglycoside donor that demonstrated good β-selectivity in a model glycosylation with benzyl alcohol.

Garner's-type aldehyde **4.54** was prepared from L-threonine **4.53** over nine steps (Figure 4.20). Aldehyde **4.54** then underwent a highly *syn*-specific chelation-assisted aldol-type reaction with thioester-isocyanide **4.55**, providing a 5.1:1 mixture of diastereomers (**4.56** and **4.57**). The diastereoselectivity of C6 can be attributed to the formation of a lithium ion chelate in the aldehyde (**4.58**), which provides enhanced Felkin-Anh selectivity. Additionally, the use of moderately polar, aprotic solvent CH_2Cl_2 and DCE allow for ion

pairing and chelation, stabilising the transition state without disrupting Li^+ coordination. It is proposed that the C5 stereochemistry is set *via* reversible deprotonation to form the more thermodynamically stable trans oxazoline intermediate.[356]

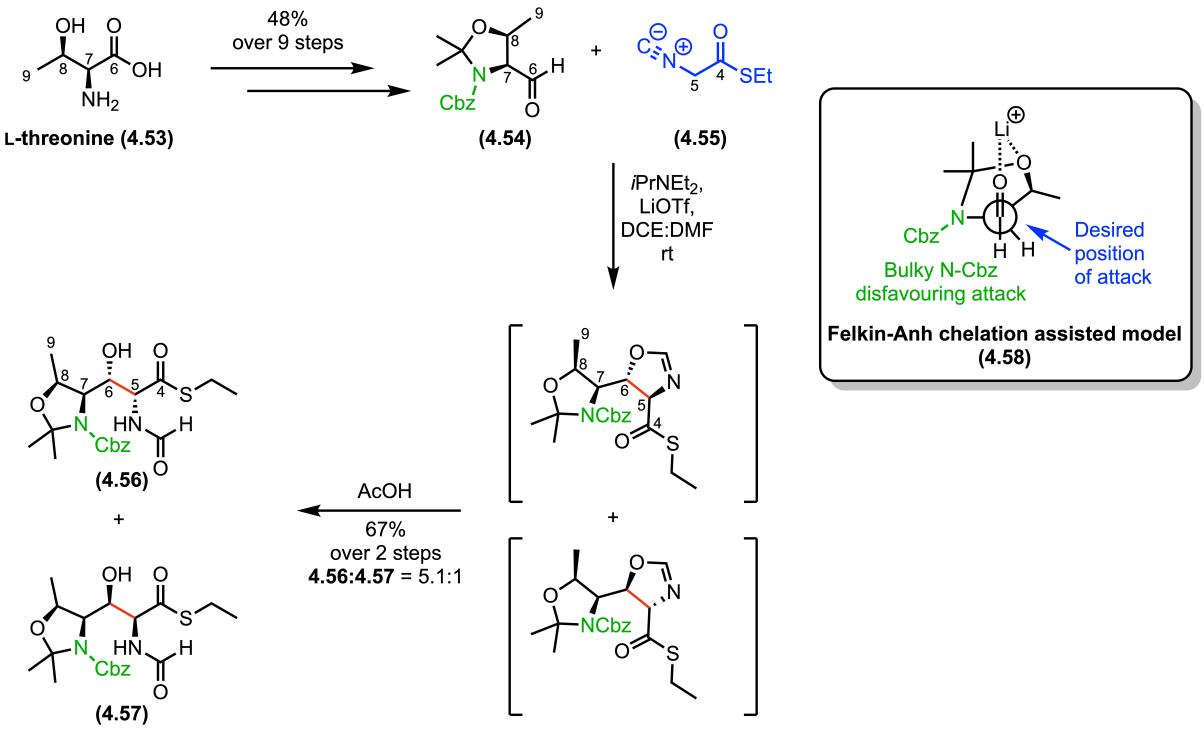


Figure 4.20. Initial synthetic steps in Li's preparation of Pse donor from L-threonine, highlighting stereocontrol of aldol-type reaction of aldehyde **4.54** and isocyanide **4.55**.

Thioester **4.56** was subjected to an *O*-silylation followed by a Fukuyama reduction to provide aldehyde **4.59** (Figure 4.21). Li then employed Ito's approach (see section 4.3.2) of an In-mediated Barbier reaction of **4.59** with isopropyl bromomethacrylate. As was observed by Ito, the Barbier reaction proceeded with low stereoselectivity. However, the stereochemistry of the newly formed alcohol **4.60** could be resolved *via* an oxidation and stereoselective 1,3-anti reduction sequence to afford triol **4.61**. Again, building on Ito's work, the final steps involved ozonolysis of the alkene to reveal the hemiacetal, which underwent thioketalisation with 4-methylbenzenethiol to provide Pse5Troc7Cbz thioglycoside donor **4.62**. Thioglycoside **4.62** could be converted to Pse5Ac7Ac **4.2** over an additional five steps, or employed directly in stereoselective glycosylation reactions.

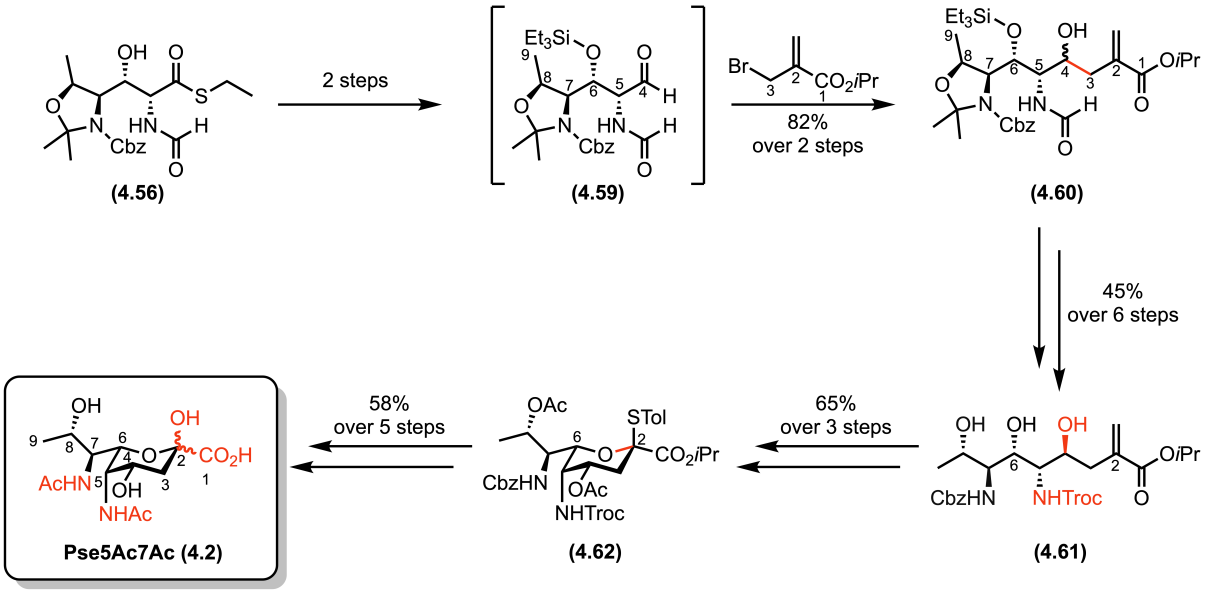


Figure 4.21. Li's synthesis of Pse-donor **4.62** from thioester **4.56**, and route to Pse5Ac7Ac (**4.2**).

4.4 Stereocontrol of Chemical Pseudaminylation

Achieving high selectivity in glycosylation reactions has long posed significant challenges in the field of carbohydrate chemistry. This selectivity is critical, as glycans in nature often exist as distinct anomeric forms, with biological function frequently dependent on a single anomer. Glycosidation of non-2-ulosonic acids poses a particular challenge due to the lack of a neighbouring substituent at the 3-position for anchimeric assistance, and the propensity for elimination to a 2,3-anhydro derivative due to electron withdrawing nature of the C1 carbonyl.[357,358] The ability to selectively synthesise either anomer of pseudaminic acid (Pse) glycosides is essential, as Pse occurs in both α- and β-anomeric configurations in nature. While α-linked Pse is commonly found on glycoproteins,[316] particularly at serine and threonine residues in Gram-negative bacteria, β-linked forms are often observed in bacterial glycans.[359,360]

A general mechanism of glycosidation of a Pse donor **4.63** is shown in Figure 4.22. A leaving group (LG) is removed, often catalysed by a Lewis acid, to form oxocarbenium ion **4.64**. This is followed by addition of an alcohol to form either an α-glycoside (**4.65**) or β-glycoside (**4.66**), or undesired glycal by-product (**4.67**).

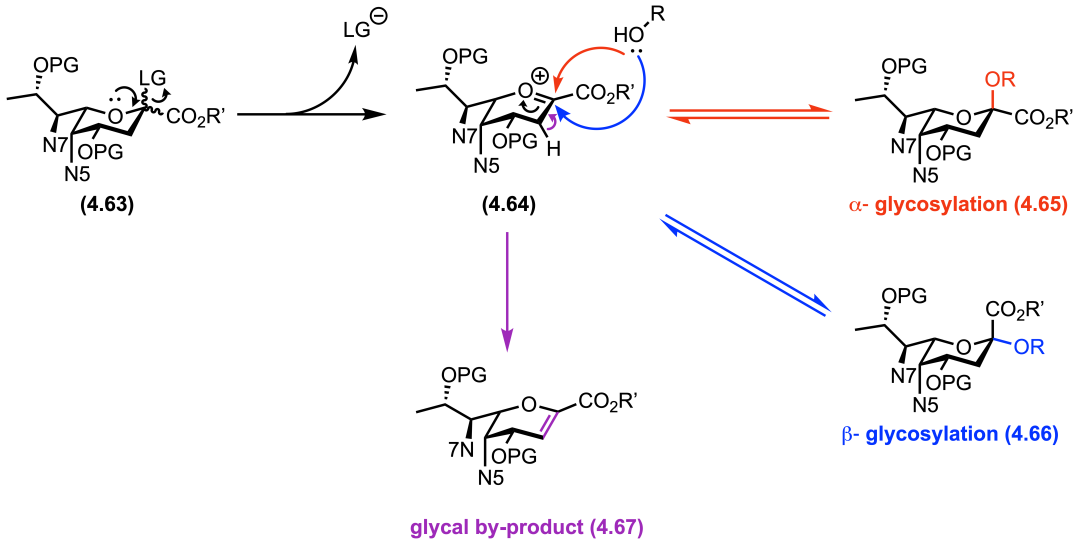


Figure 4.22. General mechanism for glycosylation of Pse donor **4.63**, where PG = protecting group, LG = leaving group, and N5 and N7 are found in various forms including azide and acetyl. Three products can be observed: α-glycoside (**4.65**), β-glycoside (**4.66**), and glycal (**4.67**).

Glycosylation strategies were initially developed using simple monosaccharide acceptors, providing a foundation that could later be extended to more complex substrates, including amino acid residues and other glycosides.

The first chemical glycosidation of Pse was reported by Ito and co-workers in 2011 (Figure 4.23).[352] After unsuccessful attempts to form a thioglycoside, they instead prepared a glycosyl phosphite donor (**4.68**), which underwent highly α-selective glycosidation with **4.69** to provide **4.70** - albeit along with a large quantity of glycal byproduct **4.71**. Interestingly, the use of the conventionally equatorial directing solvent, MeCN, still led to predominant formation of the axial alpha anomer. However, it's important to note that these glycosylations were conducted at either 0 °C or room temperature instead of the cryogenic temperatures that are typically employed for challenging glycosylations.

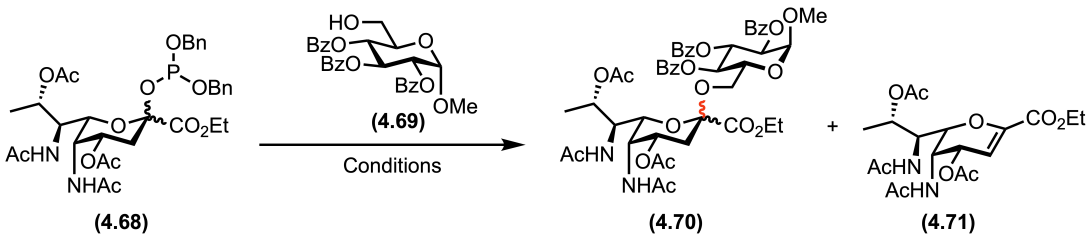


Figure 4.23. Ito's approaches towards glycosidation of Pse donors. Conditions: TMSOTf, CH_3CN, 0 °C, 3h (28% α:β = 10:1 **4.70**, 45% **4.71**), or TMSOTf , CH_2Cl_2, rt, 6 h (35% α **4.70**, 62% **4.71**).

Both Crich and Li developed glycosylation methods involving thioglycosides. Although Li was initially able to demonstrate good selectivity with a *p*-tolylthio anomeric leaving group, they later adopted an adamantane thioglycoside donor[360] (**4.74**) in analogy to that used by Crich (**4.72**).[361] The adamantane thiol leaving group possesses higher electron density on the sulfur atom due to the large number of inductively electron donating alkyl groups. This enhanced reactivity at the S-atom facilitated activation at cryogenic temperatures with the *N*-iodosuccinimide (NIS)/triflic acid (TfOH) promoter system. Notably, both donors also employed carbamate or azido groups as N5 and N7 substituents, which do not interfere with acid promoted glycosylations.

While Crich demonstrated the first β-selective pseudaminylation methods (**4.73**), Li developed conditions for generation of both α- and β- glycosides (**4.76** and **4.75**) from the common thioglycoside donor **4.74** (Figure 4.24).

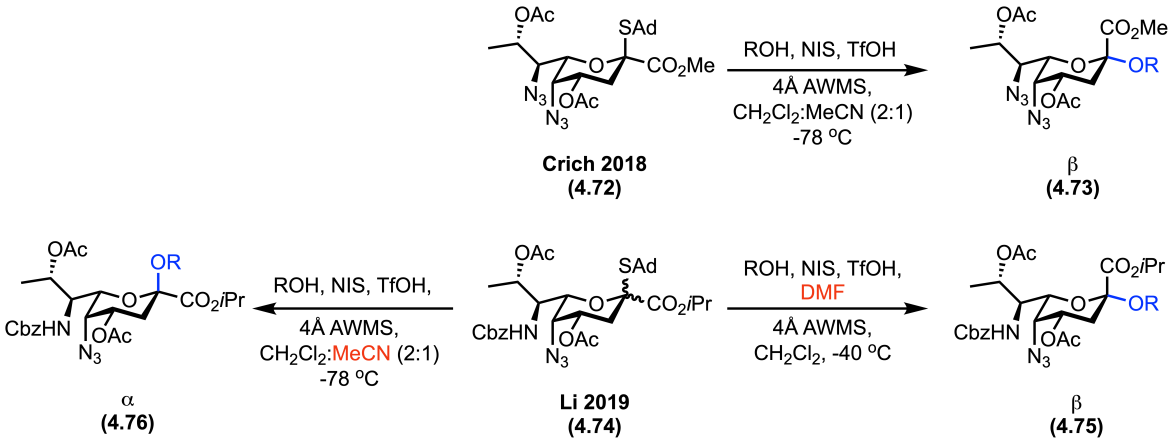


Figure 4.24. Crich and Li's analogous routes to providing α- and β-Pse glycosides.

Using identical reaction conditions, Crich and Li both demonstrated that glycosylation of Pse5N$_3$7N$_3$ (Crich) and Pse5N$_3$7NHCbz (Li) thioglycoside donors - differing in their C1-ester substituents and N7 substitution - proceed with high β-selectivity. Specifically, activation of donors **4.72** and **4.74** with NIS and TfOH in a CH_2Cl_2:MeCN (2:1 v/v) co-solvent system at –78 °C resulted in excellent β-selectivity across a broad range of alcohol acceptors. This selectivity is attributed to the well-established solvent effect of acetonitrile in glycosylation reactions. Acetonitrile is proposed to trap the oxocarbenium

ion intermediate **4.77**, forming an axial glycosyl nitrilium ion **4.78** that undergoes nucleophilic substitution *via* an S_N2-like pathway to form β-glycoside **4.75** (Figure 4.25).

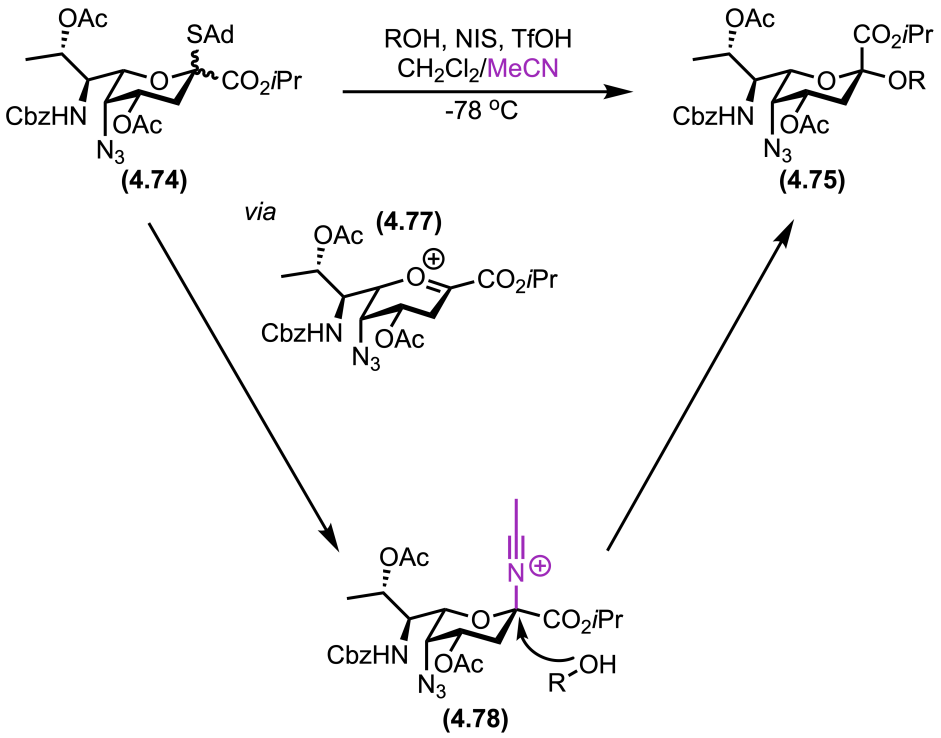


Figure 4.25. Mechanistic proposal for β-selectivity observed in glycosidation of Li's Pse donor **4.74** when co-solvent system CH_2Cl_2/MeCN is used.

Interestingly, Li's initial studies employed a Pse5Troc7Cbz glycosyl donor (**4.79**). When subjected to the same reaction conditions as those used for the corresponding Pse5$N_3$7Cbz donor, glycosylation proceeded with unselective or axial selectivity (**4.80**). This observation suggests that differences in N5 protecting group can contribute to variations in anomeric selectivity. It was proposed that the axial *N*-Troc group at C5 engages in remote anchimeric assistance to some degree during the glycosylation event (**4.81**), partially blocking the β-face of the oxocarbenium ion intermediate (**4.82**) (Figure 4.26).

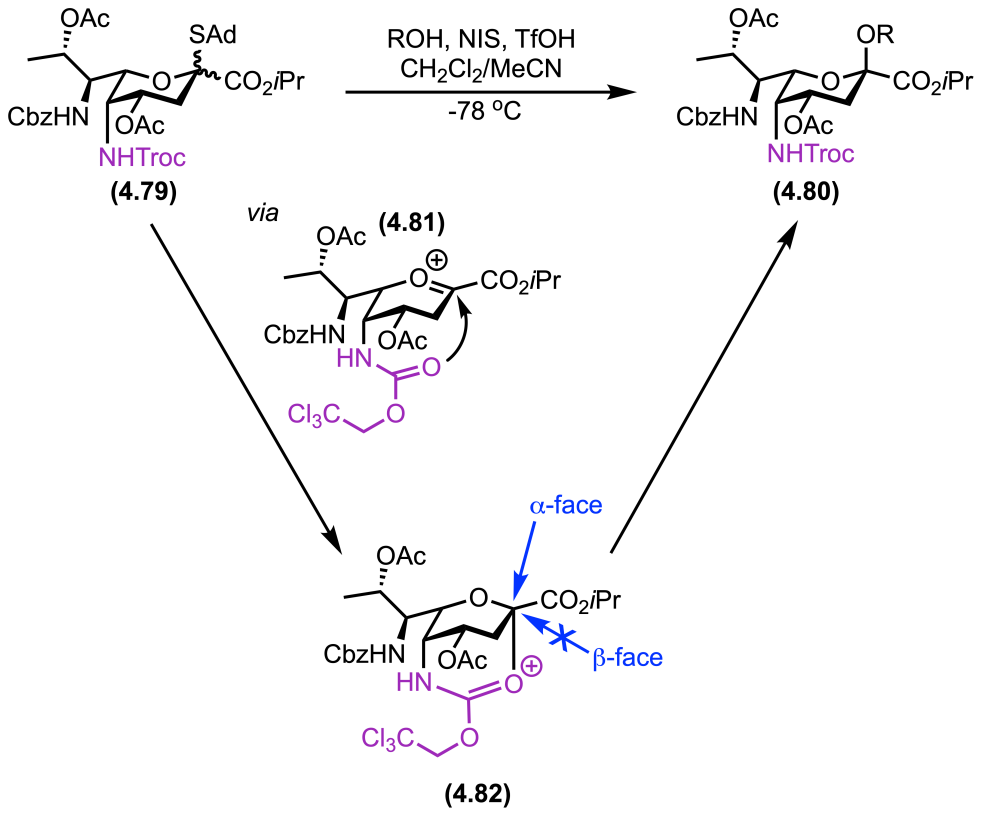


Figure 4.26. Postulated anchimeric effect from 5-NHTroc substituent in Li's Pse donor **4.79** eroding β-stereoselectivity when the co-solvent system CH_2Cl_2/MeCN is used.

In Li's methodology, *N*,*N*-dimethylformamide (DMF) was used as a stereodirecting additive to provide excellent α- stereoselectivity for glycosidation of donor **4.74**.[362] This was built on prior work that demonstrated highly axial-selective glycosylations in the presence of DMF owing to the formation of *N,N*-dimethylformaminium intermediates from reaction with oxocarbenium ion **4.77**,[363] such as **4.83** and **4.84**. The more reactive equatorial *N,N*-dimethylformaminium ion **4.84** is proposed to lead to the major product **4.76** through S_N2-like inversion by the alcohol nucleophile in an example of Curtin-Hammett kinetics (Figure 4.27).

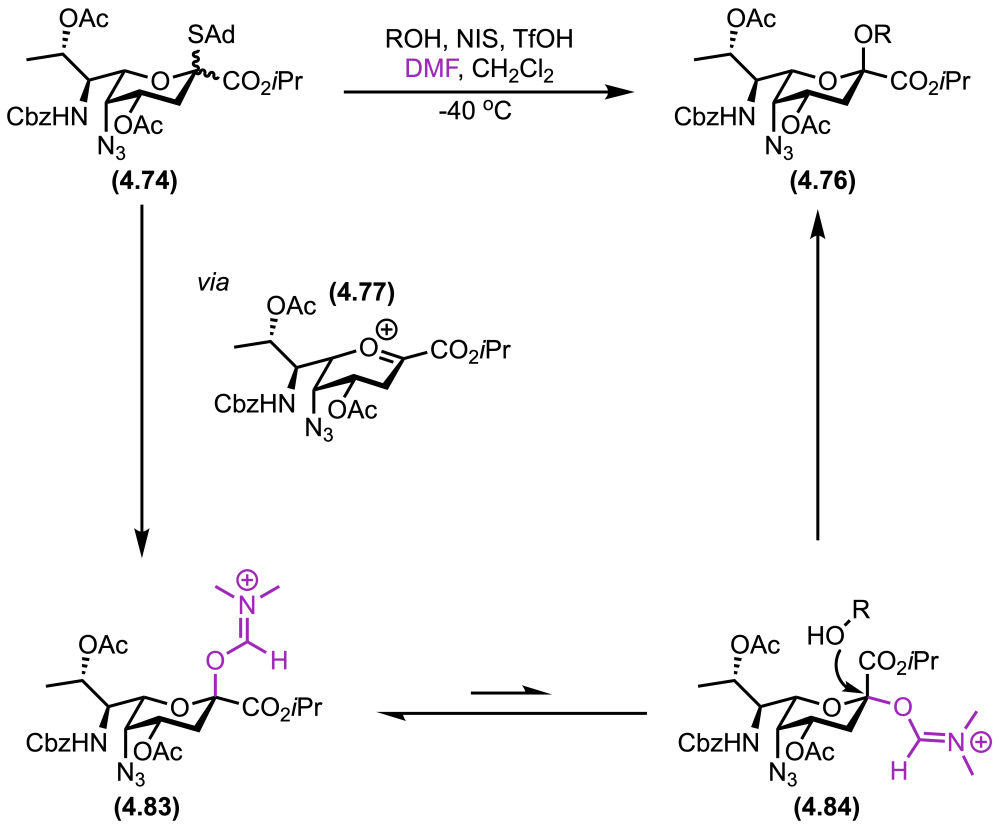


Figure 4.27. Mechanistic explanation for α- selectivity observed in glycosidation of Pse donor **4.74** when DMF is used as an additive.

4.5 Chapter Aims

The primary goal of the research presented in this chapter was to design and execute syntheses of Pse derivatives found in Gram-negative bacteria. These glycoconjugates were designed for screening against the Pse5Ac7Ac-specific monoclonal antibody previously developed by Tang *et al*. with the aim of evaluating the binding affinity and selectivity of the antibody. While Tang *et al*. demonstrated that native bacterial flagella presenting Pse exhibit an α-glycosidic linkage, both α and β linked Pse pseudaminosides were synthesised to probe whether they are recognised by the antibody.

A parallel aim of this work was to address a series of synthetic problems that were encountered when applying Li's pseudaminic acid donor to Tang's synthesis of α-pseudaminylated peptides. Namely, this work sought to address several low yielding steps in the synthesis of Li's versatile Pse5$N_3$7Cbz donor, while incorporating a C1 ester protecting group that could be removed under milder conditions following solid-phase peptide synthesis (SPPS).

4.6 Results and Discussion

4.6.1 Synthetic Methodology

A Pse-donor was required that would enable the formation of both α-glycosides (**4.85**) and orthogonally protected amines, allowing for the synthesis of multiple variants of *N*-substituted Pse donors. Both Li and Crich's syntheses provided a Pse-donor (**4.52** and **4.74**) that met these requirements (Figure 4.28).

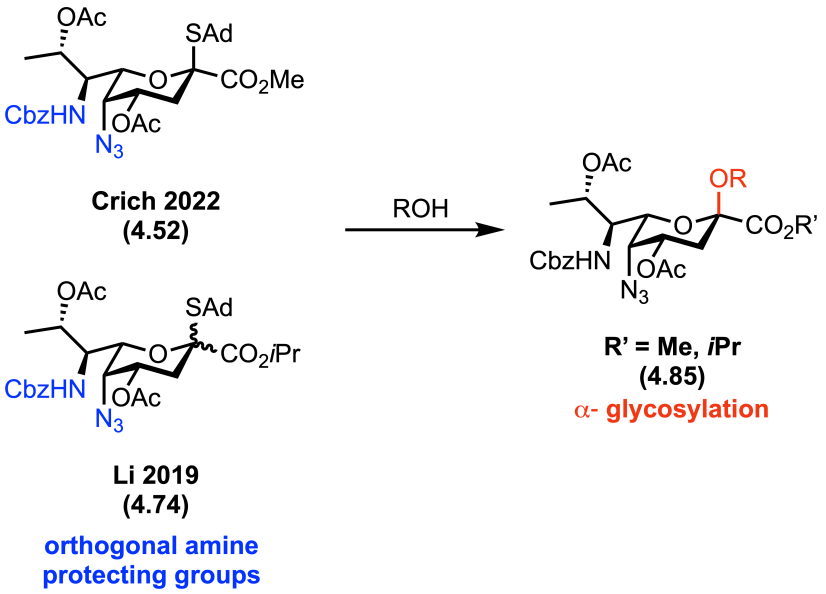


Figure 4.28. Functional group requirements for the Pse donor to be synthesised.

Ultimately, Li's synthesis was selected for several reasons. The use of the inexpensive starting material, L-*allo*-threonine, provided greater flexibility for trialling and optimising the synthetic pathway. With only two carbon stereocentres set, a range of stereocontrolled strategies could be explored to access the required donor. This is in contrast to Crich's approach which relied on protecting group manipulations, oxidation–reduction sequences, and S_N2 reactions. Although not a primary goal of this work, Li's route also offers the possibility of preparing other NulO's beyond Pse, such as legionaminic acid (Leg), acetaminic acid (Aci) and their corresponding 8-epi isomers, by starting with different threonine diastereomers or through epimerisation of intermediates/minor diastereomers. Additionally, the preparation of Pse donors *via* Li's route has been extensively worked on within the Payne group, providing both prior expertise and ready access to reagents and intermediates.

4.6.2 Limitations of Current Synthesis

Although Li's synthesis is well-established and has been used successfully in the Payne Research Group, it still has a number of limitations and areas where the synthetic strategy could be optimised.

1) Use of isopropyl ester

Firstly, Tang and Li's use of a C1-isopropyl ester protected pseudaminyl donor (**4.86**) necessitates strongly alkaline conditions for the late-stage unmasking of the C1 carboxylic acid. While these conditions are not necessarily problematic for glycans, they are not well tolerated by pseudaminylated peptides. As encountered in the work by Tang *et al.*, the use of strongly alkaline conditions or prolonged exposure to basic conditions resulted in peptide epimerisation and β-elimination of the pseudaminyl moiety from the peptide (**4.87**) (Figure 4.29).

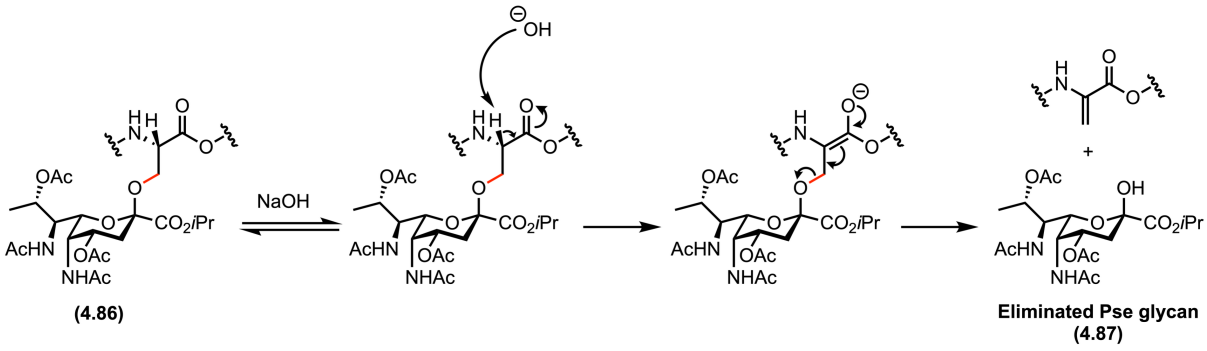


Figure 4.29. β-elimination of Pse from glycopeptide, shown proceeding through an E1cb mechanism. Key bond broken shown in red.

To circumvent this, Tang *et al.* proposed the use of a less hindered methyl ester protecting group on C1 that would undergo rapid hydrolysis under milder conditions, as was shown previously by the Payne group for the synthesis of sialylated glycopeptides.[364]

However, the bulky isopropyl ester was shown to be important in the synthesis of the pseudaminyl donor as it suppresses lactonisation during the formamide hydrolysis step.[349] Specifically, when the hydrolysis of formamide **4.88** was conducted with a C1 methyl ester (as opposed to isopropyl ester), an intramolecular lactonisation occurred, providing butyrolactone **4.89** (Figure 4.30).

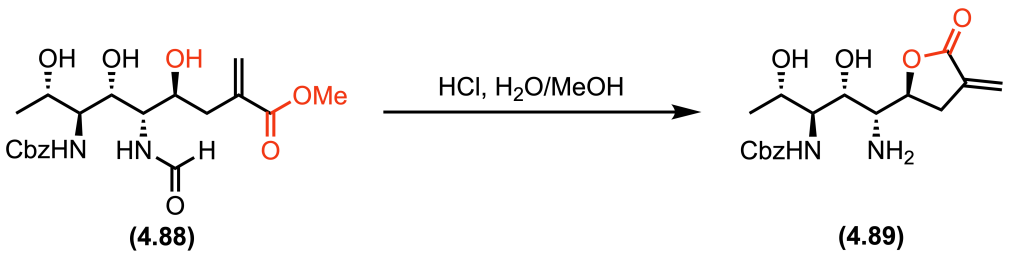


Figure 4.30. Formation of γ-butyrolactone by-product (**4.89**) under acidic conditions. Reacting functional groups (hydroxyl, methyl ester) and lactone functionality formed shown in red.

As a result, Tang *et al.* attempted to substitute the isopropyl ester for a methyl ester at a later stage in the synthesis (Figure 4.31). However, both transesterification under basic conditions (NaOMe, MeOH) or *via* hydrolysis (LiOH, H_2O) resulted in formation of oxazolidines **4.90/4.91** and **4.92/4.93** respectively. Although Tang trialled this on Pse5Troc7Cbz (**4.79**), the formation of an oxazolidinone between alcohol C8 and NCbz on C7 suggested that this process would still not be suitable for the desired Pse5N$_3$7Cbz donor **4.52**.

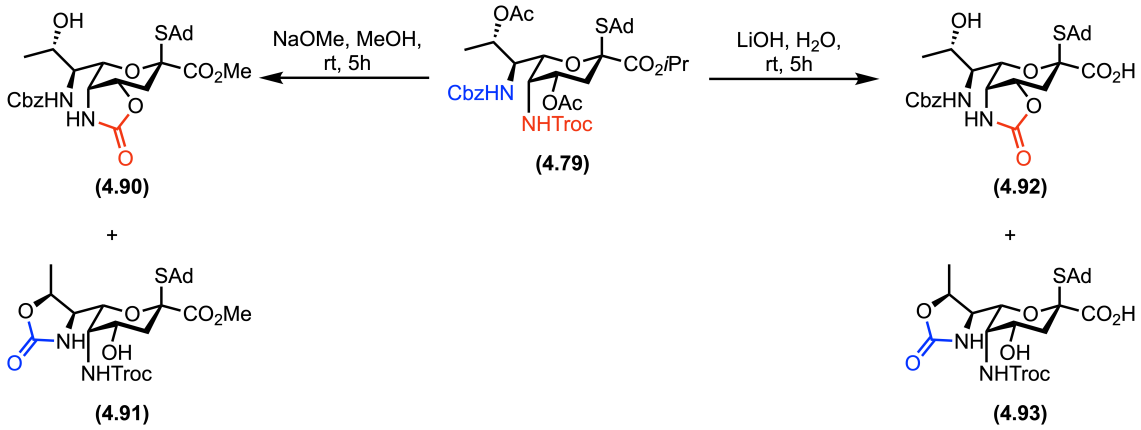


Figure 4.31. Formation of oxazolidinones during late-stage transesterification of Pse5Troc7Cbz thioglycoside donor as observed by Tang *et al*. Oxazolidine formation was seen between both C4-OH and C5-NHTroc (red), and C7-Cbz and C8-OH (blue).

Tang *et al.* also attempted transesterification at a much later stage in the synthesis of a Pse5Ac7Ac glycosylserine building block (**4.94**) (Figure 4.32), before incorporation into a peptide. At this stage, both NHCbz and NHTroc groups had been converted to NHAc, and there was no risk of oxazolidinone formation. However, it was not possible to selectively hydrolyse the isopropyl ester in the presence of the *tert*-butyl ester on the serine moiety.

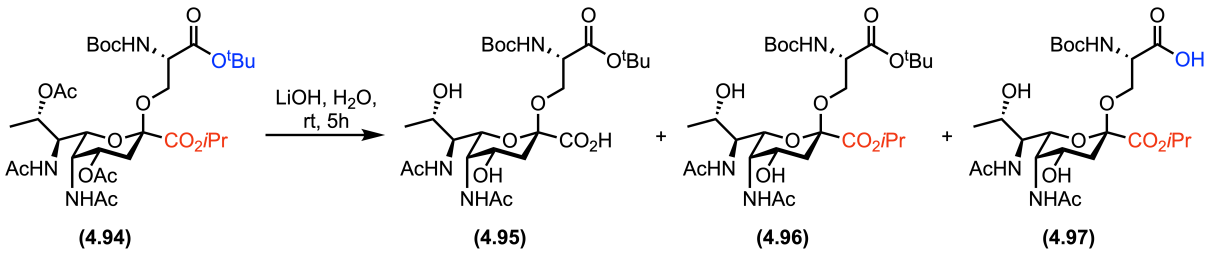


Figure 4.32. Saponification of isopropyl ester **4.94**, resulting a mixture of products. Desired product **4.95** was obtained, alongside lack of isopropyl ester hydrolysis (red, **4.96**) and undesired hydrolysis of *tert*-butyl ester group (blue, **4.97**).

To address the issues with the previous method, a new strategy was developed for glycosylamino acid synthesis, avoiding the use of a *tert*-butyl ester for serine protection. Instead, a *tert*-butyldiphenylsilyl (TBDPS) protected 'serinol' acceptor was used, allowing oxidation of the primary alcohol to a carboxylic acid following transesterification of the glycan (Figure 4.33). In this strategy, the α-selective glycosylation method was applied to thioglycoside donor **4.79** and TBDPS-protected serinol acceptor **4.98**, yielding the pseudaminylated serinol derivative **4.99** exclusively as the α-anomer. Both the NHTroc and NHCbz substituents were converted to NHAc through separate reductive acetylation procedures to yield the bis(acetamide) **4.100**. The isopropyl ester was then hydrolysed and replaced with a methyl ester through alkylation with methyl iodide, followed by re-acetylation of the C6 and C8 alcohols to form **4.101**. Finally, desilylation and oxidation furnished the desired Alloc-Ser(α-Pse(CO$_2$Me)-OH building block **4.102**, which was successfully incorporated into pseudaminylated peptides.

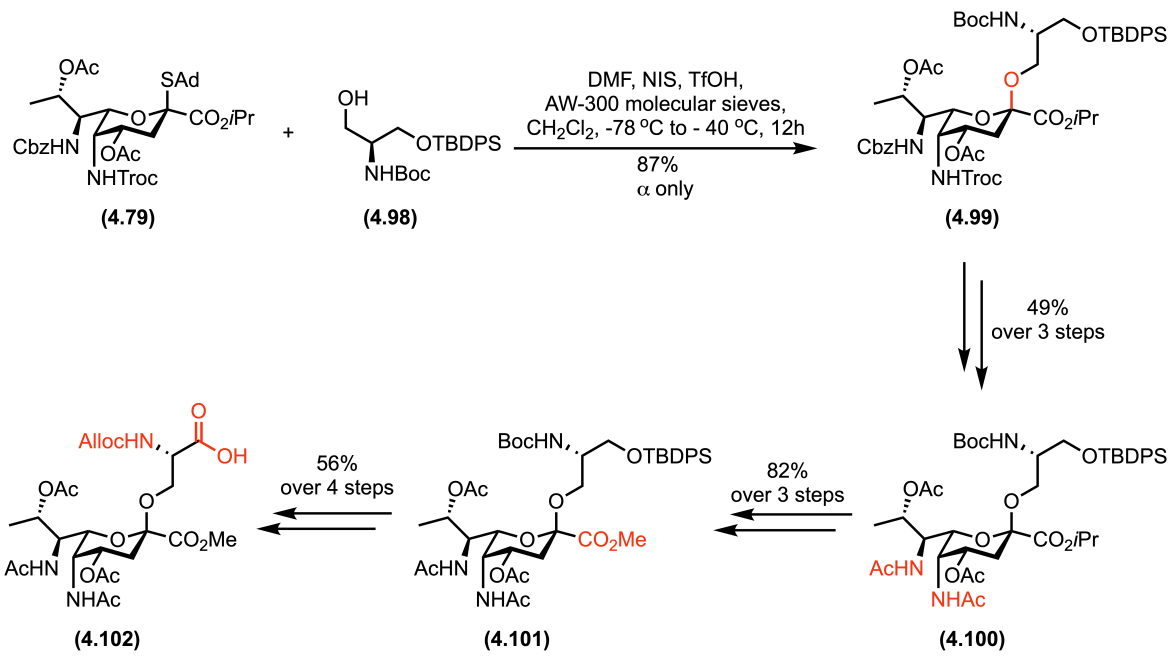


Figure 4.33. Synthesis of Alloc-Ser(α-Pse(CO_2Me))-OH building block 4.102. Key transformations are shown in red.

Although Tang *et al*. successfully synthesised the glycosyl amino acid **4.102**, the need to replace the isopropyl ester with a methyl ester added an extra seven linear steps to the synthetic route (not including the steps required to prepare the serinol acceptor). Therefore, it was decided that investigating alternative C1 protecting group strategies would be necessary to streamline access to pseudaminic acid derivatives and pseudaminylated peptides in the future.

2) Installation of azide

The 5-azido donors (**4.52** and **4.74**) are more versatile targets than the Troc-protected analogue, as they can be used to access both α- and β-pseudaminosides (*vide supra*). The Li Research Group attempted direct conversion of Pse5$NH_2$7Cbz adamantyl thioglycoside (**4.103**) to the corresponding Pse5$N_3$7Cbz donor but were unsuccessful in generating the azide intermediate under various diazotransfer conditions, necessitating installation of the azide functionality prior to cyclisation (Figure 4.34).

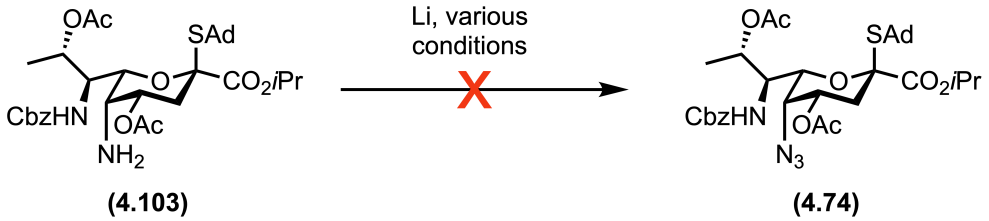


Figure 4.34. Li's unsuccessful trials to convert amine **4.103** into azide **4.74**. Exact conditions trialled were not reported.

Consequently, Tang *et al.* pursued a stepwise conversion starting from linear intermediate **4.104** (Figure 4.35). Formyl deprotection liberated the free amine, which was subsequently diazotised using triflic azide to form **4.105**. However, the azide was found to undergo azido–ene cycloaddition, forming bicyclic triazoline **4.106** as a significant byproduct. To minimise loss of material, **4.105** had to be immediately subjected to ozonolysis, acetylation, and thioglycosylation to afford the stable thioglycoside donor **4.74**.

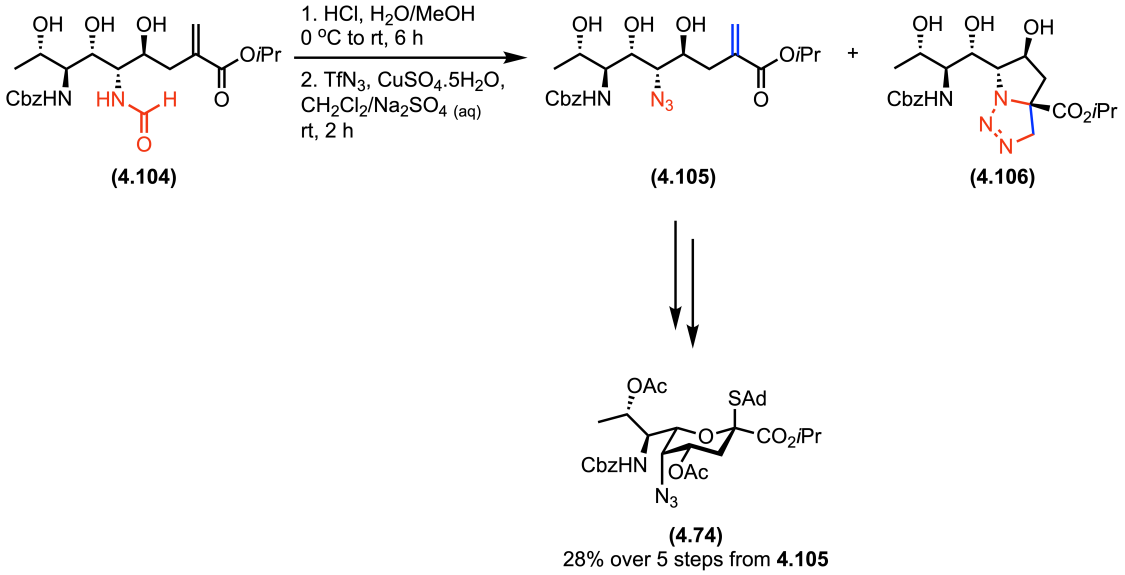


Figure 4.35. Synthesis of Pse5N$_3$7Cbz adamantyl thioglycoside donor **4.74**, highlighting the deleterious azide-alkene cycloaddition side reaction.

With the aim of developing a more robust synthetic strategy towards Li's Pse5N$_3$7Cbz glycosyl donor and glycosylamino acids, we proposed to trial a variety of different means of installing the azide, as well as alternative C1 ester groups/surrogates.

4.7 Synthesis of Pseudaminic acid analogues

4.7.1 Preparation of aldehyde

All synthetic routes proceeded from Li's common intermediate, Garner's type aldehyde **4.54**. Li's synthetic route was followed from commercially available L-*allo*-threonine (**4.18**) to the corresponding aldehyde **4.54** (Figure 4.36). On a 20 g scale, the amine of L-*allo*-threonine was first protected as a Cbz carbamate, followed by methyl esterification of the carboxylic acid (**4.107**). The resulting intermediate was then protected as an oxazoline (**4.108**) using 2,2-dimethoxypropane and $BF_3{\cdot}OEt_2$ as a Lewis acid catalyst.

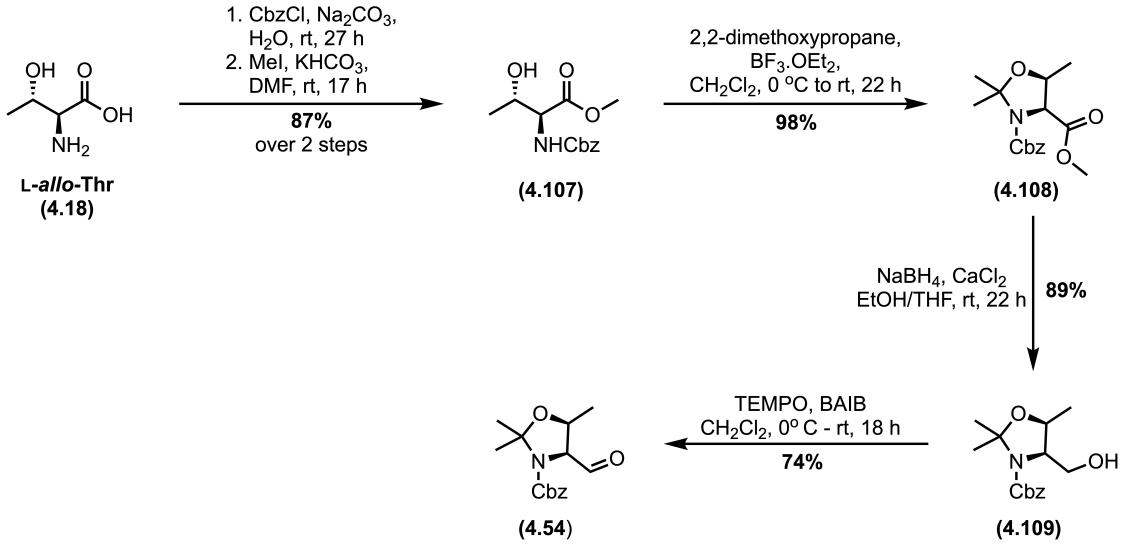


Figure 4.36. Synthesis of Garner's-type aldehyde (**4.54**) from L-*allo*-Thr (**4.18**) *via* Li's synthetic route.

Attempts to directly reduce the methyl ester to the aldehyde with DIBAL-H proved unsuccessful, yielding the over-reduced primary alcohol **4.109**. Instead, reduction was achieved using *in situ* generated calcium borohydride in an EtOH/THF co-solvent system. $Ca(BH_4)_2$ was selected for its enhanced chemoselectivity and compatibility with sensitive functional groups. Ca^{2+} is a relatively large and diffuse ion with a lower charge density compared to smaller monovalent cations such as Li^+. This imparts better solvation in ethanol and a better solvent separation of the ion pair with BH_4^-.[365] Ethanol serves multiple roles; modulating reactivity by forming nucleophilic boronate intermediates and preventing calcium salt precipitation, while also acting as the proton source post-reduction. The resulting alcohol **4.109** was then oxidised to the aldehyde **4.54** using catalytic TEMPO and bis(acetoxy)iodobenzene in CH_2Cl_2. The oxidation was

performed under anhydrous conditions to suppress over-oxidation *via* the aldehyde hydrate. However, minor formation of the corresponding carboxylic acid was observed despite careful monitoring. Aldehyde **4.54** was obtained in 56% overall yield over five steps.

4.7.2 Aldol-type reaction of Garner's aldehyde

In Li's synthesis, aldol-type reaction between aldehyde **4.54** and thioester-isocyanide **4.55** served to form the C5-C6 bond as well as set the stereochemistry at those positions (**4.56** and **4.57**) (Figure 4.37A). As an alternative approach, we proposed the aldol reaction of methyl 2-azido acetate **4.110** and Garner's type aldehyde **4.54**, which would effectively install the azide at an early stage and circumvent the need for several low-yielding N5 protecting group manipulations, forming a mixture of diastereomers at C5 and C6 (**4.11**) (Figure 4.37B). As an added advantage, this strategy would also remove the need for synthesising a thioester isocyanide, in favour of a commercially available azido ester.

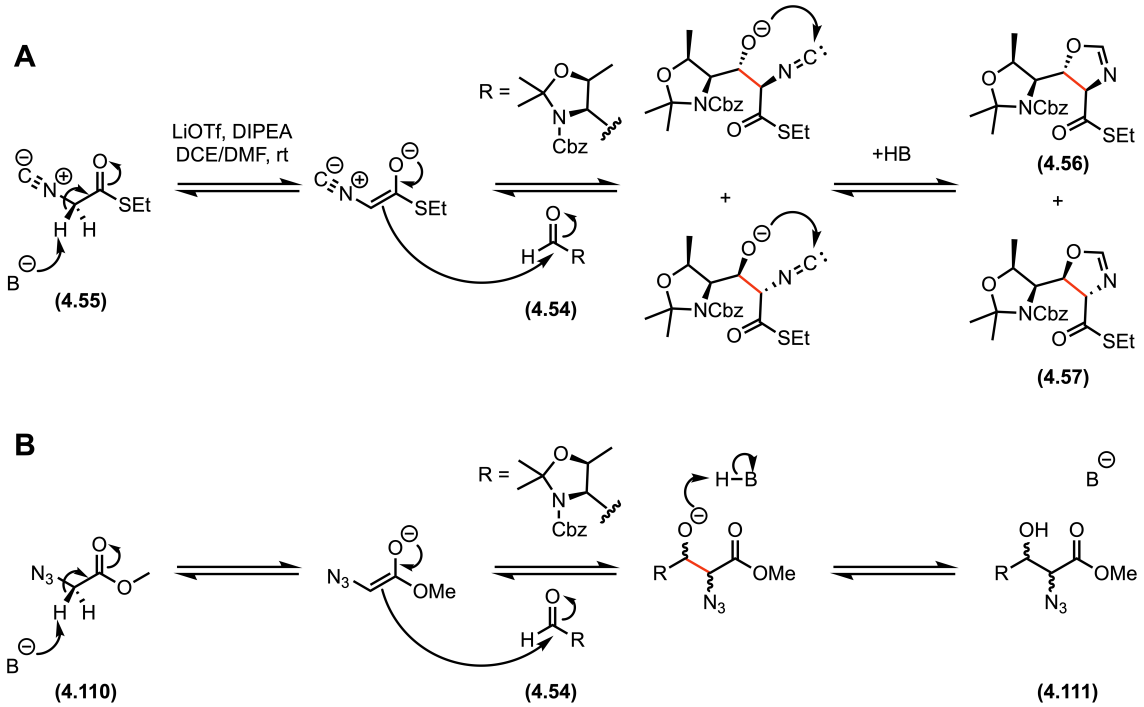


Figure 4.37. Comparing two different C5-6 bond formation strategies. **A)** Li's aldol-like strategy employing a thioester isocyanide, and **B)** Proposed aldol reaction employing methyl 2-azido acetate. C5-C6 bond formation indicated in red.

Additionally, it was envisioned that any undesired diastereomers arising from the aldol reaction could be employed directly in the synthesis of acinetaminic acid (Aci, **4.113**), which bears opposite stereochemistry at C5, or indirectly through Mitsunobu inversion at C6 to provide either Pse (**4.112**) or Aci (**4.113**) scaffolds (Figure 4.38). Although there is no literature precedent for aldol reactions of alpha azido-esters with aliphatic aldehydes, there are multiple examples of successful aldol reactions between aryl aldehydes and both methyl[366] and ethyl[367–369] 2-azido acetate, including aldol condensations.[370]

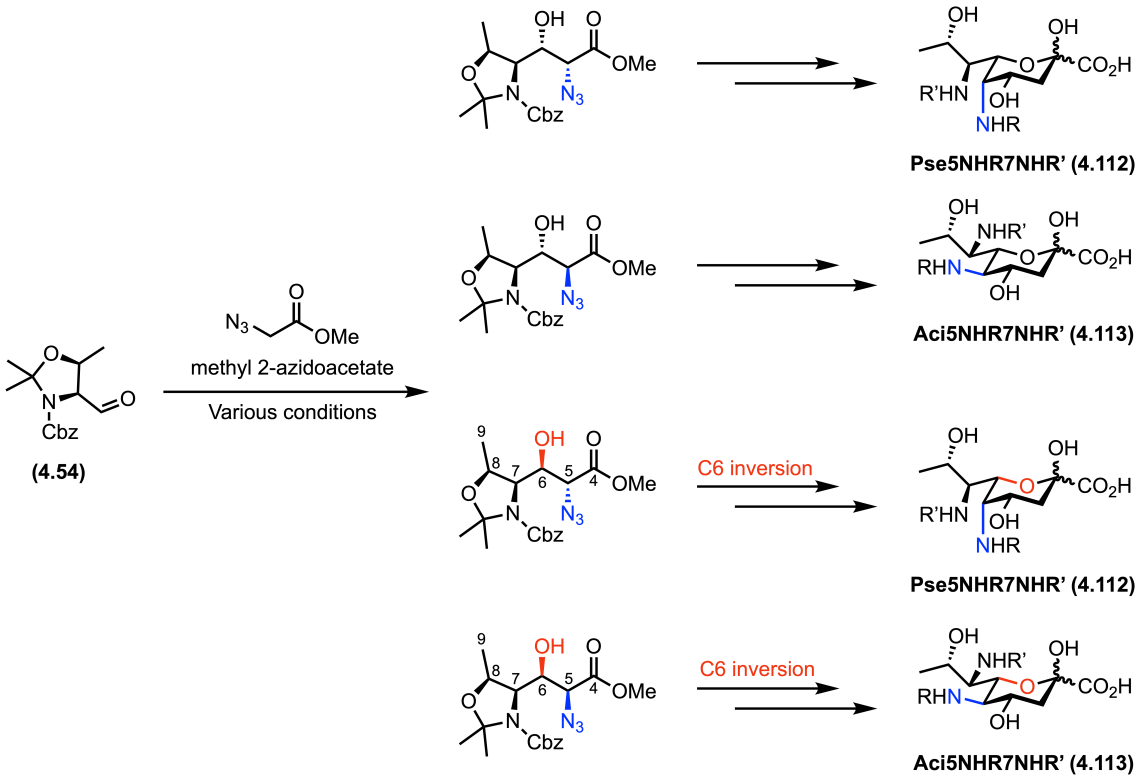


Figure 4.38. Four potential diastereomers produced from reaction of Garner-type aldehyde (**4.54**) with methyl 2-azido acetate, showing potential to convert these to desired nonulosonic acid variants Pse (**4.112**) and Aci (**4.113**).

Additionally, direct catalytic asymmetric aldol reactions of an α-azido amide with aryl aldehydes have been demonstrated,[371] indicating that stereoselectivity can be controlled. Boron chelation models would initially be trialled, offering a stereoselective pathway for the desired addition products (Figure 4.39).

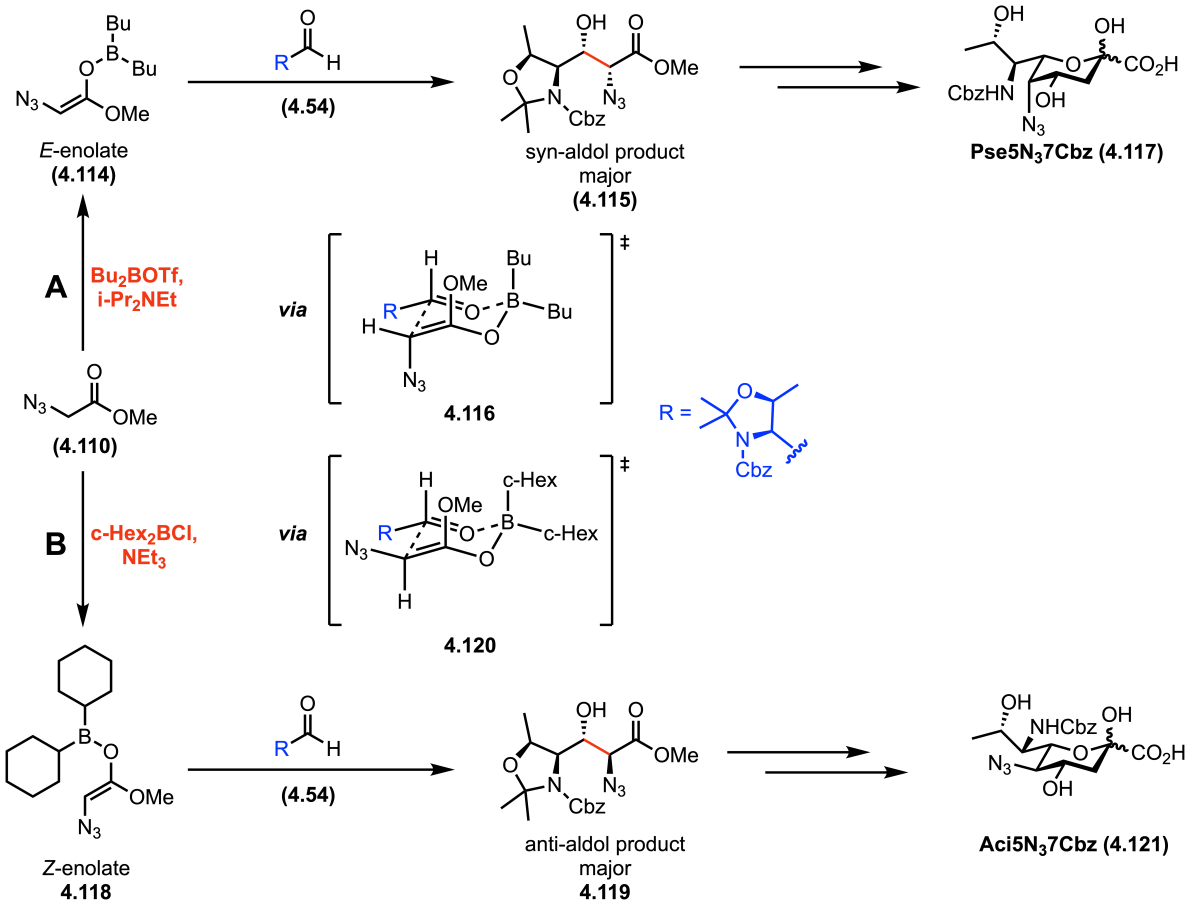


Figure 4.39. Proposed methodology of selective aldol reaction *via* differing boron-chelation models. Route A) allowing access to Pse (**4.117**) scaffolds and route B) to Aci (**4.121**) scaffolds. The bond formation from the aldol reaction is shown in red.

Lithium chelation-promoted aldol reactions, as used by Li,[349] usually only provide moderate stereoselectivity, as the transition state is quite open and loose[372] due to weak coordination of lithium ions (Li-O bond lengths of 1.9 – 2.2 Å). In comparison, boron chelation[373] provides much more rigid transition states (B-O bond lengths of 1.4 – 1.5 Å), and offer greater stereoselectivity. The conformation of the initial organoboron-carbonyl adduct determines the trajectory of deprotonation, and therefore whether the *E* or *Z* enolate is formed.[373]

To generate the correct Pse stereochemistry we proposed generating the *E* ester enolate (**4.114**) through use of a dibutyl boron Lewis acid (Figure 4.39A). This would be expected to engage the aldehyde (**4.54**) in a Zimmerman-Traxler transition state in which the bulky R group of the aldehyde occupies a pseudo-equatorial position to minimise 1,3-diaxial

strain (**4.116**). The *syn*-aldol product (**4.115**) should result as the major product, providing the correct C5 and C6 stereochemistry for Pse donor **4.117**.

Analogously, the use of bulky and large alkyl groups attached to boron such as cyclohexyl (c-Hex), would be expected to proceed via the *Z* ester enolate (**4.118**) and pass through a Zimmerman-Traxler transition state (**4.120**) resulting in the *anti*-aldol product (**4.119**) as the major product (Figure 4.39B). This would be expected to provide the correct C5 and C6 stereochemistry for an Aci donor, **4.121**, making this a potential versatile route to access a range of nonulsonic acids in future work.

It has been demonstrated that it is crucial to conduct aldol reactions with alpha azido carbonyls with catalytic base (0.2 eq).[374] The aldol reaction was trialled with conditions based on the chelation models outlined in Figure 4.39. Initially, methyl 2-azidoacetate (**4.110**, 1.5 eq.) was treated with a dialkylboron Lewis acid (2.0 eq) in anhydrous CH_2Cl_2 or THF at –78 °C. A base was then added to generate the corresponding boron enolate. Initial reactions employed 0.2 eq of base; however, in the absence of observable reactivity upon addition of aldehyde (**4.54**), subsequent trials increased the base loading to 1.0 and 2.0 eq. Aldehyde (**4.54**, 1.0 eq) was added as a solution at -78 °C, and the reaction mixture was maintained at this temperature for varying durations before being gradually warmed to room temperature in an attempt to initiate conversion (Table 4.2). Reaction progress was monitored by quenching aliquots and analysing by LC-MS. Unfortunately, all attempts using boron enolates under these conditions failed to yield the desired product (**4.122**); only unreacted **4.54** was observed in each case.

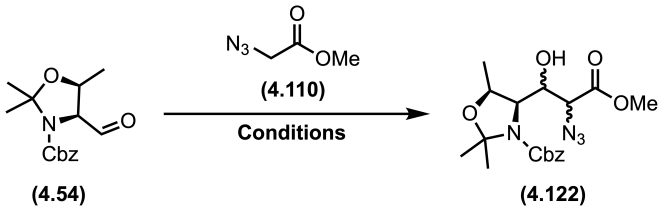


Table 4.2: Conditions and results of attempted aldol reactions.

Conditions	Results
i). 4.110 (1.5 eq), Bu_2BOTf (2.0 eq), DIPEA (0.2 - 2.2 eq), CH_2Cl_2, -78°C, 1 h **ii). 4.54** (1 eq), CH_2Cl_2, -78°C to 0 °C, 3 h	No reaction
i). 4.110 (1.5 eq), c-Hex_2BCl (2 eq), NEt_3 (0.2-2.2 eq), THF, -78°C, 1 h **ii). 4.54** (1 eq), THF, -78°C 3 h, 0 °C, 5 h	No reaction

As a result of the unsuccessful initial trials, **4.110** and **4.54** were subjected to a range of more conventional aldol reaction conditions (Table 4.3).These included the use of strong lithium bases (LiHMDS, LDA), milder sodium alkoxides (NaOMe), and the comparatively weak inorganic base K_2CO_3. Additional variables explored included the order of reagent addition (e.g., entry 3, where azide (**4.110**) was added to a preformed solution of LDA), variation in base equivalents, solvent systems (THF, MeOH), reaction temperatures, and durations. Despite these efforts, none of the conditions tested led to any observable conversion of aldehyde (**4.54**) to the desired aldol product.

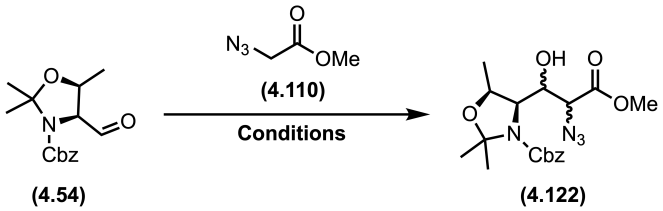


Table 4.3. Conditions and result of attempted aldol reaction.

Conditions	Results
i). 4.110 (1.5 eq), LiHMDS (2 eq), THF, -78 °C, 1 h **ii). 4.54** (1 eq), THF, -78 °C 3 h, 0 °C 5 h	No reaction
i). 4.110 (1.5 eq), LDA (2 eq), THF, -78 °C, 1 h **ii). 4.54** (1 eq), THF, -78°C 3 h, 0 °C 5 h	No reaction
i). 4.110 (1.5 eq) added to LDA (3 eq) in THF, -78 °C, 1 h **ii). 4.54** (1 eq), THF, -78 °C 3 h, 0 °C 5 h	No reaction

i). 4.110 (1.5 eq), NaOMe in MeOH (5 eq), THF, -78°C, 1 h **ii). 4.54** (1 eq), THF, -78°C to 0 °C, overnight	No reaction
i). 4.110 (1.2 eq), K_2CO_3 (3 eq), MeOH, 0 °C - rt, 5 h **ii). 4.54** (1 eq), MeOH, 0 °C, overnight	No reaction

The likely cause of the unsuccessful reaction was the significant steric hindrance associated with aldehyde **4.54**. It has been previously reported that α-azido ketones (**4.123**) are prone to decomposition via nitrogen extrusion, a pathway that competes with enolate addition to the electrophile (E+) (Figure 4.40).[374] It has been shown that use of catalytic amounts of base allowed for the generation of a low steady-state concentration of enolate (**4.124**) in the presence of excess aldehyde, favouring aldol condensation (**4.125**). However, due to the delicate kinetic balance between productive condensation and base-promoted decomposition of the enolate (**4.126** to **4.127**), any steric or electronic factor that slows the rate of C–C bond formation significantly compromises the yield of the desired aldol product. Notably, it has also been observed that α-branched aldehydes failed to afford aldol adducts in synthetically useful yields.[374]

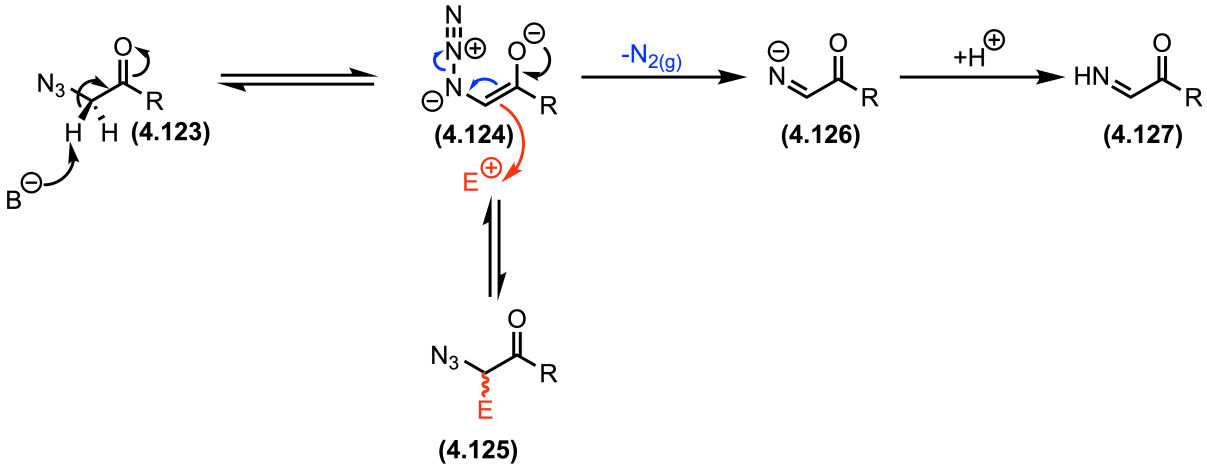


Figure 4.40. α-azido carbonyl decomposition pathway, competing with enolate addition to the electrophile (E+).[374]

In our case, this issue was likely compounded by use of an ester-derived enolate rather than a ketone, further reducing the acidity of the α-proton and lowering the enolate concentration. Based on these findings and the failure of multiple attempted conditions,

alternative strategies for the optimisation of the Pse5N$_3$7Cbz donor synthesis were pursued.

4.7.3 Li's route to *syn*-aldol product

Li's route was followed to produce aldol-like adducts **4.56** and **4.57** (Figure 4.41). As outlined in section 4.3.7, aldehyde **4.54** underwent a highly *syn*-specific chelation-assisted aldol-type reaction with thioester-isocyanide, followed by acid-catalysed hydrolysis of oxazolines **4.128** and **4.129** to provide a mixture of diastereomers (47% of **4.56** and 30% of **4.57**). As seen by Li, desired diastereomer **4.56** was provided as the major product.

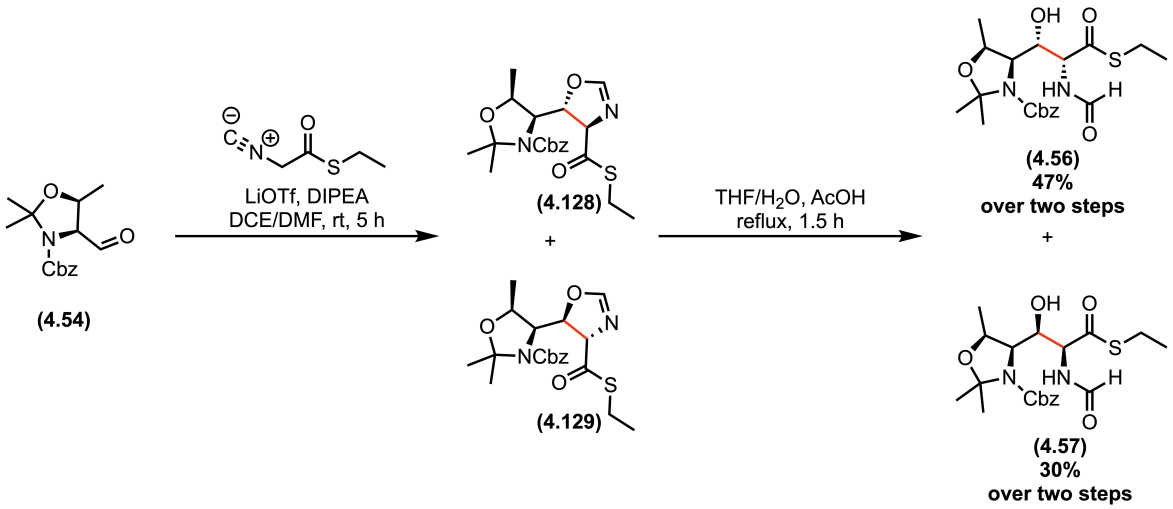


Figure 4.41. Aldol-type reaction of aldehyde **4.54** to produce diastereomers **4.56** and **4.57**, with the key bond formation shown in red.

As undesired diastereomer **4.57** was produced as a significant byproduct, it was envisioned that alcohol inversion by a Mitsunobu reaction could provide a route to a similar Aci donor from this material in the future (Figure 4.42).

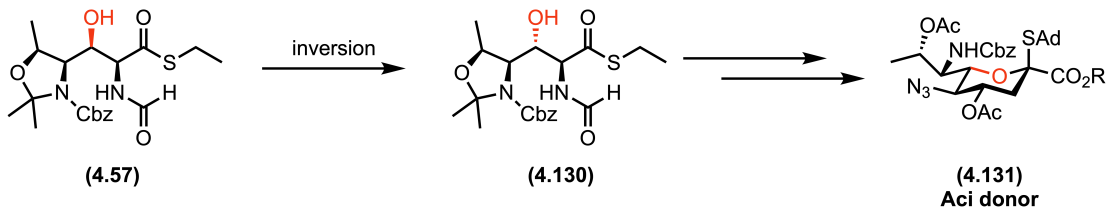


Figure 4.42. Proposal for conversion of undesired diastereomer **4.57** into Aci donor **4.131** *via* Mitsunobu inversion.

The reaction of alcohols with silanols under Mitsunobu conditions to give corresponding silyl ether has been reported.[375] Successful inversion of secondary alcohols into both trimethyl silyl and triethylsilyl (TES) ethers has been achieved. This strategy is well-suited to substrate **4.57** as the subsequent step in Li's synthesis involves a TES protection of alcohol **4.56**.

The reported conditions were applied to substrate **4.57**, beginning with preformation of the corresponding oxyphosphonium **4.132**, followed by addition of alcohol **4.57**. However, no formation of the desired product (**4.133**) was observed; only unreacted starting material was recovered (Figure 4.43).

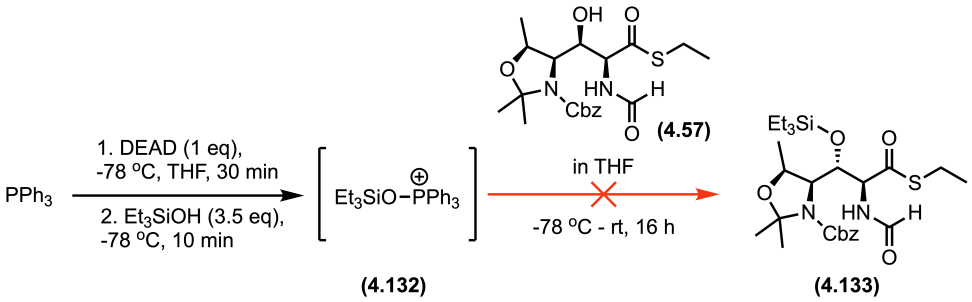


Figure 4.43. Attempted triethyl silanol Mitsunobu of alcohol **4.57**.

It was proposed that the combination of the sterically hindered substrate (**4.57**) and the bulky TES nucleophile inhibited the required S_N2 inversion at alcohol **4.57**. Consequently, more classical Mitsunobu conditions were trialled, utilising less hindered and more acidic acetic acid as a nucleophile. PPh_3 was reacted with DIAD to produce a betaine intermediate *in situ*, to which alcohol **4.57** and AcOH was added.[376] After 1 h stirring at room temperature, TLC indicated consumption of starting material. Upon purification and analysis, the product obtained was identified by nuclear magnetic resonance (NMR) as elimination product **4.134**, with no formation of desired acetate (Figure 4.44).

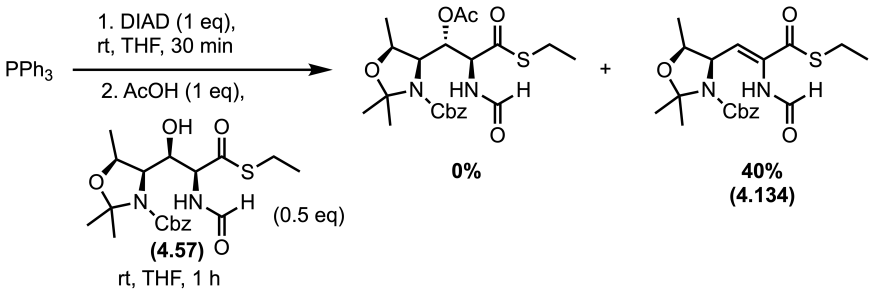


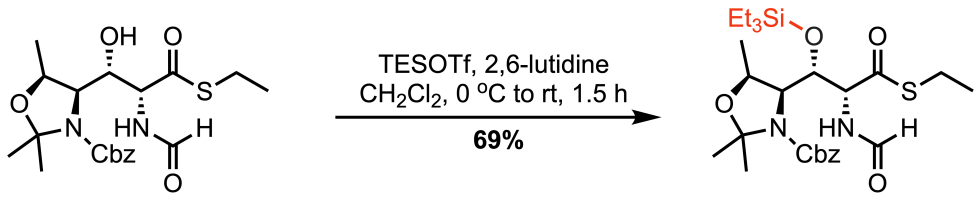
Figure 4.44. Mitsunobu trial on alcohol **4.57**, resulting in undesired elimination product **4.134**.

This observation is consistent with literature reports of serine esters undergoing elimination rather than substitution under Mitsunobu conditions.[377] Although substrate **4.57** is not a serine ester *per se*, it features a hindered secondary alcohol, and an α-proton rendered more acidic by the presence of an electron-withdrawing *N*-formyl group. Under the reaction conditions, elimination *via* a likely E1cB mechanism is thought to be favoured over substitution due to both the steric hindrance around the alcohol and the increased lability of the α-proton.

As a result of these unsuccessful attempts, efforts to invert the alcohol of the unwanted diastereomer were discontinued, and the major Pse configured diastereomer **4.56** was carried forward into subsequent steps for further optimisation trials.

4.7.4 Strategies for the installation of the C1 – C3 fragment

The synthetic route from Tang *et al.*[316] was followed to produce triethylsilyl ether **4.135** in 69% yield (Figure 4.45).



(4.56) **(4.135)**

Figure 4.45. Generation of TES-ether intermediate **4.135**.

At this point, Li's synthesis would proceed with a Fukuyama reduction of the thioester to produce aldehyde **4.59**, followed by In-mediated Barbier reaction with isopropyl 2-(bromomethyl)acrylate to install the C1-C3 fragment and provide isopropyl enoate **4.60** (Figure 4.46A). However as noted in section 4.6.2, the isopropyl ester ultimately requires harsh deprotection conditions, which are not compatible with peptides. Additionally, the C2 olefin is prone to undergo azido-ene cycloaddition after diazotisation at N5. Therefore, we proposed the use of a 3-(bromomethyl)furan (**4.136**) as an alternative C1-

C3 synthon, in which both the C1 ester and C2 alkene would be masked as a furan (Figure 4.46B).

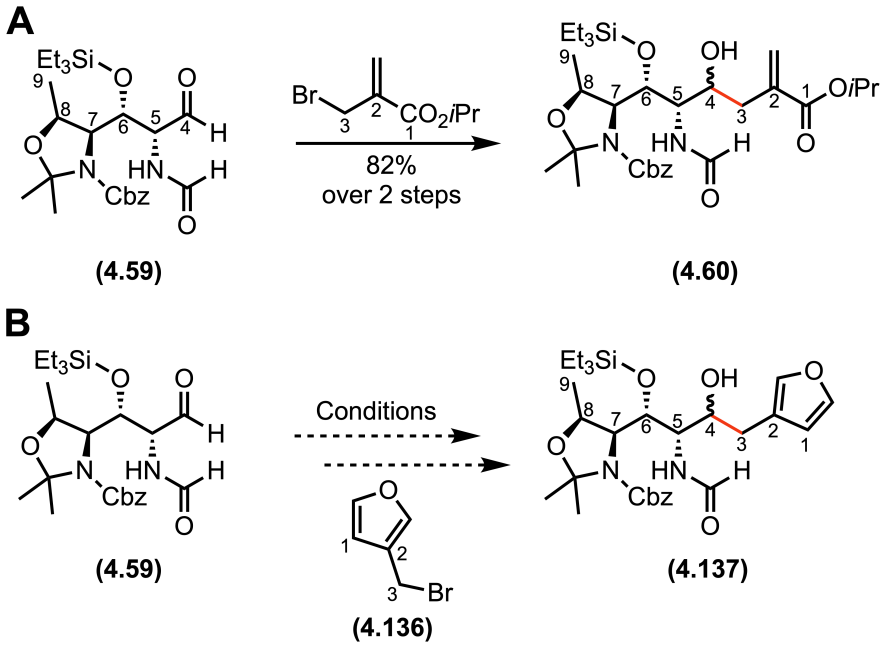


Figure 4.46. Comparison of two routes for installation of C1-C3 fragment. **A)** Li's Barbier route *via* isopropyl methacrylate and **B)** Proposed route *via* 3-(bromomethyl)furan. Key bond formation is highlighted in red.

It was proposed that either a Barbier reaction or Fukuyama ketone synthesis could be employed for alkylation with 3-(bromomethyl)furan (**4.136**). The furan could then be unmasked at a later stage by a tandem ozonolysis and Pinnick oxidation[378] to provide ketoacid **4.139**, which would spontaneously cyclise to the lactol **4.117** (Figure 4.47).

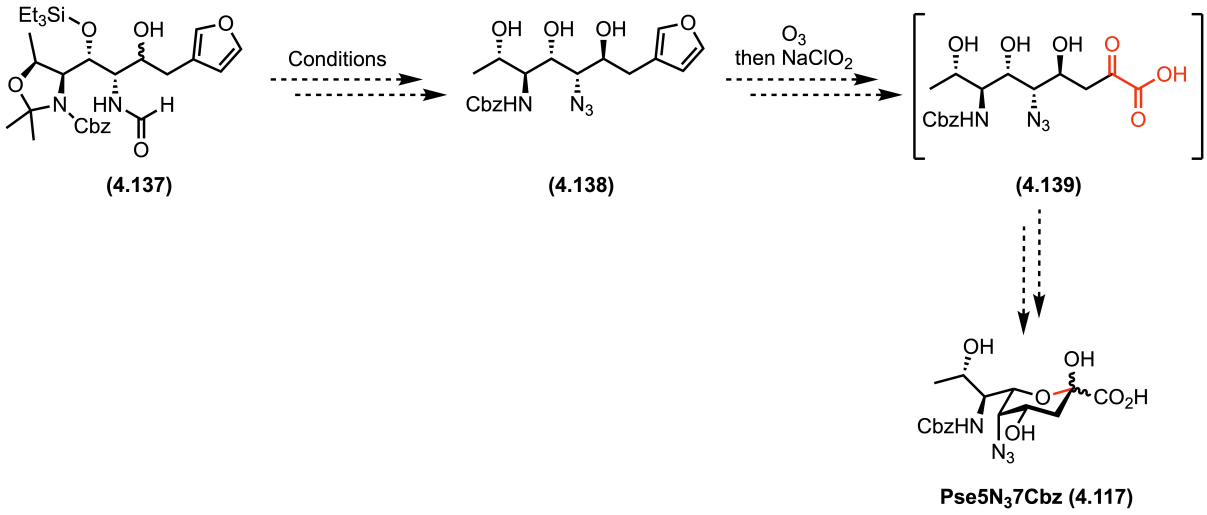


Figure 4.47. Proposed ozonolytic opening of furan to produce lactol **4.117** *via* 2-ketoacid **4.139**.

3-(Bromomethyl)furan (**4.136**) was prepared quantitatively from furan-3-ylmethanol (**4.140**) using PBr_3. A Fukuyama-type coupling of thioesters with alkyl halides has been reported previously.[379] This method was trialled first as it would deliver a C4 ketone, which could be stereoselectively reduced to set the stereochemistry at C4. This would save two steps in comparison with Li's synthesis, which employs an oxidation-reduction sequence (via the ketone) to set the stereochemistry at C4. Unfortunately, neither of the reported conditions A or B (Figure 4.48) trialled led to formation of the desired ketone product (**4.141**). We attributed this failure to a combination of reagent quality, and the oxygen sensitivity of the alkyl zinc intermediate.

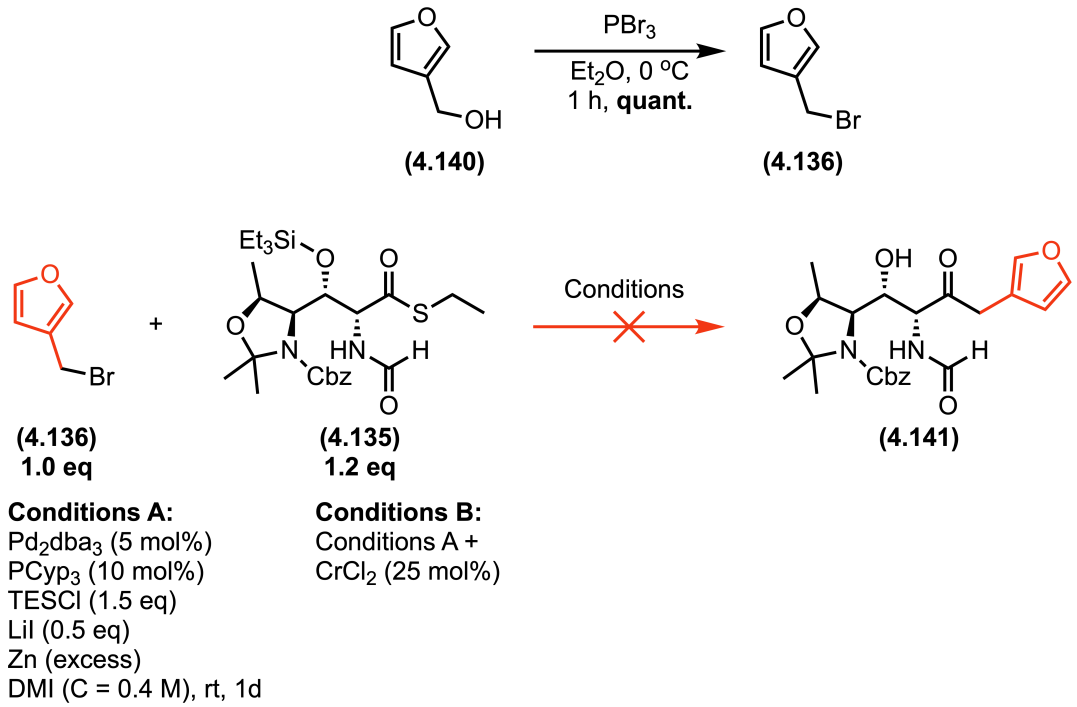
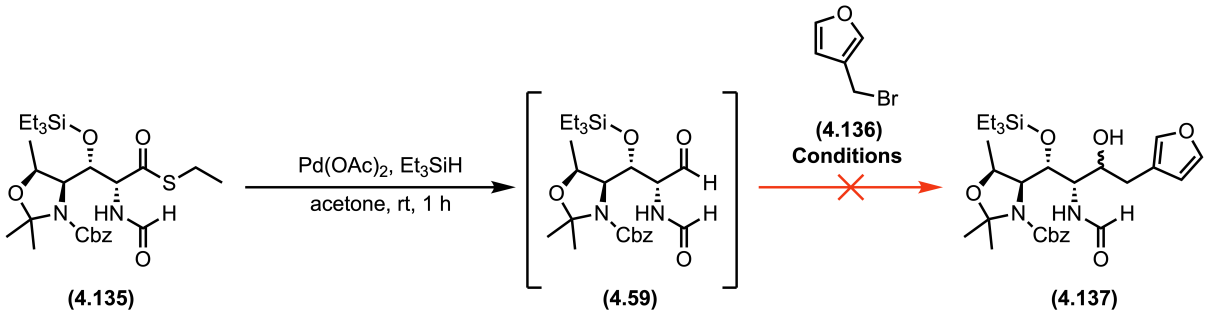


Figure 4.48. Formation of 3-(bromomethyl)furan (**4.136**) and attempted Fukuyama-type coupling.

Given the failure of the direct Fukuyama-like substitution, a Fukuyama reduction followed by Barbier reaction was next investigated. After successful Fukuyama reduction to the aldehyde (**4.59**), a range of conditions employing Zn and In were screened for the subsequent Barbier reaction with 3-(bromomethyl)furan (Figure 4.49). However, none of the conditions afforded synthetically useful quantities of the target compound **4.137**.



Conditions
A) Zn (1.3 eq), **4.136** (1.25 eq), sat. aq. NH_4Cl:THF (5:1 v/v), rt, 2 h
B) Zn (3 eq), **4.136** (3 eq), sat. aq. NH_4Cl:THF (5:1 v/v), rt, 2 h
C) Zn (3 eq) and **4.136** (3 eq) pre-activated in NH_4Cl:THF (5:1 v/v), rt, 1 h, then **4.59**, rt, 2 h
D) In (3 eq), **4.136** (3 eq), DMF, rt, 2 h
E) In (3 eq) and **4.136** (3 eq) pre-activated in DMF rt, 1 h, then **4.59**, rt, 2 h

Figure 4.49. Attempted Barbier reaction of aldehyde **4.59** with 3-(bromomethyl)furan (**4.136**) *via* a variety of conditions.

It is possible that the failure of the Barbier reaction was due to the instability of the 3-(bromomethyl)furan, which was found to be highly prone to polymerisation. To mitigate decomposition, it was stored in anhydrous diethyl ether containing K_2CO_3 as a stabilising agent. However, the compound's instability is likely a key factor in its synthetic utility, exemplified by its comparatively high commercial cost and lack of literature precedent describing its use in Barbier or Grignard-type reactions. Due to these limitations, alternative synthetic routes were explored.

The next synthetic possibility explored was to purposely form a C1-4 γ-butyrolactone (**4.142**) as a masked ester surrogate, which could be ozonolysed (**4.143**) and opened through transesterification with MeOH (**4.144**) at a later stage in the synthesis, followed by spontaneous cyclisation to Pse donor **4.145**. (Figure 4.50). In spite of the γ-butyrolactone being viewed as an undesirable side reaction during formamide hydrolysis in Li's attempts to use a C1 methyl ester (see section 4.6.2), we proposed that it could serve two useful functions, namely 1) serving as a masked methyl ester surrogate throughout the synthesis, and 2) potentially constraining the alkene to prevent the azido-ene reactivity following diazotisation.

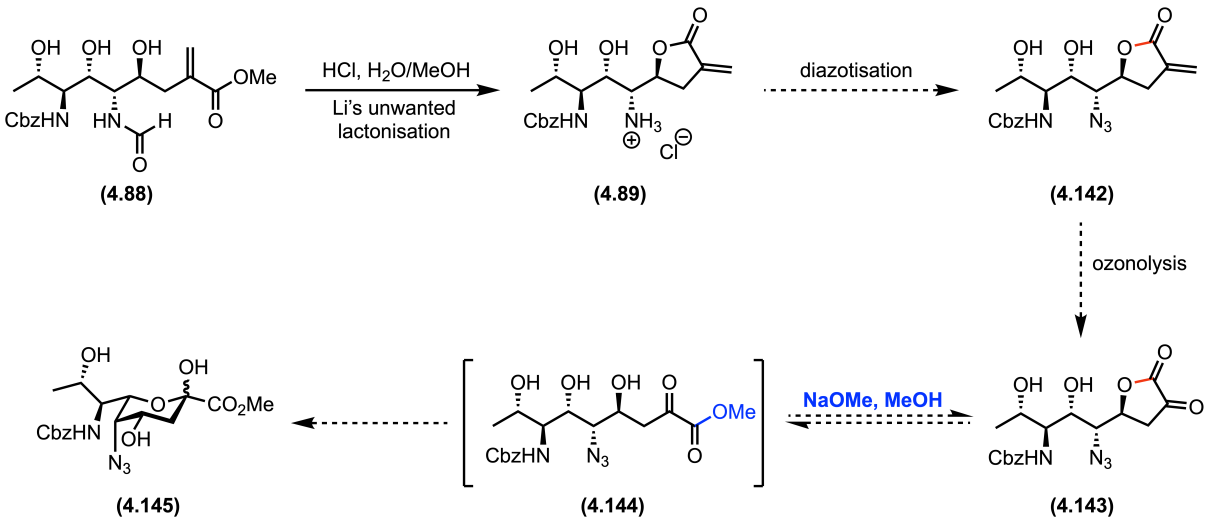


Figure 4.50. Proposed route to Pse5N$_3$7Cbz donor (**4.145**) employing Li's γ-butyrolactone side product (**4.89**) as a masked methyl ester surrogate.

Methyl ester **4.146** was installed first by Fukuyama reduction of thioester **4.135**, followed by Barbier reaction of with methyl 2-(bromomethyl)acrylate (Figure 4.51). Under Li's conditions, use of an In-mediated Barbier reaction, **4.146** was only obtained in 31% yield over two steps. A different approach utilising zinc for the Barbier reaction pleasingly resulted in methyl ester **4.146** in 71% yield as a mixture of diastereomers. Advantageously, unlike the In Barbier reaction, the route using Zn did not require pre-activation of the metal with the bromo methacrylate prior to addition to aldehyde. Methyl ester **4.146** was used in subsequent steps.

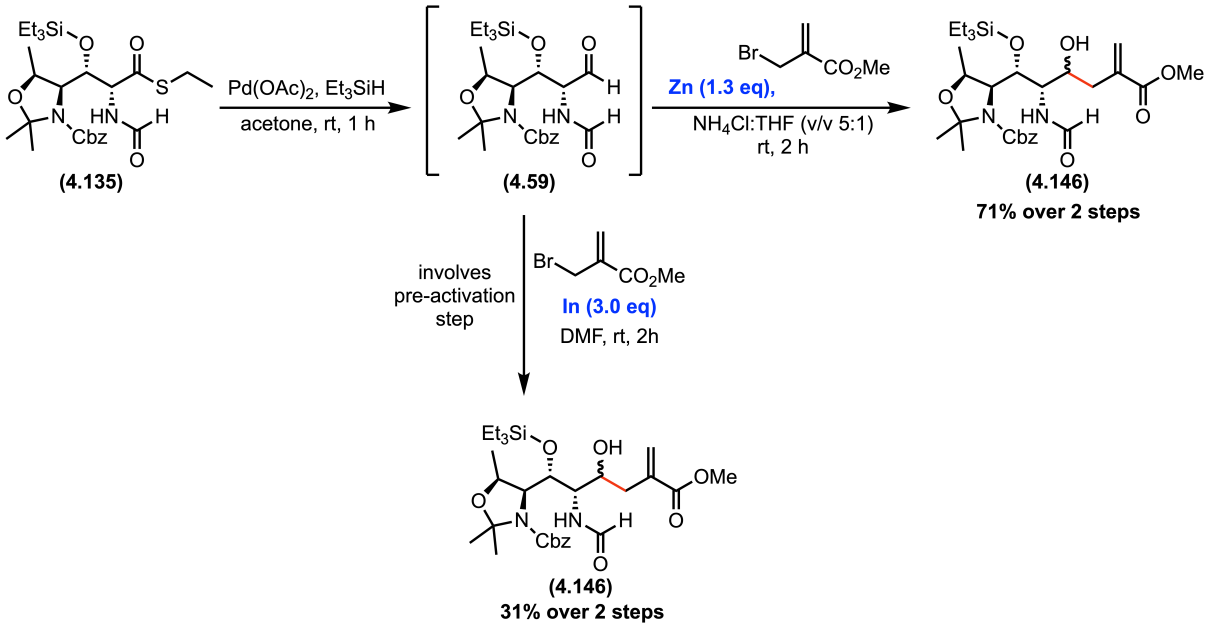


Figure 4.51. Comparison of the In- and Zn-mediated Barbier reaction of methyl 2-(bromomethyl)butyrate to aldehyde **4.59**.

4.7.5 Attempted late-stage installation of Azide

Before attempting to deprotect the N5 formyl group and simultaneously form the γ-butyrolactone, we first sought to investigate Li's lack of success in achieving diazotransfer on thioglycoside donor **4.147** (Figure 4.52). We reasoned it would be ideal to perform any manipulations on N5 at this stage in the synthesis, where lactonisation and azido-ene cyclisation could be circumvented entirely. Although structurally similar to Li's substrate, we proposed that formamide **4.148** could be stripped back to the corresponding 5-amino-4,8-diol, which may prove a less hindered substrate for diazotisation, as well as avoid potential side reactions such as O→N acetyl migration from the neighbouring acetyl group.

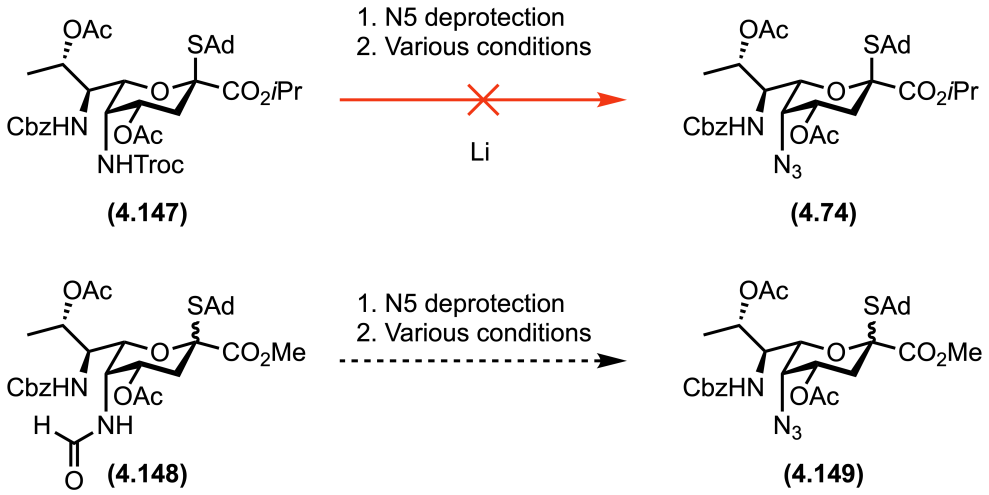


Figure 4.52. Unsuccessful diazotisation of **4.147** to **4.74** by Li; Proposed substrate (**4.148**) to trial various diazotisation conditions on.

Thioglycoside **4.148** was synthesised from linear precursor **4.146** *via* a route analogous to that reported by Li, over seven steps with an overall yield of 18% (Figure 4.53). The alcohol intermediate **4.146**, obtained as a mixture of epimers, was subjected to a stepwise oxidation–reduction sequence to access the desired epimer. Namely, oxidation of the secondary alcohol provided ketone **4.149**, which then underwent TES deprotection using tetra-*n*-butylammonium fluoride (TBAF) buffered with acetic acid. The resulting ketone was stereoselectively reduced using sodium triacetoxyborohydride ($NaBH(OAc)_3$), affording the 1,3-anti diol **4.150**. This reactant enables intramolecular hydride delivery through a chair-like transition state, favouring pseudo-equatorial

placement of substituents. Subsequent removal of the isopropylidene protecting group with 1:9 v/v TFA:H_2O at 0 °C for 15 minutes generated crude intermediate **4.151**, which was directly subjected to ozonolysis of the olefin. The resulting ketone spontaneously cyclised to form the corresponding ketal. Global *O*-acetylation of the crude material furnished glycosyl acetate **4.152** as a mixture of α- and β-anomers. Finally, activation with 1-adamantanethiol (1-AdSH) in the presence of Lewis-acid catalyst $BF_3{\cdot}OEt_2$ yielded thioglycoside donor **4.148** as a mixture of anomers.

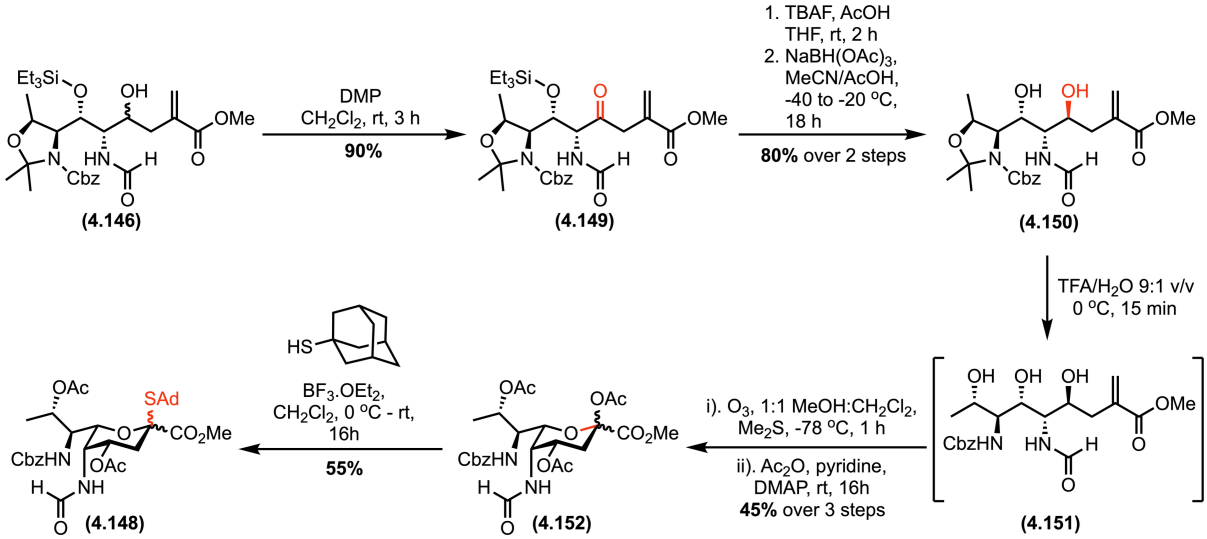


Figure 4.53. Synthesis of thioglycoside **4.148** from linear **4.146**.

With intermediate **4.148** in hand, a series of conditions for azide installation were investigated (Figure 4.54). Treatment of **4.148** with aqueous HCl in MeOH resulted in deprotection of the formamide and *O*-acetyl groups, affording the corresponding free ammonium ion **4.153**.

Subsequent attempts to convert ammonium **4.153** to the corresponding azide using standard diazotisation strategies were unsuccessful. Neither Stick's reagent nor triflic azide (TfN_3) produced the desired azide product (**4.154**). One proposed explanation for this was that the amine of **4.153** may form an intramolecular hydrogen bond with the C4 alcohol, thereby reducing its nucleophilicity.

To test this hypothesis, **4.153** was treated with *N,O*-bis(trimethylsilyl)acetamide (BSA) with the aim of affording the crude tri-TMS intermediate (**4.155**). In addition to removing

the H-bonding interaction, we proposed that this would also increase the nucleophilicity of the amine lone pair through silylation. The use of excess BSA would also serve to deprotonate the Stick's reagent (HCl salt) in situ. Interestingly, LC-MS analysis indicated that only a single hydroxyl group had undergone silylation; however, the site of silylation could not be defined. *N*-silyl groups are known to be labile under aqueous conditions, and therefore the extent of *N*-silylation could also not be determined. The resulting material was subjected directly to diazotisation conditions, and the free amine was expected to be unmasked *in situ* via cleavage of the labile *N*-TMS group. However, no azide product (**4.156**) was observed. It was proposed that silylation occurred preferentially at C8, or the additional silylation at C4 introduced excessive steric hindrance, further inhibiting the diazotisation.

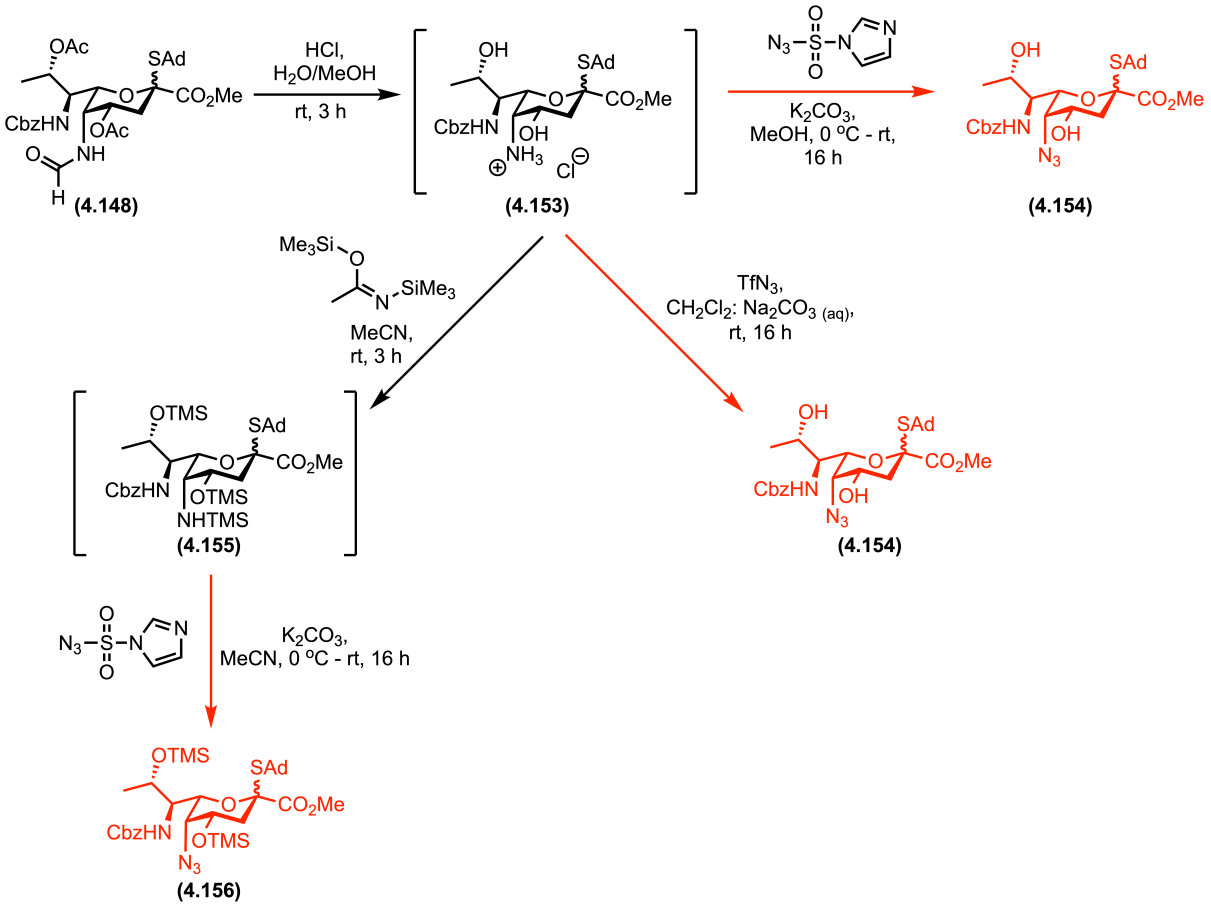


Figure 4.54. Late-stage diazotisation conditions trialled on thioglycoside **1.148**.

As the formation of the desired azide donor appeared to be impeded by a combination of steric and/or electronic factors, efforts were redirected towards the diazotisation of linear intermediate **4.151**.

4.7.6 Azide installation on linear substrate

Initial diazotisation conditions were trialled *via* the methodology outlined in Figure 4.55. Namely, acid-catalysed hydrolysis of formamide **4.151** was initially conducted on an analytical scale. LC-MS analysis confirmed quantitative deprotection, resulting in the corresponding ammonium salt (**4.157**). Upon treatment with basic diazotisation conditions, the ammonium intermediate was deprotonated and underwent rapid intramolecular cyclisation *via* a 6-exo-trig pathway, affording the thermodynamically favoured six-membered lactam (**4.158**). The presence of the lactam was supported by LC-MS data, which showed no change in mass or retention time following treatment with excess sodium hydroxide. In contrast, had a lactone (cyclic ester) been formed, it would be expected to undergo base-mediated hydrolysis, resulting in a mass increase of +18 Da (**4.160**). Additionally, lactone formation would not have precluded azide formation, and mass of azide **4.159** or **4.142** was not observed (Figure 4.56). The absence of such shifts supports lactam formation.

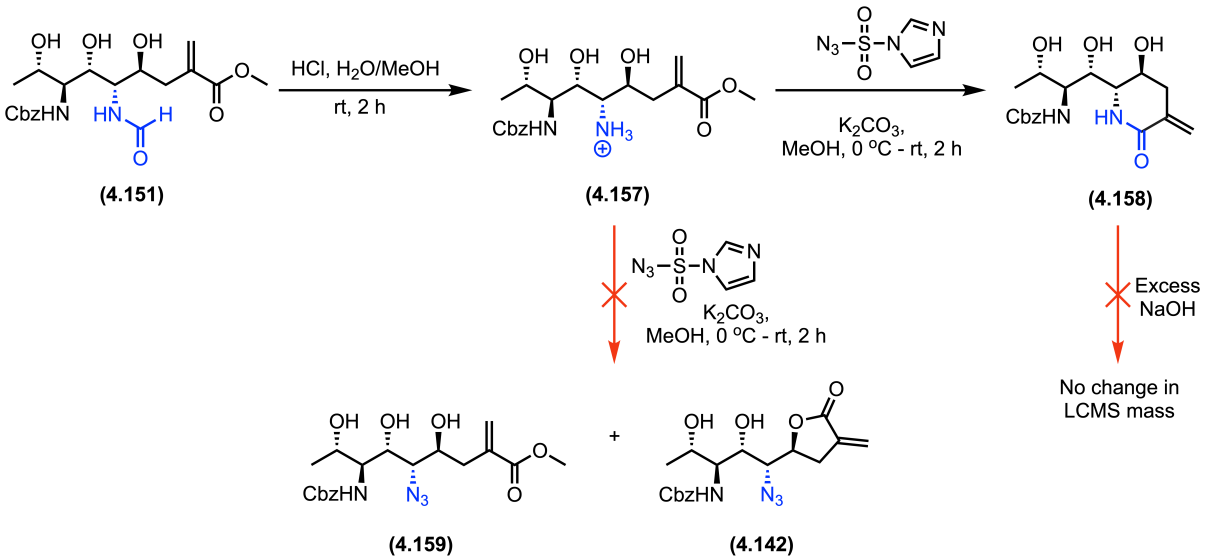


Figure 4.55. Formamide hydrolysis of **4.151**, resulting in ammonium salt **4.157**, which formed lactam **4.158** upon treatment with basic diazotisation conditions.

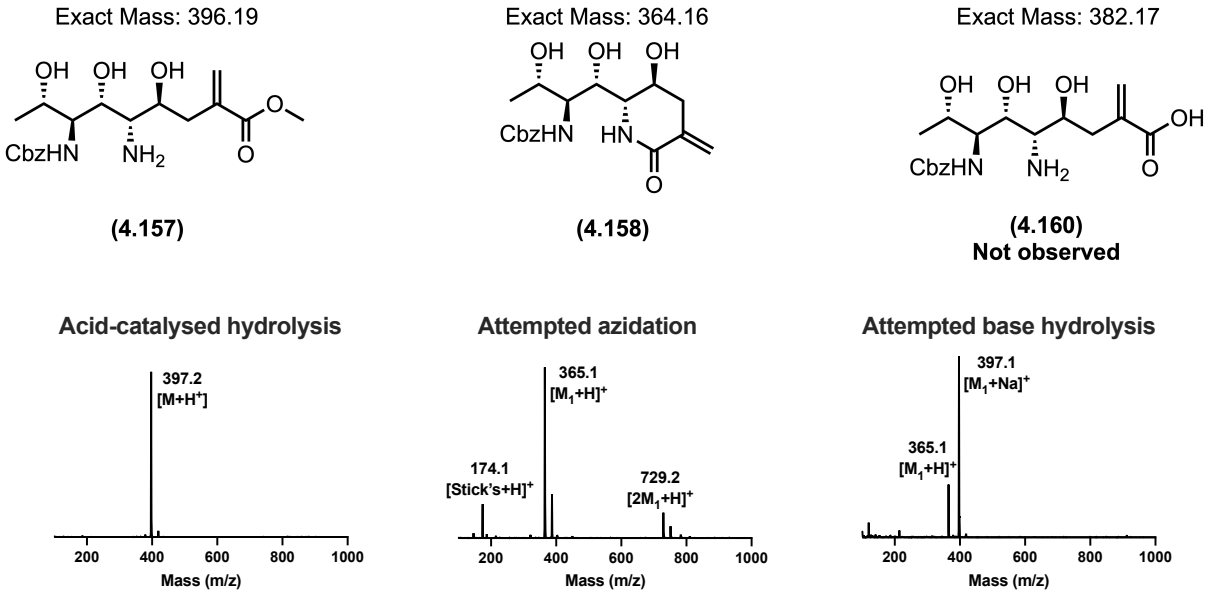


Figure 4.56. LC-MS data from acid-catalysed hydrolysis, followed by attempted diazotisation and base-catalysed hydrolysis of substrate. Acid catalysed hydrolysis resulted in **4.157**, (M = 396.2), with both attempted diazotisation and subsequent treatment with aqueous base resulting formation of lactam **4.158** (M_1 = 364.1).

To prevent lactamisation, it was proposed that the formamide and methyl ester on **4.150** could be hydrolysed under aqueous basic conditions to produce free amino carboxylate **4.161** (Figure 4.57). This was proposed as a route to prevent lactamisation, due to the decreased electrophilicity of a formamide carbonyl compared to a methyl ester carbonyl, resulting in preferential hydrolysis of methyl ester to a carboxylate first. A carboxylate is significantly less electrophilic than a methyl ester and would not be expected to undergo cyclisation with an amine. **4.161** could be subject to diazotisation to form **4.162**, and remethylated to provide methyl ester **4.163**.

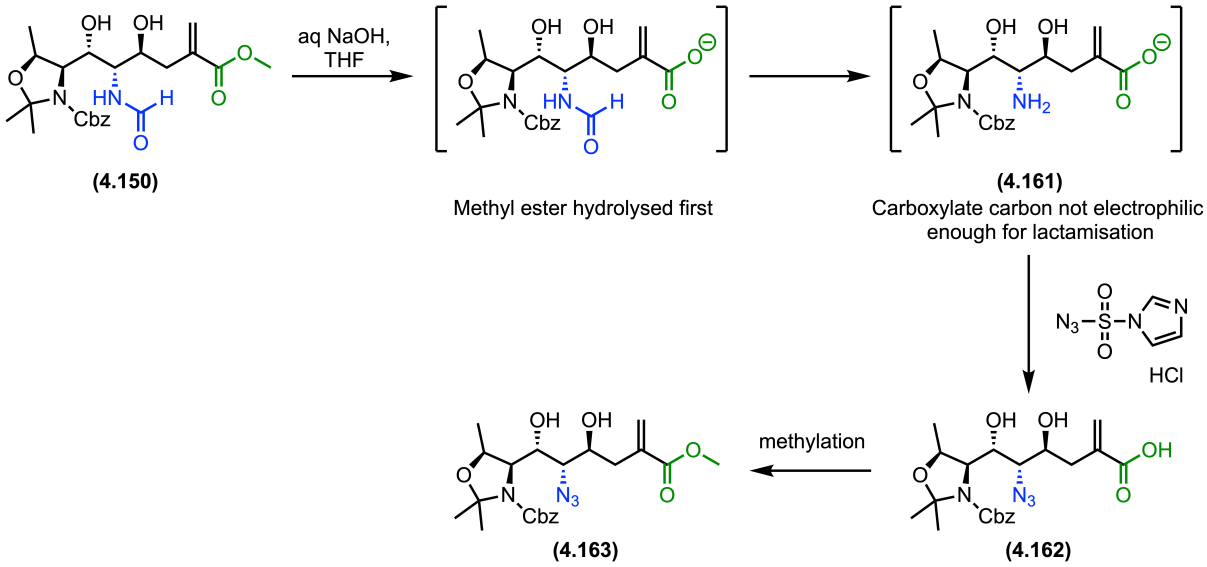


Figure 4.57. Proposed basic hydrolysis followed by diazotisation and methylation to produce methyl ester **4.163**.

However, under these conditions, lactamisation (**4.164**) was still the predominant reaction. Some alternative substrates were trialled to investigate the impact of substrate on the formation of lactam or azide (Figure 4.58). Thankfully, when the same basic hydrolysis conditions were attempted on the isopropylidene deprotected derivative (**4.151**) or TES protected derivative (**4.146**), both underwent successful hydrolysis to the desired amino carboxylates **4.165** and **4.67** respectively, with only minimal formation of the corresponding lactam side-products. The resulting intermediates **4.165** and **4.167** were subsequently buffered to pH 9 and treated with Stick's reagent at 0 °C, after which LC-MS analysis indicated mass shifts corresponding to the formation of the desired azide products **4.166** and **4.168** (Figure 4.59).

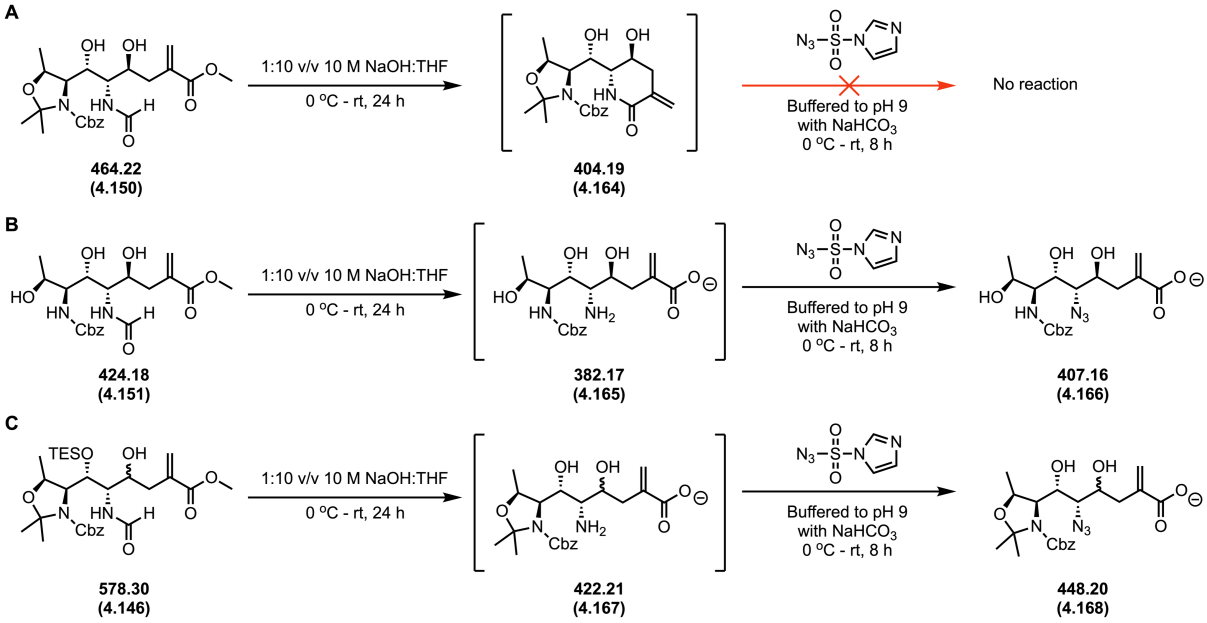


Figure 4.58. Trialled base-catalysed hydrolysis followed by diazotisation of **4.150**, **4.151** and **4.146**. Both lactam formation and desired azides were observed.

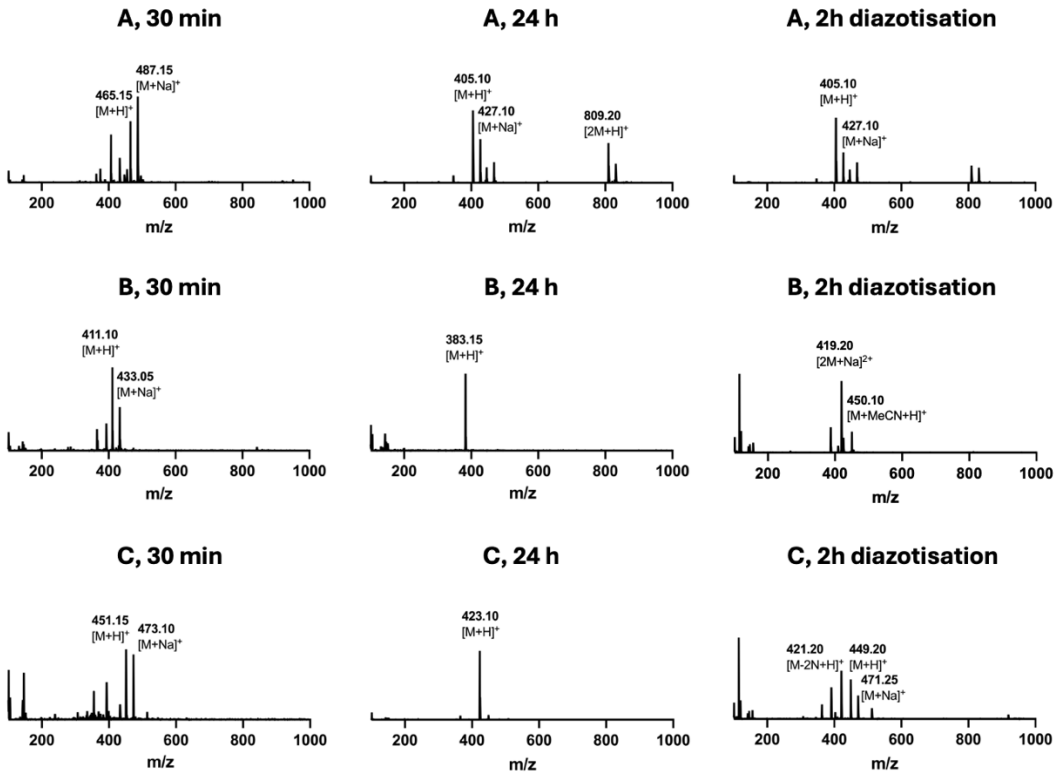


Figure 4.59. LC-MS analysis of reactions ester/formamide hydrolysis and diazotisation reactions. Conditions A resulted in irreversible formation of lactam (**4.164**) indicated by the mass 405.10, while B and C formed desired azides (**4.166**) and (**4.168**) indicated by masses 419.20 and 449.20 respectively.

The outcomes observed upon basic hydrolysis of compounds **4.150**, **4.151**, and **4.146** can be rationalised by considering the conformational and electronic influences of the oxazolidine and TES groups. In compound **4.150**, the presence of the oxazolidine ring likely induces a Thorpe–Ingold-like effect,[380] pre-organising the molecule for intramolecular attack of the free nitrogen on the methyl ester. This effect is due to a combination of lowering the enthalpic barrier by relieving ground-state strain upon cyclisation, reducing the entropic barrier by limiting non-reactive conformers, and lowering the free energy of activation due to poor solvation of the hindered nitrogen. In contrast, compound **4.151** lacks this conformational constraint, resulting in a more flexible backbone that disfavours cyclisation and instead undergoes complete hydrolysis. Compound **4.146**, despite retaining the oxazolidine ring, does not lactamise due to the bulky TES group. The TES ether likely disrupts the reactive conformation**,** hinders nucleophilic approach, and slows formamide hydrolysis, allowing the ester to be cleaved first and preventing cyclisation.

To further investigate the substituent effect of hydrolysis, di-TES compound **4.169** was synthesised, along with mono-TES compounds **4.170** and **4.171**. Compound **4.169** was treated with 10M NaOH in THF (Figure 4.60). After five days of heating at 50 °C, LC-MS indicated that **4.169** had reacted approximately 80%, producing di-TES acid **4.172** and mono-TES acid **4.173**, with no formamide hydrolysis indicated (Figure 4.61).

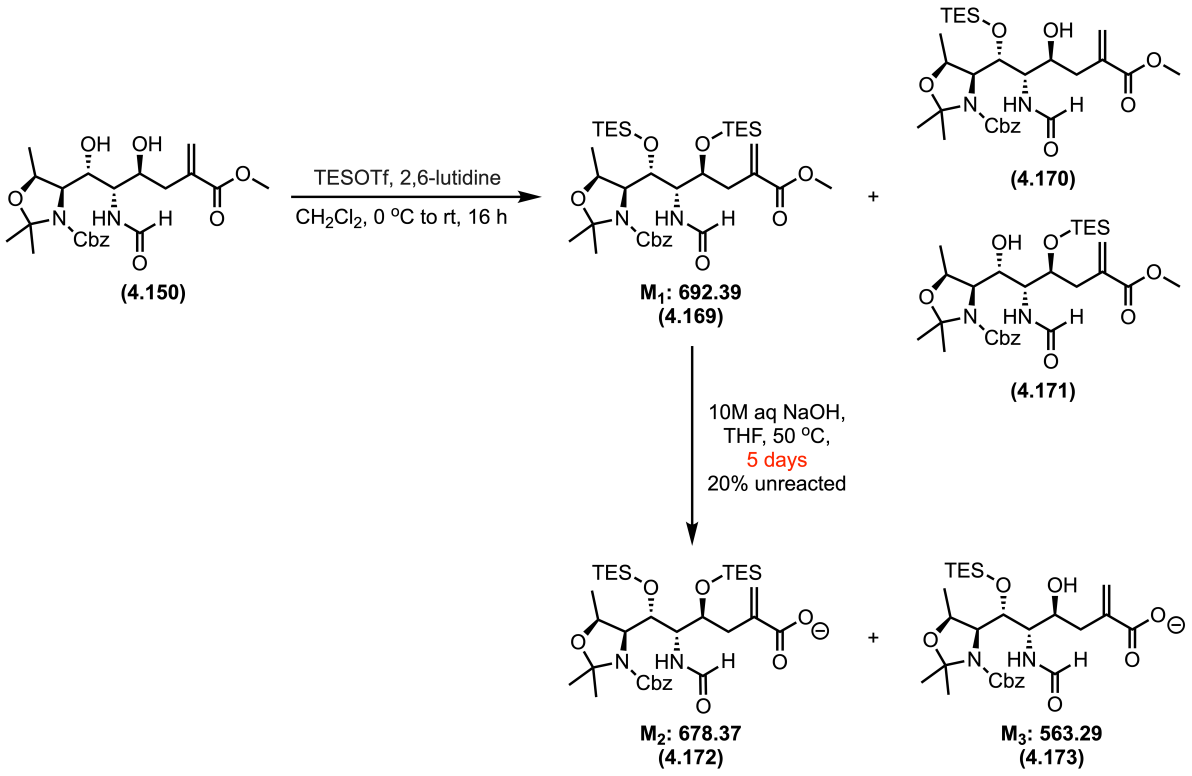


Figure 4.60. Formation of di-TES **4.169** and mono-TES compounds **4.170** and **4.171**, and subsequent hydrolysis of **4.169** with 10M NaOH.

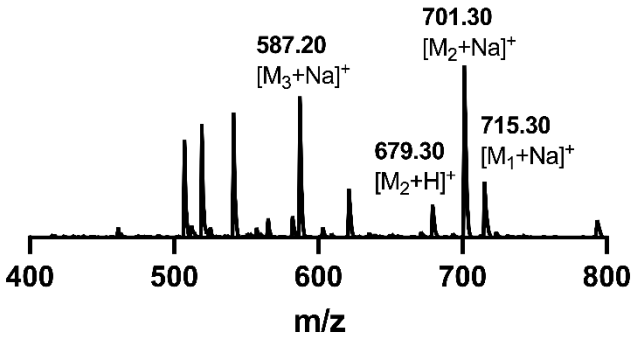


Figure 4.61. LC-MS analysis of di-TES hydrolysis trial, measured after reacting for five days. Spectrum has been cropped for clarity to display only the mass range between 400 and 800 Da.

In this case, it was clear that the steric bulk of the alcohol protecting groups prohibited formamide hydrolysis, rendering this route unviable. This indicates that the mono-TES **4.146** was likely slowing formamide hydrolysis sufficiently to prevent lactam formation.

Although some of the tested conditions showed promising results, the primary objective was the synthesis of both N5 and N7-substituted variants of Pse. While the initial goal was to generate glycopeptides or glycosyl amino acids using a thioglycoside donor, it

was ultimately determined that simple α-methyl glycosides (the native configuration of Pse in glycopeptides) would be sufficient to assess binding to the monoclonal antibody reported by Tang *et al.*[316] This approach could be accomplished *via* direct glycosylation of N5-formyl and N7-Cbz glycosyl acetate **4.152** to produce the α-variants.

4.7.7 Final synthesis of Pse variants

It was decided that α methyl glycosides bearing N5-Acetyl groups and N7 variations were to be synthesised. The methyl glycoside was deemed to mimic the first two atoms of a serine or threonine residue sufficiently to be able to determine affinity to the antibody generated by Tang *et al.* Additionally, the crystal structure revealed that the antibody interacts exclusively with the glycan moiety and not the peptide, an additional rationale for preparing the corresponding methyl glycoside. Since glycosylation of **4.152** is under thermodynamic control it would be expected to deliver the α-anomer, which benefits from anomeric stabilisation and placement of the larger methyl ester functionality in an equatorial position.

Glycosyl acetate **4.152** was treated with $SOCl_2$ in anhydrous methanol to produce methyl glycoside **4.174**, which was then reacetylated with Ac_2O in pyridine, producing **4.175** predominantly as the α–anomer in 15% yield over two steps (Figure 4.62).

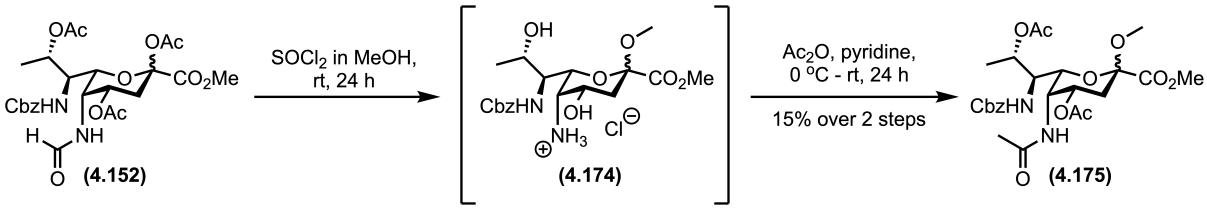


Figure 4.62. Preparation of acetylated methyl glycoside **4.175** from glycosyl acetate **4.152**.

With 20 mg of **4.175** in hand, it was decided that three α-Pse variants could be synthesised. Given the flexible binding pocket around N7, we targeted the methyl glycosides of three most common N5-acetyl-N7-acyl variants in bacteria from Table 4.1: Pse5Ac7Ac (**4.176**), Pse5Ac7Fo (**4.177**) and Pse5Ac7(3_RHb) (**4.178**) (Figure 4.63).

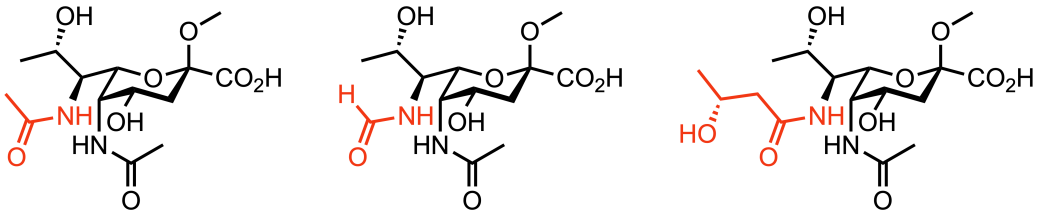


Figure 4.63. Three Pse5NAc7NAcyl variants chosen for synthesis and screening, due to their bacterial prevalence.

In order to install the three respective *N*-acyl groups, the corresponding NHS-esters (**4.180**, **4.181**, **4.182**) were prepared from *N*-hydroxy succinimide (**4.179**) as outlined in Figure 4.64.

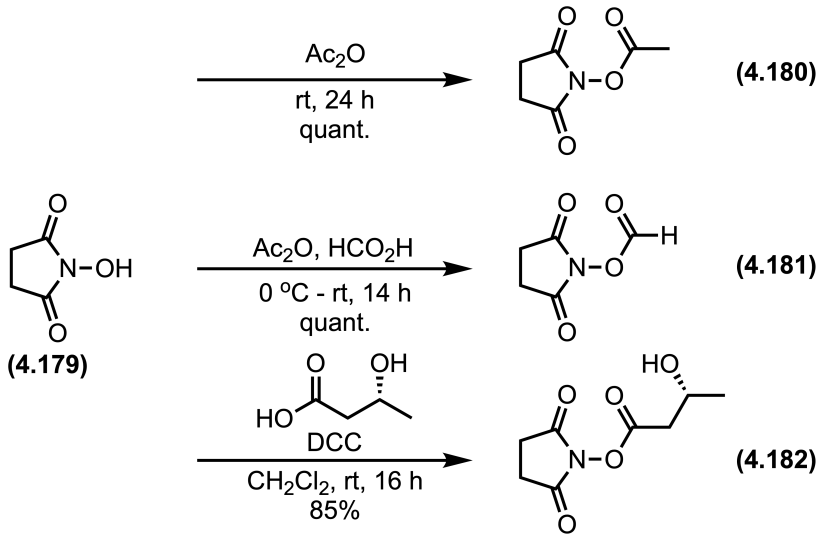


Figure 4.64. Preparation of NHS-esters of acids to be coupled to N7.

Mindful of the possibility of O→N acetyl migration from the O8 to N7, we chose to first remove the acetyl groups and simultaneously hydrolyse the methyl ester (Figure 4.65). Therefore, acetylated tri-ester **4.175** was first treated with LiOH (10 equiv.) in H_2O:THF at 40 °C to produce carboxylic acid **4.184**. Oxazolidinone by-product **4.183**, resulting from intramolecular substitution of the benzyl carbamate, was observed by LCMS, but thankfully was hydrolysed to free amine **4.184** under prolonged heating. **4.184** was dissolved in H_2O:THF (1:1 v/v) and treated with the respective NHS ester and NEt_3. After purification by HPLC on a hydrophilic interaction liquid chromatography (HILIC) column,

the final compounds **4.176**, **4.177**, and **4.178** were provided with yields of and 21%, 16%, and 19% respectively (Figure 4.65).

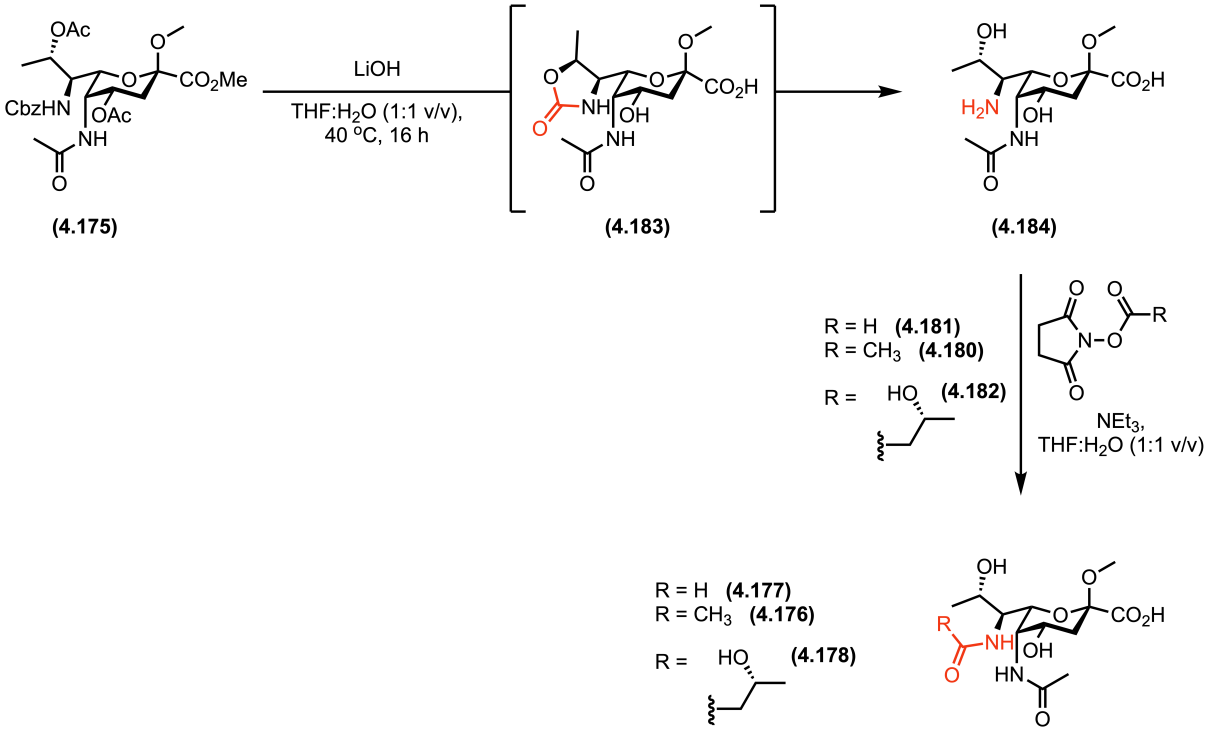


Figure 4.65. Preparation of final α-methyl Pse5NAc7NAcyl variants.

4.8 Binding Studies of Synthesised N7-variable Pseudaminylated Methyl Glycosides (performed with Professor Ethan Goddard-Borger, Walter and Eliza Hall Institute)

The aim of this evaluation was to determine the specificity of the anti-Pse monoclonal antibody 1E8, developed by Tang *et al*. to differently substituted natural Pse derivatives. To investigate this, we evaluated the group of Pse α methyl glycosides (**4.176**, **4.177**, and **4.178**) synthesised in Section 4.7.7, which lack the peptide component normally found in bacterial glycoconjugates, isolating the impact of the carbohydrate epitope itself.

The binding of these derivatives was assessed by surface plasmon resonance (SPR). In these experiments, sensorgrams recorded the increase in signal as the molecules associated with the immobilised antibody, followed by a decrease in signal during the

dissociation phase. The signal corresponds to changes in the refractive index at the sensor surface, reported as response units (RU), which is directly proportional to the mass of compound bound. Stronger binding is indicated by higher response units at a given concentration and a slower rate of dissociation, while weaker ligands show lower signals and faster dissociation. Binding responses were recorded across a series of analyte concentrations, allowing for an equilibrium dissociation constant (K_D) to be determined, providing a quantitative measure of antibody-ligand affinity.

The SPR binding data are shown in the sensorgrams below, in which increasing concentrations of each analyte were injected over the immobilised 1E8 antibody to generate association and dissociation curves. The K_D values along with the χ^2 goodness-of-fit statistics are shown on each plot.

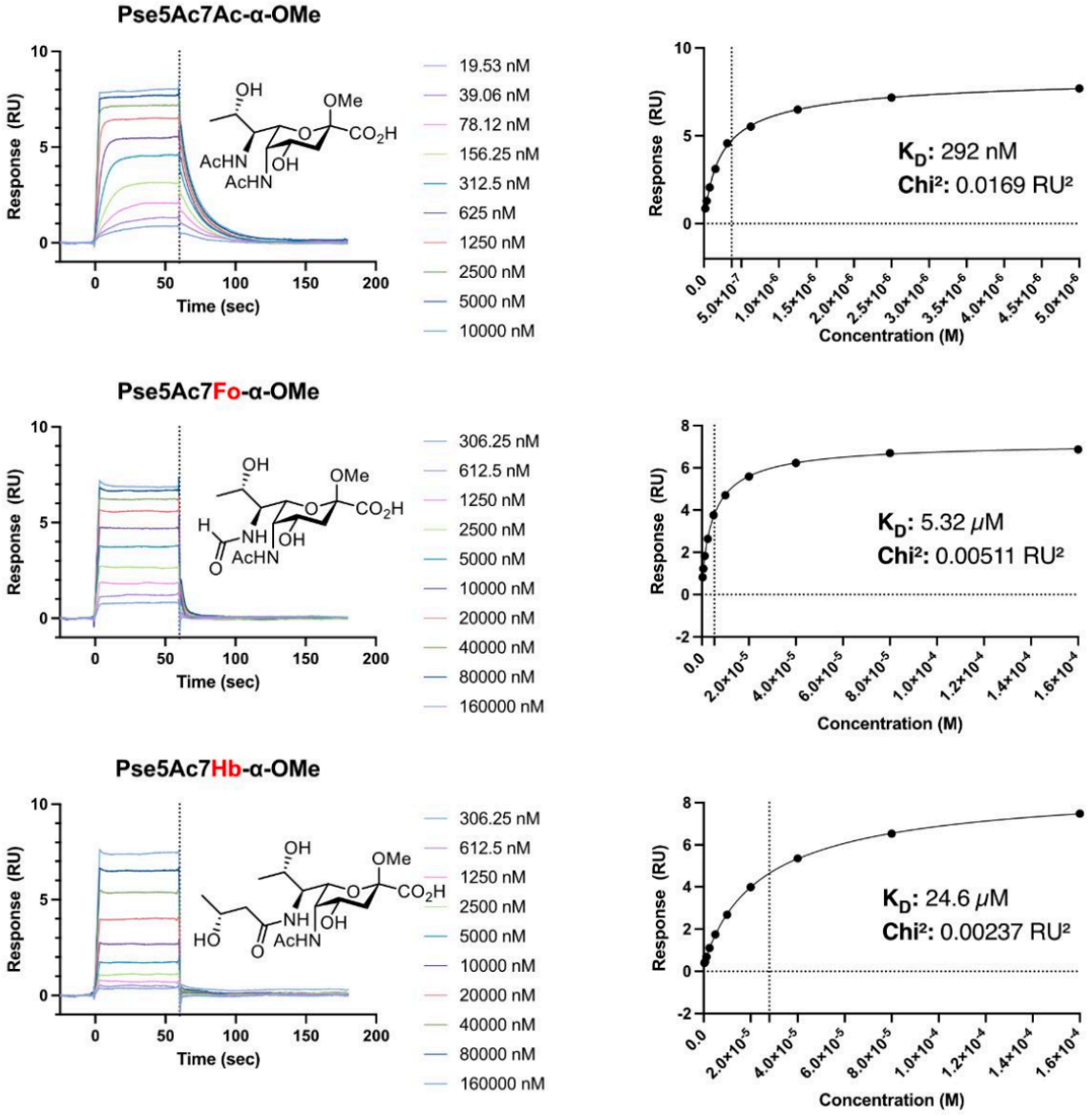


Figure 4.66. SPR Sensorgrams (left) show binding responses across a concentration series for α-OMe Pse5Ac7Ac (**4.176**), α-OMe Pse5Ac7Fo (**4.77**), and α-OMe Pse5Ac7Hb (**4.78**). Steady-state fits of response versus concentration (right) were used to calculate equilibrium dissociation constants (K_D) and χ^2 values, shown on each plot. Goodness-of-fit statistics (χ^2 in RU^2) were low across fits (0.002-0.017 RU^2), indicating acceptable model fits.

Previously, Tang *et al.* showed that the original serinyl-α-Pse5Ac7Ac bound to 1E8 with a K_D of 69nM. In comparison, the Pse5Ac7Ac α-methyl glycoside (**4.176**) bound with a K_D of 292 nM, only ~4-fold weaker. This indicates that a linkage (glycan, amino acid, or peptide) to Pse is not essential for recognition by the antibody, corroborating the X-ray structure and additionally validating the methyl glycoside as an acceptable model for probing antibody specificity. Substitution at the C7 position resulted in progressively weaker

binding. The formyl analogue (Pse5Ac7Fo, **4.177**) showed an ~18-fold reduction in affinity (K_D = 5.32 μM), while the larger hydroxybutyryl analogue (Pse5Ac7Hb, **4.178**) showed an ~84-fold reduction (K_D = 24.6 μM). These binding affinities highlight that while the antibody can tolerate some acyl group substitutions at C7, increasing the steric bulk or altering hydrogen-bonding ability, as seen with Pse5Ac7Hb, significantly disrupts recognition.

4.9 Conclusions and Future Work

This chapter described the synthesis of Pseudaminic acid (Pse) derivatives for use as biological probes. Additionally, the feasibility and challenges associated with the chemical synthesis were highlighted, with multiple alternative routes explored. By adapting Li/Tang's threonine-derived strategy, three α-methyl glycosides with variable N7 substituents were prepared. This allowed for exploration of binding affinity of the recently developed Pse-specific monoclonal antibody from Tang *et al.,* showing the specificity of the antibody for Pse and its ability to accommodate naturally occurring structural variants.

The synthetic work illustrated the limitations of existing protecting groups (e.g. isopropyl ester at C1, challenges with azide installation, and undesirable side-reactions) that complicated downstream glycosidation strategies. It was shown that an easier to cleave C1 methyl ester could be utilised in the synthesis of the methyl glycoside, however, efforts to install the azide functionality both earlier and after cyclisation were shown to be unsuccessful.

Promisingly, alteration of formamide hydrolysis conditions on the linear methyl ester substrate indicated that diazotisation could be performed without major formation of side products. The viability of this route will be explored in future work, allowing for generation of an orthogonal glycosyl donor Pse5$N_3$7Cbz which could be used to access both α and β Pse glycosides with variable substituents at N5 and N7. Preparation of additional Pse derivatives would allow for further probing of antibody specificity and substrate tolerance but also glycopeptides and glycoproteins bearing Pse moieties with defined acylation patterns to study structure-activity relationships.

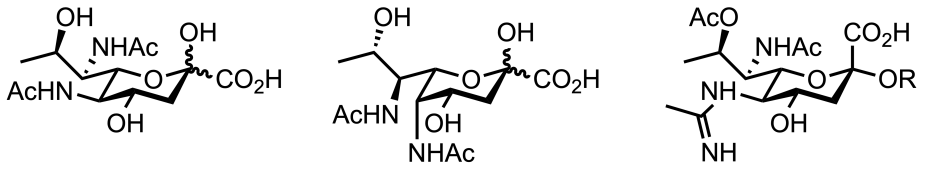
Downstream, optimised access to Pse derivatives could allow for detailed mapping of glycosylation sites, uncovering of new pseudaminylated protein targets in pathogenic bacteria, and development of novel therapeutic antibodies targeting Gram-negative pathogens. Continued progress at the interface of carbohydrate chemistry and immunology is a promising approach to addressing the urgent need for new anti-infective strategies.

Chapter 5: Total Synthesis of Legionaminic Acid

5.1 Background on Legionaminic Acid

5.1.1 Identification of Legionaminic Acid

Legionaminic acid (Leg, **5.1**), like Pse (**5.2**), is a nonulosonic acid (NulO) first identified in bacterial lipopolysaccharides. Originally characterised by Knirel *et al.* in 1994,[381] Leg was detected in the LPS of *Legionella pneumophila* (serogroup 1), the bacteria responsible for the respiratory infection Legionnaires' disease. Structural elucidation by NMR spectroscopy and chemical analysis revealed an α–(2→4)-linked homopolymer of a 5-acetamidino-7-acetamido-8-*O*-acetyl derivative of 3,5,7,9-tetradeoxynon-2-ulosonic acid (**5.3**) (Figure 5.1). The configuration was proposed to be D-glycero-L-galacto, and the structure represented the first example of a homopolymeric acidic nonulosonic acid in bacterial LPS. While this core structure differs stereochemically from Pse, both compounds share the characteristic nine-carbon backbone and multiple deoxysugar modifications typical of bacterial NulOs.



Legionaminic acid (5.1) **Pse5Ac7Ac (5.2)** **α-Leg5Am7Ac8Ac (5.3)**

Figure 5.1. Structures of legionaminic Acid (Leg) (**5.1**), α-Leg5Am7Ac8Ac (**5.1**) first identified by Knirel, and Pse5Ac7Ac (**5.2**).

5.1.2 Leg and analogues in bacteria

As with Pse, Leg is a 5,7-diamino derivative (**5.4**) of Neu5Ac (**5.5**), found naturally with a variety of N substitutions at these positions (Figure 5.2) across a range of bacteria (Table 5.1).[382]

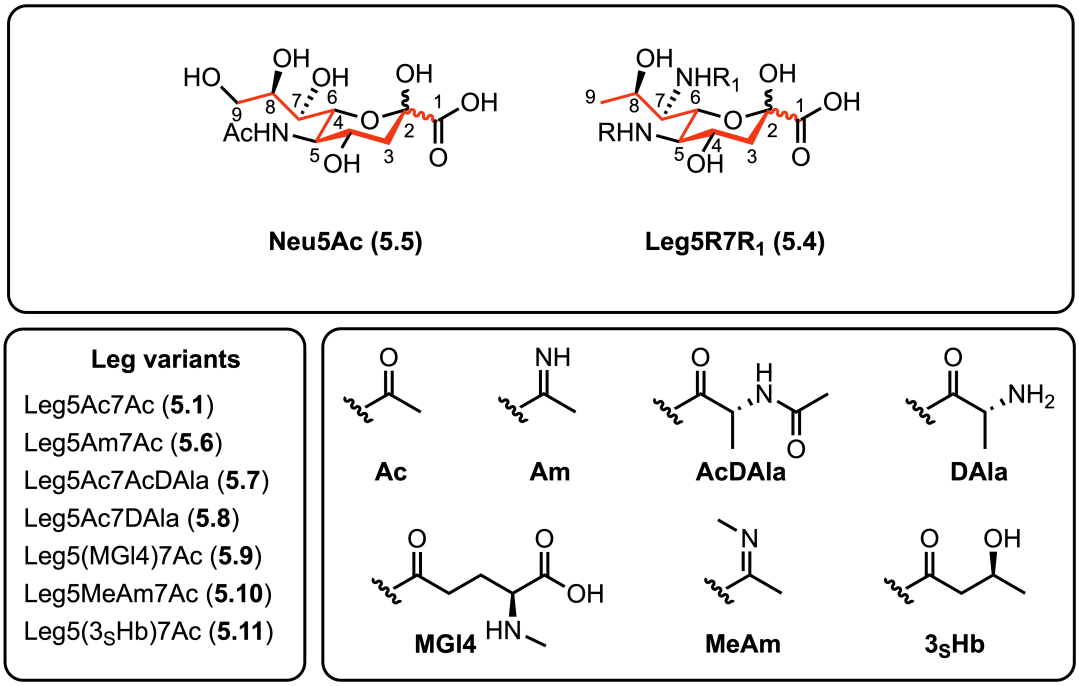


Figure 5.2. Comparison of the structures of sialic acid (Neu5Ac, **5.5**) and legionaminic acid (Leg), with common N5 and N7 substitutions of Leg.

Table 5.1. Pathogenic and opportunistic bacteria reported to express legionaminic acid-linked glycans.

Leg derivative	Family	Species/strain	Antigen
Leg5Ac7Ac (**5.1**)	Enterobacteriaceae	*Enterobacter cloacae C6285*[383]	LPS
	Campylobacteraceae	*Campylobacter jejuni* 11168[319,384]	Flagellum
	Vibrionaceae	*Vibrio parahaemolyticus* O2[385]	LPS
		Vibrio alginolyticus 945-80[386]	
	Moraxellaceae	*Acinetobacter baumannii* O24[386], K27[8]	CPS
	Enterococcaceae	*Enterococcus faecium*[387]	CPS
	Porphyromonadaceae	*Tannerella forsythia* FDC92A2[388]	S-layer
Leg5Am7Ac (**5.6**)	Pseudomonadaceae	*Pseudomonas fluorescens* ATCC 49271[386]	LPS
	Campylobacteraceae	*Campylobacter coli* VC167[389]	Flagellum
		Campylobacter jejuni 11168[384]	
	Legionellaceae	*Legionella pneumophila* serogroup 1[381]	LPS
	Vibrionaceae	*Vibrio salmonicida* NCMB 2262[386]	LPS
Leg5Ac7AcDAla (**5.7**)	Vibrionaceae	*Vibrio vulnificus* CMCP6[390]	LPS
		Vibrio parahaemolyticus KX-V212[385]	
Leg5Ac7DAla (**5.8**)	Enterobacteriaceae	*Escherichia coli* O161[391]	LPS
Leg5MGl47Ac (**5.9**)	Clostridiaceae	*Clostridium botulinum*[392]	LPS
Leg5MeAm7Ac (**5.10**)	Campylobacteracea	*Campylobacter coli* VC167[389],11168[384]	Flagellum
Leg5(3SHb)7Ac (**5.11**)	Moraxellaceae	*Acinetobacter baumannii* O24[10]	CPS

5.1.3 Anomeric nomenclature

Unlike Pse, the anomeric nomenclature in Leg is consistent with that of sialic acids, as it shares the same configuration at the highest-numbered stereogenic centre (C8). Therefore, an axial glycosidic linkage is designated as β and an equatorial linkage as α, following conventional sialic acid stereochemical rules (Figure 5.3).

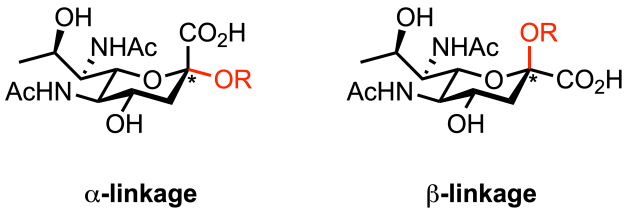


Figure 5.3. Legionaminic acid anomeric nomenclature. The anomeric centre is indicated by *.

5.2 Previous Syntheses

Legionaminic acid (Leg), like Pse, is difficult to obtain in its free form from bacterial sources. Although first identified in *Legionella pneumophila* as part of the *O*-antigen polysaccharide, Leg was not isolated as a free sugar but instead characterised within oligosaccharide fragments from the parent LPS.[381] To date, there have been no reports of the successful isolation of free Leg directly from bacterial sources. As a result, access to Leg is limited to chemical,[386,394–396] chemoenzymatic[397] or biosynthetic[398] strategies. As with Pse, chemical synthesis of Leg remains challenging due to its large number of stereogenic centres and structural similarity to other nonulosonic acids, requiring careful stereocontrol and carefully planned synthetic routes. In accordance with our work on generating a therapeutic pan-specific antibody tool for Pse,[316] the ability to access Leg and its analogues, opens up the possibility of generating mAb therapies to treat bacterial infections.

Strategies to synthesise Leg have followed similar methodologies to those of Pse. Common synthetic and biosynthetic precursors to Leg are summarised in Figure 5.4. Biosynthesis from GlcNAc (**5.12**)[398] and chemoenzymatic synthesis from D-fucose (**5.13**)[397] have been reported. The first total synthesis of Leg was completed by Knirel *et al*. in 2001[386] from benzyl β-D-fucopyranoside (synthesised from **5.13**), mimicking key

intermediates from the biosynthetic pathway.[398] The alternative approaches to synthesising Leg adopt one of two strategies; use of the amino acid D-*allo*-threonine (**5.14**)[396] (often synthesised from cheaper D-threonine), which naturally possesses the correct stereochemistry at C7 and C8, or use of Neu5Ac[394,395] (**5.5**) which contains the nine-carbon backbone found in Leg.

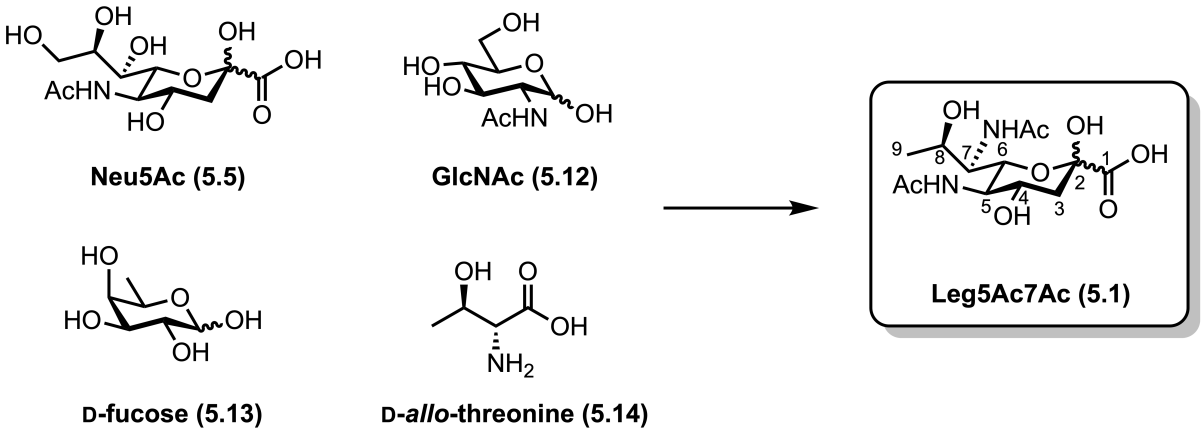


Figure 5.4. Previously used precursors for chemical (**5.5**, **5.13**, **5.14**), chemoenzymatic (**5.14**), and biosynthetic (**5.12**) synthesis of legionaminic acid (Leg).

The following sections detail key reported strategies for the chemical syntheses of Leg and Leg derivatives.

5.2.1 Synthetic Route by Knirel and co-workers

Knirel reported the synthesis of Leg5Ac7Ac (**5.1**) acid *via* an analogous route to his synthesis of Pse reported in the same publication.[386] 2,4-diacetamido-2,4,6-trideoxy-D-mannose (**5.15**), a key intermediate in the biosynthetic pathway reported by Hassan *et al.*,[398] was prepared from commercially available benzyl β-D-fucopyranoside (**5.16**) over eight steps with a 38% overall yield (Figure 5.5).

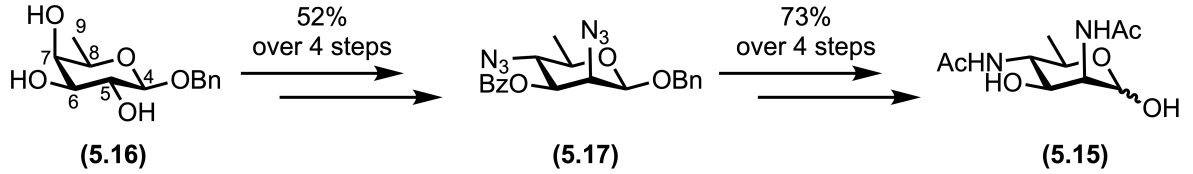


Figure 5.5. Knirel's synthesis of legionaminic acid precursor **5.15** from benzyl β-D-fucopyranoside **5.16**, highlighting the C4-C9 fragment being installed by starting material **5.16**.

Specifically, triol **5.16** was converted to di-azide **5.17** through a sequence of protecting group manipulations followed by nucleophilic substitution with sodium azide. Azide **5.17** was subjected to benzoyl ester deprotection with sodium methoxide, followed by hydrogenation of the azide and benzyl ether groups and reacetylation, providing a corresponding bis *N*-acetylated hemiacetal **5.15**.

The final step of the synthesis was a Knoevenagel condensation and decarboxylation to provide Leg5Ac7Ac (**5.1**) with a 7% yield (3% yield over 9 steps). Undesired 4-*epi*-5,7-diacetamido-legionaminic acid (**5.18**) was also formed in 10% yield (4% yield over 9 steps) (Figure 5.6). The absolute configurations of the synthetic compounds were determined by NMR comparison of Leg derivatives isolated from bacterial sources.

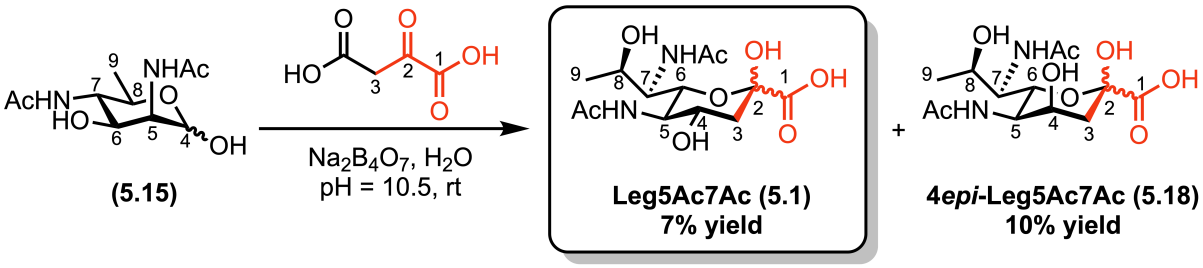


Figure 5.6. The final step of Knirel's synthesis of Leg5Ac7Ac (**5.1**) encompassing a Knoevenagel condensation and decarboxylation. Leg5Ac7Ac (**5.1**) was provided in 7% yield along with 4-*epi* derivative (**5.18**).

Although this synthetic route provides access to Leg5Ac7Ac in relatively few steps, it presents several limitations in its ability to generate Leg glycosides. Namely, the lack of stereocontrol in final Knoevenagel condensation would create purification challenges, and the early installation of the disarming *N*-acetyl groups, would lead to a relatively unreactive glycosyl donor.[399,400]

5.2.2 Synthetic Route by Seeberger and co-workers

Seeberger and co-workers reported the total chemical synthesis of a β-glycoside of Leg5Ac7Ac.[396] Beginning from D-threonine, the synthesis accessed Leg glycoside **5.19** in 21 steps with a 6% overall yield.

A key α-hydroxy aldehyde intermediate **5.20** was first prepared from D-threonine (**5.21**) (Figure 5.7). D-threonine (**5.21**) was first converted to D-*allo*-threonine methyl ester (**5.22**) over five steps, followed by conversion to aldehyde **5.23** over a further three steps. A Cram-chelate organometallic addition of 2-lithiofuran to aldehyde **5.23** proceeded with high diastereoselectivity, favouring nucleophilic attack on the *si*-face, establishing the C6 stereocentre and introducing the C5 functionality (**5.24**). Furan moiety **5.25** was subjected to ozonolysis, methylation, and a reduction-oxidation to yield the corresponding α-hydroxy aldehyde (**5.20**).

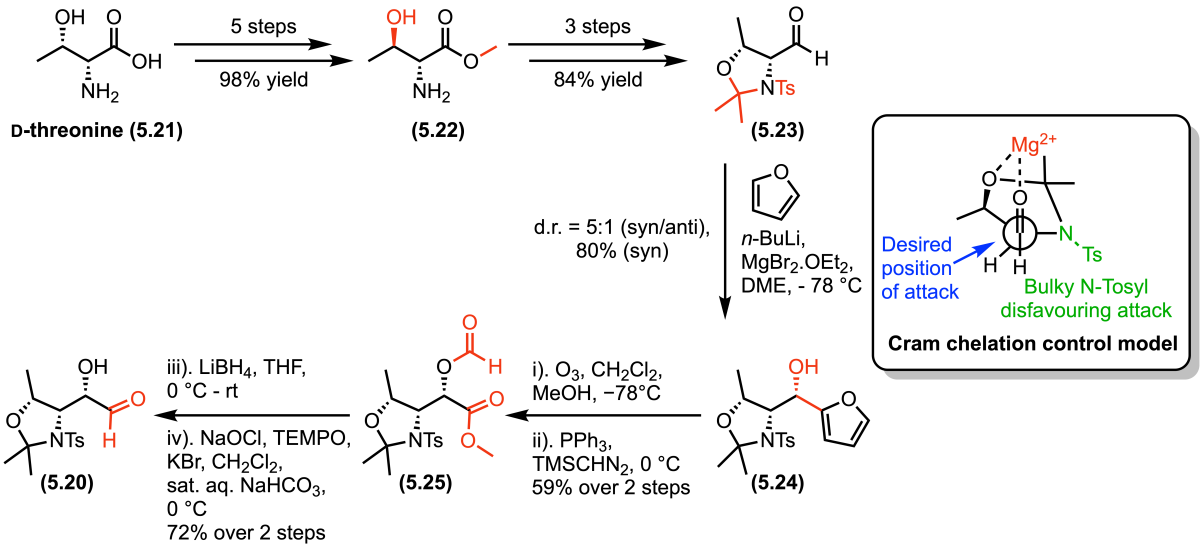


Figure 5.7. Seeberger's route to α-hydroxy aldehyde **5.20**.

The 9-carbon backbone of Leg was established using a Petasis borono-Mannich reaction followed by an indium-mediated Barbier reaction as key C-C bond forming steps (Figure 5.8). Aldehyde **5.20** was subjected to a Petasis borono-Mannich reaction to provide aminal **5.21**. The reaction proceeds *via* initial condensation of the α-hydroxy aldehyde (**5.20**) with allyl amine to form iminium ion **5.21**, which coordinates to (*E*)-styrylboronic acid to generate the key stereochemically dictating tetrahedral boronate intermediate **5.22**.[401] Attack at the *Re* face (**5.23**) is favoured by minimisation of allylic strain compared to attack at the *Si* face (**2.24**), generating the allylic amine **5.25** in (19:1 dr). Pd(0)-catalysed deallylation followed by acetylation then gave amide **5.26**. Notably, the formation of free amine on N5 could allow for N diversification at this step; however, the harsh conditions utilised in the remainder of the synthesis likely preclude this. Oxidative

cleavage of *N*-cinnamylacetamide **5.26** formed intermediate aldehyde **5.27**, which was subjected to an Indium-mediated Barbier reaction to provided enoate **5.28**, encompassing the full 9-carbon backbone of Leg (**5.1**) in a *d.r.* of 2.5:1 (*syn*:*anti*).

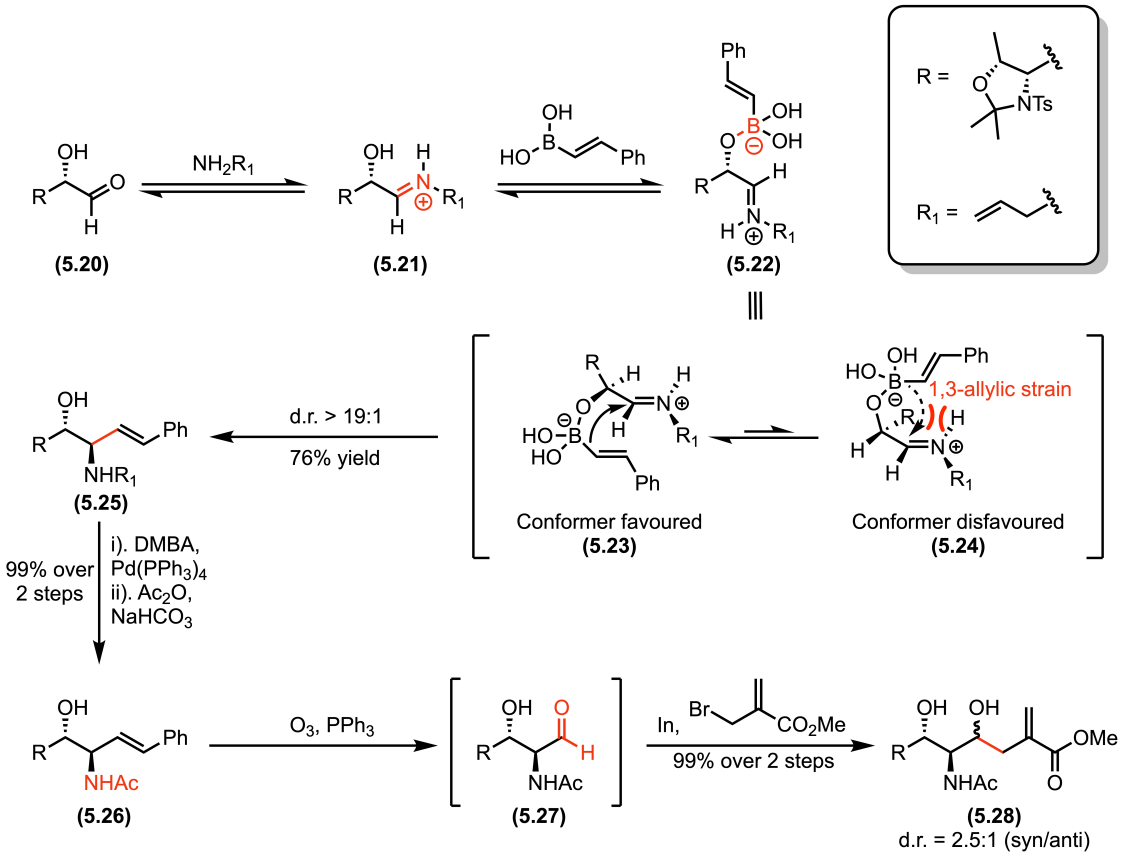


Figure 5.8. Conversion of α-hydroxy aldehyde **5.20** to enoate **5.28**, highlighting diastereoselectivity of Petasis Borono-Mannich reaction.

The desired diastereomer of **5.28** was subjected three further steps to form donor **5.29**. Donor **5.29** was subjected to dehydrative glycosidation and subsequent acetal hydrolysis to provide the β-anomer of glycoside **5.30** in 63% yield (Figure 5.9). A minor amount of α-anomer was also detected, however, it co-eluted with decomposition products and could not be isolated. Glycoside **5.30** was then sequentially deprotected through a series of manipulations including a Birch reduction of the tosylamide and benzyl thioether, followed by *N*-acetylation, to form the desired Leg5Ac7Ac glycoside (**5.31**) Notably, this final-stage modification introduces a strategic handle and N7 amine, enabling potential diversification at this position for future analogue development.

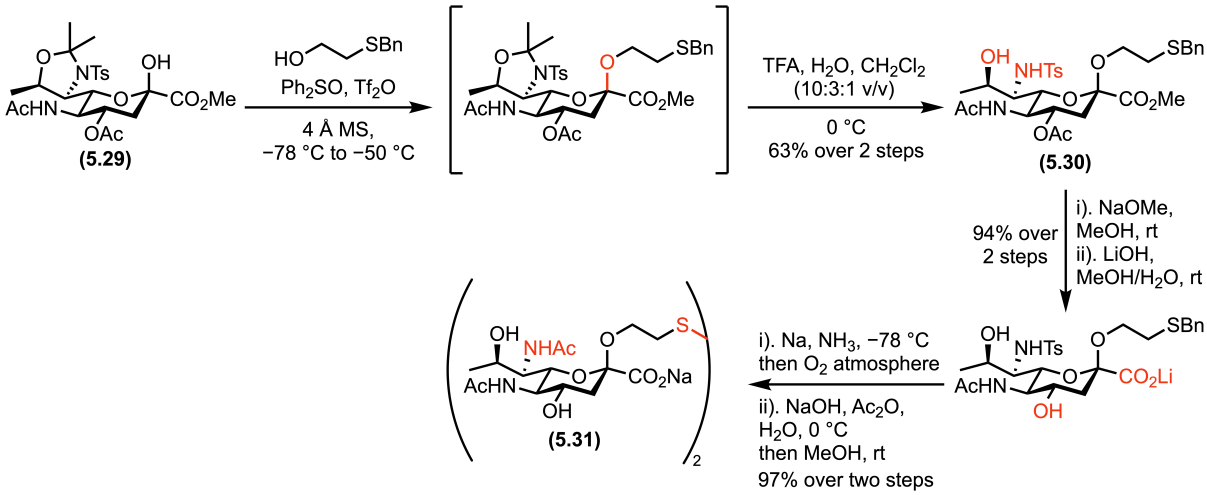


Figure 5.9. Synthesis of β-Leg5Ac7Ac glycoside (**5.31**) from Leg donor **5.29**.

Although notable as the first total synthesis of Leg, Seeberger's route has several limitations. Many of the intermediates were reported to be unstable and prone to decomposition, resulting in challenging purification and handling. Additionally, the use of Birch reduction conditions in the penultimate step limits the functionality that can be incorporated in the aglycone and at the N5 position. Most importantly, the synthetic strategy does not enable access to the α-glycoside (equatorial anomer), the native glycosidic linkage observed in bacterial legionaminic acid-containing glycosides.

5.2.3 Synthetic Routes by Crich and co-workers

Crich and co-workers have reported two syntheses of legionaminic acid. Both 2017[402] and 2022[394] syntheses begin from sialic acid (**1.3**).

5.2.3.1 Crich's 2017 Synthesis

Popik *et al.* synthesised a legionaminic acid donor (**5.32**) from Neu5Ac (**5.5**) in 15 steps with 17% overall yield, that could be used to prepare α-(equatorial) glycosides (**5.33**) (Figure 5.10).

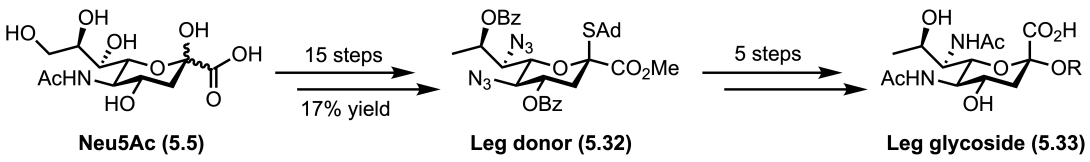


Figure 5.10. Popik's route to Leg glycoside (**5.33**); Neu5Ac (**5.5**) was converted to Leg donor **5.32** over 15 steps with a 17% overall yield, which was subsequently glycosidated and deprotected to provide a range of equatorial glycoside of Leg.

Popik's route began from known sialic acid thioglycoside **5.34**, which was obtained from sialic acid in 65% yield over six literature steps (Figure 5.11). To effect C9 deoxygenation, Popik prepared a terminal iodide with 4,8-*O*-benzoyl protecting groups (**5.35**). Alkyl iodide **5.35** was radically deiodinated with AIBN and tris(trimethylsilyl)silane (TTMS) and diazotised at the N5 to form C9 deoxy azide **5.36**. An oxidation and stereoselective reduction sequence provided (7*S*)-alcohol **5.37**, which was triflated and displaced with NaN_3 to yield 5,7-diazido Leg thioglycoside donor **5.32**.

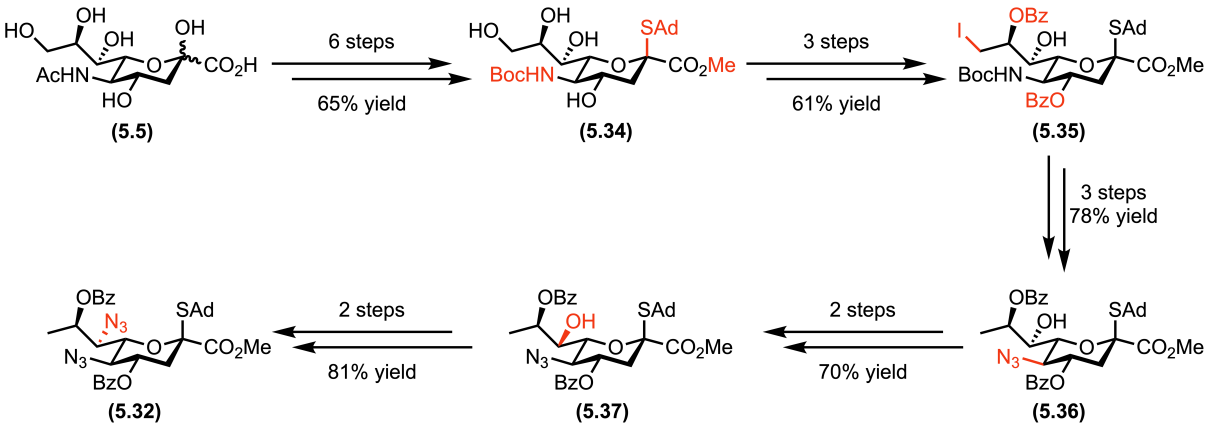


Figure 5.11. Popik's route to Leg di-azido donor **5.32** from Neu5Ac (**5.5**).

Previous work conducted by the Crich group[350] identified optimal conditions for the equatorial stereoselective glycosidation of other neuraminic acid adamantyl thioglycosides that were applied to Leg donor **5.32** (Figure 5.12). Stereoselectivity was dependent on use of nitrile co-solvent (MeCN), taking advantage of the 'nitrile effect' (see section 4.4), at −78 °C using *N*-iodosuccinimide (NIS) and trifluoromethanesulfonic acid (TfOH) as promoters.

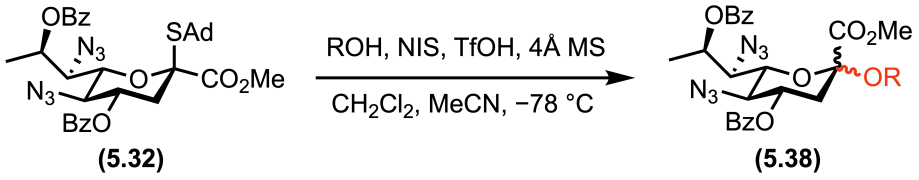
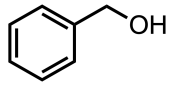
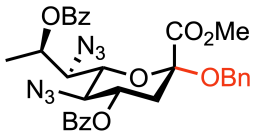
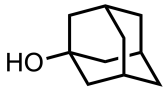
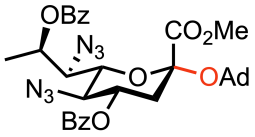
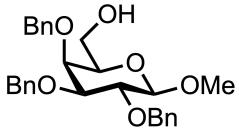
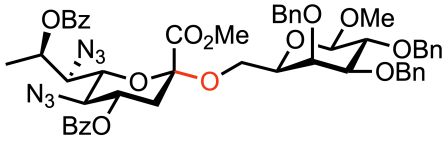


Figure 5.12. Popik's conditions for glycosylation of Leg donor **5.32** utilising established conditions from the Crich group, producing predominantly equatorial glycosides (**5.38**).

Popik's conditions proceeded with good yields, showing preference for the α-glycoside for a range of primary (**5.39**) and tertiary (**5.40**) alcohols, as well as glycans (**5.41**) (Table 5.2).

Table 5.2. Examples of Popik's glycosidation reactions, highlighting tolerance of conditions to a range of acceptors.

ROH	Product	Yield
	 **(5.39)**	96%, α only
	 **(5.40)**	73%, 4.2:1 (α:β)
	 **(5.41)**	87%, 6.1:1 (α:β)

5.2.3.2 Crich's 2022 Synthesis

In 2022, Arachchige *et al.* published an alternative route to the same Leg donor (**5.32**), which proceeded from Neu5Ac (**5.5**) in 15 steps with 18% overall yield (Figure 5.13). In this route, **5.42** was deacetylated to form common intermediate **5.34**, which was oxidatively cleaved, and the resulting aldehyde was elaborated *via* a stereoselective samarium (II) iodide (SmI_2) mediated aza-pinacol reaction to reinstall the side chain with the correct Leg stereochemistry. This route circumvented the need for regioselective manipulations in the previous synthesis.

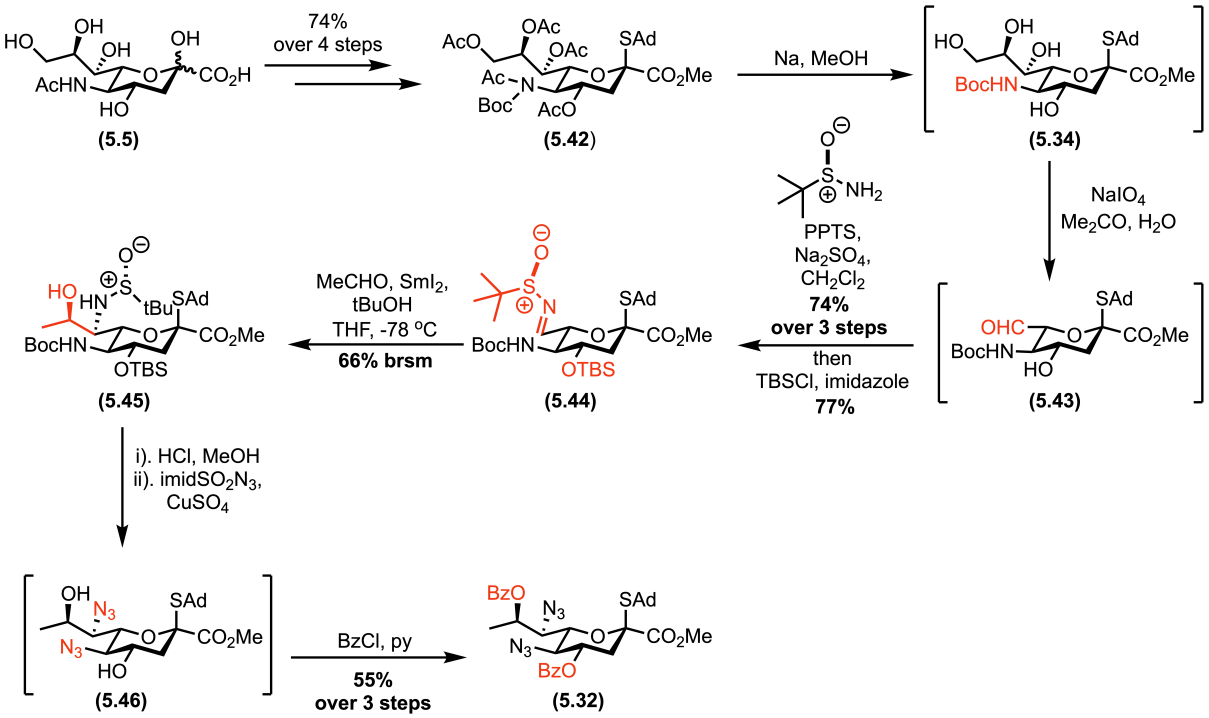


Figure 5.13. Arachchige's route to Leg donor **5.32** from Neu5Ac (**5.5**).

Crich's second generation route began with $NaIO_4$-mediated glycol cleavage of sialic acid thioglycoside **5.34**. The resulting crude aldehyde **5.43** was converted to the (*R*)-Ellman's sulfinimine derivative and *tert*-butyldimethylsilyl (TBS) protected to give **5.44.** To reinstall the C8-C9 side chain, samarium (II) iodide (SmI_2) mediated aza-pinacol reaction was conducted with acetaldehyde. Diastereomeric α-hydroxy sulfinamides were produced in 54% overall yield with 3:1 selectivity for the desired diastereomer (**5.45**). Ellman's auxiliary was removed using HCl in methanol, revealing a free amine at C7, which was immediately treated with Stick's reagent to form diazide **5.46**. Subsequent benzoylation conditions provided Leg donor **5.32** in 55% yield over three steps.

Notably, the key side chain exchange *via* $NaIO_4$-mediated oxidative cleavage and installation of a single enantiomer of Ellman's sulfinamide (**5.44**, **5.45**, and **5.46**) allowed formation of a range of nonulosonic acids donors to be synthesised: legionaminic acid (**5.32**), acetaminic acid (Aci, **5.48**), pseudaminic acid (**5.50** and **5.51**), and various 8-*epi* diastereomers (**5.47** and **5.49**) of these sugars were synthesised (Figure 5.14).

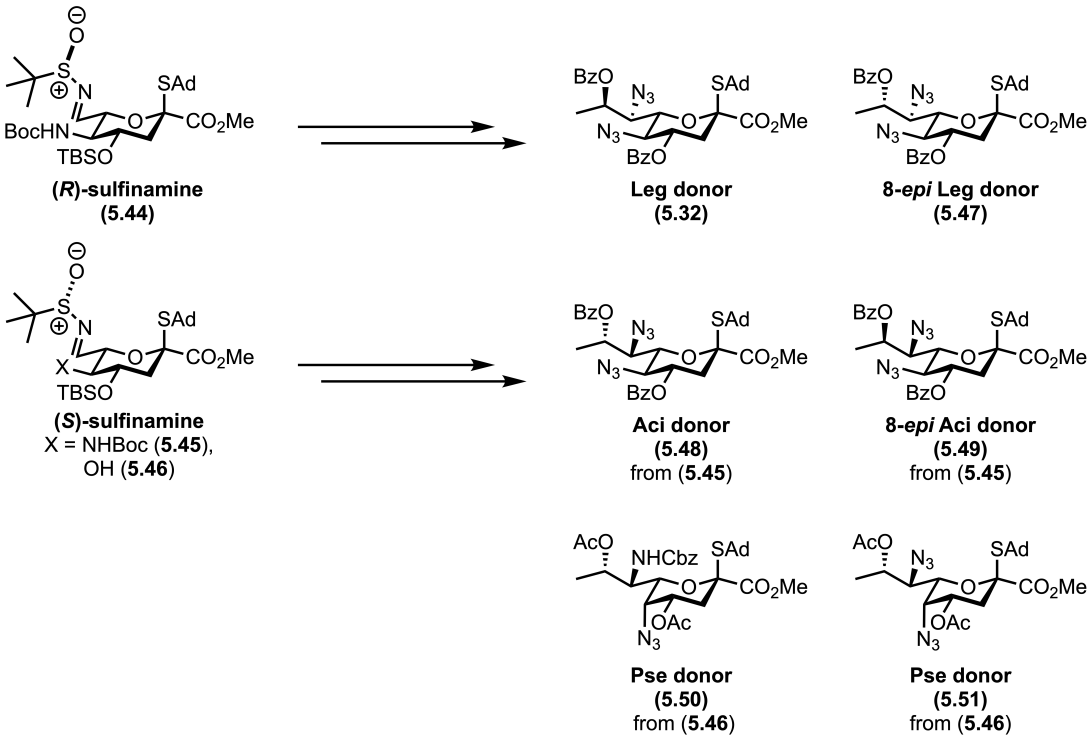


Figure 5.14. Arachchige's route from common Ellman's sulfinimines to various nonulosonic acid donors, including Leg, Pse, and acetaminic acid (Aci).

Although Arachchige did not report any glycosylations using these donors in the present study, previous work by Popik[395], Dhakal,[350] and Lu[363] has demonstrated a range of successful α- and β- selective glycosylations employing either these specific donors or structurally analogous systems.

5.3 Chapter Aims

The primary goal of the research presented in this chapter was the synthesis of an equatorial (α) glycoside of legionaminic acid (Leg). This glycoside, ideally a serine or threonine glycoside, would be used for two purposes. First, access to Leg would enable screening against the Pse5Ac7Ac-specific monoclonal antibody previously developed by Tang, with the aim of evaluating its binding affinity and selectivity. Second, as with Pse5Ac7Ac, a suitable Leg derivative could be used for the generation of a monoclonal antibody specific for α-Leg5Ac7Ac with potential application in the treatment of bacterial infections caused by Leg-expressing pathogens.

Additionally, it was envisioned that Leg variants, as outlined in Table 5.1, could be synthesised and screened against the newly developed α-Leg5Ac7Ac specific antibody to assess binding specificity and selectivity. Ideally, this work would extend to the synthesis of a broader set of nonulosonic acids, including 8-epimers and acetaminic acid, for both antibody generation and profiling against pre-existing monoclonal antibodies.

5.4 Results and Discussion

5.4.1 Selection of Synthesis

A Leg donor was required that could selectively enable the formation of an equatorial α-glycoside, the native glycosidic linkage observed in Leg-containing bacterial glycoconjugates. Both of Crich's routes produced common Leg donor **5.32**, which was shown to meet this requirement (Figure 5.15).

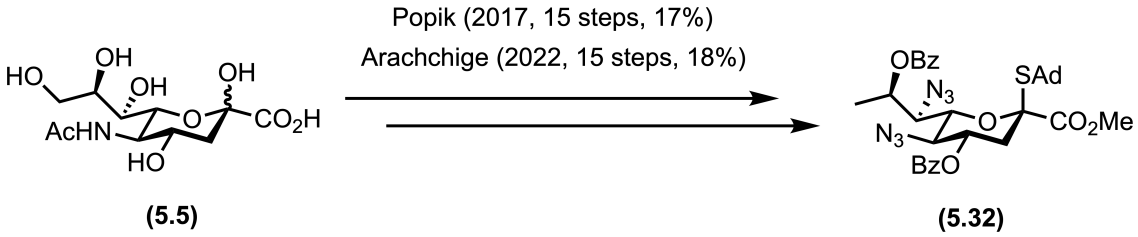


Figure 5.15. Crich's syntheses resulting in common Leg-donor **5.32**.

Both routes started from commercially available Neu5Ac (**5.5**), and led to almost identical yields (17% Popik *et al.*, 18% Arachchige *et al.*) over 15 steps. The route from Arachchige *et al.* through oxidative cleavage and stereoselective reinstallation of C8-C9 side chain using an Ellman's sulfinamide was initially selected for this work due to its demonstrated versatility in accessing a broader set of nonulosonic acids.

1.5 Modified Route to Legionaminic acid via an Ellman's sulfinimine

The synthetic route from Arachchige *et al.*[394] starting from sialic acid was broadly adopted for this work, with modifications to the reagents and conditions used in specific steps. Specifically, Neu5Ac (**5.5**) was first converted to methyl ester *via* treatment with trimethyl orthoformate and thionyl chloride in methanol, followed by peracetylation with acetic anhydride and pyridine to form **5.52** (Figure 5.16). A milder trimethyl orthoformate-mediated methyl esterification was selected over the Amberlyst H^+ catalysed Fischer esterification employed by Arachchige *et al.*, to reduce the risk of forming the methyl glycoside. Thioglycoside **5.53** was formed from glycosyl acetate using 1-adamantane thiol (AdSH) in the presence of Lewis acid catalyst $BF_3.OEt_2$. The desired thioglycoside (**5.53**) was obtained in 55% yield from glycosyl acetate **5.52** (Figure 5.16). The moderate axial selectivity was suboptimal and is likely due to a reduction in kinetic selectivity under

the ambient conditions and prolonged reaction times employed. Notably, the reaction could not be performed at sub-zero temperature, as typically used for enhancing selectivity. This is likely due to the highly electron-deficient nature of the peracetylated glycosyl acetate donor.

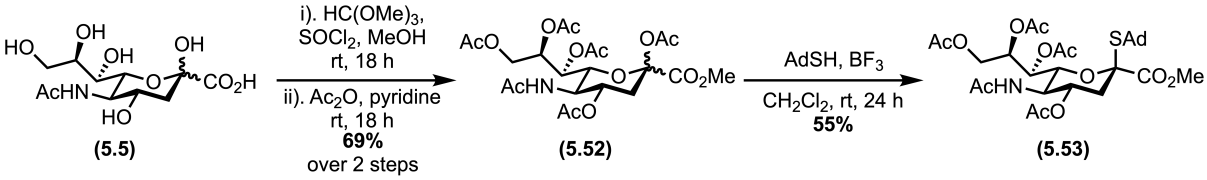


Figure 5.16. Conversion of Neu5Ac (**5.55**) to axial thioglycoside **5.53**, following Arachchige's procedure.

Acetamide **5.53** was next converted to corresponding imide **5.42** in 99% yield by treatment with Boc_2O and catalytic DMAP in refluxing THF overnight (Figure 5.17). These comparatively forcing conditions, compared to a standard Boc protection (Boc_2O, $NaHCO_3$, rt), were required due to the decreased nucleophilicity of the amide nitrogen relative to a free amine. Treatment of **5.42** with catalytic NaOH in MeOH, which produced *in situ* NaOMe,[205] provided tetra-ol **5.34** *via* transesterification. Tetra-ol **5.34** was then subjected to oxidative cleavage with sodium metaperiodate ($NaIO_4$) in aqueous acetone to provide aldehyde **5.43**. For this step the use of water as a co-solvent both promoted solubility and consumption of an intermediate C8-C9 cleavage product, *via* hydration of the C8 aldehyde (**5.54**). This intermediate allowed for subsequent cleavage of the C7-C8 bond to provide the desired C7 aldehyde. Without isolation, aldehyde **5.43** was condensed with the (*R*)-enantiomer of the Ellman sulfinamide to give sulfinimine **5.55** in 71% yield over three steps. Sulfinimine **5.55** was silylated with TBSCl and imidazole to give silyl ether **5.44**.

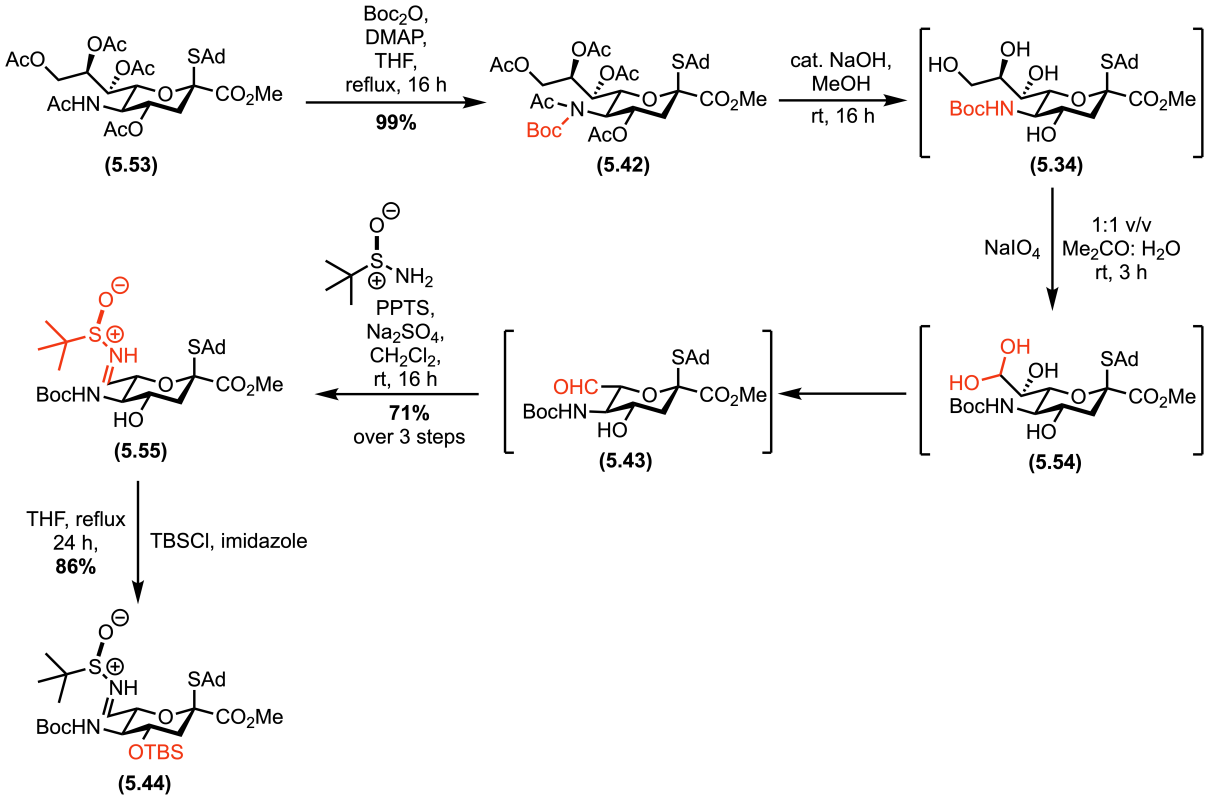


Figure 5.17. Preparation of chiral sulfinimine **5.44** *via* a modification of the route previously reported by Arachchige *et al.* from Neu5Ac (**5.5**).

With **5.44** in hand, the aim was to stereoselectively reinstall the side chain as performed by Arachchige *et al. via* a samarium diiodide-mediated aza-pinacol reaction with acetaldehyde to generate α-hydroxy sulfinamide **5.45** (see Figure 5.18 for conditions reported by Arachchige *et al.*).

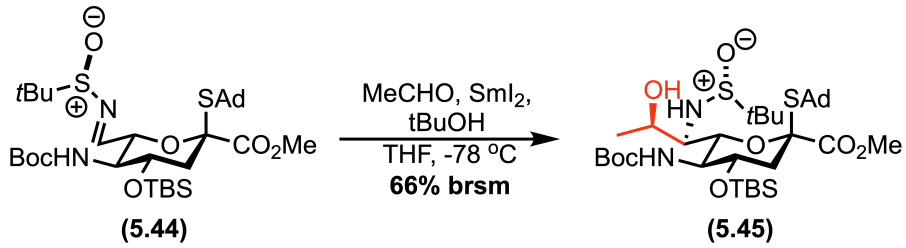


Figure 5.18. Installation of C8-C9 side chain, simultaneously setting stereochemistry of C7 and C8, reported by Arachchige *et al.*[394]

First reported by Zhong *et al.*,[403] the use of SmI_2-mediated single-electron transfer (SET) reduction has been shown to facilitate the stereoselective synthesis of enantiopure amino acids from Ellman's sulfinimines. The anti-diastereomer was obtained as the

major product. Samarium, a lanthanide, shows a strong preference for the +3 oxidation state. As a result, samarium(II) iodide (SmI_2) readily undergoes SET, donating an electron to generate the thermodynamically favoured Sm(III) species. While no mechanistic rationale has been reported for the observed diastereoselectivity, it is possible that the reaction proceeds *via* a seven-membered twist-chair transition state, the lowest energy conformation of a cycloheptane ring system (Figure 5.19).[404]

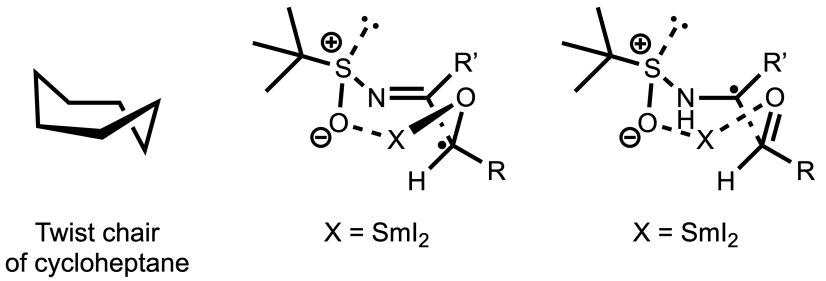


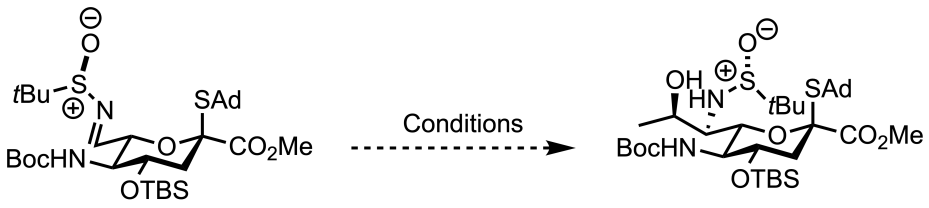
Figure 5.19. Proposed mechanistic explanation for anti-selectivity observed during SmI_2 mediated aza-pinacol, highlighting seven membered twist-chair transition state and two possibilities for C-centred radicals primed for sulfinimine attack.

This proposal reflects a similar stereoelectronic rationale to the well-established six-membered transition state observed in classical Ellman-type additions.[405] It is proposed that the bulky *tert*-butyl group adopts a pseudo-bowsprit orientation to minimise steric interactions by pointing away from the ring. The aldehyde R group (e.g. methyl) likely favours a similar orientation, with the *t*Bu and aldehyde R groups occupying opposing pseudo-bowsprit position on opposite faces of the twist-chair. Additionally, the R' group of the sulfinimine adopts a pseudo-equatorial position to avoid steric clash with the aldehyde substituent.

The transition state is likely stabilised through chelation of oxophilic Sm(II) to both the aldehyde oxygen and the sulfinyl oxygen, resulting in a cyclic transition state that enforces facial selectivity during C–C bond formation. This model is supported by experimental observations that aldehydes bearing bulkier substituents consistently afford higher levels of anti-diastereoselectivity, consistent with preferential placement of the larger group into the less hindered pseudo-bowsprit position.[403,406] Although not directly analogous to the present system, related cross-coupling reactions involving nitrones and carbonyl compounds have been shown to proceed via initial reduction of

the nitrone, generating an α-aza-stabilised nucleophilic radical that subsequently couples with the carbonyl electrophile.[407,408] In the present system, irrespective of whether acetaldehyde or the sulfinimine is reduced first, both pathways are proposed to occur through a similar transition state geometry.

The conditions trialled for the SmI_2-mediated aza-pinacol side-chain reinstallation based on the prior work from Arachchige *et al.* are outlined in Figure 5.20 and Table 5.3.



(5.44) **(5.45)**

Figure 5.20. Attempted reinstallation of side chain via SmI_2-mediated aza-pinacol, generating α-hydroxy sulfinamide **5.45** with Leg stereochemistry.

Table 5.3. Conditions and results of side chain re-installation.

Conditions	Results
*t*BuOH (3 eq), THF, rt, argon atmosphere then rt to -78 °C, acetaldehyde* (5 eq) followed by SmI_2** (0.1 M in THF, 5 eq) *Freshly purified, **SmI_2 prepared from Arachchige's procedure	No reaction
*t*BuOH (3 eq), THF, rt, argon atmosphere then rt to -78 °C, acetaldehyde* (5 eq) followed by SmI_2** (0.1 M in THF, 5 eq) *Freshly purified, **SmI_2 commercial pre-made solution	No reaction
*t*BuOH (3 eq), THF, rt, argon atmosphere then rt to -78 °C, acetaldehyde* (5 eq) followed by SmI_2** (0.1 M in THF, 5 eq), **-78 °C to -40 °C** *Freshly purified, **SmI_2 commercial pre-made solution	No reaction

*t*BuOH (3 eq), THF, rt, argon atmosphere then rt to -78 °C, acetaldehyde* (5 eq) followed by SmI_2** (0.1 M in THF, **20 eq**), -78 °C to rt *Freshly purified, **SmI_2 commercial pre-made solution	No reaction

Unfortunately, none of the SmI_2-based conditions trialled resulted in observable conversion of the starting material. Both freshly prepared SmI_2 and a commercially sourced solution were trialled, alongside variations in temperature and equivalents of reductant added. To determine whether reagent quality was limiting the transformation, a control experiment was conducted using phenylacetaldehyde. No formation of the desired pinacol product was observed, suggesting that reagent quality was the limiting factor. An alternative approach involving a Luche-type organocerium addition of TMS-acetylene to the sulfinimine was also trialled;[409] however, no conversion of starting material was observed under these conditions (Figure 5.21).

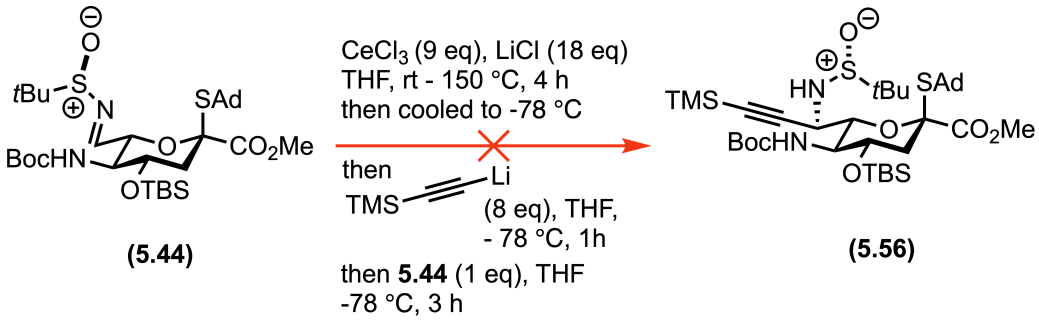


Figure 5.21. Trial of Luche-type chemistry involving TMS acetylene.

Due to the challenges in reinstalling the C8-C9 side chain, attributable to both the sensitivity of the reaction conditions and inconsistent reagent quality, it was decided to adopt the synthetic route reported by Popik *et al.*[395] to access the desired Leg donor (**5.32**). The route from Popik *et al.* (section 5.2.3.1), while containing some common intermediates to that of the Arachchige *et al.* route, differs in that it relies on the functionalisation of the pre-existing C9 backbone of sialic acid, avoiding the need for C-C bond formation that proved intractable in our hands.

5.5 Synthesis of Legionaminic acid donor

The routes from Popik *et al.* and Arachchige *et al.* diverged at the formation of *N*-Boc tetraol **5.34**, involving an initial regioselective sulfonylation of the primary (C9) alcohol with 2,4,6-triisopropylbenzenesulfonyl chloride (Tris-Cl), followed by substitution with iodide (Figure 5.22). Initial attempts at regioselective sulfonylation provided the desired sulfonate product in 55% yield. Notably, 20% of the C8-*O*-Tris regioisomer was also isolated, and the use of excess Tris-Cl led to the formation of large amounts of triisopropylbenzenesulfonate by-products, making purification challenging. To increase the regioselectivity for sulfonylation, the reaction mixture was cooled to 0 °C prior to portion wise addition of Tris-Cl (4 eq). After maintaining the reaction at 0 °C for 2 h, the mixture was warmed to rt at stirred for a further 18 h. Pleasingly, the desired product (**5.57**) was obtained in an improved yield of 66%, along with 12% of the C8-*O*-Tris product. **5.57** underwent a S_N2 reaction with excess sodium iodide at 40 °C in acetone to give terminal iodo derivative **5.58** in 94% yield.

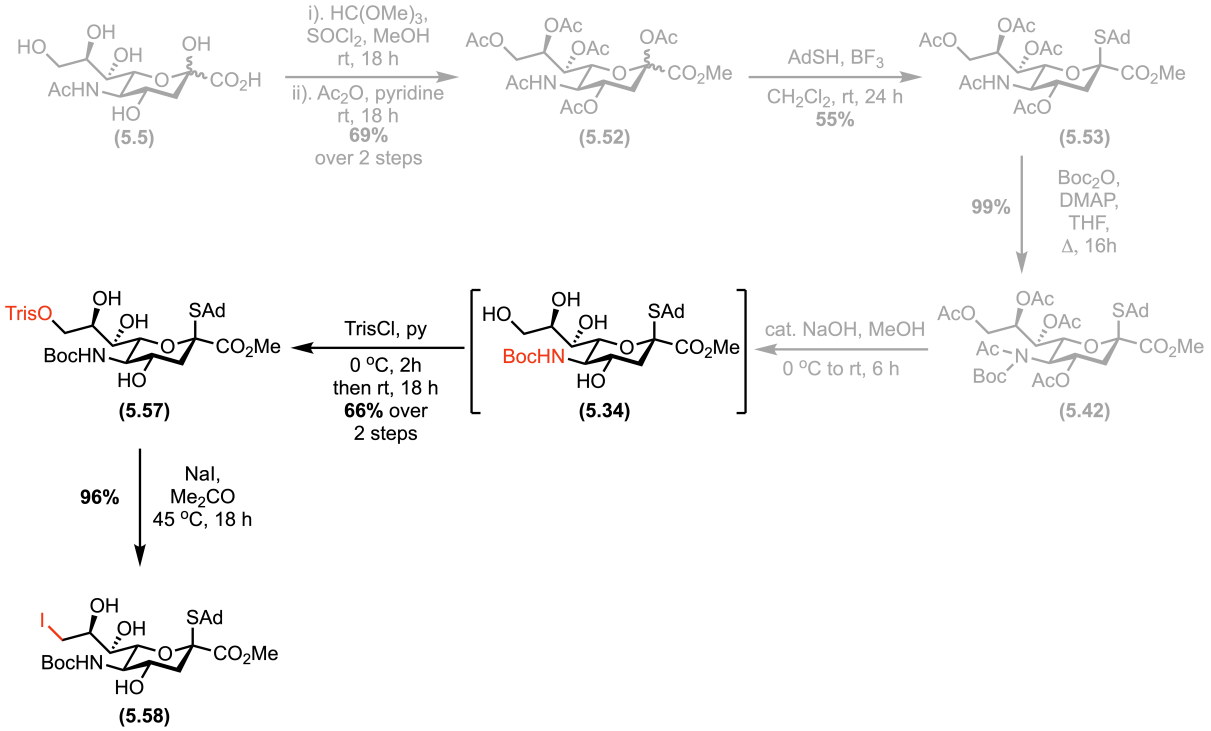


Figure 5.22. Convergence of the synthetic routes from Popik *et al.* and Arachchige *et al.*, showing the generation of iodide **5.58** from **5.34** *via* the route from Popik *et al.*

Selective benzoylation of the two least hindered alcohols (C4 and C7) in previously prepared intermediate **5.58** with benzoyl chloride in pyridine at 0 °C gave the 4,9-di-*O*-benzoate **5.35** in 91% yield. We were concerned about the strongly alkaline conditions needed to deprotect benzoyl esters that can cause β-elimination of amino acid glycosides. However, it was noted by Popik *et al.* that use of the more base-labile *O*-acetyl groups could not be introduced with sufficient 4,8-regioselectivity. **5.35** was deiodinated with AIBN and tris(trimethylsilyl)silane (TTMS) in benzene at 60 °C, and intermediate **5.59** was taken up in methanol and treated with hydrogen chloride in ether, completing removal of the Boc group, providing amine **5.60** as the hydrochloride salt. The free amine was treated with Stick's diazotransfer reagent, triethylamine, and catalytic copper(II) sulfate in aqueous acetonitrile. $CuSO_4$ was included to accelerate the diazotransfer by acting as a Lewis acid, particularly beneficial for sterically hindered or otherwise slow reacting substrates. Azide **5.36** was provided in 62% yield over three steps. The azide on C7 was installed *via* a S_N2 reaction with NaN_3. To obtain the correct stereochemistry, the alcohol on C7 needed to be inverted. To this end, (*R*)-alcohol **5.36** was oxidised with DMP to ketone **5.61** in 85% yield, followed by stereoselective reduction with Luche's reagent in methanolic dichloromethane at -78 °C to give an 85:15 mixture of epimeric alcohols. The desired (*S*)-alcohol epimer **5.37** was isolated in 82% yield, with the observed stereoselectivity attributed to a Cram-chelate-controlled reduction in which the C8 *O*-benzoyl group coordinates the lanthanide centre. Triflation of **5.37** with triflic anhydride produced triflate **5.62**, which was subject to an S_N2 reaction with NaN_3 in DMF at 0 °C to provide the donor (**5.32**) in 65% yield over two steps.

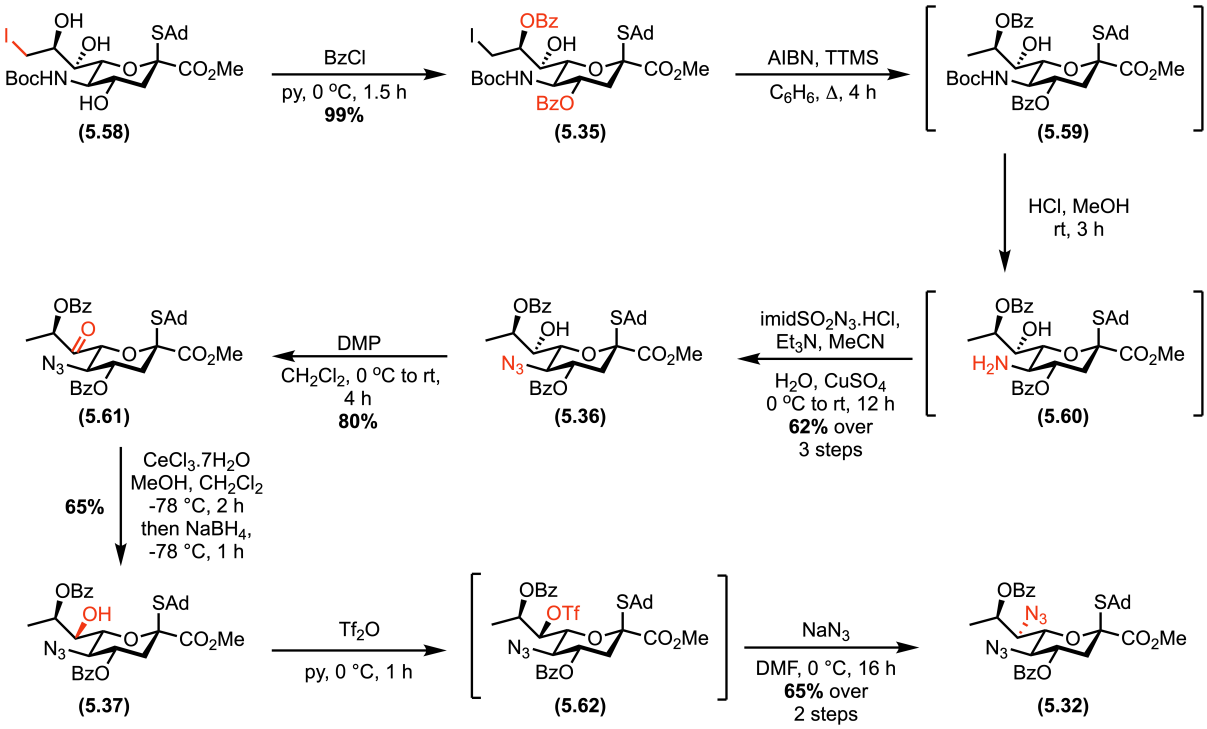


Figure 5.23. Synthesis of benzoyl-protected Leg5$N_3$7N_3 glycosyl donor (**5.32**) from iodide **5.58** following the methodology reported by Popik *et al*.

5.5.1 Glycosidation of donor

In addition to screening for affinity against the 1E8 antibody generated by Tang *et al*. a key aim was also to generate antibodies capable of selectively recognising Leg. As a result, the synthetic sugar would need to be covalently conjugated to an immunogenic carrier protein, such as keyhole limpet hemocyanin (KLH). To facilitate this conjugation, Leg donor **5.32** was glycosidated with bifunctional linker Fmoc-2-(2-hydroxyethoxy)ethyl carbamate **5.63** to provide glycoside **5.64**. (Figure 5.24).

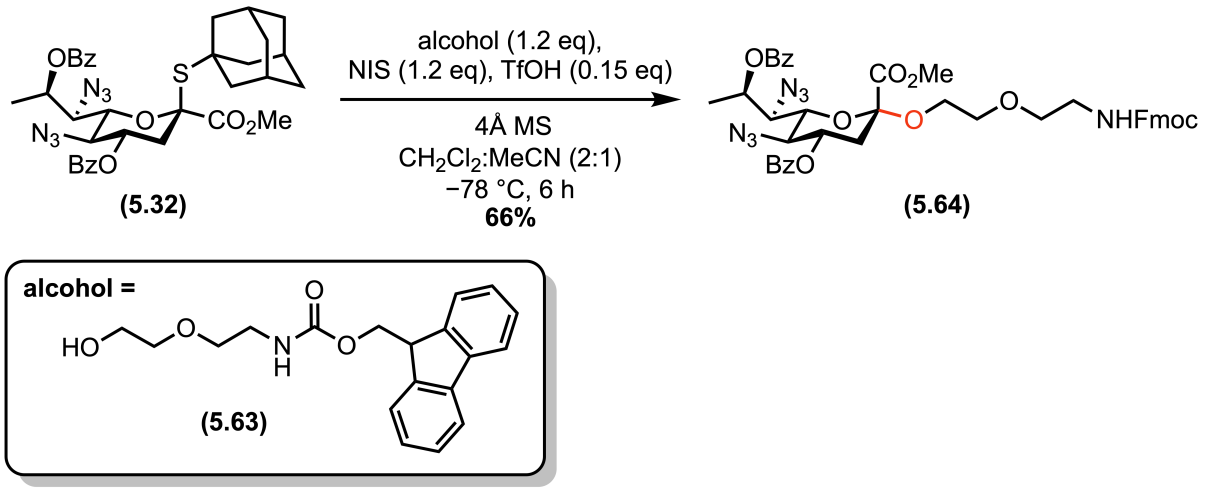


Figure 5.24. Glycosidation of Leg donor **5.32** with alcohol **5.63** to form α-glycoside **5.64**.

Glycosidation of donor **5.32** with alcohol **5.63** was promoted using NIS and triflic acid in a CH_2Cl_2:MeCN (2:1 v/v) co-solvent system at -78 °C in the presence of 4 Å molecular sieves, affording the equatorial α-glycoside **5.6** in 66% yield. Activation of the thioglycoside donor proceeds *via* attack of electrophilic iodine on the anomeric sulfur, forming a covalent S-I adduct with a triflate counterion.[410] Triflic acid is used to protonate the carbonyl of the NIS, activating it and increase the electrophilicity of the iodine.[411,412] This activation of the thioether promoting formation of the oxocarbenium ion. The oxocarbenium can be intercepted by acetonitrile, producing an axial glycosyl nitrilium cation.[413] This directs nucleophilic substitution through an S_N2-like pathway to provide α (equatorial) selectivity. The solvent combination plays complementary roles: dichloromethane as a non-polar solvent that can solubilise the donor and allow for controlled generation of the reactive intermediate, while acetonitrile is critical for stereochemical control. The low reaction temperature ensures kinetic control, ensuring the reaction proceeds through the stereodirecting nitrilium pathway before alternative pathways can occur, while also minimising elimination and decomposition. Molecular sieves remove any water present, suppressing hydrolysis of the activated donor. Together, these conditions facilitate efficient donor activation and provide high α-selectivity for glycoside formation.

A gated decoupled ^{13}C NMR experiment was used to confirm the anomeric configuration of the synthesised legionaminic acid derivative. Selective decoupling was removed for

the C3 methylene protons, allowing determination of ^{2}JCH coupling between C3-H_{ax} and the ester carbonyl C1. A doublet at the C1 resonance (168.0 ppm) of J = 6.2 Hz is consistent with the α-anomer, in which the dihedral angle between the C1-C2-C3-H_{ax} system has the required dihedral geometry and thus orbital alignment required for strong ^{2}JCH coupling (Figure 5.25). In comparison, had the β-anomer be formed, a singlet would be observed. This diagnostic pattern aligns with previously reported methods for assigning sialic acid configuration *via* ^{13}C NMR.[414]

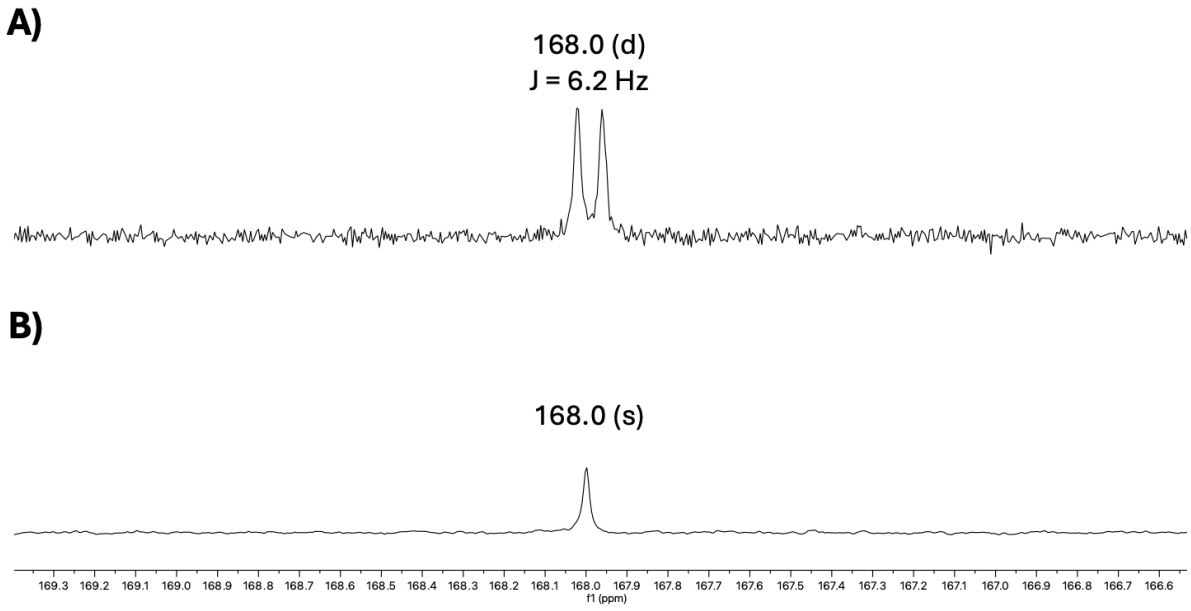


Figure 5.25. A) Selective C3 decoupling removal in ^{13}C NMR spectrum of **5.64**, showing C1 as a doublet (168.9 ppm, J = 6.2 Hz). **B)** Decoupled ^{13}C NMR spectrum of **5.64**, showing C1 as a singlet (168.0 ppm).

Following glycosylation, the azide functionalities on **5.64** were reduced to the corresponding primary amines using zinc and re-acetylated with acetic anhydride to provide the *N*-acetyl derivative (**5.65**). While the transformation proceeded successfully, the overall yield was low due to irreversible benzoyl migration. Subsequent global deprotection was carried out in a one-pot procedure using 10 equivalents of NaOH in methanol, allowing simultaneous cleavage of the methyl ester, benzoyl, and Fmoc protecting groups. This resulted in the desired α-PEG2-NH_2-Leg5Ac7Ac derivative (**5.66**) as the mixed acetate/formate salt in 11% yield over two steps (Figure 5.26, Figure 5.27). Although LC-MS analysis indicated clean conversion from intermediate **5.65** to the final

product, the low isolated yield is attributed to significant material losses during multiple rounds of purification on specialised chromatographic media.

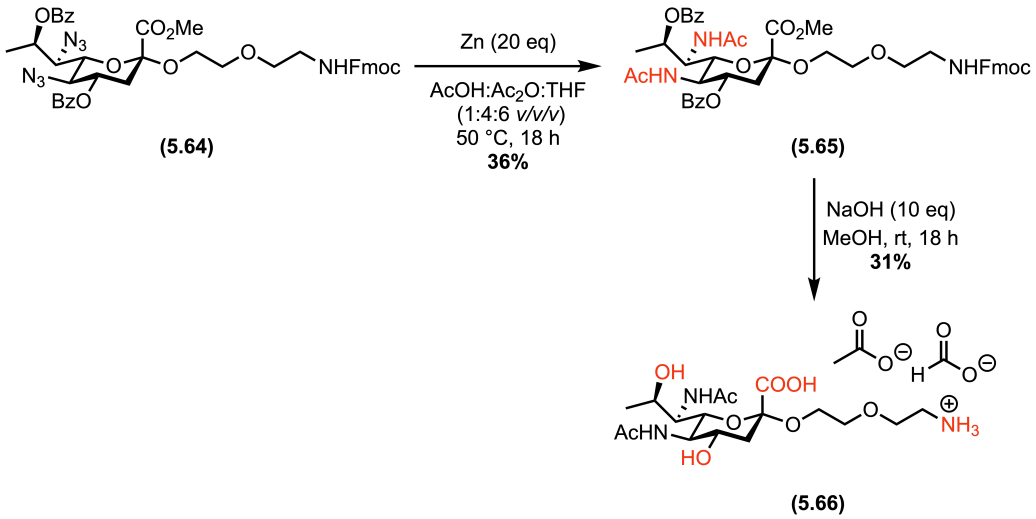


Figure 5.26. Conversion of di-azide **5.64** to di-acetamide **5.65**, following by global ester and Fmoc deprotection to provide **5.66** in 11% overall yield.

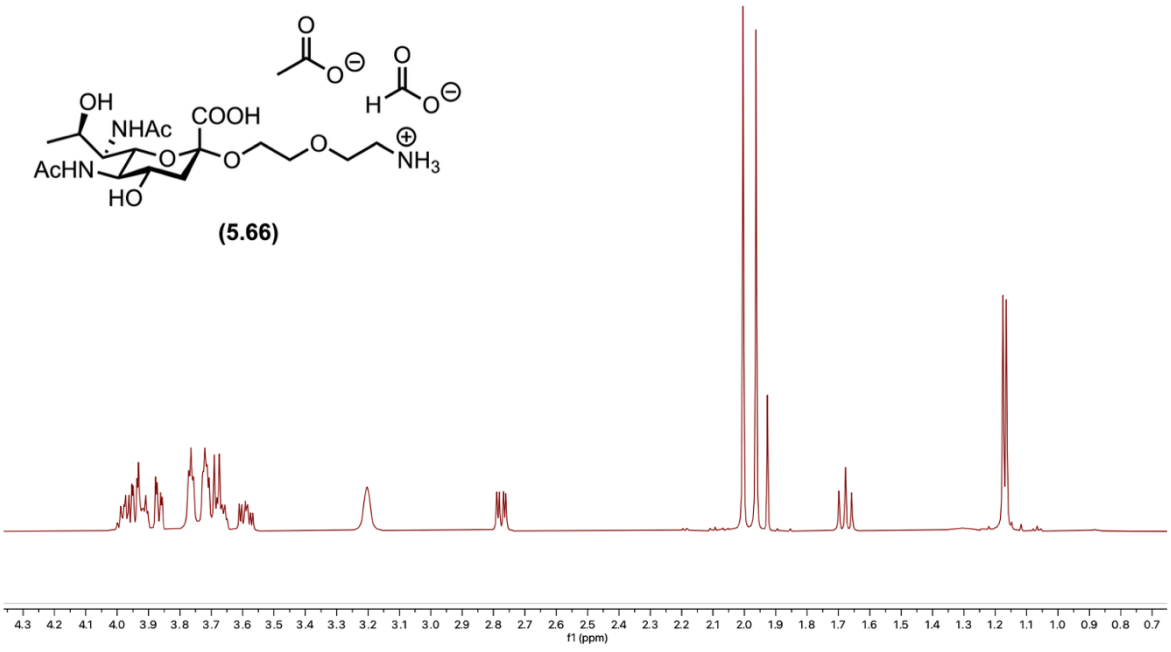


Figure 5.27. ^{1}H-NMR spectrum with water suppression for final Leg glycoside (**5.66**), produced as the mixed acetate/formate salt. The spectrum is cropped from 0.7 to 4.3 ppm for clarity.

5.6 Binding Evaluation of Synthesised legionaminic acid glycoside (performed with Professor Ethan Goddard-Borger, Walter and Eliza Hall Institute)

Similar to the binding experiments performed in chapter 4, binding experiments on the Leg glycoside (**5.66**) was performed in order to determine the specificity of the monoclonal antibody 1E8 developed by Tang *et al*. Specifically, these experiments would enable us to determine whether the 1E8 antibody had exclusive specificity for Pse analogues or whether it bound to other nonulosonic acids such as Leg.

The binding experiments of Leg glycoside (**5.66**) to the 1E8 antibody was determined in an identical manner to that of section 4.8. The SPR binding data is shown in the sensorgram below, in which increasing concentrations of **5.66** were injected over the immobilised 1E8 antibody to generate association and dissociation curves (Figure 5.28).

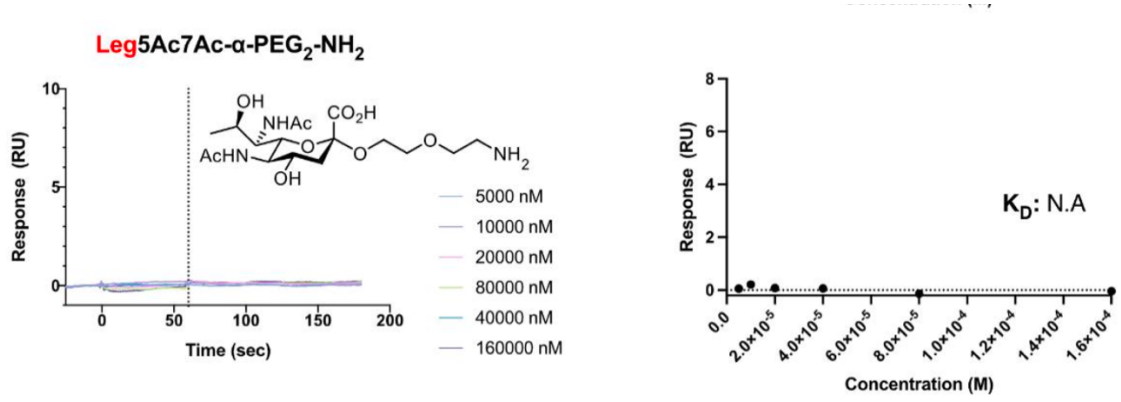


Figure 5.28. Sensorgram (left) show binding responses across a concentration series for legionaminic acid glycoside (**5.66**).

In contrast to the Pse derivatives that exhibited dissociation constants in the nanomolar range, the Leg glycoside (**5.66**) did not show any measurable binding with 1E8. Across the whole concentration series (5 μM to 160 μM), the sensorgram remained flat with no increase in response units observed above the background level. Consequently, no binding curve could be fitted, and no dissociation constant was determined. This lack of interaction indicated that 1E8 does not cross-react with the closely related nonulosonic

acid legionaminic acid, highlighting the antibody's exquisite selectivity for pseudaminic acids.

5.7 Conclusions and Future Work

This chapter described the successful synthesis of a Leg glycoside. This allowed for screening against a recently developed Pse monoclonal antibody, which pleasingly exhibited no observable binding to the synthesised Leg glycoside, illustrating the high specificity of the antibody for pseudaminic acid over other nonulosonic acids. Future work will involve the use of the Leg glycoside for the generation of Leg-specific mAbs. Specifically, conjugation of the Leg glycoside to KLH, an immunogenic carrier protein will serve as an immunogen for immunization of an animal for raising Leg-antibodies. The free amine on the linker will first be reacted with Traut's reagent (2-iminothiolane hydrochloride) to afford a free thiol group. This would allow for conjugation to maleimide-activated KLH, in which maleimide groups are covalently introduced onto lysine side chains using a NHS-maleimide crosslinker. The use of a thiol would allow for a Michael-type 1,4-conjugate addition with the maleimide, in which the thiol acts as a soft nucleophile and attacks the electron-deficient β-carbon of the maleimide double bond. The thiol and maleimide can react under mild aqueous conditions to form stable thioether bonds, which would yield a multivalent Leg–KLH glycoconjugate suitable for immunisation (Figure 5.29).

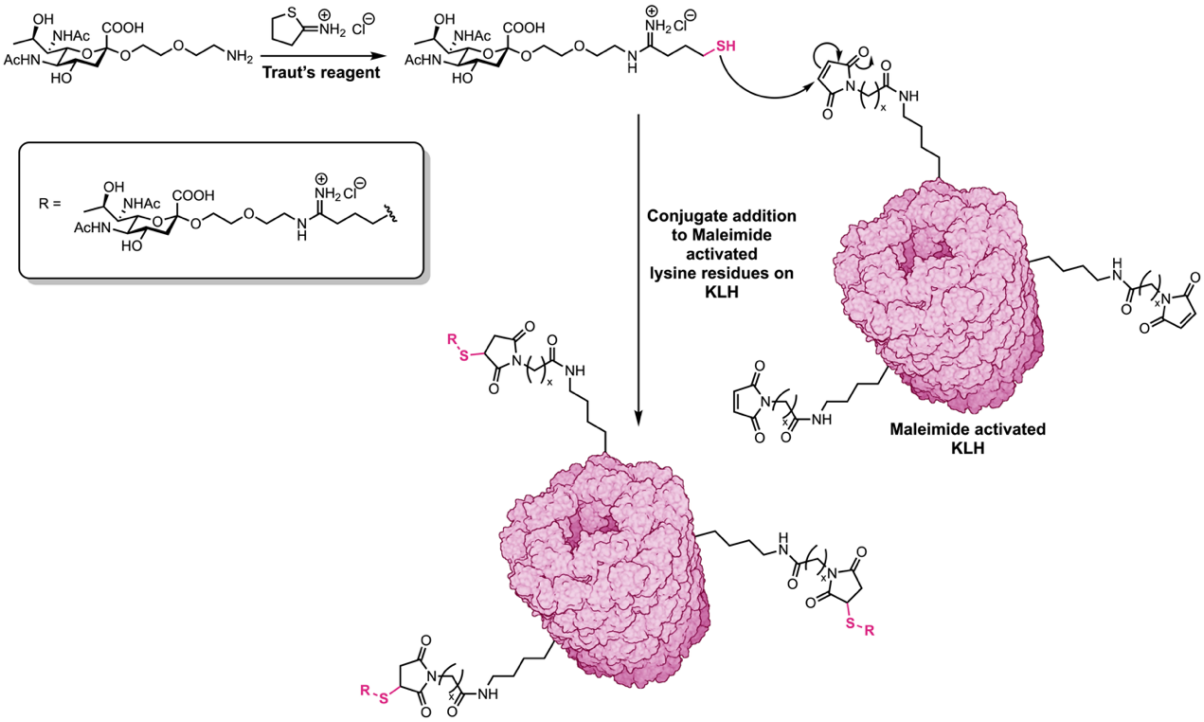


Figure 5.29. Proposed conversion of α-PEG2-NH2-Leg5Ac7Ac to a thiol, and subsequent conjugation *via* Michael addition to maleimide activated KLH, resulting in a multivalent Leg-KLH glycoconjugate.

Chapter 6: Experimental

6.1 General Experimental Materials

6.1.1 Solution-Phase Chemistry Materials

All solution-phase reactions were performed in glassware that had been dried by heating *in vacuo* and placed under a nitrogen atmosphere, unless otherwise specified. All reagents and solvents were used as received unless otherwise noted. Anhydrous MeOH, THF, DMF, MeCN, and CH_2Cl_2 were obtained using the PureSolv® solvent purification system, and subsequent drying over 4Å molecular sieves.

Unless otherwise stated, reactions were carried out under an atmosphere of dry nitrogen or argon and at room temperature (25 °C). Reactions undertaken at -78 °C utilised a bath of dry ice and acetone. Reactions carried out at 0 °C employed a bath of water and ice. Reactions carried out at above room temperature utilised a magnetic stirrer with heating and a multi-well heating mantle for direct heating of the reaction flask.

The reactions were stirred magnetically and monitored *via* analytical thin-layer chromatography (TLC) using commercially available aluminium-backed silica plates (Merck Silica Gel 60F-254) or liquid chromatography-mass spectrometry (LC-MS). The visualisation of TLC plates was executed with an ultraviolet lamp (λ = 254 nm) or stained with solutions of potassium permanganate, ninhydrin, vanillin, phosphomolybdic acid, sulfuric acid, and developed with heat. Purification by flash column chromatography was performed using 230–400 mesh Kieselgel 60 silica eluting with gradients as specified.

6.1.2 Solid-Phase Chemistry Materials

Peptide grade *N*,*N*-dimethylformamide (DMF) for peptide synthesis was purchased from RCI Labscan. Wash grade DMF was purchased from Ajax. Gradient grade acetonitrile (MeCN) for chromatography was purchased from Sigma Aldrich and ultrapure water (Type 1) was obtained from a Merck Millipore Direct-Q 5 Water Purification System. Standard Fmoc-protected amino acids (Fmoc-Xaa-OH), coupling reagents, and resins were purchased from Mimotopes or Novabiochem. Fmoc-SPPS was performed *via* automated synthesis on a Syro I peptide synthesiser (Biotage). Desalting was conducted

in reverse-phase C18 Supelco cartridges (Discovery® DSC-18 SPE Tube) purchased from Merck. Manual SPPS was conducted in polypropylene syringes with Teflon filters (Torviq). All other reagents were purchased from Sigma Aldrich, AK Scientific or Merck and used as received.

6.2 General Experimental Methods

6.2.1 Nuclear Magnetic Resonance Spectroscopy

^{1}H NMR, ^{13}C NMR and 2D NMR spectra were recorded at 300 K using a Bruker DRX600, DRX500, DRX400 or DRX300 spectrometer. Chemical shifts are reported in parts per million (ppm) and are referenced to solvent residual signals: DMSO-d_6 δ 2.50 [^{1}H] and δ 39.52 [^{13}C], CD_3CN δ 1.94 [^{1}H] and δ 1.32 [^{13}C], $CDCl_3$ δ 7.26 [^{1}H] and δ 77.16 [^{13}C], MeOD-d_4 δ 3.31 [^{1}H] and δ 49.00 [^{13}C], D_2O δ 4.79 [^{1}H]. ^{1}H NMR data is reported as chemical shift in parts per million (ppm). The data are reported as chemical shift, multiplicity (s = singlet, d = doublet, t = triplet, q = quartet, quin. = quintet, dd = doublet of doublets, dt = doublet of triplets, dq = doublet of quartets, tt = triplet of triplets, td = triplet of doublets, qd = quartet of doublets, ddd = doublet of doublet of doublets, ddt = doublet of doublet of triplets, m = multiplet, br = broad, app. = apparent), coupling constant (*J* Hz), relative integral, and assignment where possible.

6.2.2 Mass Spectrometry

High resolution electrospray ionisation (ESI) (+/-) mass spectra were measured on a Bruker–Daltonics Apex Ultra 7.0T Fourier transform mass spectroscopy (FT) or on a Waters Micromass Q-Tof Premier mass spectrometer. Low resolution ESI(+/-) mass spectra were obtained on a Shimadzu 2020 ESI mass spectrometer operating in positive/negative ion mode. Analytical UPLC-MS was performed on a Shimadzu UPLC-MS system consisting of a LC-M20A pump and a SPD-M30A diode array detector coupled to a Shimadzu 2020 mass spectrometer (ESI) operating in positive and/or negative mode. Separations on the UPLC-MS system were performed using a Waters Acquity UPLC BEH C18 1.7 µm 130 Å (2.1 x 50 mm) column at a total flow rate of 0.60 mL/min. Separations were performed using a mobile phase of 0.1% formic acid in water (Solvent C) and 0.1% formic acid in MeCN (Solvent D).

6.2.3 Infrared (IR) Absorption Spectrometry

Infrared (IR) absorption spectra were recorded on a Bruker ALPHA Spectrometer with Attenuated Total Reflection (ATR) capability or on a Shimadzu IRAffinity-1 spectrometer. IR absorption frequencies are reported in wavenumbers (cm^{-1}). Characteristic peaks corresponding to key functional groups in each compound were selected as representative signals.

6.2.4 Optical Rotation

Optical rotations were recorded at ambient temperature (298K) on a Perkin–Elmer 341 polarimeter at 589 nm (sodium D line) with a cell path length of 1 dm. Specific rotations $[\alpha]^{25}_{D}$ are reported in units of deg cm^2 g^{-1}.

6.2.5 Preparative Reversed-Phase HPLC

Preparative and semi-preparative reversed-phase high performance liquid chromatography (HPLC) was performed using a Waters 600 Multisolvent Delivery System and pump with Waters 486 Tuneable absorbance detector operating at 210-300 nm. Preparative purification of peptides used a Waters X-Bridge® C18 reversed-phase column (OBD™, 5 µm, 30 × 150 mm) at a flow rate of 38 mL min^{-1} or a Waters X-Bridge® C18 OBDTM Column (OBD™, 5 µm, 10 × 250 mm) at a flow rate of 14 mL min^{-1}. Semi-preparative purification of peptides using a Waters X-Bridge® C18 OBD™, Semi-Prep Column (5 µm, 10 × 250 mm) at a flow rate of 5 mL min^{-1}. Separations were performed using a mobile phase of 0.1% TFA in water (Solvent A) and 0.1% TFA in MeCN (Solvent B), or 0.1% formic in water (Solvent C) and 0.1% formic acid in MeCN (Solvent D) and a linear gradient as specified.

6.2.6 Preparative Reversed-Phase Mass-Directed HPLC

Preparative and semi-preparative reversed-phase mass-directed high performance liquid chromatography (HPLC) was performed using a Shimadzu LC-20AP binary preparative pump system equipped with a Shimadzu SPD-M20A photodiode array detector (operating at 210–300 nm) and a Shimadzu LCMS-2020 single quadrupole mass

detector for mass-triggered fraction collection. Preparative purification of peptides used a Waters XBridge® C18 OBD™ reversed-phase column (5 µm, 30 × 150 mm) at a flow rate of 38 mL min^{-1} or a Waters XBridge® C18 OBD™ column (5 µm, 10 × 250 mm) at a flow rate of 14 mL min^{-1}. Semi-preparative purification of peptides used a Waters XBridge® C18 OBD™ semi-prep column (5 µm, 10 × 250 mm) at a flow rate of 5 mL min^{-1}. Separations were performed using a mobile phase of 0.1% trifluoroacetic acid (TFA) in water (Solvent A) and 0.1% TFA in acetonitrile (Solvent B), or 0.1% formic acid in water (Solvent C) and 0.1% formic acid in acetonitrile (Solvent D), and a linear gradient as specified.

6.2.7 Analytical Reversed-Phase HPLC

Analytical UPLC-MS was performed on a Waters Alliance e2695 HPLC system equipped with a 2998 PDA detector (λ = 210–400 nm). Separations were performed on a Waters XBridge® Peptide BEH300 5 µm, 4.6 × 250 mm (C18) column at 40 °C with a flow rate of 1.0 mL min^{-1}. Separations were performed using a mobile phase of 0.1% formic acid in water (Solvent C) and 0.1% formic acid in MeCN (Solvent D) using linear gradients, unless otherwise specified. Analytical RP-HPLC traces were processed using GraphPad Prism where 0 min refers to the start of the gradient. Peptide were reported as pure where UPLC analysis identified the product as having >95% purity.

6.3 General Solution Phase Procedures

6.3.1 *N*-nitrosylation of piperidinylmethanols

The desired piperidinylmethanol was dissolved in water to a concentration of 0.2 M. To the stirring solution was added a pre-mixed solution of $NaNO_2$ (4 eq) in an equivalent volume of water to provide a final concentration of 0.1 M. Acetic acid (3 eq) was added dropwise and the solution was stirred at room temperature under a nitrogen atmosphere for 24 h. The solution was basified to pH 9 with solid K_2CO_3 and the aqueous layer was extracted three times with EtOAc. The organic phase was dried over Na_2SO_4 and concentrated *in vacuo*. The crude product was purified by flash column chromatography (0-10% MeOH:CH_2Cl_2) to provide the desired *N*-nitrosylated piperidinylmethanol product.

6.3.2 Reduction and Boc protection on *N*-nitrosylated piperidinylmethanols

To a flask containing the desired *N*-nitrosylated piperidinylmethanol isomer was added zinc powder (3 eq) and 4 M HCl (4 eq). This reaction was allowed to stir for five minutes, before TLC indicated complete consumption of starting material. The mixture was filtered through a celite pad soaked in water and washed through with water. To the filtered solution was added $NaHCO_3$ (10 eq) to make a saturated solution. Di-*tert*-butyl decarbonate (Boc_2O) (10 eq) in THF (THF:water, final v/v 1:10) was added to the saturated solution. The reaction mixture was left to stir at rt for 48 h. Upon completion, the layers were separated, and the aqueous layer extracted three times with EtOAc. The combined THF layer and EtOAc were combined, washed with water, dried over Na_2SO_4, and concentrated *in vacuo*. The crude product was purified by flash column chromatography (3:7:90 NH_3:MeOH:CH_2Cl_2) to provide the desired *tert*-butyl ((hydroxymethyl)piperidinyl)carbamate product.

6.3.3 Acrylation of *tert*-butyl ((hydroxymethyl)piperidinyl)carbamates

The desired *tert*-butyl ((hydroxymethyl)piperidinyl)carbamate isomer was dissolved in CH_2Cl_2 to a concentration of 0.4 M. *Tert*-butyl acrylate (5 eq) and tetra-*n*-butylammonium bromide (TBAB) (0.2 eq) were added to the solution, followed by dropwise addition of

10 M NaOH (5 eq). The reaction was stirred at room temperature under a nitrogen atmosphere for 3 h. Upon completion, the mixture was quenched with water (H_2O:CH_2Cl_2, 1:1 v/v) and the aqueous phase was extracted three times with CH_2Cl_2. The combined organic layers were washed with brine, dried over Na_2SO_4, concentrated *in vacuo*, and co-evaporated three times with toluene. The crude product was purified by flash column chromatography (0-10% MeOH:CH_2Cl_2) to provide the desired *tert*-butyl 3-((1-((*tert*-butoxycarbonyl)amino)piperidinyl)methoxy)propanoate product.

6.3.4 Simultaneous *N*-Boc and *tert*-butyl ester deprotection

The desired *tert*-butyl 3-((1-((*tert*-butoxycarbonyl)amino)piperidinyl)methoxy) propanoate product was dissolved in a 95:5 v/v mixture of TFA:H_2O to a final concentration of 1.0 M. The mixture was allowed to stir at room temperature for 3 h. Upon completion, the crude mixture was concentrated in vacuo and azeotroped three times with toluene to remove any residual TFA. The desired product was provided as TFA salt and used directly in the next step.

6.3.5 Amide Couplings with Rimonabant-NHS ester

Rimonabant-NHS ester (**2.34**) was added to a solution of hydrazine TFA salt (1 eq), as prepared by general procedure 6.3.4, and *i*Pr_2NEt (4 eq) in dry DMF to a final concentration of 0.3 M. The reaction was stirred at rt for 2 h. The mixture was concentrated *in vacuo* and LC-MS revealed a mixture of product and an impurity with +96 mass on top of product. The residue was submitted to *t*BuOH:1M aq NaOH (1:1 v/v) at 60 °C for 1 h, which resulted in hydrolysis of the impurity to the desired product. The mixture was taken up in brine and MeCN, and the organic layer was separated. The aqueous layer was extracted a further two times with MeCN, then the combined organic layers were dried over $MgSO_4$, concentrated, and purified by C18 flash chromatography (0 to 65% MeCN in H_2O, 0.1% TFA), over 15 column volumes. The relevant fractions were combined and evaporated to dryness affording the product as a white foam as the di-TFA salt. The two TFA anions were inferred from ^{1}H and ^{19}F NMR with trifluoroethanol internal standard.

6.3.6 Benzyloxycarbonyl/ azide hydrogenolysis

To the benzyloxycarbonyl protected amine or azide in MeOH (final concentration 0.01 M) was added catalytic Pd/C (10 wt%). The system was placed under a hydrogen atmosphere using a triple layer balloon and hydrogenolysed for 2 h. The solution was filtered through a celite pad saturated with MeOH to remove the Pd and the filtrate was concentrated to dryness. The crude product was used in subsequent reactions without any further purification.

6.3.7 Amide coupling of tri-GalNAc to PEG linkers

To a solution of N_3-PEG-acid (1.1 eq) or Cbz-PEG-acid (1.1 eq) in dry DMF (final concentration 0.03 M) was added HATU (1.1 eq) followed by NMM (2.5 eq). The solution was stirred for 5 min followed by the addition of tri-GalNAc amine (**2.48**) (1 eq), prepared from **2.47** according to general procedure 6.3.6. The mixture was stirred for 1 h at rt and then loaded directly onto a preequilibrated C18 flash column and eluted with 0 for 5 CV then 0 to 60% MeCN in H_2O over 15 CV (0.1% formic acid). The pure fractions (LC-MS) were concentrated under reduced pressure to afford the desired amide.

6.3.8 Deacetylation of tri-GalNAc conjugates

To a solution of the tri-GalNac conjugate in MeOH (final concentration 0.2 M) was added NaOH (1 eq), and the mixture was stirred for 2 h at rt. The mixture was neutralised with amberlite IRC 120 H^+ resin, filtered, and concentrated to dryness to afford the desired deacetylated product.

6.3.9 Amide coupling of tri-GalNAc-linker moiety to isomeric rimonabant structures

To a solution of the respective carboxylic acid bis(Tfa) salt (1.1 eq) in DMF was added HATU (1.15 eq), followed by NMM (6 eq), and the mixture was stirred for 1 min before addition of the amine (1.0 eq). The mixture was stirred at rt for 1 h, after which LC-MS indicated completion. The reaction mixture was loaded directly onto a pre-equilibrated C13 flash column and the product was eluted (0 to 65% MeCN in H_2O, 0.1% TFA), over 15

column volumes. The relevant fractions were combined and evaporated to dryness to afford the desired product.

6.3.10 Preparation of α-MeO-Pse N7 variants

Triester **4.175** (2.0 mg, 3.71 mmol, 1 equiv.) was dissolved in THF/H_2O (1:1 v/v, 0.5 mL). LiOH (1.8 mg, 20 equiv.) was added, and the reaction was stirred at 40 °C for 16 h. Upon completion, as determined by LC-MS, the mixture was cooled to rt and concentrated under a stream of nitrogen to remove THF. The remaining mixture was diluted with water, neutralised with acetic acid, and lyophilised.

The crude material was taken up in THF/H_2O (1:1 v/v, 0.5 mL) and treated with either *N*-acetoxysuccinimide (**4.180**), *N*-formyloxysuccinimide (**4.181**), or *N*-(*R*-3-hydroxybutyryloxy)succinimide (**4.182**) (5 eq) followed by Et_3N (2.6 µL, 10 eq) and stirred at rt for 3 h. Upon completion, as determined by LC-MS, the mixture was concentrated, diluted with H_2O, and neutralised with acetic acid. The crude material was desalted by reverse phase HPLC [Waters X-Bridge BEH C18 120 Å, semi prep; 0% B for 10 min to 20% B over 10 min; A = 0.1% formic acid in H_2O, B = 0.1% formic acid in MeCN, elution ~ 10 min (LC-MS)]. The desalted material was lyophilised and re-dissolved in MeOH/MeCN (1:4 v/v, ~0.3 mL). This solution was further purified on an Atlantis HILIC silica column [95% B for 5 min to 50% B over 45 min, solutions A and B identical to those above, elution ~ 30 min (LC-MS)].

6.4 General Peptide Synthesis Procedures

6.4.1 Automated Solid-Phase Peptide Synthesis at 40 °C

Rink amide resin in a polypropylene vessels was treated with 40 vol.% piperidine in DMF (800 µL) for 4 min, drained, then treated with 20 vol.% piperidine in DMF (800 µL) for 4 min, drained, and washed with DMF (4 × 1.2 mL). The resin was then treated with a solution of Fmoc-Xaa-OH (200 µmol, 4 eq) and Oxyma® (220 µmol, 4.4 eq.) in DMF (400 µL), a 1 wt.% solution of 1,3-diisopropyl-2-thiourea in DMF (400 µL), followed by a solution of DIC (200 µmol, 4.4 eq.) in DMF (400 µL). Coupling reactions were conducted at 40 °C for 30 min with intermittent shaking. The resin was then drained and washed with DMF (4 × 1.2 mL) before being treated with a solution of 5 vol.% Ac_2O and 10 vol.% iPr_2NEt in DMF (800 µL) for 6 min at room temperature, drained and washed with DMF (4 × 1.2 mL). These steps were repeated until the desired peptide sequence was obtained.

6.4.2 Automated Solid-Phase Peptide Synthesis at 75 °C

Rink amide resin in polypropylene vessels was treated with 40 vol.% piperidine in DMF (800 µL) for 4 min, drained, then treated with 20 vol.% piperidine in DMF (800 µL) for 4 min, drained, and washed with DMF (4 × 1.2 mL). The resin was then treated with a solution of Fmoc-Xaa-OH (200 µmol, 4 eq) and Oxyma® (220 µmol, 4.4 eq.) in DMF (400 µL), a 1 wt.% solution of 1,3-diisopropyl-2-thiourea in DMF (400 µL), followed by a solution of DIC (200 µmol, 4.4 eq) in DMF (400 µL). Coupling reactions were conducted at 75 °C for 15 min with intermittent shaking. For Fmoc-Cys(Trt)-OH and Fmoc-His(Trt)-OH, coupling reactions were conducted at 50 °C for 30 min. The resin was then drained and washed with DMF (4 × 1.2 mL) before being treated with a solution of 5 vol.% Ac_2O and 10 vol.% *i*Pr_2NEt in DMF (800 µL) for 6 min at room temperature, drained and washed with DMF (4 × 1.2 mL). These steps were repeated until the desired peptide sequence was obtained.

6.4.3 Modified Automated SPPS for Coupling Chloroacetic Acid

Rink amide resin in polypropylene vessels was treated with 40 vol.% piperidine in DMF (800 µL) for 4 min, drained, then treated with 20 vol.% piperidine in DMF (800 µL) for 4

min, drained, and washed with DMF (4 × 1.2 mL). The resin was then treated with a solution of chloroacetic acid (200 µmol, 4 eq) and Oxyma® (220 µmol, 4.4 eq.) in DMF (400 µL), a 1 wt.% solution of 1,3-diisopropyl-2-thiourea in DMF (400 µL), followed by a solution of DIC (200 µmol, 4.4 eq) in DMF (400 µL). The coupling was conducted at 75 °C for 15 min with intermittent shaking. The resin was then drained and washed with DMF (4 × 1.2 mL).

6.4.4 Modified Automated SPPS for Coupling Speciality Amino Acids

Rink amide resin in polypropylene vessels was treated with 40 vol.% piperidine in DMF (800 µL) for 4 min, drained, then treated with 20 vol.% piperidine in DMF (800 µL) for 4 min, drained, and washed with DMF (4 × 1.2 mL). The resin was then treated with a solution of Fmoc-Xaa-OH (100 µmol, 2 eq.) and Oxyma® (110 µmol, 2.2 eq.) in DMF (400 µL), a 1 wt.% solution of 1,3-diisopropyl-2- thiourea in DMF (400 µL), followed by a solution of DIC (200 µmol, 2.2 eq.) in DMF (400 µL). Coupling reactions were conducted at 40 °C for 30 min with intermittent shaking. The resin was then drained and washed with DMF (4 × 1.2 mL) before being treated with a solution of 5 vol.% Ac_2O and 10 vol.% *i*Pr_2NEt in DMF (800 µL) for 6 min at room temperature, drained and washed with DMF (4 × 1.2 mL).

6.4.5 Manual SPPS for Coupling Fmoc-Ser(β-GalNAc(OAc)$_3$)-OH

The peptide on Rink amide resin was treated with 20 vol.% piperidine in DMF (2 x 5 mL) for 5 min, filtered, then washed with DMF (5 × 5 mL), CH_2Cl_2 (5 × 5 mL) and DMF (5 × 5 mL). The resin was then treated with a solution of Fmoc-Ser(β-GalNAc(OAc)$_3$)-OH (**2.99**) (1.2 eq), HATU (1.1 eq), HOBt (1.2 eq) and 2,4,6-trimethylpyridine (1.5 eq) in DMF (0.1 M with respect to resin loading) and shaken at room temperature for 2 h. The resin was drained and washed with DMF (5 × 5 mL), CH_2Cl_2 (5 × 5 mL) and DMF (5 × 5 mL).

6.4.6 Manual SPPS for Coupling Chloroacetic Acid

The peptide on Rink amide resin was prepared up until residue prior to incorporation of speciality amino acid according to general procedure **6.4.2** or **6.4.5**. The resin was treated with 20 vol.% piperidine in DMF (2 x 5 mL) for 5 min, filtered, then washed with

DMF (5 × 5 mL), CH_2Cl_2 (5 × 5 mL) and DMF (5 × 5 mL). The resin was then treated with a solution of chloroacetic acid (3 eq), Oxyma® (4 eq) and DIC (3.5 eq) in DMF (0.1 M with respect to resin loading) and shaken at room temperature for 2 h. The resin was drained and washed with DMF (5 × 5 mL) and CH_2Cl_2 (5 × 5 mL).

6.4.7 Simultaneous Resin Cleavage and Global Side Chain Deprotection

To the resin-bound peptide was added a solution of TFA/*i*Pr_3SiH/H_2O (95:2.5:2.5 v/v/v) and the resin shaken at rt for 2 h. The cleavage solution was collected and diluted with diethyl ether (35 mL) to precipitate the peptide. The resulted suspension was centrifuged at 4 °C twice and the supernatant was discarded.

6.4.8 Cyclisation of Chloroacetyl-Cysteinyl Peptides A

The crude peptide (50 µmol) was dissolved in 5 vol.% *i*Pr_2NEt in DMSO. The peptide solution stirred at rt until the cyclisation was complete as judged by UPLC-MS analysis.

6.4.9 Cyclisation of Chloroacetyl-Cysteinyl Peptides B

The crude peptide (50 µmol) was dissolved in 5 vol.% *i*Pr_2NEt in 1:1 v/v MeCN/H_2O. The peptide solution was stirred at rt until the cyclisation was complete as judged by UPLC-MS analysis, at which point it was quenched with formic acid to take the pH to ~4. The peptide solution was lyophilised to produce crude peptide.

6.4.10 Neopentyl deprotection in ligation buffer

Following cyclisation in DMSO with 3 vol.% *i*Pr_2NEt and purification (General Procedure 6.4.8) by preparative RP-HPLC, purified cyclised material was dissolved in buffer (6 M Gdn.HCl, 1 M HEPES, pH 7.5). The reaction was stirred vigorously at 50 °C for 16 h until judged complete *via* LC-MS.

6.4.11 Deacetylation of GalNAc incorporated peptides

The lyophilised peptide (50 µmol) was dissolved in MeOH, and NaOH was added until the pH was ~10. The peptide solution was stirred at rt until the deacetylation was complete

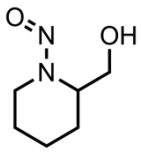
as judged by UPLC-MS analysis, at which point it was quenched with formic acid to take the pH to ~4. The MeOH was removed *via* evaporation.

6.5 Experimental Data for Chapter 2

6.5.1 Synthesis of Modified Rimonabant Scaffolds

N.B. *N*-nitrosyl amines have two configurational isomers (*cis* and *trans*) in equilibrium, resulting in distinguishable peaks in NMR.[415]

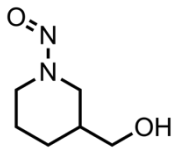
(2.18): (1-nitrosopiperidin-2-yl)methanol



2.18 was prepared according to general procedure **6.3.1** on a 20.0 g scale to provide **2.18** as a yellow oil (11.5 g, 46%). NMR data is reported for the major isomer (2.8:1 mixture of isomers).

IR (thin film): 3375 (O-H stretch), 1427 (N=O stretch), 1363 (N=O symmetric stretch) cm^{-1}; **^{1}H NMR** (500 MHz, MeOD) δ 4.40 (dt_{app}, *J* = 14.0, 4.7 Hz, 1H), 4.01 (dd, *J* = 11.7, 8.2 Hz, 1H), 3.80 (dd, *J* = 11.6, 5.8 Hz, 1H), 3.60 (qd_{app}, *J* = 11.2, 7.0 Hz, 1H), 3.26 (ddd, *J* = 14.2, 10.5, 3.9 Hz, 1H), 1.90 – 1.87 (m, 2H), 1.73 – 1.66 (m, 2H), 1.53 – 1.38 (m, 2H) ppm; **^{13}C NMR** (126 MHz, MeOD) δ 63.0, 61.8, 38.6, 28.3, 25.8, 21.7 ppm; **HRMS** (ESI+) *m/z* Calc. for $C_6H_{12}N_2O_2$ $[M + Na]^+$: 167.0797, found 167.0788.

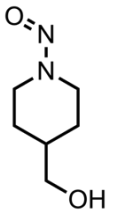
(2.19): (1-nitrosopiperidin-3-yl)methanol



2.19 was prepared according to general procedure **6.3.1** on a 20.0 g scale to provide **2.19** as a yellow oil (11.1 g, 44%). NMR data is reported for both isomers (1:1 mixture of isomers).

IR (thin film): 3389 (O-H stretch), 1421 (N=O stretch), 1352 (N=O symmetric stretch) cm^{-1}; **^{1}H NMR** (500 MHz, MeOD) δ 4.89 (dd, *J* = 13.3, 4.4 Hz, 1H), 4.74 – 4.66 (m, 2H), 4.57 (dt_{app}, *J* = 13.2, 4.0 Hz, 1H), 3.78 (td_{app}, *J* = 12.3, 3.7 Hz, 1H), 3.65 – 3.55 (m, 2H), 3.52 – 3.45 (m, 2H), 3.40 (dd, *J* = 11.1, 7.0 Hz, 1H), 2.86 (ddd, *J* = 14.5, 11.3, 4.0 Hz, 1H), 2.66 (dd, *J* = 13.3, 10.6 Hz, 1H), 1.99 ($dquin._{app}$, *J* = 11.7, 3.9 Hz, 1H), 1.92 – 1.86 (m, 3H), 1.78 (dq_{app}, *J* = 11.9, 3.8 Hz, 1H), 1.68 (dddd, *J* = 15.9, 12.0, 8.1, 4.3 Hz, 1H), 1.59 (dq_{app}, *J* = 10.7, 5.3 Hz, 1H), 1.53 – 1.33 (m, 3H) ppm; **^{13}C NMR** (126 MHz, MeOD) δ 65.1, 64.8, 54.2, 51.8, 43.3, 41.2, 40.8, 39.8, 27.8, 27.7, 26.4, 24.5 ppm; **HRMS** (ESI+) *m/z* Calc. for $C_6H_{12}N_2O_2$ $[M + Na]^+$: 167.0797, found 167.0791.

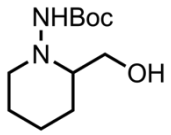
(2.20): (1-nitrosopiperidin-4-yl)methanol



2.20 was prepared according to general procedure **6.3.1** on a 20.0 g scale to provide **2.20** as a yellow oil (6.8 g, 27%).

IR (thin film): 3373 (O-H stretch), 1420 (N=O stretch), 1351 (N=O symmetric stretch) cm^{-1}; **^{1}H NMR** (500 MHz, MeOD) δ 5.03 – 4.95 (m, 1H), 4.70 (dddd, *J* = 13.3, 4.6, 2.7, 1.6 Hz, 1H), 3.77 (dddd, *J* = 13.4, 12.4, 3.6, 1.0 Hz, 1H), 3.45 (d, *J* = 6.3 Hz, 2H), 2.68 (dddd, *J* = 13.7, 12.6, 3.9, 1.0 Hz, 1H), 2.03 (dddd, *J* = 13.3, 6.0, 3.5, 2.3 Hz, 1H), 1.95 – 1.88 (m, 1H), 1.84 (dddd, *J* = 15.7, 6.1, 4.0, 2.5 Hz, 1H), 1.38 (dddd, *J* = 13.3, 12.6, 11.4, 4.8 Hz, 1H), 1.07 (tdd_{app}, *J* = 13.2, 11.6, 4.9 Hz, 1H) ppm; **^{13}C NMR** (126 MHz, MeOD) δ 66.8, 51.0, 40.0, 39.5, 30.3, 28.6 ppm; **HRMS** (ESI+) *m/z* Calc. for $C_6H_{12}N_2O_2$ $[M + Na]^+$: 167.0797, found 167.0791.

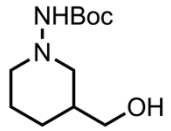
(2.24): *tert*-butyl (2-(hydroxymethyl)piperidin-1-yl)carbamate



2.24 was prepared according to general procedure **6.3.2** from **2.18** on a 20.0 g scale to provide as a white solid (10.3 g, 32%).

mp 135–136 °C; **IR** (thin film): 3420 (O-H stretch), 3263 (N-H stretch), 1692 (C=O carbamate stretch) cm^{-1}; **^{1}H NMR** (500 MHz, MeOD) δ 3.61 (dd, *J* = 11.6, 4.8 Hz, 1H), 3.42 (dd, *J* = 11.6, 2.7 Hz, 1H), 3.03 (dddd, *J* = 10.9, 3.8, 3.6, 1.4 Hz, 1H), 2.56 (ddd, *J* = 10.8, 10.7, 5.1 Hz, 1H), 2.39 – 2.32 (m, 1H), 1.77 – 1.70 (m, 2H), 1.65 – 1.55 (m, 3H), 1.46 (s, 9H), 1.31 – 1.21 (m, 1H) ppm; **^{13}C NMR** (126 MHz, MeOD) δ 158.5, 81.0, 66.9, 64.3, 58.1, 29.2, 28.7, 26.4, 24.6 ppm; **HRMS** (ESI+) *m/z* Calc. for $C_{11}H_{22}N_2O_3$ $[M + Na]^+$: 253.1528, found 253.1523.

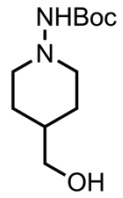
(2.25) *tert*-butyl (3-(hydroxymethyl)piperidin-1-yl)carbamate



2.25 was prepared according to general procedure **6.3.2** from **2.19** on a 20.0 g scale to provide **2.25** as a white solid (9.0 g, 28%).

mp 137–138 °C; **IR** (thin film): 3381 (O-H stretch), 3250 (N-H stretch), 1703 (C=O carbamate stretch) cm^{-1}; **^{1}H NMR** (500 MHz, MeOD) δ 3.44 (dd, *J* = 10.9, 5.8 Hz, 1H), 3.37 (dd, *J* = 11.0, 7.2 Hz, 1H), 3.06 (dd, *J* = 10.6, 3.6 Hz, 1H), 2.94 (dd, *J* = 9.7, 4.3 Hz, 1H), 2.43 – 2.31 (m, 1H), 2.17 (t_{app}, *J* = 10.4 Hz, 1H), 1.88 (dqd_{app}, *J* = 9.8, 6.6, 3.0 Hz, 1H), 1.74 – 1.61 (m, 3H), 1.45 (s, 9H), 0.98 – 0.87 (m, 1H) ppm; **^{13}C NMR** (126 MHz, MeOD) δ 155.9, 79.2, 64.6, 59.2, 56.2, 38.7, 27.3, 25.9, 23.9 ppm; **HRMS** (ESI+) *m/z* Calc. for $C_{11}H_{22}N_2O_3$ $[M + Na]^+$: 253.1528, found 253.1523.

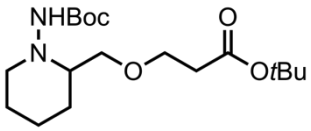
(2.26) *tert*-butyl (4-(hydroxymethyl)piperidin-1-yl)carbamate



2.26 was prepared according to general procedure **6.3.2** from **2.20** on a 17.0 g scale to provide **2.26** as a white solid (6.9 g, 25%).

mp 169–170 °C; **IR** (thin film): 3350 (O-H stretch), 3214 (N-H stretch), 1710 (C=O carbamate stretch) cm^{-1}; **^{1}H NMR** (400 MHz, MeOD) δ 3.40 – 3.37 (m, 2H), 3.01 (ddd, *J* = 11.3, 3.1, 3.1 Hz, 2H), 2.48 – 2.38 (m, 2H), 1.76 – 1.68 (m, 2H), 1.44 (s, 9H), 1.41 – 1.39 (m, 1H), 1.39 – 1.28 (m, 2H) ppm; **^{13}C NMR** (101 MHz, MeOD) δ 157.3, 80.6, 67.6, 56.9, 38.8, 29.4, 28.7 ppm; **HRMS** (ESI+) *m/z* Calc. for $C_{11}H_{22}N_2O_3$ $[M + Na]^+$: 253.1528, found 253.1523.

(2.32) *tert*-butyl 3-((1-((*tert*-butoxycarbonyl)amino)piperidin-2-yl)methoxy) propanoate

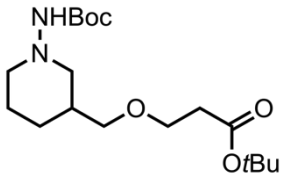


2.32 was prepared according to general procedure **6.3.3** from **2.24** on a 3.00 g scale to provide **2.32** as a colourless oil (3.25 g, 70%).

IR (thin film): 3287 (N-H stretch), 1722 (C=O ester/carbamate stretch) cm^{-1}; **^{1}H NMR** (500 MHz, MeOD) δ 3.62 (t, *J* = 6.2 Hz, 2H), 3.58 (dd, *J* = 9.7, 4.3 Hz, 1H), 3.33 – 3.28 (m, 2H), 3.02 – 2.95 (m, 1H), 2.58 – 2.50 (m, 2H), 2.46 (t, *J* = 6.4 Hz, 2H), 1.87 – 1.77 (m, 1H), 1.72 – 1.66 (m, 1H), 1.63 – 1.56 (m, 1H), 1.45 (s_{app}, 18 H), 1.40 – 1.28 (m, 1H), 1.28 – 1.16 (m, 1H) ppm; **^{13}C NMR** (126 MHz, MeOD) δ 172.9, 157.7, 81.7, 80.5, 74.3, 68.0, 65.1, 58.5, 37.3,

30.3, 28.8, 28.4, 26.4, 24.4 ppm; **HRMS** (ESI+) *m/z* Calc. for $C_{11}H_{22}N_2O_3$ [M + Na]$^+$: 381.2365, found 381.2360.

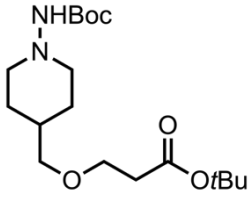
(2.33): *tert*-butyl 3-((1-((*tert*-butoxycarbonyl)amino)piperidin-3-yl)methoxy) propanoate



2.33 was prepared according to general procedure **6.3.3** from **2.25** on a 3.00 g scale to provide **2.33** as a colourless oil (3.50 g, 75%).

IR (thin film): 3286 (N-H stretch), 1720 (C=O ester/carbamate stretch) cm^{-1}; **^{1}H NMR** (500 MHz, MeOD) δ 3.69 – 3.56 (m, 2H), 3.34 (dd, *J* = 9.4, 5.5 Hz, 1H), 3.25 (dd, *J* = 9.4, 7.4 Hz, 1H), 3.05 (ddt, *J* = 10.3, 3.3, 1.5 Hz, 1H), 2.97 – 2.89 (m, 1H), 2.44 (d, *J* = 6.1 Hz, 2H), 2.41 – 2.32 (m, 1H), 2.20 – 2.12 (m, 1H), 2.05 – 1.95 (m, 1H), 1.73 – 1.58 (m, 3H), 1.45 (s, 8H), 1.44 (s, 8H), 0.99 – 0.87 (m, 1H) ppm; **^{13}C NMR** (126 MHz, MeOD) δ 171.6, 155.8, 80.3, 79.2, 73.5, 66.4, 59.5, 56.2, 36.4, 36.0, 27.3, 27.0, 26.1, 23.9 ppm; **HRMS** (ESI+) *m/z* Calc. for $C_{11}H_{22}N_2O_3$ [M + H]$^+$: 359.2546, found 359.2541.

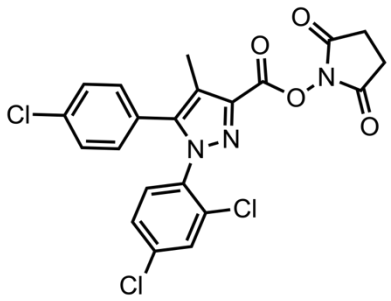
(2.31): *tert*-butyl 3-((1-((*tert*-butoxycarbonyl)amino)piperidin-4-yl)methoxy) propanoate



2.31 was prepared according to general procedure **6.3.3** from **2.26** on a 3.00 g scale to provide **2.31** as a colourless oil (3.75 g, 80%).

IR (thin film): 3276 (N-H stretch), 1721 (C=O ester/carbamate stretch) cm^{-1}; **^{1}H NMR** (500 MHz, MeOD) δ 3.63 (t, *J* = 6.1 Hz, 2H), 3.28 (d_{app}, *J* = 6.6 Hz, 2H), 2.99 (dt_{app}, *J* = 11.0, 3.7 Hz, 2H), 2.44 (t, *J* = 6.1 Hz, 2H), 2.41 (dd, *J* = 10.8, 2.9 Hz, 2H), 1.75 – 1.66 (m, 2H), 1.45 (s, 9H), 1.44 (s, 9H), 1.41 – 1.33 (m, 3H) ppm; **^{13}C NMR** (126 MHz, MeOD) δ 172.9, 157.3, 81.7, 80.6, 76.6, 67.8, 56.8, 37.3, 36.4, 29.7, 28.7, 28.4 ppm; **HRMS** (ESI+) *m/z* Calc. for $C_{11}H_{22}N_2O_3$ $[M + Na]^+$: 381.2365, found 381.2360.

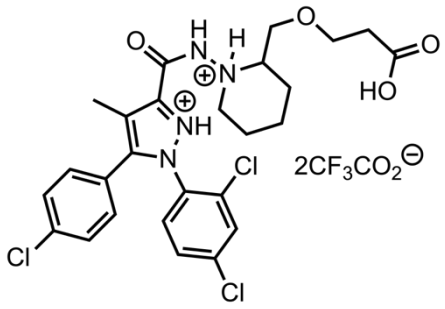
(2.34): Rimonabant *O*-succinimide (Rim-OSu)



To a suspension of rimonabant carboxylic acid (5.0 g, 13 mmol) and *N*-hydroxysuccinimide (1.5 g, 13 mmol) in anhydrous CH_2Cl_2 was added *N*,*N*'-dicyclohexylcarbodiimide (DCC) (2.7 g, 13 mmol), and the resulting mixture was stirred at rt for 16 h. The resulting suspension was filtered, and the filtrate was concentrated *in vacuo* affording the desired rimonabant-NHS ester (**2.23**) as a beige solid (5.5 g, 88%).

mp 226–227 °C; **IR** (thin film): 1802 and 1771 (C=O succinimide symmetric and asymmetric stretch), 1737 (C=O ester stretch), 1606 (C=N pyrazole stretch) cm^{-1}; **^{1}H NMR** (500 MHz, $CDCl_3$) δ 7.39 (d, *J* = 2.2 Hz, 1H), 7.35 (d, *J* = 8.5 Hz, 1H), 7.32 – 7.28 (m, 3H), 7.08 – 7.05 (m, 2H), 2.95 – 2.87 (m, 4H), 2.32 (s, 3H) ppm; **^{13}C NMR** (126 MHz, $CDCl_3$) δ 169.2, 157.8, 143.5, 138.4, 136.6, 135.6, 135.6, 132.9, 131.0, 130.6, 130.4, 129.2, 128.1, 126.5, 121.3, 25.8, 9.6 ppm.

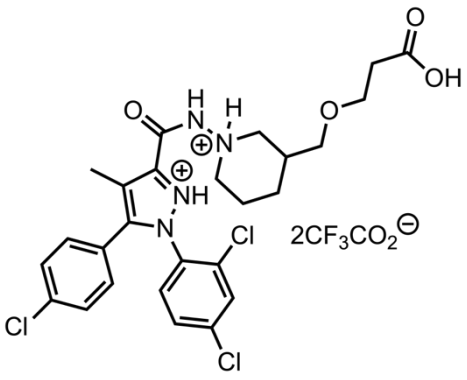
(2.38): 5-(4-Chlorophenyl)-1-[5-(3,4-dichlorophenyl)-4-methylpyrazol-1-yl]carbonyl]-2-[(2-(2-carboxyethoxy)ethyl)amino]piperidine di(trifluoroacetate)



2.38 was prepared according to general procedure **6.3.5** from **2.35** on a 0.84 g scale to provide **2.38** as an amorphous solid (0.26 g, 19%).

^{1}H NMR (400 MHz, MeOD) δ 7.60 – 7.53 (m, 2H), 7.46 (dd, *J* = 8.5, 2.3 Hz, 1H), 7.37 (d, *J* = 8.5 Hz, 2H), 7.21 (d, *J* = 8.5 Hz, 2H), 3.68 (dd, *J* = 10.4, 5.5 Hz, 1H), 3.65 – 3.54 (m, 2H), 3.52 (dd, *J* = 10.4, 4.1 Hz, 1H), 3.41 – 3.32 (m, 1H), 3.11 (ddd, *J* = 12.6, 6.2, 3.7 Hz, 1H), 2.95 (td, *J* = 11.6, 3.2 Hz, 1H), 2.41 (t, *J* = 6.4 Hz, 2H), 2.32 (s, 3H), 1.96 – 1.73 (m, 4H), 1.71 – 1.56 (m, 1H), 1.49 – 1.33 (m, 1H) ppm; **^{13}C NMR** (101 MHz, MeOD) δ 175.1, 162.7, 144.8, 144.5, 137.5, 137.3, 136.3, 134.1, 132.6, 132.5, 131.1, 129.9, 129.3, 128.4, 119.2, 73.5, 67.9, 66.3, 58.7, 35.5, 29.0, 25.4, 23.7, 9.5 ppm; **HRMS** (ESI+) *m/z* Calc. for $C_{26}H_{27}Cl_3N_4O_4$ $[M + H]^+$: 565.1176, found 565.1171.

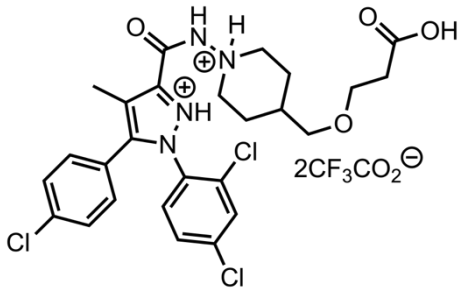
(2.39): 5-(4-Chlorophenyl)-1-[5-(3,4-dichlorophenyl)-4-methylpyrazol-1-yl]carbonyl]-3-[(2-(2-carboxyethoxy)ethyl)amino]piperidine di(trifluoroacetate)



2.39 was prepared according to general procedure **6.3.5** from **2.36** on a 0.96 g scale to provide **2.39** as an amorphous solid (0.47 g, 30%).

^{1}H NMR (400 MHz, MeOD) δ 7.58 (d, *J* = 2.3 Hz, 1H), 7.54 (d, *J* = 8.5 Hz, 1H), 7.46 (dd, *J* = 8.5, 2.2 Hz, 1H), 7.38 (d, *J* = 8.5 Hz, 2H), 7.20 (d, *J* = 8.5 Hz, 2H), 3.75 – 3.64 (m, 2H), 3.49 (dt, *J* = 9.3, 4.7 Hz, 2H), 3.45 – 3.34 (m, 2H), 2.96 (td, *J* = 10.6, 4.8 Hz, 1H), 2.82 (t, *J* = 10.9 Hz, 1H), 2.55 (t, *J* = 6.1 Hz, 2H), 2.33 (s, 3H), 2.28 – 2.18 (m, 1H), 1.91 (dq, *J* = 10.6, 5.3 Hz, 2H), 1.77 (dd, *J* = 13.5, 4.0 Hz, 1H), 1.31 – 1.16 (m, 1H) ppm; **^{13}C NMR** (101 MHz, MeOD) δ 175.4, 162.2, 144.8, 144.1, 137.6, 137.2, 136.4, 134.1, 132.5, 132.4, 131.1, 129.9, 129.3, 128.3, 119.4, 74.3, 67.8, 60.5, 57.7, 36.9, 35.7, 26.5, 24.3, 9.4 ppm; **HRMS** (ESI+) *m/z* Calc. for $C_{26}H_{27}Cl_3N_4O_4$ $[M + H]^+$: 565.1176, found 565.1171.

(2.40): 5-(4-Chlorophenyl)-1-[5-(3,4-dichlorophenyl)-4-methylpyrazol-1-yl]carbonyl]-4-[(2-(2-carboxyethoxy)ethyl)amino]piperidine di(trifluoroacetate)

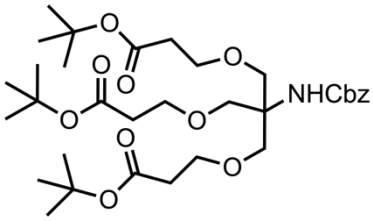


2.40 was prepared according to general procedure **6.3.5** from **2.37** on a 0.83 g scale to provide **2.40** as an amorphous solid (0.37 g, 27%).

^{1}H NMR (400 MHz, MeOD) δ 7.57 (d, *J* = 2.3 Hz, 1H), 7.54 (d, *J* = 8.5 Hz, 1H), 7.46 (dd, *J* = 8.5, 2.2 Hz, 1H), 7.37 (d, *J* = 8.5 Hz, 2H), 7.20 (d, *J* = 8.5 Hz, 2H), 3.70 (t, *J* = 6.1 Hz, 2H), 3.42 (dd, *J* = 11.3, 3.4 Hz, 2H), 3.37 (d, *J* = 6.2 Hz, 2H), 3.01 – 2.90 (m, 2H), 2.54 (t, *J* = 6.1 Hz, 2H), 2.32 (s, 3H), 1.94 – 1.85 (m, 2H), 1.81 – 1.70 (m, 1H), 1.70 – 1.55 (m, 2H) ppm; **^{13}C NMR** (101 MHz, MeOD) δ 175.4, 162.3, 144.8, 144.3, 137.5, 137.2, 136.3, 134.1, 132.5, 132.4, 131.1, 129.9, 129.3, 128.3, 119.3, 75.9, 67.7, 56.8, 35.8, 35.5, 28.6, 9.4 ppm; **HRMS** (ESI+) *m/z* Calc. for $C_{26}H_{27}Cl_3N_4O_4$ $[M + H]^+$: 565.1176, found 565.1171.

6.5.2 Synthesis of tri-GalNAc ASGPR binder

(2.44) (Benzyloxycarbonyl)tris[[2-(tert-butoxycarbonyl)ethoxy]methyl]methylamine

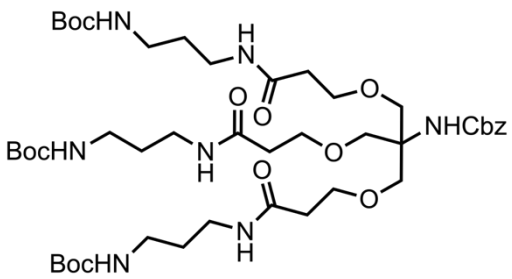


To a solution of tris[[2-(*tert*-butoxycarbonyl)ethoxy]methyl]methylamine (5.0 g, 9.9 mmol) in a 1:1 mixture of CH_2Cl_2:sat. aq $NaHCO_3$ (100 mL) at 0 °C was added benzyl chloroformate (CbzCl) (2.8 mL, 20 mmol, 2 eq) dropwise. Following the addition, the mixture was allowed to warm to rt and stirred for 24 h. Upon completion, the mixture was diluted with CH_2Cl_2 and the organic layer was collected. The aqueous layer was extracted a further two times with CH_2Cl_2, and the combined organic layers were washed with brine, dried over $MgSO_4$, and the solvent was removed under reduced pressure. The crude material was purified by silica gel flash chromatography (0-50% EtOAc:hexanes) to afford the **2.44** as a viscous oil (4.0 g, 64%).

^{1}H NMR (300 MHz, $CDCl_3$) δ 7.37 – 7.28 (m, 5H), 5.03 (s, 2H), 3.66 (s, 6H), 3.63 (t, *J* = 6.4 Hz, 6H), 2.43 (t, *J* = 6.4 Hz, 6H), 1.43 (s, 27H) ppm.

This is in agreement with the spectral data reported by Destecroix *et al.*[416]

(2.46): (Benzyloxycarbonyl)tris[[2-[N-(tert-butoxycarbonyl)-3-aminopropanoyl] ethoxy]methyl]methylamine

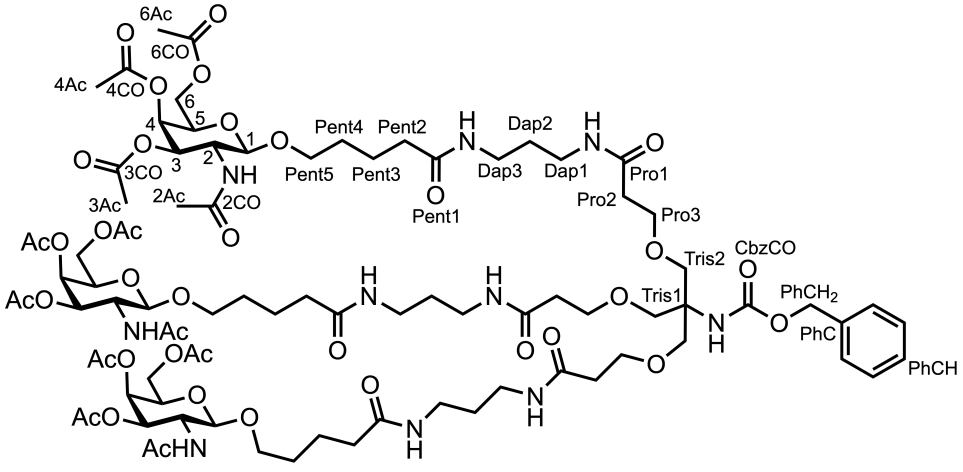


2.44 (3.8 g, 5.9 mmol) was dissolved in a 95:5 v/v mixture of TFA:H_2O (50 mL) and stirred at rt for 2 hours. Upon completion, determined by LC-MS, the mixture was concentrated under a stream of nitrogen and then co-evaproated three times with toluene. The crude acid was dissolved in dry DMF (30 mL) and then treated with HATU (6.78 g, 17.8 mmol, 3 eq) followed by NMM (3.92 mL, 35.6 mmol, 6 eq). The mixture was stirred at rt for five minutes before adding *N*-Boc-1,3-propanediamine (3.11 mL, 17.8 mmol, 3 eq). The mixture was stirred at room temperature for 1 h. Upon completion, determined by LC-MS, the mixture was concentrated under vacuum. The crude mixture was purified by silica gel flash chromatography (0-10% MeOH:CH_2Cl_2) to afford the product **2.46** as an off-white solid (3.20 g, 57%).

^{1}H NMR (500 MHz, DMSO-d6) δ 7.79 (t, *J* = 5.7 Hz, 3H), 7.39 – 7.26 (m, 5H), 6.72 (t, *J* = 5.8 Hz, 3H), 4.49 (s, 1H), 4.98 (s, 2H), 3.55 (t, *J* = 6.4 Hz, 6H), 3.48 (s, 6H), 3.03 (q_{app}, *J* = 6.6 Hz, 6H), 2.91 (q_{app}, *J* = 6.6 Hz, 6H), 2.27 (t, *J* = 6.4 Hz, 6H), 1.49 (quin.$_{app}$, *J* = 7.0 Hz, 6H), 1.36 (s, 27H) ppm.

This is in agreement with the spectral data reported by Prakash *et al.*[417]

(2.47): Benzyloxycarbonyltris{[2-[3-[5-(((2R,3R,4R,5R,6R)-3-acetamido-4,5-diacetoxy-6-(acetoxymethyl)tetrahydro-2H-pyran-2-yl)oxy)pentanoyl]amino] propanoyl]ethoxy}methyl}methylamine



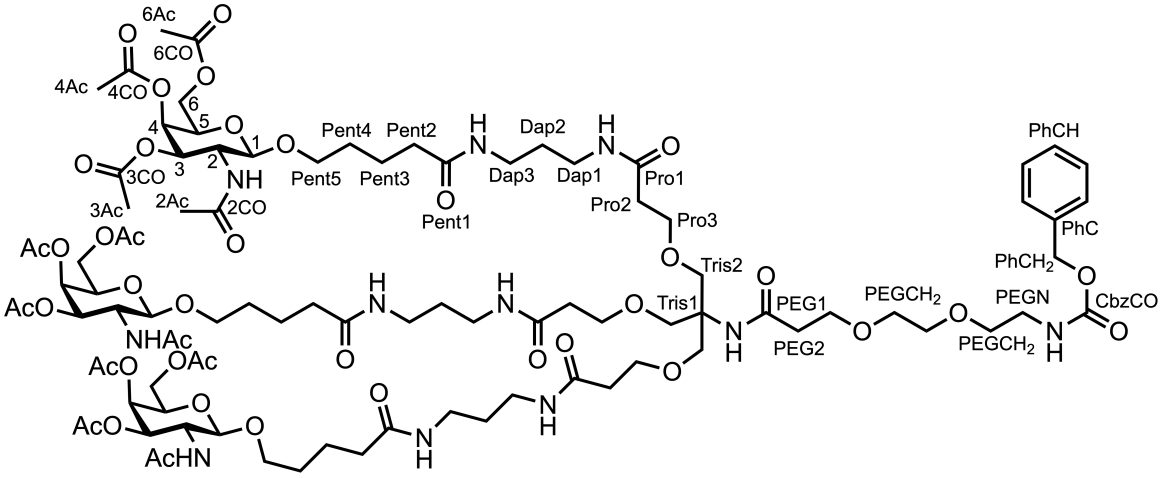
2.46 was dissolved in a 95:5 v/v mixture of TFA:H_2O to a final concentration of 1.0 M. The mixture was allowed to stir at room temperature for 3 h. Upon completion, the crude mixture was concentrated *in vacuo* and co-evaporated with toluene three times to remove any residual TFA. The desired product was provided as TFA salt and used directly in the next step. To a mixture of 5-(((2*R*,3*R*,4*R*,5*R*,6*R*)-3-Acetamido-4,5-diacetoxy-6-(acetoxymethyl)tetrahydro-2H-pyran-2-yl)oxy)pentanoic acid (0.30 g, 0.67 mmol, 3.15 eq) and NMM (0.15 mL, 1.35 mmol, 6.3 eq) in anhydrous DMF (2.5 mL) was added HATU (0.26 g, 0.67 mmol, 3.15 eq), and the mixture was stirred for 2 min before adding this solution to the triamine. More NMM (0.07 mL, 0.64 mmol, 3 eq) was added, and the mixture was stirred for 2h at rt, then concentrated to dryness under a stream of nitrogen. The material was too polar for phase extraction, so the crude mixture was loaded directly on to a silica gel flash column and eluted with 0 to 20% MeOH in CH_2Cl_2. Concentration of the relevant fractions and drying under high vacuum afforded the product (**2.47**) as a pale-yellow foam (352 mg, 85%).

$[\alpha]^{25}_D$ -12.4 (*c* 10, MeOH); **^{1}H NMR** (400 MHz, MeOD) δ 7.38 – 7.25 (m, 5H, 5xPhCH), 5.33 (dd, $J_{4,3}$ = 3.3 Hz, $J_{4,5}$ = 1.1 Hz, 3H, H-4), 5.06 (dd, $J_{3,2}$ = 11.2 Hz, $J_{3,4}$ = 3.4 Hz, 3H, H-3), 5.03 (s, 2H, $PhCH_2$), 4.56 (d, $J_{1,2}$ = 8.4 Hz, 3H, H-1), 4.20 – 4.09 (m, 6H, H-6), 4.08 (dd, $J_{2,3}$ = 11.3 Hz, $J_{2,1}$ = 8.4 Hz, 6H, H-2), 4.01 (td, $J_{5,6}$ = 6.6 Hz, $J_{5,4}$ = 1.2 Hz, 3H, H-5), 3.86 (dt, *J* = 9.6, 5.8 Hz, 3H, Pent5'), 3.66 (t, *J* = 6.0 Hz, 6H, Pro3), 3.63 (s, 6H, Tris2), 3.52 (dt, *J* = 9.7, 6.1 Hz, 3H, Pent5''), 3.26 – 3.15 (m, 12H, Dap1, Dap3', Dap3''), 2.41 (t, *J* = 6.0 Hz, 6H, Pro2', Pro2''), 2.19 (t, *J* = 7.3 Hz, 6H, Pent2), 2.14 (s, 9H, 4Ac), 2.02 (s, 9H, 6Ac), 1.95 (s, 9H, 3Ac), 1.93 (s, 9H, 2Ac), 1.72 – 1.62 (m, 12H, Pent3, Dap2), 1.62 – 1.52 (m, 6H, Pent4) ppm; **^{13}C NMR** (101 MHz, MeOD) δ 176.0 (Pent1), 174.0 (Pro1), 173.6 (2CO), 172.1 (4CO, 6CO), 171.7 (3CO), 164.4 (CbzCO), 138.4 (PhC), 129.5 (2xPhCH), 129.0 (PhCH), 128.9 (2xPhCH), 102.7 (C-1), 72.2 (C-3), 71.8 (C-5), 70.4 (Pent5, Tris2), 68.7 (Pro3), 68.2 (C-4), 67.1 (PhCH2), 62.7 (C-6), 60.4 (Tris1), 51.7 (C-2), 38.0 (Dap3), 37.9 (Dap1), 37.8 (Pro2), 36.7 (Pent2), 30.4 (Dap2), 30.1 (Pent4), 23.7 (Pent3), 22.9 (2Ac), 20.6 (6Ac), 20.6 (3Ac, 4Ac) ppm.

This is in agreement with Spiegel and co-workers.[71]

6.5.3 Synthesis of tri-GalNAc linker intermediates

(2.53): Cbz-PEG2-peracetylated tri-GalNAc

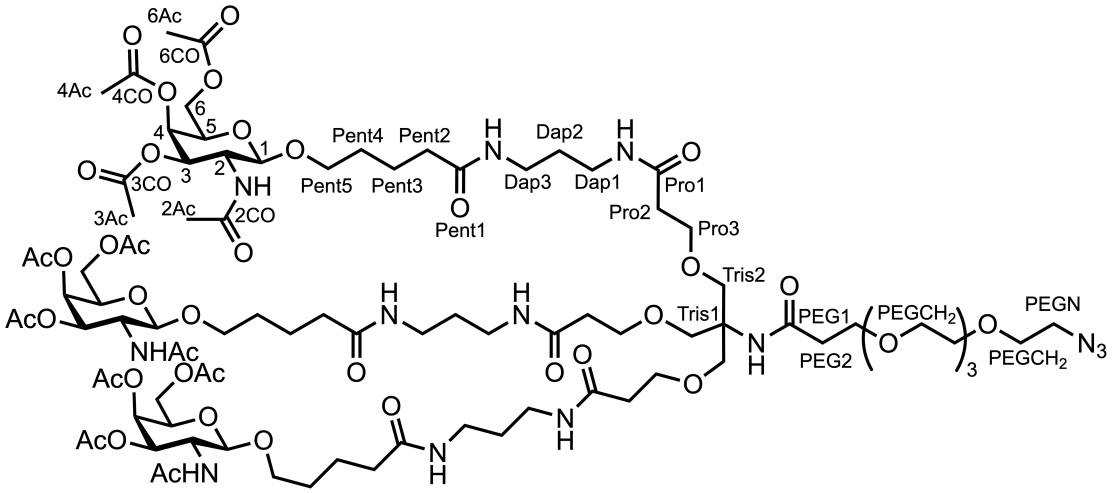


2.53 was prepared according to general procedure **6.3.7** using CbzNH-PEG2-carboxylic acid, with **2.48** (0.37 g, 0.19 mmol) prepared from **2.47** *via* general procedure **6.3.6**, to provide the desired product **2.53** as a colourless amorphous solid (0.28 g, 78%).

IR (thin film): 3293 (N-H stretch), 1746 (C=O ester stretch), 1646 (C=O amide stretch), 1544 (N-H amide bend) cm^{-1}; **^{1}H NMR** (500 MHz, MeOD) δ 7.39 – 7.27 (m, 5H, 5xPhCH), 5.34 (d, $J_{4,3}$ = 3.3 Hz, 3H, H-4), 5.08 (s, 2H, $PhCH_2$), 5.07 (dd, $J_{3,2}$ = 11.2 Hz, $J_{3,4}$ = 3.4 Hz, 3H, H-3), 4.56 (d, $J_{1,2}$ = 8.5 Hz, 3H, H-1), 4.16 (dd, $J_{6',6''}$ = 11.1 Hz, $J_{6',5}$ = 6.8 Hz, 3H, H-6'), 4.13 (dd, $J_{6'',6'}$ = 11.2 Hz, $J_{6'',5}$ 4.9 Hz, 3H, H-6''), 4.08 (dd, $J_{2,3}$ = 11.4 Hz, $J_{2,1}$ = 8.6 Hz, 3H, H-2), 4.01 (t_{app}, $J_{5,6'}$ = 6.6 Hz, $J_{5,6''}$ = 6.6 Hz, 3H, H-5), 3.87 (dt, J = 9.7, 5.9 Hz, 3H, Pent5'), 3.71 – 3.65 (m, 14H, Tris2, Pro3, $PEGCH_2$), 3.61 – 3.59 (m, 4H, $PEGCH_2$), 3.55 (d, J = 5.9 Hz, 2H, $PEGCH_2$), 3.54 – 3.49 (m, 3H, Pent5''), 3.31 – 3.29 (m, 2H, PEGN), 3.22 (q, J = 7.0 Hz, 12H, Dap1, Dap3), 2.47 – 2.44 (m, 2H, PEG2), 2.43 – 2.39 (m, 6H, Pro2), 2.21 (t, J = 7.4 Hz, 6H, Pent2), 2.14 (s, 9H, 4Ac), 2.03 (s, 9H, 6Ac), 1.95 (s, 9H, 3Ac), 1.93 (s, 9H, 2Ac), 1.72 – 1.64 (m, 12H, Pent3, Dap2), 1.63 – 1.56 (m, 6H, Pent4) ppm; **^{13}C NMR** (126 MHz, MeOD) δ 176.0 (Pent1), 173.9 (Pro1), 173.6 (2CO), 172.1 (4CO, 6CO), 171.8 (3CO), 158.9 (CbzCO), 129.5 (5xPhCH), 129.0 (PhC), 128.8 (5xPhCH), 102.7 (C-1), 72.2 (C-3), 71.8 (C-5), 71.3 ($PEGCH_2$), 70.9 ($PEGCH_2$), 70.4 (Pent5), 70.2 (Tris2), 68.7 (Pro3), 68.4 ($PEGCH_2$, C-4), 68.2 (C-4), 67.4 ($PhCH_2$), 62.7 (C-6), 61.5 (Tris1), 51.6 (C-2), 41.8 (PEGn), 38.2 (PEG2), 37.9 (Dap3), 37.8 (Dap1, Dap3), 37.7 (Pro2), 36.7 (Pent2), 30.4 (Dap2), 30.1 (Pent4), 23.7

(Pent3), 22.9 (2Ac), 20.6 (3Ac, 4Ac, 6Ac) ppm; **HRMS** (ESI+) *m/z* Calc. for $C_{94}H_{147}N_{11}O_{41}$ $[M + 2Na + 2H]^{2+}$: 1066.9854, found 1066.9801.

(2.54): N_3-PEG4-peracetylated tri-GalNAc

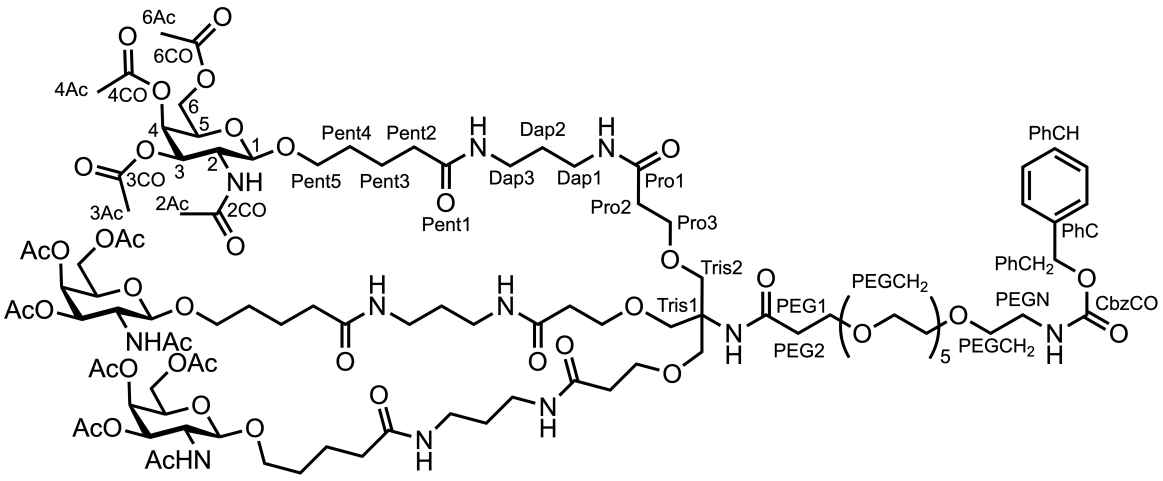


2.54 was prepared according to general procedure 6.3.7 using N_3-PEG4-carboxylic acid, with **2.48** (0.34g, 0.18 mmol) prepared from **2.47** *via* general procedure **6.3.6**, to provide the desired product **2.54** as a colourless amorphous solid (0.33 g, 66%).

IR (thin film): 3292 (N-H stretch), 2106 (N_3 stretch), 1747 (C=O ester stretch), 1647 (C=O amide stretch), 1544 (N-H amide bend) cm^{-1}; **^{1}H NMR** (500 MHz, MeOD) δ 5.34 (dd, $J_{4,3}$ = 3.5 Hz, $J_{4,5}$ = 1.1 Hz, 3H, H-4), 5.06 (dd, $J_{3,2}$ = 11.3 Hz, $J_{3,4}$ = 3.4 Hz, 3H, H-3), 4.56 (d, $J_{1,2}$ = 8.4 Hz, 3H, H-1), 4.14 (dd, $J_{6',6''}$ = 8.6 Hz, $J_{6,5}$ = 6.6 Hz, 6H, H-6), 4.08 (dd, $J_{2,3}$ = 11.3 Hz, $J_{2,1}$ = 8.5 Hz, 3H, H-2), 4.01 (td, $J_{5,6}$ = 6.6 Hz, $J_{5,4}$ 1.2 Hz, 3H, H-5), 3.87 (dt, *J* = 9.8, 5.8 Hz, 3H, Pent5'), 3.70 – 3.61 (m, 28H, Tris2, Pro3, $PEGCH_2$), 3.53 (dt, *J* = 9.8, 6.2 Hz, 3H, Pent5''), 3.38 (t, *J* = 4.9 Hz, 2H, CH_2N_3), 3.25 – 3.19 (m, 12H, Dap1, Dap3). 2.46 – 2.44 (m, 2H, PEG2), 2.44 – 2.41 (m, 6H, Pro2), 2.23 – 2.18 (m, 6H, Pent2), 2.15 (s, 9H, 4Ac), 2.03 (s, 9H, 6Ac), 1.95 (s, 9H, 3Ac), 1.93 (s, 9H, 2Ac), 1.72 – 1.68 (m, 6H, Dap2), 1.68 – 1.65 (m, 6H, Pent3), 1.63 – 1.55 (m, 6H, Pent4) ppm; **^{13}C NMR** (126 MHz, MeOD) δ 176.0 (Pent1), 173.9 (Pro1), 173.9 (PEG1), 173.6 (2CO), 172.1 (4CO, 6CO), 171.7 (3CO), 102.7 (C-1), 72.2 (C-3), 71.8 (C-5), 71.7 ($PEGCH_2$), 71.6 ($PEGCH_2$), 71.6 ($PEGCH_2$), 71.5 ($PEGCH_2$), 71.3 ($PEGCH_2$), 71.1 ($PEGCH_2$), 70.4 (Pent5), 70.2 (Tris2, Pro3), 68.7 ($PEGCH_2$), 68.4 ($PEGCH_2$), 68.2 (C-4), 62.7 (C-6), 61.5 (Tris1), 51.8 (CH_2N_3), 51.6 (C-2), 38.2 (PEG2), 37.9 (Dap3), 37.8

(Dap1), 37.7 (Pro2), 36.8 (Pent2), 30.4 (Dap2), 30.1 (Pent4), 23.7 (Pro3), 22.9 (2Ac), 20.6 (6Ac), 20.6 (3Ac, 4Ac) ppm; **HRMS** (ESI+) *m/z* Calc. for $C_{90}H_{147}N_{13}O_{41}$ $[M + 2Na + 2H]^{2+}$: 1056.9885, found 1056.9831.

(2.55): Cbz-PEG6-peracetylated tri-GalNAc

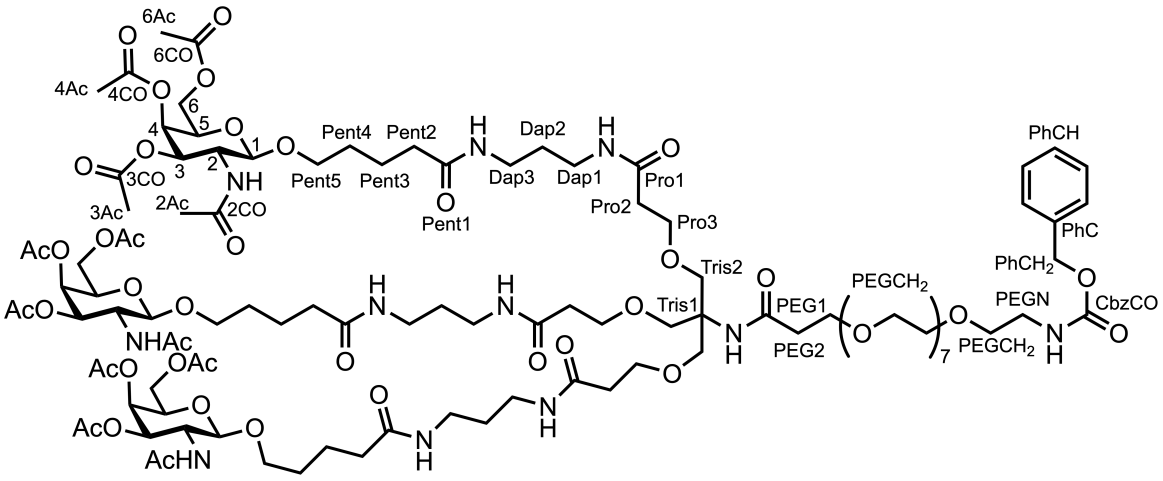


2.55 was prepared according to general procedure 6.3.7 using CbzNH-PEG6-carboxylic acid, with **2.48** (0.60 g, 0.31 mmol) prepared from **2.47** *via* general procedure **6.3.6**,, to provide the desired product **2.55** as a colourless amorphous solid (0.26 g, 73%).

IR (thin film): 3293 (N-H stretch), 1746 (C=O ester stretch), 1647 (C=O amide stretch), 1544 (N-H amide bend) cm^{-1}; **1H NMR** (500 MHz, MeOD) δ 7.41 – 7.24 (m, 5H, 5 x PhCH), 5.34 (dd, $J_{4,3}$ = 3.4 Hz, $J_{4,5}$ = 1.1 Hz, 3H, H-4), 5.08 (s, 2H, $PhCH_2$), 5.06 (dd, J = 11.4, $J_{3,4}$ = 3.3 Hz, 3H, H-3), 4.56 (d, $J_{1,2}$ = 8.4 Hz, 3H, H-1), 4.16 (dd, $J_{6',6''}$ = 11.2 Hz, $J_{6',5}$ = 6.9 Hz, 3H, H-6'), 4.12 (t_{app}, $J_{6'',6'}$ = 5.6 Hz, $J_{6'',5}$ = 5.6 Hz, 3H, H-6''), 4.08 (dd, $J_{2,3}$ = 11.3 Hz, $J_{2,1}$ = 8.5 Hz, 3H, H-2), 4.01 (td_{app}, $J_{5,6'}$ = 6.6 Hz, $J_{5,6''}$ = 6.6 Hz, $J_{5,4}$ = 1.2 Hz, 3H, H-5), 3.87 (dt, J = 9.7, 5.8 Hz, 3H, Pent5'), 3.67 (s, 10H, Pro3, $PEGCH_2$), 3.63 – 3.61 (m, 24H, Tris2, $PEGCH_2$), 3.55 – 3.54 (m, 2H, $PEGCH_2$), 3.53 – 3.50 (m, 3H, Pent5''), 3.30 – 3.29 (m, 2H, PEGn), 3.24 – 3.19 (m, 12H, Dap1, Dap3), 2.46 – 2.44 (m, 2H, PEG2), 2.42 (t, J = 5.6 Hz, 6H, Pro2), 2.23 – 2.19 (m, 6H, Pent2), 2.14 (s, 9H, 4Ac), 2.03 (s, 9H, 6Ac), 1.95 (s, 9H, 3Ac), 1.93 (s, 9H, 2Ac), 1.72 – 1.65 (m, 12H, Pent3, Dap2), 1.62 – 1.57 (m, 6H, Pent4) ppm; **^{13}C NMR** (126 MHz, MeOD) δ 176.0 (Pent1), 173.9 (Pro1), 173.9 (PEG1), 173.6 (2CO), 172.1 (4CO, 6CO), 171.7

(3CO), 158.9 (CbzCO), 129.5 (5xPhCH), 129.0 (PhC), 128.9 (5xPhCH), 102.7 (C-1), 72.2 (C-3), 71.8 (C-5), 71.6 ($PEGCH_2$), 71.5 ($PEGCH_2$), 71.5 ($PEGCH_2$), 71.3 ($PEGCH_2$), 71.3 ($PEGCH_2$), 70.9 ($PEGCH_2$), 70.4 (Pent5), 70.2 (Tris2), 68.7 (Pro3), 68.4 ($PEGCH_2$), 68.2 (C-4), 67.4 ($PhCH_2$), 62.7 (C-6), 61.5 (Tris1), 51.6 (C-2), 41.8 (PEGn), 38.2 (PEG2), 37.9 (Dap3), 37.8 (Dap1), 37.7 (Pro2), 36.8 (Pent2), 30.4 (Dap2), 30.1 (Pent4), 23.7 (Pent3), 22.9 (2Ac), 20.6 (6Ac), 20.6 (3Ac, 4Ac) ppm; **HRMS** (ESI+) *m/z* Calc. for $C_{102}H_{163}N_{11}O_{45}$ $[M + 2Na + 2H]^{2+}$: 1155.0378, found 1155.0323.

(2.56): Cbz-PEG8-peracetylated tri-GalNAc



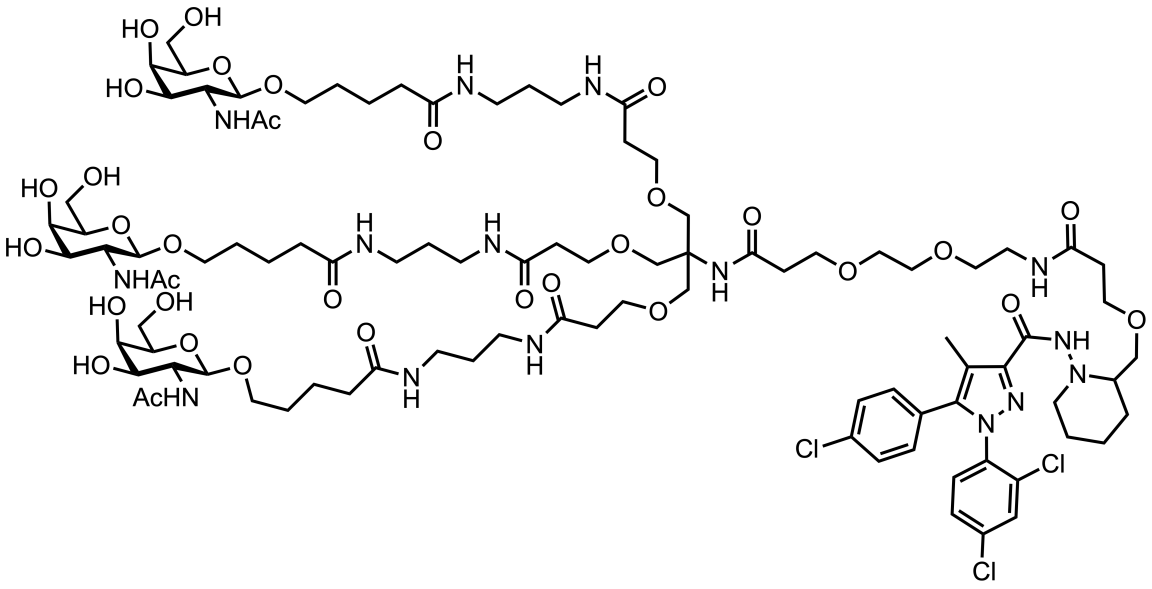
2.56 was prepared according to general procedure 6.3.7 using CbzNH-PEG8-carboxylic acid, with **2.48** (0.60 g, 0.31 mmol) prepared from **2.47** *via* general procedure **6.3.6**,, to provide the desired product **2.56** as a colourless amorphous solid (0.25 g, 70%).

IR (thin film): 3293 (N-H stretch), 1746 (C=O ester stretch), 1646 (C=O amide stretch), 1543 (N-H amide bend) cm^{-1}; **^{1}H NMR** (500 MHz, MeOD) δ 7.40 – 7.25 (m, 5H, 5xPhCH), 5.34 (dd, $J_{4,3}$ = 3.4 Hz, $J_{4,5}$ = 1.1 Hz, 3H, H-4), 5.08 (s, 2H, $PhCH_2$), 5.06 (dd, $J_{3,2}$ = 11.0 Hz, $J_{3,4}$ = 3.4 Hz, 3H, H-3), 4.56 (d, $J_{1,2}$ = 8.4 Hz, 3H, H-1), 4.16 (dd, $J_{6',6''}$ = 11.2 Hz, $J_{6',5}$ = 6.9 Hz, 3H, H-6'), 4.12 (t_{app}, $J_{6'',6'}$ = 5.6 Hz, $J_{6'',5}$ = 5.6 Hz, 3H, H-6''), 4.08 (dd, $J_{2,3}$ = 11.3 Hz, $J_{2,1}$ = 8.5 Hz, 3H, H-2), 4.01 (td, $J_{5,6''}$ = 6.6 Hz, $J_{5,6'}$ = 6.6 Hz, $J_{5,4}$ = 1.2 Hz, 3H, H-5), 3.87 (dt, *J* = 9.7, 5.8 Hz, 3H, Pent5'), 3.70 – 3.66 (m, 12H, Pro3, $PEGCH_2$), 3.64 – 3.62 (m, 12H, Tris2, $PEGCH_2$), 3.62 – 3.58 (m, 16H, $PEGCH_2$), 3.56 – 3.53 (m, 4H, $PEGCH_2$), 3.53 – 3.50 (m, 3H, Pent5''), 3.31 – 3.28 (m, 2H, PEGn), 3.24 – 3.17 (m, 12H, Dap1, Dap3), 2.45 (t, *J* = 6.3 Hz, 2H, PEG2), 2.43 (t, *J* = 6.1 Hz, 6H, Pro2), 2.26 – 2.16 (m, 6H, Pent2), 2.14 (s, 9H, 4Ac), 2.03 (s, 9H,

6Ac), 1.95 (s, 9H, 3Ac), 1.93 (s, 9H, 2Ac), 1.73 – 1.63 (m, 12H, Pent3, Dap2), 1.62 – 1.55 (m, 6H, Pent4) ppm; **^{13}C NMR** (126 MHz, MeOD) δ 176.0 (Pent1), 173.9 (Pro1), 173.9 (PEG1), 173.6 (2CO), 172.1, 171.7, 158.9 (CbzCO), 129.5 (5xPhCH), 129.0 (PhC), 128.9 (5xPhCH), 102.7 (C-1), 72.2 (C-3), 71.8 (C-5), 71.6 ($PEGCH_2$), 71.5 ($PEGCH_2$), 71.5 ($PEGCH_2$), 71.3 ($PEGCH_2$), 70.9 ($PEGCH_2$), 70.4 (Pent5), 70.2 (Tris2), 68.7 (Pro3), 68.4 ($PEGCH_2$), 68.2 (C-4), 67.4 ($PEGCH_2$), 62.7, 61.5, 51.6 (C-2), 41.8 (PEGn), 38.2 (PEG2), 37.9 (Dap3), 37.8 (Dap1), 37.7 (Pro2), 36.8 (Pent2), 30.4 (Dap2), 30.1 (Pent4), 23.7 (Pent3), 22.9 (2Ac), 20.6 (6Ac), 20.6 (3Ac, 4Ac) ppm; **HRMS** (ESI+) *m/z* Calc. for $C_{106}H_{171}N_{11}O_{47}$ $[M + 2Na + 2H]^{2+}$: 1199.0640, found 1199.0588.

6.5.4 Synthesis of final rimonabant-based bifunctional molecules

(2.61): LYTAC-1,2-PEG2

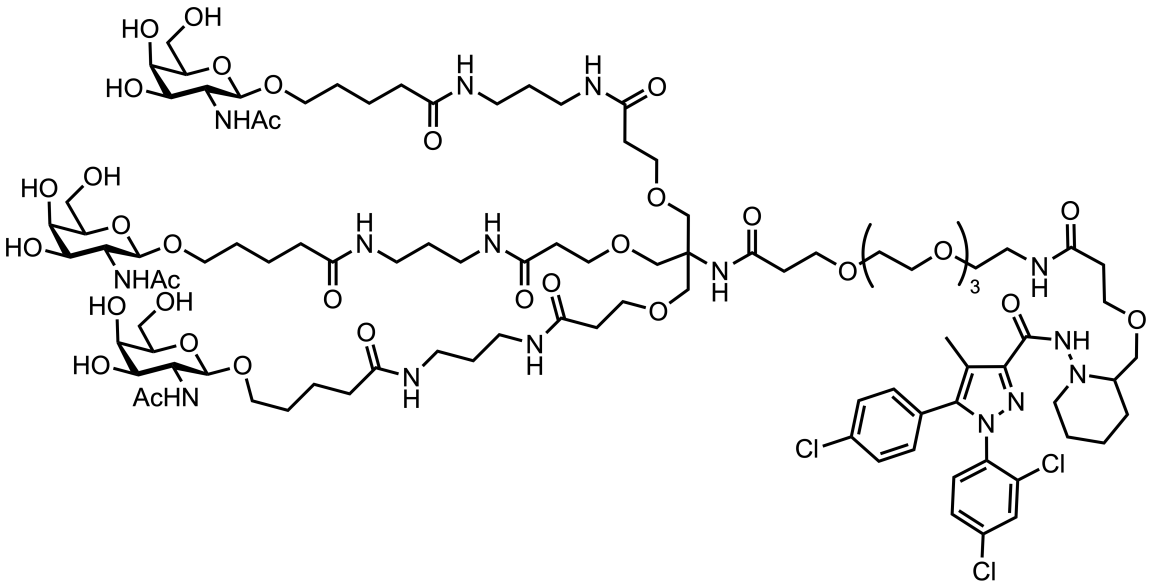


2.61 was prepared in three steps, first through deacetylation and hydrogenolysis of **2.53** according to general procedures **6.3.8** and **6.3.6** respectively, to form free amine **2.57**. Free amine **2.57** (53 mg, 0.03 mmol) was then subjected to amide coupling with **2.38** as outlined in general procedure **6.3.9.** Desired product **2.61** was obtained as a colourless amorphous solid (52 mg, 73%).

HRMS (ESI+) *m/z* Calc. for $C_{94}H_{148}Cl_3N_{15}O_{33}$ $[M + 2H + 2Na]^{2+}$: 1083.9691, found 1083.9611.

NMR data is reported in Table 6.1.

(2.62): LYTAC-1,2-PEG4

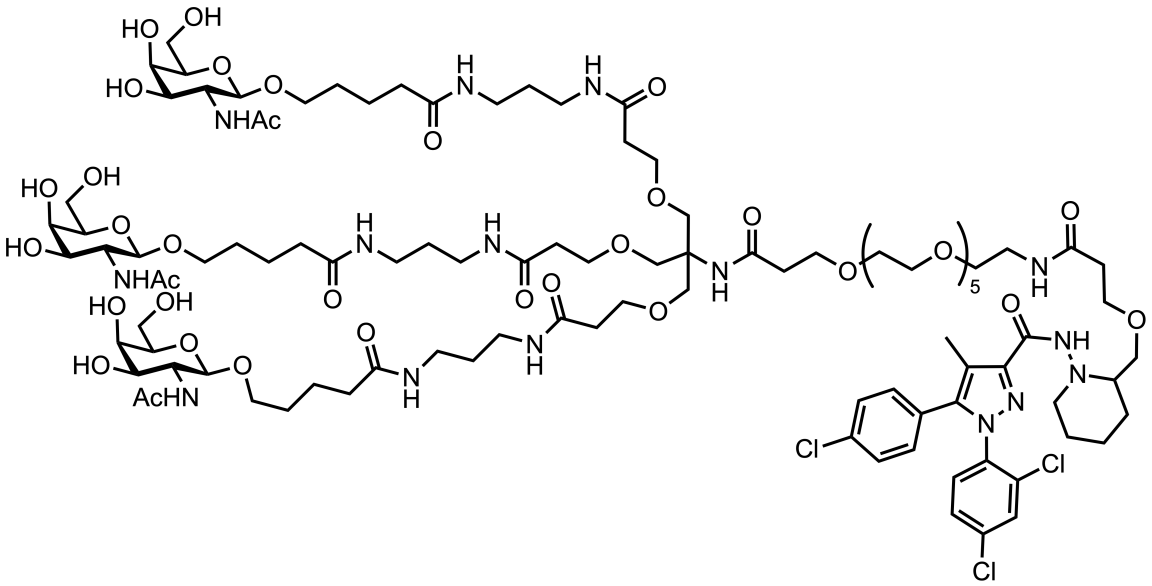


2.62 was prepared in three steps, first through deacetylation and hydrogenolysis of **2.54** according to general procedures **6.3.8** and **6.3.6** respectively, to form free amine **2.58**. Free amine **2.58** (60 mg, 0.04 mmol) was then subjected to amide coupling with **2.38** as outlined in general procedure **6.3.9.** Desired product **2.62** was obtained as a colourless amorphous solid (44 mg, 55%).

HRMS (ESI+) *m/z* Calc. for $C_{98}H_{156}Cl_3N_{15}O_{35}$ $[M + 2H + 2Na]^{2+}$: 1127.9953, found 1127.9874.

NMR data is reported in Table 6.1.

(2.63): LYTAC-1,2-PEG6

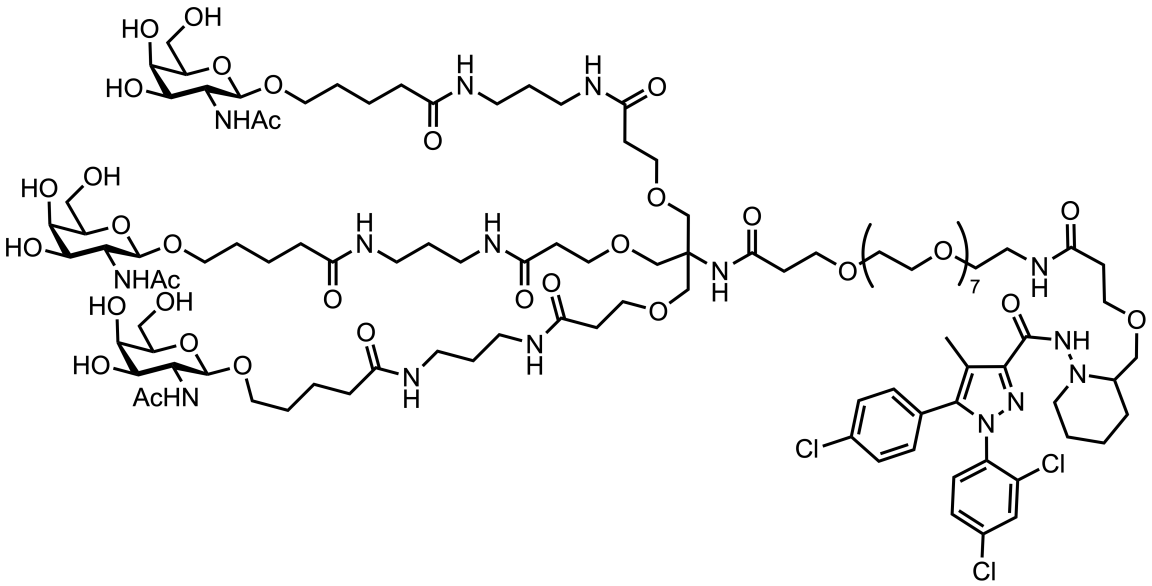


2.63 was prepared in three steps, first through deacetylation and hydrogenolysis of **2.55** according to general procedures **6.3.8** and **6.3.6** respectively, to form free amine **2.59**. Free amine **2.59** (48 mg, 0.03 mmol) was then subjected to amide coupling with **2.38** as outlined in general procedure **6.3.9.** Desired product **2.63** was obtained as a colourless amorphous solid (43 mg, 74%).

HRMS (ESI+) *m/z* Calc. for $C_{102}H_{164}Cl_3N_{15}O_{37}$ $[M + 2H + 2Na]^{2+}$: 1172.0215, found 1172.0134.

NMR data is reported in Table 6.1.

(2.64): LYTAC-1,2-PEG8

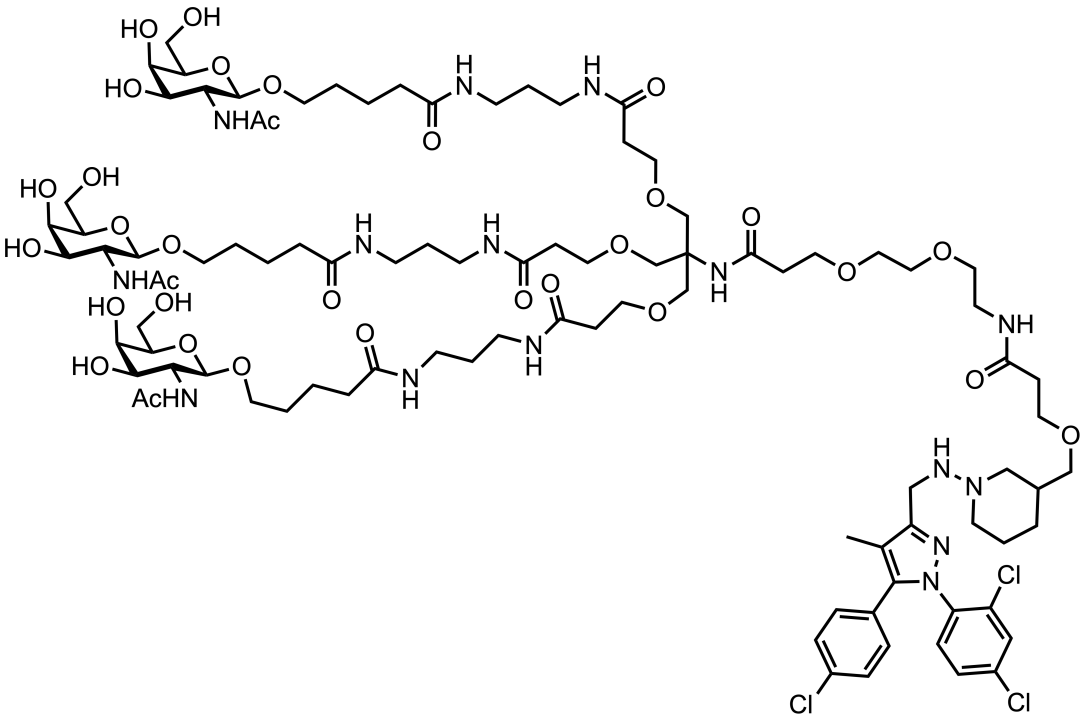


2.64 was prepared in three steps, first through deacetylation and hydrogenolysis of **2.55** according to general procedures **6.3.8** and **6.3.6** respectively, to form free amine **2.59**. Free amine **2.59** (46 mg, 0.03 mmol) was then subjected to amide coupling with **2.38** as outlined in general procedure **6.3.9.** Desired product **2.64** was obtained as a colourless amorphous solid (39 mg, 74%).

HRMS (ESI+) *m/z* Calc. for $C_{106}H_{174}Cl_3N_{15}O_{39}$ $[M + 2H + 2Na]^{2+}$: 1216.0477, found 1216.0400.

NMR data is reported in Table 6.1.

(2.65): LYTAC-1,3-PEG2

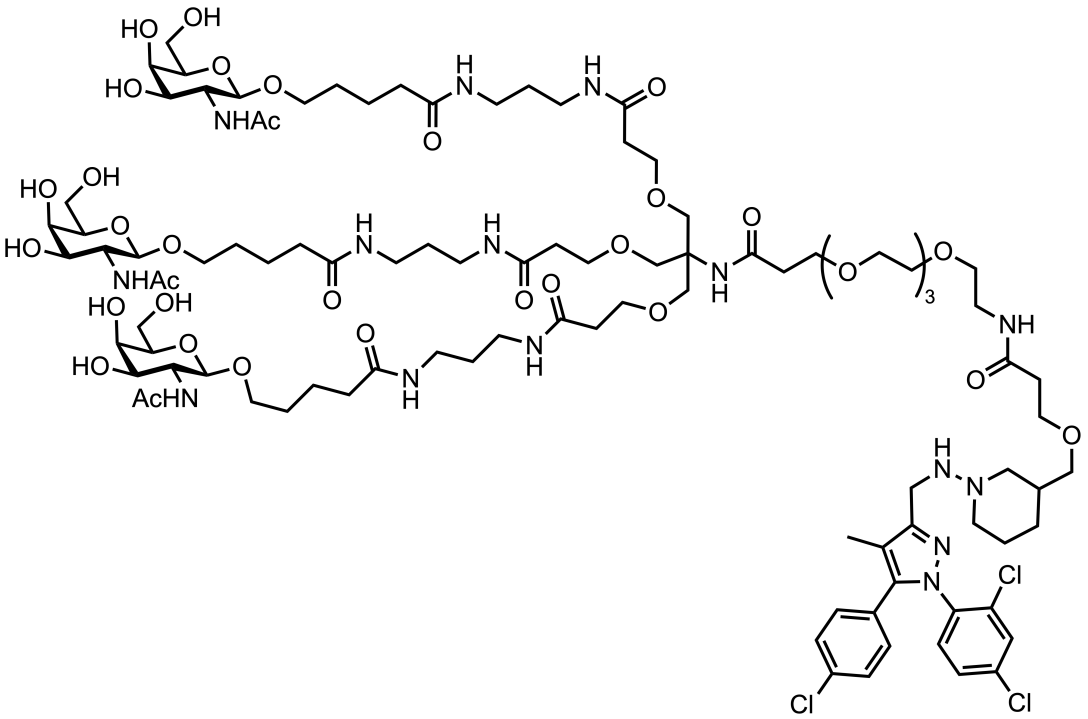


2.65 was prepared in three steps, first through deacetylation and hydrogenolysis of **2.53** according to general procedures **6.3.8** and **6.3.6** respectively, to form free amine **2.57**. Free amine **2.57** (53 mg, 0.03 mmol) was then subjected to amide coupling with **2.39** as outlined in general procedure **6.3.9.** Desired product **2.65** was obtained as a colourless amorphous solid (48 mg, 67%).

HRMS (ESI+) *m/z* Calc. for $C_{94}H_{148}Cl_3N_{15}O_{33}$ $[M + 2H + 2Na]^{2+}$: 1083.9691, found 1083.9611.

NMR data is reported in Table 6.2.

(2.66): LYTAC-1,3-PEG4

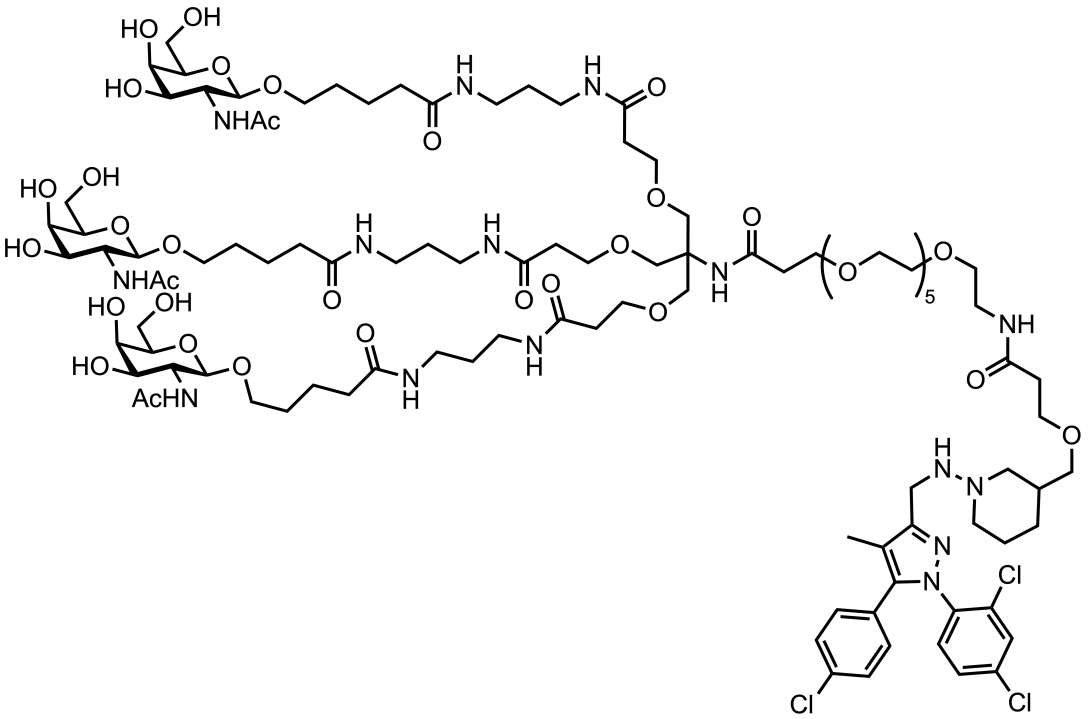


2.66 was prepared in three steps, first through deacetylation and hydrogenolysis of **2.54** according to general procedures **6.3.8** and **6.3.6** respectively, to form free amine **2.58**. Free amine **2.58** (58 mg, 0.4 mmol) was then subjected to amide coupling with **2.39** as outlined in general procedure **6.3.9.** Desired product **2.66** was obtained as a colourless amorphous solid (45 mg, 58%).

HRMS (ESI+) *m/z* Calc. for $C_{98}H_{156}Cl_3N_{15}O_{35}$ $[M + 2H + 2Na]^{2+}$: 1127.9953, found 1127.9874.

NMR data is reported in Table 6.2.

(2.67): LYTAC-1,3-PEG6

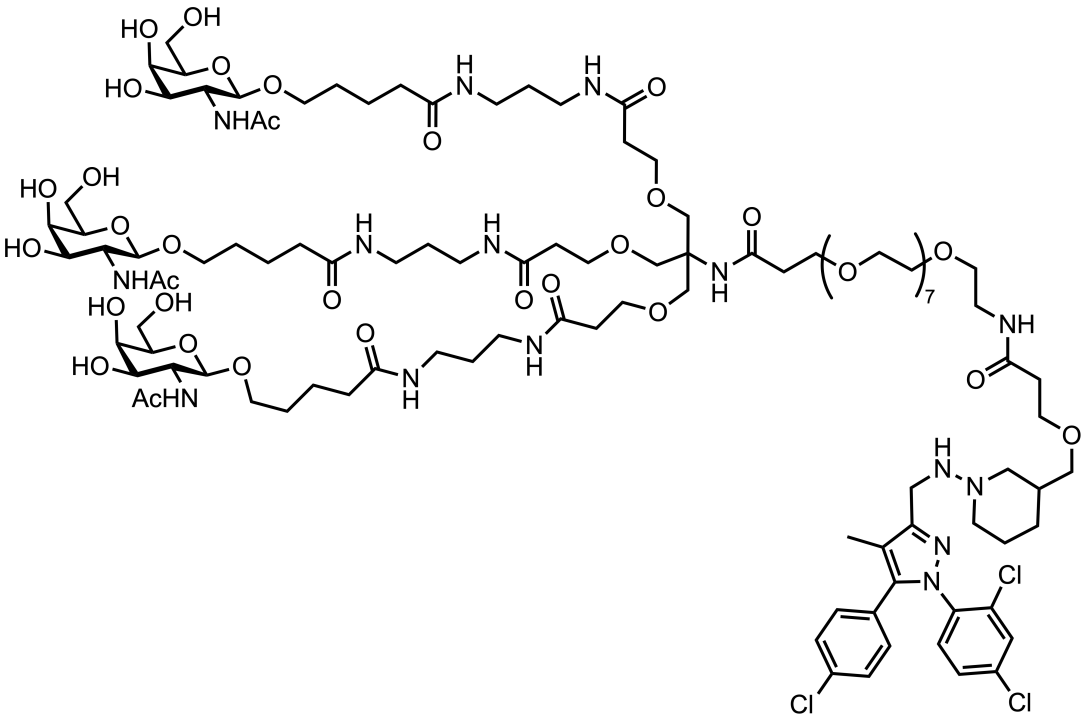


2.67 was prepared in three steps, first through deacetylation and hydrogenolysis of **2.55** according to general procedures **6.3.8** and **6.3.6** respectively, to form free amine **2.59**. Free amine **2.59** (49 mg, 0.03 mmol) was then subjected to amide coupling with **2.39** as outlined in general procedure **6.3.9.** Desired product **2.67** was obtained as a colourless amorphous solid (40 mg, 68%).

HRMS (ESI+) *m/z* Calc. for $C_{102}H_{164}Cl_3N_{15}O_{37}$ $[M + 2H + 2Na]^{2+}$: 1172.0215, found 1172.0134.

NMR data is reported in Table 6.2.

(2.68): LYTAC-1,3-PEG8

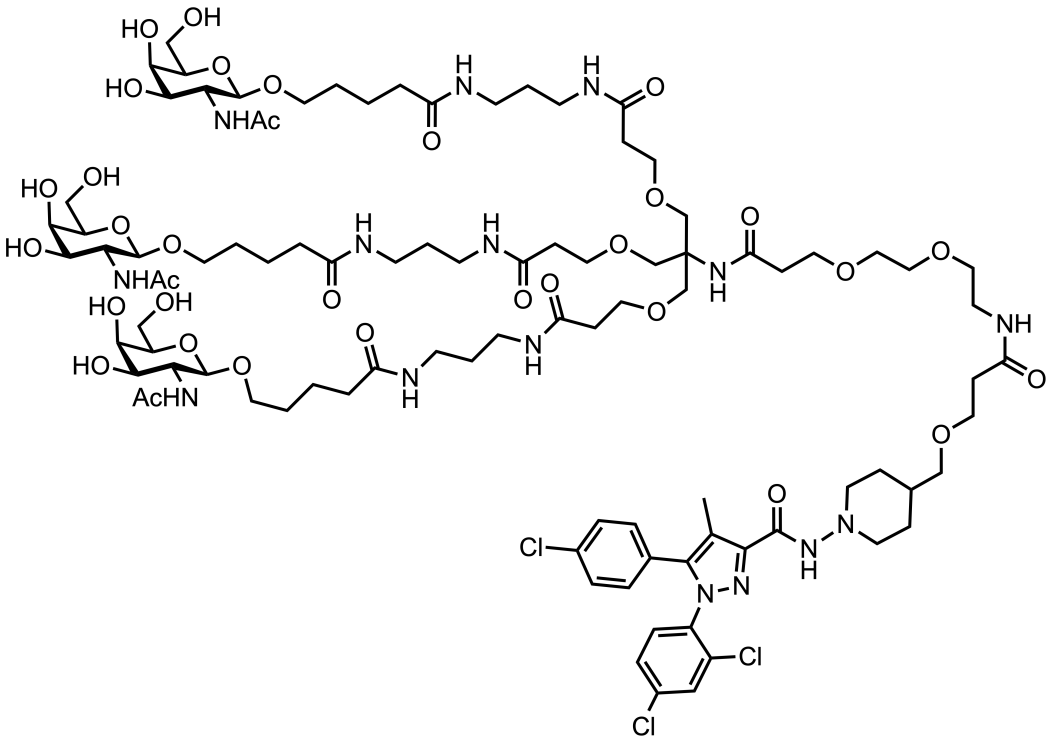


2.68 was prepared in three steps, first through deacetylation and hydrogenolysis of **2.56** according to general procedures **6.3.8** and **6.3.6** respectively, to form free amine **2.60**. Free amine **2.60** (46 mg, 0.03 mmol) was then subjected to amide coupling with **2.39** as outlined in general procedure **6.3.9.** Desired product **2.68** was obtained as a colourless amorphous solid (43 mg, 82%).

HRMS (ESI+) *m/z* Calc. for $C_{106}H_{174}Cl_3N_{15}O_{39}$ $[M + 2H + 2Na]^{2+}$: 1216.0477, found 1216.0400.

NMR data is reported in Table 6.2.

(2.69): LYTAC-1,4-PEG2

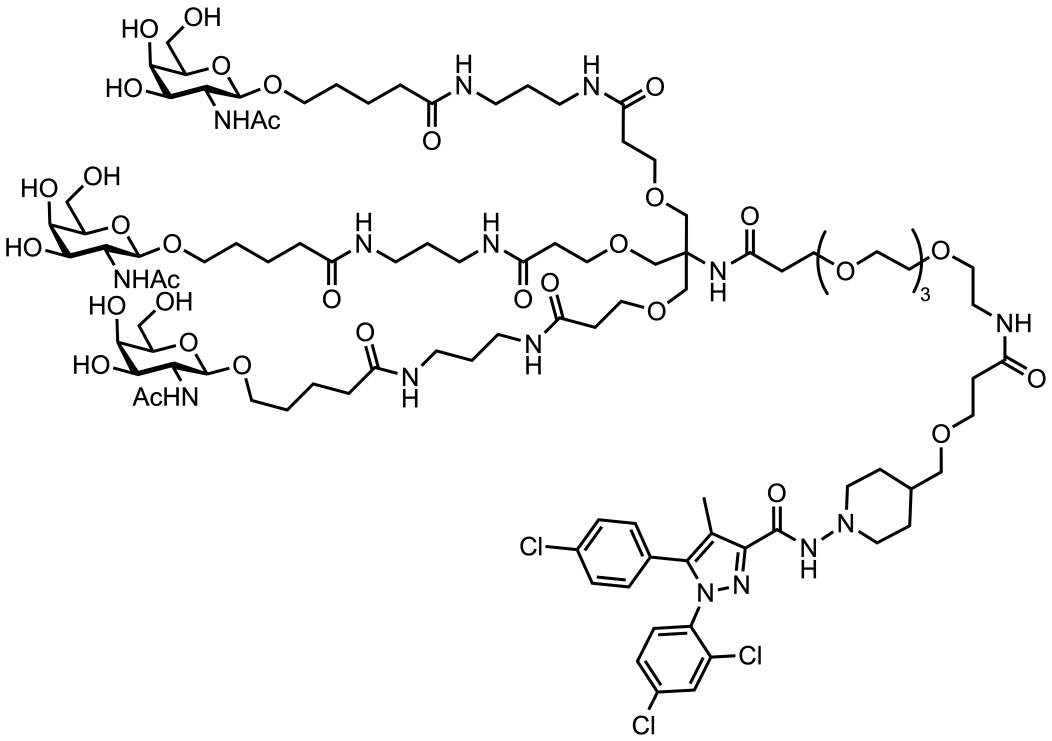


2.69 was prepared in three steps, first through deacetylation and hydrogenolysis of **2.53** according to general procedures **6.3.8** and **6.3.6** respectively, to form free amine **2.57**. Free amine **2.57** (53 mg, 0.03 mmol) was then subjected to amide coupling with **2.40** as outlined in general procedure **6.3.9.** Desired product **2.69** was obtained as a colourless amorphous solid (55 mg, 77%).

HRMS (ESI+) *m/z* Calc. for $C_{94}H_{148}Cl_3N_{15}O_{33}$ $[M + 2H + 2Na]^{2+}$: 1083.9691, found 1083.9611.

NMR data is reported in Table 6.3.

(2.70): LYTAC-1,4-PEG4

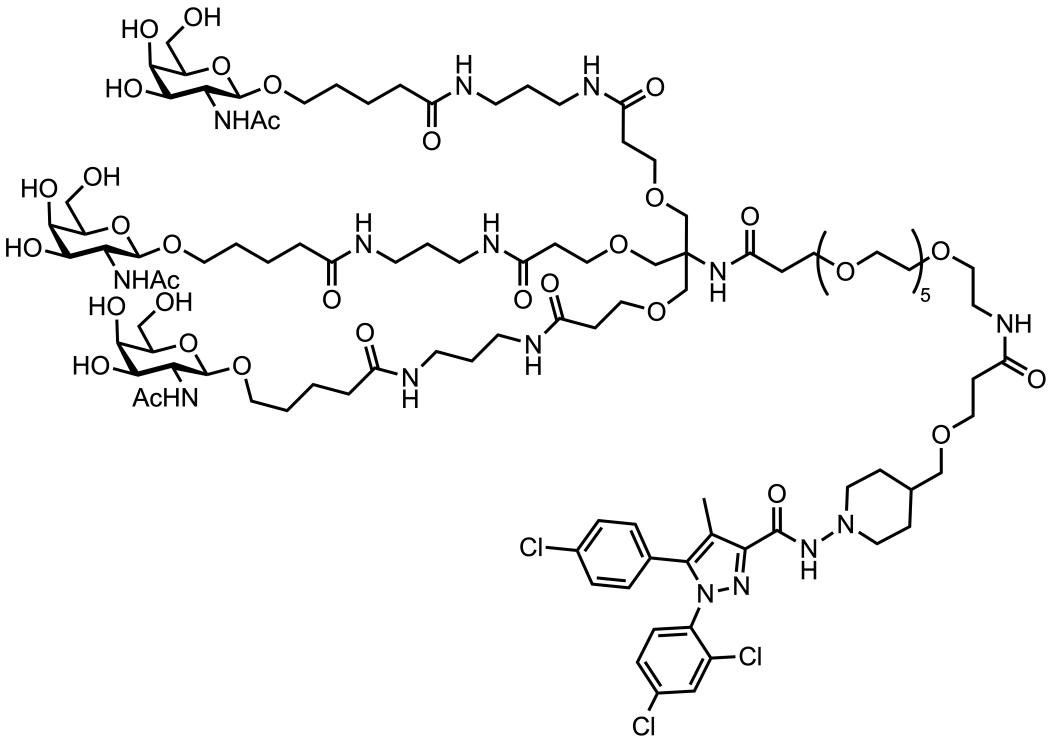


2.70 was prepared in three steps, first through deacetylation and hydrogenolysis of **2.54** according to general procedures **6.3.8** and **6.3.6** respectively, to form free amine **2.58**. Free amine **2.58** (56 mg, 0.03 mmol) was then subjected to amide coupling with **2.40** as outlined in general procedure **6.3.9.** Desired product **2.70** was obtained as a colourless amorphous solid (47 mg, 63%).

HRMS (ESI+) *m/z* Calc. for $C_{98}H_{156}Cl_3N_{15}O_{35}$ $[M + 2H + 2Na]^{2+}$: 1127.9953, found 1127.9874.

NMR data is reported in Table 6.3.

(2.71): LYTAC-1,4-PEG6

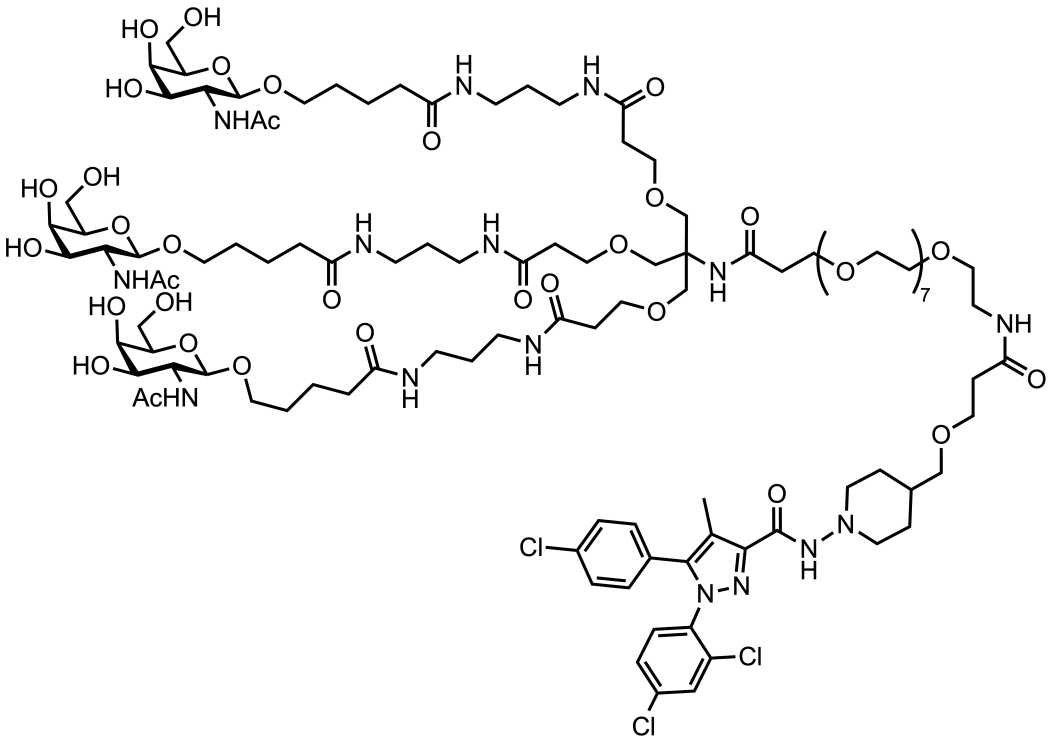


2.71 was prepared in three steps, first through deacetylation and hydrogenolysis of **2.55** according to general procedures **6.3.8** and **6.3.6** respectively, to form free amine **2.59**. Free amine **2.59** (49 mg, 0.03 mmol) was then subjected to amide coupling with **2.40** as outlined in general procedure **6.3.9.** Desired product **2.71** was obtained as a colourless amorphous solid (46 mg, 78%).

HRMS (ESI+) *m/z* Calc. for $C_{102}H_{164}Cl_3N_{15}O_{37}$ $[M + 2H + 2Na]^{2+}$: 1172.0215, found 1172.0134.

NMR data is reported in Table 6.3.

(2.72): LYTAC-1,4-PEG8



2.72 was prepared in three steps, first through deacetylation and hydrogenolysis of **2.56** according to general procedures **6.3.8** and **6.3.6** respectively, to form free amine **2.60**. Free amine **2.60** (48 mg, 0.03 mmol) was then subjected to amide coupling with **2.40** as outlined in general procedure **6.3.9.** Desired product **2.72** was obtained as a colourless amorphous solid (45 mg, 81%).

HRMS (ESI+) *m/z* Calc. for $C_{106}H_{174}Cl_3N_{15}O_{39}$ $[M + 2H + 2Na]^{2+}$: 1216.0477, found 1216.0400.

NMR data is reported in Table 6.3.

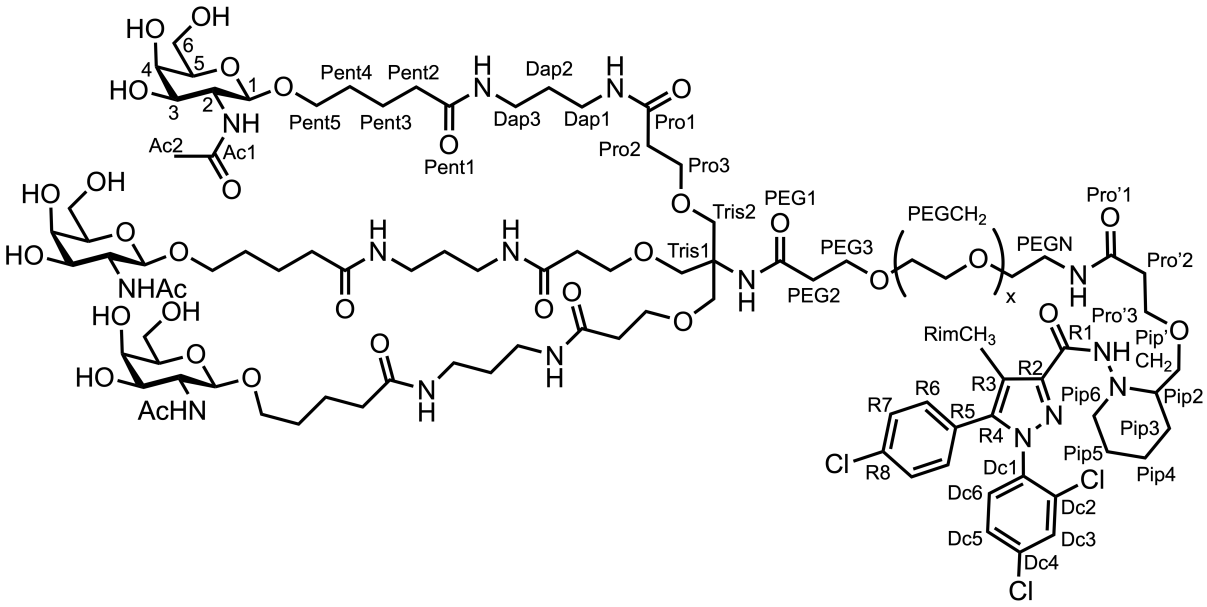


Figure 6.1. Labelled structure of LYTAC-1,2-x, where x = 1 (-PEG2, **2.61**), 3 (-PEG4, **2.62**), 5 (-PEG6, **2.63**), and 7 (-PEG8, **2.64**).

Table 6.1. ^{1}H (500/800 MHz) and ^{13}C NMR (126/201 MHz) shifts (ppm) of LYTAC-1,2- compounds, where x = 1 (-PEG2, **2.61**), 3 (-PEG4, **2.62**), 5 (-PEG6, **2.63**), and 7 (-PEG8, **2.64**).

x	**1 (2.61)**		**3 (2.62)**		**5 (2.63)**		**7 (2.64)**	
	δ_H	δ_C	δ_H	δ_C	δ_H	δ_C	δ_H	δ_C
Ac1	-	173.9	-	173.9	-	174.0	-	174.0
Ac2	1.98 (s)	23.2	1.99 (s)	23.2	1.99 (s)	23.2	1.99 (s)	23.2
Dap1	3.23 (m)	37.9	3.23 (m)	37.9	3.23 (m)	38.0	3.23 (m)	38.0
Dap2	1.70 (m)	30.1	1.70 (m)	30.1	1.70 (m)	30.1	1.70 (m)	30.1
Dap3	3.20 (m)	37.8	3.21 (m)	37.8	3.20 (m)	37.8	3.21 (m)	37.9
Dc1	-	128.6	-	128.6	-	128.5	-	128.6
Dc2	-	137.4	-	137.4	-	137.4	-	137.4
Dc3	7.58 (m)	131.1	7.58 (m)	131.1	7.58 (m)	131.1	7.59 (m)	131.1
Dc4	-	137.3	-	137.3	-	137.3	-	137.3
Dc5	7.48 (m)	129.3	7.48 (m)	129.3	7.48 (m)	129.4	7.48 (m)	129.4
Dc6	7.57 (d, 3.4 Hz)	132.5	7.57 (d, 3.2 Hz)	132.5	7.57 (d, 3.2 Hz)	132.4	7.58 (d, 3.3 Hz)	132.5
1	4.36 (d, 8.4 Hz)	103.0	4.36 (d, 8.4 Hz)	103.0	4.36 (d, 8.4 Hz)	103.0	4.36 (d, 8.4 Hz)	103.0

2	3.94 (dd, 10.8,8.6 Hz)	54.3	3.94 (dd, 10.8,8.6 Hz)	54.3	3.93 (dd, 10.8,8.6 Hz)	54.3	3.93 (dd, 10.6,8.3 Hz)	54.3
3	3.61 (m)	73.3	3.62 (m)	73.3	3.62 (m)	73.3	3.62 (m)	73.3
4	3.85 (dd, 3.2,0.9 Hz)	69.7	3.85 (dd, 3.4,0.8 Hz)	69.7	3.84 (dd, 3.4,0.9 Hz)	69.7	3.84 (dd, 3.4,0.8 Hz)	69.7
5	3.49 (m)	76.7	3.49 (m)	76.7	3.49 (m)	76.7	3.49 (m)	76.7
6	3.76 (t, 6.0 Hz)	62.6	3.76 (t, 6.0 Hz)	62.6	3.76 (t, 6.1 Hz)	62.5	3.75 (t, 6.1 Hz)	62.6
PEG1	-	173.8	-	173.8	-	173.9	-	173.9
PEG2	2.45 (t, 6.3 Hz)	37.7	2.45 (t, 6.3 Hz)	37.7	2.45 (t, 6.4 Hz)	37.7	2.45 (t, 6.3 Hz)	37.7
PEG3	3.70 (m)	71.2	3.70 (m)	71.2	3.70 (m)	71.2	3.70 (m)	71.3
PEG	3.32 (m)	40.3	3.31 (m)	40.3	3.32 (m)	40.3	3.33 (m)	40.3
PEGCH2	3.59 (m)	68.4, 68.5, 68.8	3.62 (m)	68.3, 68.4, 71.4 - 71.6	3.62 (m)	68.4, 68.5, 71.4 - 71.6	3.62 (m)	68.3, 68.4, 71.4 - 71.6
Pent1	-	176.1	-	176.1	-	176.1	-	176.1
Pent2	2.21 (t, 7.4 Hz)	38.2	2.21 (t, 7.5 Hz)	38.2	2.21 (t, 7.6 Hz)	38.2	2.21 (t, 7.4 Hz)	38.2
Pent3	1.67 (m)	23.8	1.67 (m)	23.8	1.67 (m)	23.8	1.68 (m)	23.8
Pent4	1.57 (m)	30.0	1.58 (m)	30.0	1.57 (m)	30.0	1.58 (m)	30.0
Pent5'	3.89 (m)	70.1	3.90 (m)	70.1	3.90 (m)	70.1	3.89 (m)	70.1
Pent5''	3.52 (m)	70.1	3.52 (m)	70.1	3.51 (m)	70.1	3.51 (m)	70.1
Pip2	2.77 (m)	64.8	2.77 (m)	64.8	2.78 (m)	64.8	2.77 (m)	64.9
Pip3'	1.85 (m)	30.4	1.84 (m)	30.4	1.85 (m)	30.4	1.84 (m)	30.4
Pip3''	1.47 (m)	30.4	1.48 (m)	30.4	1.47 (m)	30.4	1.47 (m)	30.4
Pip4	1.31 (m)	24.4	1.30 (m)	24.4	1.31 (m)	24.4	1.32 (m)	24.4
Pip5	1.74 (m)	26.4	1.74 (m)	26.4	1.74 (m)	26.3	1.75 (m)	26.4
Pip6'	2.71 (m)	57.9	2.70 (m)	57.9	2.71 (m)	57.9	2.71 (m)	58.0
Pip6''	3.13 (m)	57.9	3.13 (m)	57.9	3.13 (m)	57.9	2.71 (m)	58.0

Pip'CH2'	3.63 (m)	74.4	3.63 (m)	74.5	3.62 (m)	74.5	3.64 (m)	74.5
Pip'CH2''	3.42 (m)	74.4	3.41 (m)	74.5	3.41 (m)	74.5	3.40 (m)	74.5
Pro1	-	174.0	-	174.0	-	174.1	-	174.1
Pro'1	-	174.0	-	174.0	-	174.0	-	174.0
Pro2	2.43 (t, 6.0 Hz)	37.7	2.43 (t, 6.0 Hz)	37.7	2.43 (t, 6.4 Hz)	37.7	2.43 (t, 6.1 Hz)	37.7
Pro'2	2.36 (t, 6.3 Hz)	36.7	2.35 (t, 6.3 Hz)	36.7	2.35 (t, 6.3 Hz)	36.7	2.34 (t, 6.5 Hz)	36.7
Pro3	3.67 (m)	68.7	3.69 (m)	68.7	3.69 (m)	68.7	3.68 (m)	68.7
Pro'3	3.62 (m)	70.1	3.62 (m)	70.1	3.62 (m)	70.1	3.62 (m)	70.1
R1	-	163.1	-	163.1	-	163.1	-	163.1
R2	-	118.8	-	118.8	-	118.8	-	118.8
R3	-	144.6	-	144.6	-	144.6	-	144.6
R4	-	145.4	-	145.4	-	145.4	-	145.4
R5	-	134.1	-	134.1	-	134.1	-	134.1
R6	7.2 (d, 8.4 Hz)	132.7	7.21 (d, 8.4 Hz)	132.7	7.21 (d, 8.4 Hz)	132.7	7.21 (d, 8.5 Hz)	132.7
R7	7.38 (d, 8.5 Hz)	129.9	7.38 (d, 8.5 Hz)	129.9	7.38 (d, 8.4 Hz)	129.9	7.38 (d, 8.5 Hz)	129.9
R8	-	136.2	-	136.2	-	136.2	-	136.2
RimCH3	2.32 (s)	9.6	2.32 (s)	9.6	2.31 (s)	9.6	2.32 (s)	9.6
Tris1	-	61.5	-	61.5	-	61.5	-	61.5
Tris2	3.66 (s)	70.6	3.66 (s)	70.6	3.67 (s)	70.6	3.67 (s)	70.6

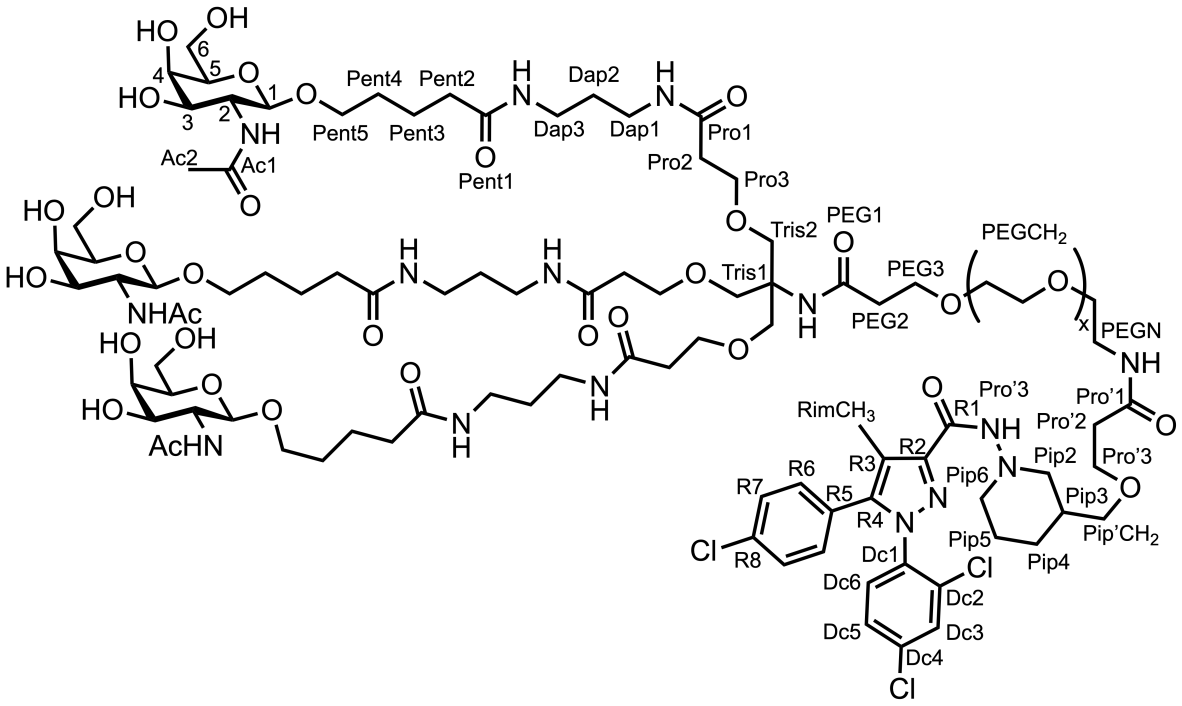


Figure 6.2. Labelled structure of LYTAC-1,3-x, where x = 1 (-PEG2, **2.65**), 3 (-PEG4, **2.66**), 5 (-PEG6, **2.67**), and 7 (-PEG8, **2.68**).

Table 6.2. ^{1}H (500/800 MHz) and ^{13}C NMR (126/201 MHz) shifts (ppm) of LYTAC-1,3- compounds, where x = 1 (-PEG2, **2.65**), 3 (-PEG4, **2.66**), 5 (-PEG6, **2.67**), and 7 (-PEG8, **2.68**).

x	**1 (2.65)**		**3 (2.66)**		**5 (2.67)**		**7 (2.68)**	
	δ_H	δ_C	δ_H	δ_C	δ_H	δ_C	δ_H	δ_C
Ac1	-	174.1	-	174.1	-	174.1	-	174.1
Ac2	1.99 (s)	23.2	1.99 (s)	23.2	1.99 (s)	23.2	1.99 (s)	23.2
Dap1	3.23 (d, 6.9 Hz)	37.8	3.23 (d, 7.0 Hz)	37.8	3.23 (d, 7.0 Hz)	37.8	3.23 (d, 7.0 Hz)	37.9
Dap2	1.69 (s)	30.4	1.69 (s)	30.4	1.69 (s)	30.4	1.69 (d, 7.2 Hz)	30.4
Dap3	3.21 (m)	37.7	3.21 (m)	37.7	3.21 (m)	37.7	3.21 (m)	37.7
Dc1	-	128.6	-	128.6	-	128.6	-	128.6
Dc2	-	137.4	-	137.4	-	137.4	-	137.4
Dc3	7.57 (d, 2.3 Hz)	131.0	7.58 (d, 2.3 Hz)	131.1	7.58 (d, 2.3 Hz)	131.1	7.58 (d, 2.3 Hz)	131.1
Dc4	-	137.3	-	137.3	-	137.3	-	137.4

Dc5	7.47 (dd, 8.5,2.4 Hz)	129.3	7.47 (dd, 8.4,2.3 Hz)	129.3	7.47 (dd, 8.4,2.3 Hz)	129.3	7.48 (dd, 8.4,2.3 Hz)	129.3
Dc6	7.56 (d, 8.4 Hz)	132.4	7.55 (d, 8.5 Hz)	132.4	7.55 (d, 8.5 Hz)	132.4	7.55 (d, 8.5 Hz)	132.4
1	4.36 (d, 8.4 Hz)	103.0	4.36 (d, 8.5 Hz)	103.0	4.36 (d, 8.5 Hz)	103.0	4.36 (d, 8.4 Hz)	103.0
2	3.94 (m)	54.3	3.94 (m)	54.3	3.94 (m)	54.3	3.93 (m)	54.3
3	3.60 (m)	73.3	3.60 (m)	73.3	3.60 (m)	73.3	3.62 (m)	73.3
4	3.85 (d, 3.4 Hz)	69.7	3.85 (d, 3.5 Hz)	69.7	3.85 (d, 3.5 Hz)	69.7	3.84 (d, 3.4 Hz)	69.7
5	3.50 (m)	76.7	3.50 (m)	76.7	3.50 (m)	76.7	3.50 (m)	76.7
6	3.76 (t, 5.8 Hz)	62.6	3.76 (t, 6.0 Hz)	62.6	3.76 (t, 6.0 Hz)	62.6	3.76 (t, 5.9 Hz)	62.6
PEG1	-	173.8	-	173.8	-	173.8	-	173.9
PEG2	2.44 (m)	37.9	2.44 (m)	38.0	2.44 (m)	38.0	2.44 (m)	37.9
PEG3	3.52 (m)	-	3.52 (m)	-	3.52 (m)	-	3.50 (m)	38.0
PEGN	3.36 (t, 5.6 Hz)	40.4	3.35 (d, 5.6 Hz)	40.4	3.35 (d, 5.6 Hz)	40.4	3.35 (d, 5.5 Hz)	40.4
PEGCH2	3.57 (m), 3.67 (m)	68.2, 68.4, 71.2, 71.3	3.61 (m), 3.68 (m)	68.2, 68.4, 70.1, 71.3 - 71.5	3.61 (m), 3.68 (m)	68.2, 68.4, 70.1, 71.3 - 71.5	3.62 (m), 3.67 (m)	68.2, 68.4, 70.1, 71.3 - 71.6
Pent1	-	176.1	-	176.1	-	176.1	-	176.1
Pent2	2.21 (t, 7.4 Hz)	36.7	2.21 (t, 7.4 Hz)	36.7	2.21 (t, 7.4 Hz)	36.7	2.21 (t, 7.6 Hz)	36.7
Pent3	1.67 (m)	23.8	1.67 (m)	23.8	1.67 (m)	23.8	1.68 (m)	23.8
Pent4	1.58 (m)	30.0	1.57 (m)	30.0	1.57 (m)	30.0	1.58 (m)	30.0
Pent5'	3.90 (m)	70.1	3.90 (m)	70.1	3.90 (m)	70.1	3.91 (m)	70.1
Pent5''	3.51 (m)	70.1	3.51 (m)	70.1	3.51 (m)	70.1	3.50 (m)	70.1
Pip1'	3.16 (m)	60.3	3.15 (m)	60.3	3.15 (m)	60.3	3.17 (m)	60.4
Pip1''	2.37 (t, 10.5 Hz)	60.3	2.37 (t, 10.4 Hz)	60.3	2.37 (t, 10.4 Hz)	60.3	2.37 (t, 10.3 Hz)	60.4

Pip2	2.10 (m)	38.1	2.08 (m)	38.2	2.08 (m)	38.2	2.09 (m)	38.2
Pip3'	1.02 (m)	27.5	1.02 (m)	27.4	1.02 (m)	27.4	1.02 (m)	27.4
Pip3''	1.71 (m)	27.5	1.72 (m)	27.4	1.72 (m)	27.4	1.70 (m)	27.4
Pip4	1.75 (m)	25.3	1.76 (m)	25.3	1.76 (m)	25.3	1.76 (m)	25.3
Pip5'	3.06 (m)	57.1	3.06 (m)	57.1	3.06 (m)	57.1	3.06 (m)	57.2
Pip5''	2.58 (m)	57.1	2.58 (m)	57.1	2.58 (m)	57.1	2.57 (m)	57.2
PipCH2'	3.39 (m)	74.9	3.39 (m)	74.9	3.39 (m)	74.9	3.39 (m)	74.9
PipCH2''	3.32 (m)	74.9	3.32 (m)	74.9	3.32 (m)	74.9	3.32 (m)	74.9
Pro1	-	174.0	-	174.0	-	174.0	-	174.1
Pro'1	-	173.9	-	173.9	-	173.9	-	174.0
Pro2	2.42 (m)	37.8	2.42 (m)	37.8	2.42 (m)	37.8	2.42 (m)	37.8
Pro'2	2.45 (m)	37.9	2.45 (m)	37.9	2.45 (m)	37.9	2.45 (m)	38.0
Pro3	3.69 (m)	68.7	3.68 (m)	68.7	3.68 (m)	68.7	3.67 (m)	68.7
Pro'3	3.67 (m)	68.4	3.68 (m)	68.4	3.68 (m)	68.4	3.67 (m)	-
R1	-	162.5	-	162.5	-	162.5	-	162.5
R2	-	118.7	-	118.7	-	118.7	-	118.7
R3	-	144.5	-	144.5	-	144.5	-	144.5
R4	-	145.4	-	145.4	-	145.4	-	145.4
R5	-	134.1	-	134.1	-	134.1	-	134.1
R6	7.20 (m)	132.6	7.20 (m)	132.6	7.20 (m)	132.6	7.20 (m)	132.7
R7	7.38 (m)	129.9	7.38 (m)	129.9	7.38 (m)	129.9	7.38 (m)	129.9
R8	-	136.2	-	136.2	-	136.2	-	136.2
RimCH3	2.31 (s)	9.6	2.31 (s)	9.6	2.31 (s)	9.6	2.32 (s)	9.5
Tris1	-	61.5	-	61.5	-	61.5	-	61.5
Tris2	3.66 (s)	70.6	3.68 (s)	70.6	3.68 (s)	70.6	3.67 (s)	70.6

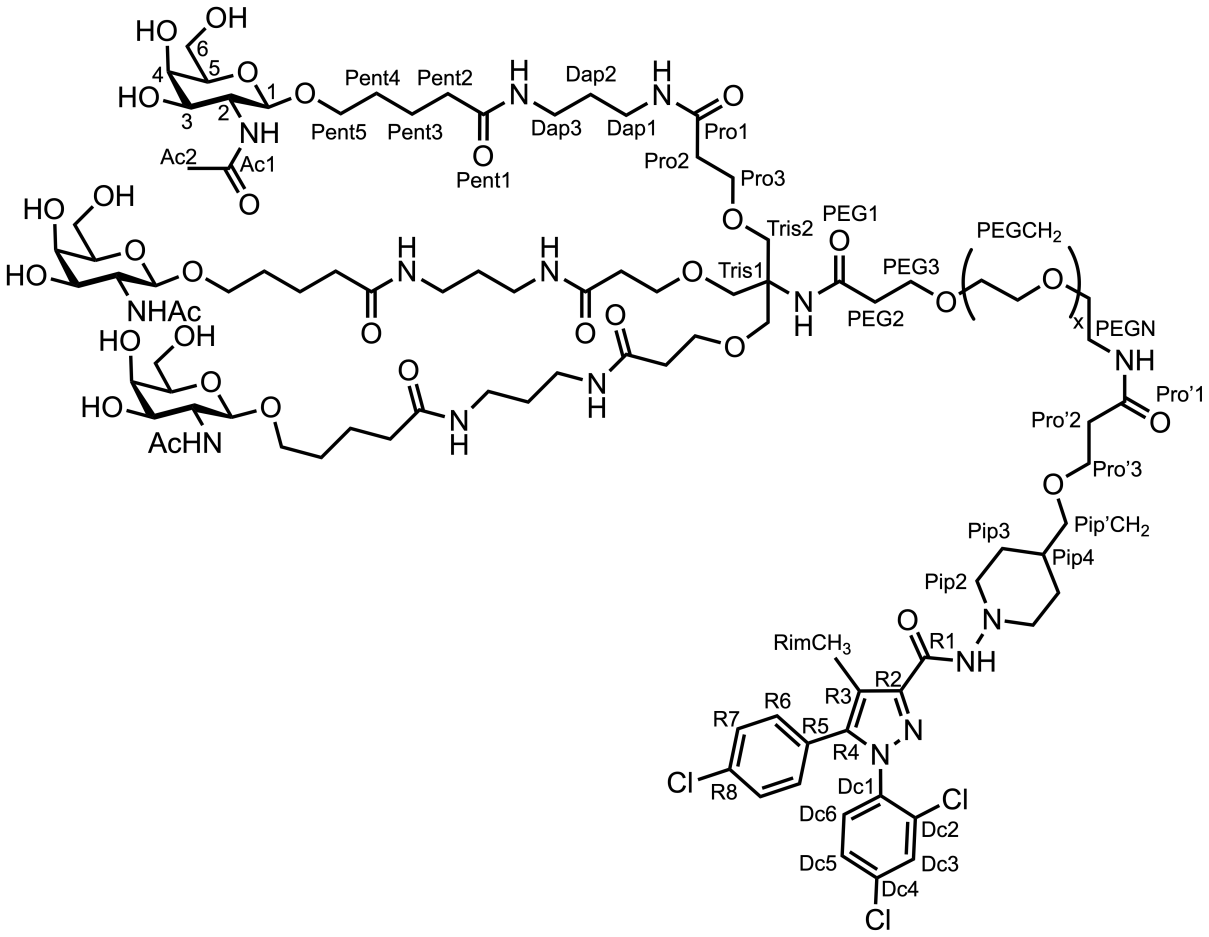


Figure 6.3. Labelled structure of LYTAC-1,4-x, where x = 1 (-PEG2, **2.69**), 3 (-PEG4, **2.70**), 5 (-PEG6, **2.71**), and 7 (-PEG8, **2.72**).

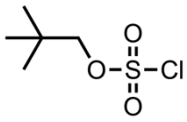
Table 6.3. ^{1}H (500/800 MHz) and ^{13}C NMR (126/201 MHz) shifts (ppm) of LYTAC-1,4- compounds, where x = 1 (-PEG2, **2.69**), 3 (-PEG4, **2.70**), 5 (-PEG6, **2.71**), and 7 (-PEG8, **2.72**).

x	**1 (2.69)**		**3 (2.70)**		**5 (2.71)**		**7 (2.72)**	
	δ_H	δ_C	δ_H	δ_C	δ_H	δ_C	δ_H	δ_C
Ac1	-	173.9	-	173.9	-	174.0	-	174.0
Ac2	1.99 (s)	23.2	1.99 (s)	23.2	1.99 (s)	23.2	1.99 (s)	23.2
Dap1	3.23 (m)	38.0	3.23 (m)	38.0	3.23 (m)	38.0	3.23 (m)	38.0
Dap2	1.70 (m)	30.4	1.70 (m)	30.4	1.70 (m)	30.4	1.70 (m)	30.4
Dap3	3.21 (m)	37.8	3.21 (m)	37.8	3.21 (m)	37.9	3.21 (m)	37.8
Dc1	-	128.6	-	128.6	-	128.5	-	128.5
Dc2	-	137.4	-	137.4	-	137.4	-	137.4
Dc3	7.57 (m)	131.0	7.57 (m)	131.0	7.57 (m)	131.0	7.57 (m)	131.0
Dc4	-	137.3	-	137.3	-	137.3	-	137.3

Dc5	7.47 (m)	129.3	7.47 (m)	129.3	7.47 (m)	129.3	7.47 (m)	129.3
Dc6	7.55 (d, 8.5 Hz)	132.6	7.55 (d, 8.5 Hz)	132.6	7.55 (d, 8.4 Hz)	132.6	7.55 (d, 8.5 Hz)	132.6
1	4.36 (d, 8.5 Hz)	103.0	4.36 (d, 8.4 Hz)	103.0	4.37 (d, 8.4 Hz)	103.0	4.37 (d, 8.4 Hz)	103.0
2	3.94 (dd, 10.6, 8.6 Hz)	54.3	3.93 (dd, 10.9,8.6 Hz)	54.3	3.93 (dd, 10.7,8.4 Hz)	54.3	3.93 (dd, 10.6,8.8 Hz)	54.3
3	3.61 (m)	73.3	3.65 (m)	73.3	3.49 (m)	73.3	3.65 (m)	73.3
4	3.85 (m)	69.7	3.85 (m)	69.7	3.85 (m)	69.7	3.85 (m)	69.7
5	3.49 (m)	76.7	3.49 (m)	76.7	3.49 (m)	76.7	3.49 (m)	76.7
6	3.76 (t, 6.0 Hz)	62.6	3.76 (t, 6.0 Hz)	62.6	3.76 (t, 6.1 Hz)	62.5	3.76 (t, 6.1 Hz)	62.5
PEG1	-	174.1	-	174.1	-	174.2	-	174.2
PEG2	3.37 (t, 5.6 Hz)	40.4	3.37 (t, 5.5 Hz)	40.4	3.37 (t, 5.5 Hz)	40.4	3.37 (t, 5.5 Hz)	40.4
PEG3	3.54 (t, 5.6 Hz)	70.6	3.55 (t, 5.5 Hz)	40.4	3.55 (t, 5.6 Hz)	70.6	3.55 (t, 5.6 Hz)	70.6
PEGN	2.45 (m)	38.2	2.45 (m)	38.2	2.45 (m)	38.2	2.44 (m)	38.2
PEGCH 2	3.67 (m)	68.1, 71.3, 71.3	3.65 (m)	68.1, 71.3 - 71.6	3.64 (m)	68.1, 71.2 - 71.5	3.65 (m)	68.1, 71.2- 71.5
Pent1	-	176.1	-	176.1	-	176.1	-	176.1
Pent2	2.21 (t, 7.5 Hz)	36.7	2.21 (t, 7.5 Hz)	36.7	2.21 (t, 7.5 Hz)	36.7	2.21 (t, 7.5 Hz)	36.7
Pent3	1.67 (m	23.8	1.66 (m)	23.8	1.67 (m)	23.8	1.67 (m)	23.8
Pent4	1.58 (m)	30.0	1.57 (m)	30.0	1.58 (m)	30.0	1.58 (m)	30.0
Pent5'	3.89 (m)	70.1	3.89 (m)	70.1	3.89 (m)	70.1	3.91 (m)	70.1
Pent5''	3.51 (m)	70.1	3.51 (m)	70.1	3.51 (m)	70.1	3.51 (m)	70.1
Pip2'	3.11 (m)	56.3	3.12 (m)	56.3	3.12 (m)	56.3	3.12 (m)	56.3
Pip2''	2.64 (m)	56.3	2.63 (m)	56.3	2.63 (m)	56.3	2.64 (m)	56.3
Pip3'	1.49 (m)	29.6	1.49 (m)	29.6	1.49 (m)	29.6	1.49 (m)	29.6
Pip3''	1.77 (m)	29.6	1.77 (m)	29.6	1.78 (m)	29.6	1.77 (m)	29.6
Pip4	1.62 (m)	36.3	1.62 (m)	36.3	1.62 (m)	36.3	1.62 (m)	36.3

Pip'CH 2'	3.31 (m)	76.5	3.33 (m)	76.5	3.33 (m)	76.5	3.33 (m)	76.5
Pip'CH 2''	3.19 (m)	76.5	3.19 (m)	76.5	3.19 (m)	76.5	3.19 (m)	76.5
Pro1	-	174.0	-	174.0	-	174.1	-	174.1
Pro'1	-	173.8	-	173.9	-	173.9	-	173.9
Pro2	2.43 (t, 6.1 Hz)	37.7	2.43 (t, 6.2 Hz)	37.7	2.42 (t. 6.1 Hz)	37.7	2.43 (t, 6.0 Hz)	37.7
Pro'2	2.47 (m)	37.7	2.46 (m)	37.7	2.46 (m)	37.6	2.46 (m)	37.6
Pro3	3.72 (m)	68.7	3.65 (m)	68.7	3.64 (m)	68.7	3.65 (m)	68.7
Pro'3	3.69 (m)	68.4	3.65 (m)	68.4	3.67 (m)	68.4	3.65 (m)	68.4
R1	-	162.5	-	162.5	-	162.5	-	162.5
R2	-	118.7	-	118.7	-	118.7	-	118.7
R3	-	144.5	-	144.5	-	144.5	-	144.5
R4	-	145.5	-	145.4	-	145.4	-	145.4
R5	-	134.1	-	134.1	-	134.1	-	134.1
R6	7.19 (m)	132.4	7.20 (m)	132.4	7.19 (m)	132.4	7.20 (m)	132.4
R7	7.37 (m)	129.9	7.37 (m)	129.9	7.37 (m)	129.9	7.37 (m)	129.9
R8	-	136.2	-	136.2	-	136.2	-	136.2
RimCH 3	2.30 (s)	9.5	2.30 (s)	9.5	2.30 (s)	9.5	2.30 (s)	9.5
Tris1	-	61.5	-	61.5	-	61.5	-	61.5
Tris2	3.66 (m)	70.1	3.65 (m)	70.1	3.64 (m)	70.1	3.65 (m)	70.1

(2.73i): neopentyl sulfurochloridate

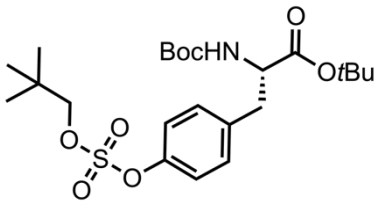


SO_2Cl_2 (50.4 mL, 620 mmol, 1.1 eq) was added to an oven-dried flask, dissolved in anhydrous ether (50 mL) and cooled to -78 ^oC. To this solution, a pre-mixed solution of neopentyl alcohol (50.0 g, 570 mmol) and pyridine (50.3 mL, 620 mmol, 1.1 eq) in anhydrous ether (110 mL) was added dropwise over 1.5 h. Upon complete addition, the mixture was warmed to rt and allowed to stir for 2.5 h. A large amount of white precipitate was formed (pyridinium chloride). Upon completion, the mixture was washed through celite soaked in ether. The ether washings were washed twice with ice cold water, dried over $MgSO_4$, and concentrated *in vacuo*. **2.73i** was obtained as a colourless liquid (96.0 g, 91%).

^{1}H NMR (500 MHz, $CDCl_3$) δ 4.17 (s, 2H), 1.05 (s, 9H) ppm.

This is in agreement with the data reported by Mihai *et al*.[418]

(2.73ii) *tert*-butyl (*S*)-2-((*tert*-butoxycarbonyl)amino)-3-(4-(((neopentyloxy)sulfonyl)oxy)phenyl) propanoate



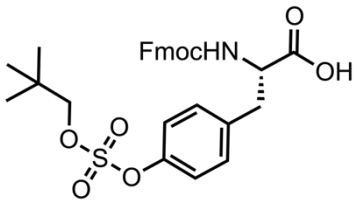
Boc-Tyr-O*t*Bu (25.0 g, 74 mmol) was placed in an oven-dried flask, dissolved in anhydrous THF (75 mL), and cooled to -78 ^oC. LiHMDS (77.8 mL, 78 mmol, 1.05 eq) was added dropwise using a cannula. The reaction was stirred for 2 min, before neopentyl sulfurochloridate (**2.73i**) was quickly added via a syringe. The reaction was warmed to rt and stirred for 21 h. Upon completion, determined by TLC, the reaction mixture was diluted with EtOAc (500 mL) and sat. aq. $NaHCO_3$ (250 mL). The organic layer was washed

twice more with $NaHCO_3$, filtered through a large plug of silica soaked in EtOAc, and washed through with EtOAc. The filtrate was dried over Na_2SO_4 and concentrated *in vacuo*. The crude material was purified by flash column chromatography (10-50% EtOAc:hexanes) to provide the desired product (**2.73ii**) as a colourless oil (15.7 g, 45%).

^{1}H NMR (500 MHz, $CDCl_3$) δ 7.22 (m, 4H), 5.01 (d, *J* = 8.1 Hz, 1H), 4.44 (q, *J* = 7.0 Hz, 1H), 4.06 (s, 2H), 3.05 (q, *J* = 8.6 Hz, 2H), 1.42 (s, 9H), 1.39 (s, 9H), 0.99 (s, 9H) ppm.

This is in agreement with the data reported by Payne and co-workers.[204]

(2.73) (*S*)-2-((((9*H*-fluoren-9-yl)methoxy)carbonyl)amino)-3-(4-(((neopentyloxy) sulfonyl)oxy)phenyl)propanoic acid



Compound **2.73ii** (15.7g, 33 mmol) was placed in a round bottom flask and dissolved in a mixture of TFA:water:triisopropylsilane (95:5:5 v/v/v, total volume 150 mL) at 0 ^oC. The mixture was stirred at 0 ^oC for 5 minutes before being warmed to rt and stirred for a further 4 h. The reaction was analysed by TLC and LCMS, using TLC to show consumption of starting material. The solvent was removed *in vacuo*, and the crude material azeotroped with toluene (3 x 100 mL) to remove any excess TFA. The crude material was redissolved in a mixture of THF:H_2O (95:5 v/v, total volume 200 mL). DIPEA (14.8 mL, 85 mmol, 3.0 eq) was added, followed by Fmoc-OSu (10.5 g, 31 mmol, 1.1 eq). The reaction was stirred at rt for 2 h. Upon completion, as determined by LCMS, the solvent was removed *in vacuo*. The crude material was redissolved in EtOAc and washed with 1M HCl (3 x 200 mL) to form the free acid. The EtOAc layer was dried over $MgSO_4$ and concentrated *in vacuo*. The now free acid was placed in an ice bath and dissolved in cold ether (approximately 15 mL/g). Dicyclohexylamine (11.3 mL, 56 mmol, 2.0 eq) was added dropwise whilst stirring, allowing formation of the dicyclohexylamine salt, which is insoluble in ether. Hexane (at room temperature, 1:1 v/v hexane:Et_2O) was added to

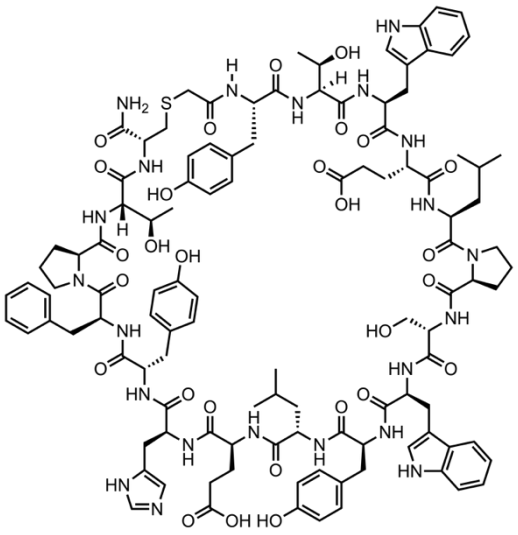
facilitate precipitation, and stirring was stopped. The mixture was allowed to precipitate at room temperature for 2 h. The desired salt was dried by vacuum filtration and washed through with cold ether (3 x 50 mL) to ensure all undesired Fmoc side products were removed. The desired salt was redissolved in EtOAc (approximately 30 mL/g) and 1M HCl (1:1 v/v with EtOAc), allowing formation of the now pure free acid and dicyclohexylamine hydrochloride precipitate. The precipitate was removed through vacuum filtration and washed with EtOAc (3 x 100 mL). The layers of the filtrate were separated, and the organic layer washed with 1 M HCl (2 x 150 mL). The organic layer was collected, dried over $MgSO_4$, and concentrated in vacuo to provide a pale orange foam. The product was coevaporated with toluene (3 x 200 mL) to remove any acetic acid formed on work up. The pure product (**2.73**) was obtained as a pale orange foam (12.5 g, 80%).

^{1}H NMR (400 MHz, $CDCl_3$) δ 7.77 (d, *J* = 7.6 Hz, 2H), 7.56 (d, *J* = 7.6 Hz, 2H), 7.41 (t, *J* = 7.5 Hz, 2H), 7.32 (ddd, *J* = 8.1, 5.0, 3.1 Hz, 2H), 7.25 – 7.12 (m, 4H), 5.21 (d, *J* = 7.7 Hz, 1H), 4.68 (d, *J* = 7.5 Hz, 1H), 4.47 (d, *J* = 6.4 Hz, 1H), 4.41 (t, *J* = 8.6 Hz, 1H), 4.21 (t, *J* = 6.9 Hz, 1H), 4.07 (s, 2H), 3.26 – 3.02 (m, 2H), 0.99 (s, 9H) ppm.

This is in agreement with the data reported by Payne and co-workers.[204]

6.5.5 Synthesis of Cyclic Peptides

(2.74): AL-02



Rink amide resin (50 µmol, ~0.6 mmol g^{-1}) was loaded with Fmoc-Cys(Trt)-OH according to general procedure **6.4.2**. The target peptide was then synthesised by iterative Fmoc-SPPS on the Syro I peptide synthesiser according to general procedure **6.4.2** with chloroacetic acid the final coupling step according to general procedure **6.4.3** to generate the resin-bound sequence chloroacetyl-YTWELPSWYLEHYFPTC. The peptide was cleaved from resin by general procedure **6.4.7**, and cyclised according to general procedure **6.4.8**. Purification by RP-HPLC (1 to 70 vol.% MeCN in H_2O with 0.1 vol.% formic acid over 50 min), followed by lyophilisation, afforded the pure peptide **2.74** as a white fluffy solid (12.1 mg, 11%).

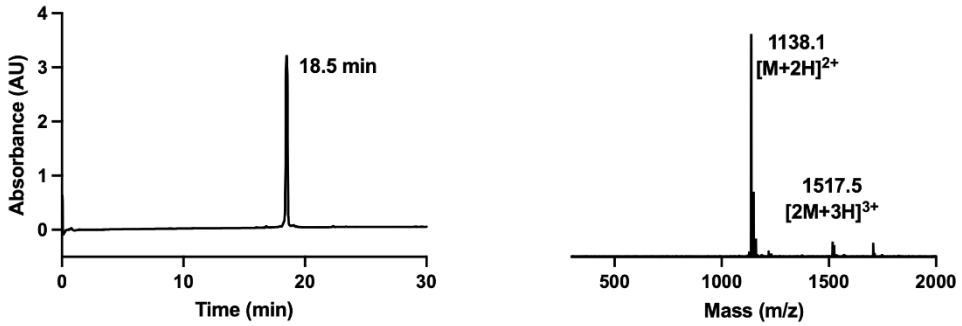
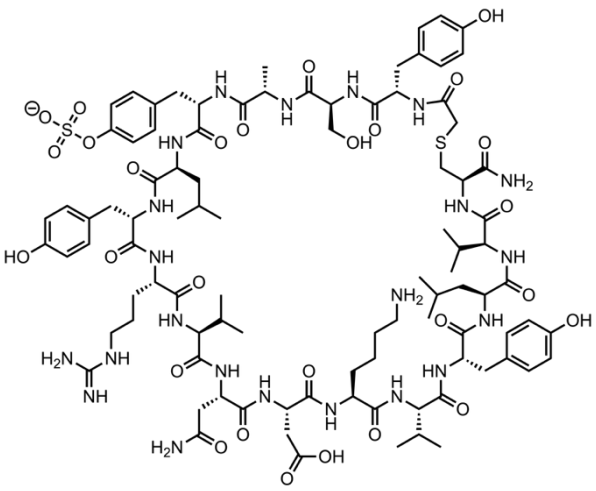


Figure 6.4. Analytical RP-HPLC: R_t = 18.5 min (1 to 70 vol.% MeCN in H_2O with 0.1 vol.% formic acid over 30 min, λ = 214 nm). **LRMS:** (+ESI) *m/z* 1517.5 $[2M+3H]^{3+}$, 1138.1 $[M+2H]^{2+}$.

(2.75): AL-06



Rink amide resin (50 µmol, ~0.6 mmol g^{-1}) was loaded with Fmoc-Cys(Trt)-OH according to general procedure **6.4.1**. The target peptide was then synthesised by iterative Fmoc-SPPS on the Syro I peptide synthesiser according to general procedure **6.4.1**, with chloroacetic acid the final coupling step according to general procedure **6.4.3** to generate the resin-bound sequence chloroacetyl-YSA**sY**LYRVNDKVYLVC. The peptide was cleaved from resin by general procedure **6.4.7**, and cyclised according to general procedure **6.4.8**. Purification by RP-HPLC (1 to 70 vol.% MeCN in H_2O with 0.1 vol.% formic acid over 50 min), followed by lyophilisation, afforded the pure neopentyl protected peptide as a white fluffy solid. The peptide was subjected to neopentyl deprotection by general procedure **6.4.10** and subsequent purification by RP-HPLC (1 to 70 vol.% MeCN in H_2O with 0.1 vol.% formic acid over 50 min), followed by lyophilisation, afforded the pure peptide **2.75** as a white fluffy solid (1.9 mg, 2%).

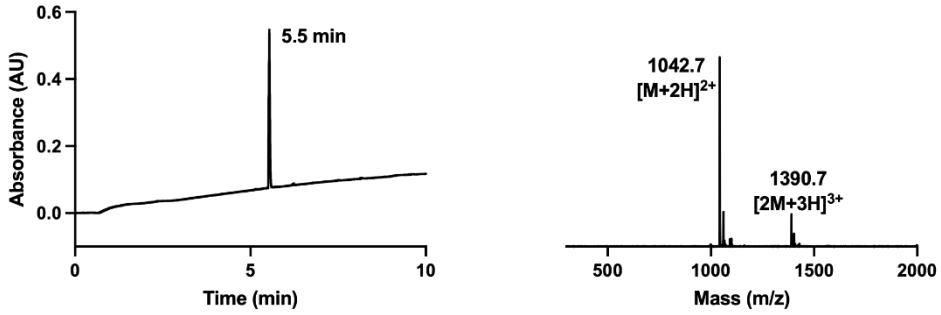
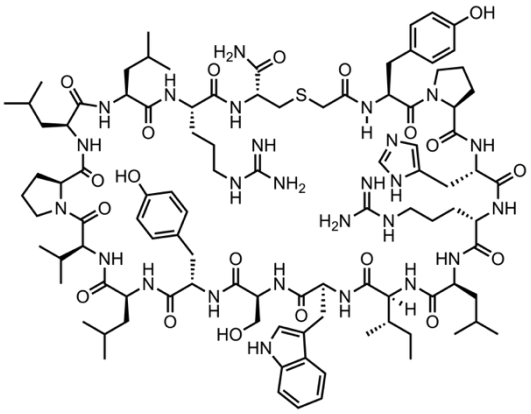


Figure 6.5. Analytical RP-HPLC: R_t = 5.5 min (1 to 80 vol.% MeCN in H_2O with 0.1 vol.% formic acid over 10 min, λ = 214 nm). **LRMS:** (+ESI) *m/z* 1390.7 $[2M+3H]^{3+}$, 1042.7 $[M+2H]^{2+}$.

(2.76): AL-08



Rink amide resin (50 µmol, ~0.6 mmol g^{-1}) was loaded with Fmoc-Cys(Trt)-OH according to general procedure **6.4.2**. The target peptide was then synthesised by iterative Fmoc-SPPS on the Syro I peptide synthesiser according to general procedure **6.4.2**, with chloroacetic acid the final coupling step according to general procedure **6.4.3** to generate the resin-bound sequence chloroacetyl-YPHRLIWSYLVPLLRC. The peptide was cleaved from resin by general procedure **6.4.7**, and cyclised according to general procedure **6.4.8**. Purification by RP-HPLC (1 to 50 vol.% MeCN in H_2O with 0.1 vol.% formic acid over 40 min), followed by lyophilisation, afforded the pure peptide **2.76** as a white fluffy solid (11.2 mg, 11%).

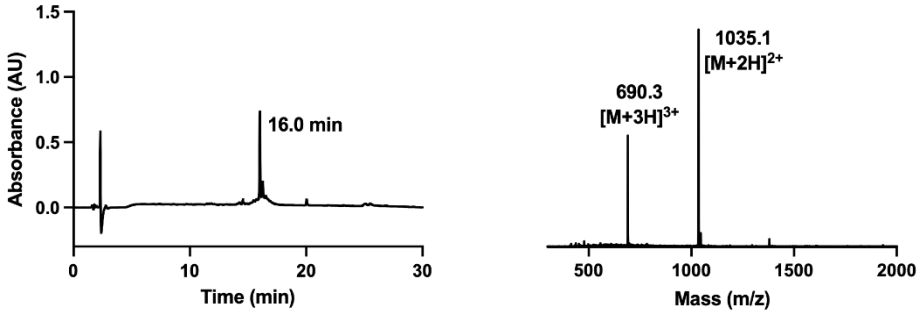
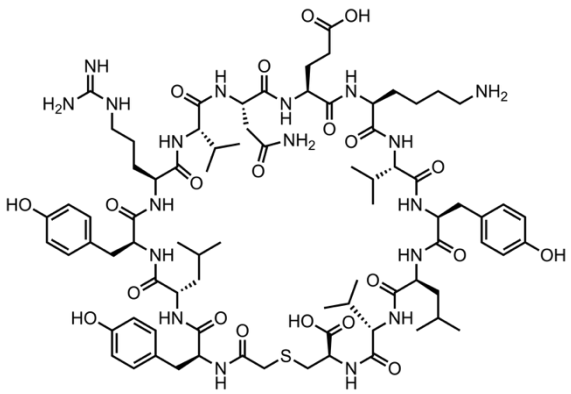


Figure 6.6. Analytical RP-HPLC: R_t = 16.0 min (1 to 80 vol.% MeCN in H_2O with 0.1 vol.% formic acid over 30 min, λ = 214 nm). **LRMS:** (+ESI) *m/z* 1035.1 $[M+2H]^{2+}$, 690.3 $[M+3H]^{3+}$.

(2.77): AL-10



Rink amide resin (50 µmol, ~0.6 mmol g^{-1}) was loaded with Fmoc-Cys(Trt)-OH according to general procedure **6.4.2**. The target peptide was then synthesised by iterative Fmoc-SPPS on the Syro I peptide synthesiser according to general procedure **6.4.2**, with chloroacetic acid the final coupling step according to general procedure **6.4.3** to generate the resin-bound sequence chloroacetyl-YLYRVNEKVYLVC. The peptide was cleaved from resin by general procedure **6.4.7**, and cyclised according to general procedure **6.4.8**. Purification by RP-HPLC (1 to 70 vol.% MeCN in H_2O with 0.1 vol.% formic acid over 40 min), followed by lyophilisation, afforded the pure peptide **2.77** as a white fluffy solid (9.9 mg, 12%).

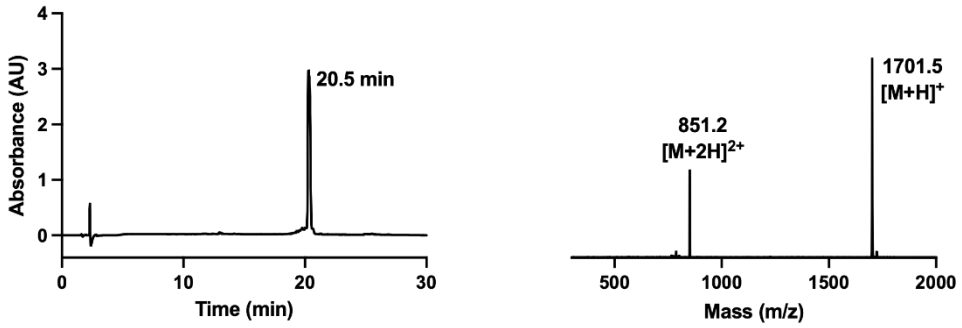
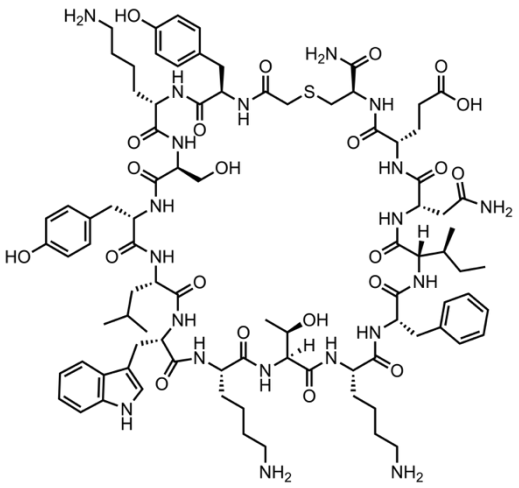


Figure 6.7. Analytical RP-HPLC: R_t = 20.5 min (1 to 80 vol.% MeCN in H_2O with 0.1 vol.% formic acid over 30 min, λ = 214 nm). **LRMS:** (+ESI) *m/z* 1701.5 $[M+H]^+$, 851.2 $[M+2H]^{2+}$.

(2.78): AD-02



Rink amide resin (50 µmol, ~0.6 mmol g^{-1}) was loaded with Fmoc-Cys(Trt)-OH according to general procedure **6.4.2**. The target peptide was then synthesised by iterative Fmoc-SPPS on the Syro I peptide synthesiser according to general procedure **6.4.2**, with chloroacetic acid the final coupling step according to general procedure **6.4.3** to generate the resin-bound sequence chloroacetyl-yKSYLWKTKFINEC. The peptide was cleaved from resin by general procedure **6.4.7**, and cyclised according to general procedure **6.4.8**. Purification by RP-HPLC (1 to 40 vol.% MeCN in H_2O with 0.1 vol.% formic acid over 40 min), followed by lyophilisation, afforded the pure peptide **2.78** as a white fluffy solid (21.7 mg, 23%).

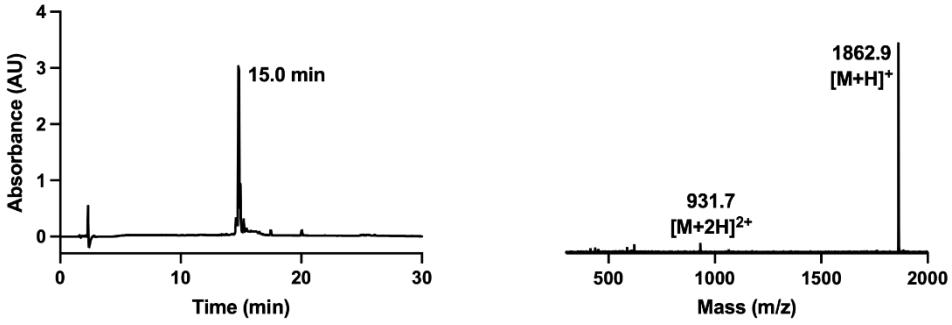
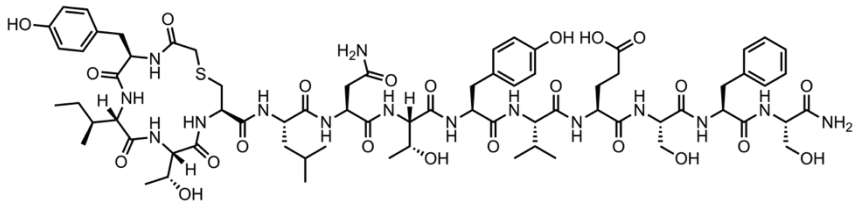


Figure 6.8. Analytical RP-HPLC: R_t = 15.0 min (1 to 80 vol.% MeCN in H_2O with 0.1 vol.% formic acid over 30 min, λ = 214 nm). **LRMS:** (+ESI) *m/z* 1862.9 $[M+H]^+$, 931.7 $[M+2H]^{2+}$.

(2.79): AD-04



Rink amide resin (50 µmol, ~0.6 mmol g^{-1}) was loaded with Fmoc-Ser(*t*Bu)-OH according to general procedure **6.4.2**. The target peptide was then synthesised by iterative Fmoc-SPPS on the Syro I peptide synthesiser according to general procedure **6.4.2**, with chloroacetic acid the final coupling step according to general procedure **6.4.3** to generate the resin-bound sequence chloroacetyl-yITCLNTYVESFS. The peptide was cleaved from resin by general procedure **6.4.7**, and cyclised according to general procedure **6.4.8**. Purification by RP-HPLC (1 to 60 vol.% MeCN in H_2O with 0.1 vol.% formic acid over 40 min), followed by lyophilisation, afforded the pure peptide **2.79** as a white fluffy solid (17.5 mg, 22%).

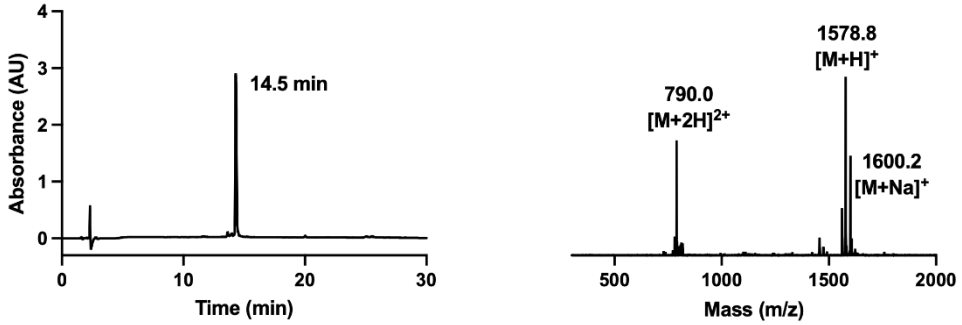
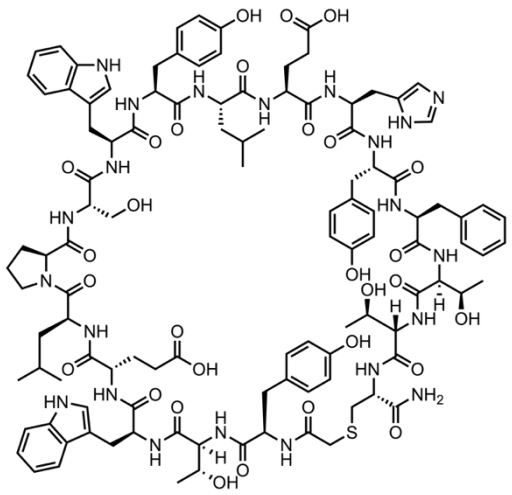


Figure 6.9. Analytical RP-HPLC: R_t = 14.5 min (1 to 80 vol.% MeCN in H_2O with 0.1 vol.% formic acid over 30 min, λ = 214 nm). **LRMS:** (+ESI) *m/z* 1600.2 $[M+Na]^+$, 1578.8 $[M+H]^+$, 790.0 $[M+2H]^{2+}$.

(2.80): AD-05



Rink amide resin (50 µmol, ~0.6 mmol g^{-1}) was loaded with Fmoc-Cys(Trt)-OH according to general procedure **6.4.2**. The target peptide was then synthesised by iterative Fmoc-SPPS on the Syro I peptide synthesiser according to general procedure **6.4.2**, with chloroacetic acid the final coupling step according to general procedure **6.4.3** to generate the resin-bound sequence chloroacetyl-yTWELPSWYLEHYFTTC. The peptide was cleaved from resin by general procedure **6.4.7**, and cyclised according to general procedure **6.4.8**. Purification by RP-HPLC (1 to 70 vol.% MeCN in H_2O with 0.1 vol.% formic acid over 40 min), followed by lyophilisation, afforded the pure peptide **2.80** as a white fluffy solid (3.3 mg, 3%).

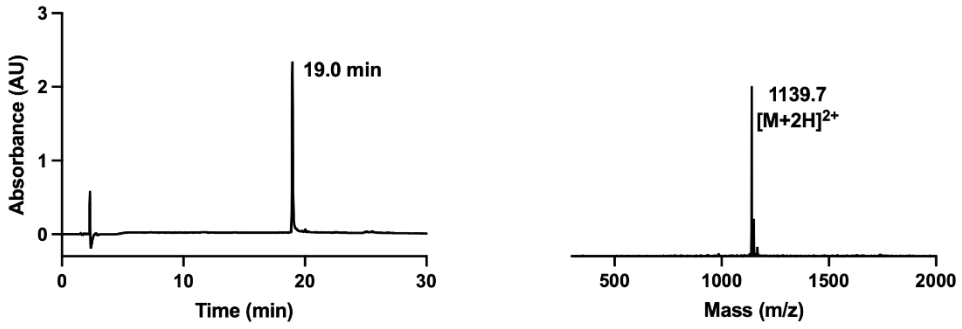
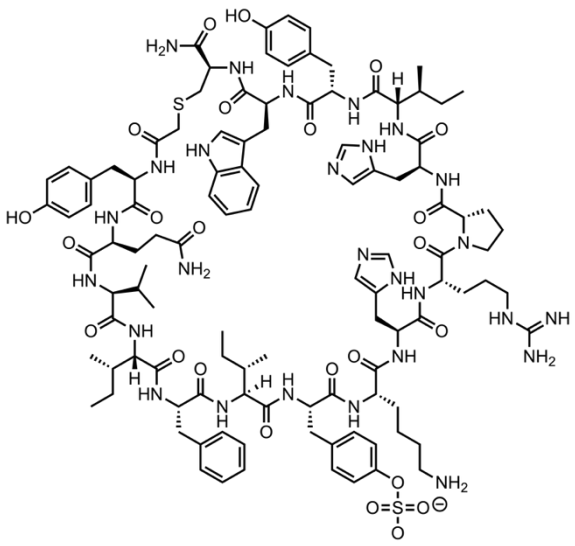


Figure 6.10. Analytical RP-HPLC: R_t = 19.0 min (1 to 80 vol.% MeCN in H_2O with 0.1 vol.% formic acid over 30 min, λ = 214 nm). **LRMS:** (+ESI) *m/z* 1139.7 $[M+2H]^{2+}$.

(2.81): AD-08



Rink amide resin (50 µmol, ~0.6 mmol g^{-1}) was loaded with Fmoc-Cys(Trt)-OH according to general procedure **6.4.1**. The target peptide was then synthesised by iterative Fmoc-SPPS on the Syro I peptide synthesiser according to general procedure **6.4.1**, with chloroacetic acid the final coupling step according to general procedure **6.4.3** to generate the resin-bound sequence chloroacetyl-ySA**sY**LYRVNDKVYLVC. The peptide was cleaved from resin by general procedure **6.4.7**, and cyclised according to general procedure **6.4.8**. Purification by RP-HPLC (1 to 80 vol.% MeCN in H_2O with 0.1 vol.% formic acid over 50 min), followed by lyophilisation, afforded the pure neopentyl protected peptide as a white fluffy solid. The peptide was subjected to neopentyl deprotection by general procedure **6.4.10** and subsequent purification by RP-HPLC (1 to 70 vol.% MeCN in H_2O with 0.1 vol.% formic acid over 50 min), followed by lyophilisation, afforded the pure peptide **2.81** as a white fluffy solid (3.2 mg, 3%).

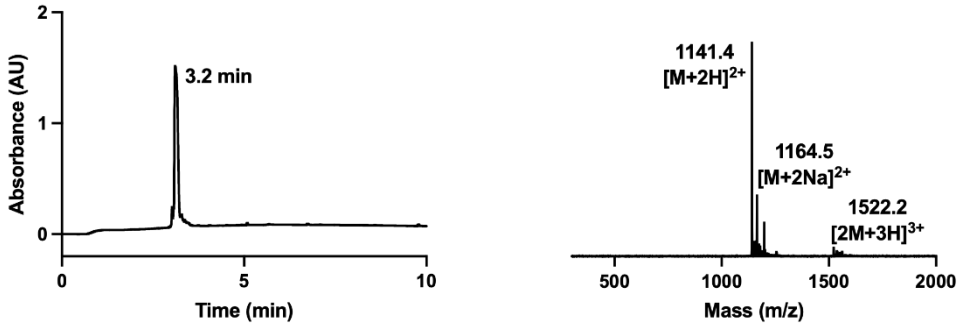
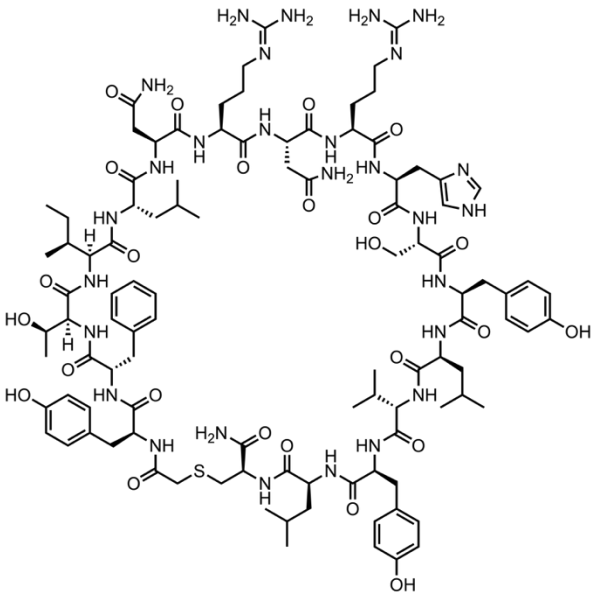


Figure 6.11. Analytical RP-HPLC: R_t = 3.2 min (1 to 100 vol.% MeCN in H_2O with 0.1 vol.% formic acid over 10 min, λ = 214 nm). **LRMS:** (+ESI) *m/z* 1522.2 $[2M+3H]^{3+}$, 1164.5 $[M+2Na]^{2+}$, 1141.4 $[M+2H]^{2+}$.

(2.82): AD-09



Rink amide resin (50 µmol, ~0.6 mmol g^{-1}) was loaded with Fmoc-Cys(Trt)-OH according to general procedure **6.4.2**. The target peptide was then synthesised by iterative Fmoc-SPPS on the Syro I peptide synthesiser according to general procedure **6.4.2**, with chloroacetic acid the final coupling step according to general procedure **6.4.3** to generate the resin-bound sequence chloroacetyl-yFTILNRNRHSYLVYLC. The peptide was cleaved from resin by general procedure **6.4.7**, and cyclised according to general procedure **6.4.8**. Purification by RP-HPLC (1 to 70 vol.% MeCN in H_2O with 0.1 vol.% formic acid over 40 min), followed by lyophilisation, afforded the pure peptide **2.82** as a white fluffy solid (4.9 mg, 4%).

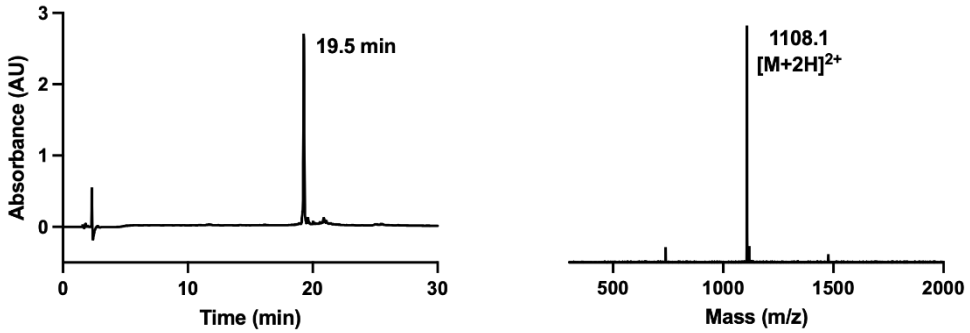
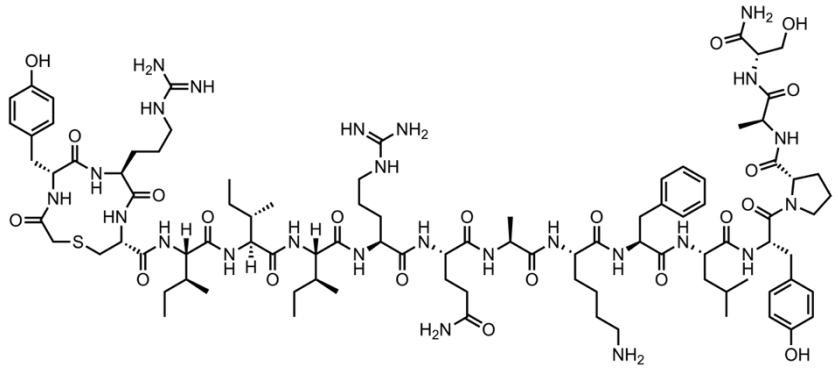


Figure 6.12. Analytical RP-HPLC: R_t = 19.5 min (1 to 80 vol.% MeCN in H_2O with 0.1 vol.% formic acid over 30 min, λ = 214 nm). **LRMS:** (+ESI) *m/z* 1108.1 $[M+2H]^{2+}$.

(2.83): AD-10



Rink amide resin (50 µmol, ~0.6 mmol g^{-1}) was loaded with Fmoc-Ser(*t*Bu)-OH according to general procedure **6.4.2**. The target peptide was then synthesised by iterative Fmoc-SPPS on the Syro I peptide synthesiser according to general procedure **6.4.2**, with chloroacetic acid the final coupling step according to general procedure **6.4.3** to generate the resin-bound sequence chloroacetyl-yRCIIIRQAKFLYPAS. The peptide was cleaved from resin by general procedure **6.4.7**, and cyclised according to general procedure **6.4.8**. Purification by RP-HPLC (1 to 55 vol.% MeCN in H_2O with 0.1 vol.% formic acid over 40 min), followed by lyophilisation, afforded the pure peptide **2.83** as a white fluffy solid (4.6 mg, 5%).

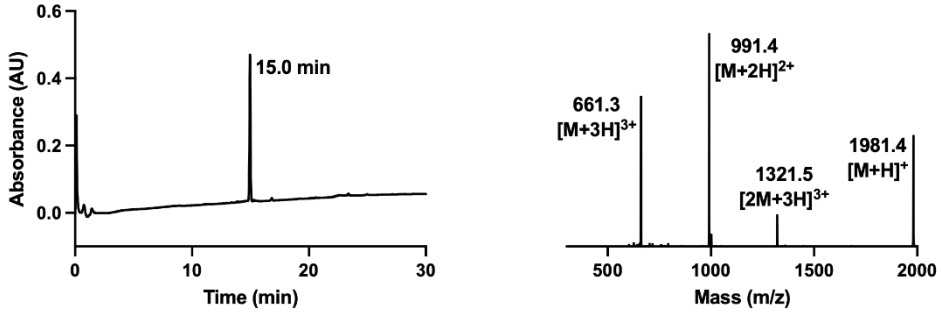
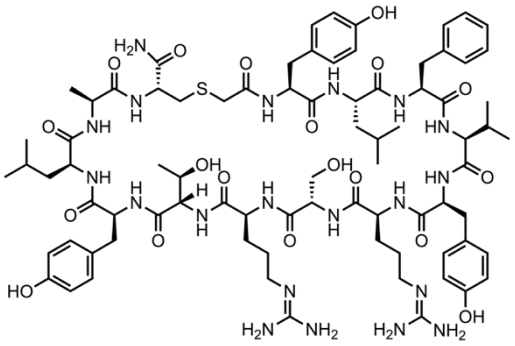


Figure 6.13. Analytical RP-HPLC: R_t = 15.0 min (1 to 70 vol.% MeCN in H_2O with 0.1 vol.% formic acid over 30 min, λ = 214 nm). **LRMS:** (+ESI) *m/z* 1981.4 $[M+H]^+$, 1321.5 $[2M+3H]^{3+}$, 991.4 $[M+2H]^{2+}$, 661.3 $[M+3H]^{3+}$.

(2.84): BL-01



Rink amide resin (50 µmol, ~0.6 mmol g^{-1}) was loaded with Fmoc-Cys(Trt)-OH according to general procedure **6.4.2**. The target peptide was then synthesised by iterative Fmoc-SPPS on the Syro I peptide synthesiser according to general procedure **6.4.2**, with chloroacetic acid the final coupling step according to general procedure **6.4.3** to generate the resin-bound sequence chloroacetyl-YLFVYRSRTYLAC. The peptide was cleaved from resin by general procedure **6.4.7**, and cyclised according to general procedure **6.4.8**. Purification by RP-HPLC (1 to 80 vol.% MeCN in H_2O with 0.1 vol.% formic acid over 40 min), followed by lyophilisation, afforded the pure peptide **2.84** as a white fluffy solid (8.2 mg, 10%).

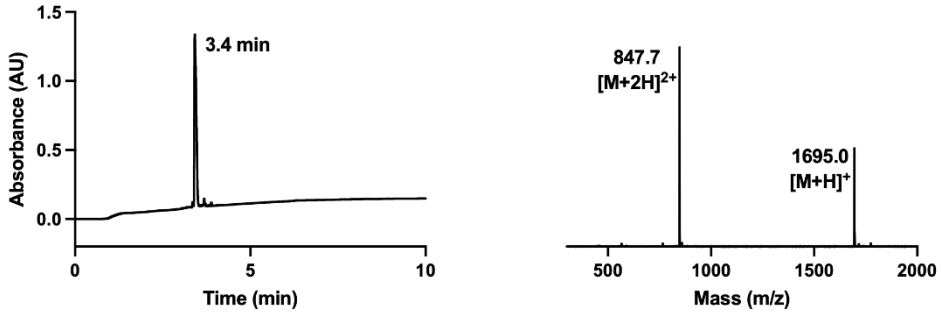
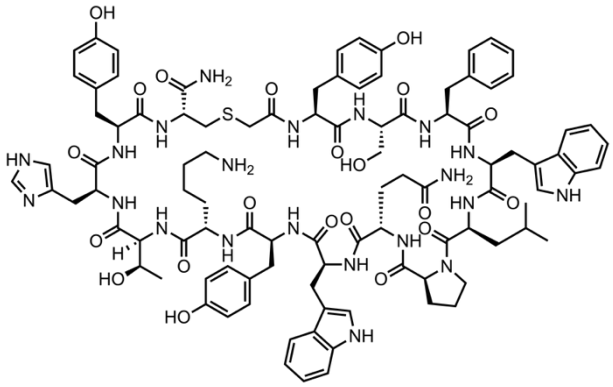


Figure 6.14. Analytical RP-HPLC: R_t = 3.4 min (1 to 100 vol.% MeCN in H_2O with 0.1 vol.% formic acid over 10 min, λ = 214 nm). **LRMS:** (+ESI) *m/z* 1695.0 $[M+H]^+$, 847.7 $[M+2H]^{2+}$.

(2.85): BL-04



Rink amide resin (50 µmol, ~0.6 mmol g^{-1}) was loaded with Fmoc-Cys(Trt)-OH according to general procedure **6.4.2**. The target peptide was then synthesised by iterative Fmoc-SPPS on the Syro I peptide synthesiser according to general procedure **6.4.2**, with chloroacetic acid the final coupling step according to general procedure **6.4.3** to generate the resin-bound sequence chloroacetyl-YSFWLPQWYKTHYC. The peptide was cleaved from resin by general procedure **6.4.7**, and cyclised according to general procedure **6.4.8**. Purification by RP-HPLC (1 to 80 vol.% MeCN in H_2O with 0.1 vol.% formic acid over 40 min), followed by lyophilisation, afforded the pure peptide **2.85** as a white fluffy solid (6.5 mg, 10%).

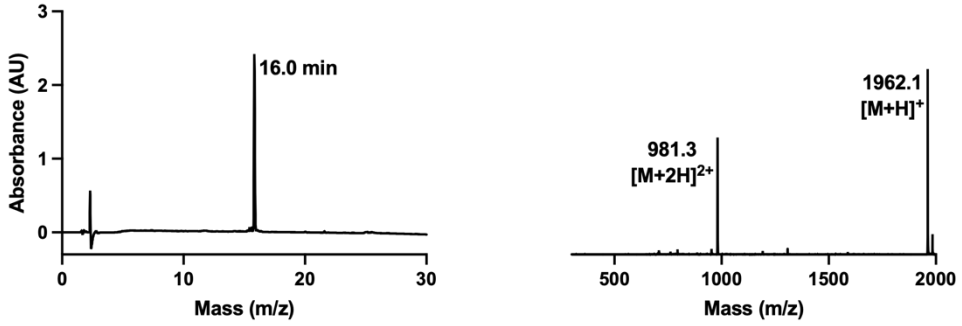
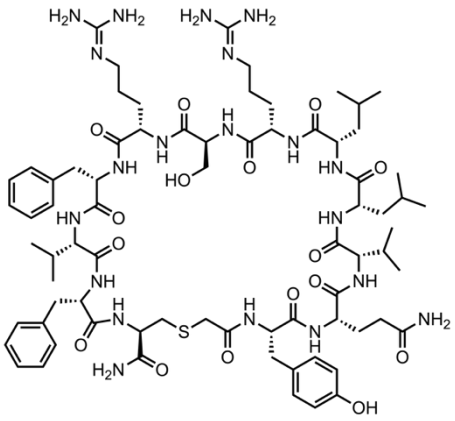


Figure 6.15. Analytical RP-HPLC: R_t = 16.0 min (1 to 80 vol.% MeCN in H_2O with 0.1 vol.% formic acid over 30 min, λ = 214 nm). **LRMS:** (+ESI) *m/z* 1962.1 $[M+H]^+$, 981.3 $[M+2H]^{2+}$.

(2.88): BL-09



Rink amide resin (50 µmol, ~0.6 mmol g^{-1}) was loaded with Fmoc-Cys(Trt)-OH according to general procedure **6.4.2**. The target peptide was then synthesised by iterative Fmoc-SPPS on the Syro I peptide synthesiser according to general procedure **6.4.2**, with chloroacetic acid the final coupling step according to general procedure **6.4.3** to generate the resin-bound sequence chloroacetyl-YQVLLRSRFVFC. The peptide was cleaved from resin by general procedure **6.4.7**, and cyclised according to general procedure **6.4.8**. Purification by RP-HPLC (1 to 80 vol.% MeCN in H_2O with 0.1 vol.% formic acid over 40 min), followed by lyophilisation, afforded the pure peptide **2.88** as a white fluffy solid (4.0 mg, 5%).

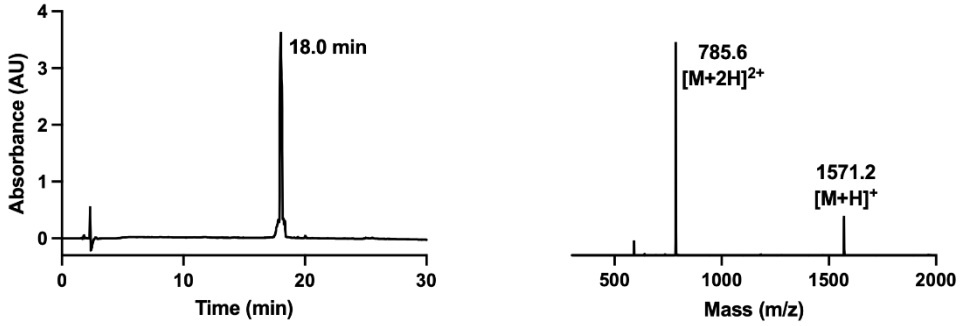
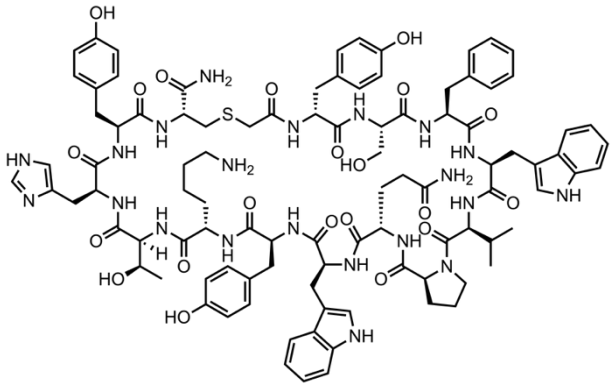


Figure 6.16. Analytical RP-HPLC: R_t = 18.0 min (1 to 80 vol.% MeCN in H_2O with 0.1 vol.% formic acid over 30 min, λ = 214 nm). **LRMS:** (+ESI) *m/z* 1571.2 $[M+H]^+$, 785.6 $[M+2H]^{2+}$.

(2.90): BD-13



Rink amide resin (50 µmol, ~0.6 mmol g^{-1}) was loaded with Fmoc-Cys(Trt)-OH according to general procedure **6.4.2**. The target peptide was then synthesised by iterative Fmoc-SPPS on the Syro I peptide synthesiser according to general procedure **6.4.2**, with chloroacetic acid the final coupling step according to general procedure **6.4.3** to generate the resin-bound sequence chloroacetyl-ySFWVPQWYKTHYC. The peptide was cleaved from resin by general procedure **6.4.7**, and cyclised according to general procedure **6.4.8**. Purification by RP-HPLC (1 to 75 vol.% MeCN in H_2O with 0.1 vol.% formic acid over 40 min), followed by lyophilisation, afforded the pure peptide **2.90** as a white fluffy solid (7.2 mg, 7%).

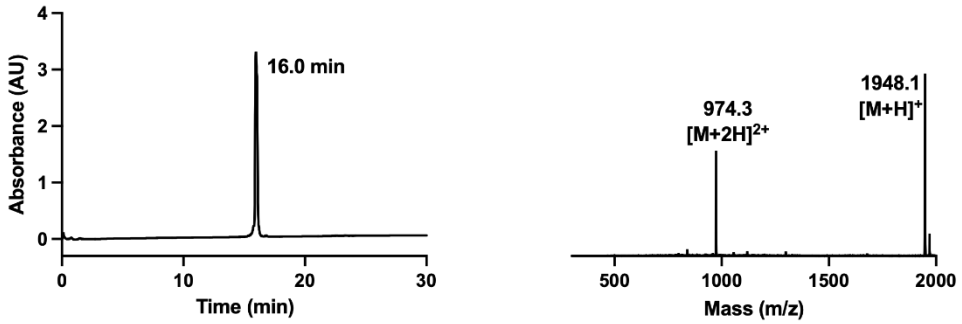
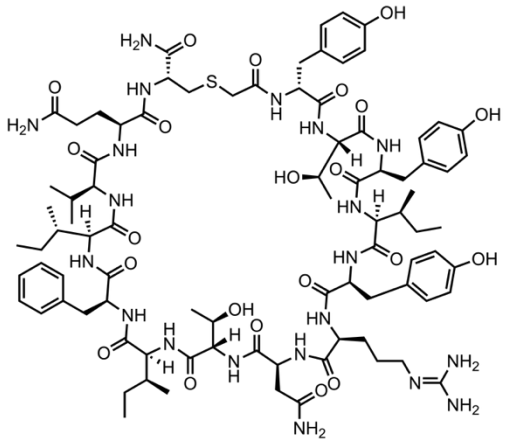


Figure 6.17. Analytical RP-HPLC: R_t = 16.0 min (1 to 70 vol.% MeCN in H_2O with 0.1 vol.% formic acid over 30 min, λ = 214 nm). **LRMS:** (+ESI) *m/z* 1948.1 $[M+H]^+$, 974.3 $[M+2H]^{2+}$.

(2.91): BD-14



Rink amide resin (50 µmol, ~0.6 mmol g^{-1}) was loaded with Fmoc-Cys(Trt)-OH according to general procedure **6.4.2**. The target peptide was then synthesised by iterative Fmoc-SPPS on the Syro I peptide synthesiser according to general procedure **6.4.2**, with chloroacetic acid the final coupling step according to general procedure **6.4.3** to generate the resin-bound sequence chloroacetyl-y TYIYRNTIFIVQC. The peptide was cleaved from resin by general procedure **6.4.7**, and cyclised according to general procedure **6.4.8**. Purification by RP-HPLC (1 to 70 vol.% MeCN in H_2O with 0.1 vol.% formic acid over 40 min), followed by lyophilisation, afforded the pure peptide **2.91** as a white fluffy solid (5.4 mg, 6%).

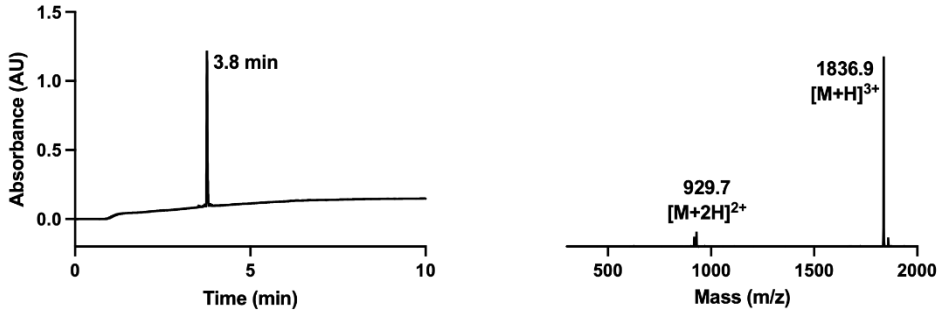
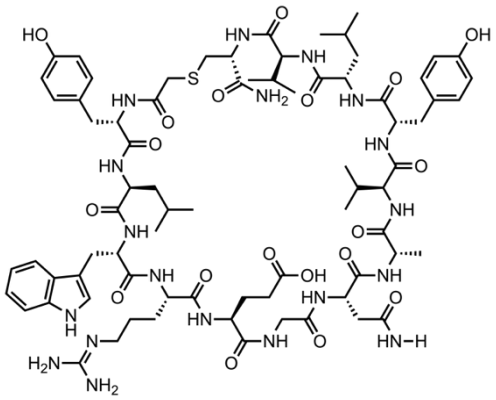


Figure 6.18. Analytical RP-HPLC: R_t = 3.8 min (1 to 100 vol.% MeCN in H_2O with 0.1 vol.% formic acid over 10 min, λ = 214 nm). **LRMS:** (+ESI) *m/z* 1836.9 $[M+H]^+$, 929.7 $[M+2H]^{2+}$.

(2.96): BL-22



Rink amide resin (50 µmol, ~0.6 mmol g^{-1}) was loaded with Fmoc-Cys(Trt)-OH according to general procedure **6.4.2**. The target peptide was then synthesised by iterative Fmoc-SPPS on the Syro I peptide synthesiser according to general procedure **6.4.2**, with chloroacetic acid the final coupling step according to general procedure **6.4.3** to generate the resin-bound sequence chloroacetyl-YLWREGNAVYLVC. The peptide was cleaved from resin by general procedure **6.4.7**, and cyclised according to general procedure **6.4.8**. Purification by RP-HPLC (1 to 70 vol.% MeCN in H_2O with 0.1 vol.% formic acid over 40 min), followed by lyophilisation, afforded the pure peptide **2.96** as a white fluffy solid (8.2 mg, 10%).

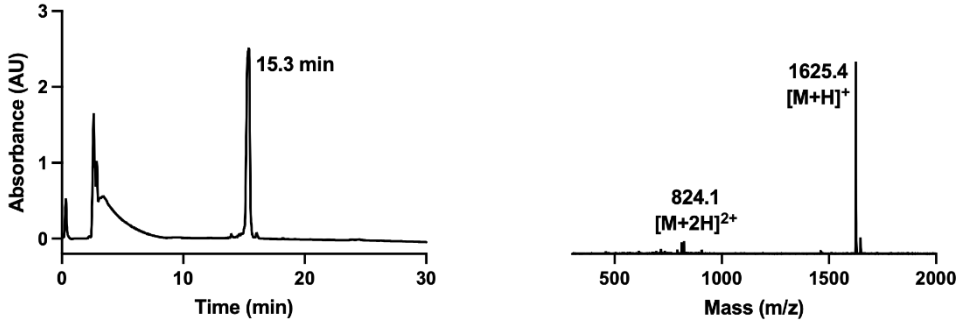
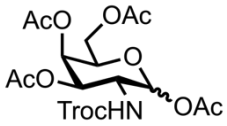


Figure 6.19. Analytical RP-HPLC: R_t = 3.8 min (1 to 70 vol.% MeCN in H_2O with 0.1 vol.% formic acid over 30 min, λ = 214 nm). **LRMS:** (+ESI) *m/z* 1625.4 $[M+H]^+$, 824.1 $[M+2H]^{2+}$.

6.5.6 Synthesis of Fmoc-Ser(*O*-β-D-GalNAc(OAc)$_3$)-OH

(2.101): 1,3,4,6-tetra-*O*-acetyl-2-*N*-(2,2,2-trichloroethoxycarbonyl)-2-amino-2-deoxy-D-galactopyranose

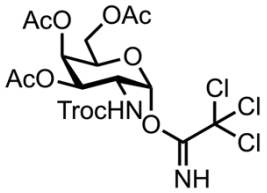


To a solution of galactosamine hydrochloride (10.8 g, 50 mmol) in H_2O (150 mL) was added $NaHCO_3$ (12.6 g, 150 mmol, 3 eq) and trichloroethyl chloroformate (TrocCl) (9.8 mL, 75 mmol, 1.5 eq). The reaction mixture was stirred at rt for 6 h. Subsequently, a solid separated out which was filtered and dried to afford the Troc-protected amine. The crude compound was added to a mixture of pyridine:Ac_2O (2:1 v/v, total volume 50 mL), and a few crystals of DMAP were added, and mixture was stirred at rt for 16 h. Upon completion, as determined by LC-MS, the mixture was concentrated *in vacuo*. The crude material was diluted with EtOAc (200 mL), washed with 1 M HCl (3 x 100 mL), sat. aq. $CuSO_4$ solution (100 mL), brine (100 mL), and sat. aq. $NaHCO_3$ solution (100 mL). The combined organic layers were dried over $MgSO_4$, filtered, and concentrated *in vacuo*. The crude product was purified by flash column chromatography (20-60% EtOAc:hexanes) to afford **2.101** as a white solid (18.8 g, 72%) as a mixture of anomers (α/β 3:4).

^{1}H NMR (300 MHz, $CDCl_3$) δ 6.27 (d, *J* = 3.7 Hz, 1H), 5.75 (d, *J* = 8.8 Hz, 1H), 5.42 (ddd, *J* = 13.2, 3.3, 1.2 Hz, 1H), 5.22 (dd, *J* = 11.3, 3.4 Hz, 1H), 5.14 (dd, *J* = 11.3, 3.2 Hz, 1H), 5.07 (d, *J* = 9.6 Hz, 1H), 4.83 (d, *J* = 12.1 Hz, 1H), 4.72 (d, *J* = 2.3 Hz, 1H), 4.62 (d, *J* = 12.1 Hz, 1H), 4.43 (ddd, *J* = 11.4, 9.6, 3.7 Hz, 1H), 4.28 – 4.21 (m, 1H), 4.19 – 4.01 (m, 6H), 2.18 (s, 3H), 2.17 (s, 3H), 2.16 (s, 3H), 2.12 (s, 3H), 2.04 (s, 3H), 2.03 (s, 3H), 2.03 (s, 3H), 2.00 (s, 3H) ppm.

This is in agreement with the data reported by Wrodnigg *et al*.[419]

(2.102): 3,4,6-tri-*O*-Acetyl-2-*N*-(2,2,2-trichloroethoxycarbonyl)-2-amino-2-deoxy-α-D-galactopyranosyl trichloroacetimidate

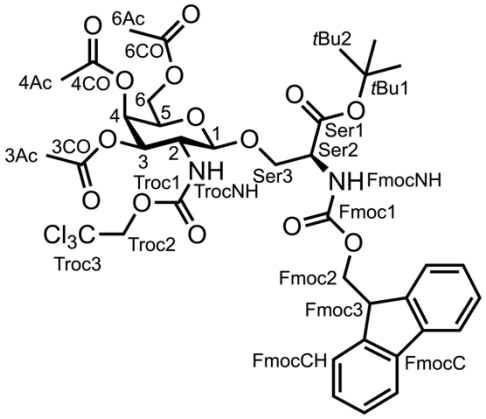


To **2.101** (8.09 g, 15 mmol) in THF (120 mL) was added glacial acetic acid (8.1 g, 15 mmol, 1 eq) and ethylenediamine (1.2 mL, 19 mmol, 1.2 eq). The reaction was stirred at rt for 2 h, before being diluted with water (200 mL). The aqueous layer was extracted with EtOAc (3 x 200 mL), washed with brine (100 mL), and the combined organic layers were dried over $MgSO_4$, filtered, and concentrated *in vacuo*. The crude material was dissolved in CH_2Cl_2 (80 mL), followed by addition of trichloroacetonitrile (7.8 mL, 77 mmol, 5 eq) and DBU (0.6 mL, 3.9 mmol, 0.25 eq). The reaction was stirred at rt for 4 h, and upon completion, concentrated *in vacuo*. The residue was purified by flash column chromatography (30% EtOAc:hexanes, 0.1% NEt_3) to provide the product (**2.102**) as a white solid (8.0 g, 83%).

^{1}H NMR (500 MHz, $CDCl_3$) δ 8.79 (s, 1H), 6.46 (d, *J* = 3.7 Hz, 1H), 5.51 (dd, *J* = 3.2, 1.4 Hz, 1H), 5.28 (dd, *J* = 11.5, 3.2 Hz, 1H), 5.12 (d, *J* = 9.6 Hz, 1H), 4.75 (d, *J* = 12.0 Hz, 1H), 4.70 (d, *J* = 12.0 Hz, 1H), 4.52 (ddd, *J* = 11.4, 9.6, 3.7 Hz, 1H), 4.40 – 4.35 (m, 1H), 4.20 – 4.05 (m, 3H), 2.19 (s, 3H), 2.02 (s, 3H), 2.02 (s, 3H) ppm.

This is in agreement with the data reported by Sun *et al*.[420]

(2.103): *N*-(9*H*-Fluoren-9-ylmethoxycarbonyl)-*O*-(3,4,6-tri-*O*-Acetyl-2-*N*-(2,2,2-trichloroethoxycarbonyl)-2-amino-2-deoxy-β-D-galactopyranosyl)-L-serine *tert*-butyl ester

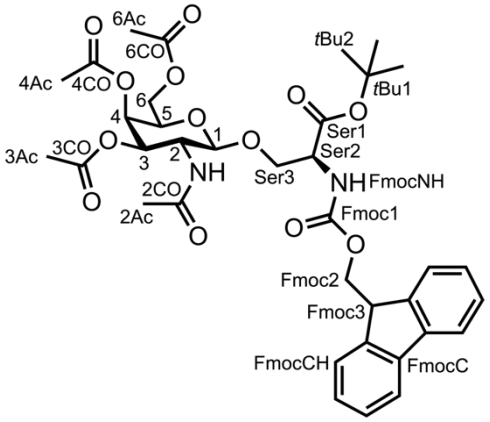


To a solution of **2.102** (1.50 g, 2.4 mmol), Fmoc-Ser-*t*Bu (1.01 g, 2.6 mmol, 1.1 eq) and 4Å MS in anhydrous CH_2Cl_2 (25 mL) was added TMSOTf (8 uL, 0.05 mmol, 0.02 eq) at -78 °C. The pale-yellow reaction mixture was stirred while slowly warming to rt over a period of 2 h. The reaction mixture was neutralised with Et_3N (1 drop), filtered through thin pad of celite saturated with CH_2Cl_2, and the filtrate concentrated *in vacuo*. The crude product was purified by flash column chromatography (20-50% EtOAc:hexanes) to provide the desired product **2.103** as a white foam (1.60 g, 79%).

$[\alpha]^{25}_D$ + 0.7 (*c* 10, $CHCl_3$); **IR** (thin film): 3314 (N-H streth), 1740 (C=O ester stretch), 1524 (N-H amide bend), 1450 (C=C aromatic stretch) cm^{-1}; **^{1}H NMR** (500 MHz, $CDCl_3$) δ 7.80 – 7.74 (m, 2H, FmocCH), 7.68 – 7.60 (m, 2H, FmocCH), 7.44 – 7.37 (m, 2H, FmocCH), 7.36 – 7.29 (m, 2H, FmocCH), 5.79 – 5.75 (m, 1H, FmocNH), 5.36 (dd, $J_{4,3}$ = 3.4 Hz, $J_{4,5}$ = 1.1 Hz, 1H, H-4), 5.20 – 5.14 (m, 1H, H-3), 5.14 (s, 1H, TrocNH), 4.80 – 4.74 (m, 1H, Troc2), 4.66 (d, $J_{1,2}$ = 8.0 Hz, 1H, H-1), 4.51 (t, *J* = 8.3 Hz, 1H, Fmoc2'), 4.48 – 4.43 (m, 1H), 4.43 – 4.38 (m, 1H, Ser2), 4.29 (d, *J* = 8.4 Hz, 1H, Fmoc2''), 4.24 (t, *J* = 7.1 Hz, 1H, Fmoc3), 4.19 – 4.15 (m, 1H, Ser3''), 4.13 (d, $J_{6,5}$ = 6.6 Hz, 2H, H-6), 3.93 (dd, *J* = 10.6, 2.9 Hz, 1H, Ser3'), 3.88 (td, $J_{5,6}$ = 6.6 Hz, $J_{5,4}$ = 1.2 Hz, 1H, H-5), 3.84 – 3.71 (m, 1H, H-2), 2.13 (s, 3H, 4Ac), 2.04 (s, 3H, 3Ac), 1.99 (s, 3H, 6Ac), 1.49 (s, 9H, *t*Bu2) ppm; **^{13}C NMR** (126 MHz, $CDCl_3$) δ 170.5

(3CO), 170.4 (6CO), 170.2 (C-4CO), 168.6 (Ser1), 156.3 (Fmoc1), 154.4 (Troc1), 141.5 (C-FmocC), 141.4 (C-FmocC), 127.9 (C-FmocCH), 127.3 (C-FmocCH), 125.2 (FmocCH), 120.2 (FmocCH), 100.6 (C-1), 95.6 (Troc3), 83.0 (*t*Bu1), 74.5 (Troc2), 70.9 (C-5), 69.3 (Ser3), 67.4 (Fmoc2), 66.8 (C-4), 61.5 (C-6), 54.6 (Ser2), 52.9 (C-2), 47.3 (Fmoc3), 28.1 (*t*Bu2), 20.8 (3Ac), 20.7 (4Ac), 20.7 (6Ac) ppm; **HRMS** (ESI+) *m/z* Calc. for $C_{37}H_{43}Cl_3N_2O_{14}$ $[M + Na]^+$: 867.1678, found 867.1672.

(2.104): *N*-(9*H*-Fluoren-9-ylmethoxycarbonyl)-*O*-(3,4,6-tri-*O*-Acetyl-2-acetyl-2-amino-2-deoxy-β-D-galactopyranosyl)-L-serine *tert*-butyl ester

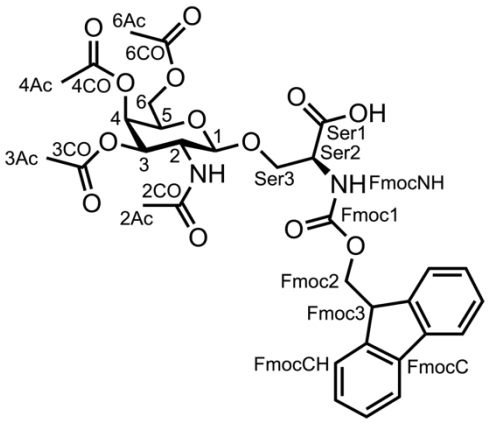


To a solution of **2.103** (800 mg, 0.9 mmol) in acetic anhydride (10 mL) was added zinc powder (620 mg, 9.5 mmol, 10 eq). The mixture was stirred vigorously at room temperature for 2 h. Upon completion, as determined by TLC, the solution was filtered through a pad of celite saturated with MeOH before being concentrated *in vacuo*, followed by co-evaporation with toluene. The crude material was purified *via* flash column chromatography (20-60% EtOAc:hexanes) to provide the desired product **2.104** as a white foam (590 mg, 88%).

$[\alpha]^{25}_D$ - 6.4 (*c* 10, $CHCl_3$); **IR** (thin film): 3310 (N-H stretch), 1742 (C=O ester stretch), 1666 (C=O carbamate stretch), 1524 (N-H amide bend), 1450 (C=C aromatic stretch) cm^{-1}; **^{1}H NMR** (500 MHz, $CDCl_3$) δ 7.81 – 7.74 (m, 2H, FmocCH), 7.68 – 7.62 (m, 2H, FmocCH), 7.43 – 7.37 (m, 2H, FmocCH), 7.35 – 7.30 (m, 2H, FmocCH), 5.75 (d, *J* = 8.0 Hz, 1H, FmocNH), 5.45 (d, *J* = 8.5 Hz, 1H, AcNH), 5.34 (d, $J_{4,3}$ = 3.4 Hz, 1H, H-4), 5.23 (dd, $J_{3,2}$ = 11.3 Hz, $J_{3,4}$ = 3.4 Hz, 1H, H-3), 4.66 (d, $J_{1,2}$ = 8.4 Hz, 1H, H-1), 4.51 – 4.40 (m, 2H, Fmoc2), 4.38

– 4.33 (m, 1H, Ser2), 4.23 (t, *J* = 6.7 Hz, 1H, Fmoc3), 4.18 (dd, *J* = 10.7, 3.9 Hz, 1H, Ser3'), 4.12 (d, $J_{6,5}$ = 6.6 Hz, 2H, H-6), 3.93 – 3.89 (m, 1H, H-2), 3.89 – 3.86 (m, 1H, Ser3''), 3.86 – 3.82 (m, 1H, H-5), 2.12 (s, 3H, 4Ac), 2.03 (s, 3H, 3Ac), 2.00 (s, 3H, 6Ac), 1.86 (s, 3H, 2Ac), 1.47 (s, 9H, *t*Bu2) ppm; **^{13}C NMR** (126 MHz, $CDCl_3$) δ 170.8 (2CO), 170.6 – 170.5 (m, 6CO), 170.5 (3CO), 170.3 (4CO), 168.7 (Ser1), 156.1 (Fmoc1), 143.9 (FmocC), 141.5 (FmocC), 127.9 (FmocCH), 127.3 (FmocCH), 125.3 (FmocCH), 120.1 (FmocCH), 101.0 (C-1), 82.9 (*t*Bu1), 70.9 (C-5), 70.0 (C-3), 69.3 (Ser3), 66.8 (Fmoc2, C-4), 61.6 (C-6), 54.9 (Ser2), 28.0 (*t*Bu2), 23.4 (2Ac), 51.6 (C-2), 47.4 (Fmoc3), 20.8 (3Ac, 4Ac, 6Ac) ppm; **HRMS** (ESI+) *m/z* Calc. for $C_{36}H_{44}N_2O_{13}$ $[M + Na]^+$: 735.2741, found 735.2736.

(2.99): *N*-(9*H*-Fluoren-9-ylmethoxycarbonyl)-*O*-(3,4,6-tri-*O*-Acetyl-2-acetyl-2-amino-2-deoxy-β-D-galactopyranosyl)-L-serine



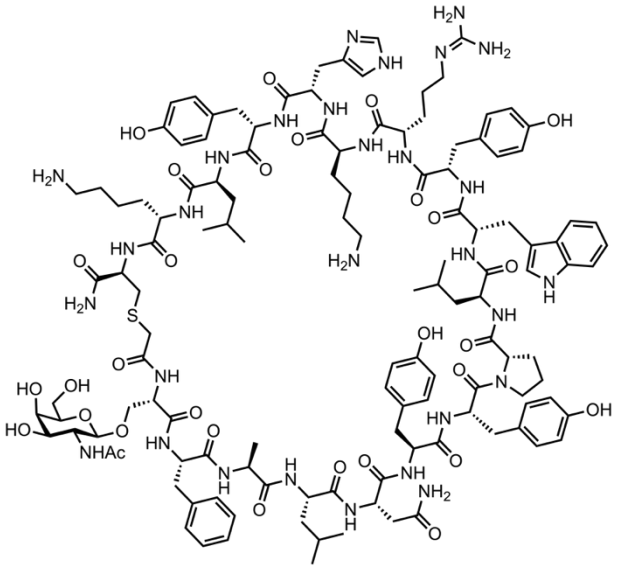
To **2.104** (1.38 g, 1.94 mmol) was added a solution TFA/H_2O (20 mL, 19:1 v/v), and the reaction was stirred at rt for 2 h. Upon completion, as determined by LC-MS, the solution was concentrated *in vacuo*, followed by co-evaporation with toluene, to provide the desired carboxylic acid **2.99** as a white foam (1.22 g, 96%).

$[\alpha]^{25}_D$ - 6.0 (*c* 10, MeOH); **IR** (thin film): 3335 (O-H, N-H stretch), 1745 (C=O ester stretch), 1720 (C=O stretch carboxylic acid), 1666 (C=O carbamate stretch), 1531 (N-H amide bend), 1450 (C=C aromatic stretch) cm^{-1}; **^{1}H NMR** (500 MHz, MeOD) δ 7.82 – 7.77 (m, 2H, FmocCH), 7.72 – 7.65 (m, 2H, FmocCH), 7.43 – 7.36 (m, 2H, FmocCH), 7.36 – 7.29 (m, 2H, FmocCH), 5.33 (dd, $J_{4,3}$ = 3.4 Hz, $J_{4,5}$ = 1.2 Hz, 1H, H-4), 5.08 (dd, $J_{3,2}$ = 11.2 Hz, $J_{3,4}$ =

3.4 Hz, 1H, H-3), 4.63 (d, $J_{1,2}$ = 8.4 Hz, 1H, H-1), 4.44 (dd, *J* = 10.5, 6.7 Hz, 1H, Fmoc2'), 4.38 (t, *J* = 4.6 Hz, 1H, Ser2), 4.33 (dd, *J* = 10.6, 6.9 Hz, 1H, Fmoc2''), 4.24 (t, *J* = 6.8 Hz, 1H, Fmoc3), 4.17 – 4.14 (m, 1H, Ser3'), 4.11 (dd, $J_{6',6''}$ = 11.9 Hz, $J_{6,5}$ = 7.0 Hz, 2H, H-6), 4.06 (dd, $J_{2,3}$ = 11.3 Hz, $J_{2,1}$ = 8.5 Hz, 1H, H-2), 3.99 (td, $J_{5,6}$ = 6.7 Hz, $J_{5,4}$ = 1.1 Hz, 1H, H-5), 3.92 (dd, *J* = 10.5, 4.0 Hz, 1H, Ser3''), 2.12 (s, 3H, 4Ac), 2.00 (s, 3H, 6Ac), 1.95 (s, 3H, 3Ac), 1.88 (s, 3H, 2Ac) ppm; **^{13}C NMR** (126 MHz, MeOD) δ 173.9 (2CO), 173.1 (Ser1), 172.1 (6CO), 172.1 (4CO), 171.7 (3CO), 158.4 (Fmoc1), 145.3 (FmocC), 142.6 (FmocC), 128.8 (FmocCH), 128.2 (FmocCH), 126.3 (FmocCH), 120.9 (FmocCH), 102.5 (C-1), 71.9 (C-3, C-5), 70.0 (Ser3), 68.1 (C-4), 68.1 (Fmoc2), 62.6 (C-6), 55.6 (Ser2), 51.5 (C-2), 48.4 (Fmoc3), 22.9 (2Ac), 20.6 (6Ac), 20.5 (4Ac), 20.5 (3Ac) ppm; **HRMS** (ESI+) *m/z* Calc. for $C_{32}H_{37}N_2O_{13}$ $[M + H]^+$: 657.2296, found 657.2290.

6.5.7 Synthesis of Cyclic Peptides incorporating GalNAc

(2.105): Gal-01



Rink amide resin (50 µmol, ~0.3 mmol g^{-1}) was loaded with Fmoc-Cys(Trt)-OH according to general procedure **6.4.1**. The target peptide was then synthesised by iterative Fmoc-SPPS on the Syro I peptide synthesiser according to general procedure **6.4.1**, with Fmoc-Phe-OH as the final coupling step to generate the resin-bound sequence FALNYYPLWYRKHYLKC. Fmoc-Ser(β-GalNAc$(OAc)_3$)-OH was coupled to the peptide on-resin by general procedure **6.4.5**, followed by coupling of chloroacetic acid by general procedure **6.4.6**. The peptide was cleaved from resin by general procedure **6.4.7**, and cyclised according to general procedure **6.4.9**. The peptide was deacetylated according to general procedure **6.4.11**. Purification by mass-directed RP-HPLC (1 to 70 vol.% MeCN in H_2O with 0.1 vol.% formic acid over 40 min), followed by lyophilisation, afforded the pure peptide **2.105** as a white fluffy solid (1.0 mg, 1%).

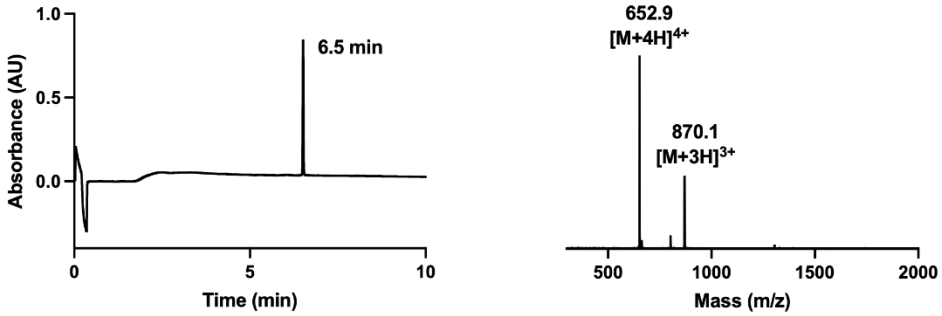
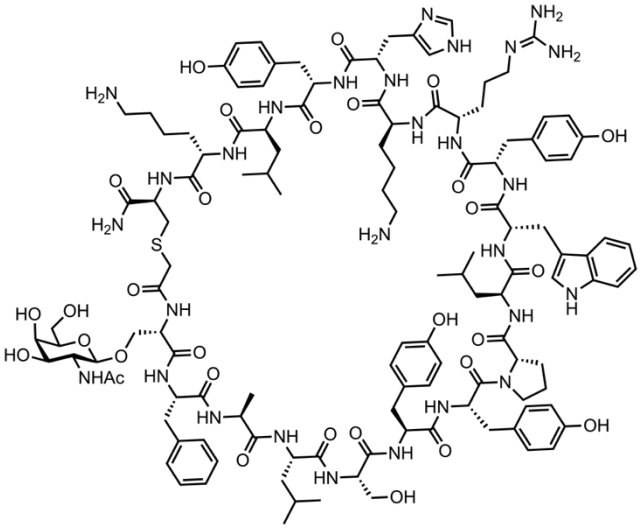


Figure 6.20. Analytical RP-HPLC: R_t = 6.5 min (1 to 60 vol.% MeCN in H_2O with 0.1 vol.% formic acid over 10 min, λ = 214 nm). **LRMS:** (+ESI) *m/z* 870.1 $[M+3H]^{3+}$, 652.9 $[M+4H]^{4+}$.

(2.106): Gal-02



Rink amide resin (50 µmol, ~0.3 mmol g^{-1}) was loaded with Fmoc-Cys(Trt)-OH according to general procedure **6.4.1**. The target peptide was then synthesised by iterative Fmoc-SPPS on the Syro I peptide synthesiser according to general procedure **6.4.1**, with Fmoc-Phe-OH as the final coupling step to generate the resin-bound sequence FALSYYPLWYRKHYLKC. Fmoc-Ser(β-GalNAc(OAc)$_3$)-OH was coupled to the peptide on-resin by general procedure **6.4.5**, followed by coupling of chloroacetic acid by general procedure **6.4.6**. The peptide was cleaved from resin by general procedure **6.4.7**, and cyclised according to general procedure **6.4.9**. The peptide was deacetylated according to general procedure **6.4.11**. Purification by mass-directed RP-HPLC (1 to 80 vol.% MeCN in H_2O with 0.1 vol.% formic acid over 40 min), followed by lyophilisation, afforded the pure peptide **2.106** as a white fluffy solid (3.1 mg, 2%).

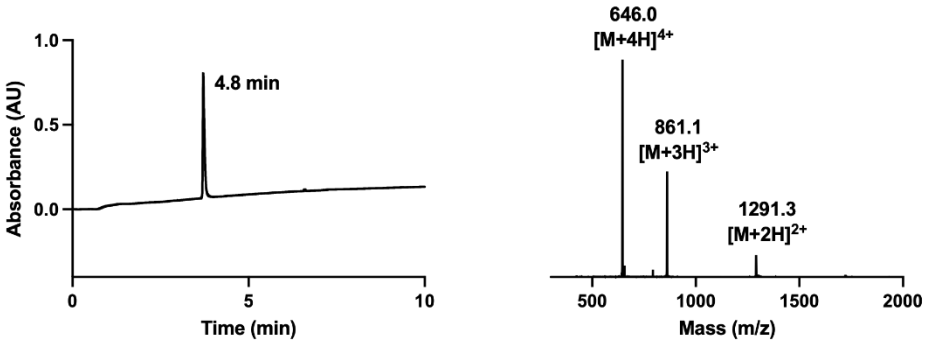
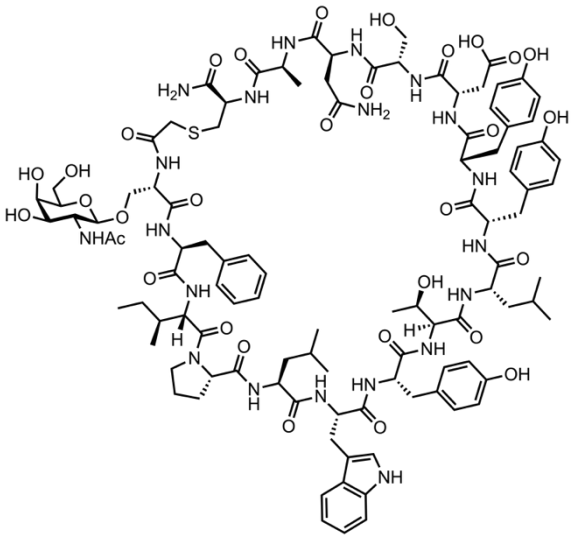


Figure 6.21. Analytical RP-HPLC: R_t = 4.8 min (1 to 70 vol.% MeCN in H_2O with 0.1 vol.% formic acid over 10 min, λ = 214 nm). **LRMS:** (+ESI) *m/z* 1291.3 $[M+2H]^{2+}$, 861.1 $[M+3H]^{3+}$, 646.0 $[M+4H]^{4+}$.

(2.107): Gal-03



Rink amide resin (50 μmol, ~0.3 mmol g^{-1}) was loaded with Fmoc-Cys(Trt)-OH according to general procedure **6.4.1**. The target peptide was then synthesised by iterative Fmoc-SPPS on the Syro I peptide synthesiser according to general procedure **6.4.1**, with Fmoc-Phe-OH as the final coupling step to generate the resin-bound sequence FIPLWYTLYYDSNAC. Fmoc-Ser(β-GalNAc$(OAc)_3$)-OH was coupled to the peptide on-resin by general procedure **6.4.5**, followed by coupling of chloroacetic acid by general procedure **6.4.6**. The peptide was cleaved from resin by general procedure **6.4.7**, and cyclised according to general procedure **6.4.9**. The peptide was deacetylated according to general procedure **6.4.11**. Purification by mass-directed RP-HPLC (1 to 80 vol.% MeCN in H_2O with 0.1 vol.% formic acid over 40 min), followed by lyophilisation, afforded the pure peptide **2.107** as a white fluffy solid (2.2 mg, 2%).

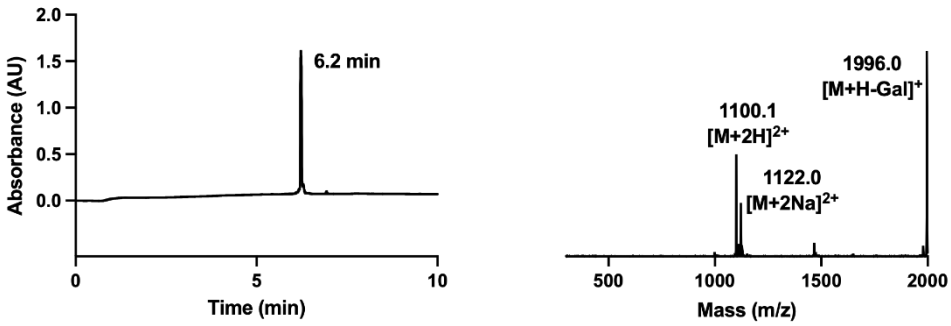
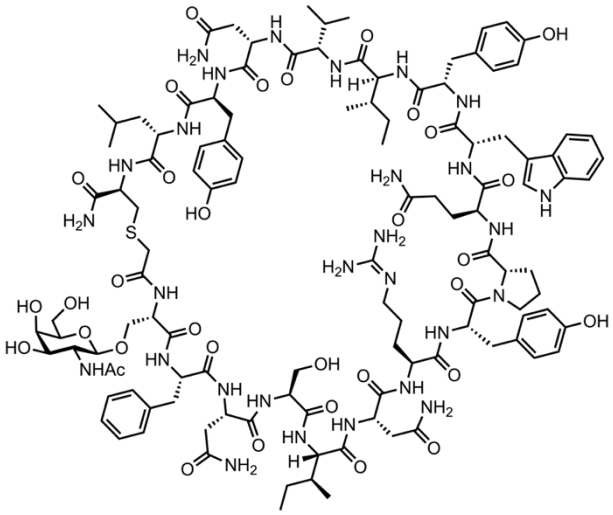


Figure 6.22. Analytical RP-HPLC: R_t = 6.2 min (1 to 70 vol.% MeCN in H_2O with 0.1 vol.% formic acid over 10 min, λ = 214 nm). **LRMS:** (+ESI) *m/z* 1996.0 $[M+H\text{-}Gal]^+$, 1122.0 $[M+2Na]^{2+}$, 1100.1 $[M+2H]^{2+}$.

(2.108): Gal-05



Rink amide resin (50 µmol, ~0.3 mmol g^{-1}) was loaded with Fmoc-Cys(Trt)-OH according to general procedure **6.4.1**. The target peptide was then synthesised by iterative Fmoc-SPPS on the Syro I peptide synthesiser according to general procedure **6.4.1**, with Fmoc-Phe-OH as the final coupling step to generate the resin-bound sequence FNSINRYPQWYIVNYLC. Fmoc-Ser(β-GalNAc(OAc)$_3$)-OH was coupled to the peptide on-resin by general procedure **6.4.5**, followed by coupling of chloroacetic acid by general procedure **6.4.6**. The peptide was cleaved from resin by general procedure **6.4.7**, and cyclised according to general procedure **6.4.9**. The peptide was deacetylated according to general procedure **6.4.11**. Purification by mass-directed RP-HPLC (1 to 80 vol.% MeCN in H_2O with 0.1 vol.% formic acid over 40 min), followed by lyophilisation, afforded the pure peptide **2.108** as a white fluffy solid (0.5 mg, 0.4%).

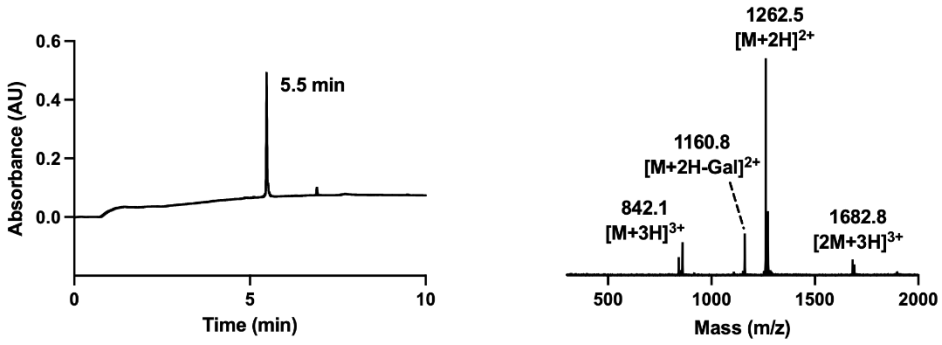
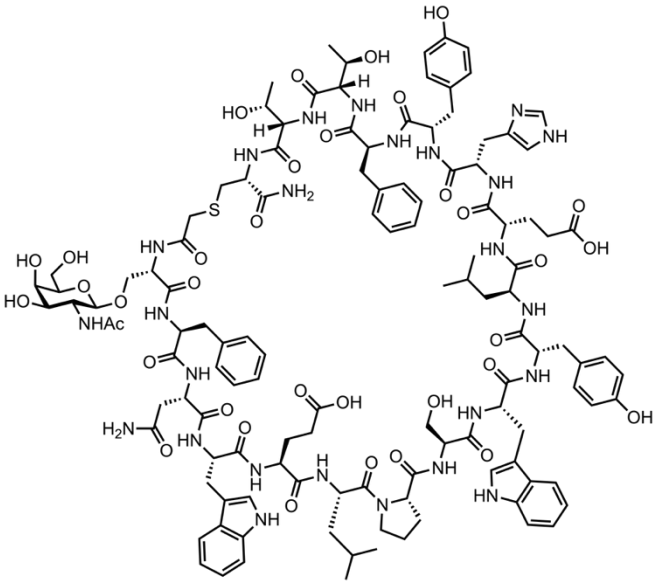


Figure 6.23. Analytical RP-HPLC: R_t = 5.5 min (1 to 70 vol.% MeCN in H_2O with 0.1 vol.% formic acid over 10 min, λ = 214 nm). **LRMS:** (+ESI) *m/z* 1682.8 $[2M+3H]^{3+}$, 1262.5 $[M+2H]^{2+}$, 1160.8 $[M+2H\text{-Gal}]^{2+}$, 842.1 $[M+3H]^{3+}$.

(2.109): Gal-06



Rink amide resin (50 µmol, ~0.3 mmol g^{-1}) was loaded with Fmoc-Cys(Trt)-OH according to general procedure **6.4.1**. The target peptide was then synthesised by iterative Fmoc-SPPS on the Syro I peptide synthesiser according to general procedure **6.4.1**, with Fmoc-Phe-OH as the final coupling step to generate the resin-bound sequence FNWELPSWYLEHYFTTC. Fmoc-Ser(β-GalNAc$(OAc)_3$)-OH was coupled to the peptide on-resin by general procedure **6.4.5**, followed by coupling of chloroacetic acid by general procedure **6.4.6**. The peptide was cleaved from resin by general procedure **6.4.7**, and cyclised according to general procedure **6.4.9**. The peptide was deacetylated according to general procedure **6.4.11**. Purification by mass-directed RP-HPLC (1 to 70 vol.% MeCN in H_2O with 0.1 vol.% formic acid over 40 min), followed by lyophilisation, afforded the pure peptide **2.109** as a white fluffy solid (4.8 mg, 4%).

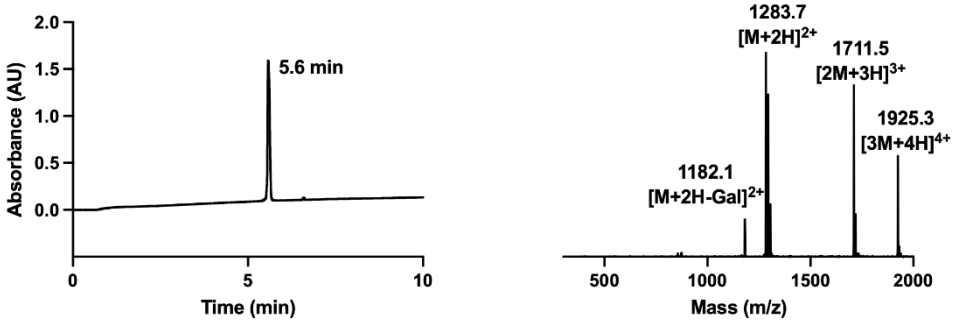
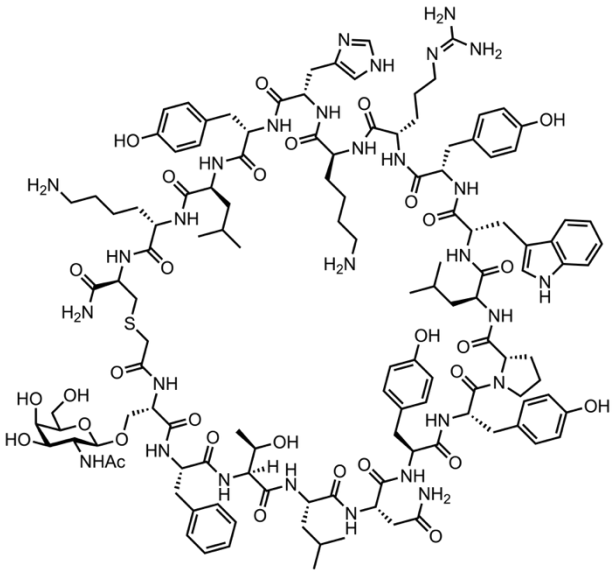


Figure 6.24. Analytical RP-HPLC: R_t = 5.6 min (1 to 70 vol.% MeCN in H_2O with 0.1 vol.% formic acid over 10 min, λ = 214 nm). **LRMS:** (+ESI) *m/z* 1925.3 $[3M+4H]^{4+}$, 1711.5 $[2M+3H]^{3+}$, 1283.7 $[M+2H]^{2+}$, 1182.1 $[M+2H\text{-}Gal]^{2+}$.

(2.110): Gal-08



Rink amide resin (50 µmol, ~0.3 mmol g^{-1}) was loaded with Fmoc-Cys(Trt)-OH according to general procedure **6.4.1**. The target peptide was then synthesised by iterative Fmoc-SPPS on the Syro I peptide synthesiser according to general procedure **6.4.1**, with Fmoc-Phe-OH as the final coupling step to generate the resin-bound sequence FTLNYYPLWYRKHYLKC. Fmoc-Ser(β-GalNAc(OAc)$_3$)-OH was coupled to the peptide on-resin by general procedure **6.4.5**, followed by coupling of chloroacetic acid by general procedure **6.4.6**. The peptide was cleaved from resin by general procedure **6.4.7**, and cyclised according to general procedure **6.4.9**. The peptide was deacetylated according to general procedure **6.4.11**. Purification by mass-directed RP-HPLC (1 to 70 vol.% MeCN in H_2O with 0.1 vol.% formic acid over 40 min), followed by lyophilisation, afforded the pure peptide **2.110** as a white fluffy solid (2.7 mg, 2%).

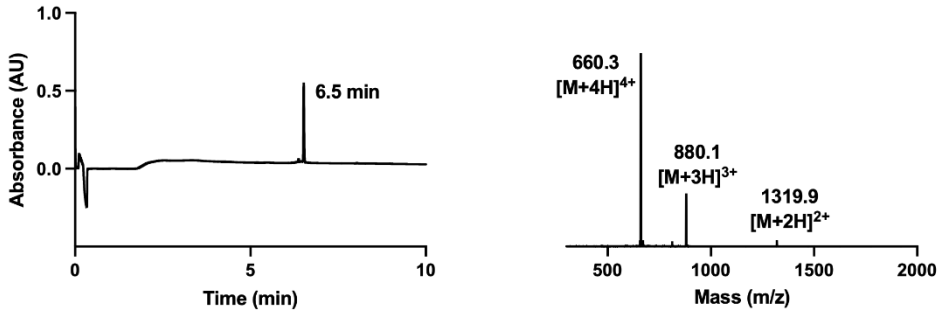
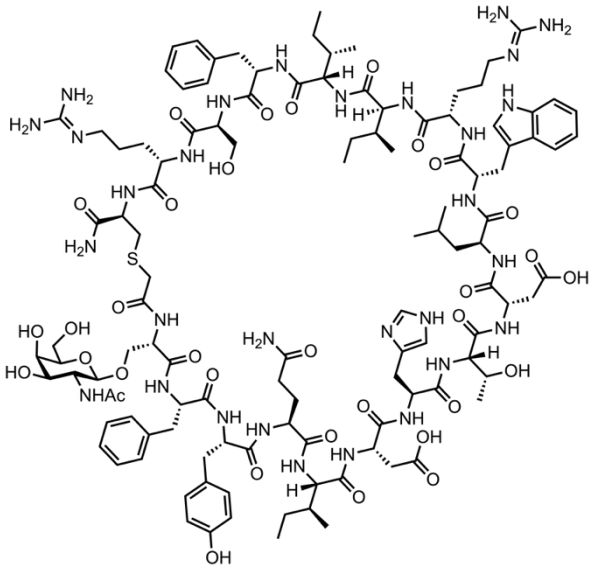


Figure 6.25. Analytical RP-HPLC: R_t = 6.5 min (1 to 60 vol.% MeCN in H_2O with 0.1 vol.% formic acid over 10 min, λ = 214 nm). **LRMS:** (+ESI) *m/z* 1319.9 $[M+2H]^{2+}$, 880.1 $[M+3H]^{3+}$, 660.3 $[M+4H]^{4+}$.

(2.111): Gal-11



Rink amide resin (50 μmol, ~0.3 mmol g^{-1}) was loaded with Fmoc-Cys(Trt)-OH according to general procedure **6.4.1**. The target peptide was then synthesised by iterative Fmoc-SPPS on the Syro I peptide synthesiser according to general procedure **6.4.1**, with Fmoc-Phe-OH as the final coupling step to generate the resin-bound sequence FYQIDHTDLWRIIFSRC. Fmoc-Ser(β-GalNAc($OAc)_3$)-OH was coupled to the peptide on-resin by general procedure **6.4.5**, followed by coupling of chloroacetic acid by general procedure **6.4.6**. The peptide was cleaved from resin by general procedure **6.4.7**, and cyclised according to general procedure **6.4.9**. The peptide was deacetylated according to general procedure **6.4.11**. Purification by mass-directed RP-HPLC (1 to 55 vol.% MeCN in H_2O with 0.1 vol.% formic acid over 40 min), followed by lyophilisation, afforded the pure peptide **2.111** as a white fluffy solid (0.4 mg, 0.3%).

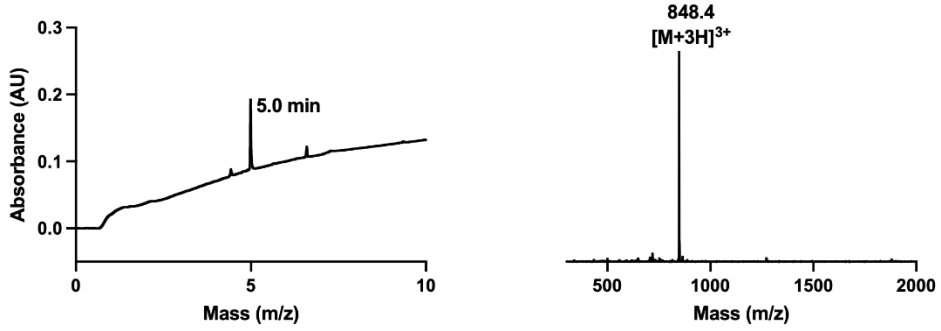
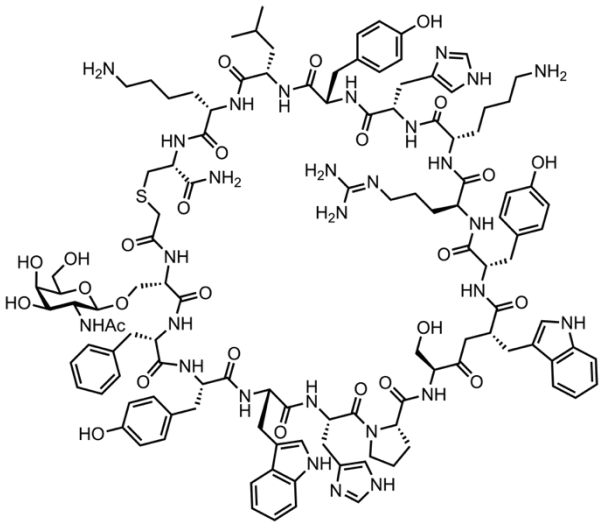


Figure 6.26. Analytical RP-HPLC: R_t = 5.0 min (1 to 70 vol.% MeCN in H_2O with 0.1 vol.% formic acid over 10 min, λ = 214 nm). **LRMS:** (+ESI) *m/z* 848.4 $[M+3H]^{3+}$.

(2.112): Gal-12



Rink amide resin (50 µmol, ~0.3 mmol g^{-1}) was loaded with Fmoc-Cys(Trt)-OH according to general procedure **6.4.1**. The target peptide was then synthesised by iterative Fmoc-SPPS on the Syro I peptide synthesiser according to general procedure **6.4.1**, with Fmoc-Phe-OH as the final coupling step to generate the resin-bound sequence FYWHPSWYRKHYLKC. Fmoc-Ser(β-GalNAc$(OAc)_3$)-OH was coupled to the peptide on-resin by general procedure **6.4.5**, followed by coupling of chloroacetic acid by general procedure **6.4.6**. The peptide was cleaved from resin by general procedure **6.4.7**, and cyclised according to general procedure **6.4.9**. The peptide was deacetylated according to general procedure **6.4.11**. Purification by mass-directed RP-HPLC (1 to 40 vol.% MeCN in H_2O with 0.1 vol.% formic acid over 40 min), followed by lyophilisation, afforded the pure peptide **2.112** as a white fluffy solid (1.3 mg, 1%).

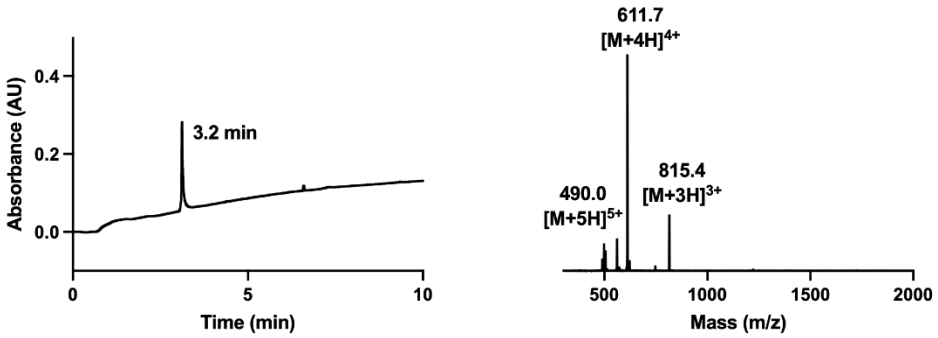
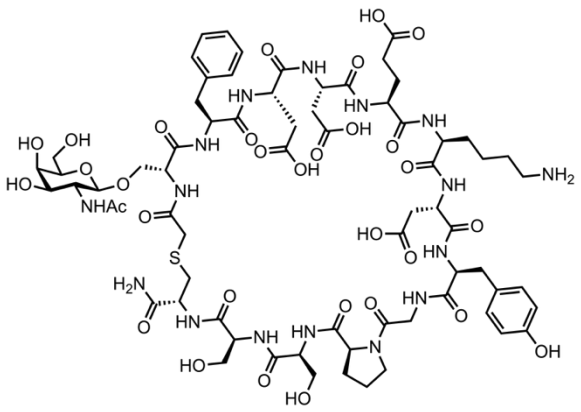


Figure 6.27. Analytical RP-HPLC: R_t = 3.2 min (1 to 70 vol.% MeCN in H_2O with 0.1 vol.% formic acid over 10 min, λ = 214 nm). **LRMS:** (+ESI) *m/z* 815.4 $[M+3H]^{3+}$, 611.7 $[M+4H]^{4+}$, 490.0 $[M+5H]^{5+}$.

(2.113): Gal-15



Rink amide resin (50 µmol, ~0.3 mmol g^{-1}) was loaded with Fmoc-Cys(Trt)-OH according to general procedure **6.4.1**. The target peptide was then synthesised by iterative Fmoc-SPPS on the Syro I peptide synthesiser according to general procedure **6.4.1**, with Fmoc-Phe-OH as the final coupling step to generate the resin-bound sequence FDDEKDYGPSSC. Fmoc-Ser(β-GalNAc$(OAc)_3$)-OH was coupled to the peptide on-resin by general procedure **6.4.5**, followed by coupling of chloroacetic acid by general procedure **6.4.6**. The peptide was cleaved from resin by general procedure **6.4.7**, and cyclised according to general procedure **6.4.9**. The peptide was deacetylated according to general procedure **6.4.11**. Purification by mass-directed RP-HPLC (1 to 60 vol.% MeCN in H_2O with 0.1 vol.% formic acid over 40 min), followed by lyophilisation, afforded the pure peptide **2.113** as a white fluffy solid (5.3 mg, 3%).

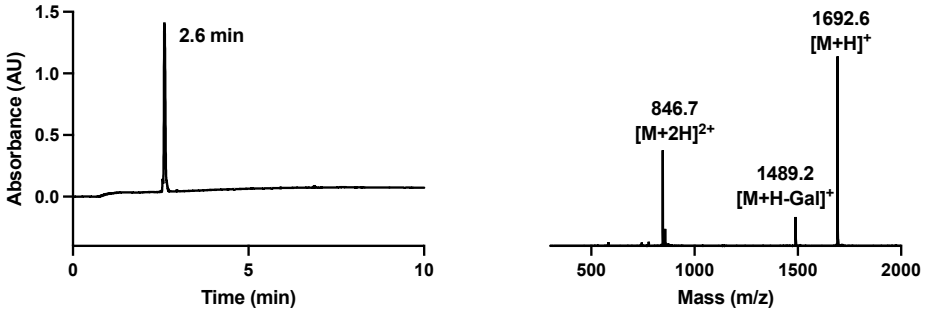
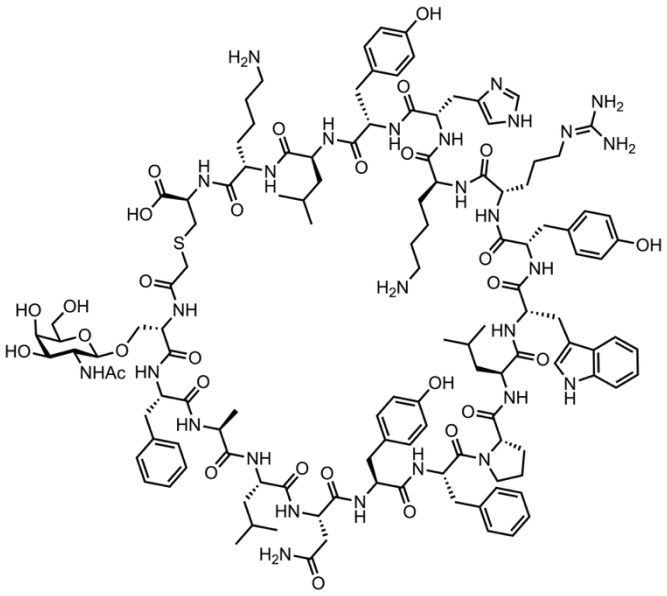


Figure 6.28. Analytical RP-HPLC: R_t = 2.6 min (1 to 70 vol.% MeCN in H_2O with 0.1 vol.% formic acid over 10 min, λ = 214 nm). **LRMS:** (+ESI) *m/z* 1692.6 $[M+H]^+$, 1489.2 $[M+H\text{-Gal}]^+$, 846.7 $[M+2H]^{2+}$.

(2.114): Gal-16



Rink amide resin (50 µmol, ~0.3 mmol g^{-1}) was loaded with Fmoc-Cys(Trt)-OH according to general procedure **6.4.1**. The target peptide was then synthesised by iterative Fmoc-SPPS on the Syro I peptide synthesiser according to general procedure **6.4.1**, with Fmoc-Phe-OH as the final coupling step to generate the resin-bound sequence FALNYFPLWYRKHYLKC. Fmoc-Ser(β-GalNAc(OAc)$_3$)-OH was coupled to the peptide on-resin by general procedure **6.4.5**, followed by coupling of chloroacetic acid by general procedure **6.4.6**. The peptide was cleaved from resin by general procedure **6.4.7**, and cyclised according to general procedure **6.4.9**. The peptide was deacetylated according to general procedure **6.4.11**. Purification by mass-directed RP-HPLC (1 to 70 vol.% MeCN in H_2O with 0.1 vol.% formic acid over 40 min), followed by lyophilisation, afforded the pure peptide **2.114** as a white fluffy solid (3.1 mg, 2%).

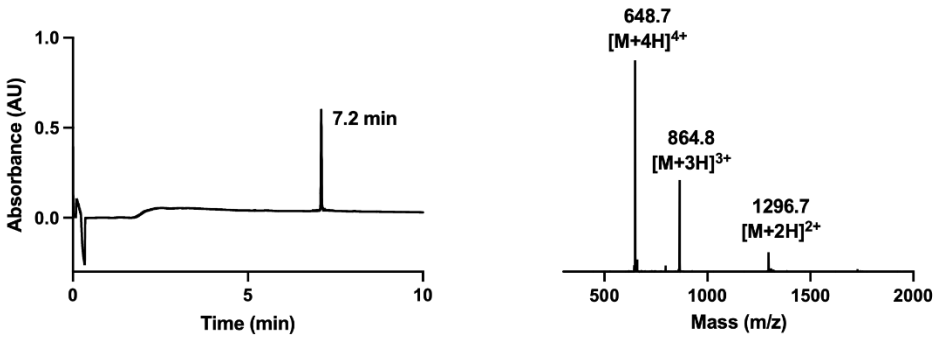
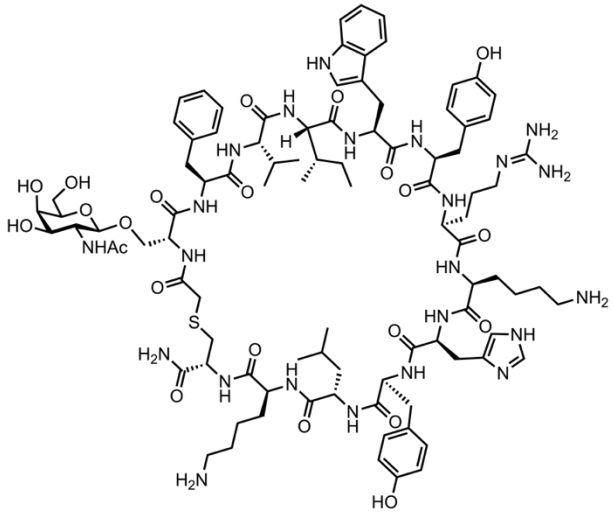


Figure 6.29. Analytical RP-HPLC: R_t = 7.2 min (1 to 60 vol.% MeCN in H_2O with 0.1 vol.% formic acid over 10 min, λ = 214 nm). **LRMS:** (+ESI) *m/z* 1296.7 $[M+2H]^{2+}$, 864.8 $[M+3H]^{3+}$, 648.7 $[M+4H]^{4+}$.

(2.115): Gal-18



Rink amide resin (50 µmol, ~0.3 mmol g^{-1}) was loaded with Fmoc-Cys(Trt)-OH according to general procedure **6.4.1**. The target peptide was then synthesised by iterative Fmoc-SPPS on the Syro I peptide synthesiser according to general procedure **6.4.1**, with Fmoc-Phe-OH as the final coupling step to generate the resin-bound sequence FVIWYRKHYLKC. Fmoc-Ser(β-GalNAc(OAc)$_3$)-OH was coupled to the peptide on-resin by general procedure **6.4.5**, followed by coupling of chloroacetic acid by general procedure **6.4.6**. The peptide was cleaved from resin by general procedure **6.4.7**, and cyclised according to general procedure **6.4.9**. The peptide was deacetylated according to general procedure **6.4.11**. Purification by mass-directed RP-HPLC (1 to 60 vol.% MeCN in H_2O with 0.1 vol.% formic acid over 40 min), followed by lyophilisation, afforded the pure peptide **2.115** as a white fluffy solid (0.8 mg, 1%).

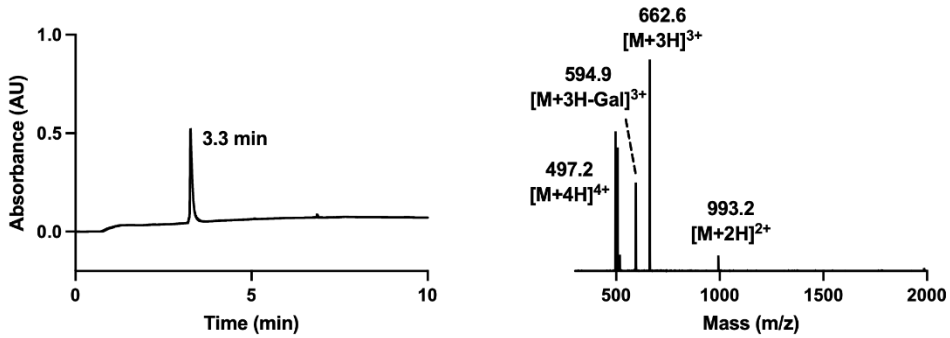
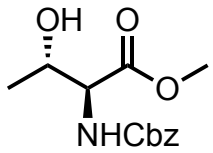


Figure 6.30. Analytical RP-HPLC: R_t = 3.3 min (1 to 70 vol.% MeCN in H_2O with 0.1 vol.% formic acid over 10 min, λ = 214 nm). **LRMS:** (+ESI) *m/z* 993.2 $[M+2H]^{2+}$, 662.6 $[M+3H]^{3+}$, 594.9 $[M+3H\text{-}Gal]^{3+}$, 497.2 $[M+4H]^{4+}$.

6.6 Experimental data for Chapter 4

6.6.1 Synthesis of psuedaminic acid intermediates

(4.107): methyl (2S,3S)-2-benzyloxycarbonylamino-3-hydroxybutyrate

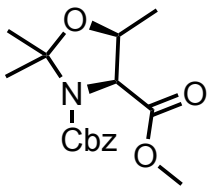


L-allo-Threonine (10.0 g, 84.0 mmol) and Na_2CO_3 (26.7 g, 252 mmol, 3.0 eq) were dissolved in water (100 mL), followed by addition of benzyl chloroformate (14.4 mL, 101 mmol, 1.2 equiv.). The reaction mixture was stirred at rt for 24 h. Upon completion, as determined by TLC (50% EtOAc:hexanes) the mixture was diluted with water (200 mL) and washed with diethyl ether (3 x 100 mL) to remove benzyl alcohol. The aqueous layer was collected and acidified with 1 M HCl to pH 3. The aqueous layer was then extracted with EtOAc (3 x 100 mL), and the combined organic layers were dried over anhydrous Na_2SO_4 and concentrated *in vacuo*. The crude intermediate was dissolved in DMF (50 mL) followed by the addition of $KHCO_3$ (16.8 g, 168 mmol, 2 eq) and iodomethane (7.8 mL, 126 mmol, 1.5 eq). The reaction mixture was stirred at rt for 17 h. Upon completion, the mixture was diluted with EtOAc (300 mL) and washed with 1 M HCl (5 x 200 mL). The organic layer was collected, dried over anhydrous $MgSO_4$ and concentrated *in vacuo*. The crude product was purified by flash column chromatography (20-50% EtOAc:hexanes) to afford the compound **4.107** as a white solid (19.4 g, 87% over two steps).

^{1}H NMR (300 MHz, $CDCl_3$) δ 7.42 – 7.28 (m, 5H), 5.68 (d, NH, *J* = 7.4 Hz, 1H), 5.12 (s, 2H), 4.44 (dd, *J* = 8.2, 3.8 Hz, 1H), 4.19 – 4.13 (m, 1H), 3.78 (s, 3H), 2.72 (br, OH, 1H), 1.21 (d, *J* = 6.5 Hz, 3H).

These data are in agreement with those reported by Tang *et al.*[316]

(4.108): 3-benzyl 4-methyl (4*S*,5*S*)-2,2,5-trimethyloxazolidine-3,4-dicarboxylate

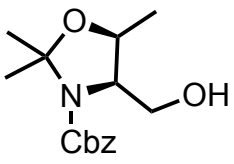


Compound **4.107** (14.0 g, 52.4 mmol) was dissolved in CH_2Cl_2 (100 mL) followed by the addition of 2,2-dimethoxypropane (32.1 mL, 262 mmol, 5.0 equiv.). The mixture was cooled to 0 °C before the dropwise addition of $BF_3.OEt_2$ (0.77 mL, 7.86 mmol, 0.15 eq). The reaction mixture was allowed to warm to rt and stirred for 24 h. Upon completion, as determined by TLC (30% EtOAc:hexanes), the mixture was quenched with triethylamine (1.5 mL) and concentrated *in vacuo*. The crude product was purified by flash column chromatography (10-30% EtOAc:hexanes) to afford the compound **4.108** as a yellow oil (15.8 g, 98%).

^{1}H NMR (300 MHz, $CDCl_3$, 2:1 mixture of two rotamers) δ 7.39 – 7.27 (m, 5H, major and minor), 5.25 – 4.99 (m, 2H, major and minor), 4.48 – 4.34 (m, 2H, major and minor), 3.77 (s, 1H, minor), 3.65 (s, 2H, major), 1.77 (s, 2H, major), 1.70 (s, 1H, minor), 1.56 (s, 2H, major), 1.50 (s, 1H, minor), 1.30 – 1.20 (m, 3H, major and minor).

These data are in agreement with those reported by Tang *et al.*[316]

(4.109): benzyl (4*R*,5*S*)-4-(hydroxymethyl)-2,2,5-trimethyloxazolidine-3-carboxylate



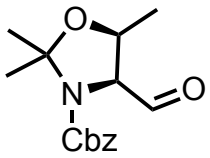
$CaCl_2$ (7.0 g, 63.5 mmol, 1.5 eq) was ground into a fine powder and dissolved in EtOH (100 mL) with the aid of ultrasonication. $NaBH_4$ (4.80 g, 127 mmol, 3.0 eq) was added to the stirring mixture, followed by the addition of a solution of **4.108** (13.0 g, 42.3 mmol) in THF (40 mL). The reaction mixture was stirred at rt for 22 h. Upon completion, as

determined by TLC (30% EtOAc:hexanes) the mixture was cooled to 0 °C, and quenched via dropwise addition of sat. aq. NH_4Cl solution (10 mL). The reaction mixture was diluted with water (300 mL), and the aqueous layer was extracted with EtOAc (4 x 200 mL). The combined organic layers were washed with 1 M HCl (200 mL), sat. aq. $NaHCO_3$ (200 mL), and brine (200 mL). The organic layer was collected, dried over anhydrous Na_2SO_4 and concentrated *in vacuo*. The crude product was purified by flash column chromatography (10-70% EtOAc:hexanes) to afford the title compound **4.109** as a yellow oil (10.6 g, 89%).

^{1}H NMR (300 MHz, $CDCl_3$, 1.3:1 mixture of two rotamers) δ 7.36 – 7.32 (m, 5H, major and minor), 5.16 (s, 1.24H, major), 5.12 (s, 0.76H, minor), 4.28 (p, *J* = 6.3 Hz, 1H, major and minor), 4.04 – 3.98 (m, 1H, major and minor), 3.95 – 3.85 (m, 2H, major and minor), 3.77 – 3.64 (m, 1H, major and minor), 2.74 (br s, 1H, major and minor), 1.62 (s, 1.11H, minor), 1.56 (s, 3H, major and minor), 1.50 (s, 2H), 1.36 (d, *J* = 6.6 Hz, 1.20H, minor), 1.30 (d, *J* = 6.5 Hz, 1.80H, major).

These data are in agreement with those reported by Tang *et al.*[316]

(4.54): benzyl (4*S*,5*S*)-4-formyl-2,2,5-trimethyloxazolidine-3-carboxylate



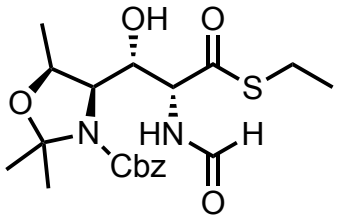
In an oven-dried flask, compound **4.109** (9.20 g, 33 mmol) was dissolved in anhydrous CH_2Cl_2 (150 mL) and placed under a nitrogen atmosphere. The reaction mixture was cooled to 0 °C before TEMPO (1.30 g, 7 mmol, 0.2 eq) and BAIB (15.91 g, 49 mmol, 1.5 eq) were added. The mixture was stirred at rt for 18 hours. Upon completion, determined by TLC, the mixture was diluted with CH_2Cl_2 (100 mL) and washed with sat. aq. $NaHCO_3$ (100 mL). The organic layer was collected, and the aqueous layer was re-extracted with CH_2Cl_2 (3 x 100 mL). The combined organic layer was washed with brine (200 mL), dried over anhydrous Na_2SO_4, and concentrated in *vacuo*. The crude material was purified by

flash column chromatography (5-30% EtOAc:hexanes) to afford the compound **4.54** as a pale-yellow oil (6.72 g, 74%).

^{1}H NMR (300 MHz, $CDCl_3$, 7:3 mixture of two rotamers) δ 9.62 (d, *J* = 2.7 Hz, 0.3 H, minor), 9.56 (d, *J* = 3.3 Hz, 0.7H, major), 7.42 – 7.25 (m, 5H, major and minor), 5.23 – 5.01 (m, 2H, major and minor), 4.49 – 4.38 (m, 1H, major and minor), 4.30 (dd, *J* = 6.6, 2.7 Hz, 0.3H, minor), 4.19 (dd, *J* = 6.6, 3.3 Hz, 0.7H, major), 1.76 (s, 2H, major), 1.67 (s, 1H, minor), 1.60 (s, 2H, major), 1.52 (s, 1H, minor), 1.36 1.30 (m, – 3H, major and minor).

These data are in agreement with those reported by Tang *et al*.[316]

(4.56): benzyl (4R,5S)-4-((1R,2R)-3-(ethylthio)-2-formamido-1-hydroxy-3-oxopropyl)-2,2,5-trimethyloxazolidine-3-carboxylate



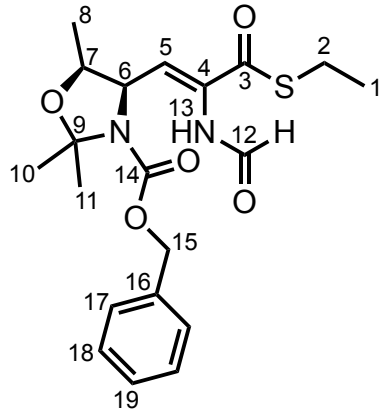
In an oven-dried flask, aldehyde 06-05 was dissolved in anhydrous dichloroethane (100 mL) and placed under a nitrogen atmosphere. To the mixture was added the thioester-isocyanide **4.55** (3.9 g, 30.5 mmol, 1.2 eq), followed by the addition of a solution of pre-dried LiOTf (4.4 g, 30.5 mmol, 1.2 eq) in anhydrous DMF (20 mL). The mixture (final concentration 0.2 M, DCE:DMF, 4:1 v/v) was allowed to stir at rt. After 30 minutes, DIPEA (0.8 mL, 4.7 mmol, 0.2 equiv.) was added dropwise, and the mixture was stirred at rt for 5 h. Upon completion, determined by TLC, the reaction mixture was concentrated *in vacuo* and diluted with EtOAc (200 mL). The resulting solution was washed with sat. aq. NH_4Cl (3 x 100 mL), followed by brine (100 mL). The organic layer was concentrated in vacuo and then redissolved in THF/H_2O (100 mL, 2:1 v/v). Acetic acid (0.5 mL) was added to the mixture and the refluxed for 90 minutes. Upon completion, the mixture was allowed to cool to rt and washed with sat. aq. $NaHCO_3$ (100 mL). The aqueous layer was extracted with EtOAc (3 x 150 mL), and the combined organic layer was washed with

brine (150 mL), dried over anhydrous Na_2SO_4, and concentrated *in vacuo*. The crude product was purified by flash column chromatography (10-50% EtOAc:hexanes) to obtain a mixture of two diastereomers. The desired diastereomer **4.56** was obtained as a pale-yellow solid (4.70 g, 47%).

^{1}H NMR (300 MHz, CD_3CN, mixture of rotamers) δ 7.98 (s, 0.56H), 7.87 (s, 0.44H), 7.33 (m, 5H), 7.12 (s, 1H), 5.21 (d, *J* = 13.3 Hz, 0.44H), 5.12 (d, *J* = 12.8 Hz, 0.56H), 5.03 (d, *J* = 12.7 Hz, 0.56H), 4.71 (d, *J* = 7.1 Hz, 0.44H), 4.62 (d, *J* = 13.0 Hz, 0.44H), 4.39 – 4.11 (m, 3H), 3.97 (br, 0.56H), 3.84 – 3.79 (m, 0.56H), 3.67 (s, 0.44H), 2.79 (q, *J* = 7.4 Hz, 2H), 1.52 – 1.39 (m, 6H), 1.32 – 1.21 (m, 3H), 1.15 (t, *J* = 7.4 Hz, 3H).

These data are in agreement with Li and co-workers.[349]

(4.134): benzyl (4*R*,5*S*)-4-((*Z*)-3-(ethylthio)-2-formamido-3-oxoprop-1-en-1-yl)-2,2,5-trimethyloxazolidine-3-carboxylate

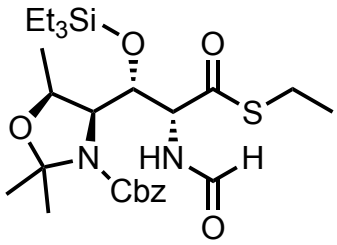


To a solution of diisopropyl azodicarboxylate (0.18 mL, 0.9 mmol, 2 eq) in THF (3 mL) was added triphenylphosphine (250 mg, 0.9 mmol, 2 eq) at rt and the mixture was stirred for 30 min. A solution of **4.57** (200 mg, 0.5 mmol,1 eq) in THF (2 mL) and acetic acid (0.05 mL, 0.9 mmol, 2 eq) in THF (2 mL) was added successively and the reaction mixture was stirred for 2 h at rt. The reaction was quenched by addition of saturated aq. NH_4Cl and the organic layer was separated. The aqueous layer was extracted three times with methyl *tert*-butyl ether and the combined organic layers were dried with MgSO4, filtered

and concentrated *in vacuo*. The crude product was purified by flash column chromatography (10-50% EtOAc:hexanes) to provide **4.134** as a colourless oil (88 mg, 40%).

IR (thin film) vmax = 3310 (N-H stretch), 1789 (C=O thioester stretch), 1712 (carbamate and formamide C=O stretch), 1512 (C=C stretch) cm^{-1}; **^{1}H NMR (500 MHz, CD_3CN)** δ 8.82 (s, 1H, 12), 8.20 (s, 1H, 13), 7.43 – 7.28 (m, 5H, 17, 18, 19), 6.19 (d, *J* = 10.8 Hz, 1H, 5), 5.16 – 5.05 (m, 2H, 15), 4.62 – 4.52 (m, 1H, 6), 4.42 – 4.30 (m, 1H, 7), 2.91 (q, *J* = 7.3 Hz, 3H, 2), 1.59 – 1.50 (m, 6H, 10, 11), 1.24 (t, *J* = 7.4 Hz, 4H, 1), 1.18 (d, *J* = 6.3 Hz, 3H, 8) ppm; **^{13}C NMR (126 MHz, CD_3CN)** δ 190.81 (3), 161.43 (12), 152.67 (14), 138.09 (16), 134.69 (4), 129.58 (17), 129.20 (18), 129.01 (19), 126.09 (5), 94.48 (9), 73.59 (7), 68.29 (15), 58.37 (6), 28.40 (11), 27.55 (10), 24.24 (2), 14.88 (1), 14.35 (8) ppm; **HRMS** (ESI-) *m/z* Calc. for $C_{19}H_{24}N_2O_6$ $[M - H]^-$: 375.1556, found 375.1562.

(4.135): benzyl (4*S*,5*S*)-4-((1*R*,2*R*)-3-(ethylthio)-2-formamido-3-oxo-1-((triethylsilyl)oxy)propyl)-2,2,5-trimethyloxazolidine-3-carboxylate



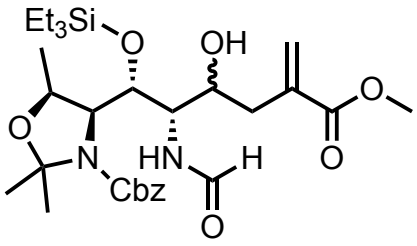
In an oven-dried flask, compound **4.56** (4.60 g, 10.8 mmol) was dissolved in anhydrous CH_2Cl_2 and placed under a nitrogen atmosphere. The mixture was cooled to 0 °C before 2,6-lutidine (3.79 mL, 32.5 mmol, 3.0 eq) was added. The reaction was left to stir for five minutes before triethylsiyl trifluoromethanesulfonate (4.90 mL, 21.7 mmol, 2.0 eq) was added dropwise. The reaction mixture was allowed to room temperature and stirred for 1.5 h. Upon complete, determined by TLC, the mixture was quenched with MeOH (50 mL). The mixture was diluted with water (50 mL), and the organic layer was washed with 1M HCl (2 x 100 mL), sat. aq. $NaHCO_3$ solution (2 x 100 mL) and brine (100 mL). The organic layer was collected, dried over anhydrous Na_2SO_4, and concentrated *in vacuo*.

The crude product was purified by flash column chromatography (20-50% EtOAc:hexanes) to afford compound **4.135** as a yellow oil (4.02 g, 69%).

^{1}H NMR (500 MHz, CD_3CN) δ 7.72 (s, 1H), 7.42 – 7.27 (m, 5H), 6.72 (s, 1H), 5.12 (d, *J* = 12.3 Hz, 1H), 5.02 (d, *J* = 12.4 Hz, 1H), 4.48 (s, 1H), 4.33 (dq, *J* = 6.7, 6.6 Hz, 1H), 4.30 – 4.27 (m, 1H), 3.95 (d, *J* = 6.2 Hz, 1H), 2.80 (q, *J* = 7.4 Hz, 2H), 1.42 (s, 3H), 1.41 (s, 3H) 1.36 (d, *J* = 6.6 Hz, 3H), 1.16 (t, *J* = 7.4 Hz, 3H), 0.90 (t, *J* = 7.9 Hz, 9H), 0.56 (q, *J* = 8.3 Hz, 6H).

These data are in agreement with Li and co-workers.[349]

(4.146): Benzyl (4*S*,5*S*)-4-((1*R*,2*S*)-2-formamido-3-hydroxy-5- (methoxy carbonyl)-1-((triethylsilyl)oxy)hex-5-en-1-yl)-2,2,5-trimethyloxazolidine-3-carboxylate



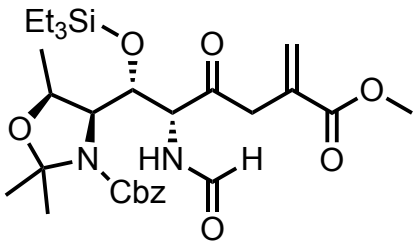
4.135 (1.50 g, 2.78 mmol) was subjected to a Fukuyama reduction by dissolving in acetone (10 mL) followed by addition of $Pd(OAc)_2$ (100 mg, 0.42 mmol, 0.15 eq).[349] To the stirring suspension, triethylsilane (1.33 mL, 8.35 mmol, 3.0 eq) was added dropwise, and the reaction left to stir at room temperature for 1 h, upon which completion was determined by TLC (30% EtOAc:hexanes). Upon completion, the mixture was concentrated *in vacuo* and resuspended in CH_2Cl_2. The mixture was filtered through a pad of celite soaked in CH_2Cl_2, the filtrate collected, and co-evaporated with CH_2Cl_2 to completely remove any acetone residue. The crude aldehyde was used directly in the Barbier reaction.

The aldehyde was dissolved in a 5:1 v/v mixture of sat. aq. NH_4Cl:THF (18 mL). Methyl 2-(bromomethyl)acrylate (0.48 mL, 3.48 mmol, 1.25 eq) and Zn powder (240 mg, 2.6 mmol, 3.0 eq) were added to this solution, and the mixture was stirred vigorously at room temperature for 2 h. Upon completion, as determined by TLC (50% EtOAc:hexanes), the

mixture was poured into water (100 mL). The aqueous layer was extracted with EtOAc (3 x 100 mL), and the combined organic layers washed with brine (100 mL), dried over $MgSO_4$, and concentrated *in vacuo*. The crude material was purified by flash column chromatography (20-70% EtOAc:hexanes) to provide the title compound **4.146** as a yellow oil containing a mixture of diastereomers (1.15 g, 71% over two steps, 3:2 mixture of diastereomers).

$[\alpha]^{25}_D$ = -17.0 (c = 1.0, $CHCl_3$); **IR** (thin film): 3306 (N-H and O-H stretch), 1767 (ester C=O stretch), 1694 (carbamate and formamide C=O stretch, C=C stretch), 1117 (Si-O stretch) cm^{-1}; **^{1}H NMR** (500 MHz, $CDCl_3$) δ 8.14 (s, 1H), 7.43 – 7.29 (m, 5H), 6.24 (d, *J* = 2.0 Hz, 1H), 5.70 (d, *J* = 2.0 Hz, 1H), 5.22 – 5.06 (m, 2H), 4.35 – 4.19 (m, 2H), 4.13 – 3.83 (m, 2H), 3.76 (s, 3H), 3.27 (m, 1H), 2.58 – 2.39 (m, 1H), 1.63 (d, *J* = 7.7 Hz, 3H), 1.54 – 1.37 (m, 6H), 0.96 (t, *J* = 7.8 Hz, 9H), 0.66 (q, *J* = 7.7 Hz, 6H) ppm; **^{13}C NMR** (126 MHz, $CDCl_3$, major isomer) δ 168.2, 162.6, 155.4, 137.5, 136.9, 135.8, 128.9, 128.3, 124.1, 93.2, 72.8, 72.4, 70.5, 68.2, 61.6, 56.2, 52.0, 37.9, 27.8, 24.9, 15.2, 6.7, 5.9 ppm; **HRMS** (ESI+) *m/z* Calc. for $C_{29}H_{46}N_2O_8Si$ [M + Na]$^+$: 601.2916, found 601.2922.

(4.149): Benzyl (4*S*,5*S*)-4-((1*R*,2*R*)-2-formamido-5-(methoxycarbonyl)-3-oxo-1-((triethylsilyl)oxy)hex-5-en-1-yl)-2,2,5-trimethyloxazolidine-3-carboxylate

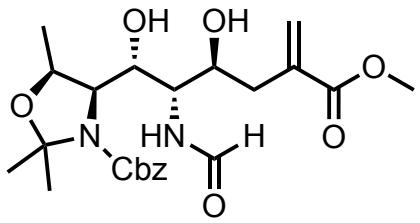


4.135 (270 mg, 0.47 mmol) was dissolved in CH_2Cl_2 (5 mL) before Dess-Martin periodinane (297 mg, 0.7 mmol, 1.5 equiv.) was added. One drop of water was added to facilitate proton transfer. The reaction mixture was stirred at rt for 3 h. Upon completion, as determined by TLC (50% EtOAc:hexanes), sat. aq. $NaHCO_3$ (20 mL) and sat. aq. $Na_2S_2O_3$ solution (20 mL) were added to the reaction mixture and the mixture was stirred vigorously. The phases were separated, and the aqueous layer was extracted with CH_2Cl_2

(2 x 50 mL). The combined organic layers were washed with sat. aq. $NaHCO_3$ (50 mL) and brine (50 mL). The organic layer was collected, dried over anhydrous Na_2SO_4, and concentrated *in vacuo*. The crude product was purified by flash column chromatography (20-70% EtOAc:hexanes) to provide the title compound **4.149** as a pale-yellow oil (250 mg, 93%).

$[\alpha]^{25}_D$ = +10.9 (c = 1.0, $CHCl_3$); **IR** (thin film): 3400 (N-H stretch), 1702 (ketone, ester, formamide, and carbamate C=O stretch), 1640 (C=C stretch), 1057 (Si-O stretch) cm^{-1}; **^{1}H NMR** (500 MHz, $CDCl_3$) δ 8.05 (br, 1H), 7.48 – 7.30 (m, 5H), 6.90 (s, 1H), 6.32 (d, *J* = 1.2 Hz, 1H), 5.59 (d, *J* = 2.3 Hz, 1H), 5.37 – 4.95 (m, 2H), 4.72 (d, *J* = 2.2 Hz, 1H), 4.31 ($quin_{app}$, *J* = 6.8 Hz, 2H), 3.97 (br, 1H), 3.71 (s, 3H), 3.65 – 3.50 (m, 2H), 1.55 (s, 3H), 1.53 (s, 3H), 1.40 (d, *J* = 6.4 Hz, 3H), 0.97 (t, *J* = 8.0 Hz, 9H), 0.62 (q, *J* = 7.9 Hz, 6H) ppm; **^{13}C NMR** (126 MHz, $CDCl_3$) δ 205.9 , 166.6, 162.0, 161.0, 134.0, 133.5, 128.8, 128.7, 128.7, 128.4, 93.4, 72.4, 69.4, 68.1, 64.6, 59.9, 52.0, 43.2, 27.5, 24.7, 15.5, 6.9, 5.0 ppm; **HRMS** (ESI+) *m/z* Calc. for $C_{29}H_{44}N_2O_8Si$ $[M + Na]^+$: 599.2759, found 599.2762.

(4.150): Benzyl (4*R*,5*S*)-4-((1*R*,2*S*,3*S*)-2-formamido-1,3-dihydroxy-5-(methoxycarbonyl)hex-5-en-1-yl)-2,2,5-trimethyloxazolidine-3-carboxylate

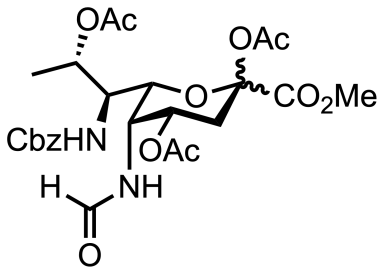


In an oven-dried flask **4.149** (200 mg, 0.3 mmol) was dissolved in anhydrous THF (5 mL). To the reaction mixture was added a pre-mixed solution of TBAF in 1M THF (0.7 mL, 0.7 mmol, 2.0 eq) and acetic acid (0.05 mL, 0.9 mmol, 2.5 eq). The reaction mixture was stirred at rt for 2 h. Upon completion, as determined by TLC (50% EtOAc:hexane), the reaction mixture was concentrated *in vacuo* to remove THF. The crude material was re-dissolved in EtOAc (30 mL), and the organic layer was washed with brine (2 x 20 mL), dried over anhydrous Na_2SO_4, and concentrated *in vacuo* to obtain the TES-deprotected

compound. The crude product was subject to the reduction reaction without further purification. For the reduction reaction, $NaBH(OAc)_3$ (368 mg, 1.7 mmol, 5 eq relative to Pse-10) was dissolved in anhydrous MeCN (6 mL, final concentration 0.3 M) before acetic acid (0.6 mL, 1:10 v/v to MeCN) was added. The mixture was cooled to -40 °C before a solution of the TES-deprotected compound in anhydrous MeCN (2 mL) was added dropwise. The reaction mixture was allowed to stir at -40 °C for 18 h. Upon completion, determined by LC-MS, the reaction mixture was quenched with sat. aq. NH_4Cl (10 mL) and diluted with EtOAc (30 mL). This mixture was washed with sat. aq. $NaHCO_3$ (2 x 30 mL) and brine (50 mL). The organic layer was collected, dried over anhydrous Na_2SO_4, and concentrated *in vacuo*. The crude product was purified by flash chromatography (20-100% EtOAc:hexanes) to provide the title compound **4.150** as a pale-yellow foam (130 mg, 81% over two steps).

$[\alpha]^{25}_D$ = +7.8 (c = 1.0, $CHCl_3$); **IR** (thin film) = 3367 (O-H and N-H stretch),1685 (ester, formamide, and carbamate C=O stretch), and 1661 (C=C stretch) cm^{-1}; **^{1}H NMR** (500 MHz, $CDCl_3$) δ 8.00 (s, 1H), 7.40 – 7.33 (m, 5H), 7.16 – 7.08 (m, 1H), 6.25 (s, 1H), 5.75 (s, 1H), 5.22 – 5.11 (m, 2H), 4.32 (qd, *J* = 6.6, 6.3 Hz, 1H), 4.22 (d, *J* = 7.7 Hz, 1H), 4.19 (ddd, *J* = 9.2, 5.8, 2.9 Hz, 1H), 3.94 (dd, *J* = 7.2, 5.5 Hz, 1H), 3.76 (s, 3H), 3.33 (dd, *J* = 6.7, 3.1 Hz, 1H), 2.51 (dd, *J* = 15.2, 5.9 Hz, 2H), 1.52 (s, 3H), 1.50 (s, 3H), 1.42 (d, *J* = 6.6 Hz, 3H) ppm; **^{13}C NMR** (126 MHz, $CDCl_3$) δ 168.1, 162.8, 155.5, 137.0, 135.8, 128.9, 128.7, 128.5, 128.2, 93.3, 72.9, 72.2, 68.8, 68.3, 62.1, 56.5, 52.2, 36.9, 27.8, 24.0, 15.3 ppm; **HRMS** (ESI+) *m/z* Calc. for $C_{23}H_{32}N_2O_8$ $[M + Na]^+$: 487.2051 found 487.2052.

(4.152): 2,4,8-tri-*O*-Acetyl-7-*N*-benzyloxycarbonyl-5-*N*-formyl-1-methylpseudaminoside

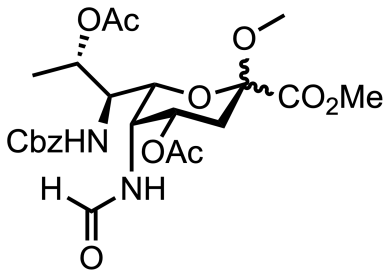


A solution of TFA/water (5.0 mL, 9:1 v/v) was cooled to 0 °C before being added to a flask containing compound **4.150** (110 mg, 0.300 mmol). The reaction mixture was stirred for at 0 °C for 15 min. Upon completion, as determined by TLC (100% EtOAc), the mixture was diluted by EtOAc (5 mL) and quenched by sat. aq. $NaHCO_3$. The solution was stirred vigorously until pH was neutral. The phases were separated, and the organic layer was dried with anhydrous $MgSO_4$ and concentrated *in vacuo* to afford the crude isopropropylidene-deprotected compound**.** This was dissolved in a mixture of CH_2Cl_2:MeOH (1:1 v/v, 8.0 mL) and cooled to -78 °C. A stream of O_3 was bubbled through the stirring reaction mixture for 1 h. Upon completion of ozonolysis, as determined by colour change of the reaction to dark blue, generation of O_3 was halted and pure O_2 was allowed to pass through the reaction mixture to remove excess O_3. Upon return of the reaction mixture to colourless, an excess of Me_2S (0.5 mL) was added to the reaction mixture and the mixture was allowed to warm to rt over 1 h. Upon completion, determined by LC-MS, the reaction mixture was concentrated *in vacuo* and co-evaporated with CH_2Cl_2 to remove excess MeOH to provide the crude ketal, which was dried under high vacuum. To the dry ketal was added pyridine (16 mL) and the solution was cooled to 0 °C before acetic anhydride (8 mL) and 3 crystals of DMAP were added. The reaction mixture was stirred at rt for 16 h. Upon completion, as determined by TLC (48:48:4 hexanes:EtOAc:MeOH), the reaction was diluted with EtOAc (100 mL), washed with 1M HCl (2 x 100 mL), sat. aq. $CuSO_4$ (100 mL), brine (100 mL), and sat. aq. $NaHCO_3$ (100 mL). The organic layer was collected, dried over anhydrous $MgSO_4$, and concentrated *in vacuo*. The crude product was purified by flash column chromatography (50% EtOAc:hexanes then 48:48:4 hexanes:EtOAc:MeOH) to provide the title compound

4.152 as a white foam containing a mixture of anomers (115 mg, 80% over three steps, 2.9:1 mixture of anomers).

IR (thin film): 3334 (N-H stretch), 1721 (C=O stretch esters and formamide), and 1532 (amide N-H bend and C-N stretch) cm^{-1}; **^{1}H NMR** (500 MHz, MeOD, major anomer) δ 8.13 (s, 1H), 7.36 – 7.30 (m, 5H), 5.13 (qd, J= 6.5, 3.3 Hz, 1H), 5.11 – 5.07 (m, 2H), 5.07 – 5.02 (m, 1H), 4.70 – 4.67 (m, 1H), 4.48 (dd, *J* = 10.5, 1.9 Hz, 1H), 4.23 (dd, *J* = 10.5, 3.3 Hz, 1H), 3.77 (s, 3H), 2.42 (dd, *J* = 13.3, 5.0 Hz, 1H), 2.10 (s, 3H), 2.09 – 2.07 (m, 1H), 1.97 (s, 3H), 1.85 (s, 3H), 1.23 (d, *J* = 6.5 Hz, 3H) ppm; **^{13}C NMR** (126 MHz, MeOD, major anomer) δ 172.4, 171.6, 170.1, 167.0, 164.5, 158.6, 138.4, 129.4, 128.8, 128.7, 97.8, 74.53, 71.05, 68.42, 67.63, 53.30, 52.93, 45.28, 32.81, 21.15, 20.84, 20.68, 13.32 ppm; **HRMS** (ESI+) *m/z* Calc. for $C_{25}H_{32}N_2O_{12}$ $[M + Na]^+$: 575.1853, found 575.1848.

(4.175): Methyl 4*O*,5*N*,8*O*-triacetyl-7-*N*-benzyloxycarbonyl-1-methyl-α-pseudaminoside

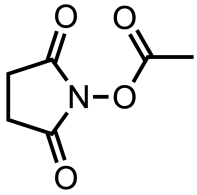


4.152 (100 mg, 0.2 mmol) was dissolved in anhydrous MeOH (10 mL) under a nitrogen atmosphere, and cooled to 0 °C. To the stirring solution, $SOCl_2$ (0.29 mL, 4.0 mmol, 20 eq) was added dropwise and the mixture was warmed to rt and stirred for 24 h. Upon completion, as determined by LC-MS, the mixture was concentrated *in vacuo* and co-evaporated with toluene. The crude material was dissolved in pyridine (5 mL) and cooled to 0 °C. Acetic anhydride (2.5 mL) was added, and the reaction was allowed to warm to rt and stirred for 24 h. Upon completion, as determined by LC-MS, the reaction was diluted with EtOAc (20 mL), washed with 1 M HCl (2 x 20 mL), brine (20 mL), and sat. aq. $NaHCO_3$ (20 mL). The organic layer was collected, dried over anhydrous $MgSO_4$, and

concentrated *in vacuo*. The material was filtered through a silica pad to provide semi-purified **4.175** (20 mg, 21%, α/β 9:1) as an off-white foam to be used directly in the next step.

IR (thin film): 3348 (N-H stretch), 1725 (C=O ester), 1651 (C=O amide), 1546 and 1536 (amide N-H bend and C-N stretch) cm^{-1}; **^{1}H NMR** (500 MHz, MeOD, major anomer) δ 7.35 (m, *J* = 8.2 Hz, 5H), 5.25 (qd, *J* = 6.3, 2.3 Hz, 1H, 8), 5.20 (ddd, *J* = 12.4, 5.4, 4.3 Hz, 1H, 4), 5.10 (d, *J* = 12.2 Hz, 2H, Cbz-CH_2'), 4.93 (d, *J* = 12.5 Hz, 2H, Cbz-CH_2''), 4.62 (s_{app}, 1H, 5), 4.23 (dd, *J* = 10.6, 3.0 Hz, 1H, 7), 3.95 (dd, *J* = 10.5, 1.9 Hz, 1H, 6), 3.84 (s, 3H, CO_2Me), 3.28 (s, 3H, OMe), 2.12 (dd, *J* = 12.5, 5.6 Hz, 1H, 3''), 1.99 (s, 3H, NHAc), 1.95 (s_{app}, 6H, 19, 2xOAc), 1.93 (dd, *J* = 13.4, 12.1 Hz, 1H, 3'), 1.25 (d, *J* = 6.6 Hz, 3H, 9) ppm; **^{13}C NMR** (126 MHz, MeOD, major anomer) δ 174.2, 172.3, 172.0, 169.7, 158.5, 138.3, 129.4, 128.9, 128.8, 100.7, 71.8, 71.4, 68.6, 67.7, 53.7, 53.3, 52.3, 47.0, 33.2, 22.6, 21.2, 21.0, 14.9 ppm; **HRMS** (ESI+) *m/z* Calc. for $C_{25}H_{34}N_2O_{11}$ $[M + Na]^+$: 561.2061, found 561.2055.

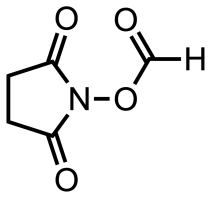
(4.180): *N*-acetoxy succinimide



N-hydroxy succinimide (120 mg, 1.0 mmol) was added to acetic anhydride (0.3 mL, 3.1 mmol, 3 eq) and stirred at room temperature for 24 h. The precipitate obtained was filtered, washed with hexane, and dried in vacuum to provide *N*-acetoxy succinimide (**4.180**) quantitatively (162 mg).

^{1}H NMR (400 MHz, $CDCl_3$) δ 2.85 (d, *J* = 3.2 Hz, 4H), 2.36 (s, 3H) ppm.

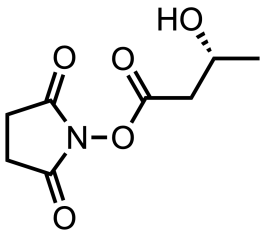
(4.181): Formyloxy succinimide



Acetic anhydride (0.8 mL, 8.3 mmol, 8 eq) was cooled to 0 °C, and formic acid (0.4 mL, 10.4 mmol, 10 eq) was added over 10 minutes. The solution was warmed to rt and stirred for 2 h. *N*-hydroxy succinimide (120 mg, 1.0 mmol, 1 eq) was then added, and the reaction mixture stirred for a further 14 h. The reaction mixture was concentrated *in vacuo*, and the resulting solid dried under high vacuum to provide the desired formyloxy succinimide quantitatively (148 mg, 1.0 mmol) as a white solid.

^{1}H NMR (400 MHz, $CDCl_3$) δ 8.20 (s, 1H), 2.87 (s, 4H) ppm.

(4.182): *N*-(*R*-3-hydroxybutyryloxy)succinimide

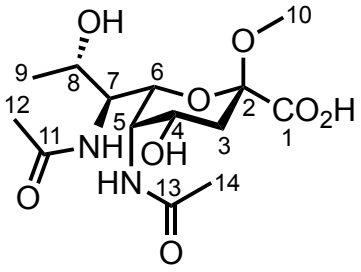


To a solution of *R*-3-hydroxybutyric acid (108 mg, 1.04 mmol, 1 eq) and *N*-hydroxysuccinimide (119 mg, 1.04 mmol, 1 eq) in dry CH_2Cl_2 (2 mL) was added DCC (214 mg, 1.04 mmol, 1 eq), and the mixture was stirred at rt for 24 h. The resulting suspension was diluted with MeCN (10 mL), filtered, and concentrated *in vacuo* to provide the desired *R*-3-hydroxybutyryl succinimide **(4.182)** as a white solid (178 mg, 85%). The material was used without further purification.

^{1}H NMR (400 MHz, $CDCl_3$) δ 4.32 (dqd, *J* = 7.7, 6.3, 4.6 Hz, 1H), 2.84 (s, 4H), 2.77 (dd, *J* = 15.4, 4.6 Hz, 2H), 2.72 (dd, *J* = 15.4, 7.7 Hz, 2H), 1.32 (d, *J* = 6.3 Hz, 3H) ppm.

6.6.2 Synthesis of final Pse N7 variants

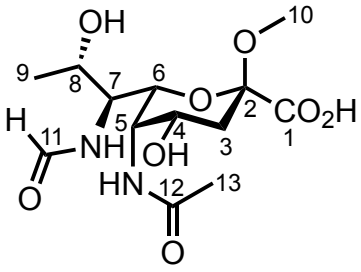
(4.176): Methyl 5,7-di-*N*-acetyl-α-pseudaminoside



4.176 was prepared according to general procedure **6.3.10**, to provide the title compound as a white foam (0.4 mg, 21%).

^{1}H NMR (800 MHz, D_2O) δ 4.18 (qd, $J_{8,9}$ = 6.8 Hz, $J_{8,7}$ = 3.6 Hz, 1H, H-8), 4.14 (dd, $J_{7,8}$ = 3.8 Hz, $J_{7,6}$ = 2.2 Hz, 1H, H-7), 4.13 (dd, $J_{5,6}$ = 10.6 Hz, $J_{5,4}$ = 3.7 Hz, 1H, H-5), 4.07 (dt, $J_{4,3ax}$ = 12.4 Hz, $J_{4,3eq}$ = 4.6 Hz, $J_{4,5}$ = 4.6 Hz, 1H, H-4), 3.73 (dd, $J_{6,5}$ = 10.4 Hz, $J_{6,7}$ = 1.7 Hz, 1H, H-6), 3.10 (s, 3H, H-10), 1.99 (dd, $J_{3eq,3ax}$ = 13.6 Hz, $J_{3eq,4}$ = 5.1 Hz, 1H, H-3_{eq}), 1.92 – 1.90 (m, 3H, 14), 1.89 (s, 3H, H-12), 1.50 (t_{app}, $J_{3ax,3eq}$ = 12.9 Hz, $J_{3ax,4}$ = 12.9 Hz, 1H, H-3_{ax}), 1.08 (d, $J_{9,8}$ = 6.5 Hz, 3H, H-9) ppm; **^{13}C NMR (201 MHz, D_2O)** δ 175.0 (C-1), 174.6 (C-13), 173.7 (C-11), 100.8 (C-2), 70.3 (C-6), 66.7 (C-8), 65.0 (C-4), 53.5 (C-7), 50.9 (C-10), 48.6 (C-5), 35.2 (C-3), 22.0 (C-12), 21.9 (C-14), 15.3 (C-9) ppm; **HRMS** (ESI-) m/z Calc. for $C_{14}H_{24}N_2O_8$ $[M - H]^-$: 347.1454, found 347.1460.

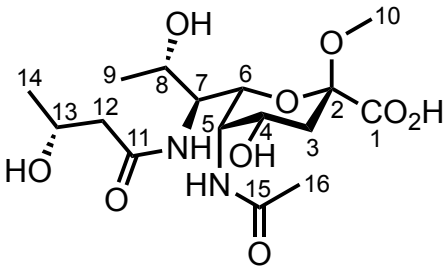
(4.177): Methyl 5-*N*-acetyl-7-*N*-formyl-α-pseudaminoside



4.177 was prepared according to general procedure **6.3.10**, to provide the title compound as a white foam (0.3 mg, 16%).

^{1}H NMR (800 MHz, D_2O) δ 8.08 (s, 1H, 11), 4.33 (dd, $J_{7,6}$ = 10.4, $J_{7,8}$ = 3.1 Hz, 1H, 7), 4.30 (qd, $J_{8,9}$ = 6.5 Hz, $J_{8,7}$ = 3.0 Hz, 1H, H-8), 4.25 (dd, $J_{5,4}$ = 4.5 Hz, $J_{5,6}$ = 1.5 Hz, 1H, H-5), 4.16 (ddd, $J_{4,3ax}$ = 12.2 Hz, $J_{4,3eq}$ = 5.0 Hz, $J_{4,5}$ = 4.0 Hz, 1H, H-4), 3.86 (dd, $J_{6,7}$ = 10.4 Hz, $J_{6,5}$ = 1.8 Hz, 1H, H-6), 3.20 (s, 3H, H-10), 2.07 (dd, $J_{3eq,3ax}$ = 13.4 Hz, $J_{3eq,4}$ = 5.0 Hz, 1H, H-3_{eq}), 2.00 (s, 3H, H-13), 1.60 (dd, $J_{3ax,3eq}$ = 13.6 Hz, $J_{3ax,4}$ = 12.2 Hz, 1H, H-3_{ax}), 1.18 (d, $J_{9,8}$ = 6.5 Hz, 3H, H-9) ppm; **^{13}C NMR (201 MHz, D_2O)** δ 174.8 (C-1), 174.7 (C-12), 163.9 (C-11), 100.7 (C-2), 70.4 (C-6), 66.3 (C-8), 65.0 (C-4), 52.2 (C-7), 51.0 (C-10), 48.6 (C-5), 35.0 (C-3), 22.0 (C-13), 15.3 (C-9) ppm; **HRMS** (ESI-) *m/z* Calc. for $C_{13}H_{22}N_2O_8$ [M - H]$^-$: 333.1299, found 333.1303.

(4.178): Methyl 5-*N*-acetyl-7-*N*-(3*R*-hydroxybutyryl)-α-pseudaminoside

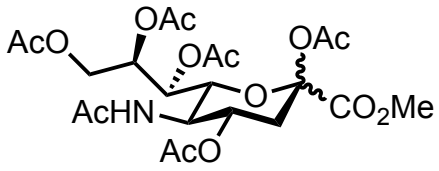


4.178 was prepared according to general procedure **6.3.10**, to provide the title compound as a white foam (0.4 mg, 18%).

^{1}H NMR (800 MHz, D_2O) δ 4.18 (qd, $J_{8,9}$ = 6.1 Hz, $J_{8,7}$ = 3.1 Hz, 1H, H-8), 4.16 (dd, $J_{7,6}$ = 10.4 Hz, $J_{7,8}$ = 3.4 Hz, 1H, H-7), 4.13 (m, 1H, H-5), 4.13 – 4.10 (m, 1H, H-13), 4.06 (dt_{app}, $J_{4,3ax}$ = 11.7 Hz, $J_{4,3eq}$ = 4.3 Hz, $J_{4,5}$ = 4.3 Hz, 1H, H-4), 3.73 (dd, $J_{6,7}$ = 10.3 Hz, $J_{6,5}$ = 1.9 Hz, 1H, H-6), 3.10 (s, 3H, H-10), 2.31 (dd, $J_{12',12''}$ = 14.2 Hz, $J_{12',13}$ = 8.6 Hz, 1H, H-12'), 2.27 (dd, $J_{12'',12'}$ = 14.7 Hz, $J_{12'',13}$ = 4.5 Hz, 1H, H-12''), 1.98 (dd, $J_{3eq,3ax}$ = 13.8 Hz, $J_{3eq,4}$ = 4.7 Hz, 1H, H-3_{eq}), 1.91 (s, 3H, H-16), 1.50 (t_{app}, $J_{3ax,3eq}$ = 12.9 Hz, $J_{3ax,4}$ = 12.9 Hz, 1H, 3_{ax}), 1.16 (d, $J_{14,13}$ = 6.1 Hz, 3H, H-14), 1.08 (d, $J_{9,8}$ = 5.9 Hz, 3H, H-9) ppm; **^{13}C NMR (201 MHz, D_2O)** δ 175.0 (C-1), 174.6 (C-15), 173.7 (C-11), 100.8 (C-2), 70.4 (C-6), 66.9 (C-8), 65.1 (C-4), 64.9 (C-13), 53.5 (C-7), 51.0 (C-10), 48.6 (C-5), 45.2 (C-12), 35.1 (C-3), 22.1 (C-14), 21.9 (C-16), 15.5 (C-9) ppm; **HRMS** (ESI-) *m/z* Calc. for $C_{16}H_{28}N_2O_9$ [M - H]$^-$: 391.1717, found 391.1722.

6.7 Experimental Data for Chapter 5

(5.52): Methyl (2,4,7,8,9-Penta-*O*-acetyl-5-acetamido-3,5-dideoxy-β-D-glycero-D-galacto-non-2-ulopyranoside)onate



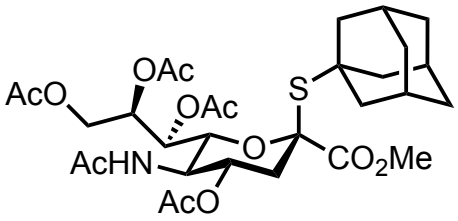
To an oven-dried flask under a nitrogen atmosphere was added sialic acid (20.0 g, 38.8 mmol) and anhydrous MeOH (350 mL). To the stirring suspension was added trimethyl orthoformate (9.5 mL, 86 mmol, 1.3 eq) in a single portion. The reaction mixture was cooled to 0 °C before dropwise addition of $SOCl_2$ (3.3 mL, 45 mmol, 0.7 eq). The suspension was allowed to warm to rt and the reaction was stirred for 18 h. Upon completion, as determined by NMR, the solution was concentrated *in vacuo* and dried under high vacuum overnight. The residue was dissolved in pyridine (200 mL) and the solution was cooled to 0 °C. Ac_2O (74 mL, 780 mmol, 12 eq) and catalytic DMAP were added, and the reaction was allowed to warm to rt and stirred for 18 h. Upon completion, as determined by TLC, the solution was concentrated *in vacuo*. The residue was redissolved in EtOAc (300 mL), washed with aq. 1M HCl (300 mL x 2), sat. aq. $NaHCO_3$ (300 mL), and brine (300 mL). The organic layer was dried over $MgSO_4$, filtered, and concentrated *in vacuo*. The residue was co-evaporated with toluene (200 mL x 3) to afford the crude glycosyl acetate. The crude material was purified by flash column chromatography on silica (MeOH:EtOAc:hexane 5:45:50) to provide the desired mixture of anomers (**5.52**) as a white foam (22.8 g, 66% over two steps).

^{1}H NMR (500 MHz, $CDCl_3$) δ 5.49 – 5.42 (m, 1H), 5.36 (dd, *J* = 5.0, 1.7 Hz, 1H), 5.28 – 5.19 (m, 1H), 5.05 (ddd, *J* = 7.2, 5.0, 2.5 Hz, 1H), 4.48 (dd, *J* = 12.4, 2.6 Hz, 1H), 4.13 – 4.08 (m,

3H), 3.77 (s, 3H), 2.53 (dd, *J* = 13.5, 4.9 Hz, 1H), 2.13 (s_{app}, 6H), 2.10 – 2.06 (m, 1H), 2.04 (s, 3H), 2.02 (s_{app}, 6H), 1.87 (s, 3H) ppm.

This is in agreement with the spectral data reported by Lorpitthaya *et al.*[421]

(5.53): Methyl (1-adamantanyl 5-(*N*-acetylacetamido)-4,7,8,9-tetra-*O*-acetyl-3,5-dideoxy-2- thio-D-glycero-β-D-galacto-non-2-ulopyranoside)onate

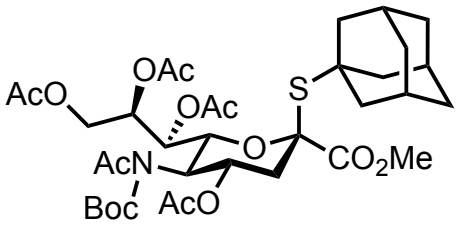


To an oven-dried flask under a nitrogen atmosphere was added **5.52** (22.8 g, 43 mmol), 1-adamantanethiol (7.9 g, 47 mmol, 1.1 eq), and anhydrous CH_2Cl_2 (250 mL). $BF_3.OEt_2$ (13.2 mL, 107 mmol, 2.5 eq) was added to the stirring solution portion wise, and the mixture was left to stir at room temperature for 16 h. Upon completion, as determined by TLC, the mixture was diluted with CH_2Cl_2 (500 mL), washed with sat. aq. $NaHCO_3$ (200 mL x 2), brine (200 mL), dried over $MgSO_4$, and concentrated *in vacuo*. The crude material was purified by flash column chromatography on silica (MeOH:EtOAc:hexanes 5:45:50) to provide β-thiosialoside **5.53** as white foam (18.4 g, 67%).

$[\alpha]^{25}_D$ - 56.9 (*c* 10, $CDCl_3$); **^{1}H NMR** (500 MHz, $CDCl_3$) δ 5.46 (t_{app}, *J* = 4.0 Hz, 1H), 5.44 (d, *J* = 10.4 Hz, 1H), 5.31 – 5.22 (m, 1H), 5.16 (d, *J* = 8.8 Hz, 1H), 5.00 (dd, *J* = 12.1, 3.0 Hz, 1H), 4.54 (dd, *J* = 10.6, 3.0 Hz, 1H), 4.20 (dd, *J* = 12.4, 9.2 Hz, 1H), 4.06 (q_{app}, *J* = 10.4 Hz, 1H), 3.82 (s, 3H), 2.52 (dd, *J* = 13.3, 3.9 Hz, 1H), 2.11 (s, 3H), 2.06 (s, 4H), 2.02 – 1.97 (m, broad, 10H), 1.97 – 1.91 (m, broad, 3H), 1.88 – 1.83 (m, broad, 6H), 1.70 – 1.59 (m, broad, 6H) ppm.

This is in agreement with the spectral data reported by Crich *et al.*[422]

(5.42): Methyl (1-Adamantanyl 5-acetamido-4,7,8,9-tetra-*O*-acetyl-3,5-dideoxy-5-*N*-(1,1-dimethylethoxy)carbonyl-2-thio-D-glycero-β-D-galacto-non-2-ulopyranoside)onate

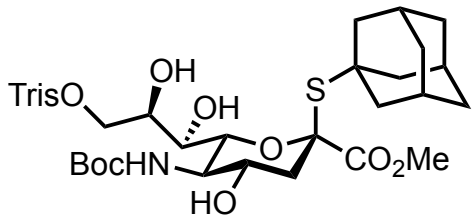


To an oven-dried flask under a nitrogen atmosphere was added **5.53** (5.8 g, 9.0 mmol) in anhydrous THF (40 mL). To the stirring solution was added di-*tert*-butyl dicarbonate (20.8 mL, 90 mmol, 10 eq) and DMAP (440 mg, 3.6 mmol, 0.4 eq). The mixture was heated at 60 °C for 16 h before it was cooled to room temperature, quenched with water (200 mL) and the THF removed *in vacuo*. The aqueous suspension was extracted with EtOAc (300 mL x 3), washed with brine (200 mL), dried over $MgSO_4$, and concentrated *in vacuo*. The crude material was purified by flash column chromatography on silica (EtOAc:hexane 10-50%) to provide **5.42** as an off-white foam (6.6 g, 99%).

$[\alpha]^{25}_D$ - 38.2 (*c* 10, $CDCl_3$); **^{1}H NMR** (500 MHz, $CDCl_3$) δ 5.65 (td_{app}, *J* = 11.1, 4.7 Hz, 1H), 5.36 (dd, *J* = 10.0, 1.6 Hz, 1H), 5.33 (s, broad, 1H), 5.14 (dd, *J* = 8.9, 1.8 Hz, 1H), 4.97 (d, *J* = 12.4 Hz, 1H), 4.76 (t, *J* = 10.4 Hz, 1H), 4.23 (dd, *J* = 12.5, 8.9 Hz, 1H), 3.83 (s, 3H), 2.63 (dd, *J* = 13.6, 4.8 Hz, 1H), 2.33 (d, *J* = 1.3 Hz, 3H), 2.07 (s, 3H), 2.04 (s, 3H), 2.02 – 1.98 (m, 9H),1.92 (s, 3H), 1.89 – 1.84 (m, 3H), 1.69 (s, broad, 9H), 1.65 (s_{app}, broad, 6H) ppm.

This is in agreement with the spectral data reported by Crich *et al.*[422]

(5.57): Methyl (1-Adamantanyl 3,5-dideoxy-5-*N*-(1,1-dimethylethoxy)-carbonyl-9-*O*-((2,4,6-triisopropylphenyl)sulfonyl)oxy-2-thio-D-glycero-β-D-galacto-non-2-ulopyranosid)onate

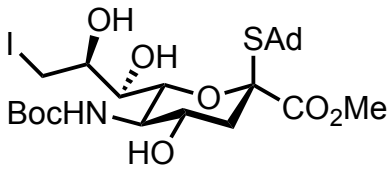


In an oven-dried flask under a nitrogen atmosphere, **5.42** (15.8 g, 21 mmol) was dissolved in anhydrous MeOH (210 mL, 0.1 M). The stirring solution was cooled to 0 °C and catalytic NaOH was added (170 mg, 4 mmol, 0.2 eq). The reaction was warmed to room temperature and allowed to stir for 6 h. Upon completion, the solution was concentrated *in vacuo* to give the crude deprotected product, which was left to dry on the high vacuum overnight. The crude product was dissolved in anhydrous pyridine (150 mL) under a nitrogen atmosphere and cooled to 0 °C. 2,4,6-triisopropylbenzenesulfonyl chloride (Tris-Cl) (25.8 g, 85 mmol, 4 eq) was added portion wise. The reaction mixture was stirred at 0 °C for 2 h then room temperature for 16 h. Upon completion, the reaction was quenched with MeOH (8.6 mL, 210 mmol, 10 eq) and concentrated *in vacuo* to remove most of the pyridine. The remaining mixture was diluted with EtOAc (400 mL) and washed with water (500 mL x 3), brine (300 mL), dried over $MgSO_4$, and concentrated *in vacuo*. The crude material was purified by flash column chromatography on silica (EtOAc:hexane:MeOH 20:78:2 to 70:28:2) to provide **5.57** as white foam (11.4 g, 66% over two steps).

$[\alpha]^{25}_D$ -49.4 (*c* 5, $CDCl_3$); **^{1}H NMR** (400 MHz, $CDCl_3$) δ 7.19 (s, 2H), 4.72 (d, *J* = 8.7 Hz, 1H), 4.52 (dd, *J* = 10.7, 2.5 Hz, 1H), 4.23 (dd, *J* = 10.7, 6.7 Hz, 2H), 4.12 (hept, *J* = 6.7 Hz, 2H), 4.08 – 3.99 (m, 2H), 3.79 (s, 3H), 3.63 (dd, *J* = 8.4, 1.2 Hz, 1H), 3.55 (dd, *J* = 9.5, 9.3 Hz, 1H), 2.91 (hept, *J* = 6.9 Hz, 1H), 2.60 (dd, *J* = 13.8, 4.7 Hz, 1H), 1.98 (s, 3H), 1.95 (s, 3H), 1.91 – 1.80 (m, 3H), 1.65 (d, *J* = 2.9 Hz, 6H), 1.42 (s, 9H), 1.27 (d, *J* = 6.8 Hz, 9H), 1.26 (d, *J* = 6.9 Hz, 9H) ppm.

This is in agreement with the spectral data reported by Crich *et al.*[395]

(5.58): Methyl (1-Adamantanyl 3,5,9-trideoxy-9-iodo-5-*N*-(1,1-dimethylethoxy)carbonyl-2-thio-D-glycero-β-D-galacto-non-2-ulopyranosid)onate

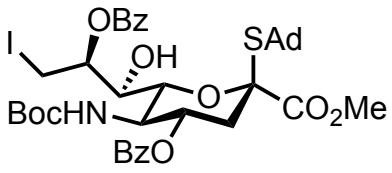


In an oven-dried flask under a nitrogen atmosphere, **5.57** (7.65 g, 9.40 mmol) was dissolved in anhydrous acetone (120 mL). Sodium iodide (9.86 g, 65.8 mmol, 7 eq) was added to the mixture, and the reaction was heated at 45 °C for 18 h. Upon completion, as determined by TLC, the reaction was concentrated *in vacuo,* and the crude material purified by flash column chromatography on silica (EtOAc:hexane 20-100%) to provide **5.58** as a pale-yellow foam (5.77 g, 96%).

$[\alpha]^{25}_{D}$ - 84.9 (*c* 10, $CDCl_3$); **^{1}H NMR** (400 MHz, $CDCl_3$) δ 4.78 (d, *J* = 8.9 Hz, 1H), 4.20 (d, *J* = 10.3 Hz, 1H), 4.07 – 3.96 (m, 1H), 3.81 (s, 3H), 3.78 (dd, *J* = 10.7, 2.9 Hz, 1H), 3.66 – 3.60 (m, 2H), 3.60 – 3.56 (m, 2H), 3.55 (br s, 1H), 2.60 (dd, *J* = 13.8, 4.6 Hz, 1H), 2.26 (br s, 2H), 2.03 – 1.96 (m, 5H), 1.97 – 1.93 (m, 2H), 1.92 – 1.88 (m, 2H), 1.87 – 1.84 (m, 1H), 1.66 (s, 6H), 1.45 (s, 9H) ppm.

This is in agreement with the spectral data reported by Crich *et al.*[395]

(5.35): Methyl (1-Adamantanyl 3,5,9-trideoxy-9-iodo-5-*N*-(1,1-dimethylethoxy)carbonyl-2-thio-D-glycero-β-D-galacto-non-2-ulopyranosid)onate



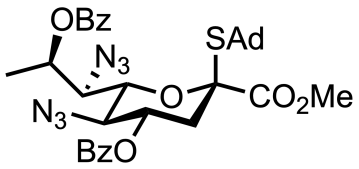
In an oven-dried flask under a nitrogen atmosphere, **5.58** (5.77 g, 9.00 mmol) was dissolved in anhydrous pyridine (180 mL) and cooled to 0 °C. Benzoyl chloride (3.66 mL, 31.5 mmol, 3.5 eq) was added dropwise, and the mixture was stirred at 0 °C for 1.5 h.

Upon completion, as determine by TLC, the mixture was diluted with EtOAc (200 mL), washed with sat. aq. NaHCO3 (200 mL), brine (200 mL), dried over $MgSO_4$, concentrated *in vacuo*. The residue was co-evaporated with toluene (100 mL x 3), and the crude material purified by flash column chromatography on silica (EtOAc:hexane, 0-50%) to provide **5.35** as a white foam (7.57 g, 99%).

$[\alpha]^{25}_D$ - 33.1 (*c* 10, $CDCl_3$); **^{1}H NMR** (400 MHz, $CDCl_3$) δ 8.10 (d, *J* = 7.3 Hz, 2H), 8.01 (d, *J* = 7.2 Hz, 2H), 7.60 (d_{app}, *J* = 7.6 Hz, 1H), 7.56 (d_{app}, *J* = 7.7 Hz, 1H), 7.51 – 7.45 (m, 2H), 7.45 – 7.40 (m, 2H), 5.62 (td_{app}, *J* = 11.2, 4.6 Hz, 1H), 5.00 (d, *J* = 8.7 Hz, 1H), 4.93 (td_{app}, *J* = 5.5, 2.5 Hz, 1H), 4.33 (dd, 10.1, 1.4 Hz, 1H), 4.26 (dd, *J* = 11.0, 2.5 Hz, 1H), 4.12 (d, *J* = 5.1 Hz, 1H), 3.94 (q_{app}, *J* = 10.0 Hz, 1H), 3.87 (dd, *J* = 11.1, 6.5 Hz, 1H), 3.82 (s, 3H), 2.75 (dd, *J* = 13.4, 4.6 Hz, 1H), 2.13 (t_{app}, *J* = 12.6 Hz, 1H), 1.96 – 1.86 (m, 6H), 1.75 (d, *J* = 11.7 Hz, 3H), 1.55 (d, *J* = 12.6 Hz, 3H), 1.47 (d, *J* = 12.5 Hz, 3H), 1.29 (s, 9H) ppm.

This is in agreement with the spectral data reported by Crich *et al.*[395]

(5.36): Methyl (1-Adamantanyl 5-azido-4,8-di-*O*-benzoyl-3,5,9-trideoxy-2-thio-D-glycero-β-D-galacto-non-2-ulopyranosid)onate



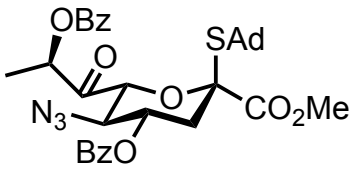
A solution of **5.35** (3.60 g, 4.24 mmol) and tris(trimethylsilyl)silane (3.92 mL, 12.7 mmol, 3 eq) in benzene (70 mL) was subjected to degassing by three freeze-pump-thaw cycles. In a separate flask, a 0.1 M solution of 2,2'-azobis(2-methylpropionnitrile) (AIBN) in benzene was prepared followed by degassing by three freeze-pump-thaw cycles. The solution containing **5.35** was stirred and heated to 60 °C, followed by dropwise addition of the AIBN solution (4.24 mL, 0.42 mmol, 0.1 eq). The reaction was stirred for 4 h, upon which completion was determined by TLC, and was cooled and concentrated *in vacuo* to dryness. The crude residue was dissolved in anhydrous methanol (15 mL), and 2 M hydrogen chloride solution in diethyl ether (30 mL) was added. The mixture was stirred at

rt for 3 h, upon which completion was determined by TLC, and then concentrated *in vacuo*. The crude residue was dissolved in acetonitrile (50 mL) and extracted with hexanes (3 x 50 mL) to remove any non-popular impurities. The acetonitrile layer was separate and concentrated to dryness to provide crude amine. This residue was taken up in a mixture of acetonitrile and water (4:1, 70 mL) and cooled to 0 °C. Triethylamine (1.77 mL, 12.7 mmol, 3 eq), $CuSO_4$ (67 mg, 0.42 mmol, 0.1 eq), and imidazole-1-sulfonyl azidehydrochloride (1.33 g, 6.35 mmol, 1.5 eq) were added to the stirring reaction mixture. The reaction was warmed to rt and stirred for 12 h, with reaction progress being monitored by TLC. After full consumption of the starting material, the mixture was diluted with EtOAc (100 mL) and washed 1M HCl (100 mL). The aqueous phase was extracted with EtOAc (100 mL x 2), and the combined organic layers were washed with brine (100 mL), dried over Na_2SO_4, and concentrated *in vacuo*. The crude material purified by flash column chromatography on silica (EtOAc:hexanes 15-50%) to provide **5.36** as a white foam (1.71 g, 62%).

$[\alpha]^{25}_D$ - 53.2 (*c* 10, $CDCl_3$); **^{1}H NMR** (300 MHz, $CDCl_3$) δ 8.10 – 7.99 (m, 4H), 7.65 – 7.53 (m, 2H), 7.53 – 7.40 (m, 4H), 5.67 (ddd, *J* = 10.8, 10.6, 4.6 Hz, 1H), 4.99 (dq, *J* = 8.6, 6.2 Hz, 1H), 4.35 (d, *J* = 10.1 Hz, 1H), 4.03 (d, *J* = 8.7 Hz, 1H), 3.91 (t_{app}, *J* = 10.0 Hz, 1H), 3.78 (s, 3H), 2.85 (dd, *J* = 13.5, 4.7 Hz, 1H), 2.13 (br s, 1H), 1.91 (dd, *J* = 13.8, 11.8 Hz, 1H), 1.86 (s, 3H), 1.76 (dd, *J* = 11.6, 1.7 Hz, 3H), 1.73 – 1.64 (m, 3H), 1.60 (d, *J* = 6.1 Hz, 3H), 1.53 (d, *J* = 12.8 Hz, 3H), 1.38 (d, *J* = 11.8 Hz, 3H) ppm.

This is in agreement with the spectral data reported by Crich *et al.*[395]

(5.61): Methyl (1-Adamantanyl 5-azido-4,8-di-*O*-benzoyl-3,5,9-trideoxy-7-oxo-2-thio-D-glycero-β-D-galacto-non-2-ulopyranosid)onate

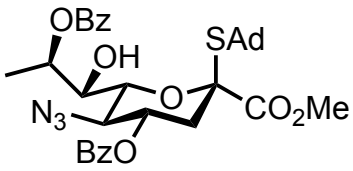


In an oven-dried flask under a nitrogen atmosphere, **5.36** (900 mg, 1.4 mmol) was dissolved in anhydrous dichloromethane (50 mL) and cooled to 0 °C. Dess-Martin periodinane (880 mg, 2.1 mmol, 1.5 eq) was added, and the reaction was warmed to rt. Upon consumption of starting material after 4 h, as determined by TLC, the mixture was diluted with diethyl ether (50 mL) and a mixture of sat. aq. $NaHCO_3$: sat. aq. $Na_2S_2O_3$ (1:1 v/v, 50 mL) was added. The layers were separated, and the organic layer was washed with brine, dried over $MgSO_4$, and concentrated *in vacuo*. The crude material was purified by flash column chromatography on silica (EtOAc:hexanes 0-20%) to provide **5.61** as a white foam (720 mg, 80%).

$[\alpha]^{25}_D$ - 90.5 (*c* 10, $CDCl_3$); **^{1}H NMR** (500 MHz, $CDCl_3$) δ 8.13 – 8.07 (m, 2H), 8.05 – 8.01 (m, 2H), 7.62 – 7.55 (m, 2H), 7.48 – 7.44 (m, 4H), 5.59 (q, *J* = 6.8 Hz, 1H), 5.49 (ddd, *J* = 11.4, 9.5, 4.8 Hz, 1H), 5.04 (d, *J* = 9.9 Hz, 1H), 3.85 (t, *J* = 9.7 Hz, 1H), 3.81 (s, 3H), 2.81 (dd, *J* = 13.7, 4.9 Hz, 1H), 2.05 (d, *J* = 11.6 Hz, 3H), 2.02 – 1.99 (m, 4H), 1.92 (d, *J* = 11.7 Hz, 3H), 1.71 (d, *J* = 6.9 Hz, 3H), 1.67 – 1.63 (m, 6H) ppm.

This is in agreement with the spectral data reported by Crich *et al.*[395]

(5.37): Methyl (1-Adamantanyl 5-azido-4,8-di-*O*-benzoyl-3,5,9-trideoxy-2-thio-D-glycero-β-L-altro-non-2-ulopyranosid)onate

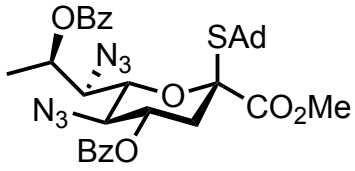


In an oven-dried flask under a nitrogen atmosphere, **5.61** (510 mg, 0.8 mmol) was dissolved in anhydrous CH_2Cl_2 (10 mL) and cooled to -78 °C. To this stirring solution was added a solution of cerium(III) chloride heptahydrate (880 mg, 2.4 mmol, 3 eq) in anhydrous methanol (15 mL). After stirring for 1 h at -78 °C, sodium borohydride (45 mg, 1.2 mmol, 1.5 eq) was added, and the reaction was monitored by TLC. After 1 h, upon consumption of starting material, the mixture was quenched with sat. aq. NH_4Cl (5 mL), warmed to rt, and concentrated *in vacuo*. The residue was redissolved in EtOAc (100 mL), washed with water (50 mL), brine (50 mL), dried over $MgSO_4$, and concentrated *in vacuo*. The crude material was purified by flash column chromatography on silica (EtOAc:hexanes 10-50%) to provide **5.37** as a white foam (300 mg, 65%) and recovered substrate **5.36** (57 mg, 11%).

$[\alpha]^{25}_D$ - 72.1 (*c* 10, $CDCl_3$); **^{1}H NMR** (500 MHz, $CDCl_3$) δ 8.08 (ddd, *J* = 22.4, 8.4, 1.2 Hz, 2H), 8.03 (dd, *J* = 8.5, 1.2 Hz, 2H), 7.61 – 7.53 (m, 2H), 7.49 – 7.43 (m, 4H), 5.59 (ddd, *J* = 11.4, 9.4, 4.9 Hz, 1H), 5.55 (q_{app}, *J* = 6.3 Hz, 1H), 4.40 (dd, *J* = 10.2, 2.8 Hz, 1H), 4.06 (t_{app}, J = 10.0 Hz, 1H), 4.05 – 4.03 (m, 1H), 3.59 (s, 3H), 2.74 (dd, *J* = 13.6, 4.8 Hz, 1H), 2.28 (br s, 1H), 2.03 – 1.97 (m, 6H), 1.95 (dd, *J* = 13.6, 11.2 Hz, 1H), 1.86 (d, *J* = 10.2 Hz, 3H), 1.69 – 1.61 (m, 6H), 1.51 (d, *J* = 6.3 Hz, 3H) ppm.

This is in agreement with the spectral data reported by Crich *et al.*[395]

(5.32): Methyl (1-Adamantanyl 5,7-diazido-4,8-di-*O*-benzoyl-3,5,7,9-tetradeoxy-2-thio-D-glycero-β-D-galacto-non-2-ulopyranosid)onate

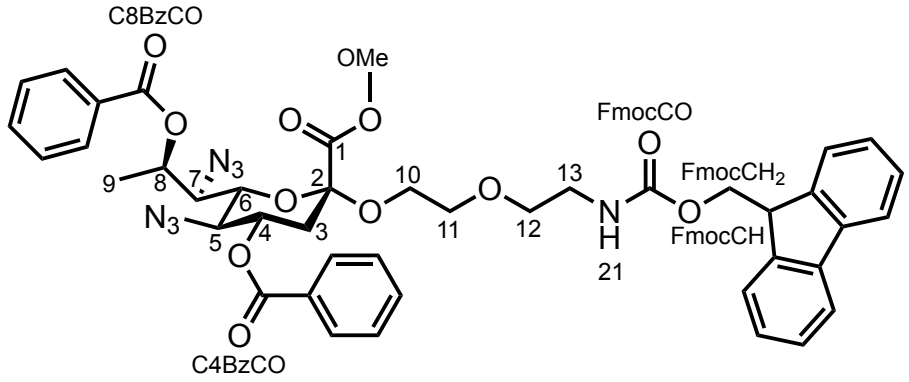


In an oven-dried flask under a nitrogen atmosphere, **5.37** (300 mg, 0.5 mmol) was dissolved in anhydrous CH_2Cl_2 (5 mL) and cooled to 0 °C. Anhydrous pyridine (370 µL, 4.6 mmol, 10 eq) was added followed by dropwise addition of triflic anhydride (230 µL, 1.39 mmol, 3 eq). The mixture was stirred at 0 °C for 1 h, and the reaction was monitored by TLC. Upon completion, the mixture was diluted with dichloromethane (20 mL) and poured into ice-cold 1 M HCl solution (20 mL). The organic phase was washed with cold water (20 mL), dried over $MgSO_4$, and concentrated *in vacuo*. The residue was dissolved in anhydrous DMF (12 mL), and the solution was cooled to 0 °C followed by addition of sodium azide (600 mg, 9.2 mmol, 20 eq). The mixture was stirred at 0 °C for 16 h, and the reaction was monitored by TLC. Upon completion, the mixture was diluted with ethyl acetate (50 mL) and washed with water (3 x 150 mL). The organic phase was washed with brine (50 mL), dried over $MgSO_4$, and concentrated *in vacuo*. The crude material was purified by flash column chromatography on silica (EtOAc:hexanes 0-30%) to provide **5.32** as a white foam (200 mg, 65%).

$[\alpha]^{25}_D$ - 64.1 (*c* 10, $CDCl_3$); **^{1}H NMR** (400 MHz, $CDCl_3$) δ 8.10 – 8.01 (m, 4H), 7.64 – 7.55 (m, 2H), 7.52 – 7.41 (m, 4H), 5.66 (ddd, *J* = 11.6, 9.8, 4.7 Hz, 1H), 5.39 (quint.$_{app}$, *J* = 6.2 Hz, 1H), 4.48 (dd, *J* = 10.1, 1.8 Hz, 1H), 3.89 (t, *J* = 10.0 Hz, 1H), 3.86 (dd, *J* = 6.6, 1.7 Hz, 1H), 3.79 (s, 3H), 2.88 (dd, *J* = 13.5, 4.7 Hz, 1H), 1.99 (dd, *J* = 13.5, 11.7 Hz, 1H), 1.95 – 1.83 (m, 6H), 1.73 (d, *J* = 11.6 Hz, 3H), 1.69 (d, *J* = 6.2 Hz, 3H), 1.57 (d, *J* = 12.4 Hz, 3H), 1.46 (d, *J* = 12.2 Hz, 3H) ppm.

This is in agreement with the spectral data reported by Crich *et al.*[395]

(5.64): Methyl [1-(Fmoc-NH–PEG$_2$–*O*)-(5,7-diazido-4,8-di-*O*-benzoyl-3,5,7,9-tetradeoxy-D-glycero-α-D-galacto-non-2-ulopyranosid)onate]

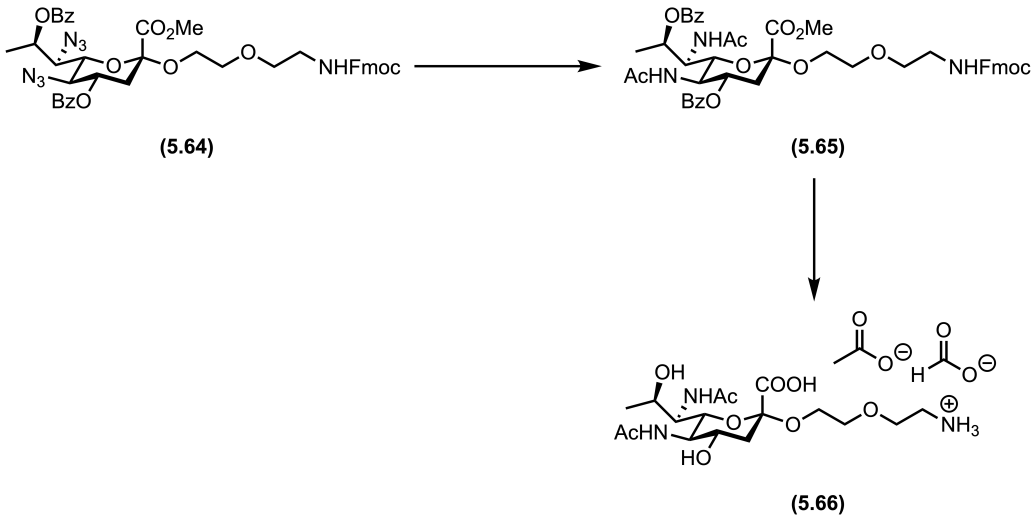


In an oven-dried flask under a nitrogen atmosphere, **5.32** (101 mg, 160 µmol), Fmoc-PEG2-alcohol (**5.63**) (64 mg, 200 µmol, 1.2 eq), and activated 4 Å acid-washed molecular sieves (300 mg) in anhydrous CH_2Cl_2:MeCN (2:1 v/v, 4 mL) were stirred at rt for 2 h. This was done to ensure minimal presence of water and maintain anhydrous reaction conditions. The mixture was cooled to −78 °C and treated with *N*-iodosuccinimide (44 mg, 200 µmol, 1.2 eq) and trifluoromethanesulfonic acid (2 µL, 25 µmol, 0.15 eq). The reaction mixture was stirred at −78 °C for 2 h, at which point completion was determined by TLC. The mixture was quenched with triethylamine (25 µL, 180 µmol, 1.1 eq). The mixture was diluted with CH_2Cl_2 (20 mL), filtered through celite, washed with sat. aq. Na_2SO_3 (20 mL), dried over $MgSO_4$, concentrated *in vacuo*. The crude material was purified by flash column chromatography on silica (EtOAc:hexanes:MeOH 30:70:0 to 48:48:4) to provide **5.64** as a white foam (90 mg, 66%).

[α]$^{25}_D$ - 6.1 (*c* 10, $CDCl_3$); **IR** (thin film) vmax = 3304 (N-H stretch), 2110 (azide stretch), 1718 (carbamate and ester C=O stretch), 1602 (aromatic C=C stretch) cm^{-1}; **^{1}H NMR** (400 MHz, $CDCl_3$) δ 8.14 – 7.91 (m, 4H), 7.73 (d, *J* = 7.5 Hz, 2H), 7.62 – 7.59 (m, 2H), 7.57 (d, *J* = 7.8 Hz, 3H), 7.47 (t, *J* = 7.7 Hz, 2H), 7.37 (t, *J* = 7.3 Hz, 2H), 7.34 – 7.20 (m, 2H), 5.60 (dq, $J_{8,7}$ = 8.6 Hz, $J_{8,9}$ = 6.2 Hz, 1H, H-8), 5.42 (s, 1H, NH), 5.16 (ddd, $J_{4,3ax}$ = 12.0 Hz, $J_{4,5}$ = 9.5 Hz, $J_{4,3eq}$ = 4.8 Hz, 1H, H-4), 4.43 – 4.29 (m, 2H, FmocCH$_2$), 4.21 (t, *J* = 7.2 Hz, 1H, FmocCH), 4.03 (dd, $J_{6,5}$ = 10.3 Hz, $J_{6,7}$ = 1.7 Hz, 1H, H-6), 3.97 (t_{app}, $J_{5,4}$ = 9.7 Hz, $J_{5,6}$ = 9.7 Hz, 1H, H-5), 3.92 (dd, *J* = 7.1, 6.1 Hz, 1H, H-10''), 3.68 (dd, $J_{7,8}$ = 8.7 Hz, $J_{7,6}$ = 1.7 Hz, 1H, H-7), 3.62 – 3.57 (m, 3H, H-10', H-11), 3.55 (t, *J* = 5.1 Hz, 2H, H-12), 3.46 (s, 3H, OMe), 3.39 (t, *J* = 5.1

Hz, 2H, H-13), 2.94 (dd, $J_{3eq,3ax}$ = 12.9 Hz, $J_{3eq,4}$ = 4.8 Hz, 1H, 3_{eq}), 2.00 (dd, $J_{3ax,3eq}$ = 12.8 Hz, $J_{3ax,4}$ = 12.3 Hz, 1H, 3_{ax}), 1.80 (s, 1H), 1.61 (d, $J_{9,8}$ = 6.2 Hz, 3H, H-9) ppm; **^{13}C NMR** (101 MHz, $CDCl_3$) δ 168.0 (C-1), 165.4 (BzCO), 165.3 (BzCO), 156.6 (FmocCO), 144.2, 144.1, 141.4, 133.7, 133.3, 130.3, 129.8, 129.8, 128.7, 128.6, 127.8, 127.1, 125.2, 120.0, 99.0 (C-2), 73.0 (C-6), 71.5 (C-4), 70.2 (C-11), 70.0 (C-12), 68.5 (C-8), 66.9 ($FmocCH_2$), 64.5 (C-10), 63.6 (C-7), 61.1 (C-5), 52.77 (OMe), 47.4 (FmocCH), 41.0 (C-13), 37.8 (C-3), 18.2 (C-9) ppm; **HRMS** (ESI+) *m/z* Calc. for $C_{43}H_{43}N_7O_{11}$ $[M + Na]^+$: 856.2920, found 856.2913.

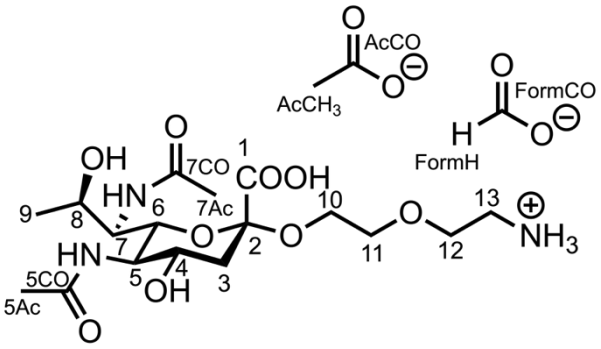
(5.66): [1-(2-aminoethoxyethoxy)-(5,7-diacetamido-3,5,7,9-tetradeoxy-D-glycero-α-D-galacto-non-2-ulopyranosid)onic acid] formate



To a stirred solution of **5.64** (40 mg, 50 µmol), in AcOH (0.2 mL), Ac_2O (0.8 mL) and THF (1.2 mL) was added nanoparticle zinc (63 mg, 960 µmol, 20 eq) in a single portion. The solution was stirred for 18 h at 55 °C before filtering through celite and co-evaporating with toluene (3 x 20 mL) to remove AcOH. The crude material was purified by reverse phase high-performance liquid chromatography (HPLC) [Waters X-Bridge BEH C18 120, semi prep, 0%B for 10 mins to 70%B over 50 mins; A = 0.1% formic acid in H_2O, B = 0.1% formic acid in MeCN] to provide the crude **5.65** as a white foam (15 mg, 36%). A crude ^{1}H-NMR of **5.65** was obtained to confirm its identity. To crude **5.65** (10 mg, 12 µmol) in MeOH (100 µL) was added NaOH (4.6 mg, 120 µmol) and the reaction was stirred at rt for 8 h. Upon completion, as determined by LC-MS, the reaction was quenched with formic acid

(20 uL) and concentrated *in vacuo*. The desalted material was dissolved in MeOH/MeCN (1:4 v/v) and purified on an Atlantis HILIC silica column (95%B for 15 min to 40%B over 60 min) to provide the desired **5.66** as a mixed formate and acetate salt (1.5 mg, 31%).

(5.65): **^{1}H NMR** (300 MHz, MeOD) δ 8.12 – 8.07 (m, 2H), 7.93 (d, *J* = 7.8 Hz, 2H), 7.74 (d, *J* = 7.5 Hz, 2H), 7.66 – 7.54 (m, 4H), 7.53 – 7.46 (m, 2H), 7.44 – 7.38 (m, 2H), 7.38 – 7.23 (m, 4H), 5.36 (dq, *J* =9.3, 6.3, 1H), 5.04 (ddd, *J* = 12.0, 10.4, 4.6 Hz, 1H), 4.54 (dt_{app}, *J* = 9.7, 3.2 Hz, 1H), 4.35 (d, *J* = 6.7 Hz, 2H), 4.29 (dd, *J* = 10.7, 2.5 Hz, 1H), 4.19 (t_{app}, *J* = 9.5 Hz, 2H), 4.02 – 3.95 (m, 1H), 3.81 (s_{app}, 1H), 3.65 – 3.58 (m, 2H), 3.55 (t_{app}, *J* = 5.3 Hz, 2H), 3.38 (s, 3H), 3.21 – 3.01 (m, 2H), 2.79 (dd, *J* = 12.5, 4.6 Hz, 1H), 2.05 (s, 3H), 1.94 (dd, *J* = 12.5, 12.1 Hz, 1H), 1.80 (s, 3H), 1.34 (d, *J* = 6.3 Hz, 3H).



(5.66): **^{1}H NMR** (600 MHz, D_2O) δ 8.47 (s, 1H, FormylH), 3.98 (dq, $J_{8,7}$ = 9.3 Hz, $J_{8,9}$ = 6.3 Hz, 1H, H-8), 3.95 (dd, $J_{6,5}$ = 10.2 Hz, $J_{6,7}$ = 3.1 Hz, 1H, H-6), 3.93 – 3.89 (m, 1H, H-10'), 3.87 (dd, $J_{7,8}$ = 9.3 Hz, $J_{7,6}$ = 3.1 Hz, 1H, H-7), 3.77 (t, *J* = 5.1 Hz, 2H, H-12), 3.72 (t, *J* = 4.4 Hz, 2H, H-11), 3.69 (dd, $J_{5,6}$ = 10.2 Hz, $J_{5,4}$ = 9.8 Hz, 2H, H-5), 3.70 – 3.64 (m, 2H, H-10''), 3.59 (ddd, $J_{4,3ax}$ = 11.9 Hz, $J_{4,5}$ = 9.8 Hz, $J_{4,3eq}$ = 4.7 Hz, 1H, H-4), 3.21 (t, *J* = 5.5 Hz, 2H, H-13), 2.78 (dd, $J_{3eq,3ax}$ = 12.5 Hz, $J_{3eq,4}$ = 4.7 Hz, 1H, H-3_{eq}), 2.01 (s, 3H, 7Ac), 1.97 (s, 3H, 5Ac), 1.93 (s, 1H, AcCH3), 1.68 (t_{app}, $J_{3ax,3eq}$ = 12.2 Hz, $J_{3ax,4}$ = 12.2 Hz, 1H, H-3_{ax}), 1.17 (d, $J_{9,8}$ = 6.3 Hz, 3H, H-9); **^{13}C NMR** (151 MHz, D_2O) δ 181.6 (AcCO), 174.0 (5CO), 173.7 (7CO), 173.4 (C-1), 171.0 (FormCO), 100.7 (C-2), 71.7 (C-6), 69.5 (C-11), 68.6 (C-4), 67.1 (C-8), 66.8 (C-12), 63.6 (C-10), 53.9 (C-7), 52.1 (C-5), 40.2 (C-3), 39.1 (C-13), 23.3 ($AcCH_3$), 22.1 (5Ac) 22.0 (7Ac), 18.0 (C-9); **HRMS** (ESI+) *m/z* Calc. for $C_{17}H_{31}N_3O_9$ $[M + Na]^+$: 444.1958, found 444.1953.

6.8 Pharmacological and Binding Methods

6.8.1 CB_1 Radioligand Binding Assay

Cell Culture

Human Embryonic Kidney 293 (HEK 293; RRID:CVCL_0045) cells were cultivated in Dulbecco's Modified Eagle's Medium (DMEM; Gibco, Thermo Fisher Scientific, Waltham, MA, USA) supplemented with 10% foetal bovine serum (FBS; New Zealand-origin, Moregate Biotech, Brisbane, Australia) and appropriate selection antibiotics, and incubated in 5% CO_2 at 37 °C in a humidified atmosphere.

Radioligand Binding Assay

Competition/displacement binding assays were performed using HEK 293 cell membranes stably expressing human CB_1 receptors N-terminally tagged with preprolactin signal sequence (pplss) and three hemagglutinin (3HA) epitopes (pplss-3HA-hCB_1; initially reported in Finlay *et al.,* 2017). For membrane preparation, HEK 293 pplss-3HA-hCB_1 cells were cultivated in DMEM (Gibco, Thermo Fisher Scientific, Waltham, MA, USA) supplemented with 10% FBS (New Zealand-origin, Moregate Biotech, Brisbane, Australia) in 175 cm^2 polystyrene flasks until 80-90% confluent. HEK 293 cells were harvested using 5 mM EDTA in PBS, sedimented and then snap frozen at −80°C. Cell pellets were resuspended in sucrose buffer (200 mM sucrose, 50 mM Tris-HCl pH 7.4, 5 mM $MgCl_2$, 2.5 mM EDTA), with “P2” membranes prepared in sucrose buffer as previously described [423]. Protein concentration was quantified using a BioRad DC protein assay (Hercules, CA, USA), according to manufacturer’s instructions.

For binding assays, unlabelled drugs (CP55940 and LYTAC), radioligand (1.5 nM [^{3}H]-CP55940; PerkinElmer, Waltham, MA, USA) and P2 membrane isolate (8 µg) were diluted in ice-cold binding buffer [50 mM HEPES pH 7.4, 1 mM $MgCl_2$, 1mM $CaCl_2$, 0.2% NZ-origin bovine serum albumin (BSA; MP Biomedicals, Santa Ana, CA, USA)] and dispensed into 96-well, polypropylene V-well plates. Plates were sealed and incubated at 30°C for one hour. During the incubation, a 96-position printed glass fibre filtermat (PerkinElmer, Waltham MA, USA) was treated with 0.1% w/v branched polyethyleneimine (PEI; Sigma-Aldrich, St. Louis, MO, USA) in water for approximately one hour. At the conclusion of the

incubation, filtermats were washed with 200 µL ice-cold wash buffer (50 mM HEPES pH 7.4, 500 mM NaCl, 0.2% BSA) under vacuum. The binding assay mixture (displacer drug, membrane and radioligand) was then filtered through the filtermat and washed a further three times with 200 µL wash buffer. The filtermat was dried overnight at room temperature, prior to the application of melt-on solid scintillator (MeltiLex®-A; PerkinElmer, Waltham MA, USA) with a heating block. Filtermats were incubated in dark conditions for 30 minutes, and then radioactivity was detected in a MicroBeta^2 TriLux Liquid Scintillation Counter (PerkinElmer, Waltham MA, USA) at two-minute counts per well, with counts corrected for detector efficiency. Data was analysed using GraphPad Prism v9 (GraphPad Software Inc., La Jolla, CA, USA) and normalised to vehicle (100% specific binding) and 1 µM CP55940 (0%), with homologous binding data modelled using pre-defined equations in GraphPad Prism.

6.8.2 *in vitro* Cannabinoid Receptor Functional Activity Assays

Assays investigating changes in membrane potential resulting from CB_1 activation were performed as previously described, and adapted for antagonist study.[424,425] Briefly, mouse AtT20 adenocarcinoma cells stably transfected with human CB_1 were cultured in DMEM containing 10% FBS, 100 U penicillin/streptomycin, and 80 µg/mL hygromycin. Cells were passaged at 80% confluency as required. Cells for assays were grown in 75 cm^2 flasks and used at 90% confluence. The day before the assay, cells were detached from the flask with trypsin/EDTA (Sigma-Aldrich, St Louis, MO, USA) and resuspended in 10 mL of Leibovitz's L-15 media supplemented with 1% FBS, 100 U penicillin/streptomycin and 15 mM glucose. The cells were plated in black-walled, clear-bottomed poly-D-lysine-coated 384-well microplates (Corning, Corning, NY, USA) at 22.5 µL/well. Cells were incubated overnight at 37 °C in ambient CO_2. Membrane potential was measured using a FLIPR Membrane Potential Assay kit blue (Molecular Devices, San Jose, CA, USA), as described previously.[426] The dye was reconstituted with assay buffer of composition (mM): NaCl 145, HEPES 22, Na_2HPO_4 0.338, $NaHCO_3$ 4.17, KH_2PO_4 0.441, $MgSO_4$ 0.407, $MgCl_2$ 0.493, $CaCl_2$ 1.26, glucose 5.56 (pH 7.4). Prior to the assay, cells were loaded with 22.5 µL/well of the dye solution without removal of the L-15, and

incubated at 37 °C with ambient CO_2 for 60 min. Fluorescence was measured using a FlexStation 3 microplate reader (Molecular Devices, San Jose, CA, USA; l_{ex} = 530 nM and l_{ex} = 565 nM). Baseline readings were taken every 2 s for at least 2 min, at which time either drug or vehicle (0.1% DMSO + 0.01% BSA in assay buffer) was added in a volume of 5 µL (first addition), followed by a second addition of a different drug or vehicle (5 µL) after an additional 5 minutes. The background fluorescence of cells without dye or dye without cells was negligible. Changes in fluorescence were expressed as a percentage of baseline fluorescence after subtraction of the vehicle, and normalised to the response produced by 10 µM CP55,940 (100%). Data is expressed as the mean ± SEM of at least 4 independent determinations performed in duplicate, unless otherwise noted. Pooled data were fit to a four-parameter logistic equation in GraphPad Prism 10 (GraphPad Software, San Diego CA, USA).

6.8.3 RaPID mRNA display selection with/ without reprogramming against ASGPR1

This work was completed by Dr Jessica Zhong, University of Sydney

tRNAs required for genetic reprogramming were prepared by *in vitro* transcription from PCR-generated DNA templates as previously described.[427] Sulfo-L-Tyr-DBE and N-ClAc-L/D-Tyr-CME reagents were synthesized as previously described.[428]

Acylation of sulfo-L-Tyr-tRNA$_{CAU}$ and N-ClAc-L/D-Tyr-tRNA$_{ini}$

A solution of 42 µM dFx flexizyme and 42 µM tRNA$_{CAU}$ substrate in 50 mM HEPES, pH 7.5 was heated to 95 °C for 2 min before being incubated at room temperature for 5 min. 1/3 vol.% of 3 M $MgCl_2$ was added and the solution was further incubated at room temperature for 5 min. Then, sulfo-L-Tyr-DBE (25 mM in DMSO) was added, resulting in a mixture of 50 mM HEPES pH 7.5, 25 µM dFx flexizyme, 25 µM tRNA$_{CAU}$, 0.6 M $MgCl_2$ and 5 mM sulfo-L-Tyr-DBE. The mixture was incubated at 0 °C for 2 h, then quenched by adding 3 M NaOAc pH 5.2 to 85 mM. The acylated tRNA were precipitated by mixing with 2 × vol.% of ethanol and 15 min centrifugation at 15,000 × g. The RNA pellets were washed twice with 70 vol.% EtOH containing 0.1 M NaOAc (pH 5.2) then once with 70 vol.% EtOH,

before dissolving in 0.2 vol.% acetic acid to give a 250 μM solution which was stored dry at -80 ˚C until use. ClAc-L/D-Tyr-$tRNA_{ini}$ was prepared in a similar manner but using ClAc-L-Tyr-CME, initiator $tRNA_{ini}$ and the eFx flexizyme.

Affinity selection against ASGPR1

To prepare a puromycin-linked mRNA library, DNA oligos comprising a T7 promoter, ribosome binding site, ATG start codon, 4–15 NNS (N = A, C, G or T; S = C or G) codons, a TGC (Cys) codon and a 3' fixed region encoding a SALSA linker were amplified by 7 cycles of PCR. The resulting library was transcribed *in vitro* using T7 RNA polymerase to generate mRNA, which was purified by denaturing urea polyacrylamide gel electrophoresis. The libraries of different lengths were then pooled proportional to theoretical diversity. The pooled mRNA library was then ligated to a puromycin-linked oligonucleotide using T4 RNA ligase.

For the initial round of selection, the mRNA library was translated using a PURExpress DRF system (New England Biolabs) with release factors 2 and 3 (RF2 and 3) added following the manufacturer's directions. Initiating and internal Met residues were reprogrammed using a custom Solution A containing only 19 aminoacylated tRNA, missing $tRNA_{ini}$ and $tRNA_{CAU}$, and 25 μM of sulfo-L-Tyr-$tRNA_{CAU}$ was added with either 25 μM N-ClAc-L or D-Tyr-$tRNA_{ini}$. For selection without sY reprogramming, only aminoacylated $tRNA_{ini}$ were added. After translation, magnesium acetate was added to 8 mM to improve puromycin coupling to the peptide chain, and finally the ribosomal complex was denatured using 20 mM EDTA.

The mRNA-peptide library was then reverse transcribed using MMLV H-reverse transcriptase. The reverse transcribed peptide-mRNA-cDNA library was panned against 120 pmol of biotinylated ASGPR1 immobilized on Dynabeads M-280 Streptavidin beads (Life Technologies) for 30 min at 4 °C. After washing with ice-cold TBS-T (50 mM Tris pH 8, 150 mM NaCl, 0.05% w/v Tween® 20), the fused peptide–mRNA/cDNA was isolated from the beads by heating to 95 °C for 5 min, and the cDNA was amplified by 25 cycles of PCR, purified by ethanol precipitation, and transcribed as above to produce the enriched mRNA library for the next round of selection. For rounds 2-7, iterative counter-selections

were used to remove peptides with affinity for the Dynabeads™ by pre-incubating the mRNA-peptide library with 50% biotin saturated Dynabeads™ consecutively 3 times (30 min at 4 ℃ each time), before incubating with 20 pmol of ASGPR1 immobilized on Dynabeads™. Sequencing of the enriched cDNA from rounds 5-7 was conducted using an iSeq100 next generation sequencer (Illumina) and analysed using customised script and CLC workbench software (Qiagen).

6.8.4 Production of biotinylated 1E8 Fab'

This work was completed by Dr Niccolay Madiedo Soler and Professor Ethan Goddard-Borger, Walter and Eliza Hall Institute

A plasmid encoding 1E8 reformatted into a mouse IgG2a (Genscript) was transfected and expressed in ExpiCHO cells following the manufacturer's instructions (ThermoFisher). 1E8 IgG2a was purified by affinity chromatography. In brief, clarified supernatant was passed through protein A resin pre-equilibrated in TBS buffer (20 mM Tris pH 7.4, 150 mM NaCl). Resin was washed with 10 column volumes of TBS prior to elution of the IgG with 100 mM glycine pH 2.7. Elution fractions were equilibrated with 1M Tris pH 9.0 and further purified by size exclusion chromatography using the Superdex® 200 increase 10/300 GL column (GE Healthcare) pre-equilibrated in PBS buffer.

To generate 1E8 F(ab')2, purified IgG was cleaved below the hinge region using IdeZ protease. Reactions were set up in PBS buffer and incubated at RT for 1h. 6xHis-tagged IdeZ and cleaved Fc were removed by reverse chromatography using Ni-NTA and protein A resin. Lastly, purified F(ab')2 was treated with 50 mM 2-MEA at RT for 20 min to generate Fab'. 2-MEA was removed by buffer exchange into PBS buffer using a Zeba spin desalting column (ThermoFisher) prior to chemical biotinylation of the Fab' with EZ-Link™ Maleimide-PEG2-Biotin following manufacturer's recommendations (ThermoFisher). Biotinylated 1E8 Fab' was further purified by size exclusion chromatography using the Superdex® 200 increase 10/300 GL column (GE Healthcare) pre-equilibrated in PBS buffer.

6.8.5 Surface plasmon resonance (SPR)

This work was completed by Dr Niccolay Madiedo Soler and Professor Ethan Goddard-Borger, Walter and Eliza Hall Institute

Binding experiments were carried out using the Biacore S200 system (GE Healthcare) in 10 mM HEPES pH 7.4, 150 mM NaCl, 0.02% Tween 20. Dilutions of Pse derivatives (**4.176**, **4.177**, and **4.178**) and Leg glycoside (**5.66**) were passed over biotinylated 1E8 Fab' immobilised onto a streptavidin-coated sensor chip (Citiva) for 60 sec at 30 µl/min. Dissociation of analytes was achieved with running buffer for 120 sec at 30 µl/min. A reference flow cell (no ligand) was included in the experiments, and the recorded data was subtracted from the experimental flow cells. Data was plotted in Prism (Graphpad).

References

(1) Davis, B. G. *Carbohydrate Chemistry*; Oxford Chemistry Primers; Oxford University Press: Oxford, **2002**.

(2) M.L. Sinnott; *Carbohydrate Chemistry and Biochemistry: Structure and Mechanism*; The Royal Society of Chemistry: Cambridge, **2007**; Chapter 1, pp 1–40.

(3) De Vivo, D. C.; Trifiletti, R. R.; Jacobson, R. I.; Ronen, G. M.; Behmand, R. A.; Harik, S. I. Defective Glucose Transport across the Blood-Brain Barrier as a Cause of Persistent Hypoglycorrhachia, Seizures, and Developmental Delay. *N. Engl. J. Med.* **1991**, *325* (10), 703–709. https://doi.org/10.1056/NEJM199109053251006.

(4) Komor, E.; Schobert, C.; Cho, B. H. Sugar Specificity and Sugar-Proton Interaction for the Hexose-Proton-Symport System of Chlorella. *Eur. J. Biochem.* **1985**, *146* (3), 649–656. https://doi.org/10.1111/j.1432-1033.1985.tb08700.x.

(5) Adero, P. O.; Amarasekara, H.; Wen, P.; Bohé, L.; Crich, D. The Experimental Evidence in Support of Glycosylation Mechanisms at the SN1–SN2 Interface. *Chem. Rev.* **2018**, *118* (17), 8242–8284. https://doi.org/10.1021/acs.chemrev.8b00083.

(6) Crich, D. Mechanism of a Chemical Glycosylation Reaction. *Acc. Chem. Res.* **2010**, *43* (8), 1144–1153. https://doi.org/10.1021/ar100035r.

(7) Breton, C.; Fournel-Gigleux, S.; Palcic, M. M. Recent Structures, Evolution and Mechanisms of Glycosyltransferases. *Curr. Opin. Struct. Biol.* **2012**, *22* (5), 540–549. https://doi.org/10.1016/j.sbi.2012.06.007.

(8) Davis, B. G.; H*and in glove*, Chemistry & Industry, (**2000**), *4*, 134-138.

(9) Ambrosi, M.; Cameron, N. R.; Davis, B. G. Lectins: Tools for the Molecular Understanding of the Glycocode. *Org. Biomol. Chem.* **2005**, *3* (9), 1593–1608. https://doi.org/10.1039/B414350G.

(10) Pinho, S.S., Alves, I., Gaifem, J. *et al.* Immune regulatory networks coordinated by glycans and glycan-binding proteins in autoimmunity and infection. *Cell Mol. Immunol.* **20**, 1101–1113 (**2023**). https://doi.org/10.1038/s41423-023-01074-1.

(11) Haji-Ghassemi, O.; Blackler, R. J.; Martin Young, N.; Evans, S. V. Antibody Recognition of Carbohydrate Epitopes†. *Glycobiology* **2015**, *25* (9), 920–952. https://doi.org/10.1093/glycob/cwv037.

(12) de Haan, N.; Nielsen, M. I.; Wandall, H. H. Reading and Writing the Human Glycocode. *Annu. Rev. Biochem.* **2024**, *93* (1), 529–564. https://doi.org/10.1146/annurev-biochem-030122-044347.

(13) Griffin, M. E.; Hsieh-Wilson, L. C. Glycan Engineering for Cell and Developmental Biology. *Cell Chem. Biol.* **2016**, *23* (1), 108–121. https://doi.org/10.1016/j.chembiol.2015.12.007.

(14) Schnaar, R. L. Glycans and Glycan-Binding Proteins in Immune Regulation: A Concise Introduction to Glycobiology for the Allergist. *J. Allergy Clin. Immunol.* **2015**, *135* (3), 609–615. https://doi.org/10.1016/j.jaci.2014.10.057.

(15) Lee, S.; Inzerillo, S.; Lee, G. Y.; Bosire, E. M.; Mahato, S. K.; Song, J. Glycan-Mediated Molecular Interactions in Bacterial Pathogenesis. *Trends Microbiol.* **2022**, *30* (3), 254–267. https://doi.org/10.1016/j.tim.2021.06.011.

(16) Whelan, W. J. *Biological Functions of Carbohydrates*; Springer: Dordrecht, **1986**.

(17) Zimmer, J. Structural Features Underlying Recognition and Translocation of Extracellular Polysaccharides. *Interface Focus* **2019**, *9* (2), 20180060. https://doi.org/10.1098/rsfs.2018.0060.

(18) Reitsma, S.; Slaaf, D. W.; Vink, H.; van Zandvoort, M. A.; oude Egbrink, M. G. The Endothelial Glycocalyx: Composition, Functions, and Visualization. *Pflügers Arch. Eur. J. Physiol.* **2007**, *454* (3), 345–359. doi.org/10.1007/s00424-007-0212-8.

(19) Strzyz P. Bend it like glycocalyx. *Nat. Rev. Mol. Cell Biol.* **2019**, *20* (7), 388. doi: 10.1038/s41580-019-0142-2.

(20) He, M., Zhou, X. & Wang, X. Glycosylation: mechanisms, biological functions and clinical implications. *Sig. Transduct. Target. Ther.*, **2024**, *194*. https://doi.org/10.1038/s41392-024-01886-1.

(21) Ninham, B. W.; Bunkin, N.; Battye, M. The Endothelial Surface Layer-Glycocalyx - Universal Nano-Infrastructure Is Fundamental to Physiology, Cell Traffic and a Complementary Neural Network. *Adv. Colloid Interface Sci.* **2025**, *338*, 103401. https://doi.org/10.1016/j.cis.2025.103401.

(22) Tsai, Y.-X.; Chang, N.-E.; Reuter, K.; Chang, H.-T.; Yang, T.-J.; Bülow, S. von; Sehrawat, V.; Zerrouki, N.; Tuffery, M.; Gecht, M.; Grothaus, I. L.; Ciacchi, L. C.; Wang, Y.-S.; Hsu, M.-F.; Khoo, K.-H.; Hummer, G.; Hsu, S.-T. D.; Hanus, C.; Sikora, M. Rapid Simulation of Glycoprotein Structures by Grafting and Steric Exclusion of Glycan Conformer Libraries. *Cell* **2024**, *187* (5), 1296-1311.e26. https://doi.org/10.1016/j.cell.2024.01.034.

(23) Saha, S.; Anilkumar, A. A.; Mayor, S. GPI-Anchored Protein Organization and Dynamics at the Cell Surface. *J. Lipid Res.* **2016**, *57* (2), 159–175. https://doi.org/10.1194/jlr.R062885.

(24) Szarpak, A.; Auzély-Velty, R. Hyaluronic Acid Single-Network Hydrogel with High Stretchable and Elastic Properties. *Carbohydr. Polym.* **2023**, *320*, 121212. https://doi.org/10.1016/j.carbpol.2023.121212.

(25) Chandran, P. L.; Horkay, F. Aggrecan, an Unusual Polyelectrolyte: Review of Solution Behavior and Physiological Implications. *Acta Biomater.* **2012**, *8* (1), 3–12. https://doi.org/10.1016/j.actbio.2011.08.011.

(26) Gao S, Jin W, Quan Y, Li Y, Shen Y, Yuan S, Yi L, Wang Y, Wang Y. Bacterial capsules: Occurrence, mechanism, and function. *NPJ Biofilms Microbiomes*. **2024**, *10* (1), 21. doi: 10.1038/s41522-024-00497-6.

(27) Lerouge, I.; Vanderleyden, J. O-Antigen Structural Variation: Mechanisms and Possible Roles in Animal/Plant–Microbe Interactions. *FEMS Microbiol. Rev.* **2002**, 26 (1), 17–47. doi.org/10.1111/j.1574-6976.2002.tb00597.x

(28) Sande, C.; Bouwman, C.; Kell, E.; Nickerson, N. N.; Kapadia, S. B.; Whitfield, C. Structural and Functional Variation in Outer Membrane Polysaccharide Export (OPX) Proteins from the Two Major Capsule Assembly Pathways Present in *Escherichia coli*. *J. Bacteriol.* **2019**, *201* (14), 10.1128/jb.00213-19. https://doi.org/10.1128/jb.00213-19.

(29) Nanra, J. S.; Buitrago, S. M.; Crawford, S.; Ng, J.; Fink, P. S.; Hawkins, J.; Scully, I. L.; McNeil, L. K.; Aste-Amézaga, J. M.; Cooper, D.; Jansen, K. U.; Anderson, A. S. Capsular Polysaccharides Are an Important Immune Evasion Mechanism for Staphylococcus Aureus. *Hum. Vaccines Immunother.* **2013**, *9* (3), 480–487. https://doi.org/10.4161/hv.23223.

(30) Buchanan, C. J.; Gaunt, B.; Harrison, P. J.; Yang, Y.; Liu, J.; Khan, A.; et al. Pathogen-Sugar Interactions Revealed by Universal Saturation Transfer Analysis. *Science* **2022**, 376 (6596), eabm3125. doi.org/10.1126/science.abm3125.

(31) Somers, W. S.; Tang, J.; Shaw, G. D.; Camphausen, R. T. Insights into the Molecular Basis of Leukocyte Tethering and Rolling Revealed by Structures of P- and E-Selectin Bound to SLeX and PSGL-1. *Cell* **2000**, *103* (3), 467–479. https://doi.org/10.1016/S0092-8674(00)00138-0.

(32) Ivetic, A.; Hoskins Green, H. L.; Hart, S. J. L-Selectin: A Major Regulator of Leukocyte Adhesion, Migration and Signaling. *Front. Immunol.* **2019**, *10*, 1068. doi.org/10.3389/fimmu.2019.01068.

(33) Macauley, M. S.; Crocker, P. R.; Paulson, J. C. Siglec-Mediated Regulation of Immune Cell Function in Disease. *Nat. Rev. Immunol.* **2014**, *14* (10), 653–666. doi.org/10.1038/nri3737

(34) Wielgat P, Rogowski K, Niemirowicz-Laskowska K, Car H. Sialic Acid-Siglec Axis as Molecular Checkpoints Targeting of Immune System: Smart Players in Pathology and Conventional Therapy. *Int. J. Mol. Sci.* **2020**, *21* (12), 4361. doi: 10.3390/ijms21124361.

(35) Ramírez-Cortés, F.; Ménová, P. Hepatocyte Targeting via the Asialoglycoprotein Receptor. *RSC Med. Chem.* **2025**, *16*, 525–544. DOI: 10.1039/D4MD00652F.

(36) Bider, M. D.; Wahlberg, J. M.; Kammerer, R. A.; Spiess, M. The Oligomerization Domain of the Asialoglycoprotein Receptor Preferentially Forms 2:2 Heterotetramers *in Vitro*. *J. Biol. Chem.* **1996**, *271* (50), 31996–32001. https://doi.org/10.1074/jbc.271.50.31996.

(37) Geffen, I.; Spiess, M. Asialoglycoprotein Receptor. In *International Review of Cytology*; Friedlander, M., Mueckler, M., Eds.; *Molecular Biology of Receptors and Transporters*; Academic Press: San Diego, **1993**, *137*, 181–219. doi.org/10.1016/S0074-7696(08)62605-4.

(38) Ashwell, G.; Harford, J. Carbohydrate-Specific Receptors of the Liver. *Annu. Rev. Biochem.* **1982**, *51* (1), 531–554. doi.org/10.1146/annurev.bi.51.070182.002531

(39) Kim, J.; Byun, I.; Kim, D. Y.; Joh, H.; Kim, H. J.; Lee, M. J. Targeted Protein Degradation Directly Engaging Lysosomes or Proteasomes. *Chem. Soc. Rev.* **2024**, *53* (7), 3253–3272. https://doi.org/10.1039/D3CS00344B.

(40) Moran, A. P.; Prendergast, M. M. Molecular Mimicry in *Campylobacter jejuni* and *Helicobacter pylori* Lipopolysaccharides: Contribution of Gastrointestinal Infections to Autoimmunity. *J. Autoimmun.* **2001**, *16* (3), 241–256. doi.org/10.1006/jaut.2000.0490

(41) Läubli, H.; Varki, A. Sialic Acid–Binding Immunoglobulin-Like Lectins (Siglecs) Detect Self-Associated Molecular Patterns to Regulate Immune Responses. *Cell. Mol. Life Sci.* **2020**, *77*, 593–605. doi.org/10.1007/s00018-019-03288-x

(42) Hao, C.; Zou, Q.; Bai, X.; Shi, W. Effect of Glycosylation on Protein Folding: From Biological Roles to Chemical Protein Synthesis. *iScience* **2025**, *28* (6), 112605. https://doi.org/10.1016/j.isci.2025.112605.

(43) Guay, K. P.; Ke, H.; Canniff, N. P.; George, G. T.; Eyles, S. J.; Mariappan, M.; Contessa, J. N.; Gershenson, A.; Gierasch, L. M.; Hebert, D. N. ER Chaperones Use a Protein Folding and Quality Control Glyco-Code. *Mol. Cell* **2023**, *83* (24), 4524-4537.e5. https://doi.org/10.1016/j.molcel.2023.11.006.

(44) Zhou, Q.; Qiu, H. The Mechanistic Impact of N-Glycosylation on Stability, Pharmacokinetics, and Immunogenicity of Therapeutic Proteins. *J. Pharm. Sci.* **2019**, *108* (4), 1366–1377. https://doi.org/10.1016/j.xphs.2018.11.029.

(45) Park, E. I.; Manzella, S. M.; Baenziger, J. U. Rapid Clearance of Sialylated Glycoproteins by the Asialoglycoprotein Receptor. *J. Biol. Chem.* **2003**, *278* (7), 4597–4602. https://doi.org/10.1074/jbc.M210612200.

(46) Varki, A.; Schnaar, R. L.; Schauer, R. Sialic Acids and Other Nonulosonic Acids. *Essentials of Glycobiology*, 4th ed.; Varki, A., Cummings, R. D., Esko, J. D., et al., Eds.; Cold Spring Harbor Laboratory Press: Cold Spring Harbor, NY, **2022**; Chapter 15. doi.org/10.1101/glycobiology.4e.015.

(47) Jiang, H.; Qin, X.; Wang, Q.; Xu, Q.; Wang, J.; Wu, Y.; Chen, W.; Wang, C.; Zhang, T.; Xing, D.; Zhang, R. Application of Carbohydrates in Approved Small Molecule Drugs: A Review. *Eur. J. Med. Chem.* **2021**, *223*, 113633. https://doi.org/10.1016/j.ejmech.2021.113633.

(48) Wang, J.; Zhang, Y.; Lu, Q.; Xing, D.; Zhang, R. Exploring Carbohydrates for Therapeutics: A Review on Future Directions. *Front. Pharmacol.* **2021**, *12*. https://doi.org/10.3389/fphar.2021.756724.

(49) von Itzstein, M. The War against Influenza: Discovery and Development of Sialidase Inhibitors. *Nat. Rev. Drug Discov.* **2007**, *6* (12), 967–974. https://doi.org/10.1038/nrd2400.

(50) Witczak, Z. J. Carbohydrate Therapeutics: New Developments and Strategies. In *Carbohydrate Drug Design*; Witczak, Z. J., Nieforth, K. A., Eds.; *ACS Symp. Ser.* **2006**, *932*, 25–46. https://doi.org/10.1021/bk-2006-0932.ch002.

(51) Josse, R. G. Acarbose for the Treatment of Type II Diabetes: The Results of a Canadian Multi-Centre Trial. *Diabetes Res. Clin. Pract.* **1995**, *28 Suppl*, S167-172. https://doi.org/10.1016/0168-8227(95)01081-n.

(52) van de Laar, F. A. Alpha-Glucosidase Inhibitors in the Early Treatment of Type 2 Diabetes. *Vasc. Health Risk Manag.* **2008**, *4* (6), 1189–1195. https://doi.org/10.2147/vhrm.s3119.

(53) Van Gaal, L.; Nobels, F.; De Leeuw, I. Effects of Acarbose on Carbohydrate Metabolism, Electrolytes, Minerals and Vitamins in Fairly Well-Controlled Non-Insulin-Dependent Diabetes Mellitus. *Z. Gastroenterol.* **1991**, *29*, 642–644.

(54) Hao, C.; Xu, H.; Yu, L.; Zhang, L. Heparin: An Essential Drug for Modern Medicine. In *Progress in Molecular Biology and Translational Science*; Zhang, L., Ed.; Academic Press: Cambridge, MA, **2019**; 163, pp 1–19. doi.org/10.1016/bs.pmbts.2019.02.002.

(55) Khodadadi Yazdi, M.; Seidi, F.; Hejna, A.; Zarrintaj, P.; Rabiee, N.; Kucinska-Lipka, J.; Saeb, M. R.; Bencherif, S. A. Tailor-Made Polysaccharides for Biomedical Applications. *ACS Appl. Bio. Mater.* **2024**, *7* (7), 4193–4230. https://doi.org/10.1021/acsabm.3c01199.

(56) Solá, R. J.; Griebenow, K. Effects of Glycosylation on the Stability of Protein Pharmaceuticals. *J. Pharm. Sci.* **2009**, *98* (4), 1223–1245. https://doi.org/10.1002/jps.21504.

(57) Varasteh Moradi, S.; M. Hussein, W.; Varamini, P.; Simerska, P.; Toth, I. Glycosylation, an Effective Synthetic Strategy to Improve the Bioavailability of Therapeutic Peptides. *Chem. Sci.* **2016**, *7* (4), 2492–2500. https://doi.org/10.1039/C5SC04392A.

(58) Frederick, C. A.; Williams, L. D.; Ughetto, G.; van der Marel, G. A.; van Boom, J. H.; Rich, A.; Wang, A. H. Structural Comparison of Anticancer Drug-DNA Complexes: Adriamycin and Daunomycin. *Biochemistry* **1990**, *29* (10), 2538–2549.

(59) Kushwaha, D.; Kushwaha, A. K.; Kumar, R.; Chauhan, D. Recent Advances in the Synthesis of Glycoconjugated Heterocycles: A Promising Strategy for Accessing Bioactive Compounds. *Bioorganic Chem.* **2025**, *162*, 108559. https://doi.org/10.1016/j.bioorg.2025.108559.

(60) Azad, C. S.; Saxena, M.; Siddiqui, A. J.; Bhardwaj, J.; Puri, S. K.; Dutta, G. P.; Anand, N.; Saxena, A. K. Synthesis of Primaquine Glyco-Conjugates as Potential Tissue Schizontocidal Antimalarial Agents. *Chem. Biol. Drug Des.* **2017**, *90* (2), 254–261. https://doi.org/10.1111/cbdd.12944.

(61) Zorc, B.; Perković, I.; Pavić, K.; Rajić, Z.; Beus, M. Primaquine Derivatives: Modifications of the Terminal Amino Group. *Eur. J. Med. Chem.* **2019**, *182*, 111640. https://doi.org/10.1016/j.ejmech.2019.111640.

(62) Ye, W.; Tang, Q.; Zhou, T.; Zhou, C.; Fan, C.; Wang, X.; Wang, C.; Zhang, K.; Liao, G.; Wen, W. Design, synthesis and biological evaluation of the positional isomers of the galactose conjugates able to target hepatocellular carcinoma cells via ASGPR-mediated cellular uptake and cytotoxicity. Eur. J. Med. Chem. **2024**, *264*, 115988. DOI:10.1016/j.ejmech.2023.115988.

(63) Nagarajan, R. Structure–Activity Relationships of Vancomycin Antibiotics. In *Glycopeptide Antibiotics*; CRC Press: Boca Raton, FL, **1994**; pp 47–67.

(64) Ward, T. J.; Gilmore, A.; Ward, K.; Vowell, C. Vancomycin Molecular Interactions: Antibiotic and Enantioselective Mechanisms. In *Chiral Recognition in Separation Methods: Mechanisms and Applications*; Berthod, A., Ed.; Springer: Berlin, Heidelberg, **2010**; pp 223–240. https://doi.org/10.1007/978-3-642-12445-7_8.

(65) Egrie, J. C.; Browne, J. K. Development and Characterization of Novel Erythropoiesis Stimulating Protein (NESP). *Br. J. Cancer* **2001**, *84* (Suppl. 1), 3–10. DOI: 10.1054/bjoc.2001.1746.

(66) Su, D.; Zhao, H.; Xia, H. Glycosylation-Modified Erythropoietin with Improved Half-Life and Biological Activity. *Int. J. Hematol.* **2010**, *91* (2), 238–244. https://doi.org/10.1007/s12185-010-0496-x.

(67) Banks, D. D. The Effect of Glycosylation on the Folding Kinetics of Erythropoietin. *J. Mol. Biol.* **2011**, *412* (3), 536–550. https://doi.org/10.1016/j.jmb.2011.07.061.

(68) Zhao, L.; Zhao, J.; Zhong, K.; Tong, A.; Jia, D. Targeted Protein Degradation: Mechanisms, Strategies and Application. *Signal Transduct. Target. Ther.* **2022**, *7* (1), 1–13. https://doi.org/10.1038/s41392-022-00966-4.

(69) Banik, S. M.; Pedram, K.; Wisnovsky, S.; Ahn, G.; Riley, N. M.; Bertozzi, C. R. Lysosome-Targeting Chimaeras for Degradation of Extracellular Proteins. *Nature* **2020**, *584* (7820), 291–297. https://doi.org/10.1038/s41586-020-2545-9.

(70) Ahn, G.; Banik, S. M.; Miller, C. L.; Riley, N. M.; Cochran, J. R.; Bertozzi, C. R. LYTACs That Engage the Asialoglycoprotein Receptor for Targeted Protein Degradation. *Nat. Chem. Biol.* **2021**, *17* (9), 937–946. https://doi.org/10.1038/s41589-021-00770-1.

(71) Caianiello, D. F.; Zhang, M.; Ray, J. D.; Howell, R. A.; Swartzel, J. C.; Branham, E. M. J.; Chirkin, E.; Sabbasani, V. R.; Gong, A. Z.; McDonald, D. M.; Muthusamy, V.; Spiegel, D. A. Bifunctional Small Molecules That Mediate the Degradation of Extracellular Proteins. *Nat. Chem. Biol.* **2021**, *17* (9), 947–953. https://doi.org/10.1038/s41589-021-00851-1.

(72) Zhou, Y.; Teng, P. *et al*;. Development of Triantennary N-Acetylgalactosamine Conjugates as Degraders for Extracellular Proteins. *ACS Cent. Sci.* **2021**, 7, 952–961. doi.org/10.1021/acscentsci.1c00146

(73) Rodrigues Mantuano, N.; Natoli, M.; Zippelius, A.; Läubli, H. Tumor-Associated Carbohydrates and Immunomodulatory Lectins as Targets for Cancer Immunotherapy. *J. Immunother. Cancer* **2020**, *8* (2), e001222. https://doi.org/10.1136/jitc-2020-001222.

(74) Miller, N. L.; Clark, T.; Raman, R.; Sasisekharan, R. Glycans in Virus–Host Interactions: A Structural Perspective. *Front. Mol. Biosci.* **2021**, *8*, 666756. https://doi.org/10.3389/fmolb.2021.666756

(75) Raglow, Z.; McKenna, M. K.; Bonifant, C. L.; Wang, W.; Pasca di Magliano, M.; Stadlmann, J.; Penninger, J. M.; Cummings, R. D.; Brenner, M. K.; Markovitz, D. M. Targeting Glycans for CAR Therapy: The Advent of Sweet CARs. *Mol. Ther.* **2022**, *30* (9), 2881–2890. https://doi.org/10.1016/j.ymthe.2022.07.006.

(76) Sletmoen, M.; Gerken, T. A.; Stokke, B. T.; Burchell, J.; Brewer, C. F. Tn and STn Are Members of a Family of Carbohydrate Tumor Antigens That Possess Carbohydrate–Carbohydrate Interactions. *Glycobiology* **2018**, *28* (7), 437–442. https://doi.org/10.1093/glycob/cwy032.

(77) Qusairy, Z.; Rada, M. Glycosylation in Cancer: Mechanisms, Diagnostic Markers, and Therapeutic Applications. *Mol. Cell. Biochem.* **2025**. https://doi.org/10.1007/s11010-025-05303-1.

(78) Kudelka, M. R.; Ju, T.; Heimburg-Molinaro, J.; Cummings, R. D. Chapter Three - Simple Sugars to Complex Disease—Mucin-Type O-Glycans in Cancer. In *Advances in Cancer Research*; Drake, R. R., Ball, L. E., Eds.; Glycosylation and Cancer; Academic Press, **2015**; *126*, 53–135. https://doi.org/10.1016/bs.acr.2014.11.002.

(79) Ju, T.; Lanneau, G. S.; Gautam, T.; Wang, Y.; Xia, B.; Stowell, S. R.; Willard, M. T.; Wang, W.; Xia, J. Y.; Zuna, R. E.; Laszik, Z.; Benbrook, D. M.; Hanigan, M. H.;

Cummings, R. D. Human Tumor Antigens Tn and Sialyl Tn Arise from Mutations in Cosmc. *Cancer Res.* **2008**, *68* (6), 1636–1646. https://doi.org/10.1158/0008-5472.CAN-07-2345.

(80) Munkley, J. The Role of Sialyl-Tn in Cancer. *Int. J. Mol. Sci.* **2016**, *17* (3), 275. https://doi.org/10.3390/ijms17030275.

(81) Kudva, A.; Modak, S. Chapter 9 - Immunotherapy for Neuroblastoma. In *Neuroblastoma*; Ray, S. K., Ed.; Academic Press, **2019**, 147–173. https://doi.org/10.1016/B978-0-12-812005-7.00009-6.

(82) Miles, D.; Roché, H.; Martin, M.; Perren, T. J.; Cameron, D. A.; Glaspy, J.; Dodwell, D.; Parker, J.; Mayordomo, J.; Tres, A.; Murray, J. L.; Ibrahim, N. K.; Group, the T. S. Phase III Multicenter Clinical Trial of the Sialyl-TN (STn)-Keyhole Limpet Hemocyanin (KLH) Vaccine for Metastatic Breast Cancer. *The Oncologist* **2011**, *16* (8), 1092–1100. https://doi.org/10.1634/theoncologist.2010-0307.

(83) Holmberg, L. A.; Sandmaier, B. M. Theratope Vaccine (STn-KLH). *Expert Opin. Biol. Ther.* **2001**, *1* (5), 881–891. https://doi.org/10.1517/14712598.1.5.881.

(84) Matsumoto, Y.; Ju, T. Aberrant Glycosylation as Immune Therapeutic Targets for Solid Tumors. *Cancers* **2023**, *15* (14), 3536. https://doi.org/10.3390/cancers15143536.

(85) Dhillon, S. Dinutuximab: First Global Approval. *Drugs* **2015**, *75* (8), 923–927. https://doi.org/10.1007/s40265-015-0399-5.

(86) Liu, CC., Ye, XS. Carbohydrate-based cancer vaccines: target cancer with sugar bullets. *Glycoconj J* **29**, 259–271 (**2012**). https://doi.org/10.1007/s10719-012-9399-9

(87) Lee, C.-J. Bacterial Capsular Polysaccharides: Immunogenicity and Vaccines. In *Polysaccharides in Medicinal Applications*; Dumitriu, S., Ed.; Routledge: New York, **1996**; pp 563–599.

(88) Qin, C.; Tian, G.; Hu, J.; Zou, X.; Yin, J. Recent Chemical Synthesis and Immunological Evaluation of Glycans Related to Bacterial Lipopolysaccharides. *Curr. Opin. Chem. Biol.* **2024**, 78, 102424. doi.org/10.1016/j.cbpa.2023.102424

(89) Javed, A.; Mandal, P. K. Bacterial Surface Capsular Polysaccharides from *Streptococcus Pneumoniae*: A Systematic Review on Structures, Syntheses, and Glycoconjugate Vaccines. *Carbohydr. Res.* **2021**, 502, 108277. doi.org/10.1016/j.carres.2021.108277

(90) Paton, J. C.; Trappetti, C. *Streptococcus Pneumoniae* Capsular Polysaccharide. *Microbiol. Spectr.* **2019**, 7 (2), GPP3-0019-2018. doi.org/10.1128/microbiolspec.gpp3-0019-2018

(91) Bentley, S. D.; Aanensen, D. M.; Mavroidi, A.; Saunders, D.; Rabbinowitsch, E.; Collins, M.; Donohoe, K.; Harris, D.; Murphy, L.; Quail, M. A.; Samuel, G.; Skovsted, I. C.; Kaltoft, M. S.; Barrell, B.; Reeves, P. R.; Parkhill, J.; Spratt, B. G. Genetic Analysis of the Capsular Biosynthetic Locus from All 90 Pneumococcal Serotypes. *PLOS Genet.* **2006**, *2* (3), e31. doi.org/10.1371/journal.pgen.0020031

(92) Brugger, S. D.; Troxler, L. J.; Rüfenacht, S.; Frey, P. M.; Morand, B.; Geyer, R.; Mühlemann, K.; Höck, S.; Thormann, W.; Furrer, J.; Christen, S.; Hilty, M. Polysaccharide Capsule Composition of Pneumococcal Serotype 19A Subtypes Is Unaltered among Subtypes and Independent of the Nutritional Environment. *Infect. Immun.* **2016**, *84* (11), 3152–3160. doi.org/10.1128/IAI.00474-16

(93) Karki, G.; Mandal, P. K. Synthetic Directions towards Capsular Polysaccharide of *Streptococcus Pneumoniae* Serotype 18C. *Tetrahedron Lett.* **2019**, *60* (42), 151153. doi.org/10.1016/j.tetlet.2019.151153.

(94) Swartley, J. S.; Liu, L.-J.; Miller, Y. K.; Martin, L. E.; Edupuganti, S.; Stephens, D. S. Characterization of the Gene Cassette Required for Biosynthesis of the (A1→6)-LinkedN-Acetyl-d-Mannosamine-1-Phosphate Capsule of Serogroup A Neisseria Meningitidis. *J. Bacteriol.* **1998**, *180* (6), 1533–1539. https://doi.org/10.1128/jb.180.6.1533-1539.1998.

(95) von Loewenich, F. D.; Wintermeyer, E.; Dümig, M.; Frosch, M. Analysis of Transcriptional Control Mechanisms of Capsule Expression in *Neisseria Meningitidis*. *Int. J. Med. Microbiol.* **2001**, *291* (5), 361–369. https://doi.org/10.1078/1438-4221-00142.

(96) Martinez, J.; Pilishvili, T.; Barnard, S.; Caba, J.; Spear, W.; Romero-Steiner, S.; Carlone, G. M. Opsonophagocytosis of Fluorescent Polystyrene Beads Coupled to Neisseria Meningitidis Serogroup A, C, Y, or W135 Polysaccharide Correlates with Serum Bactericidal Activity. *Clin. Vaccine Immunol.* **2002**, *9* (2), 485–488. https://doi.org/10.1128/CDLI.9.2.485-488.2002.

(97) Ada, G.; Isaacs, D. Carbohydrate—Protein Conjugate Vaccines. *Clin. Microbiol. Infect.* **2003**, *9* (2), 79–85. https://doi.org/10.1046/j.1469-0691.2003.00530.x.

(98) Berger, A. Science Commentary: Why Conjugate Vaccines Protect Longer. *BMJ* **1998**, *316* (7144), 1571. https://doi.org/10.1136/bmj.316.7144.1571.

(99) Trotter, C. L.; Maiden, M. C. Meningococcal Vaccines and Herd Immunity: Lessons Learned from Serogroup C Conjugate Vaccination Programs. *Expert Rev. Vaccines* **2009**, *8* (7), 851–861. https://doi.org/10.1586/erv.09.48.

(100) Nielsen, T. B.; Pantapalangkoor, P.; Luna, B. M.; Bruhn, K. W.; Yan, J.; Dekitani, K.; Hsieh, S.; Yeshoua, B.; Pascual, B.; Vinés, E. D.; Lemmens, N.; Durant, J.; Dufresne, E.; Ho, T.; DiGiandomenico, A.; Keller, A. E.; Zurawski, D. V.; Hujer, A. M.; Domitrovic, T. N.; Rudin, S. D.; Hujer, K. M.; Marshall, S. H.; Perez, F.; Bonomo, R. A.; Spellberg, B. Monoclonal Antibody Protects against *Acinetobacter Baumannii* Infection by

Enhancing Bacterial Clearance and Evading Sepsis. *Nat. Med.* **2017**, *23* (1), 49–54. doi.org/10.1038/nm.4238

(101) Szijártó, V.; Guachalla, L. M.; Visram, Z. C.; Hartl, K.; Varga, C.; Mirkina, I.; Zmajkovic, J.; Badarau, A.; Zauner, G.; Pleban, C.; Magyarics, Z.; Nagy, E.; Nagy, G. Bactericidal Monoclonal Antibodies Specific to the Lipopolysaccharide O Antigen from Multidrug-Resistant Escherichia Coli Clone ST131-O25b:H4 Elicit Protection in Mice. *Antimicrob. Agents Chemother.* **2015**, *59* (6), 3109–3116. https://doi.org/10.1128/AAC.04494-14.

(102) Pietri, G. P.; Bertuzzi, S.; Karnicar, K.; Unione, L.; Lisnic, B.; Malic, S.; Miklic, K.; Novak, M.; Calloni, I.; Santini, L.; Usenik, A.; Romano, M. R.; Adamo, R.; Jonjic, S.; Turk, D.; Jiménez-Barbero, J.; Lenac Rovis, T. Antigenic Determinants Driving Serogroup-Specific Antibody Response to *Neisseria Meningitidis* C, W, and Y Capsular Polysaccharides: Insights for Rational Vaccine Design. *Carbohydr. Polym.* **2024**, *341*, 122349. https://doi.org/10.1016/j.carbpol.2024.122349.

(103) Yang, X.; Wei, R.; Liu, H.; Wei, T.; Zeng, P.; Cheung, Y. C.; Heng, H.; Chan, E. W.; Li, X.; Chen, S. Discovery of a Monoclonal Antibody That Targets Cell-Surface Pseudaminic Acid of Acinetobacter Baumannii with Direct Bactericidal Effect. *ACS Cent. Sci.* **2024**, *10* (2), 439–446. https://doi.org/10.1021/acscentsci.3c01507.

(104) Wu, Y.; Qiu, Y.; Feng, Y.; Stoddart, J. F. Automating Glycan Assembly in Solution. *ACS Cent. Sci.* **2022**. https://doi.org/10.1021/acscentsci.2c01043.

(105) He, H.; Xu, L.; Sun, R.; Zhang, Y.; Huang, Y.; Chen, Z.; Li, P.; Yang, R.; Xiao, G. An Orthogonal and Reactivity-Based One-Pot Glycosylation Strategy for Both Glycan and Nucleoside Synthesis: Access to TMG-Chitotriomycin, Lipochitooligosaccharides and Capuramycin. *Chem. Sci.* **2021**, *12* (14), 5143–5151. https://doi.org/10.1039/D0SC06815B.

(106) Ágoston, K.; Streicher, H.; Fügedi, P. Orthogonal Protecting Group Strategies in Carbohydrate Chemistry. *Tetrahedron Asymmetry* **2016**, *27* (16), 707–728. https://doi.org/10.1016/j.tetasy.2016.06.010.

(107) Axford, J.; Alavi, A.; Cummings, R.; Lauc, G.; Opdenakker, G.; Reis, C.; Rudd, P. Translational Glycobiology: From Bench to Bedside. *J. R. Soc. Med.* **2019**, *112* (10), 424–427. https://doi.org/10.1177/0141076819865863.

(108) Astronomo, R. D.; Burton, D. R. Carbohydrate Vaccines: Developing Sweet Solutions to Sticky Situations? *Nat. Rev. Drug Discov.* **2010**, 9 (4), 308–324. doi.org/10.1038/nrd3012

(109) Arias, I. M.; Alter, H. J.; Boyer, J. L.; Cohen, D. E.; Shafritz, D. A.; Thorgeirsson, S. S.; Wolkoff, A. W., Eds. *The Liver: Biology and Pathobiology*, 6th ed.; Wiley-Blackwell: Hoboken, NJ, **2020**.

(110) Hippocrates. *On the Sacred Disease*. In *Hippocratic Writings*; Lloyd, G. E. R., Ed.; Penguin Classics: London, **1983**.

(111) Lihui Qin, James M. Crawford,. *1* - Anatomy and Cellular Functions of the Liver. In *The Liver: Biology and Pathobiology*; Elsevier: Amsterdam, Netherlands, **2018**; 1–30. https://doi.org/10.1016/B978-0-323-37591-7.00001-X.

(112) Hansel, M. C.; Gramignoli, R.; Skvorak, K. J.; Dorko, K.; Marongiu, F.; Blake, W.; Davila, J.; Strom, S. C. The History and Use of Human Hepatocytes for the Study and Treatment of Liver Metabolic Diseases. *Curr. Protoc. Toxicol.* **2014**, *62*, 14.12.1–14.12.23. https://doi.org/10.1002/0471140856.tx1412s62.

(113) Sevior, D. K.; Pelkonen, O.; Ahokas, J. T. Hepatocytes: The Powerhouse of Biotransformation. *Int. J. Biochem. Cell Biol.* **2012**, *44* (2), 257–261. https://doi.org/10.1016/j.biocel.2011.11.011.

(114) Klover, P. J.; Mooney, R. A. Hepatocytes: Critical for Glucose Homeostasis. *Int. J. Biochem. Cell Biol.* **2004**, *36* (5), 753–758. https://doi.org/10.1016/j.biocel.2003.10.002.

(115) Grant, D. M. Detoxification Pathways in the Liver. *J. Inherit. Metab. Dis.* **1991**, *14* (4), 421–430. https://doi.org/10.1007/BF01797915.

(116) Boyer, J. L.; Soroka, C. J. Bile Formation and Secretion: An Update. *J. Hepatol.* **2021**, *75* (1), 190–201. https://doi.org/10.1016/j.jhep.2021.02.011.

(117) Cheemerla, S.; Balakrishnan, M. Global Epidemiology of Chronic Liver Disease. *Clin. Liver Dis.* **2021**, *17* (5), 365–370. https://doi.org/10.1002/cld.1061.

(118) Moon, A. M.; Singal, A. G.; Tapper, E. B. Contemporary Epidemiology of Chronic Liver Disease and Cirrhosis. *Clin. Gastroenterol. Hepatol. Off. Clin. Pract. J. Am. Gastroenterol. Assoc.* **2020**, *18* (12), 2650–2666. https://doi.org/10.1016/j.cgh.2019.07.060.

(119) Deloitte Access Economics. *The Social and Economic Cost of Primary Liver Cancer in Australia*; Gastroenterological Society of Australia: Melbourne, **2019**. Available at: liver.org.au

(120) Huang, D. Q.; Terrault, N. A.; Tacke, F.; Gluud, L. L.; Arrese, M.; Bugianesi, E.; Loomba, R. Global Epidemiology of Cirrhosis — Aetiology, Trends and Predictions. *Nat. Rev. Gastroenterol. Hepatol.* **2023**, *20* (6), 388–398. https://doi.org/10.1038/s41575-023-00759-2.

(121) Michalopoulos, G. K.; Bhushan, B. Liver Regeneration: Biological and Pathological Mechanisms and Implications. *Nat. Rev. Gastroenterol. Hepatol.* **2021**, *18* (1), 40–55. https://doi.org/10.1038/s41575-020-0342-4.

(122) Younossi, Z. M.; Rinella, M. E.; Sanyal, A. J.; Harrison, S. A.; Brunt, E. M.; Goodman, Z.; Cohen, D. E.; Loomba, R. From NAFLD to MAFLD: Implications of a Premature Change in Terminology. *Hepatology* **2021**, *73* (3), 1194–1198. https://doi.org/10.1002/hep.31420.

(123) Moon, A. M.; Singal, A. G.; Tapper, E. B. Contemporary Epidemiology of Chronic Liver Disease and Cirrhosis. *Clin. Gastroenterol. Hepatol. Off. Clin. Pract. J. Am. Gastroenterol. Assoc.* **2020**, *18* (12), 2650–2666. https://doi.org/10.1016/j.cgh.2019.07.060.

(124) Ludwig, J.; Viggiano, T. R.; McGill, D. B.; Ott, B. J. Nonalcoholic Steatohepatitis Mayo Clinic Experiences With a Hitherto Unnamed Disease. *Mayo Clin. Proc.* **1980**, *55* (7), 434–438. https://doi.org/10.1016/S0025-6196(24)00530-5.

(125) Nassir, F.; Rector, R. S.; Hammoud, G. M.; Ibdah, J. A. Pathogenesis and Prevention of Hepatic Steatosis. *Gastroenterol. Hepatol.* **2015**, *11* (3), 167–175.

(126) Yeh, M. M.; Brunt, E. M. Pathological Features of Fatty Liver Disease. *Gastroenterology* **2014**, *147* (4), 754–764. https://doi.org/10.1053/j.gastro.2014.07.056.

(127) Lackner, C.; Tiniakos, D. Fibrosis and Alcohol-Related Liver Disease. *J. Hepatol.* **2019**, *70* (2), 294–304. https://doi.org/10.1016/j.jhep.2018.12.003.

(128) Bataller, R.; Brenner, D. A. Liver Fibrosis. *J. Clin. Invest.* **2005**, *115* (2), 209–218. https://doi.org/10.1172/JCI24282.

(129) Hallsworth, K.; Adams, L. A. Lifestyle Modification in NAFLD/NASH: Facts and Figures. *JHEP Rep.* **2019**, *1* (6), 468–479. https://doi.org/10.1016/j.jhepr.2019.10.008.

(130) Ginès, P.; Krag, A.; Abraldes, J. G.; Solà, E.; Fabrellas, N.; Kamath, P. S. Liver Cirrhosis. *The Lancet* **2021**, *398* (10308), 1359–1376. https://doi.org/10.1016/S0140-6736(21)01374-X.

(131) Baiocchini, A.; Grillo, L. R.; Ettorre, G. M. Pathology of Hepatocellular Carcinoma. In *Hepatocellular Carcinoma*; Ettorre, G. M., Ed.; Springer International Publishing: Cham, **2023**, 45–52. https://doi.org/10.1007/978-3-031-09371-5_6.

(132) El–Serag, H. B.; Rudolph, K. L. Hepatocellular Carcinoma: Epidemiology and Molecular Carcinogenesis. *Gastroenterology* **2007**, *132* (7), 2557–2576. https://doi.org/10.1053/j.gastro.2007.04.061.

(133) Brunt, E. M. Pathology of Fatty Liver Disease. *Mod. Pathol.* **2007**, *20*, S40–S48. https://doi.org/10.1038/modpathol.3800680.

(134) Kořínková, L.; Pražienková, V.; Černá, L.; Karnošová, A.; Železná, B.; Kuneš, J.; Maletínská, L. Pathophysiology of NAFLD and NASH in Experimental Models: The

Role of Food Intake Regulating Peptides. *Front. Endocrinol.* **2020**, *11*. https://doi.org/10.3389/fendo.2020.597583.

(135) Marsano, L. S.; Mendez, C.; Hill, D.; Barve, S.; Mcclain, C. J. Diagnosis and Treatment of Alcoholic Liver Disease and Its Complications. *Alcohol Res. Health* **2003**, *27* (3), 247–256.

(136) Beaton, M. D. Current Treatment Options for Nonalcoholic Fatty Liver Disease and Nonalcoholic Steatohepatitis. *Can. J. Gastroenterol. Hepatol.* **2012**, *26* (6), 725468. https://doi.org/10.1155/2012/725468.

(137) Vilar-Gomez, E.; Martinez-Perez, Y.; Calzadilla-Bertot, L.; Torres-Gonzalez, A.; Gra-Oramas, B.; Gonzalez-Fabian, L.; Friedman, S. L.; Diago, M.; Romero-Gomez, M. Weight Loss Through Lifestyle Modification Significantly Reduces Features of Nonalcoholic Steatohepatitis. *Gastroenterology* **2015**, *149* (2), 367-378.e5. https://doi.org/10.1053/j.gastro.2015.04.005.

(138) Verrill, C.; Markham, H.; Templeton, A.; Carr, N. J.; Sheron, N. Alcohol-Related Cirrhosis--Early Abstinence Is a Key Factor in Prognosis, Even in the Most Severe Cases. *Addict. Abingdon Engl.* **2009**, *104* (5), 768–774. https://doi.org/10.1111/j.1360-0443.2009.02521.x.

(139) Lassailly, G.; Caiazzo, R.; Ntandja-Wandji, L.-C.; Gnemmi, V.; Baud, G.; Verkindt, H.; Ningarhari, M.; Louvet, A.; Leteurtre, E.; Raverdy, V.; Dharancy, S.; Pattou, F.; Mathurin, P. Bariatric Surgery Provides Long-Term Resolution of Nonalcoholic Steatohepatitis and Regression of Fibrosis. *Gastroenterology* **2020**, *159* (4), 1290-1301.e5. https://doi.org/10.1053/j.gastro.2020.06.006.

(140) Gofton, C.; George, J. Updates in fatty liver disease: Pathophysiology, diagnosis and management. *Aust. J. Gen. Pract.* **2021**, *50*(10), 702-707. https://doi.org/10.31128/AJGP-05-21-5974.

(141) Cusi, K.; Orsak, B.; Bril, F.; Lomonaco, R.; Hecht, J.; Ortiz-Lopez, C.; Tio, F.; Hardies, J.; Darland, C.; Musi, N.; Webb, A.; Portillo-Sanchez, P. Long-Term Pioglitazone Treatment for Patients With Nonalcoholic Steatohepatitis and Prediabetes or Type 2 Diabetes Mellitus. *Ann. Intern. Med.* **2016**, *165* (5), 305–315. https://doi.org/10.7326/M15-1774.

(142) Staels, B.; Butruille, L.; Francque, S. Treating NASH by Targeting Peroxisome Proliferator-Activated Receptors. *J. Hepatol.* **2023**, *79* (5), 1302–1316. https://doi.org/10.1016/j.jhep.2023.07.004.

(143) Rotman, Y.; Sanyal, A. J. Pioglitazone for the Treatment of NASH in Patients with Prediabetes or Type 2 Diabetes Mellitus—Authors' Response. *Gut* **2018**, *67* (3), 624–625. https://doi.org/10.1136/gutjnl-2017-314263.

(144) Masubuchi, Y. Metabolic and Non-Metabolic Factors Determining Troglitazone Hepatotoxicity: A Review. *Drug Metab. Pharmacokinet.* **2006**, *21* (5), 347–356. https://doi.org/10.2133/dmpk.21.347.

(145) Sanyal, A. J.; Chalasani, N.; Kowdley, K. V.; McCullough, A.; Diehl, A. M.; Bass, N . M.; Neuschwander-Tetri, B. A.; Lavine, J. E.; Tonascia, J.; Unalp, A.; Van Natta, M.; Clark, J.; Brunt, E. M.; Kleiner, D. E.; Hoofnagle, J. H.; Robuck, P. R. Pioglitazone, Vitamin E, or Placebo for Nonalcoholic Steatohepatitis. *N. Engl. J. Med.* **2010**, 362 (18), 1675–1685. doi.org/10.1056/NEJMoa0907929

(146) Pioglitazone versus Vitamin E versus Placebo for the Treatment of Nondiabetic Patients with Nonalcoholic Steatohepatitis: PIVENS Trial Design. *Contemp. Clin. Trials* **2009**, *30* (1), 88–96. https://doi.org/10.1016/j.cct.2008.09.003.

(147) Newsome, P. N.; Buchholtz, K.; Cusi, K.; Linder, M.; Okanoue, T.; Ratziu, V.; Sanyal, A. J.; Sejling, A.-S.; Harrison, S. A. A Placebo-Controlled Trial of Subcutaneous Semaglutide in Nonalcoholic Steatohepatitis. *N. Engl. J. Med.* **2021**, *384* (12), 1113–1124. https://doi.org/10.1056/NEJMoa2028395.

(148) Armstrong, M. J.; Hull, D.; Guo, K.; Barton, D.; Hazlehurst, J. M.; Gathercole, L. L.; Nasiri, M.; Yu, J.; Gough, S. C.; Newsome, P. N.; Tomlinson, J. W. Glucagon-like Peptide 1 Decreases Lipotoxicity in Non-Alcoholic Steatohepatitis. *J. Hepatol.* **2016**, *64* (2), 399–408. https://doi.org/10.1016/j.jhep.2015.08.038.

(149) Herz, A. Endogenous Opioid Systems and Alcohol Addiction. *Psychopharmacology* **1997**, *129* (2), 99–111. https://doi.org/10.1007/s002130050169.

(150) Ray, L. A.; Chin, P. F.; Miotto, K. Naltrexone for the Treatment of Alcoholism: Clinical Findings, Mechanisms of Action, and Pharmacogenetics. *CNS Neurol. Disord. Drug Targets* **2010**, *9* (1), 13–22. https://doi.org/10.2174/187152710790966704.

(151) Plosker, G. L. Acamprosate: A Review of Its Use in Alcohol Dependence. *Drugs* **2015**, *75* (11), 1255–1268. https://doi.org/10.1007/s40265-015-0423-9.

(152) Lovinger, D. M.; White, G.; Weight, F. F. Ethanol Inhibits NMDA-Activated Ion Current in Hippocampal Neurons. *Science* **1989**, *243* (4899), 1721–1724. https://doi.org/10.1126/science.2467382.

(153) Mann, K.; Kiefer, F.; Spanagel, R.; Littleton, J. Acamprosate: Recent Findings and Future Research Directions. *Alcohol. Clin. Exp. Res.* **2008**, *32* (7), 1105–1110. https://doi.org/10.1111/j.1530-0277.2008.00690.x.

(154) Agabio, R.; Leite-Morris, K. A.; Addolorato, G.; Colombo, G. Targeting the $GABA_B$ Receptor for the Treatment of Alcohol Use Disorder. In *GABAB Receptor*; Colombo, G., Ed.; Springer International Publishing: Cham, **2016**, 287–307. https://doi.org/10.1007/978-3-319-46044-4_15.

(155) de Beaurepaire, R. A Review of the Potential Mechanisms of Action of Baclofen in Alcohol Use Disorder. *Front. Psychiatry* **2018**, *9*, 506. https://doi.org/10.3389/fpsyt.2018.00506.

(156) Colombo, G.; Gessa, G. L. Suppressing Effect of Baclofen on Multiple Alcohol-Related Behaviors in Laboratory Animals. *Front. Psychiatry* **2018**, *9*, 475. https://doi.org/10.3389/fpsyt.2018.00475.

(157) Addolorato, G.; Leggio, L.; Ferrulli, A.; Cardone, S.; Vonghia, L.; Mirijello, A.; Abenavoli, L.; D'Angelo, C.; Caputo, F.; Zambon, A.; Haber, P. S.; Gasbarrini, G. Effectiveness and Safety of Baclofen for Maintenance of Alcohol Abstinence in Alcohol-Dependent Patients with Liver Cirrhosis: Randomised, Double-Blind Controlled Study. *The Lancet* **2007**, *370* (9603), 1915–1922. https://doi.org/10.1016/S0140-6736(07)61814-5.

(158) Maisel, N. C.; Blodgett, J. C.; Wilbourne, P. L.; Humphreys, K.; Finney, J. W. Meta-Analysis of Naltrexone and Acamprosate for Treating Alcohol Use Disorders: When Are These Medications Most Helpful? *Addiction* **2013**, *108* (2), 275–293. https://doi.org/10.1111/j.1360-0443.2012.04054.x.

(159) Morley, K. C.; Baillie, A.; Fraser, I.; Furneaux-Bate, A.; Dore, G.; Roberts, M.; Abdalla, A.; Phung, N.; Haber, P. S. Baclofen in the Treatment of Alcohol Dependence with or without Liver Disease: Multisite, Randomised, Double-Blind, Placebo-Controlled Trial. *Br. J. Psychiatry* **2018**, *212* (6), 362–369. https://doi.org/10.1192/bjp.2018.13.

(160) Mosoni, C.; Dionisi, T.; Vassallo, G. A.; Mirijello, A.; Tarli, C.; Antonelli, M.; Sestito, L.; Rando, M. M.; Tosoni, A.; De Cosmo, S.; Gasbarrini, A.; Addolorato, G. Baclofen for the Treatment of Alcohol Use Disorder in Patients with Liver Cirrhosis: 10 Years After the First Evidence. *Front. Psychiatry* **2018**, *9*, 474. https://doi.org/10.3389/fpsyt.2018.00474.

(161) Thursz, M. R.; Richardson, P.; Allison, M.; Austin, A.; Bowers, M.; Day, C. P.; Downs, N.; Gleeson, D.; MacGilchrist, A.; Grant, A.; Hood, S.; Masson, S.; McCune, A.; Mellor, J.; O'Grady, J.; Patch, D.; Ratcliffe, I.; Roderick, P.; Stanton, L.; Vergis, N.; Wright, M.; Ryder, S.; Forrest, E. H.; STOPAH Trial. Prednisolone or Pentoxifylline for Alcoholic Hepatitis. *N. Engl. J. Med.* **2015**, *372* (17), 1619–1628. https://doi.org/10.1056/NEJMoa1412278.

(162) Mathurin, P.; O'Grady, J.; Carithers, R. L.; Phillips, M.; Louvet, A.; Mendenhall, C. L.; Ramond, M.-J.; Naveau, S.; Maddrey, W. C.; Morgan, T. R. Corticosteroids Improve Short-Term Survival in Patients with Severe Alcoholic Hepatitis: Meta-Analysis of Individual Patient Data. *Gut* **2011**, *60* (2), 255–260. https://doi.org/10.1136/gut.2010.224097.

(163) Louvet, A.; Wartel, F.; Castel, H.; Dharancy, S.; Hollebecque, A.; Canva–Delcambre, V.; Deltenre, P.; Mathurin, P. Infection in Patients With Severe Alcoholic

Hepatitis Treated With Steroids: Early Response to Therapy Is the Key Factor. *Gastroenterology* **2009**, *137* (2), 541–548. https://doi.org/10.1053/j.gastro.2009.04.062.

(164) European Association for the Study of the Liver. EASL Clinical Practice Guidelines for the Management of Patients with Decompensated Cirrhosis. *J. Hepatol.* **2018**, *69* (2), 406–460. https://doi.org/10.1016/j.jhep.2018.03.024.

(165) Uhlén, M.; Fagerberg, L.; Hallström, B. M.; Lindskog, C.; Oksvold, P.; Mardinoglu, A.; Sivertsson, Å.; Kampf, C.; Sjöstedt, E.; Asplund, A.; Olsson, I.; Edlund, K.; Lundberg, E.; Navani, S.; Szigyarto, C. A.-K.; Odeberg, J.; Djureinovic, D.; Takanen, J. O.; Hober, S.; Alm, T.; Edqvist, P.-H.; Berling, H.; Tegel, H.; Mulder, J.; Rockberg, J.; Nilsson, P.; Schwenk, J. M.; Hamsten, M.; von Feilitzen, K.; Forsberg, M.; Persson, L.; Johansson, F.; Zwahlen, M.; von Heijne, G.; Nielsen, J.; Pontén, F. Tissue-Based Map of the Human Proteome. *Science* **2015**, *347* (6220), 1260419. https://doi.org/10.1126/science.1260419.

(166) Howlett, A. C.; Blume, L. C.; Dalton, G. D. CB1 Cannabinoid Receptors and Their Associated Proteins. *Curr. Med. Chem.* **2010**, *17* (14), 1382–1393. https://doi.org/10.2174/092986710790980023.

(167) Hua, T.; Vemuri, K.; Nikas, S. P.; Laprairie, R. B.; Wu, Y.; Qu, L.; Pu, M.; Korde, A.; Jiang, S.; Ho, J.-H.; Han, G. W.; Ding, K.; Li, X.; Liu, H.; Hanson, M. A.; Zhao, S.; Bohn, L. M.; Makriyannis, A.; Stevens, R. C.; Liu, Z.-J. Crystal Structures of Agonist-Bound Human Cannabinoid Receptor CB1. *Nature* **2017**, *547* (7664), 468–471. https://doi.org/10.1038/nature23272.

(168) Osei-Hyiaman, D.; DePetrillo, M.; Pacher, P.; Liu, J.; Radaeva, S.; Bátkai, S.; Harvey-White, J.; Mackie, K.; Offertáler, L.; Wang, L.; Kunos, G. Endocannabinoid Activation at Hepatic CB1 Receptors Stimulates Fatty Acid Synthesis and Contributes to Diet-Induced Obesity. *J. Clin. Invest.* **2005**, *115* (5), 1298–1305. https://doi.org/10.1172/JCI23057.

(169) Jeong, W.; Osei-Hyiaman, D.; Park, O.; Liu, J.; Bátkai, S.; Mukhopadhyay, P.; Horiguchi, N.; Harvey-White, J.; Marsicano, G.; Lutz, B.; Gao, B.; Kunos, G. Paracrine Activation of Hepatic CB1 Receptors by Stellate Cell-Derived Endocannabinoids Mediates Alcoholic Fatty Liver. *Cell Metab.* **2008**, *7* (3), 227–235. https://doi.org/10.1016/j.cmet.2007.12.007.

(170) Purohit, V.; Rapaka, R.; Shurtleff, D. Role of Cannabinoids in the Development of Fatty Liver (Steatosis). *AAPS J.* **2010**, *12* (2), 233–237. https://doi.org/10.1208/s12248-010-9178-0.

(171) Osei-Hyiaman, D.; DePetrillo, M.; Pacher, P.; Liu, J.; Radaeva, S.; Bátkai, S.; Harvey-White, J.; Mackie, K.; Offertáler, L.; Wang, L.; Kunos, G. Endocannabinoid Activation at Hepatic CB_1 Receptors Stimulates Fatty Acid Synthesis and Contributes

to Diet-Induced Obesity. *J. Clin. Invest.* **2005**, *115* (5), 1298–1305. https://doi.org/10.1172/JCI23057.

(172) Nakagawa, H. Lipogenesis and MASLD: Re-Thinking the Role of SREBPs. *Arch. Toxicol.* **2025**, *99*, 2299–2312. https://doi.org/10.1007/s00204-025-04052-w.

(173) Kim, C.-W.; Addy, C.; Kusunoki, J.; Anderson, N. N.; Deja, S.; Fu, X.; Burgess, S. C.; Li, C.; Ruddy, M.; Chakravarthy, M.; Previs, S.; Milstein, S.; Fitzgerald, K.; Kelley, D. E.; Horton, J. D. Acetyl CoA Carboxylase Inhibition Reduces Hepatic Steatosis but Elevates Plasma Triglycerides in Mice and Humans: A Bedside to Bench Investigation. *Cell Metab.* **2017**, *26* (2), 394-406.e6. https://doi.org/10.1016/j.cmet.2017.07.009.

(174) Osei-Hyiaman, D.; Liu, J.; Zhou, L.; Godlewski, G.; Harvey-White, J.; Jeong, W.; Bátkai, S.; Marsicano, G.; Lutz, B.; Buettner, C.; Kunos, G. Hepatic CB1 Receptor Is Required for Development of Diet-Induced Steatosis, Dyslipidemia, and Insulin and Leptin Resistance in Mice. *J. Clin. Invest.* **2008**, *118* (9), 3160–3169. https://doi.org/10.1172/JCI34827.

(175) Gary-Bobo, M.; Elachouri, G.; Gallas, J.-F.; Janiak, P.; Marini, P.; Ravinet-Trillou, C.; Chabbert, M.; Cruccioli, N.; Pfersdorff, C.; Roque, C.; Arnone, M.; Croci, T.; Soubrie, P.; Oury-Donat, F.; Maffrand, J.-P.; Scatton, B.; Lacheretz, F.; Le Fur, G.; Herbert, J.-M.; Bensaid, M. Rimonabant Reduces Obesity-Associated Hepatic Steatosis and Features of Metabolic Syndrome in Obese Zucker fa/fa Rats. *Hepatology* **2007**, *46* (1), 122–129. https://doi.org/10.1002/hep.21641.

(176) Rinaldi-Carmona, M.; Barth, F.; Héaulme, M.; Shire, D.; Calandra, B.; Congy, C.; Martinez, S.; Maruani, J.; Néliat, G.; Caput, D. SR141716A, a Potent and Selective Antagonist of the Brain Cannabinoid Receptor. *FEBS Lett.* **1994**, *350* (2–3), 240–244. https://doi.org/10.1016/0014-5793(94)00773-x.

(177) Curioni, C.; André, C. Rimonabant for Overweight or Obesity. *Cochrane Database Syst. Rev.* **2006**, (4), CD006162. https://doi.org/10.1002/14651858.CD006162.pub2.

(178) Van Gaal, L. F.; Rissanen, A. M.; Scheen, A. J.; Ziegler, O.; Rössner, S. Effects of the Cannabinoid-1 Receptor Blocker Rimonabant on Weight Reduction and Cardiovascular Risk Factors in Overweight Patients: 1-Year Experience from the RIO-Europe Study. *The Lancet* **2005**, *365* (9468), 1389–1397. https://doi.org/10.1016/S0140-6736(05)66374-X.

(179) Sayburn, A. European Drugs Agency Withdraws Antiobesity Drug. *BMJ* **2008**, *337*, a2301. https://doi.org/10.1136/bmj.a2301.

(180) Cohen, D.; Arnaud, C. Seventeen Years since Rimonabant's Downfall: Reassessing Its Suicidality Risk Profile. *Obesity* **2024**, *32* (6), 1161–1170. https://doi.org/10.1002/oby.24019.

(181) Mitchell, P. B.; Morris, M. J. Depression and Anxiety with Rimonabant. *The Lancet* **2007**, *370* (9600), 1671–1672. https://doi.org/10.1016/S0140-6736(07)61705-X.

(182) Mackie, K. Distribution of Cannabinoid Receptors in the Central and Peripheral Nervous System. In *Cannabinoids*; Pertwee, R. G., Ed.; Springer: Berlin, Heidelberg, **2005**; 299–325. https://doi.org/10.1007/3-540-26573-2_10.

(183) Kano, M.; Ohno-Shosaku, T.; Hashimotodani, Y.; Uchigashima, M.; Watanabe, M. Endocannabinoid-Mediated Control of Synaptic Transmission. *Physiol. Rev.* **2009,** *89* (1), 309–380. https://doi.org/10.1152/physrev.00019.2008

(184) Rogawski, M. A. Revisiting AMPA Receptors as an Antiepileptic Drug Target: Revisiting AMPA Receptors as an Antiepileptic Drug Target. *Epilepsy Curr.* **2011**, *11* (2), 56–63. https://doi.org/10.5698/1535-7511-11.2.56.

(185) Miura, M.; Watanabe, M.; Offermanns, S.; Simon, M. I.; Kano, M. Group I Metabotropic Glutamate Receptor Signaling via Gαq/Gα11 Secures the Induction of Long-Term Potentiation in the Hippocampal Area CA1. *J. Neurosci.* **2002**, *22* (19), 8379–8390. https://doi.org/10.1523/JNEUROSCI.22-19-08379.2002.

(186) Sallard, E.; Letourneur, D.; Legendre, P. Electrophysiology of Ionotropic GABA Receptors. *Cell. Mol. Life Sci. CMLS* **2021**, *78* (13), 5341–5370. https://doi.org/10.1007/s00018-021-03846-2.

(187) Root, D. H.; Mejias-Aponte, C. A.; Zhang, S.; Wang, H.-L.; Hoffman, A. F.; Lupica, C. R.; Morales, M. Single Rodent Mesohabenular Axons Release Glutamate and GABA. *Nat. Neurosci.* **2014**, *17* (11), 1543–1551. https://doi.org/10.1038/nn.3823.

(188) Lawther, B. K.; Kumar, S.; Krovvidi, H. Blood–Brain Barrier. *Contin. Educ. Anaesth. Crit. Care Pain* **2011**, *11* (4), 128–132. https://doi.org/10.1093/bjaceaccp/mkr018.

(189) Mendiguren, A.; Pineda, J. Effect of the CB1 Receptor Antagonists Rimonabant and AM251 on the Firing Rate of Dorsal Raphe Serotonergic Neurons. *Br. J. Pharmacol.* **2009**, *158* (6), 1579–1587. doi.org/10.1111/j.1476-5381.2009.00419.x.

(190) O'Sullivan, S. E.; Yates, A. S.; Porter, R. K. The Peripheral Cannabinoid Receptor Type 1 (CB1) as a Molecular Target for Modulating Body Weight in Man. *Molecules* **2021**, *26*, 6178. doi.org/10.3390/molecules26206178.

(191) Bányai, B.; Vass, Z.; Kiss, S.; Balogh, A.; Brandhuber, D.; Karvaly, G.; Kovács, K.; Nádasy, G. L.; Hunyady, L.; Dörnyei, G.; Horváth, E. M.; Szekeres, M. Role of CB1 Cannabinoid Receptors in Vascular Responses and Vascular Remodeling of the Aorta in Female Mice. *Int. J. Mol. Sci.* **2023**, *24* (22), 16429. doi.org/10.3390/ijms242216429.

(192) Fonseca, B. M.; Rebelo, I. Cannabis and Cannabinoids in Reproduction and Fertility: Where We Stand. *Reprod. Sci.* **2022**, *29* (9), 2429–2439. https://doi.org/10.1007/s43032-021-00588-1.

(193) Rajagopal, S.; Shenoy, S. K. GPCR Desensitization: Acute and Prolonged Phases. *Cell. Signal.* **2018**, *41*, 9–16. https://doi.org/10.1016/j.cellsig.2017.01.024.

(194) Hislop, J. N.; von Zastrow, M. Role of Ubiquitination in Endocytic Trafficking of G-Protein-Coupled Receptors. *Traffic* **2011**, *12* (2), 137–148. doi.org/10.1111/j.1600-0854.2010.01139.x

(195) Pohl, C.; Dikic, I. Cellular Quality Control by the Ubiquitin-Proteasome System and Autophagy. *Science* **2019**, *366* (6467), 818–822. https://doi.org/10.1126/science.aax3769.

(196) Hu, B.; Hu, J. Complete Elimination of Estrogen Receptor α by PROTAC Estrogen Receptor α Degrader ERD-148 in Breast Cancer Cells. *Breast Cancer Res. Treat.* **2023**, *198* (3), 557–571. doi.org/10.1007/s10549-023-07136-2

(197) Chen, Q.-H.; Munoz, E.; Ashong, D. Insight into Recent Advances in Degrading Androgen Receptor for Castration-Resistant Prostate Cancer. *Cancers* **2024**, *16* (3), 663. https://doi.org/10.3390/cancers16030663.

(198) Burslem, G. M.; Crews, C. M. Proteolysis-Targeting Chimeras as Therapeutics and Tools for Biological Discovery. *Cell* **2020**, *181* (1), 102–114. https://doi.org/10.1016/j.cell.2019.11.031.

(199) Echeazarra, L.; García del Caño, G.; Barrondo, S.; González-Burguera, I.; Saumell-Esnaola, M.; Aretxabala, X.; López de Jesús, M.; Borrega-Román, L.; Mato, S.; Ledent, C.; Matute, C.; Goicolea, M. A.; Sallés, J. Fit-for-Purpose Based Testing and Validation of Antibodies to Amino- and Carboxy-Terminal Domains of Cannabinoid Receptor 1. *Histochem. Cell Biol.* **2021**, *156* (5), 479–502. https://doi.org/10.1007/s00418-021-02025-5.

(200) Chu, C.-M.; Hung, M.-S.; Hsieh, M.-T.; Kuo, C.-W.; D, S. T.; Song, J.-S.; Chiu, H.-H.; Chao, Y.-S.; Shia, K.-S. Bioisosteric Replacement of the Pyrazole 3-Carboxamide Moiety of Rimonabant. A Novel Series of Oxadiazoles as CB1 Cannabinoid Receptor Antagonists. *Org. Biomol. Chem.* **2008**, *6* (18), 3399–3407. https://doi.org/10.1039/B807648K.

(201) Basu, S.; Ray, A.; Dittel, B. N. Cannabinoid Receptor 2 Is Critical for the Homing and Retention of Marginal Zone B Lineage Cells and for Efficient T-Independent Immune Responses. *J. Immunol.* **2011**, *187* (11), 5720–5732. https://doi.org/10.4049/jimmunol.1102195.

(202) Hua, T.; Vemuri, K.; Pu, M.; Qu, L.; Han, G. W.; Wu, Y.; Zhao, S.; Shui, W.; Li, S.; Korde, A.; Laprairie, R. B.; Stahl, E. L.; Ho, J.-H.; Zvonok, N.; Zhou, H.; Kufareva, I.; Wu, B.; Zhao, Q.; Hanson, M. A.; Bohn, L. M.; Makriyannis, A.; Stevens, R. C.; Liu, Z.-J. Crystal Structure of the Human Cannabinoid Receptor CB1. *Cell* **2016**, *167* (3), 750-762.e14. https://doi.org/10.1016/j.cell.2016.10.004.

(203) Veronese, F. M.; Pasut, G. PEGylation, Successful Approach to Drug Delivery. *Drug Discov. Today* **2005**, *10* (21), 1451–1458. https://doi.org/10.1016/S1359-6446(05)03575-0.

(204) Dr Leo Corcilius, PhD thesis; Stereoselective Synthesis of Plant and Animal-Derived *O*-linked Glycopeptides, The University of Sydney, **2016**.

(205) Ren, B.; Wang, M.; Liu, J.; Ge, J.; Zhang, X.; Dong, H. Zemplén Transesterification: A Name Reaction That Has Misled Us for 90 Years. *Green Chem.* **2015**, *17* (3), 1390–1394. https://doi.org/10.1039/C4GC02006E.

(206) Lehninger, A. L.; Nelson, D. L.; Cox, M. M. *Lehninger Principles of Biochemistry*, 7th ed.; W. H. Freeman and Company: New York, **2017**.

(207) Rosson, E.; Lux, F.; David, L.; Godfrin, Y.; Tillement, O.; Thomas, E. Focus on Therapeutic Peptides and Their Delivery. *Int. J. Pharm.* **2025**, *675*, 125555. https://doi.org/10.1016/j.ijpharm.2025.125555.

(208) Driggers, E. M.; Hale, S. P.; Lee, J.; Terrett, N. K. The Exploration of Macrocycles for Drug Discovery--an Underexploited Structural Class. *Nat. Rev. Drug Discov.* **2008**, *7* (7), 608–624. https://doi.org/10.1038/nrd2590.

(209) Bozovičar, K.; Bratkovič, T. Small and Simple, yet Sturdy: Conformationally Constrained Peptides with Remarkable Properties. *Int. J. Mol. Sci.* **2021**, *22* (4), 1611. https://doi.org/10.3390/ijms22041611.

(210) Dougherty, P. G.; Qian, Z.; Pei, D. Macrocycles as Protein-Protein Interaction Inhibitors. *Biochem. J.* **2017**, *474* (7), 1109–1125. https://doi.org/10.1042/BCJ20160619.

(211) Goto, Y.; Suga, H. The RaPID Platform for the Discovery of Pseudo-Natural Macrocyclic Peptides. *Acc. Chem. Res.* **2021**, *54* (18), 3604–3617. https://doi.org/10.1021/acs.accounts.1c00391.

(212) Roberts, R. W.; Szostak, J. W. RNA-Peptide Fusions for the in Vitro Selection of Peptides and Proteins. *Proc. Natl. Acad. Sci. U. S. A.* **1997**, *94* (23), 12297–12302. https://doi.org/10.1073/pnas.94.23.12297.

(213) Keefe, A. D. Protein Selection Using mRNA Display. *Curr. Protoc. Mol. Biol.* **2001**, *Chapter 24*, Unit 24.5. https://doi.org/10.1002/0471142727.mb2405s53.

(214) Goto, Y.; Katoh, T.; Suga, H. Flexizymes for Genetic Code Reprogramming. *Nat. Protoc.* **2011**, *6* (6), 779–790. https://doi.org/10.1038/nprot.2011.331.

(215) Wang, J.; Zhang, W.; Cao, W.; Liu, K.; Su, S.; Ma, J.; Li, X. Selective Synthesis of α- and β-Glycosides of N-Acetyl Galactosamine Using Rare Earth Metal Triflates. *Front. Chem.* **2022**, *10*. https://doi.org/10.3389/fchem.2022.1029911.

(216) Zhang, J.; Kováč, P. An Alternative Method for Regioselective, Anomeric Deacylation of Fully Acylated Carbohydrates. *J. Carbohydr. Chem.* **1999**, *18* (4), 461–469. https://doi.org/10.1080/07328309908544010.

(217) Schmidt, R. R. New Methods for the Synthesis of Glycosides and Oligosaccharides—Are There Alternatives to the Koenigs-Knorr Method? [New Synthetic Methods (56)]. *Angew. Chem. Int. Ed.* **1986**, *25* (3), 212–235. https://doi.org/10.1002/anie.198602121.

(218) Zhang, Y.; Muthana, S. M.; Barchi, J. J.; Gildersleeve, J. C. Divergent Behavior of Glycosylated Threonine and Serine Derivatives in Solid Phase Peptide Synthesis. *Org. Lett.* **2012**, *14* (16), 4026–4029. https://doi.org/10.1021/ol301723e.

(219) Ramírez-Cortés, F.; Ménová, P. Hepatocyte Targeting via the Asialoglycoprotein Receptor. *RSC Med. Chem.* **2025**, *16* (2), 525–544. https://doi.org/10.1039/D4MD00652F.

(220) Magasanik, B. Research on Bacteria in the Mainstream of Biology. *Science* **1988**, *240* (4858), 1435–1439. https://doi.org/10.1126/science.3287618.

(221) Ikuta, K. S. *et al.*; Global Mortality Associated with 33 Bacterial Pathogens in 2019: A Systematic Analysis for the Global Burden of Disease Study 2019. *The Lancet* **2022**, *400* (10369), 2221–2248. https://doi.org/10.1016/S0140-6736(22)02185-7.

(222) *Sherris & Ryan's Medical Microbiology, 8th Edition*.

(223) Murray, P. R.; Rosenthal, K. S.; Pfaller, M. A. *Medical Microbiology E-Book: Medical Microbiology E-Book*; Elsevier Health Sciences, **2020**.

(224) Croxen, M. A.; Law, R. J.; Scholz, R.; Keeney, K. M.; Wlodarska, M.; Finlay, B. B. Recent Advances in Understanding Enteric Pathogenic *Escherichia coli*. *Clin. Microbiol. Rev.* **2013**, *26* (4), 822–880. https://doi.org/10.1128/CMR.00022-13.

(225) Coburn, B.; Grassl, G. A.; Finlay, B. B. Salmonella, the Host and Disease: A Brief Review. *Immunol. Cell Biol.* **2007**, *85* (2), 112–118. https://doi.org/10.1038/sj.icb.7100007.

(226) Unemo, M.; Shafer, W. M. Antimicrobial Resistance in Neisseria Gonorrhoeae in the 21st Century: Past, Evolution, and Future. *Clin. Microbiol. Rev.* **2014**, *27* (3), 587–613. https://doi.org/10.1128/CMR.00010-14.

(227) Kaakoush, N. O.; Castaño-Rodríguez, N.; Mitchell, H. M.; Man, S. M. Global Epidemiology of Campylobacter Infection. *Clin. Microbiol. Rev.* **2015**, *28* (3), 687–720. https://doi.org/10.1128/CMR.00006-15.

(228) Fields, B. S.; Benson, R. F.; Besser, R. E. Legionella and Legionnaires' Disease: 25 Years of Investigation. *Clin. Microbiol. Rev.* **2002**, *15* (3), 506–526. https://doi.org/10.1128/CMR.15.3.506-526.2002.

(229) Arias, C. A.; Murray, B. E. The Rise of the Enterococcus: Beyond Vancomycin Resistance. *Nat. Rev. Microbiol.* **2012**, *10* (4), 266–278. https://doi.org/10.1038/nrmicro2761.

(230) Tong, S. Y. C.; Davis, J. S.; Eichenberger, E.; Holland, T. L.; Fowler, V. G. Staphylococcus Aureus Infections: Epidemiology, Pathophysiology, Clinical Manifestations, and Management. *Clin. Microbiol. Rev.* **2015**, *28* (3), 603–661. https://doi.org/10.1128/CMR.00134-14.

(231) Podschun, R.; Ullmann, U. Klebsiella Spp. as Nosocomial Pathogens: Epidemiology, Taxonomy, Typing Methods, and Pathogenicity Factors. *Clin. Microbiol. Rev.* **1998**, *11* (4), 589–603. https://doi.org/10.1128/CMR.11.4.589.

(232) Peleg, A. Y.; Seifert, H.; Paterson, D. L. *Acinetobacter baumannii*: Emergence of a Successful Pathogen. *Clin. Microbiol. Rev.* **2008**, *21* (3), 538–582. https://doi.org/10.1128/CMR.00058-07.

(233) Driscoll, J. A.; Brody, S. L.; Kollef, M. H. The Epidemiology, Pathogenesis and Treatment of *Pseudomonas aeruginosa* Infections. *Drugs* **2007**, *67* (3), 351–368. https://doi.org/10.2165/00003495-200767030-00003.

(234) Cress, B. F.; Englaender, J. A.; He, W.; Kasper, D.; Linhardt, R. J.; Koffas, M. A. G. Masquerading Microbial Pathogens: Capsular Polysaccharides Mimic Host-Tissue Molecules. *FEMS Microbiol. Rev.* **2014**, *38* (4), 660–697. https://doi.org/10.1111/1574-6976.1205.

(235) Galinier, A.; Delan-Forino, C.; Foulquier, E.; Lakhal, H.; Pompeo, F. Recent Advances in Peptidoglycan Synthesis and Regulation in Bacteria. *Biomolecules* **2023**, *13* (5), 720. https://doi.org/10.3390/biom13050720.

(236) Castañeda-Barba, S.; Top, E. M.; Stalder, T. Plasmids, a Molecular Cornerstone of Antimicrobial Resistance in the One Health Era. *Nat. Rev. Microbiol.* **2024**, *22* (1), 18–32. https://doi.org/10.1038/s41579-023-00926-x.

(237) Gault, J.; Ferber, M.; Machata, S.; Imhaus, A.-F.; Malosse, C.; Charles-Orszag, A.; Millien, C.; Bouvier, G.; Bardiaux, B.; Péhau-Arnaudet, G.; Klinge, K.; Podglajen, I.; Ploy, M. C.; Seifert, H. S.; Nilges, M.; Chamot-Rooke, J.; Duménil, G. Neisseria Meningitidis Type IV Pili Composed of Sequence Invariable Pilins Are Masked by Multisite Glycosylation. *PLoS Pathog.* **2015**, *11* (9), e1005162. https://doi.org/10.1371/journal.ppat.1005162.

(238) Wielert, I.; Kraus-Römer, S.; Volkmann, T. E.; Craig, L.; Higgins, P. G.; Maier, B. Pilin Antigenic Variants Impact Gonococcal Lifestyle and Antibiotic Tolerance by Modulating Interbacterial Forces. *PLoS Biol.* **2025**, *23* (1), e3003022. https://doi.org/10.1371/journal.pbio.3003022.

(239) Berg, H., Anderson, R. Bacteria Swim by Rotating their Flagellar Filaments. *Nature* **1973**, *245*, 380–382. https://doi.org/10.1038/245380a0.

(240) Chang, Y.; Carroll, B. L.; Liu, J. Structural Basis of Bacterial Flagellar Motor Rotation and Switching. *Trends Microbiol.* **2021**, *29* (11), 1024–1033. https://doi.org/10.1016/j.tim.2021.03.009.

(241) Adler, J. “Chemotaxis in Bacteria.” *Science* **1966**, 153 (3737), 708-716.

(242) Chaban, B.; Hughes, H. V.; Beeby, M. The Flagellum in Bacterial Pathogens: For Motility and a Whole Lot More. *Semin. Cell Dev. Biol.* **2015**, *46*, 91–103. https://doi.org/10.1016/j.semcdb.2015.10.032.

(243) De Maayer, P.; Cowan, D. A. Flashy Flagella: Flagellin Modification Is Relatively Common and Highly Versatile among the Enterobacteriaceae. *BMC Genomics* **2016**, *17* (1), 377. https://doi.org/10.1186/s12864-016-2735-x.

(244) *Bergey’s Manual of Systematic Bacteriology*. SpringerLink. https://link.springer.com/series/4157.

(245) Coico, R. Gram Staining. *Curr. Protoc. Microbiol.* **2006**, *00* (1), A.3C.1-A.3C.2. https://doi.org/10.1002/9780471729259.mca03cs00.

(246) Alberts, B.; Johnson, A.; Lewis, J.; Raff, M.; Roberts, K.; Walter, P. *Molecular Biology of the Cell*, 4th ed.; Garland Science, 2002.

(247) Rohde, M. The Gram-Positive Bacterial Cell Wall. *Microbiol. Spectr.* **2019**, *7* (3), 10.1128/microbiolspec.gpp3-0044–2018. https://doi.org/10.1128/microbiolspec.gpp3-0044-2018.

(248) Gumbart, J. C.; Beeby, M.; Jensen, G.; Roux, B. Assembly and Architecture of Gram-Positive and -Negative Cell Walls. *Biophys. J.* **2013**, *104* (2), 642a. https://doi.org/10.1016/j.bpj.2012.11.3544.

(249) Popescu, A.; Doyle, R. J. The Gram Stain after More than a Century. *Biotech. Histochem. Off. Publ. Biol. Stain Comm.* **1996**, *71* (3), 145–151. https://doi.org/10.3109/10520299609117151.

(250) Willey, J. M.; Sherwood, L.; Woolverton, C. J. *Prescott’s Microbiology*; McGraw-Hill Education, **2017**.

(251) Caroff, M.; Novikov, A. LPS Structure, Function, and Heterogeneity. In *Endotoxin Detection and Control in Pharma, Limulus, and Mammalian Systems*; Williams, K. L., Ed.; Springer International Publishing: Cham, **2019**, 53–93. https://doi.org/10.1007/978-3-030-17148-3_3.

(252) Schumann, A.; Gaballa, A.; Wiedmann, M. The Multifaceted Roles of Phosphoethanolamine-Modified Lipopolysaccharides: From Stress Response and Virulence to Cationic Antimicrobial Resistance. *Microbiol. Mol. Biol. Rev.* **2024**, *88* (1), e00193-23. https://doi.org/10.1128/mmbr.00193-23.

(253) Whitfield, C.; Kelly, S. D.; Stanton, T. D.; Wyres, K. L.; Clarke, B. R.; Forrester, T. J. B.; Kowalczyk, A. O-Antigen Polysaccharides in Klebsiella Pneumoniae: Structures and Molecular Basis for Antigenic Diversity. *Microbiol. Mol. Biol. Rev.* **2025**, *89* (2), e00090-23. https://doi.org/10.1128/mmbr.00090-23.

(254) Maher, C.; Hassan, K. A. The Gram-Negative Permeability Barrier: Tipping the Balance of the In and the Out. *mBio* **2023**, *14* (3), e01205-23. https://doi.org/10.1128/mbio.01205-23.

(255) Delcour, A. H. Outer Membrane Permeability and Antibiotic Resistance. *Biochim. Biophys. Acta BBA - Proteins Proteomics* **2009**, *1794* (5), 808–816. https://doi.org/10.1016/j.bbapap.2008.11.005.

(256) Livermore, D. M. Permeation of β-Lactam Antibiotics into *Escherichia coli*, *Pseudomonas aeruginosa*, and Other Gram-Negative Bacteria. *Rev. Infect. Dis.* **1988**, *10* (4), 691–698. https://doi.org/10.1093/clinids/10.4.691.

(257) Macesic, N.; Uhlemann, A.-C.; Peleg, A. Y. Multidrug-Resistant Gram-Negative Bacterial Infections. *The Lancet* **2025**, *405* (10474), 257–272. https://doi.org/10.1016/S0140-6736(24)02081-6.

(258) Saxena, D.; Maitra, R.; Bormon, R.; Czekanska, M.; Meiers, J.; Titz, A.; Verma, S.; Chopra, S. Tackling the Outer Membrane: Facilitating Compound Entry into Gram-Negative Bacterial Pathogens. *Npj Antimicrob. Resist.* **2023**, *1* (1), 17. https://doi.org/10.1038/s44259-023-00016-1.

(259) Gauba, A.; Rahman, K. M. Evaluation of Antibiotic Resistance Mechanisms in Gram-Negative Bacteria. *Antibiotics* **2023**, *12* (11), 1590. https://doi.org/10.3390/antibiotics12111590.

(260) Upmanyu, N.; Malviya, V. N. 18 - Antibiotics: Mechanisms of Action and Modern Challenges. In *Microorganisms for Sustainable Environment and Health*; Chowdhary, P., Raj, A., Verma, D., Akhter, Y., Eds.; Elsevier, **2020**; 367–382. https://doi.org/10.1016/B978-0-12-819001-2.00018-8.

(261) Fleming, A. On the Antibacterial Action of Cultures of a Penicillium, with Special Reference to Their Use in the Isolation of B. Influenzae. 1929. *Bull. World Health Organ.* **2001**, *79* (8), 780–790.

(262) Schatz, A.; Bugle, E.; Waksman, S. A. Streptomycin, a Substance Exhibiting Antibiotic Activity Against Gram-Positive and Gram-Negative Bacteria.*. *Exp. Biol. Med.* **1944**, *55* (1), 66–69. https://doi.org/10.3181/00379727-55-14461.

(263) Sarkar, P.; Yarlagadda, V.; Ghosh, C.; Haldar, J. A Review on Cell Wall Synthesis Inhibitors with an Emphasis on Glycopeptide Antibiotics. *MedChemComm* **2017**, *8* (3), 516–533. https://doi.org/10.1039/c6md00585c.

(264) Wang, F.; Zhou, H.; Olademehin, O. P.; Kim, S. J.; Tao, P. Insights into Key Interactions between Vancomycin and Bacterial Cell Wall Structures. *ACS Omega* **2018**, *3* (1), 37–45. https://doi.org/10.1021/acsomega.7b01483.

(265) Suginaka, H.; Blumberg, P. M.; Strominger, J. L. Multiple Penicillin-Binding Components in *Bacillus subtilis*, *Bacillus cereus*, *Staphylococcus aureus*, and *Escherichia coli*. *J. Biol. Chem.* **1972**, *247* (17), 5279–5288.

(266) Yocum, R. R.; Rasmussen, J. R.; Strominger, J. L. The Mechanism of Action of Penicillin. Penicillin Acylates the Active Site of *Bacillus stearothermophilus* D-Alanine Carboxypeptidase. *J. Biol. Chem.* **1980**, *255* (9), 3977–3986. https://doi.org/10.1016/S0021-9258(19)85621-1.

(267) Booth, S.; Lewis, R. J. Structural Basis for the Coordination of Cell Division with the Synthesis of the Bacterial Cell Envelope. *Protein Sci.* **2019**, *28* (12), 2042–2054. https://doi.org/10.1002/pro.3722.

(268) Zhydzetski, A.; Głowacka-Grzyb, Z.; Bukowski, M.; Żądło, T.; Bonar, E.; Władyka, B. Agents Targeting the Bacterial Cell Wall as Tools to Combat Gram-Positive Pathogens. *Molecules* **2024**, *29* (17), 4065. https://doi.org/10.3390/molecules29174065.

(269) Wilson, D. Ribosome-targeting antibiotics and mechanisms of bacterial resistance. *Nat Rev. Microbiol.* **2014**, *12*, 35–48. https://doi.org/10.1038/nrmicro3155

(270) Lang, M.; Carvalho, A.; Baharoglu, Z.; Mazel, D. Aminoglycoside Uptake, Stress, and Potentiation in Gram-Negative Bacteria: New Therapies with Old Molecules. *Microbiol. Mol. Biol. Rev.* **2023**, *87* (4), e00036-22. https://doi.org/10.1128/mmbr.00036-22

(271) Garneau-Tsodikova, S.; Labby, K. J. Mechanisms of Resistance to Aminoglycoside Antibiotics: Overview and Perspectives. *MedChemComm* **2016**, *7* (1), 11–27. https://doi.org/10.1039/C5MD00344J.

(272) Hooper, D. C. Mechanisms of Action and Resistance of Older and Newer Fluoroquinolones. *Clin. Infect. Dis.* **2000**, *31* (Supplement_2), S24–S28. https://doi.org/10.1086/314056.

(273) Kherroubi, L.; Bacon, J.; Rahman, K. M. Navigating Fluoroquinolone Resistance in Gram-Negative Bacteria: A Comprehensive Evaluation. *JAC-Antimicrob. Resist.* **2024**, *6* (4), dlae127. https://doi.org/10.1093/jacamr/dlae127.

(274) Fernández-Villa, D.; Aguilar, M. R.; Rojo, L. Folic Acid Antagonists: Antimicrobial and Immunomodulating Mechanisms and Applications. *Int. J. Mol. Sci.* **2019**, *20* (20), 4996. https://doi.org/10.3390/ijms20204996.

(275) Minato, Y.; Thiede, J. M.; Kordus, S. L.; McKlveen, E. J.; Turman, B. J.; Baughn, A. D. *Mycobacterium tuberculosis* Folate Metabolism and the Mechanistic Basis for para-Aminosalicylic Acid Susceptibility and Resistance. *Antimicrob. Agents Chemother.* **2015**, *59* (9), 5097–5106. https://doi.org/10.1128/AAC.00647-15.

(276) Venkatesan, M., Fruci, M., Verellen, L.A. *et al*. Molecular mechanism of plasmid-borne resistance to sulfonamide antibiotics. *Nat Commun* **2023**, *14*, 4031. https://doi.org/10.1038/s41467-023-39778-7.

(277) Rammelkamp, C. H.; Maxon, T. *Resistance of Staphylococcus aureus to the Action of Penicillin*. *Proc. Soc. Exp. Biol. Med.* **1942**, *51* (3), 386–389. https://doi.org/10.3181/00379727-51-13986.

(278) *Antimicrobial resistance*. https://www.who.int/news-room/fact-sheets/detail/antimicrobial-resistance.

(279) O'Neill, J. *Tackling Drug-Resistant Infections Globally: Final Report and Recommendations*; Report; Government of the United Kingdom, **2016**.

(280) O'Neill, J. Antimicrobial Resistance: A Top Ten Global Public Health Threat. *eClinicalMedicine* **2021**, *41*, 101221. https://doi.org/10.1016/j.eclinm.2021.101221.

(281) Murray, C. J. L. *et al*.; Global Burden of Bacterial Antimicrobial Resistance in 2019: A Systematic Analysis. *The Lancet* **2022**, *399* (10325), 629–655. https://doi.org/10.1016/S0140-6736(21)02724-0.

(282) Mourabiti, F.; Jouga, F.; Sakoui, S.; El Hosayny, O.; Zouheir, Y.; Soukri, A.; El Khalfi, B. Mechanisms, Therapeutic Strategies, and Emerging Therapeutic Alternatives for Carbapenem Resistance in Gram-Negative Bacteria. *Arch. Microbiol.* **2025**, *207* (3), 58. https://doi.org/10.1007/s00203-025-04252-z.

(283) Darby, E.M., Trampari, E., Siasat, P. *et al*. Molecular mechanisms of antibiotic resistance revisited. *Nat. Rev. Microbiol.* **2023**, *21*, 280–295. https://doi.org/10.1038/s41579-022-00820-y

(284) Belay, W. Y.; Getachew, M.; Tegegne, B. A.; Teffera, Z. H.; Dagne, A.; Zeleke, T. K.; Abebe, R. B.; Gedif, A. A.; Fenta, A.; Yirdaw, G.; Tilahun, A.; Aschale, Y. Mechanism of Antibacterial Resistance, Strategies and next-Generation Antimicrobials to Contain Antimicrobial Resistance: A Review. *Front. Pharmacol.* **2024**, *15*. https://doi.org/10.3389/fphar.2024.1444781.

(285) Nikaido, H.; Vaara, M. Molecular Basis of Bacterial Outer Membrane Permeability. *Microbiol. Rev.* **1985**, *49* (1), 1–32. https://doi.org/10.1128/mr.49.1.1-32.1985.

(286) Su, Y.; Zou, G.; Huang, X.; Bi, J.; Meng, L.; Zhao, W.; Li, T. Molecular Characterization and Resistance Mechanisms of Ertapenem-Non-Susceptible Carbapenem-Resistant Klebsiella Pneumoniae Co-Harboring ESBLs or AmpC Enzymes with Porin Loss or Efflux Pump Overexpression. *J. Bacteriol.* **2025**, *207* (7), e0014825. https://doi.org/10.1128/jb.00148-25.

(287) Agreles, M. A. A.; de Moura, A. L. P.; Lima, K. F. A.; Aires, C. A. M.; de Almeida Campos, L. A.; Cavalcanti, I. M. F. Resistance in Gram-Negative Bacilli: The

Emergence of RND Efflux Pumps. *Future Microbiol.* **2025**, *20* (12), 817–831. https://doi.org/10.1080/17460913.2025.2536375.

(288) Nikaido, H.; Pagès, J.-M. Broad-Specificity Efflux Pumps and Their Role in Multidrug Resistance of Gram-Negative Bacteria. *FEMS Microbiol. Rev.* **2012**, *36* (2), 340–363. https://doi.org/10.1111/j.1574-6976.2011.00290.x.

(289) Ruppé, É.; Woerther, P.-L.; Barbier, F. Mechanisms of Antimicrobial Resistance in Gram-Negative Bacilli. *Ann. Intensive Care* **2015**, *5* (1), 61. https://doi.org/10.1186/s13613-015-0061-0.

(290) Luo, L.; Li, Q.; Xing, C.; Li, C.; Pan, Y.; Sun, H.; Yu, X.; Wen, K.; Shen, J.; Wang, Z. Antibody-Based Therapy: An Alternative for Antimicrobial Treatment in the Post-Antibiotic Era. *Microbiol. Res.* **2025**, *290*, 127974. https://doi.org/10.1016/j.micres.2024.127974.

(291) Kolberg, J.; Jones, C. Monoclonal Antibodies with Specificities for Streptococcus Pneumoniae Group 9 Capsular Polysaccharides. *FEMS Immunol. Med. Microbiol.* **1998**, *20* (4), 249–255. https://doi.org/10.1111/j.1574-695X.1998.tb01134.x.

(292) Reyes, F.; Amin, N.; Otero, O.; Aguilar, A.; Cuello, M.; Valdés, Y.; García, L. G.; Cardoso, D.; Camacho, F. Four Monoclonal Antibodies against Capsular Polysaccharides of *Neisseria Meningitidis* Serogroups A, C, Y and W135: Its Application in Identity Tests. *Biologicals* **2013**, *41* (4), 275–278. https://doi.org/10.1016/j.biologicals.2013.05.002.

(293) Soliman, C.; Pier, G. B.; Ramsland, P. A. Antibody Recognition of Bacterial Surfaces and Extracellular Polysaccharides. *Curr. Opin. Struct. Biol.* **2020**, *62*, 48–55. https://doi.org/10.1016/j.sbi.2019.12.001.

(294) Haiko, J.; Westerlund-Wikström, B. The Role of the Bacterial Flagellum in Adhesion and Virulence. *Biology* **2013**, *2* (4), 1242–1267. https://doi.org/10.3390/biology2041242.

(295) Rukavina, T.; Tićac, B.; Susa, M.; Jendrike, N.; Jonjić, S.; Lucin, P.; Marre, R. Protective Effect of Antilipopolysaccharide Monoclonal Antibody in Experimental *Klebsiella* Infection. *Infect. Immun.* **1997**, *65*, 1754–1760. https://doi.org/10.1128/iai.65.5.1754-1760.1997.

(296) Lee, S.; Inzerillo, S.; Lee, G. Y.; Bosire, E. M.; Mahato, S. K.; Song, J. Glycan-Mediated Molecular Interactions in Bacterial Pathogenesis. *Trends Microbiol.* **2022**, *30* (3), 254–267. https://doi.org/10.1016/j.tim.2021.06.011.

(297) Reeves, P. Role of O-Antigen Variation in the Immune Response. *Trends Microbiol.* **1995**, *3* (10), 381–386. https://doi.org/10.1016/S0966-842X(00)88983-0.

(298) Viðarsson, G.; Jónsdóttir, I.; Jónsson, S.; Valdimarsson, H. Opsonization and Antibodies to Capsular and Cell Wall Polysaccharides of *Streptococcus*

pneumoniae. *J. Infect. Dis.* **1994**, *170* (3), 592–599. https://doi.org/10.1093/infdis/170.3.592.

(299) Nanra, J. S.; Buitrago, S. M.; Crawford, S.; Ng, J.; Fink, P. S.; Hawkins, J.; Scully, I. L.; McNeil, L. K.; Aste-Amézaga, J. M.; Cooper, D.; Jansen, K. U.; Anderson, A. S. Capsular Polysaccharides Are an Important Immune Evasion Mechanism for Staphylococcus Aureus. *Hum. Vaccines Immunother.* **2013**, *9* (3), 480–487. https://doi.org/10.4161/hv.23223.

(300) Ramachandran, G.; Tennant, S. M.; Boyd, M. A.; Wang, J. Y.; Tulapurkar, M. E.; Pasetti, M. F.; Levine, M. M.; Simon, R. Functional Activity of Antibodies Directed towards Flagellin Proteins of Non-Typhoidal Salmonella. *PLoS ONE* **2016**, *11* (3), e0151875. https://doi.org/10.1371/journal.pone.0151875.

(301) Merino, S.; Tomás, J. M. Gram-Negative Flagella Glycosylation. *Int. J. Mol. Sci.* **2014**, *15* (2), 2840–2857. https://doi.org/10.3390/ijms15022840.

(302) Singh, B.; Mortezaei, N.; Savarino, S. J.; Uhlin, B. E.; Bullitt, E.; Andersson, M. Antibodies Damage the Resilience of Fimbriae, Causing them to be Stiff and Tangled. *J. Bacteriol.* **2017**, *199* (1), e00665-16. https://doi.org/10.1128/JB.00665-16.

(303) Oz, T.; Guvenek, A.; Yildiz, S.; Karaboga, E.; Tamer, Y. T.; Mumcuyan, N.; Ozan, V. B.; Senturk, G. H.; Cokol, M.; Yeh, P.; Toprak, E. Strength of Selection Pressure Is an Important Parameter Contributing to the Complexity of Antibiotic Resistance Evolution. *Mol. Biol. Evol.* **2014**, *31* (9), 2387–2401. https://doi.org/10.1093/molbev/msu191.

(304) Mettu, R.; Chen, C.-Y.; Wu, C.-Y. Synthetic Carbohydrate-Based Vaccines: Challenges and Opportunities. *J. Biomed. Sci.* **2020**, *27* (1), 9. https://doi.org/10.1186/s12929-019-0591-0.

(305) Weintraub, A. Immunology of Bacterial Polysaccharide Antigens. *Carbohydr. Res.* **2003**, *338* (23), 2539–2547. https://doi.org/10.1016/j.carres.2003.07.008.

(306) Avci, F. Y.; Kasper, D. L. How Bacterial Carbohydrates Influence the Adaptive Immune System. *Annu. Rev. Immunol.* **2010**, *28*, 107–130. https://doi.org/10.1146/annurev-immunol-030409-101159.

(307) Broecker, F.; Anish, C.; Seeberger, P. H. Generation of Monoclonal Antibodies against Defined Oligosaccharide Antigens. In *Carbohydrate-Based Vaccines: Methods and Protocols*; Lepenies, B., Ed.; Springer: New York, NY, **2015**, 57–80. https://doi.org/10.1007/978-1-4939-2874-3_5.

(308) Broecker, F.; Hanske, J.; Martin, C. E.; Baek, J. Y.; Wahlbrink, A.; Wojcik, F.; Hartmann, L.; Rademacher, C.; Anish, C.; Seeberger, P. H. Multivalent Display of Minimal Clostridium Difficile Glycan Epitopes Mimics Antigenic Properties of Larger Glycans. *Nat. Commun.* **2016**, *7* (1), 11224. https://doi.org/10.1038/ncomms11224.

(309) Briles, D. E.; Tart, R. C.; Swiatlo, E.; Dillard, J. P.; Smith, P.; Benton, K. A.; Ralph, B. A.; Brooks-Walter, A.; Crain, M. J.; Hollingshead, S. K.; McDaniel, L. S. Pneumococcal Diversity: Considerations for New Vaccine Strategies with Emphasis on Pneumococcal Surface Protein A (PspA). *Clin. Microbiol. Rev.* **1998**, *11* (4), 645–657. https://doi.org/10.1128/CMR.11.4.645.

(310) King, L. M.; Andrejko, K. L.; Kobayashi, M.; Xing, W.; Cohen, A. L.; Self, W. H.; Resser, J. J.; Whitney, C. G.; Baughman, A.; Kio, M.; Grijalva, C. G.; Traenkner, J.; Rouphael, N.; Lewnard, J. A. Pneumococcal Serotype Distribution and Coverage of Existing and Pipeline Pneumococcal Vaccines. *J. Infect. Dis.* **2025**, jiaf376. https://doi.org/10.1093/infdis/jiaf376.

(311) Wantuch, P. L.; Knoot, C. J.; Robinson, L. S.; Vinogradov, E.; Scott, N. E.; Harding, C. M.; Rosen, D. A. Capsular Polysaccharide Inhibits Vaccine-Induced O-Antigen Antibody Binding and Function across Both Classical and Hypervirulent K2:O1 Strains of Klebsiella Pneumoniae. *PLoS Pathog.* **2023**, *19* (5), e1011367. https://doi.org/10.1371/journal.ppat.1011367.

(312) Que, Y.-A.; Lazar, H.; Wolff, M.; François, B.; Laterre, P.-F.; Mercier, E.; Garbino, J.; Pagani, J.-L.; Revelly, J.-P.; Mus, E.; Perez, A.; Tamm, M.; Rouby, J.-J.; Lu, Q.; Chastre, J.; Eggimann, P. Assessment of Panobacumab as Adjunctive Immunotherapy for the Treatment of Nosocomial Pseudomonas Aeruginosa Pneumonia. *Eur. J. Clin. Microbiol. Infect. Dis. Off. Publ. Eur. Soc. Clin. Microbiol.* **2014**, *33* (10), 1861–1867. https://doi.org/10.1007/s10096-014-2156-1.

(313) Hanot, M.; Lohou, E.; Sonnet, P. Anti-Biofilm Agents to Overcome Pseudomonas Aeruginosa Antibiotic Resistance. *Pharmaceuticals* **2025**, *18* (1), 92. https://doi.org/10.3390/ph18010092.

(314) Zunk, M.; Kiefel, M. J. The Occurrence and Biological Significance of the α-Keto-Sugars Pseudaminic Acid and Legionaminic Acid within Pathogenic Bacteria. *RSC Adv.* **2013**, *4* (7), 3413–3421. https://doi.org/10.1039/C3RA44924F.

(315) Salah Ud-Din, A. I. M.; Roujeinikova, A. Flagellin Glycosylation with Pseudaminic Acid in Campylobacter and Helicobacter: Prospects for Development of Novel Therapeutics. *Cell. Mol. Life Sci.* **2018**, *75* (7), 1163–1178. https://doi.org/10.1007/s00018-017-2696-5.

(316) Tang, A. H.; Karlic, K. I.; Soler, N. M.; Corcilius, L.; Lehmann, C.; Debowski, A.; Dale, A. L.; Zavan, L.; Cielesh, M.; Adewale, A. P.; Moulton, K. D.; Li, L.; Guan, C.; Kaparakis-Liaskos, M.; Howden, B. P.; Wei, R.; Li, X.; Dube, D. H.; Cordwell, S. J.; Larance, M.; Stubbs, K. A.; Carter, G. P.; Scott, N. E.; Goddard-Borger, E. D.; Payne, R. J. Uncovering Bacterial Pseudaminylation with Pan-Specific Antibody Tools. bioRxiv **2025**, p 2025.07.13.664564. https://doi.org/10.1101/2025.07.13.664564.

(317) Knirel, Y. A.; Vinogradov, E. V.; L'vov, V. L.; Kocharova, N. A.; Shashkov, A. S.; Dmitriev, B. A.; Kochetkov, N. K. Sialic Acids of a New Type from the

Lipopolysaccharides of *Pseudomonas aeruginosa* and *Shigella boydii*. *Carbohydr. Res.* **1984**, *133* (2), C5–C8. https://doi.org/10.1016/0008-6215(84)85213-1.

(318) Nemanichvili, N.; Spruit, C. M.; Berends, A. J.; Gröne, A.; Rijks, J. M.; Verheije, M. H.; de Vries, R. P. Wild and Domestic Animals Variably Display Neu5Ac and Neu5Gc Sialic Acids. *Glycobiology* **2022**, *32* (9), 791–802. https://doi.org/10.1093/glycob/cwac033.

(319) Zunk, M.; Kiefel, M. J. The Occurrence and Biological Significance of the α-Keto-Sugars Pseudaminic Acid and Legionaminic Acid within Pathogenic Bacteria. *RSC Adv.* **2013**, *4* (7), 3413–3421. https://doi.org/10.1039/C3RA44924F.

(320) Guo, X.; Li, P.; Liu, H.; Li, X. Recent Progress on the Chemical Synthesis of Bacterial Non-2-Ulosonic Acids. *Org. Chem. Front.* **2023**, *10* (13), 3429–3446. https://doi.org/10.1039/D3QO00637A.

(321) Han, R.; Perepelov, A. V.; Wang, Y.; Filatov, A. V.; Wang, M.; Shashkov, A. S.; Wang, L.; Knirel, Y. A. Structural and Genetic Characterization of the O-Antigen of Enterobacter Cloacae C5529 Related to the O-Antigen of E. Cloacae G3054. *Carbohydr. Res.* **2017**, *443–444*, 49–52. https://doi.org/10.1016/j.carres.2017.02.006.

(322) Kenyon, J. J.; Arbatsky, N. P.; Shneider, M. M.; Popova, A. V.; Dmitrenok, A. S.; Kasimova, A. A.; Shashkov, A. S.; Hall, R. M.; Knirel, Y. A. The K46 and K5 Capsular Polysaccharides Produced by *Acinetobacter baumannii* NIPH 329 and SDF Have Related Structures and the Side-Chain Non-Ulosonic Acids Are 4-O-Acetylated by Phage-Encoded O-Acetyltransferases. *PLoS ONE* **2019**, *14* (6), e0218461. https://doi.org/10.1371/journal.pone.0218461.

(323) Kasimova, A. A.; Dudnik, A. G.; Shashkov, A. S.; Shneider, M. M.; Christofferson, A.; Shelenkov, A. A.; Mikhailova, Y. V.; Kenyon, J. J.; Knirel, Y. A. The K218 Capsular Polysaccharide Produced by Acinetobacter Baumannii Isolate 52-249 Includes 5,7-Di-N-Acetylpseudaminic Acid Linked by a KpsS3 Glycosyltransferase. *Int. J. Biol. Macromol.* **2022**, *218*, 310–316. https://doi.org/10.1016/j.ijbiomac.2022.07.135.

(324) Kenyon, J. J.; Marzaioli, A. M.; Hall, R. M.; De Castro, C. Structure of the K2 Capsule Associated with the KL2 Gene Cluster of *Acinetobacter baumannii*. *Glycobiology* **2014**, *24* (6), 554–563. https://doi.org/10.1093/glycob/cwu024.

(325) Senchenkova, S. N.; Shashkov, A. S.; Shneider, M. M.; Arbatsky, N. P.; Popova, A. V.; Miroshnikov, K. A.; Volozhantsev, N. V.; Knirel, Y. A. Structure of the Capsular Polysaccharide of *Acinetobacter baumannii* ACICU Containing Di-*N*-Acetylpseudaminic Acid. *Carbohydr. Res.* **2014**, *391*, 89–92. https://doi.org/10.1016/j.carres.2014.04.002.

(326) Kenyon, J. J.; Marzaioli, A. M.; Hall, R. M.; De Castro, C. Structure of the K6 Capsular Polysaccharide from *Acinetobacter baumannii* Isolate RBH4. *Carbohydr. Res.* **2015**, *409*, 30–35. https://doi.org/10.1016/j.carres.2015.03.016.

(327) Kenyon, J. J.; Arbatsky, N. P.; Sweeney, E. L.; Shashkov, A. S.; Shneider, M. M.; Popova, A. V.; Hall, R. M.; Knirel, Y. A. Production of the K16 Capsular Polysaccharide by *Acinetobacter baumannii* ST25 Isolate D4 Involves a Novel Glycosyltransferase Encoded in the KL16 Gene Cluster. *Int. J. Biol. Macromol.* **2019**, *128*, 101–106. https://doi.org/10.1016/j.ijbiomac.2019.01.080.

(328) Iovine, A.; Filatov, A. V.; Kasimova, A. A.; Sharar, N. S.; Ambrose, S. J.; Dmitrenok, A. S.; Shneider, M. M.; Shpirt, A. M.; Perepelov, A. V.; Knirel, Y. A.; Hall, R. M.; De Castro, C.; Kenyon, J. J. Structure of the K58 Capsular Polysaccharide Produced by *Acinetobacter baumannii* Isolate MRSN 31468 Includes Pse5Ac7Ac That Is 4-O-Acetylated by a Phage-Encoded Acetyltransferase. *Carbohydr. Res.* **2025**, *547*, 109324. https://doi.org/10.1016/j.carres.2024.109324.

(329) Lee, I.-M.; Yang, F.-L.; Chen, T.-L.; Liao, K.-S.; Ren, C.-T.; Lin, N.-T.; Chang, Y.-P.; Wu, C.-Y.; Wu, S.-H. Pseudaminic Acid on Exopolysaccharide of *Acinetobacter baumannii* Plays a Critical Role in Phage-Assisted Preparation of Glycoconjugate Vaccine with High Antigenicity. *J. Am. Chem. Soc.* **2018**, *140* (28), 8639–8643. https://doi.org/10.1021/jacs.8b04078.

(330) Ardissone, S.; Kint, N.; Viollier, P. H. Specificity in Glycosylation of Multiple Flagellins by the Modular and Cell Cycle Regulated Glycosyltransferase FlmG. *eLife* **2020**, *9*, e60488. https://doi.org/10.7554/eLife.60488.

(331) Casillo, A.; Ricciardelli, A.; Parrilli, E.; Tutino, M. L.; Corsaro, M. M. Cell-Wall Associated Polysaccharide from the Psychrotolerant Bacterium *Psychrobacter arcticus* 273-4: Isolation, Purification and Structural Elucidation. *Extremophiles* **2020**, *24* (1), 63–70. https://doi.org/10.1007/s00792-019-01113-8.

(332) Sharypova, L. A.; Chataigné, G.; Fraysse, N.; Becker, A.; Poinsot, V. Overproduction and Increased Molecular Weight Account for the Symbiotic Activity of the rkpZ-Modified K Polysaccharide from *Sinorhizobium meliloti* Rm1021. *Glycobiology* **2006**, *16* (12), 1181–1193. https://doi.org/10.1093/glycob/cwl042.

(333) Zdorovenko, E. L.; Kadykova, A. A.; Varbanets, L. D.; Shashkov, A. S.; Kiprianova, E. A.; Brovarskaya, O. S.; Knirel, Y. A. Structure of the O-Specific Polysaccharides of *Pseudomonas chlororaphis* subsp. *chlororaphis* UCM B-106. *Carbohydr. Res.* **2016**, *433*, 1–4. https://doi.org/10.1016/j.carres.2016.06.013.

(334) Kaszowska, M.; Stojkovic, K.; Niedziela, T.; Lugowski, C. The O-Antigen of *Plesiomonas shigelloides* Serotype O36 Containing Pseudaminic Acid. *Carbohydr. Res.* **2016**, *434*, 1–5. https://doi.org/10.1016/j.carres.2016.07.007.

(335) Senchenkova, S. N.; Zhang, Y.; Perepelov, A. V.; Guo, X.; Shashkov, A. S.; Weintraub, A.; Liu, B.; Widmalm, G.; Knirel, Y. A. Structure and Gene Cluster of the O-Antigen of Escherichia Coli O165 Containing 5-N-Acetyl-7-N-[(R)-3-Hydroxybutanoyl]Pseudaminic Acid. *Glycobiology* **2016**, *26* (4), 335–342. https://doi.org/10.1093/glycob/cwv106.

(336) Kasimova, A. A.; Shneider, M. M.; Arbatsky, N. P.; Popova, A. V.; Shashkov, A. S.; Miroshnikov, K. A.; Balaji, V.; Biswas, I.; Knirel, Y. A. Structure and Gene Cluster of the K93 Capsular Polysaccharide of *Acinetobacter baumannii* B11911 Containing 5-N-Acetyl-7-N-[(R)-3-Hydroxybutanoyl]pseudaminic Acid. *Biochemistry (Moscow)* **2017**, *82*, 483–489. https://doi.org/10.1134/S0006297917040101.

(337) Schauer, R.; Kamerling, J. P. Exploration of the Sialic Acid World. *Adv. Carbohydr. Chem. Biochem.* **2018**, *75*, 1–213. https://doi.org/10.1016/bs.accb.2018.09.001.

(338) Castric, P.; Cassels, F. J.; Carlson, R. W. Structural Characterization of the Pseudomonas Aeruginosa 1244 Pilin Glycan. *J. Biol. Chem.* **2001**, *276* (28), 26479–26485. https://doi.org/10.1074/jbc.M102685200.

(339) Kokoulin, M.S.; Kuzmich, A.S.; Romanenko, L.A.; Chikalovets, I.V.; Chernikov, O.V. Structure and In Vitro Bioactivity against Cancer Cells of the Capsular Polysaccharide from the Marine Bacterium *Psychrobacter marincola*. *Mar. Drugs* **2020**, *18*, 268. https://doi.org/10.3390/md18050268.

(340) Lee, I.-M.; Wu, H.-Y.; Angata, T.; Wu, S.-H. Bacterial Pseudaminic Acid Binding to Siglec-10 Induces a Macrophage Interleukin-10 Response and Suppresses Phagocytosis. *Chem. Commun.* **2024**, *60* (21), 2930–2933. https://doi.org/10.1039/D4CC00077C.

(341) Kleikamp, H. B. C.; Lin, Y. M.; McMillan, D. G. G.; Geelhoed, J. S.; Naus-Wiezer, S. N. H.; Baarlen, P. van; Saha, C.; Louwen, R.; Sorokin, D. Y.; Loosdrecht, M. C. M. van; Pabst, M. Tackling the Chemical Diversity of Microbial Nonulosonic Acids – a Universal Large-Scale Survey Approach. *Chem. Sci.* **2020**, *11* (11), 3074–3080. https://doi.org/10.1039/C9SC06406K.

(342) Andolina, G.; Wei, R.; Liu, H.; Zhang, Q.; Yang, X.; Cao, H.; Chen, S.; Yan, A.; Li, X. D.; Li, X. Metabolic Labeling of Pseudaminic Acid-Containing Glycans on Bacterial Surfaces. *ACS Chem. Biol.* **2018**, *13* (10), 3030–3037. https://doi.org/10.1021/acschembio.8b00822.

(343) Champasa, K.; Longwell, S. A.; Eldridge, A. M.; Stemmler, E. A.; Dube, D. H. Targeted Identification of Glycosylated Proteins in the Gastric Pathogen *Helicobacter Pylori* (*Hp*)*. *Mol. Cell. Proteomics* **2013**, *12* (9), 2568–2586. https://doi.org/10.1074/mcp.M113.029561.

(344) Zhu, D.; Zhang, H.; Yu, W.; Jin, L.; Ma, Y.; Yang, X.; Li, X.; Chen, S. Synthetic Pseudaminic-Acid-Based Antibacterial Vaccine Confers Effective Protection against *Acinetobacter baumannii* Infection. *ACS Cent. Sci.* **2021**, *7* (10), 1647–1655. https://doi.org/10.1021/acscentsci.1c00656

(345) Lee, I.-M.; Tu, I.-F.; Yang, F.-L.; Wu, S.-H. Bacteriophage Tail-Spike Proteins Enable Detection of Pseudaminic-Acid-Coated Pathogenic Bacteria and Guide the Development of Antiglycan Antibodies with Cross-Species Antibacterial Activity. *J.*

Am. Chem. Soc. **2020**, *142* (46), 19446–19450. https://doi.org/10.1021/jacs.0c07314.

(346) Knirel, Y. A.; Kocharova, N. A.; Shashkov, A. S.; Dmitriev, B. A.; Kochetkov, N. K.; Stanislavsky, E. S.; Mashilova, G. M. Somatic Antigens of Pseudomonas Aeruginosa. *Eur. J. Biochem.* **1987**, *163* (3), 639–652. https://doi.org/10.1111/j.1432-1033.1987.tb10913.x.

(347) Liu, F.; Tanner, M. E. PseG of Pseudaminic Acid Biosynthesis: A UDP-sugar hydrolase as a masked glycosyltransferase. *J. Biol. Chem.* **2006**, *281* (30), 20902–20909. https://doi.org/10.1074/jbc.M602972200.

(348) Pradhan, K.; Kulkarni, S. S. Synthesis of Nonulosonic Acids. *Eur. J. Org. Chem.* **2020**, (44), 6819–6830. https://doi.org/10.1002/ejoc.202000250.

(349) Liu, H.; Zhang, Y.; Wei, R.; Andolina, G.; Li, X. Total Synthesis of Pseudomonas Aeruginosa 1244 Pilin Glycan via de Novo Synthesis of Pseudaminic Acid. *J. Am. Chem. Soc.* **2017**, *139* (38), 13420–13428. https://doi.org/10.1021/jacs.7b06055.

(350) Dhakal, B.; Crich, D. Synthesis and Stereocontrolled Equatorially Selective Glycosylation Reactions of a Pseudaminic Acid Donor: Importance of the Side-Chain Conformation and Regioselective Reduction of Azide Protecting Groups. *J. Am. Chem. Soc.* **2018**, *140* (44), 15008–15015. https://doi.org/10.1021/jacs.8b09654.

(351) Siyabalapitiya Arachchige, S.; Crich, D. Syntheses of Legionaminic Acid, Pseudaminic Acid, Acetaminic Acid, 8-Epi-Acetaminic Acid, and 8-Epi-Legionaminic Acid Glycosyl Donors from N-Acetylneuraminic Acid by Side Chain Exchange. *Org. Lett.* **2022**, *24* (16), 2998–3002. https://doi.org/10.1021/acs.orglett.2c00894.

(352) Lee, Y. J.; Kubota, A.; Ishiwata, A.; Ito, Y. Synthesis of Pseudaminic Acid, a Unique Nonulopyranoside Derived from Pathogenic Bacteria through 6-Deoxy-AltdiNAc. *Tetrahedron Lett.* **2011**, *52* (3), 418–421. https://doi.org/10.1016/j.tetlet.2010.11.078.

(353) Tsvetkov, Y. E.; Shashkov, A. S.; Knirel, Y. A.; Zähringer, U. Synthesis and NMR Spectroscopy of Nine Stereoisomeric 5,7-Diacetamido-3,5,7,9-Tetradeoxynon-2-Ulosonic Acids. *Carbohydr. Res.* **2001**, *335* (4), 221–243. https://doi.org/10.1016/S0008-6215(01)00235-X.

(354) Williams, J. T.; Corcilius, L.; Kiefel, M. J.; Payne, R. J. Total Synthesis of Native 5,7-Diacetylpseudaminic Acid from N-Acetylneuraminic Acid. *J. Org. Chem.* **2016**, *81* (6), 2607–2611. https://doi.org/10.1021/acs.joc.5b02754.

(355) Buda, S.; Crich, D. Oxidative Deamination of N-Acetyl Neuraminic Acid: Substituent Effects and Mechanism. *J. Am. Chem. Soc.* **2016**, *138* (3), 1084–1092. https://doi.org/10.1021/jacs.5b13015.

(356) Lee, S.-H.; Yoon, J.; Nakamura, K.; Lee, Y.-S. Efficient Syntheses and Ring-Opening Reactions of Trans- and Cis-Oxazoline-5-Carboxylates. *Org. Lett.* **2000**, *2* (9), 1243–1246. https://doi.org/10.1021/ol005681h.

(357) Christensen, H. M.; Oscarson, S.; Jensen, H. H. Common Side Reactions of the Glycosyl Donor in Chemical Glycosylation. *Carbohydr. Res.* **2015**, *408*, 51–95. https://doi.org/10.1016/j.carres.2015.02.007.

(358) Zhang, J.; Jie, J.; Yan, S.; Zhang, H.; Chen, J.; Wu, J.; Qin, L.; Liu, G.; Su, H.; Xing, G. Single Electron/Energy Transfer Photocatalysis: α-/β-Switchable Synthesis of 3-Deoxy-D-manno-oct-2-ulosonic Acid *O*-Glycosides. *Chem. Sci.* **2016**, *7* (2), 1207–1212. https://doi.org/10.1039/D5SC02980E.

(359) Cheung, Y. C.; Guo, X.; Yang, X.; Wei, R.; Chan, E. W.; Li, X.; Chen, S. KpsS1 Mediates the Glycosylation of Pseudaminic Acid in Bacterial Surface Structures. *Chem. Eur. J.* **2024**, *30*, e202400703. https://doi.org/10.1002/chem.202400703.

(360) Wei, R.; Liu, H.; Tang, A. H.; Payne, R. J.; Li, X. A Solution to Chemical Pseudaminylation via a Bimodal Glycosyl Donor for Highly Stereocontrolled α- and β-Glycosylation. *Org. Lett.* **2019**, *21* (10), 3584–3588. https://doi.org/10.1021/acs.orglett.9b00990.

(361) Crich, D.; Li, W. α-Selective Sialylations at −78 °C in Nitrile Solvents with a 1-Adamantanyl Thiosialoside. *J. Org. Chem.* **2007**, *72* (20), 7794–7797. https://doi.org/10.1021/jo7012912.

(362) Mulani, S. K.; Hung, W.-C.; Ingle, A. B.; Shiau, K.-S.; Mong, K.-K. T. Modulating Glycosylation with Exogenous Nucleophiles: An Overview. *Org. Biomol. Chem.* **2014**, *12* (8), 1184–1197. https://doi.org/10.1039/C3OB42129E.

(363) Lu, S.-R.; Lai, Y.-H.; Chen, J.-H.; Liu, C.-Y.; Mong, K.-K. Tony. Dimethylformamide: An Unusual Glycosylation Modulator. *Angew. Chem. Int. Ed.* **2011**, *50* (32), 7315–7320. https://doi.org/10.1002/anie.201100076

(364) Corcilius, L.; Payne, R. J. Stereoselective Synthesis of Sialylated Tumor-Associated Glycosylamino Acids. *Org. Lett.* **2013**, *15* (22), 5794–5797. https://doi.org/10.1021/ol402845e.

(365) Brown, H. C.; Narasimhan, S.; Choi, Y. M. Selective Reductions. 30. Effect of Cation and Solvent on the Reactivity of Saline Borohydrides for Reduction of Carboxylic Esters. Improved Procedures for the Conversion of Esters to Alcohols by Metal Borohydrides. *J. Org. Chem.* **1982**, *47* (24), 4702–4708. https://doi.org/10.1021/jo00145a018.

(366) Valiullina, Z. R.; Lobov, A. N.; Selezneva, N. K.; Miftakhov, M. S. Pyrrolidine Synthons for β-Lactams. *Russ. J. Org. Chem.* **2016**, *52* (3), 349–354. https://doi.org/10.1134/S1070428016030106.

(367) Venkatraman, S.; Velazquez, F.; Gavalas, S.; Wu, W.; Chen, K. X.; Nair, A. G.; Bennett, F.; Huang, Y.; Pinto, P.; Jiang, Y.; Selyutin, O.; Vibulbhan, B.; Zeng, Q.; Lesburg, C.; Duca, J.; Heimark, L.; Huang, H.-C.; Agrawal, S.; Jiang, C.; Ferrari, E.; Li, C.; Kozlowski, J.; Rosenblum, S.; Shih, N.-Y.; Njoroge, F. G. Optimization of Potency and Pharmacokinetics of Tricyclic Indole Derived Inhibitors of HCV NS5B Polymerase. Identification of Ester Prodrugs with Improved Oral Pharmacokinetics. *Bioorg. Med. Chem.* **2014**, *22* (1), 447–458. https://doi.org/10.1016/j.bmc.2013.11.007.

(368) Velázquez, F.; Venkatraman, S.; Lesburg, C. A.; Duca, J.; Rosenblum, S. B.; Kozlowski, J. A.; Njoroge, F. G. Synthesis of New 4,5-Dihydrofuranoindoles and Their Evaluation as HCV NS5B Polymerase Inhibitors. *Org. Lett.* **2012**, *14* (2), 556–559. https://doi.org/10.1021/ol203177g.

(369) Moser, D.; Jana, K.; Sparr, C. Atroposelective PIII/PV=O Redox Catalysis for the Isoquinoline-Forming Staudinger–Aza-Wittig Reaction. *Angew. Chem. Int. Ed.* **2023**, *62* (39), e202309053. https://doi.org/10.1002/anie.202309053.

(370) Murakami, Y.; Watanabe, T.; Suzuki, H.; Kotake, N.; Takahashi, T.; Toyonari, K.; Ohno, M.; Takase, K.; Suzuki, T.; Kondo, K. New Findings on the Hemetsberger-Knittel Reaction (Synthetic Studies on Indoles and Related Compounds. XLIII). *Chem. Pharm. Bull.* **1997**, *45* (11), 1739–1744. https://doi.org/10.1248/cpb.45.1739.

(371) Weidner, K.; Sun, Z.; Kumagai, N.; Shibasaki, M. Direct Catalytic Asymmetric Aldol Reaction of an α-Azido Amide. *Angew. Chem. Int. Ed.* **2015**, *54* (21), 6236–6240. https://doi.org/10.1002/anie.201501607.

(372) Li, Y.; Paddon-Row, M. N.; Houk, K. N. Transition Structures for the Aldol Reactions of Anionic, Lithium, and Boron Enolates. *J. Org. Chem.* **1990**, *55* (2), 481–493. https://doi.org/10.1021/jo00289a020.

(373) Evans, D. A.; Vogel, E.; Nelson, J. V. Stereoselective Aldol Condensations via Boron Enolates. *J. Am. Chem. Soc.* **1979**, *101* (20), 6120–6123. https://doi.org/10.1021/ja00514a045.

(374) Patonay, T.; Hoffman, R. V. Base-Promoted Reactions of .Alpha.-Azido Ketones with Aldehydes and Ketones: A Novel Entry to α-Azido-β-Hydroxy Ketones and 2,5-Dihydro-5-Hydroxyoxazoles. *J. Org. Chem.* **1995**, *60* (8), 2368–2377. https://doi.org/10.1021/jo00113a015.

(375) Clive, D. L. J.; Kellner, D. A New Method for Silylation of Hydroxylic Compounds: Reaction of Phenols and Alcohols with Silanols Mediated by Diethyl Azodicarboxylate and Triphenylphosphine. *Tetrahedron Lett.* **1991**, *32* (49), 7159–7160. https://doi.org/10.1016/0040-4039(91)80464-H.

(376) Camp, D.; Jenkins, I. D. The Mechanism of the Mitsunobu Esterification Reaction. Part I. The Involvement of Phosphoranes and Oxyphosphonium Salts. *J. Org. Chem.* **1989**, *54* (13), 3045–3049. https://doi.org/10.1021/jo00274a016.

(377) Marvin, C. C. 6.02 Synthesis of Amines and Ammonium Salts. In *Comprehensive Organic Synthesis (Second Edition)*; Knochel, P., Ed.; Elsevier: Amsterdam, **2014**; 34–99. https://doi.org/10.1016/B978-0-08-097742-3.00603-0.

(378) Cochran, B. M. One-Pot Oxidative Cleavage of Olefins to Synthesize Carboxylic Acids by a Telescoped Ozonolysis–Oxidation Process. *Synlett* **2016**, *27* (2), 245–248. https://doi.org/10.1055/s-0035-1560659.

(379) Lee, J. H.; Kishi, Y. One-Pot Ketone Synthesis with Alkylzinc Halides Prepared from Alkyl Halides via a Single Electron Transfer (SET) Process: New Extension of Fukuyama Ketone Synthesis. *J. Am. Chem. Soc.* **2016**, *138* (22), 7178–7186. https://doi.org/10.1021/jacs.6b03897.

(380) Jung, M. E.; Piizzi, G. Gem-Disubstituent Effect: Theoretical Basis and Synthetic Applications. *Chem. Rev.* **2005**, *105* (5), 1735–1766. https://doi.org/10.1021/cr940337h.

(381) Knirel, Y. A.; Rietschel, E. Th.; Marre, R.; Zähringer, U. The Structure of the O-Specific Chain of Legionella Pneumophila Serogroup 1 Lipopolysaccharide. *Eur. J. Biochem.* **1994**, *221* (1), 239–245. https://doi.org/10.1111/j.1432-1033.1994.tb18734.x.

(382) McDonald, N. D.; Boyd, E. F. Structural and Biosynthetic Diversity of Nonulosonic Acids (NulOs) That Decorate Surface Structures in Bacteria. *Trends Microbiol.* **2021**, *29* (2), 142–157. https://doi.org/10.1016/j.tim.2020.08.002.

(383) Filatov, A. V.; Wang, M.; Wang, W.; Perepelov, A. V.; Shashkov, A. S.; Wang, L.; Knirel, Y. A. Structure and Genetics of the O-Antigen of *Enterobacter Cloacae* C6285 Containing Di-*N*-Acetyllegionaminic Acid. *Carbohydr. Res.* **2014**, *392*, 21–24. https://doi.org/10.1016/j.carres.2014.01.012.

(384) Logan, S. M.; Hui, J. P. M.; Vinogradov, E.; Aubry, A. J.; Melanson, J. E.; Kelly, J. F.; Nothaft, H.; Soo, E. C. Identification of Novel Carbohydrate Modifications on *Campylobacter jejuni* 11168 Flagellin Using Metabolomics-Based Approaches. *FEBS J.* **2009**, *276* (4), 1014–1023. https://doi.org/10.1111/j.1742-4658.2008.06840.x.

(385) Hashii, N.; Isshiki, Y.; Iguchi, T.; Kondo, S. Structural Characterization of the Carbohydrate Backbone of the Lipopolysaccharide of *Vibrio Parahaemolyticus* O-Untypeable Strain KX-V212 Isolated from a Patient. *Carbohydr. Res.* **2003**, *338* (23), 2711–2719. https://doi.org/10.1016/j.carres.2003.06.003.

(386) Tsvetkov, Y. E.; Shashkov, A. S.; Knirel, Y. A.; Zähringer, U. Synthesis and Identification in Bacterial Lipopolysaccharides of 5,7-Diacetamido-3,5,7,9-Tetradeoxy-D-Glycero- D -Galacto- and -D-Glycero-D-Talo-Non-2-Ulosonic Acids. *Carbohydr. Res.* **2001**, *331* (3), 233–237. https://doi.org/10.1016/S0008-6215(01)00041-6.

(387) Kodali, S.; Vinogradov, E.; Lin, F.; Khoury, N.; Hao, L.; Pavliak, V.; Jones, C. H.; Laverde, D.; Huebner, J.; Jansen, K. U.; Anderson, A. S.; Donald, R. G. K. A Vaccine Approach for the Prevention of Infections by Multidrug-Resistant *Enterococcus faecium*. *J. Biol. Chem.* **2015**, *290* (32), 19512–19526. https://doi.org/10.1074/jbc.M115.655852.

(388) Friedrich, V.; Janesch, B.; Windwarder, M.; Maresch, D.; Braun, M. L.; Megson, Z. A.; Vinogradov, E.; Goneau, M.-F.; Sharma, A.; Altmann, F.; Messner, P.; Schoenhofen, I. C.; Schäffer, C. Tannerella Forsythia Strains Display Different Cell-Surface Nonulosonic Acids: Biosynthetic Pathway Characterization and First Insight into Biological Implications. *Glycobiology* **2017**, *27* (4), 342–357. https://doi.org/10.1093/glycob/cww129.

(389) McNally, D. J.; Aubry, A. J.; Hui, J. P. M.; Khieu, N. H.; Whitfield, D.; Ewing, C. P.; Guerry, P.; Brisson, J.-R.; Logan, S. M.; Soo, E. C. Targeted Metabolomics Analysis of *Campylobacter Coli* VC167 Reveals Legionaminic Acid Derivatives as Novel Flagellar Glycans*. *J. Biol. Chem.* **2007**, *282* (19), 14463–14475. https://doi.org/10.1074/jbc.M611027200.

(390) McDonald, N. D.; DeMeester, K. E.; Lewis, A. L.; Grimes, C. L.; Boyd, E. F. Structural and Functional Characterization of a Modified Legionaminic Acid Involved in Glycosylation of a Bacterial Lipopolysaccharide. *J. Biol. Chem.* **2018**, *293* (49), 19113–19126. https://doi.org/10.1074/jbc.RA118.004966.

(391) Li, X.; Perepelov, A. V.; Wang, Q.; Senchenkova, S. N.; Liu, B.; Shevelev, S. D.; Guo, X.; Shashkov, A. S.; Chen, W.; Wang, L.; Knirel, Y. A. Structural and Genetic Characterization of the O-Antigen of *Escherichia Coli* O161 Containing a Derivative of a Higher Acidic Diamino Sugar, Legionaminic Acid. *Carbohydr. Res.* **2010**, *345* (11), 1581–1587. https://doi.org/10.1016/j.carres.2010.04.008.

(392) Twine, S. M.; Paul, C. J.; Vinogradov, E.; McNally, D. J.; Brisson, J.-R.; Mullen, J. A.; McMullin, D. R.; Jarrell, H. C.; Austin, J. W.; Kelly, J. F.; Logan, S. M. Flagellar Glycosylation in *Clostridium botulinum*. *FEBS J.* **2008**, *275* (18), 4428–4444. https://doi.org/10.1111/j.1742-4658.2008.06589.x.

(393) Haseley, S. R.; Wilkinson, S. G. Structural Studies of the Putative O-Specific Polysaccharide of Acinetobacter Baumannii O24 Containing 5,7-Diamino-3,5,7,9-Tetradeoxy-L-Glycerol-D-Galacto-Nonulosonic Acid. *Eur. J. Biochem.* **1997**, *250* (2), 617–623. https://doi.org/10.1111/j.1432-1033.1997.0617a2.

(394) Siyabalapitiya Arachchige, S.; Crich, D. Syntheses of Legionaminic Acid, Pseudaminic Acid, Acetaminic Acid, 8-Epi-Acetaminic Acid, and 8-Epi-Legionaminic Acid Glycosyl Donors from N-Acetylneuraminic Acid by Side Chain Exchange. *Org. Lett.* **2022**, *24* (16), 2998–3002. https://doi.org/10.1021/acs.orglett.2c00894.

(395) Popik, O.; Dhakal, B.; Crich, D. Stereoselective Synthesis of the Equatorial Glycosides of Legionaminic Acid. *J. Org. Chem.* **2017**, *82* (12), 6142–6152. https://doi.org/10.1021/acs.joc.7b00746.

(396) Matthies, S.; Stallforth, P.; Seeberger, P. H. Total Synthesis of Legionaminic Acid as Basis for Serological Studies. *J. Am. Chem. Soc.* **2015**, *137* (8), 2848–2851. https://doi.org/10.1021/jacs.5b00455.

(397) Santra, A.; Xiao, A.; Yu, H.; Li, W.; Li, Y.; Ngo, L.; McArthur, J. B.; Chen, X. A Diazido Mannose Analogue as a Chemoenzymatic Synthon for Synthesizing Di-N-Acetyllegionaminic Acid-Containing Glycosides. *Angew. Chem. Int. Ed.* **2018**, *57* (11), 2929–2933. https://doi.org/10.1002/anie.201712022.

(398) Hassan, M. I.; Lundgren, B. R.; Chaumun, M.; Whitfield, D. M.; Clark, B.; Schoenhofen, I. C.; Boddy, C. N. Total Biosynthesis of Legionaminic Acid, a Bacterial Sialic Acid Analogue. *Angew. Chem. Int. Ed.* **2016**, *55* (39), 12018–12021. https://doi.org/10.1002/anie.201606006.

(399) Fraser-Reid, B.; Konradsson, P.; Mootoo, D. R.; Udodong, U. Direct Elaboration of Pent-4-Enyl Glycosides into Disaccharides. *J. Chem. Soc. Chem. Commun.* **1988**, No. 12, 823–825. https://doi.org/10.1039/C39880000823.

(400) Jensen, H. H.; Nordstrøm, L. U.; Bols, M. The Disarming Effect of the 4,6-Acetal Group on Glycoside Reactivity: Torsional or Electronic? *J. Am. Chem. Soc.* **2004**, *126* (30), 9205–9213. https://doi.org/10.1021/ja047578j.

(401) Candeias, N. R.; Montalbano, F.; Cal, P. M. S. D.; Gois, P. M. P. Boronic Acids and Esters in the Petasis-Borono Mannich Multicomponent Reaction. *Chem. Rev.* **2010**, *110* (10), 6169–6193. https://doi.org/10.1021/cr100108k.

(402) Popik, O.; Dhakal, B.; Crich, D. Stereoselective Synthesis of the Equatorial Glycosides of Legionaminic Acid. *J. Org. Chem.* **2017**, *82* (12), 6142–6152. https://doi.org/10.1021/acs.joc.7b00746.

(403) Zhong, Y.-W.; Dong, Y.-Z.; Fang, K.; Izumi, K.; Xu, M.-H.; Lin, G.-Q. A Highly Efficient and Direct Approach for Synthesis of Enantiopure β-Amino Alcohols by Reductive Cross-Coupling of Chiral N-Tert-Butanesulfinyl Imines with Aldehydes. *J. Am. Chem. Soc.* **2005**, *127* (34), 11956–11957. https://doi.org/10.1021/ja054401w.

(404) Bocian, D. F.; Pickett, H. M.; Rounds, T. C.; Strauss, H. L. Conformations of Cycloheptane. *J. Am. Chem. Soc.* **1975**, *97* (4), 687–695. https://doi.org/10.1021/ja00837a001.

(405) Yang, J. *Six-Membered Transition States in Organic Synthesis*; John Wiley & Sons, Inc.: Hoboken, NJ, **2008**. https://doi.org/10.1002/9780470199053.

(406) Lin, X.; Bentley, P. A.; Xie, H. Auxiliary Strategies for the Preparation of β-Amino Alcohols with Reductive Cross-Coupling and a Synthesis of (−)-Cytoxazone.

Tetrahedron Lett. **2005**, *46* (45), 7849–7852. https://doi.org/10.1016/j.tetlet.2005.09.002.

(407) Burchak, O. N.; Masson, G.; Py, S. SmI_2-Mediated Reductive Cross-Coupling Reactions of α-Cyclopropyl Nitrones. *Synlett* **2010**, 11, 1623–1626. doi.org/10.1055/s-0030-1258084

(408) Szostak, M.; Fazakerley, N. J.; Parmar, D.; Procter, D. J. Cross-Coupling Reactions Using Samarium(II) Iodide. *Chem. Rev.* **2014**, *114* (11), 5959–6039. https://doi.org/10.1021/cr400685r.

(409) Trost, B. M.; Waser, J.; Meyer, A. Total Synthesis of (−)-Pseudolaric Acid B. *J. Am. Chem. Soc.* **2008**, *130* (48), 16424–16434. https://doi.org/10.1021/ja806724x.

(410) Demchenko, A. V., Ed. *Handbook of Chemical Glycosylation: Advances in Stereoselectivity and Therapeutic Relevance*; Wiley-VCH: Weinheim, Germany, **2008**. DOI: 10.1002/9783527621644.

(411) Stachulski, A. V. Glucuronidation of Alcohols Using the Bromosugar–Iodonium Reagent Method. *Tetrahedron Lett.* **2001**, *42* (37), 6611–6613. https://doi.org/10.1016/S0040-4039(01)01333-8.

(412) Crich, D.; Sun, S. Are Glycosyl Triflates Intermediates in the Sulfoxide Glycosylation Method? A Chemical and 1H, 13C, and 19F NMR Spectroscopic Investigation. *J. Am. Chem. Soc.* **1997**, *119* (46), 11217–11223. https://doi.org/10.1021/ja971239r.

(413) Bohé, L.; Crich, D. A Propos of Glycosyl Cations and the Mechanism of Chemical Glycosylation. *Comptes Rendus Chim.* **2011**, *14* (1), 3–16. https://doi.org/10.1016/j.crci.2010.03.016.

(414) Hori, H.; Nakajima, T.; Nishida, Y.; Ohrui, H.; Meguro, H. A Simple Method to Determine the Anomeric Configuration of Sialic Acid and Its Derivatives by 13C-NMR. *Tetrahedron Lett.* **1988**, *29* (48), 6317–6320. https://doi.org/10.1016/S0040-4039(00)82335-7.

(415) Chow, Y. L.; Colón, C. J. Nuclear Magnetic Resonance Studies on the Configurations and Conformations of Heterocyclic Nitrosamines. *Can. J. Chem.* **1968**, *46* (17), 2827–2833. https://doi.org/10.1139/v68-468.

(416) Destecroix, H.; Renney, C. M.; Mooibroek, T. J.; Carter, T. S.; Stewart, P. F. N.; Crump, M. P.; Davis, A. P. Affinity Enhancement by Dendritic Side Chains in Synthetic Carbohydrate Receptors. *Angew. Chem. Int. Ed.* **2015**, *54* (7), 2057–2061. https://doi.org/10.1002/anie.201409124.

(417) Prakash, T. P.; Graham, M. J.; Yu, J.; Carty, R.; Low, A.; Chappell, A.; Schmidt, K.; Zhao, C.; Aghajan, M.; Murray, H. F.; Riney, S.; Booten, S. L.; Murray, S. F.; Gaus, H.; Crosby, J.; Lima, W. F.; Guo, S.; Monia, B. P.; Swayze, E. E.; Seth, P. P. Targeted Delivery

of Antisense Oligonucleotides to Hepatocytes Using Triantennary *N*-Acetyl Galactosamine Improves Potency 10-Fold in Mice. *Nucleic Acids Res.* **2014**, *42* (13), 8796–8807. https://doi.org/10.1093/nar/gku531.

(418) Mihai, M. T.; Williams, B. D.; Phipps, R. J. Para-Selective C–H Borylation of Common Arene Building Blocks Enabled by Ion-Pairing with a Bulky Countercation. *J. Am. Chem. Soc.* **2019**, *141* (39), 15477–15482. https://doi.org/10.1021/jacs.9b07267.

(419) Wrodnigg, T. M.; Lundt, I.; Stütz, A. E. Synthesis of N-Protected Galactosamine Building Blocks from D-Tagatose via the Heyns Rearrangement. *J. Carbohydr. Chem.* **2006**, *25* (1), 33–41. https://doi.org/10.1080/07328300500495795.

(420) Sun, B.; Pukin, A. V.; Visser, G. M.; Zuilhof, H. An Efficient Glycosylation Reaction for the Synthesis of Asialo GM2 Analogues. *Tetrahedron Lett.* **2006**, *47* (41), 7371–7374. https://doi.org/10.1016/j.tetlet.2006.08.008.

(421) Lorpitthaya, R.; Suryawanshi, S. B.; Wang, S.; Pasunooti, K. K.; Cai, S.; Ma, J.; Liu, X.-W. Total Synthesis of Sialic Acid by a Sequential Rhodium-Catalyzed Aziridination and Barbier Allylation of D-Glycal. *Angew. Chem. Int. Ed.* **2011**, *50* (50), 12054–12057. https://doi.org/10.1002/anie.201104516.

(422) Crich, D.; Li, W. α-Selective Sialylations at −78 °C in Nitrile Solvents with a 1-Adamantanyl Thiosialoside. *J. Org. Chem.* **2007**, *72* (20), 7794–7797. https://doi.org/10.1021/jo7012912.

(423) Finlay, D. B.; Cawston, E. E.; Grimsey, N. L.; Hunter, M. R.; Korde, A.; Vemuri, V. K.; Makriyannis, A.; Glass, M. Gαs Signalling of the CB1 Receptor and the Influence of Receptor Number. *Br. J. Pharmacol.* **2017**, *174* (15), 2545–2562. https://doi.org/10.1111/bph.13866.

(424) Knapman, A.; Santiago, M.; Du, Y. P.; Bennallack, P. R.; Christie, M. J.; Connor, M. A Continuous, Fluorescence-Based Assay of μ-Opioid Receptor Activation in AtT-20 Cells. *J. Biomol. Screen.* **2013**, *18* (3), 269–276. https://doi.org/10.1177/1087057112461376.

(425) Eric Sparkes, Axelle Timmerman, Jack W. Markham, Rochelle Boyd, Rebecca Gordon, Katelyn A. Walker, Richard C. Kevin, David E. Hibbs, Samuel D. Banister, Elizabeth A. Cairns, Christophe Stove, and Adam Ametovski; *ACS Chemical Neuroscience* **2024** *15* (9), 1787-1812; DOI: 10.1021/acschemneuro.3c00818

426) Knapman, A.; Santiago, M.; Du, Y. P.; Bennallack, P. R.; Christie, M. J.; Connor, M. A Continuous, Fluorescence-Based Assay of μ-Opioid Receptor Activation in AtT-20 Cells. *J. Biomol. Screen.* **2013**, *18* (3), 269–276. https://doi.org/10.1177/1087057112461376.

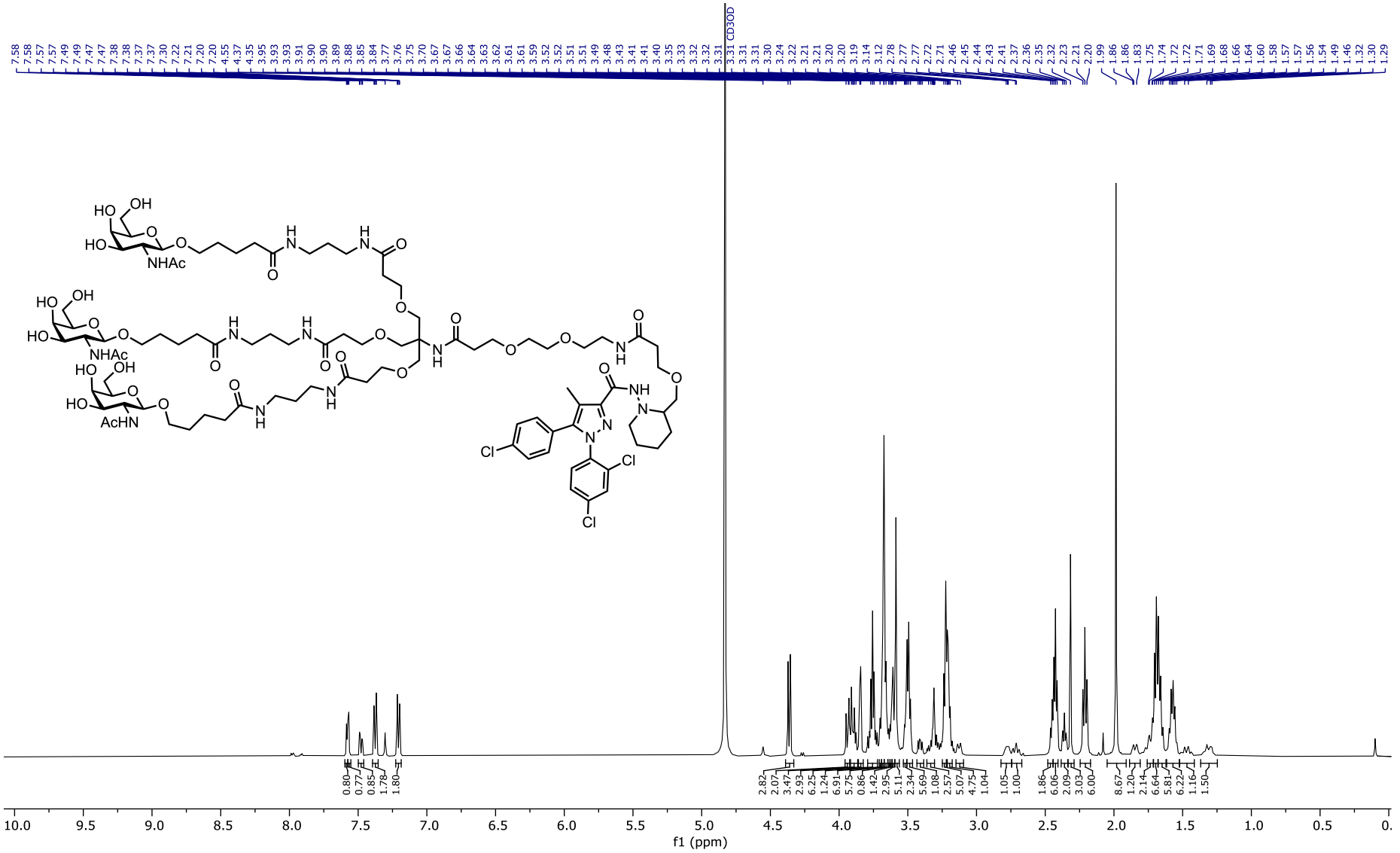
(427) Passioura, T.; Liu, W.; Dunkelmann, D.; Higuchi, T.; Suga, H. Display Selection of Exotic Macrocyclic Peptides Expressed under a Radically Reprogrammed 23 Amino

Acid Genetic Code. *J. Am. Chem. Soc.* **2018**, *140* (37), 11551–11555. https://doi.org/10.1021/jacs.8b03367.

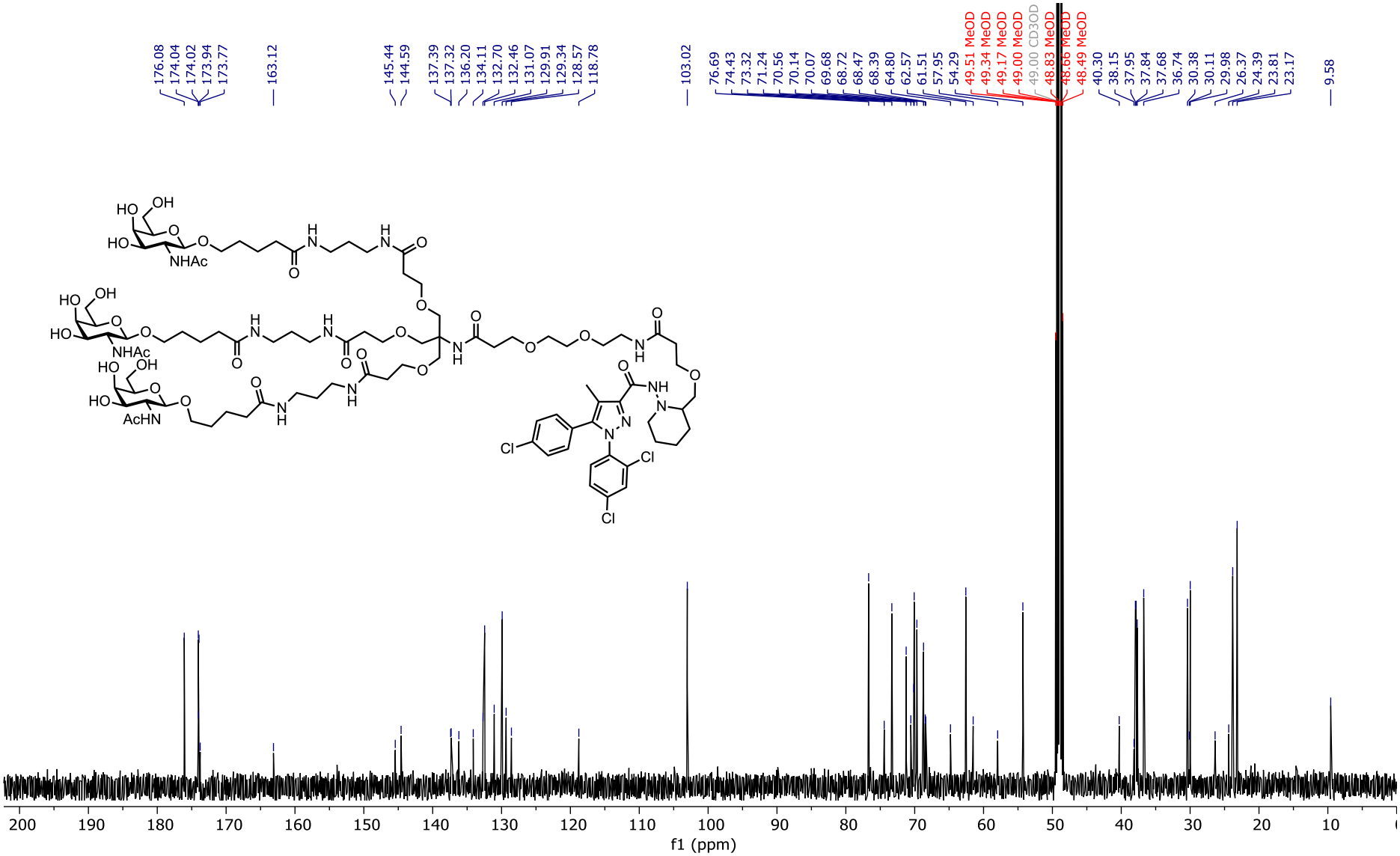
(428) Johansen-Leete, J.; Passioura, T.; Foster, S. R.; Bhusal, R. P.; Ford, D. J.; Liu, M.; Jongkees, S. A. K.; Suga, H.; Stone, M. J.; Payne, R. J. Discovery of Potent Cyclic Sulfopeptide Chemokine Inhibitors via Reprogrammed Genetic Code mRNA Display. *J. Am. Chem. Soc.* **2020**, *142* (20), 9141–9146. https://doi.org/10.1021/jacs.0c03152.

Appendix I: Exemplar NMR Data

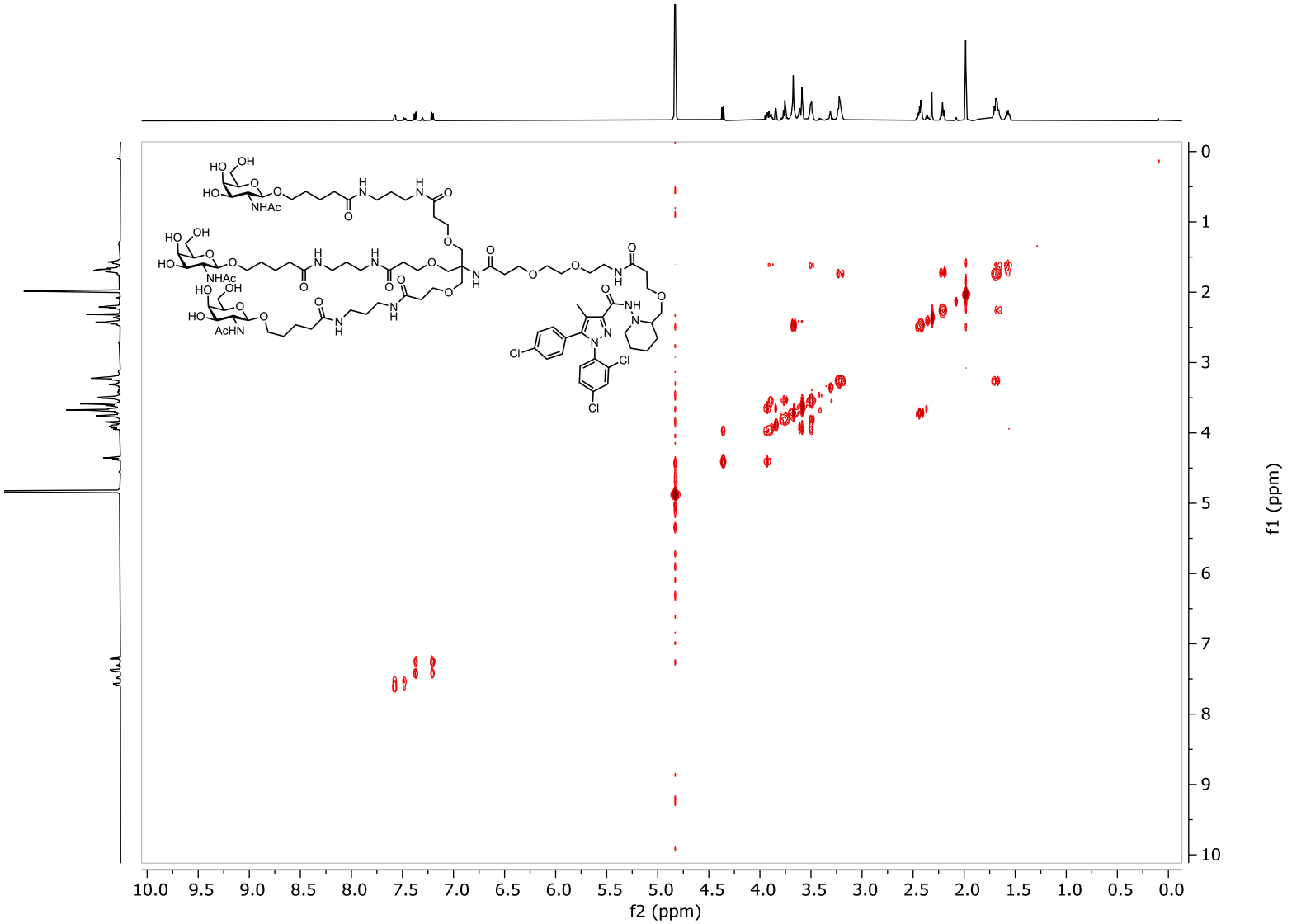
Compound LYTAC-1,2-PEG2 **(2.61)** **^{1}H NMR** (500 MHz, MeOD)



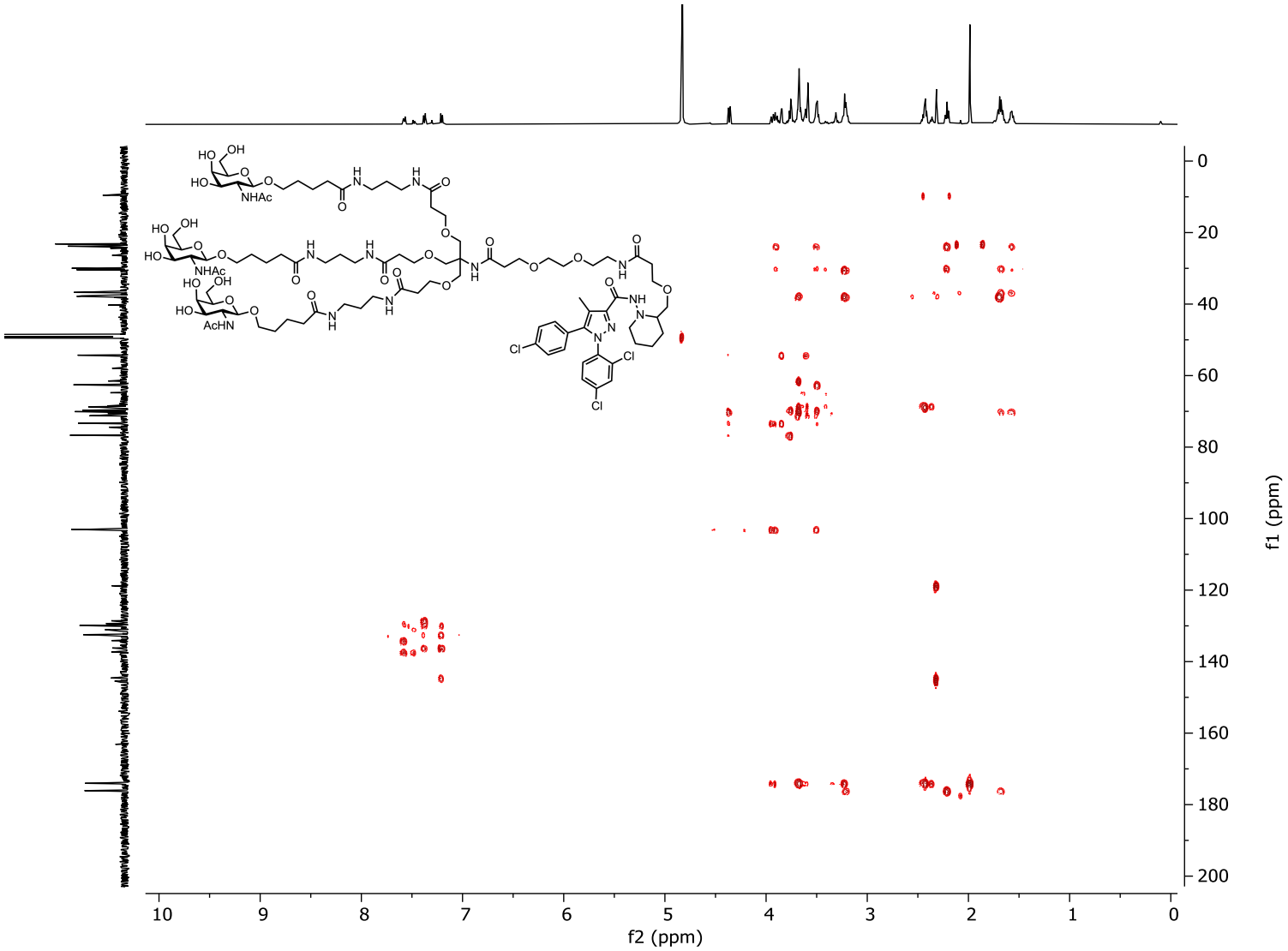
Compound LYTAC-1,2-PEG2 **(2.61)** **^{13}C NMR** (126 MHz, MeOD)



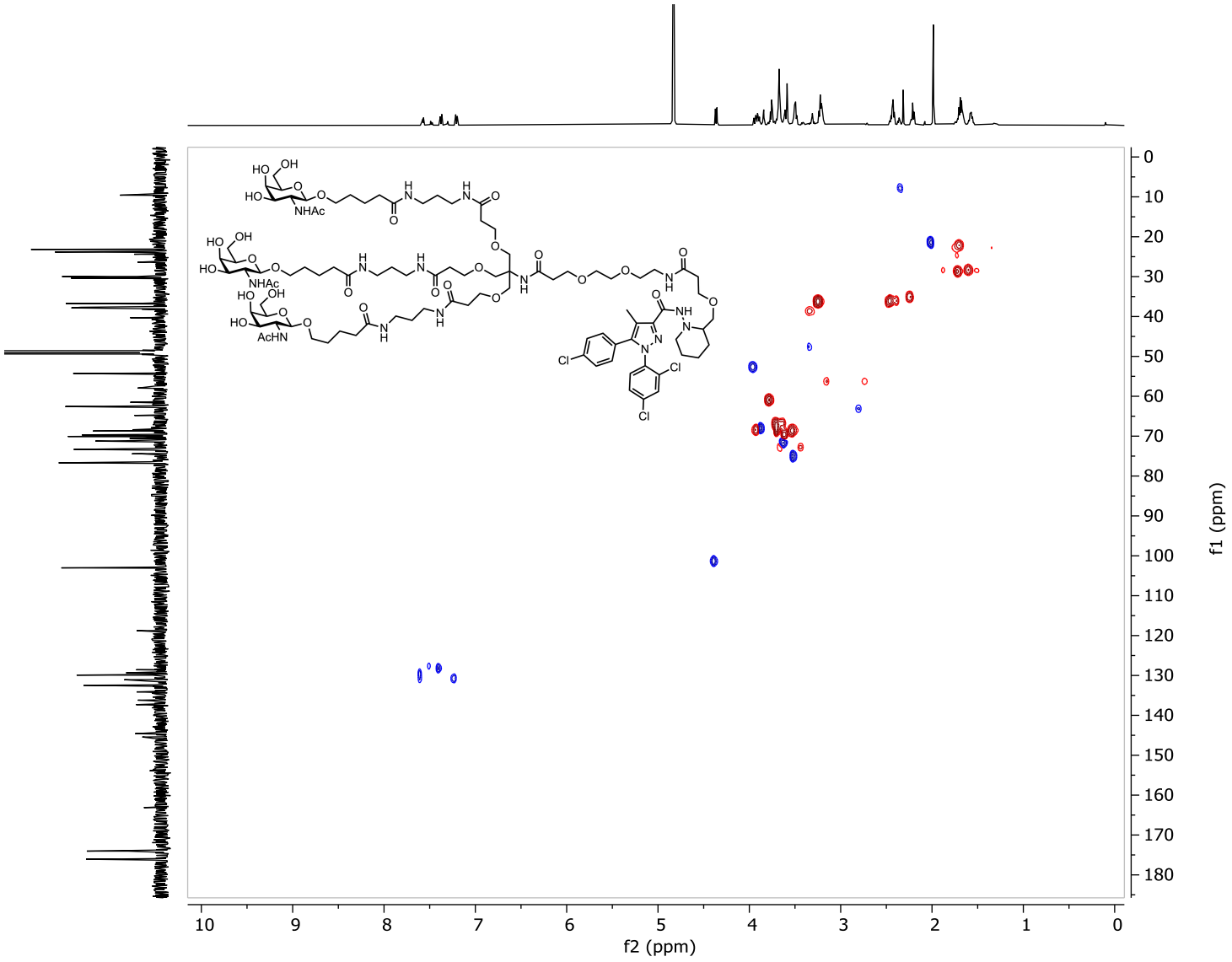
Compound LYTAC-1,2-PEG2 **(2.61) COSY** (500 MHz, MeOD)



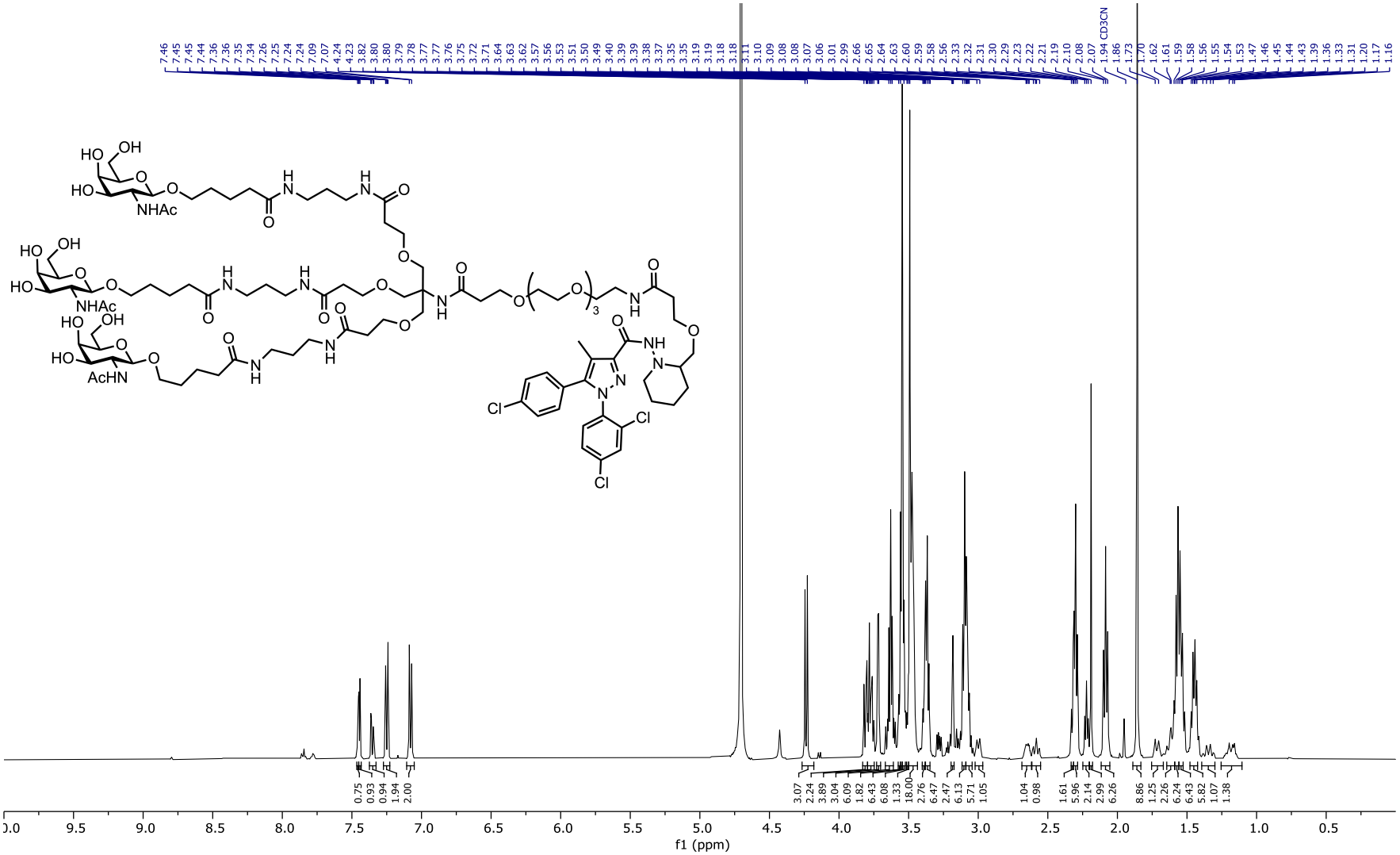
Compound LYTAC-1,2-PEG2 **(2.61) HMBC** (500/126 MHz, MeOD)



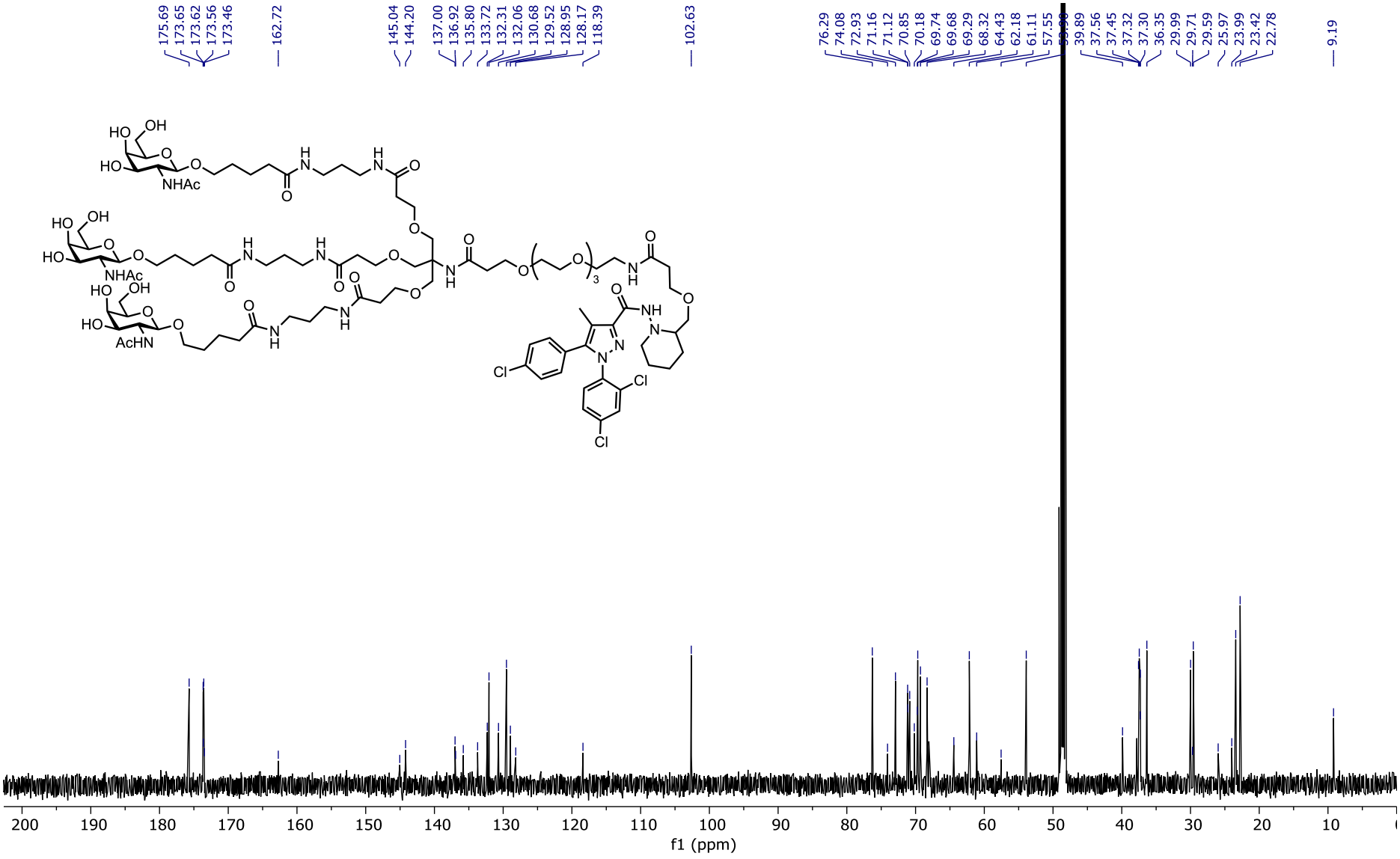
Compound LYTAC-1,2-PEG2 **(2.61) HSQC** (500/126 MHz, MeOD)



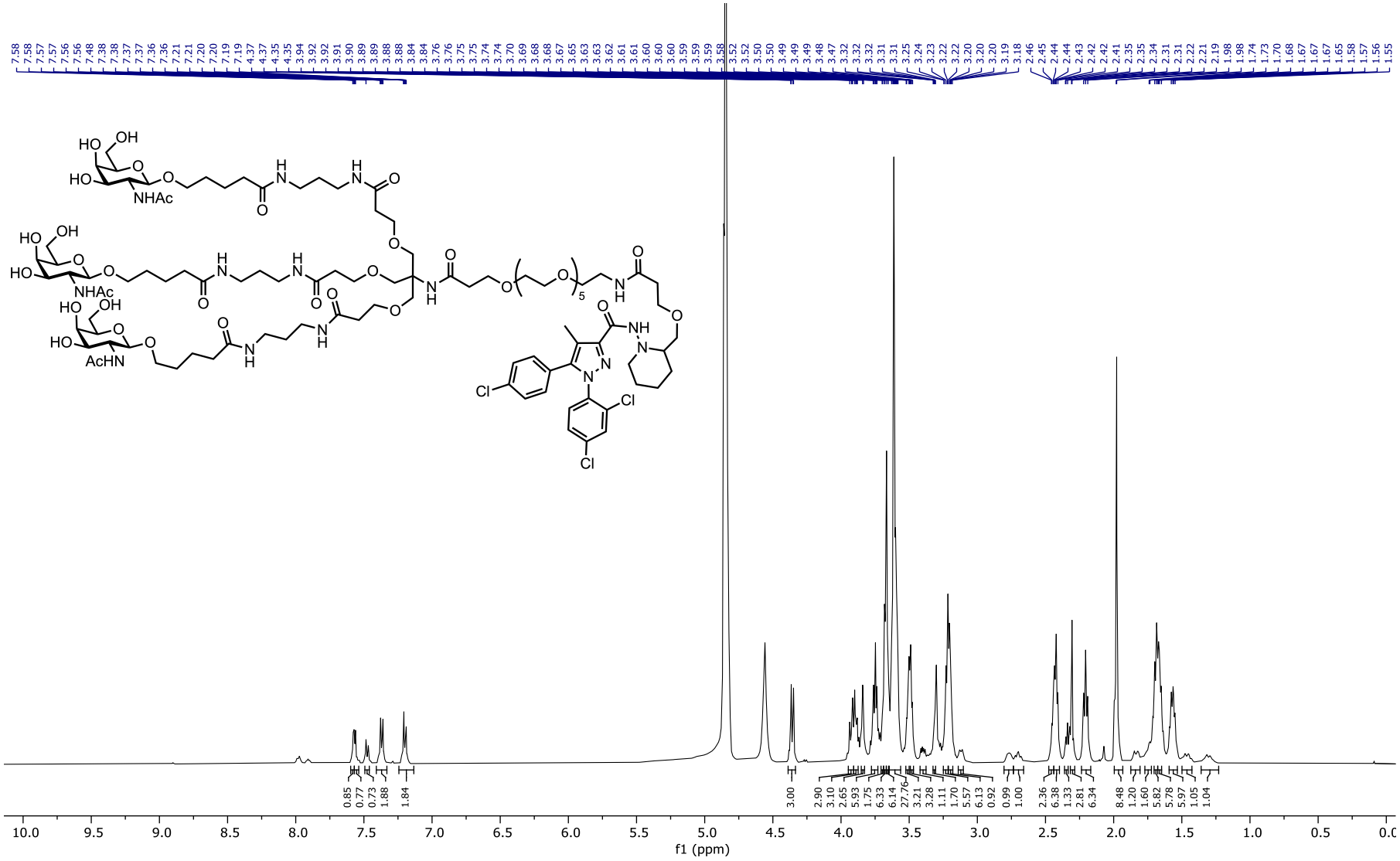
Compound LYTAC-1,2-PEG4 **(2.62)** **^{1}H NMR** (500 MHz, MeOD)



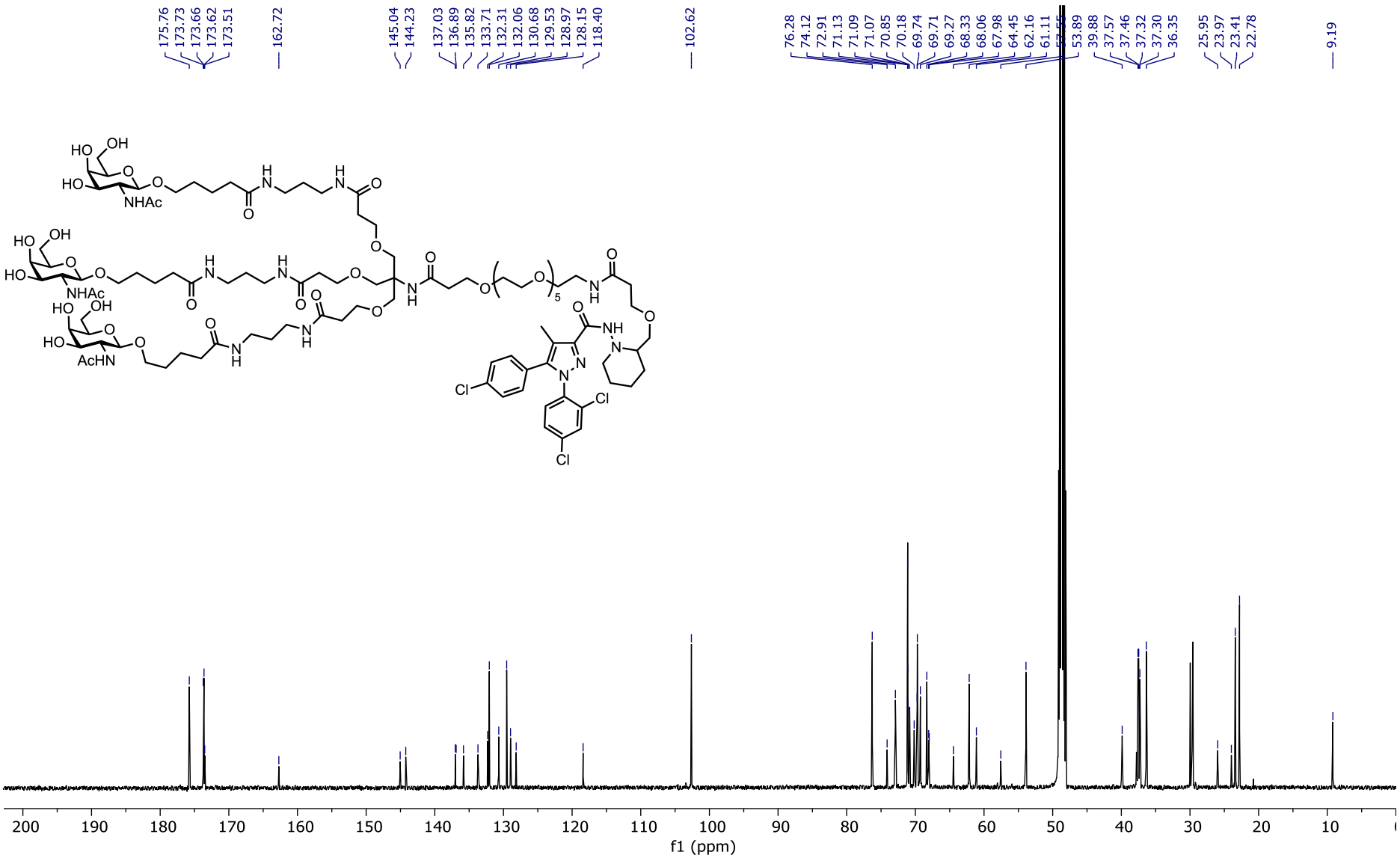
Compound LYTAC-1,2-PEG4 **(2.62)** **^{13}C NMR** (126 MHz, MeOD)



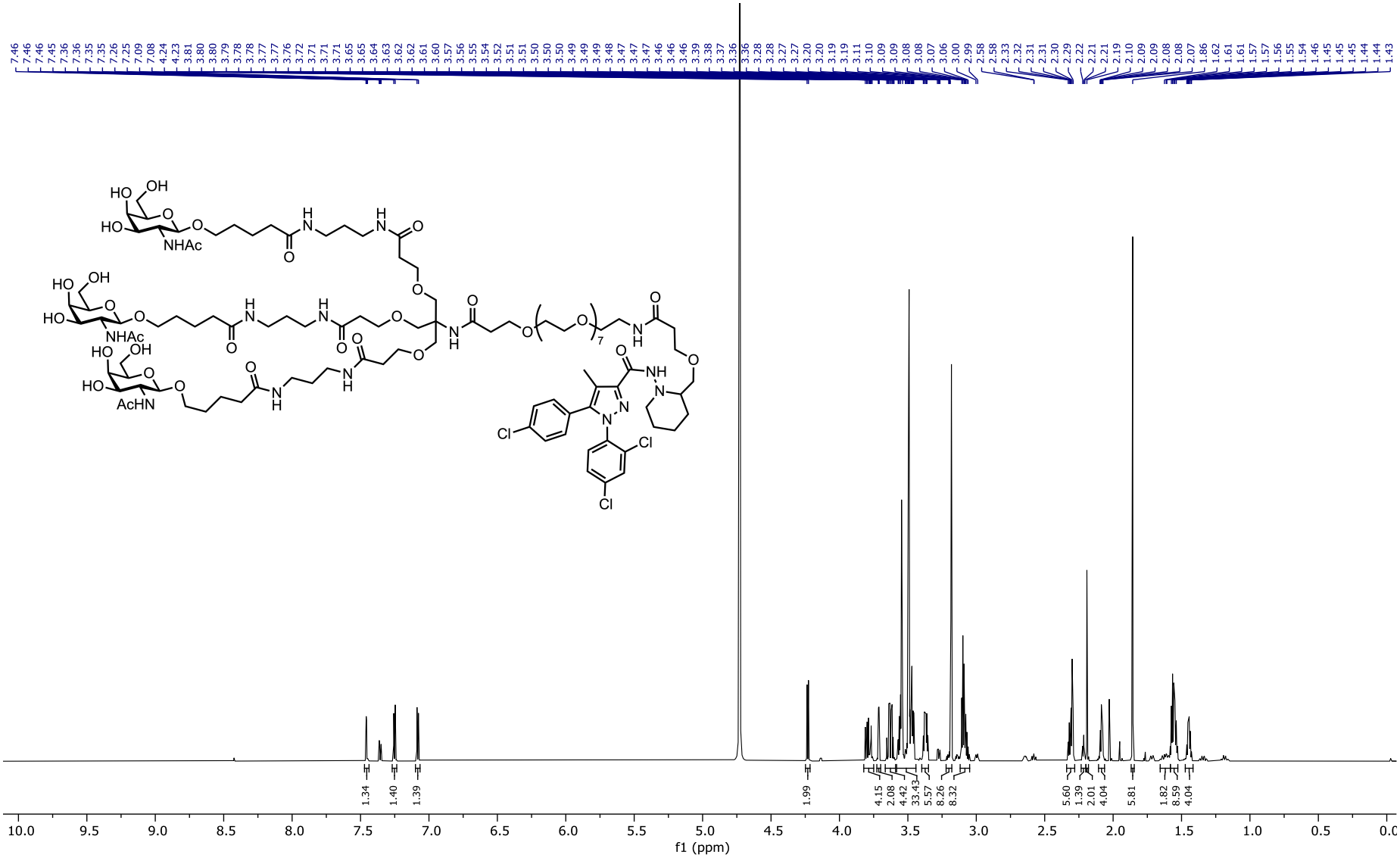
Compound LYTAC-1,2-PEG6 **(2.63)** **^{1}H NMR** (500 MHz, MeOD)



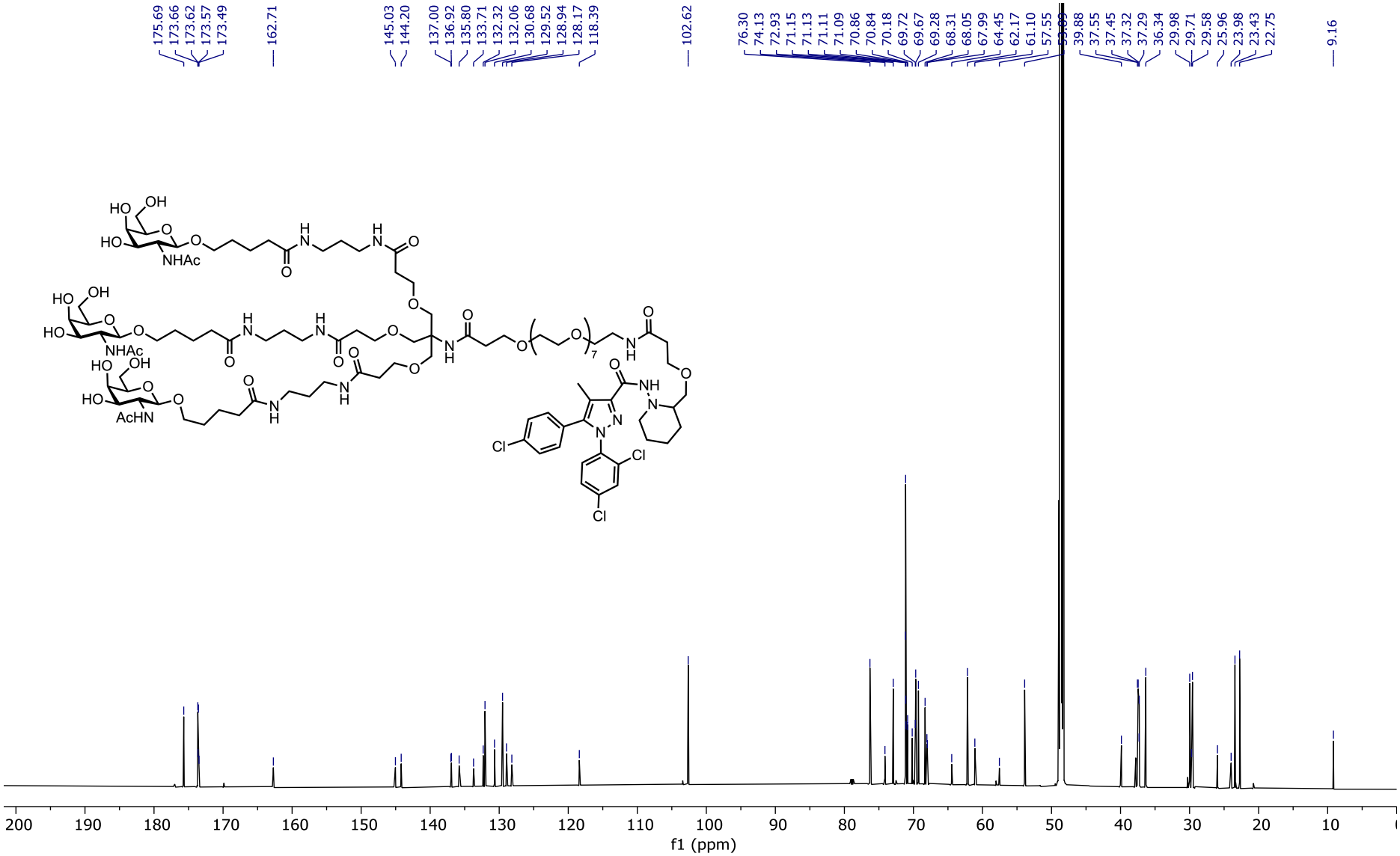
Compound LYTAC-1,2-PEG6 **(2.63)** **^{13}C NMR** (126 MHz, MeOD)



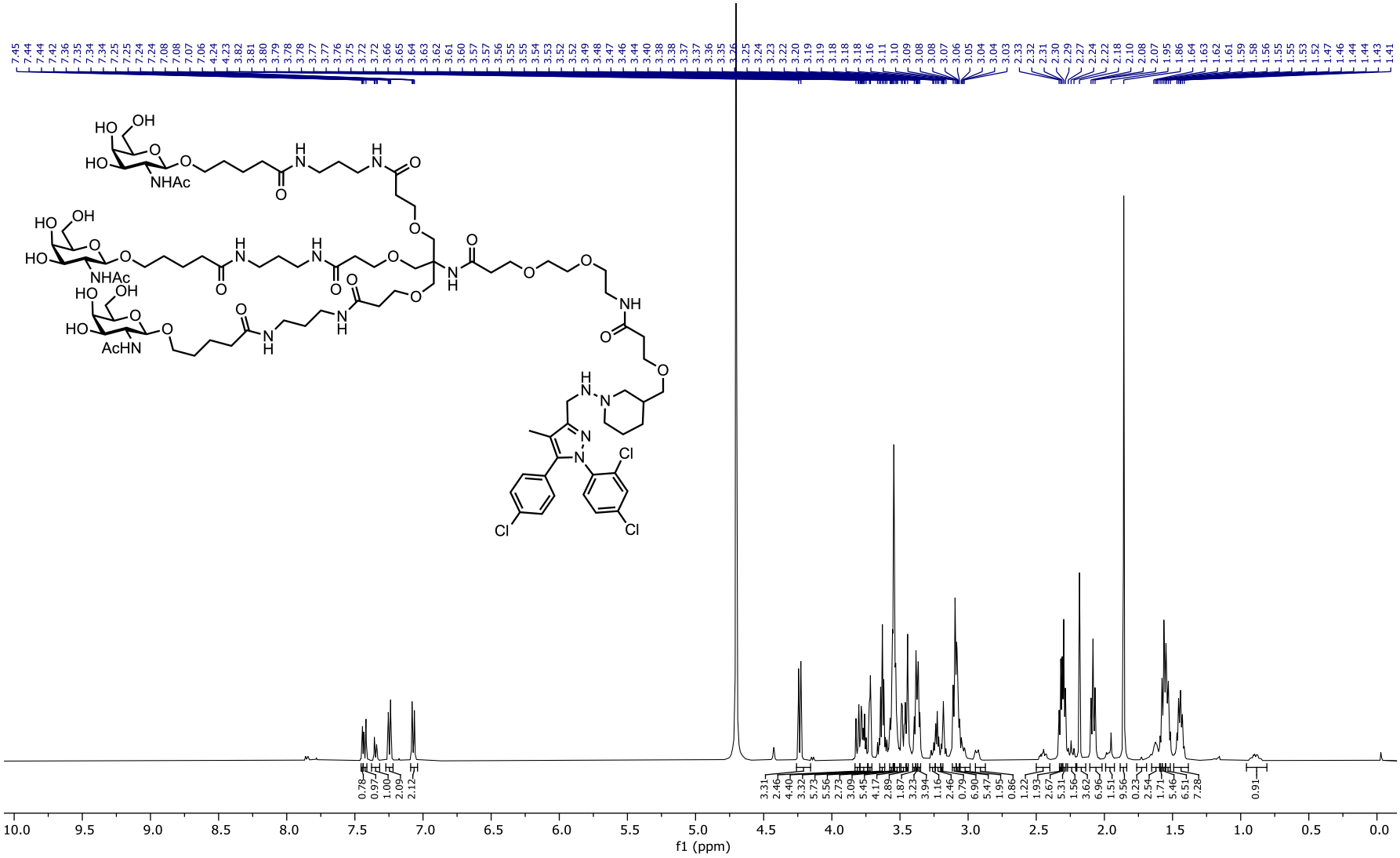
Compound LYTAC-1,2-PEG8 **(2.64)** **^{1}H NMR** (800 MHz, MeOD)



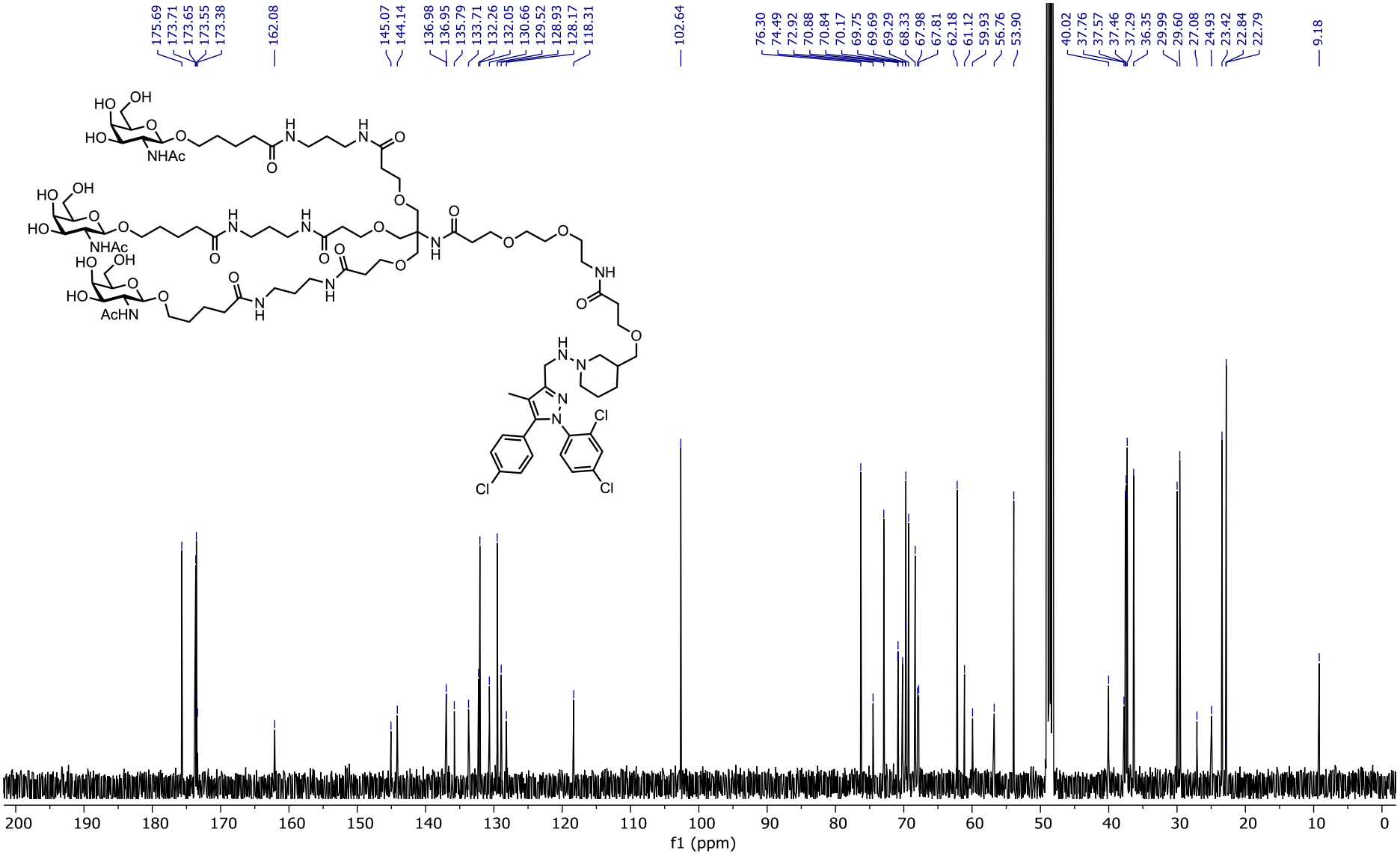
Compound LYTAC-1,2-PEG8 **(2.64)** **^{13}C NMR** (201 MHz, MeOD)



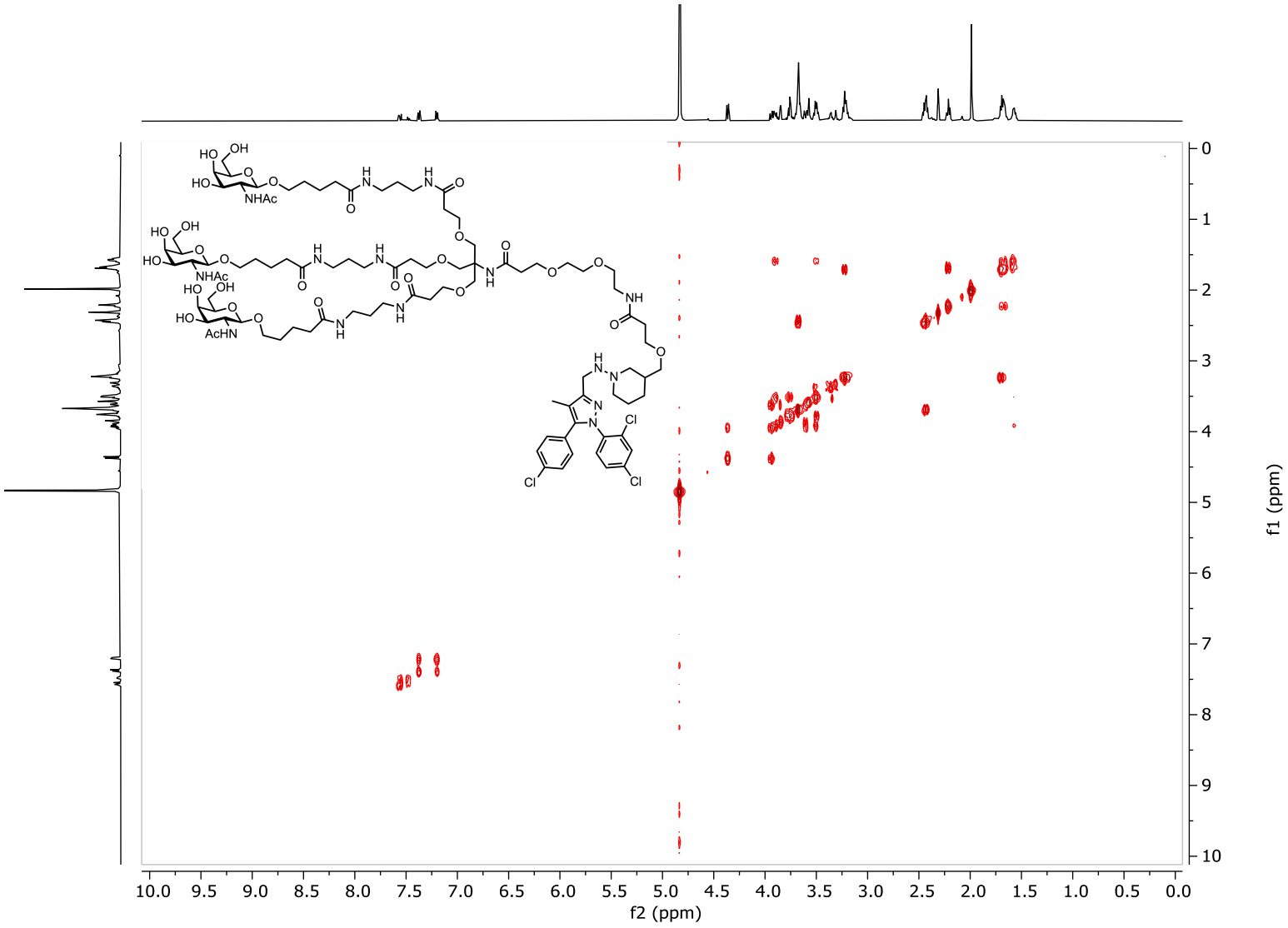
Compound LYTAC-1,3-PEG2 **(2.65)** **^{1}H NMR** (500 MHz, MeOD)



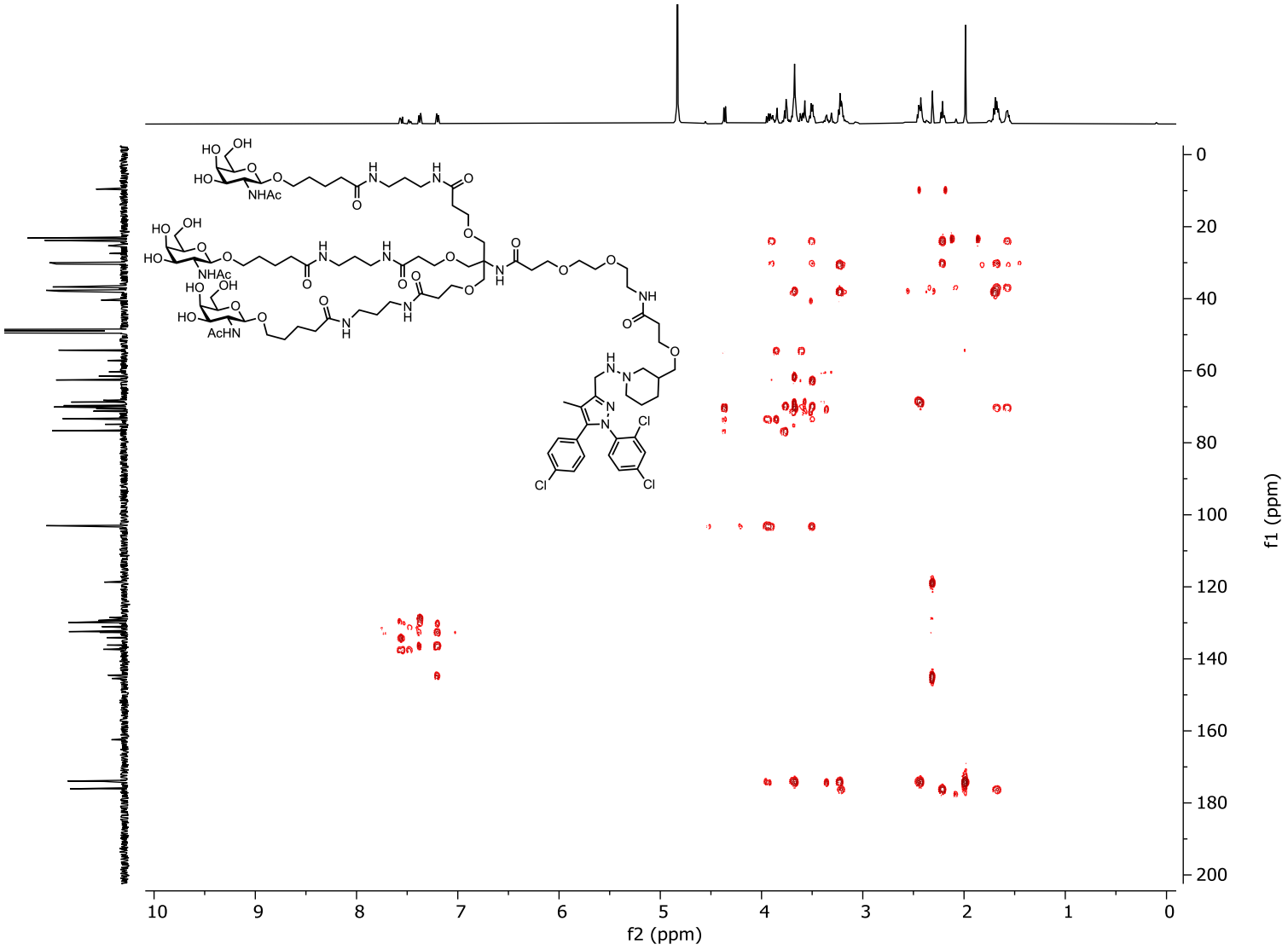
Compound LYTAC-1,3-PEG2 **(2.65)** **^{13}C NMR** (500 MHz, MeOD)



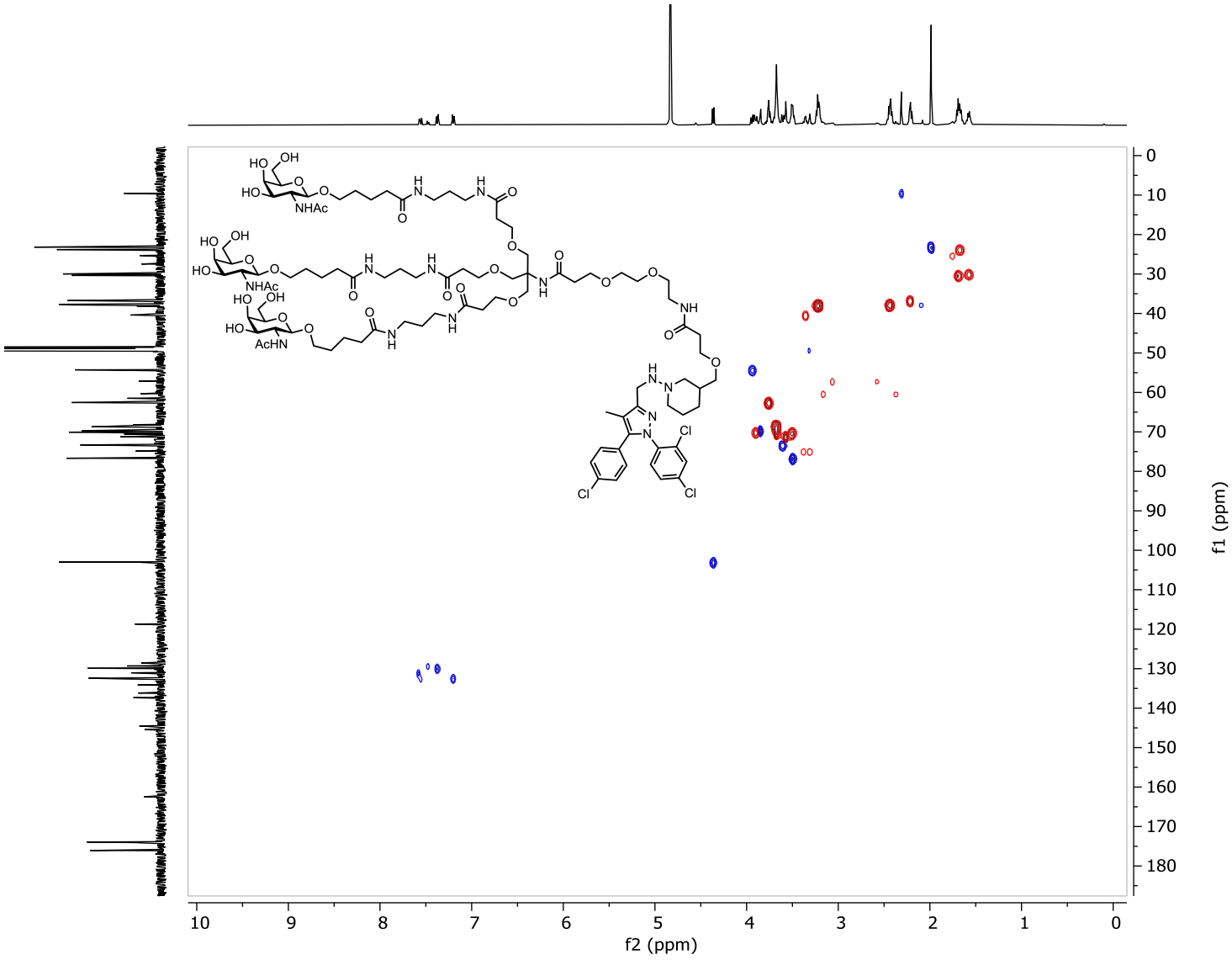
Compound LYTAC-1,3-PEG2 **(2.65) COSY** (500 MHz, MeOD)



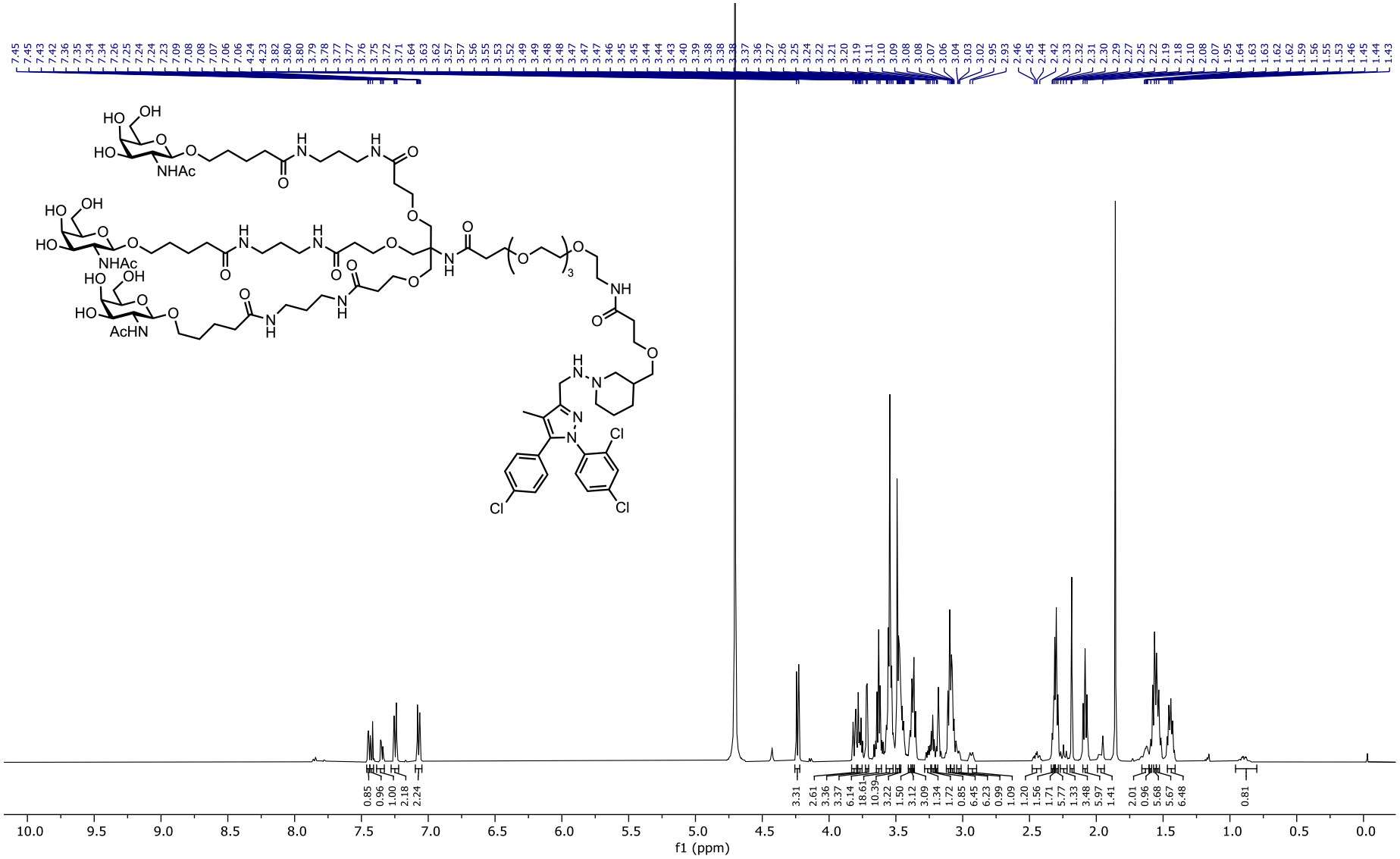
Compound LYTAC-1,3-PEG2 **(2.65) HMBC** (500/126 MHz, MeOD)



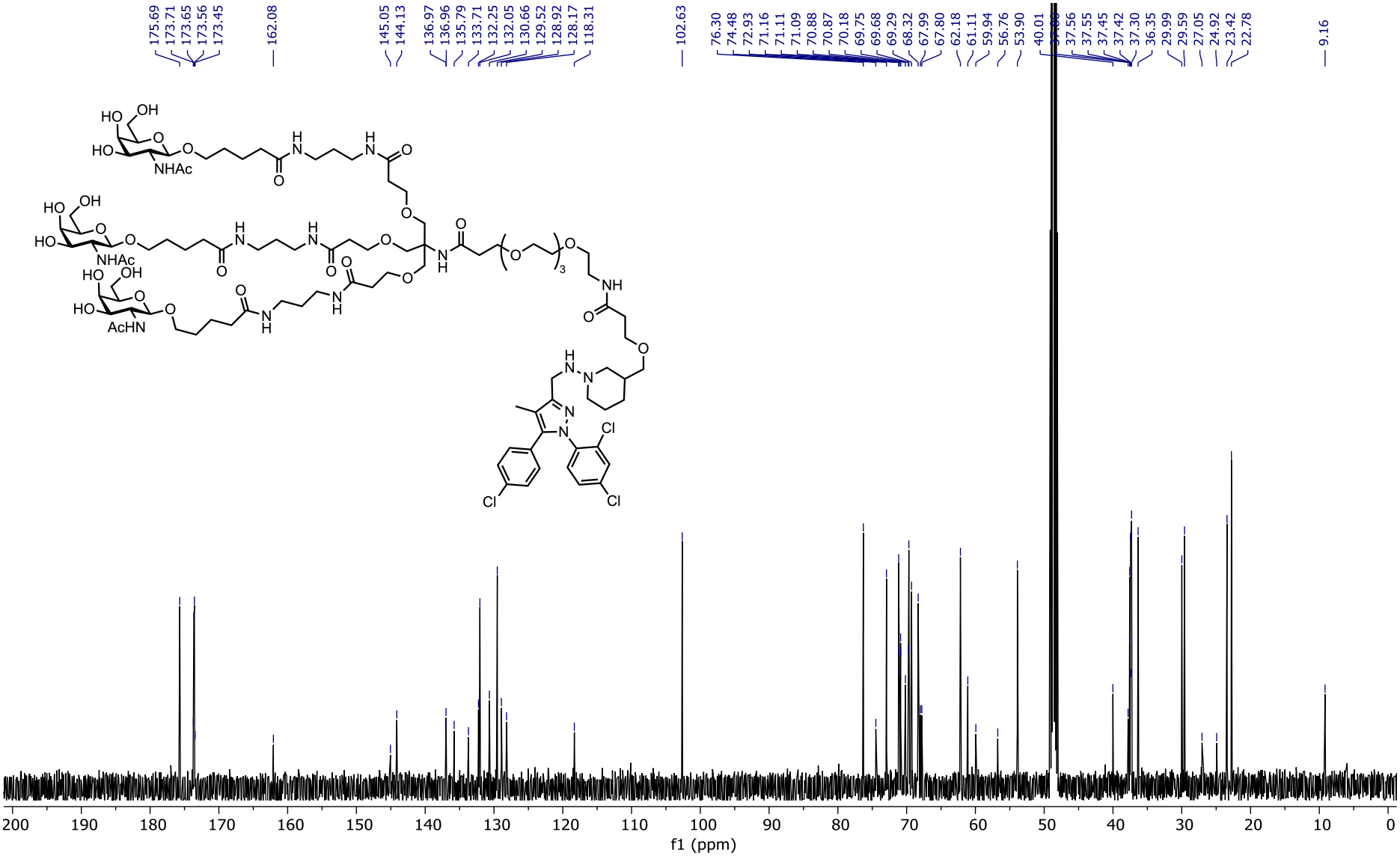
Compound LYTAC-1,3-PEG2 **(2.65) HSQC** (500/126 MHz, MeOD)



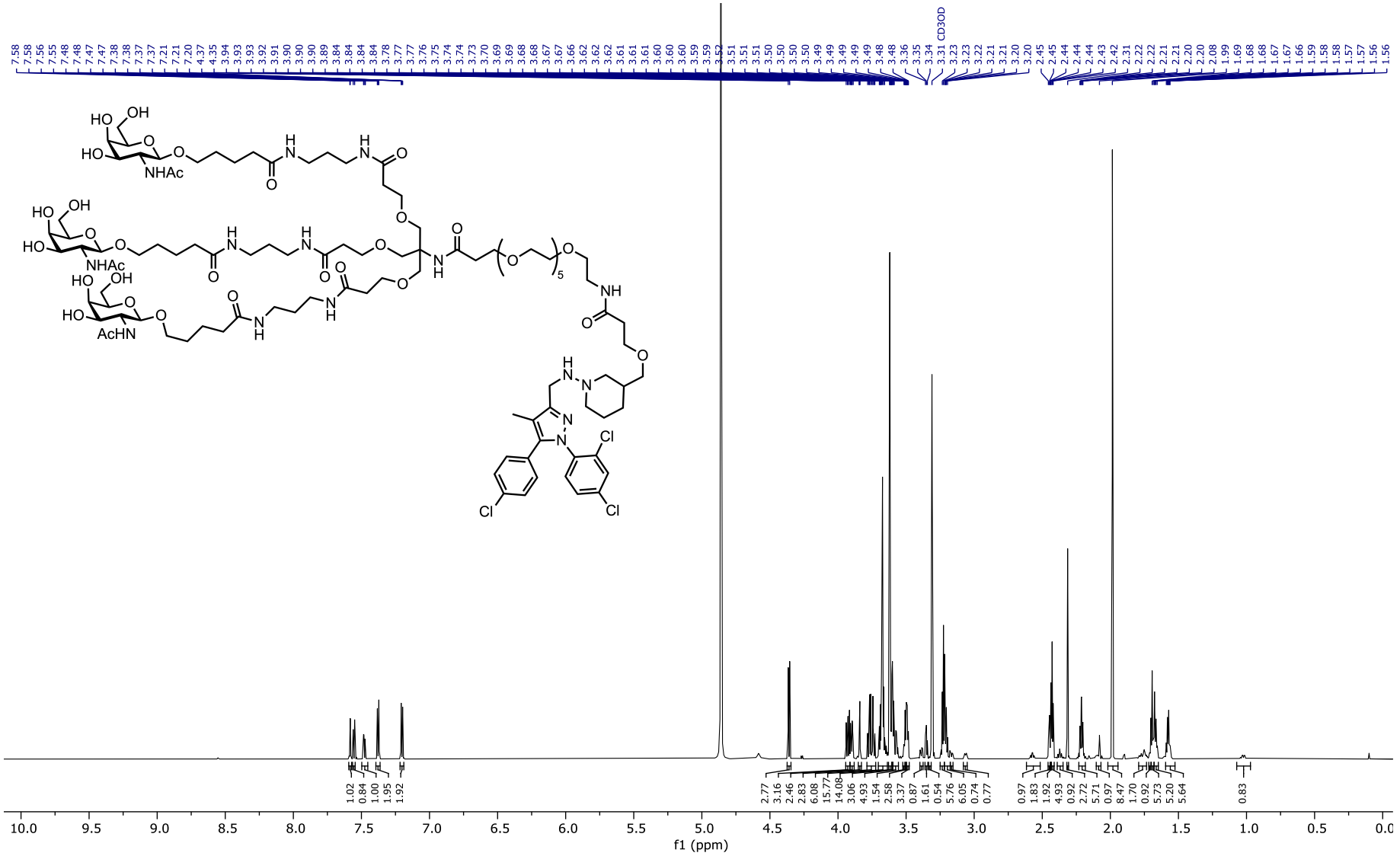
Compound LYTAC-1,3-PEG4 **(2.66)** **^{1}H NMR** (500 MHz, MeOD)



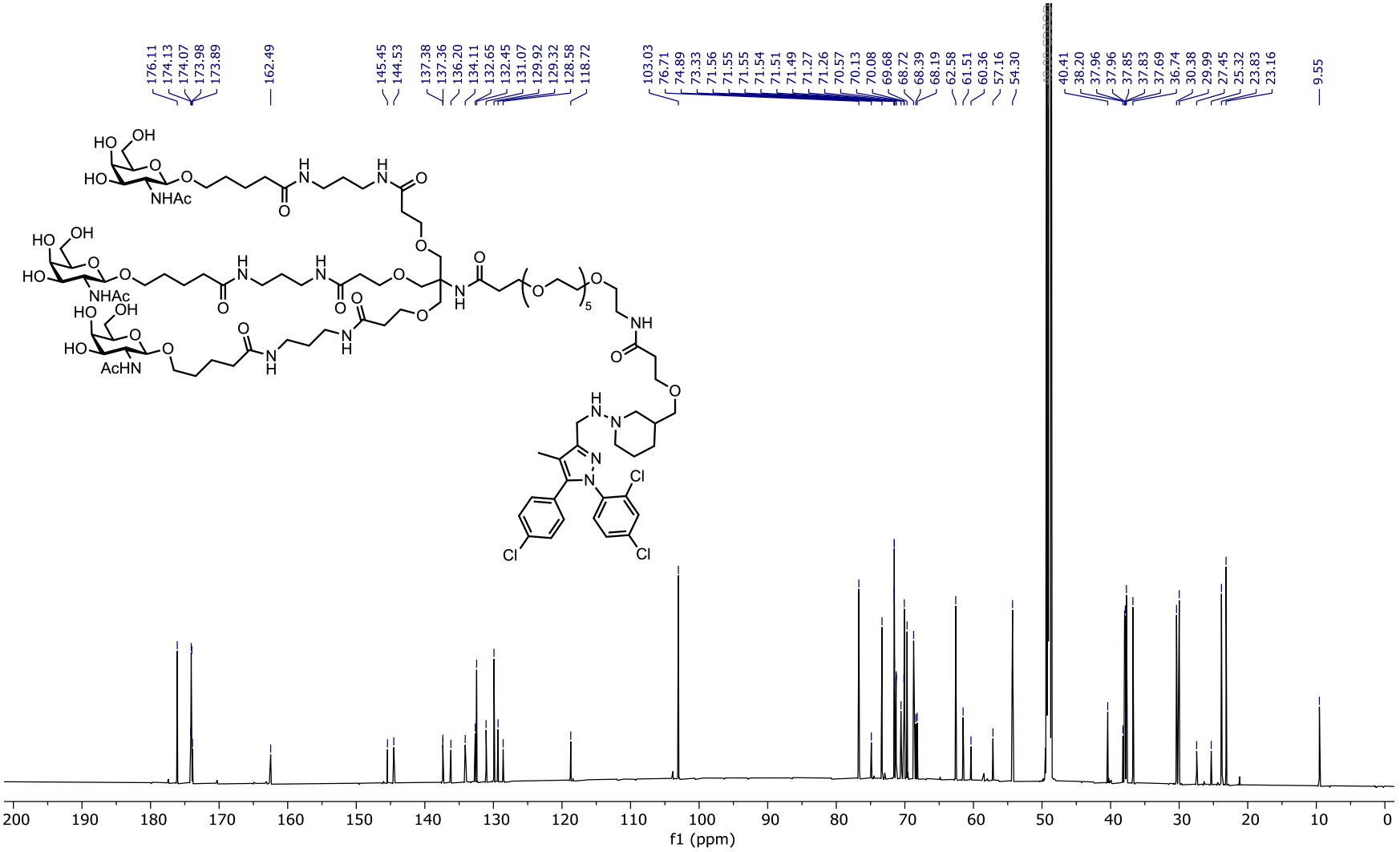
Compound LYTAC-1,3-PEG4 **(2.66)** **^{13}C NMR** (126 MHz, MeOD)



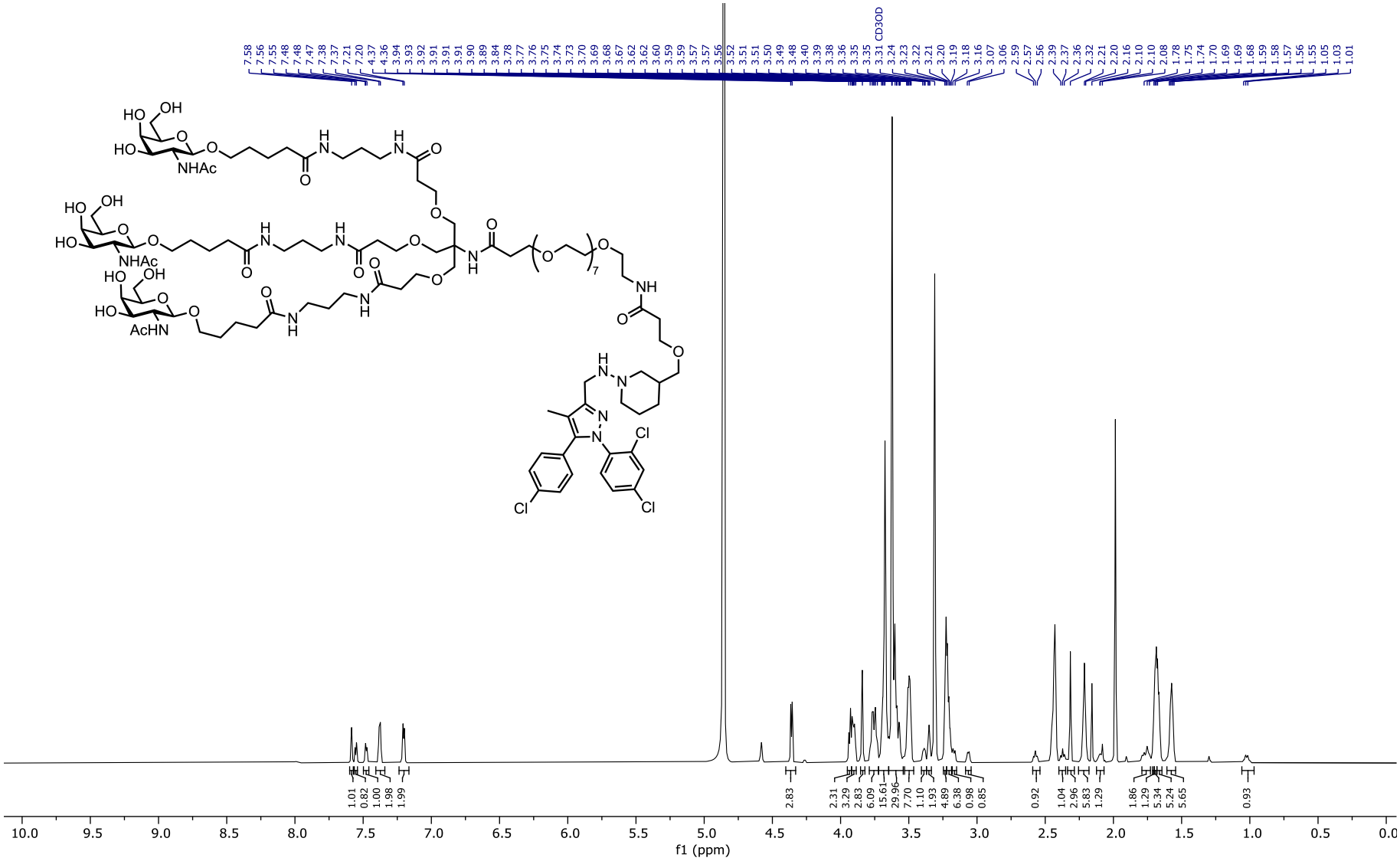
Compound LYTAC-1,3-PEG6 **(2.67)** **^{1}H NMR** (800 MHz, MeOD)



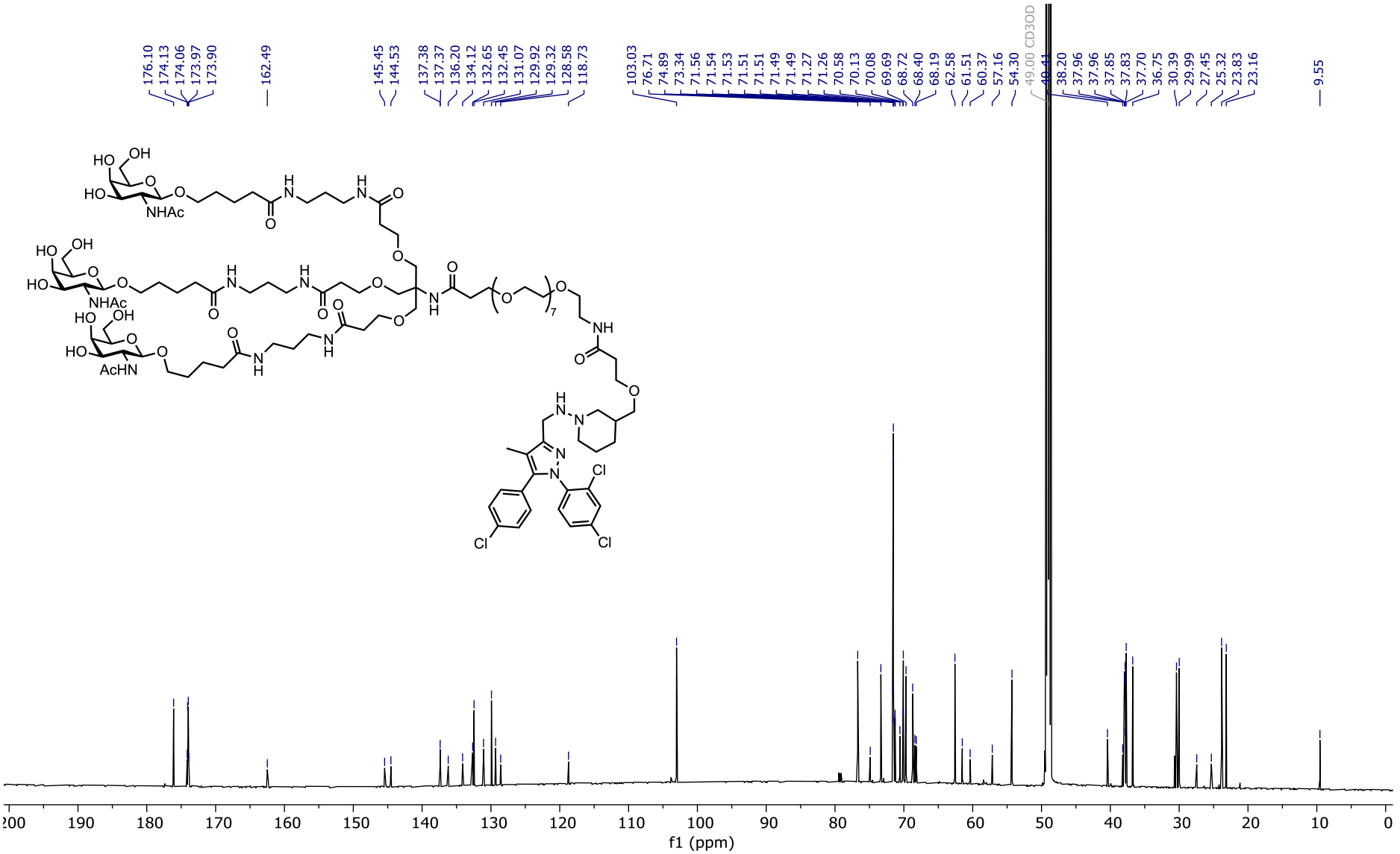
Compound LYTAC-1,3-PEG6 **(2.67)** **^{13}C NMR** (201 MHz, MeOD)



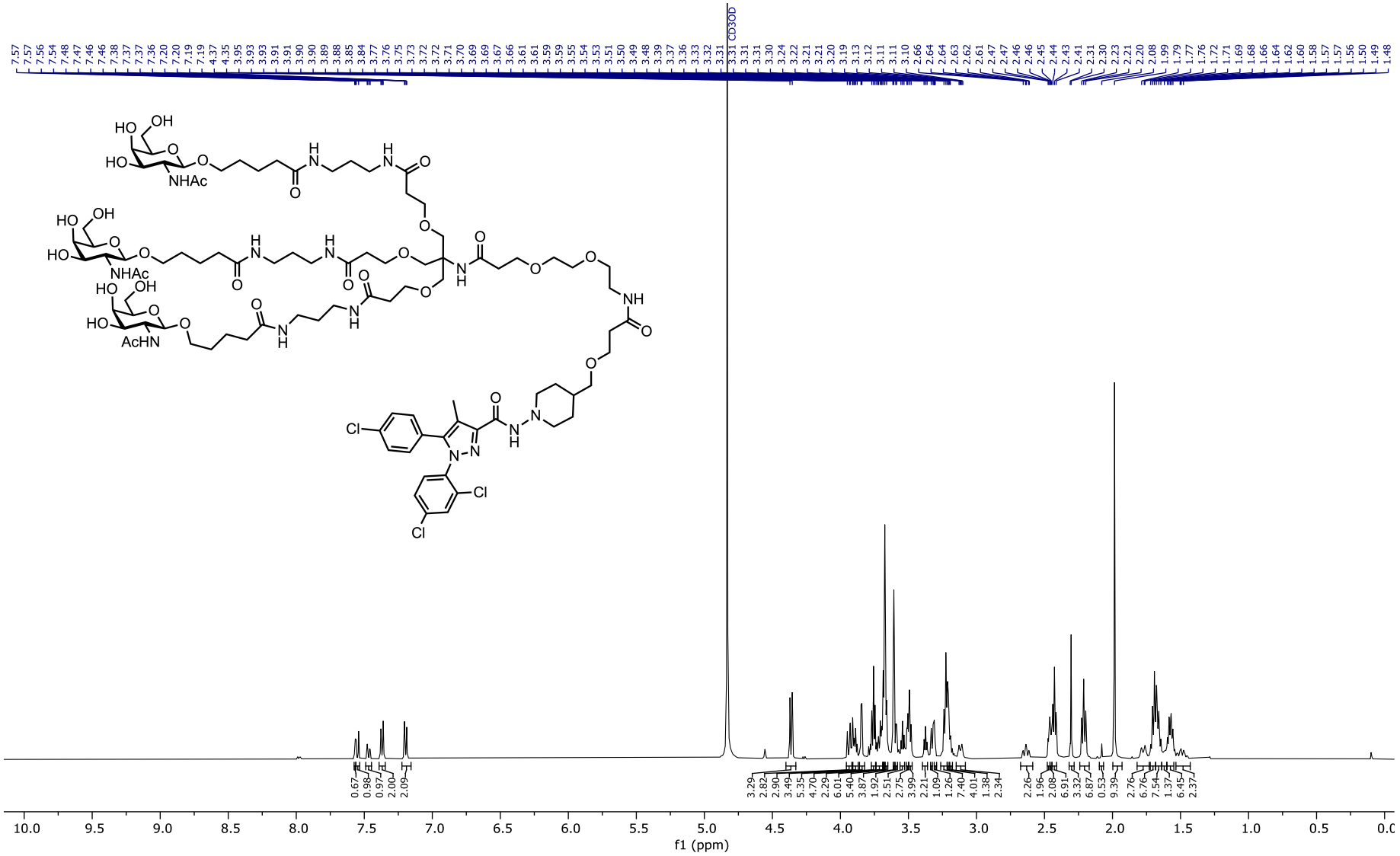
Compound LYTAC-1,3-PEG8 **(2.68)** **^{1}H NMR** (800 MHz, MeOD)



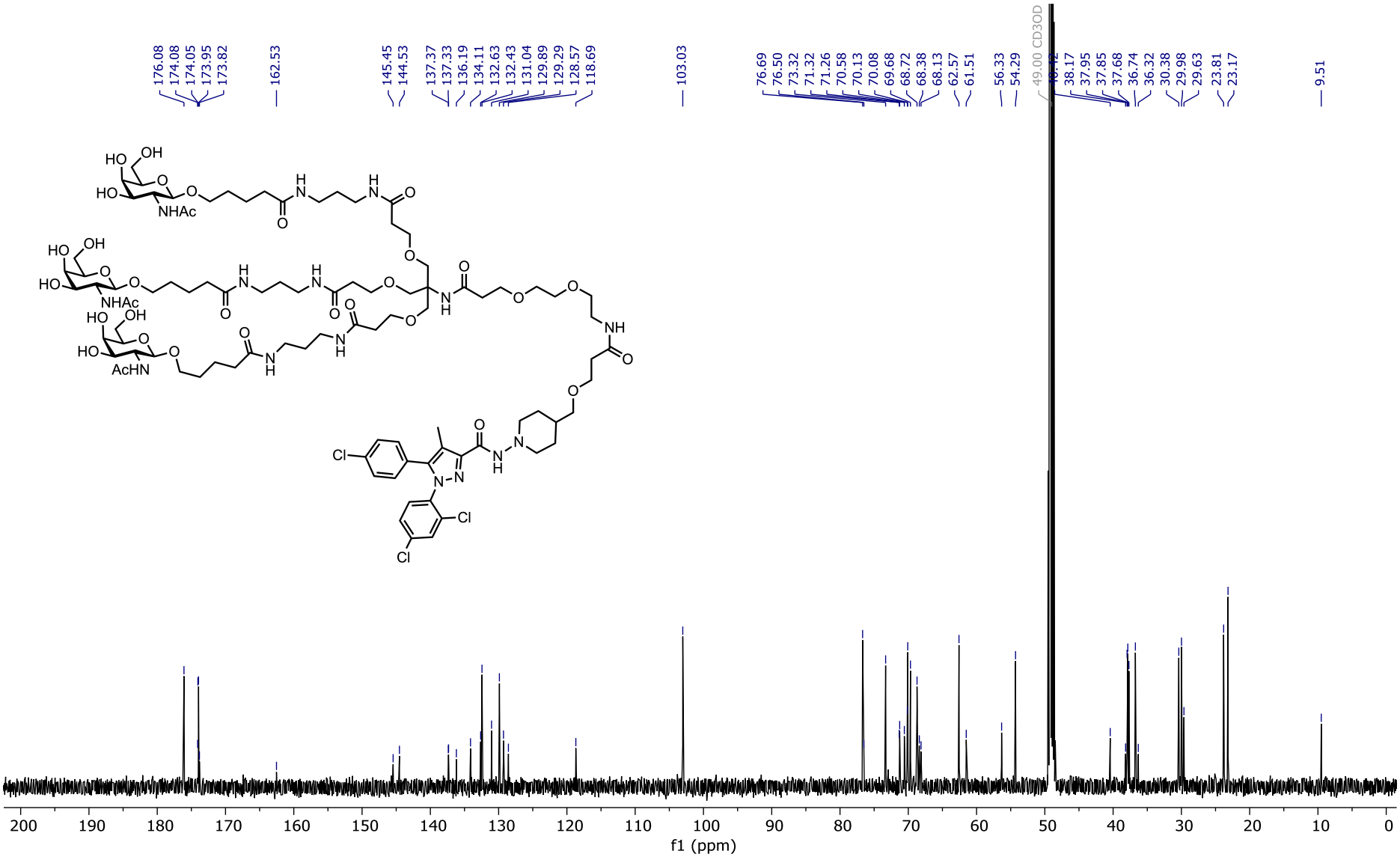
Compound LYTAC-1,3-PEG8 **(2.68)** **^{13}C NMR** (201 MHz, MeOD)



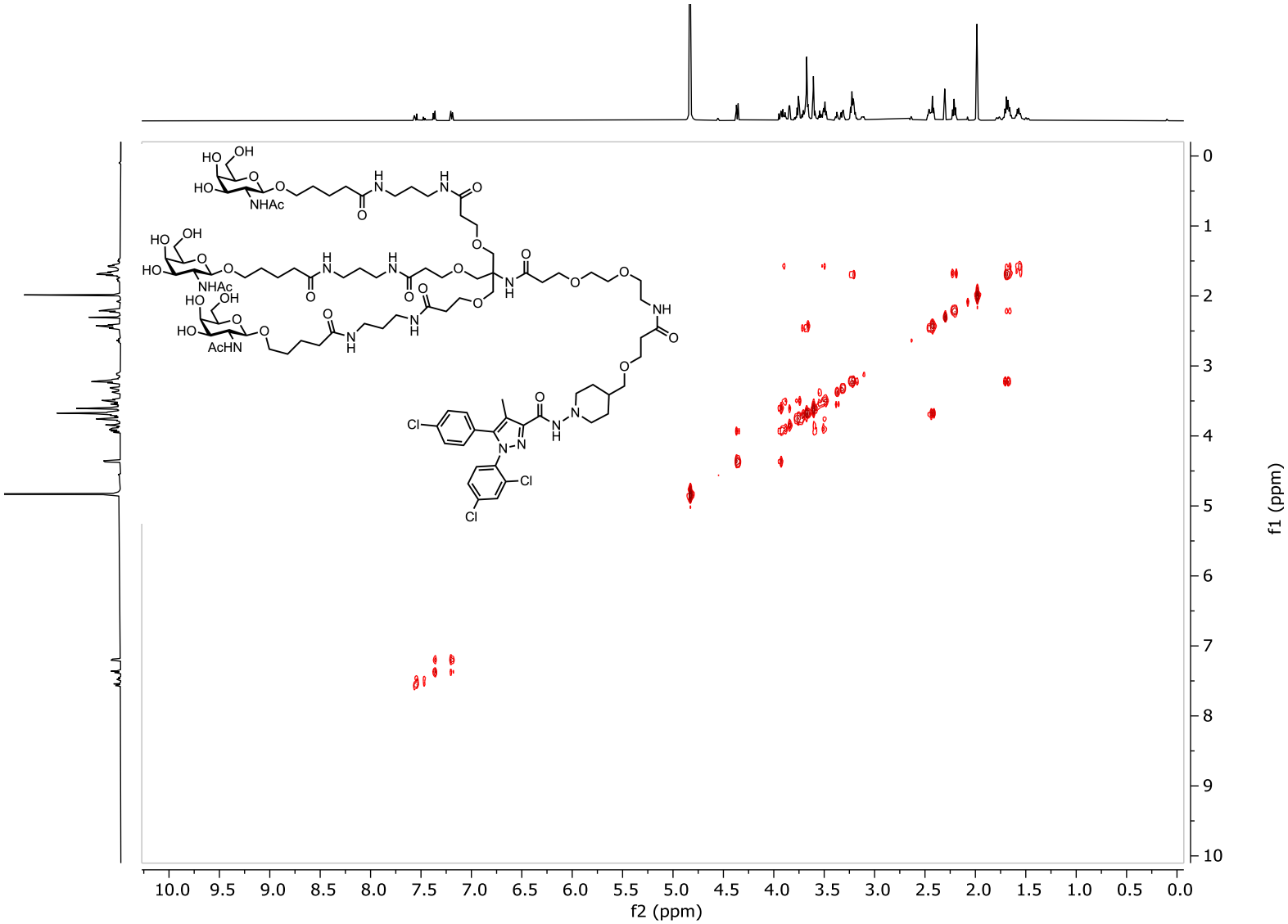
Compound LYTAC-1,4-PEG2 **(2.69)** **^{1}H NMR** (500 MHz, MeOD)



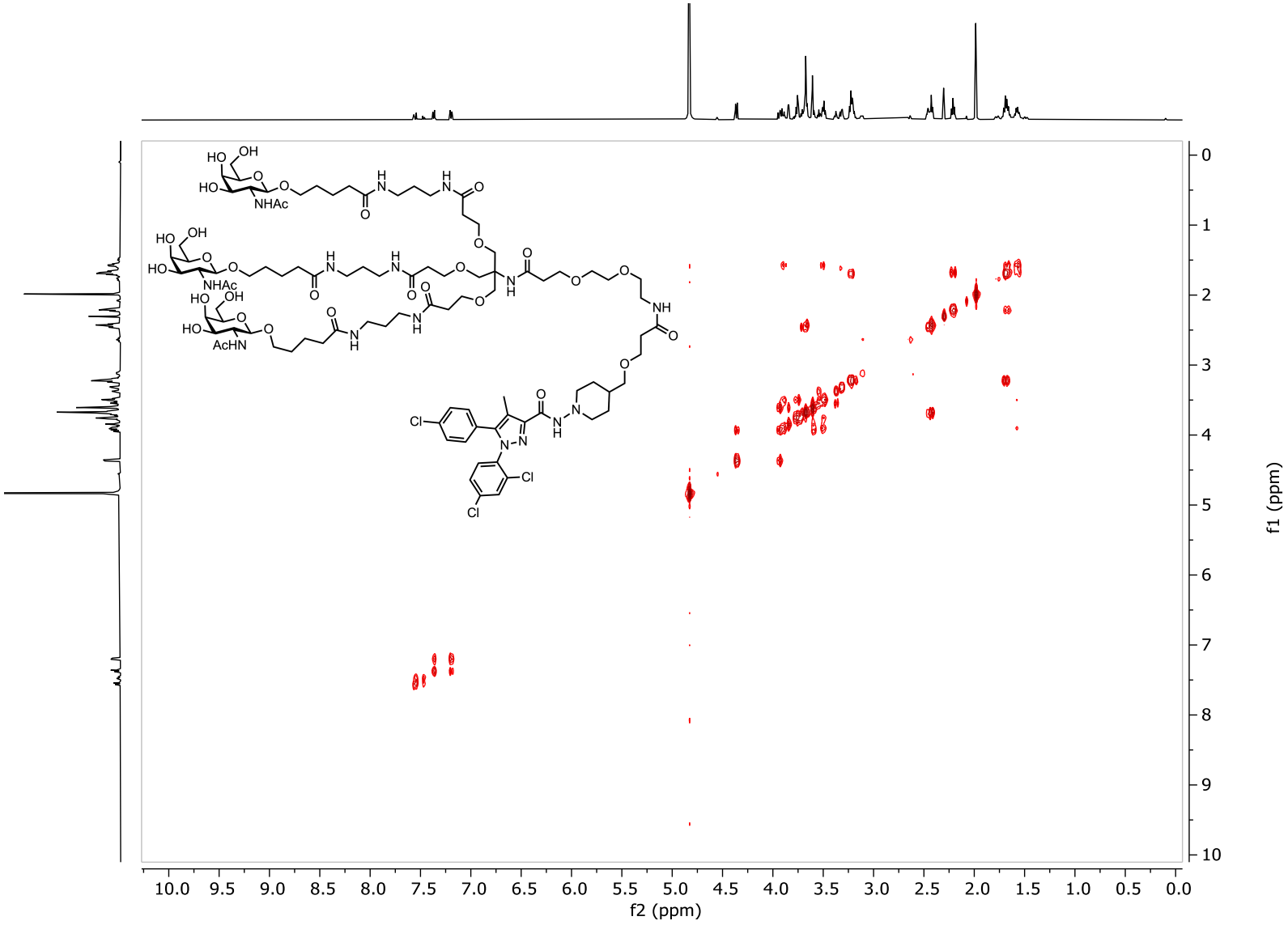
Compound LYTAC-1,4-PEG2 **(2.69)** **^{13}C NMR** (126 MHz, MeOD)



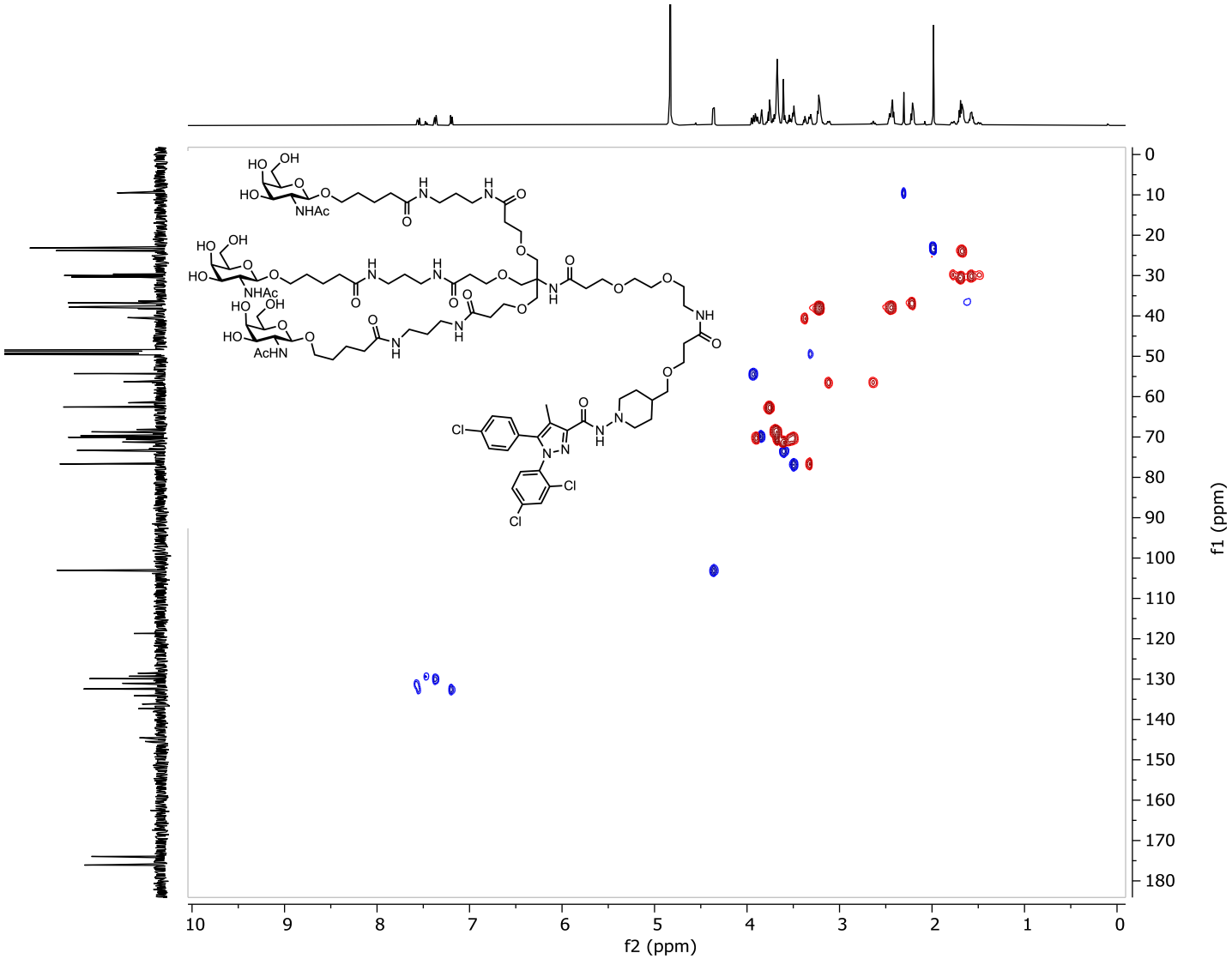
Compound LYTAC-1,4-PEG2 **(2.69) COSY** (500 MHz, MeOD)



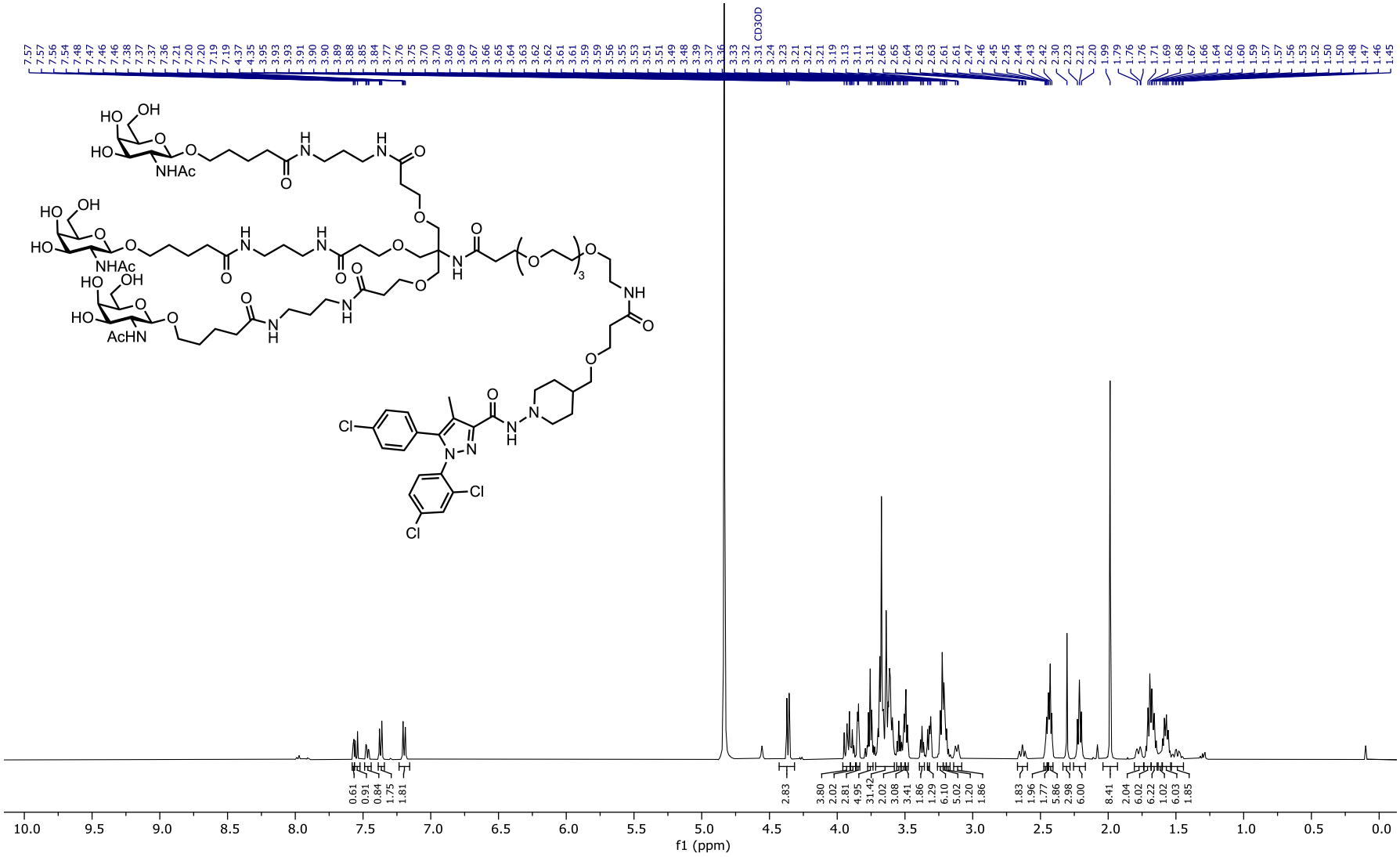
Compound LYTAC-1,4-PEG2 **(2.69) HMBC** (500/126 MHz, MeOD)



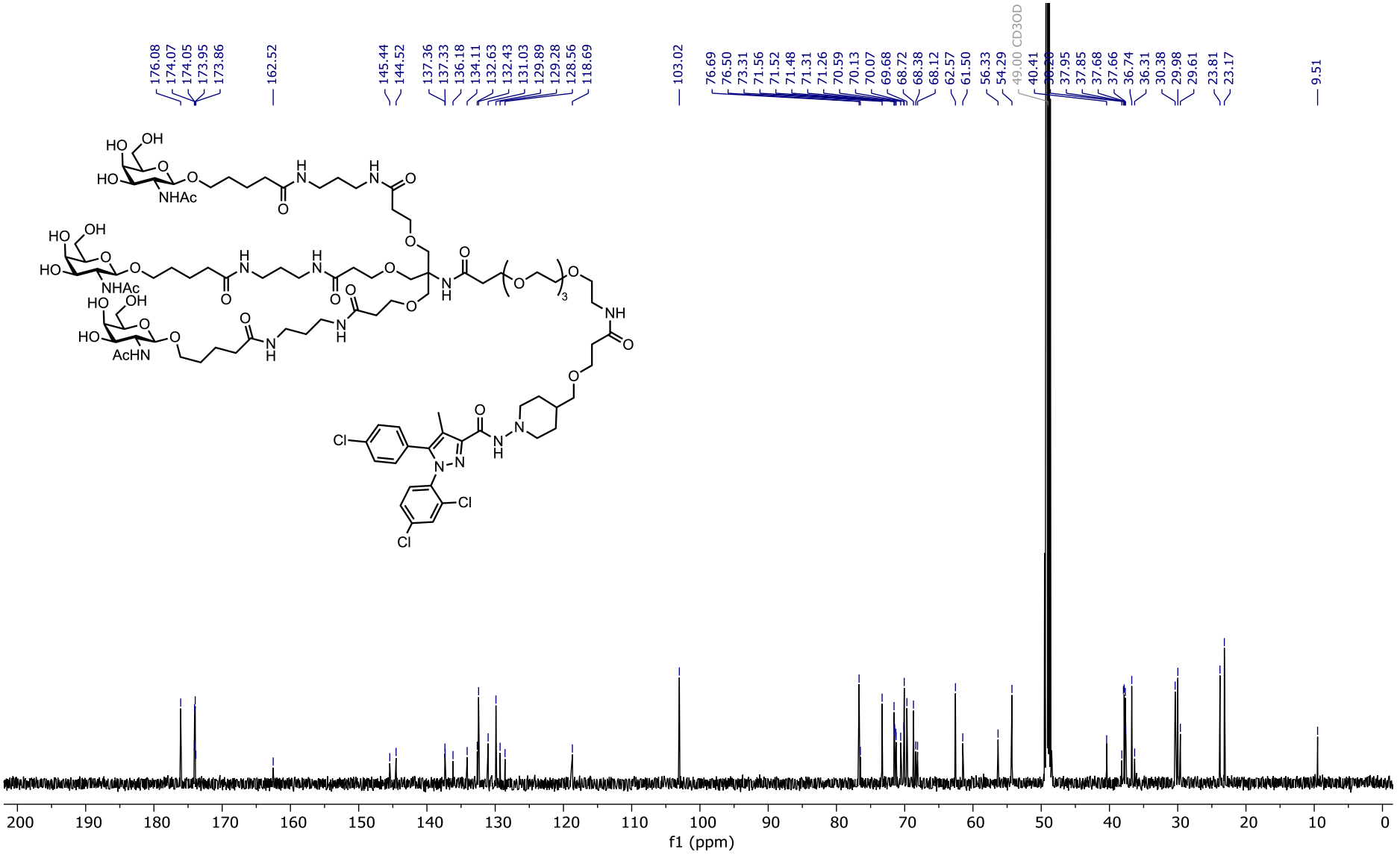
Compound LYTAC-1,4-PEG2 **(2.69) HSQC** (500/126 MHz, MeOD)



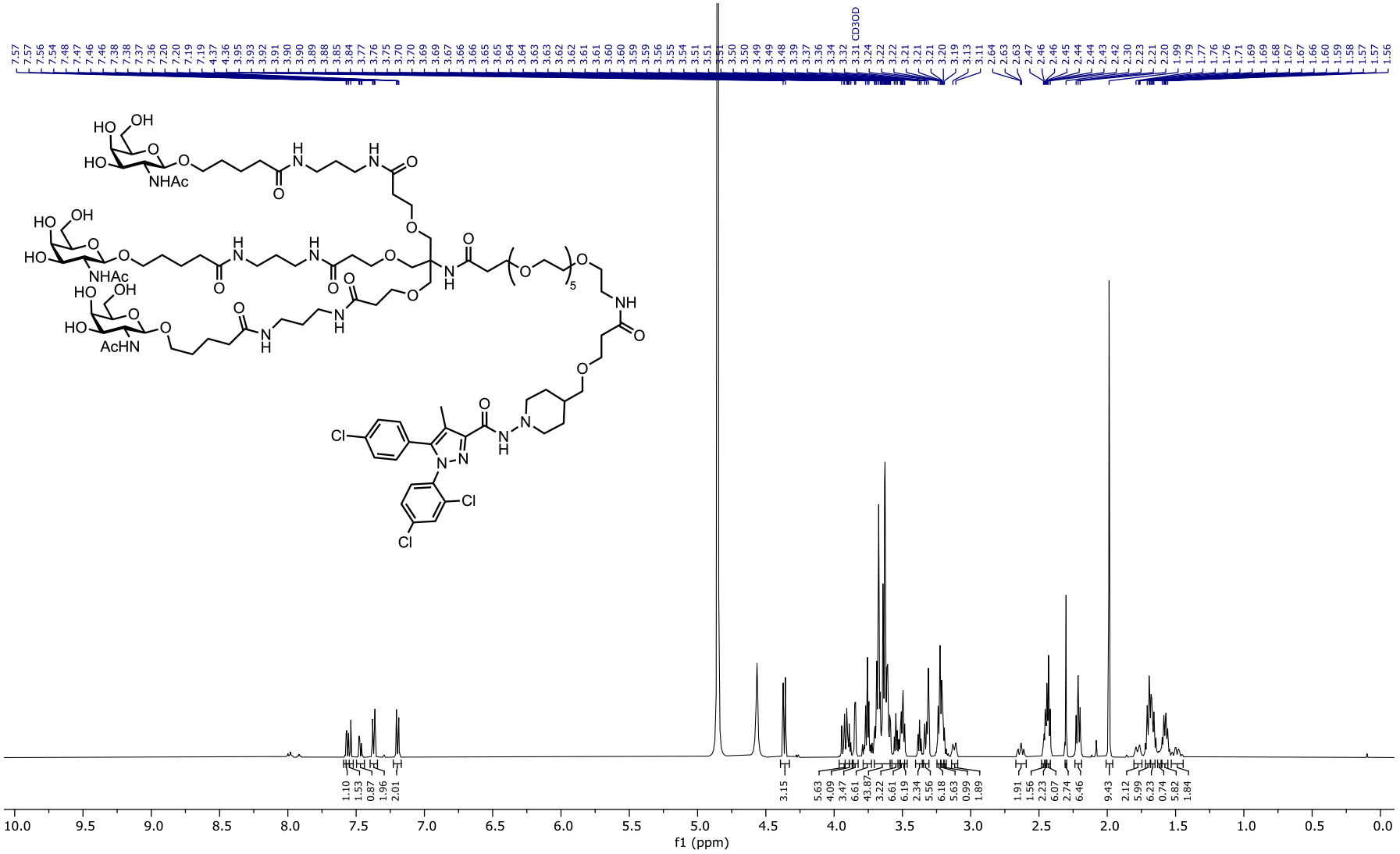
Compound LYTAC-1,4-PEG4 **(2.70)** **^{1}H NMR** (500 MHz, MeOD)



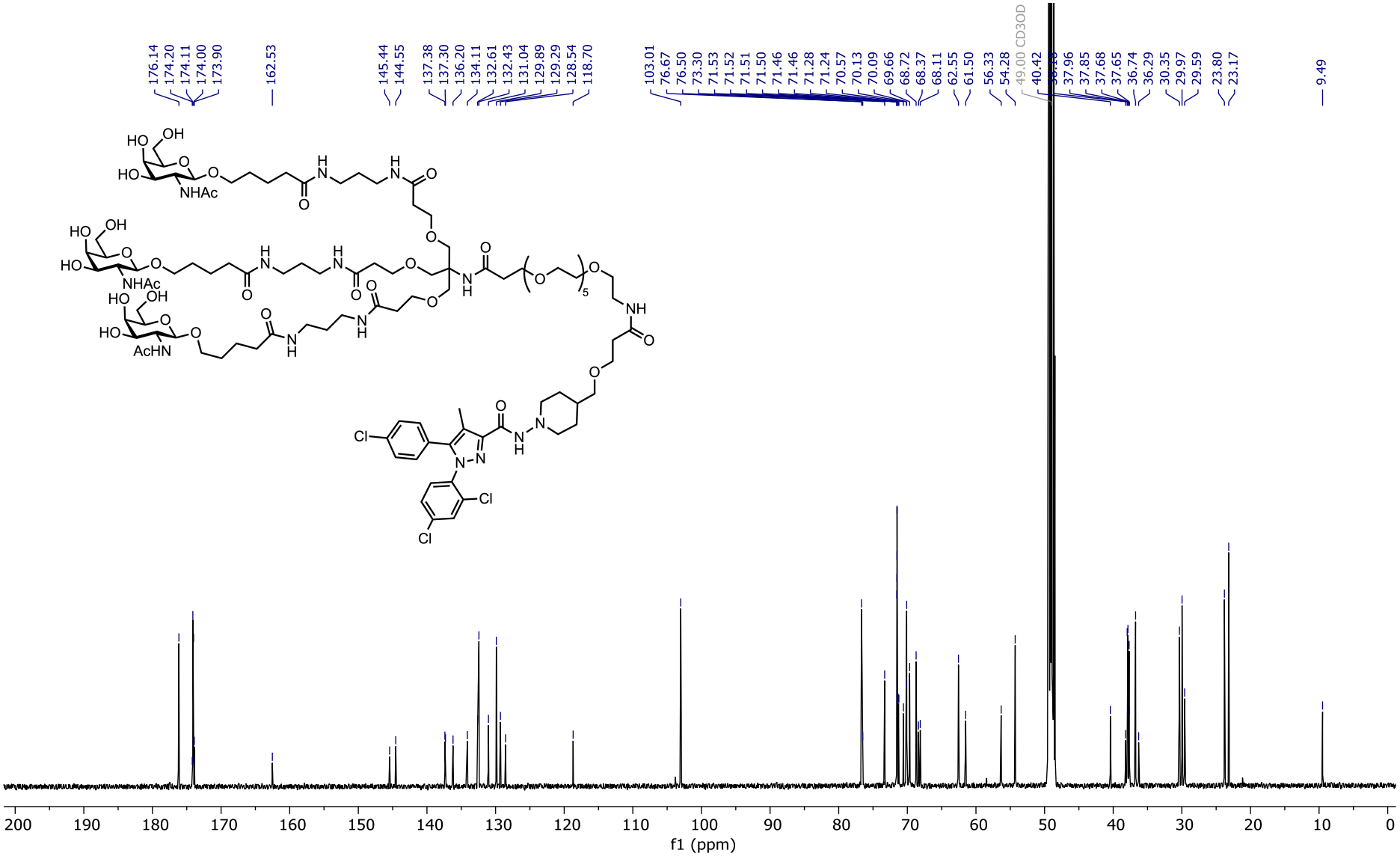
Compound LYTAC-1,4-PEG4 **(2.70)** **^{13}C NMR** (126 MHz, MeOD)



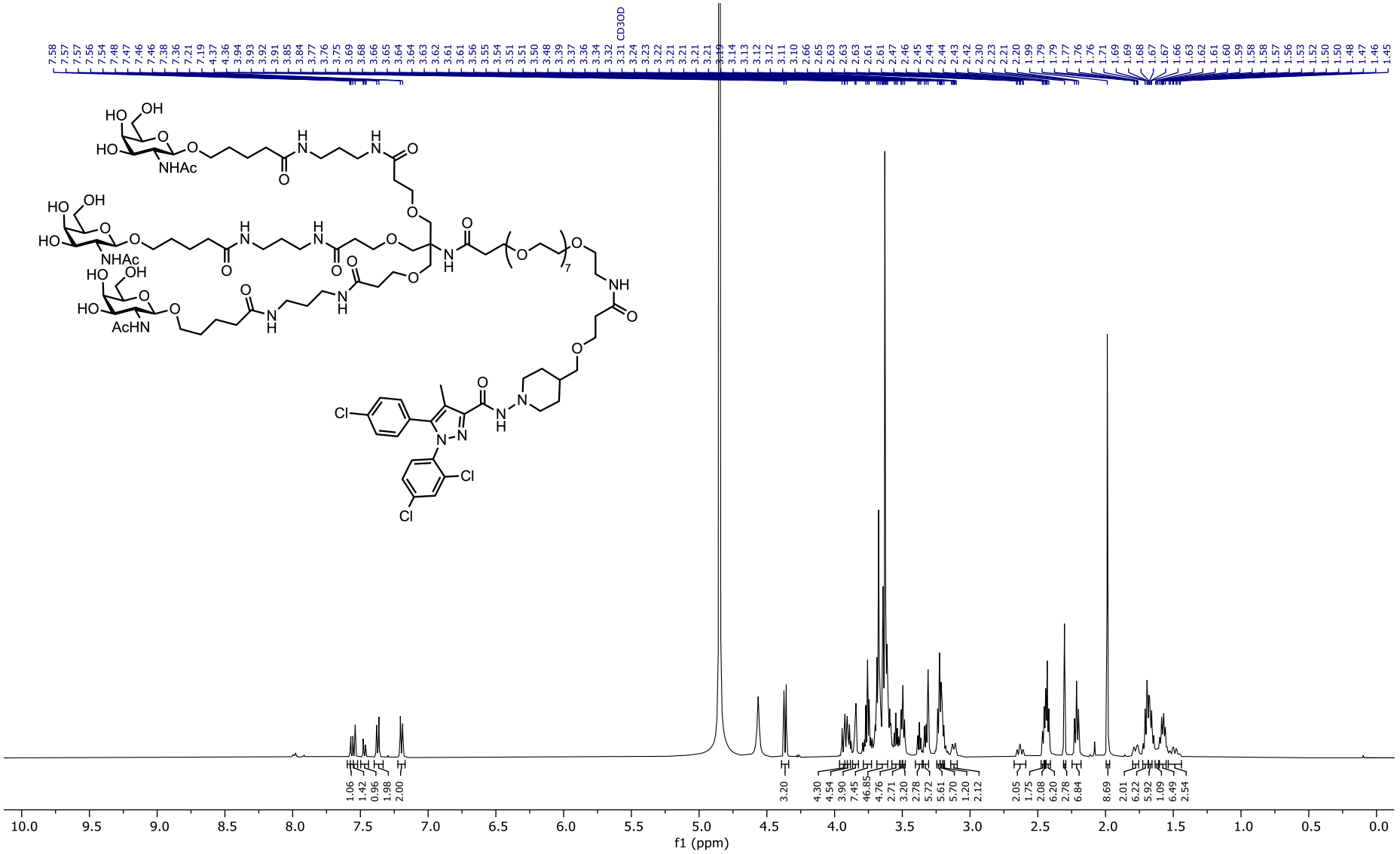
Compound LYTAC-1,4-PEG6 **(2.71) ^{1}H NMR** (500 MHz, MeOD)



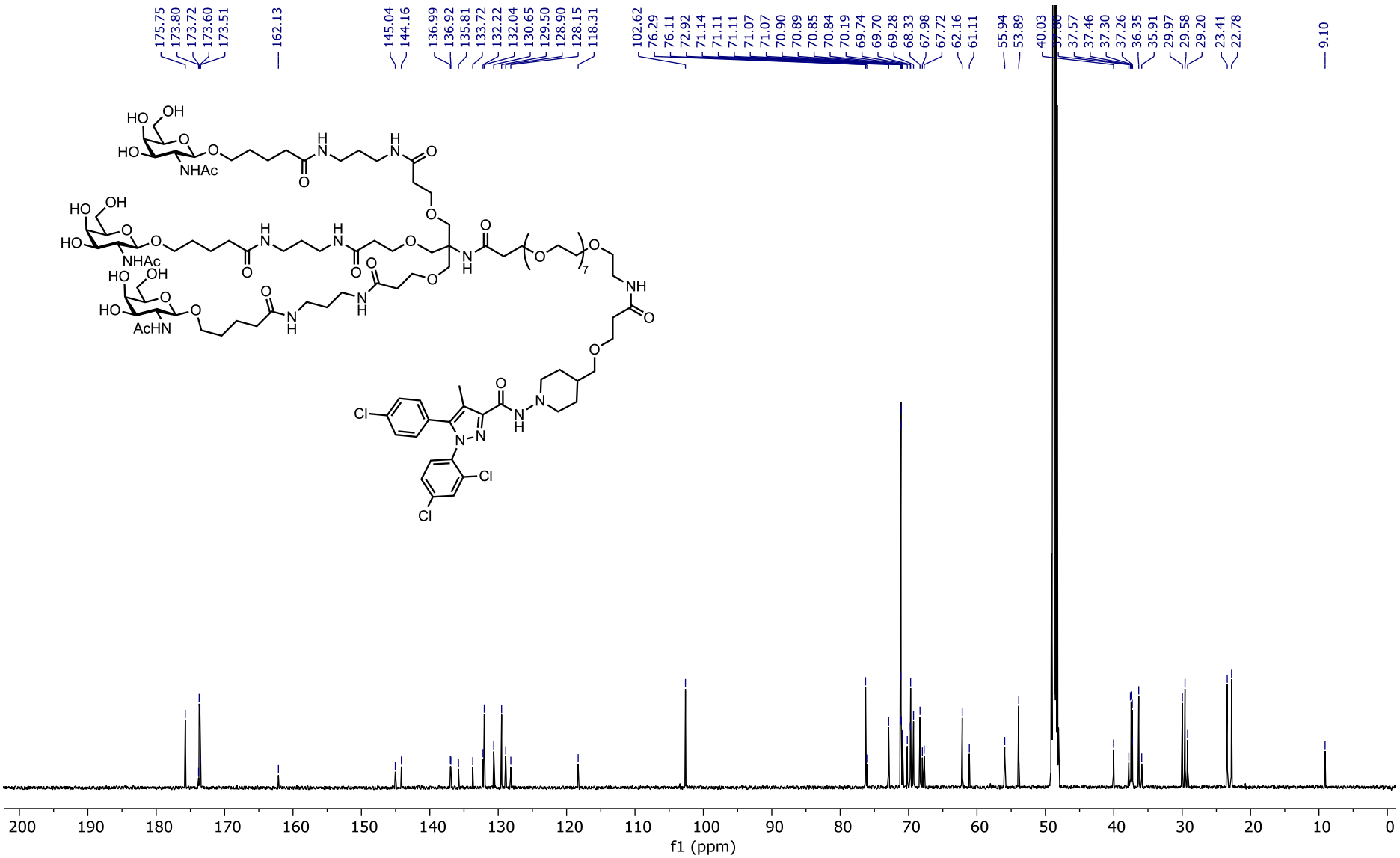
Compound LYTAC-1,4-PEG6 **(2.71)** **^{13}C NMR** (126 MHz, MeOD)



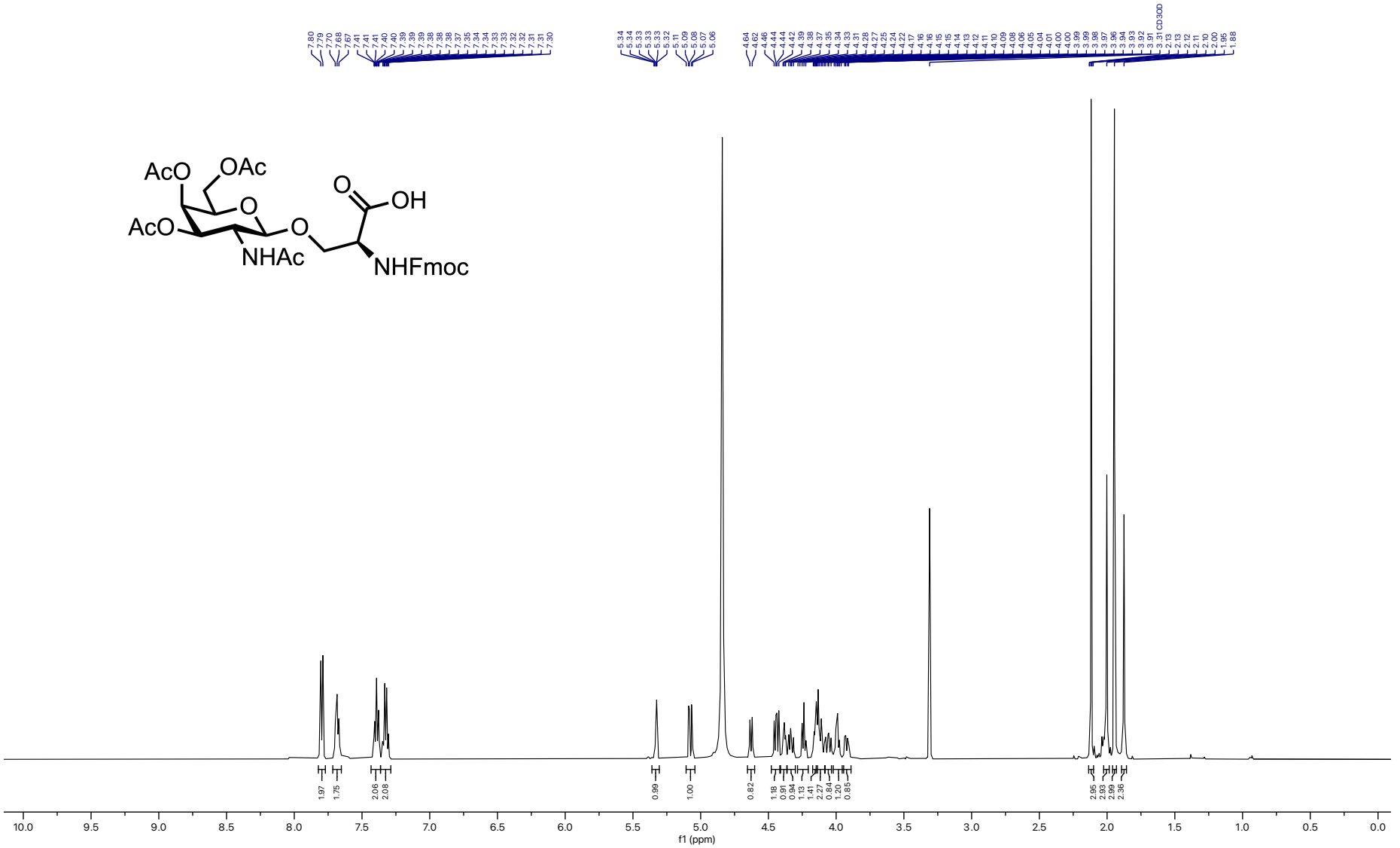
Compound LYTAC-1,4-PEG8 **(2.72)** **^{1}H NMR** (800 MHz, MeOD)



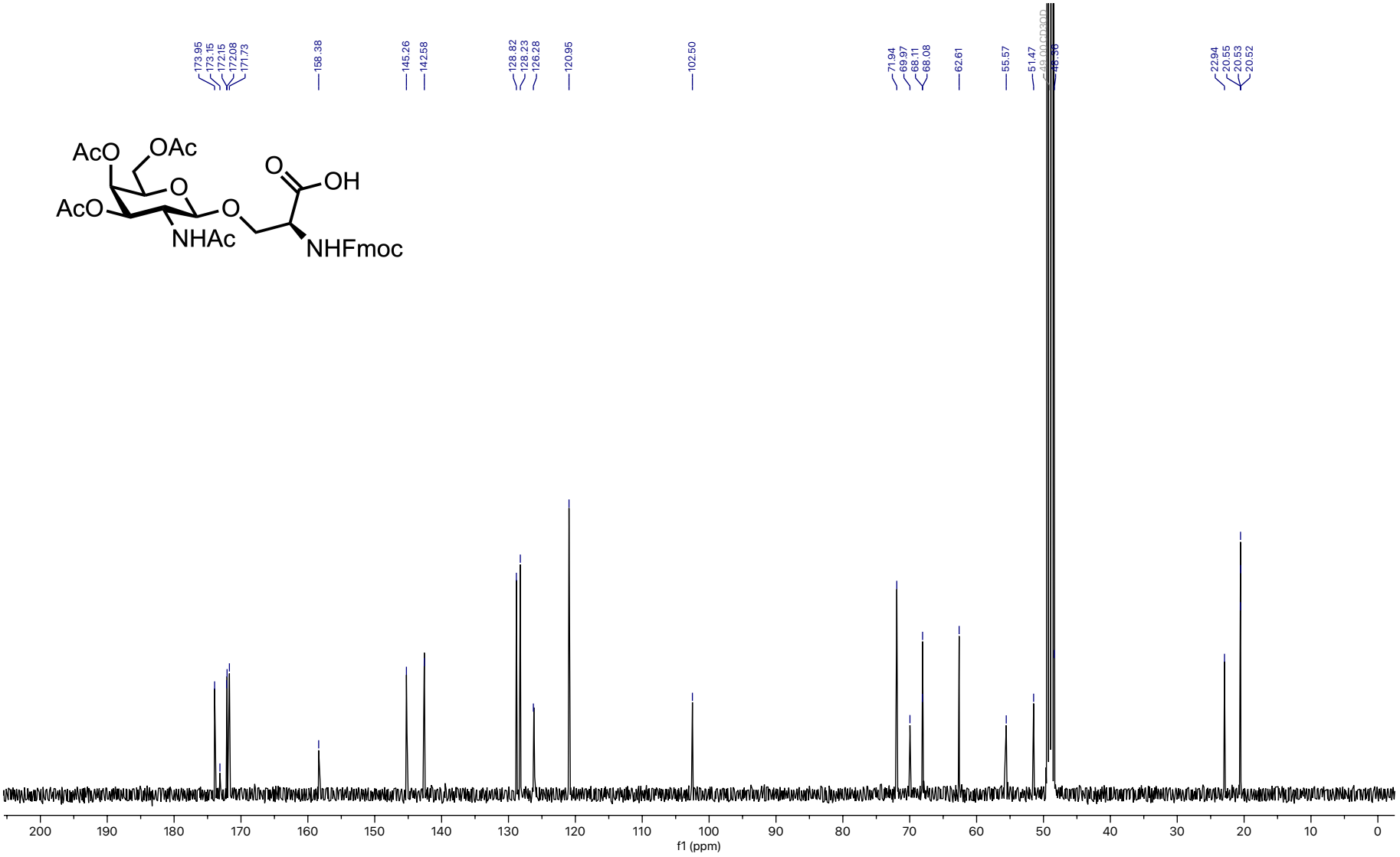
Compound LYTAC-1,4-PEG8 **(2.72)** **^{13}C NMR** (201 MHz, MeOD)



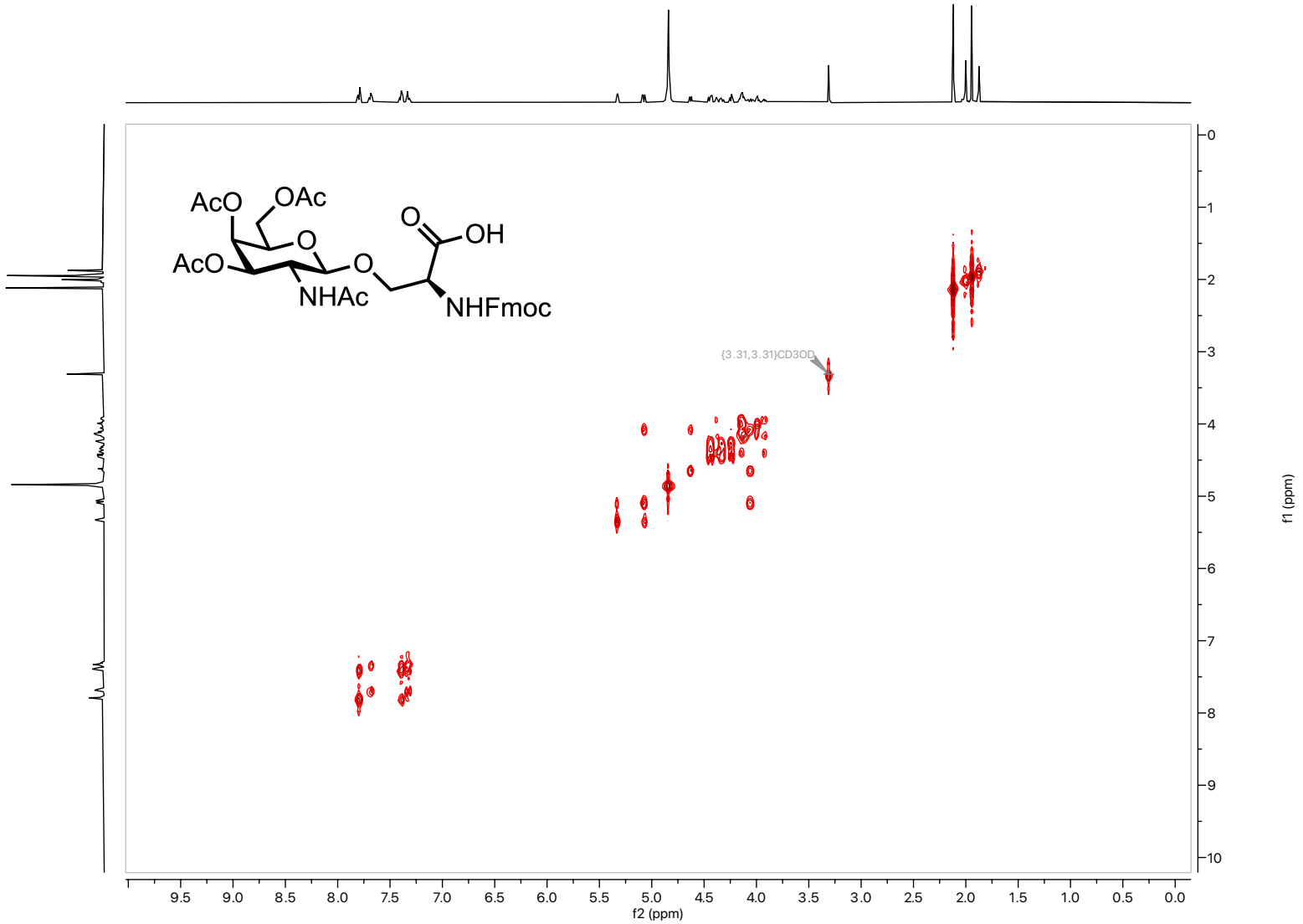
Compound Fmoc-β-Ser-GalNAc(OAc)$_3$-OH **(2.99)** **^{1}H NMR** (500 MHz, MeOD)



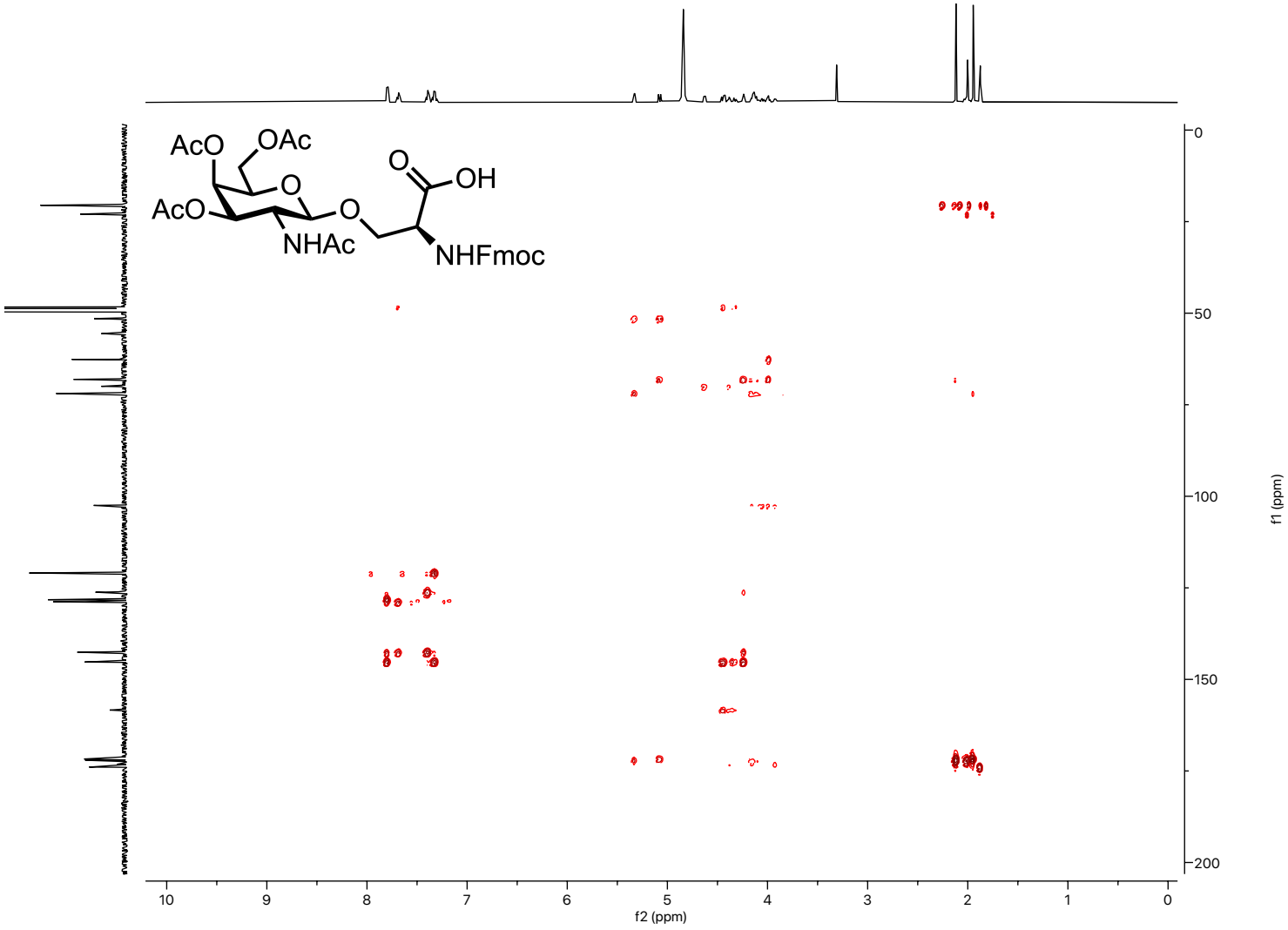
Compound Fmoc-β-Ser-GalNAc(OAc)$_3$-OH **(2.99)** **^{13}C NMR** (126 MHz, MeOD)



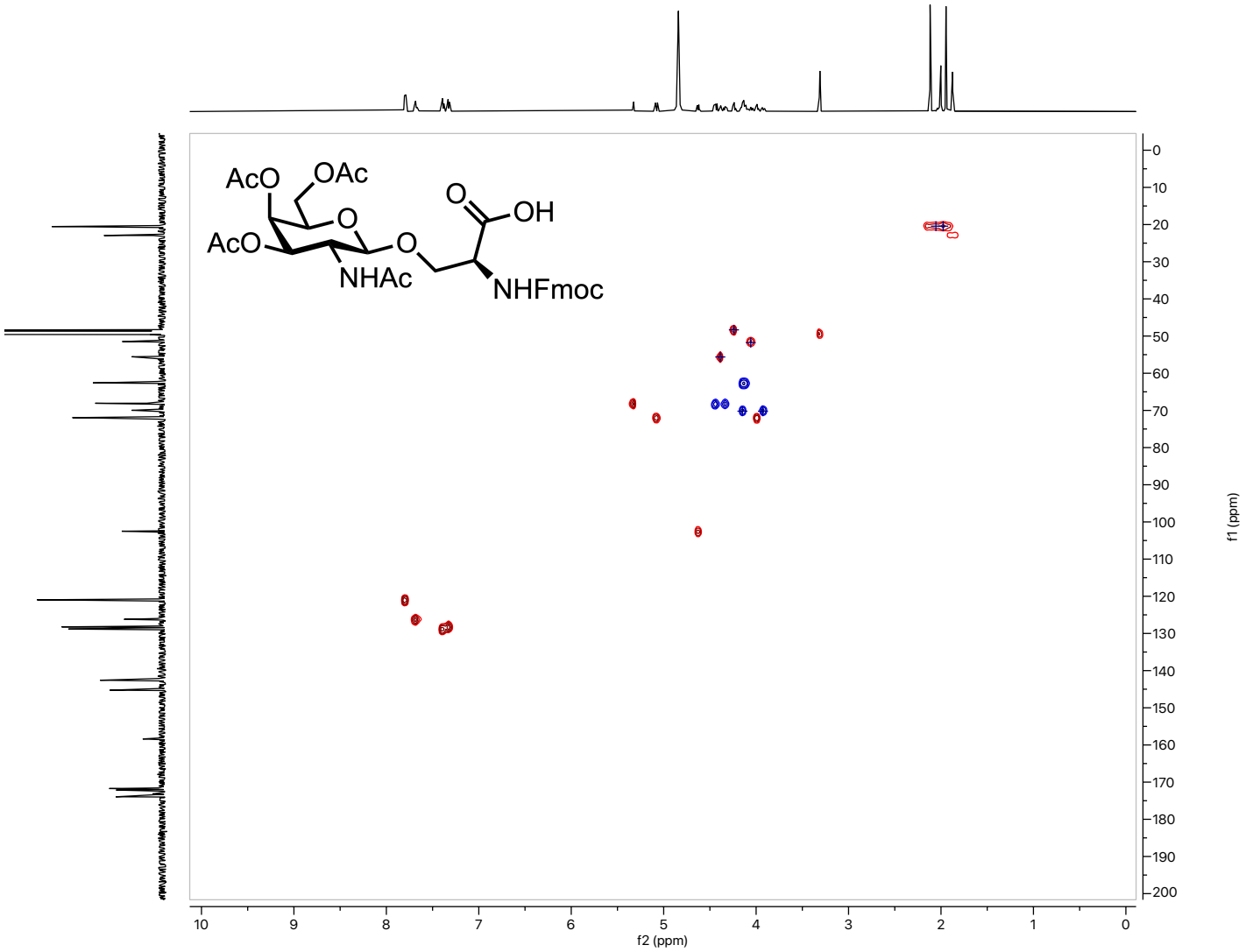
Compound Fmoc-β-Ser-GalNAc(OAc)$_3$-OH **(2.99) COSY** (500 MHz, MeOD)



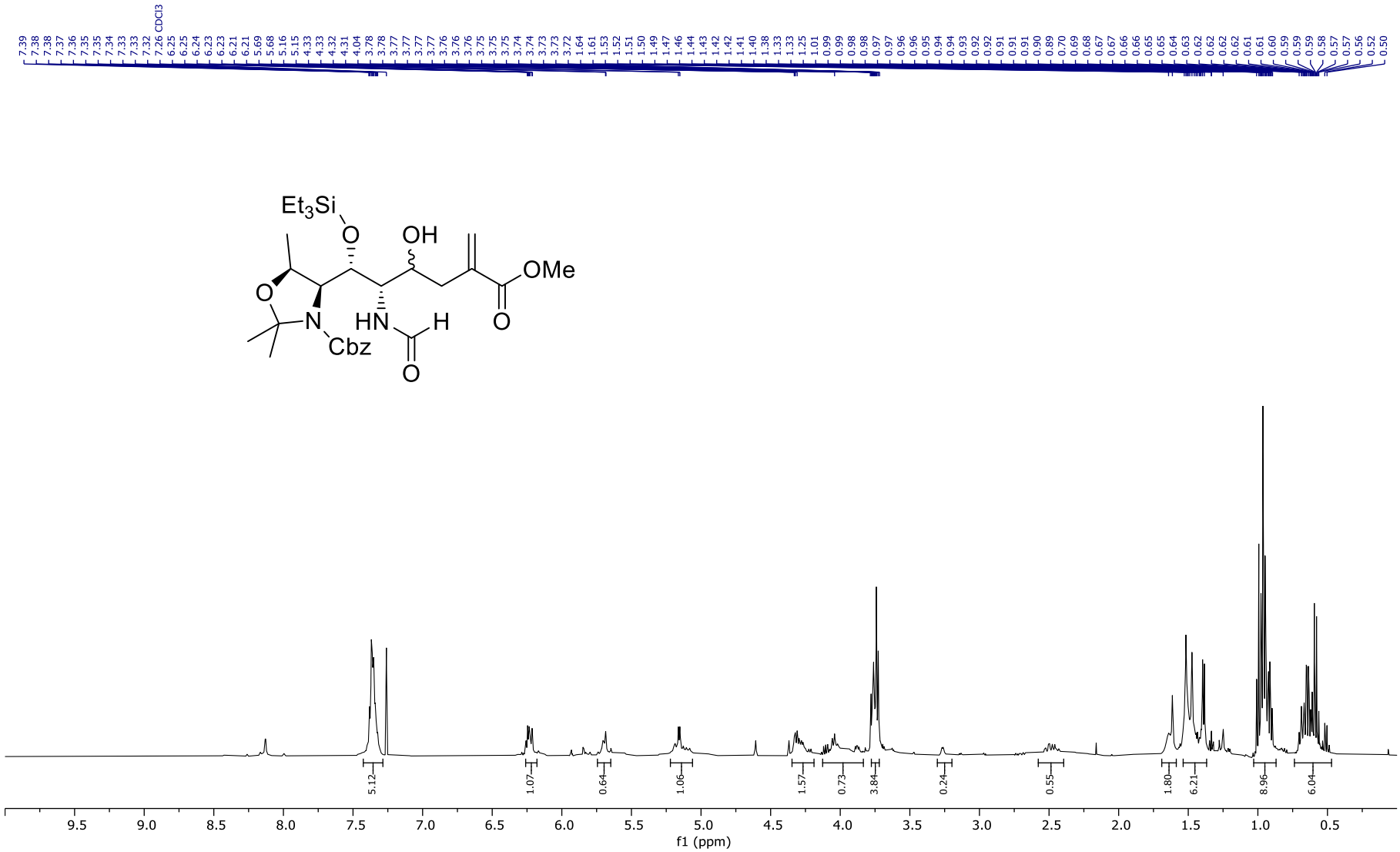
Compound Fmoc-β-Ser-GalNAc(OAc)$_3$-OH **(2.99) HMBC** (500/126 MHz, MeOD)



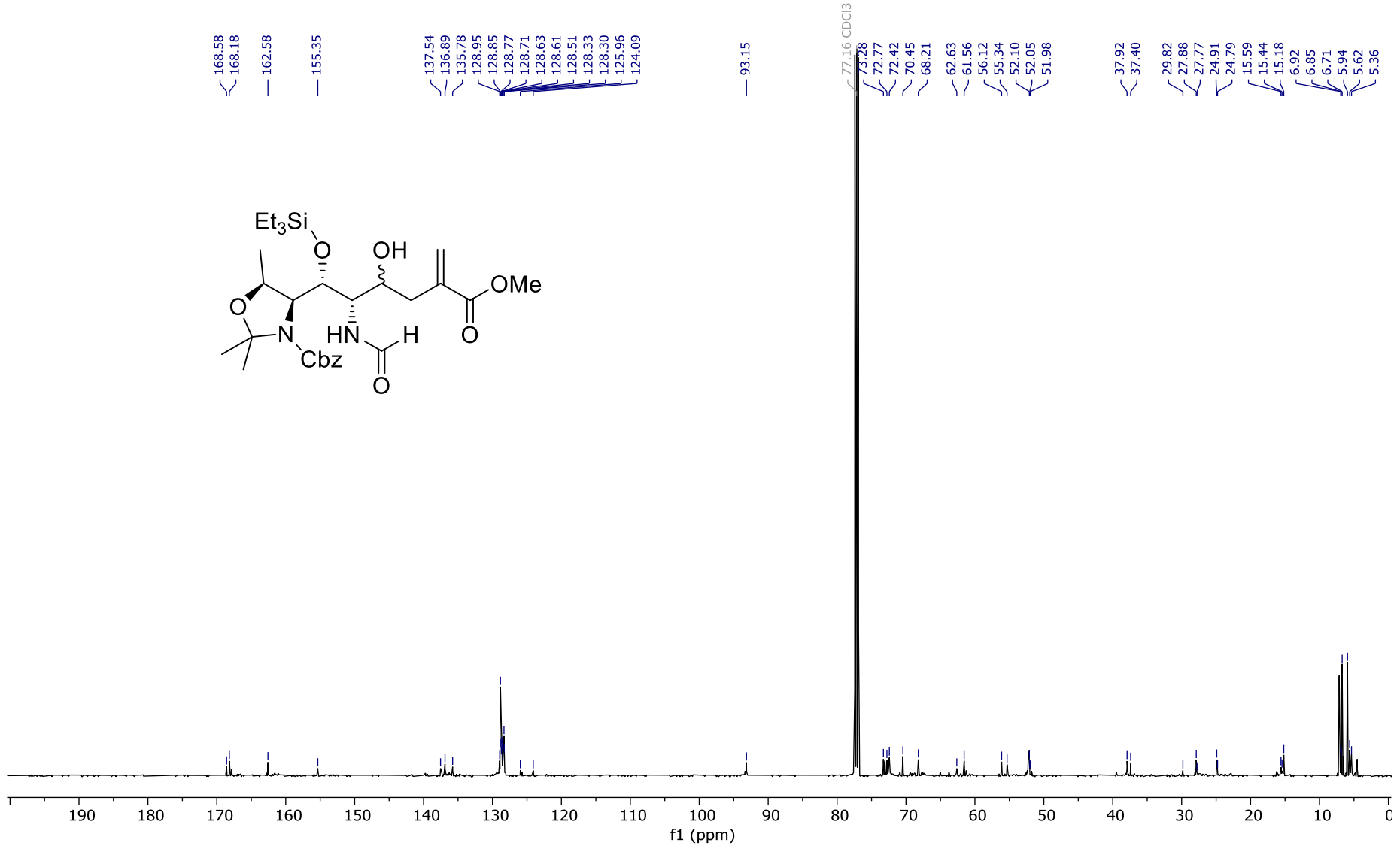
Compound Fmoc-β-Ser-GalNAc(OAc)$_3$-OH **(2.99) HSQC** (500/126 MHz, MeOD)



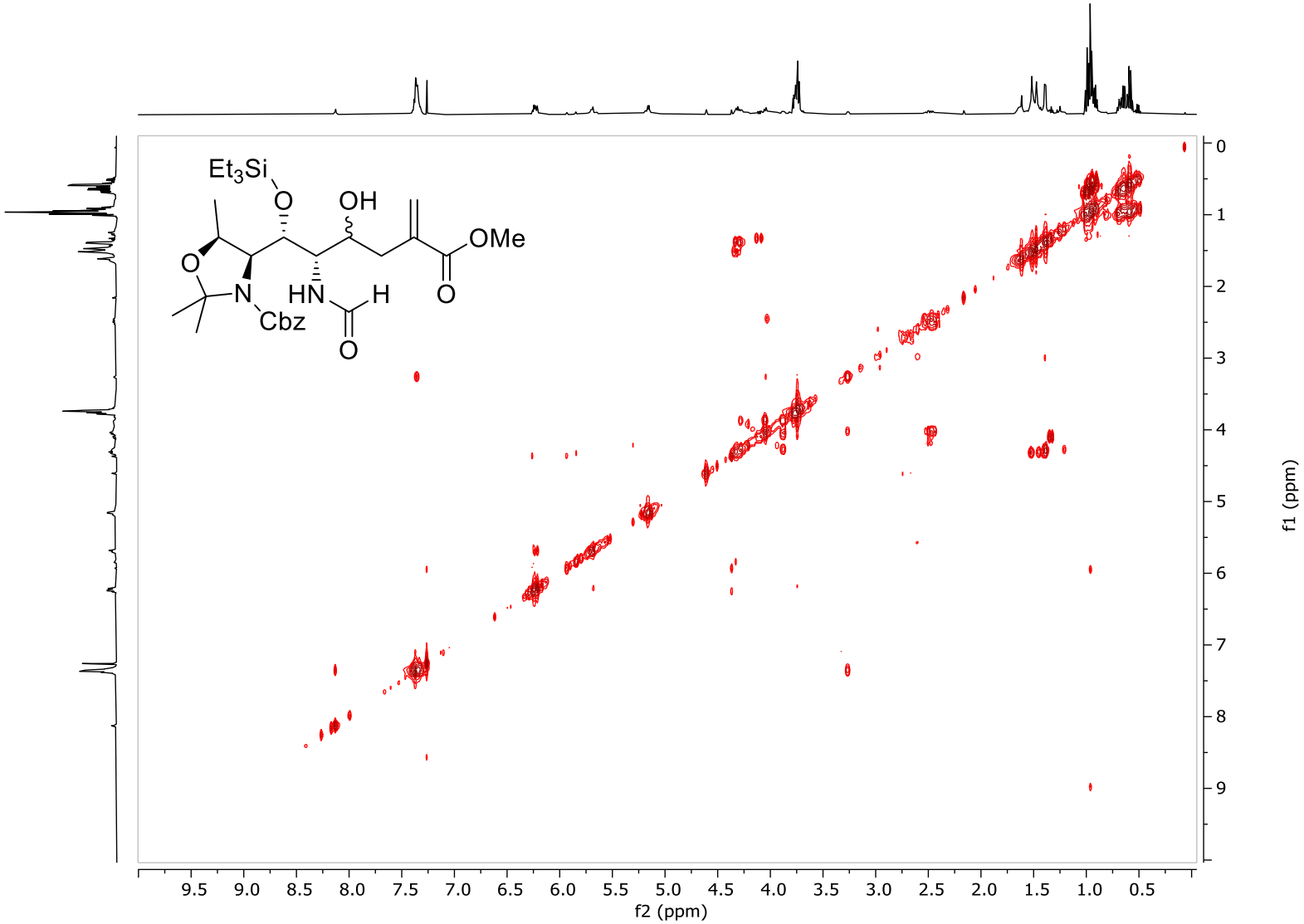
Compound **4.146** **^{1}H NMR** (500 MHz, $CDCl_3$)



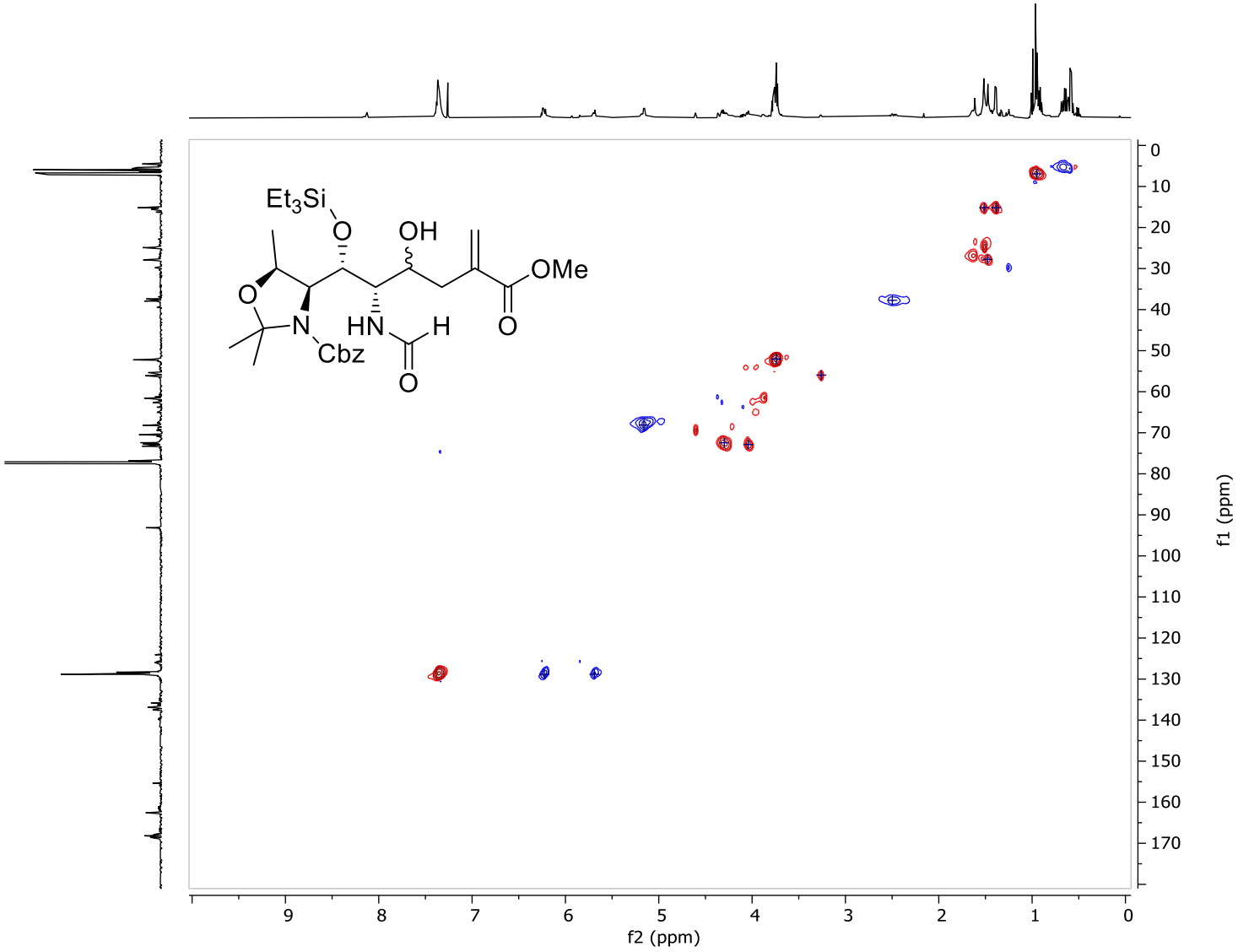
Compound **4.146** **^{13}C NMR** (126 MHz, $CDCl_3$)



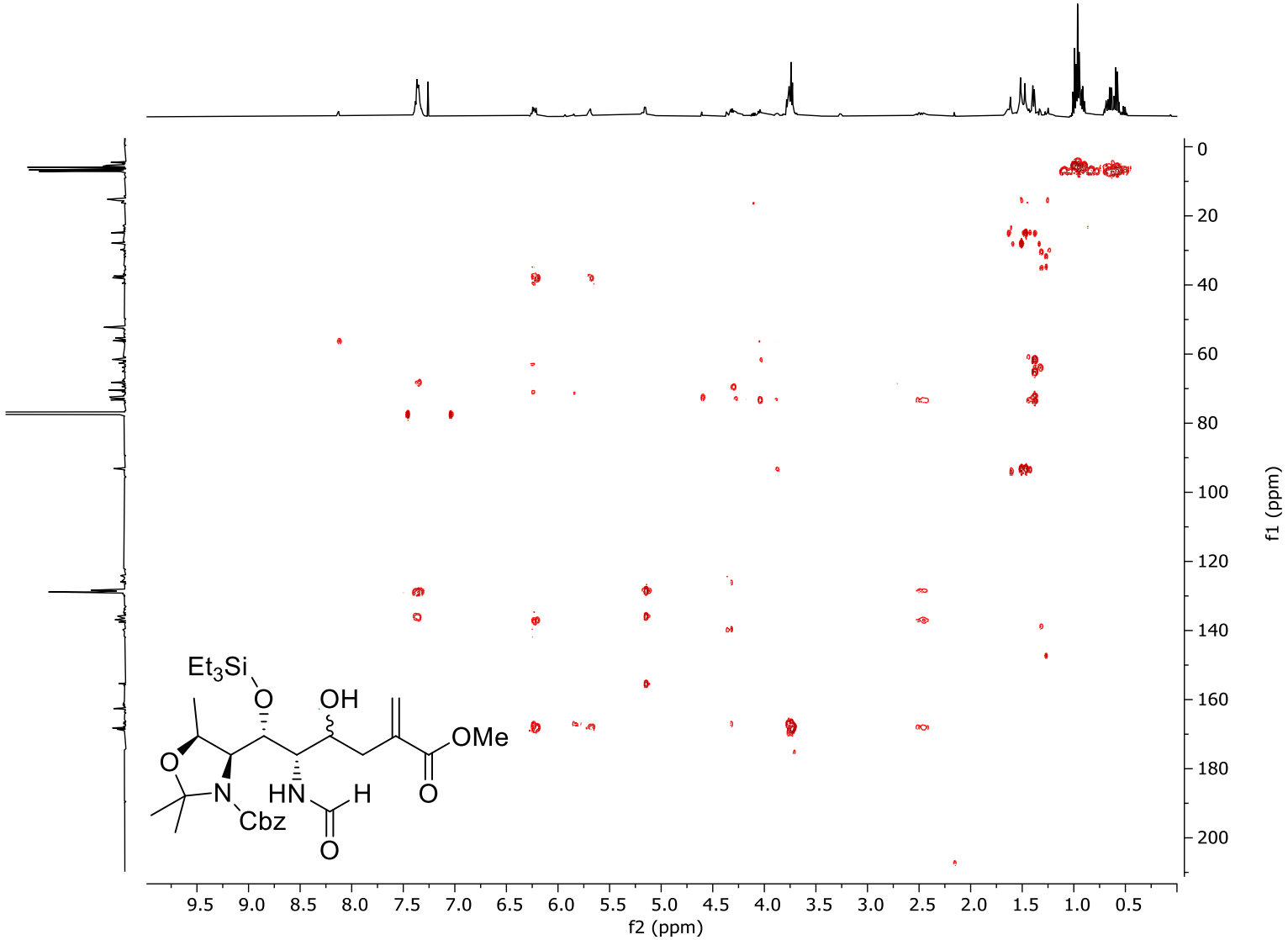
Compound **4.146 COSY** (500 MHz, $CDCl_3$)



Compound **4.146 HSQC** (500/126 MHz, $CDCl_3$)



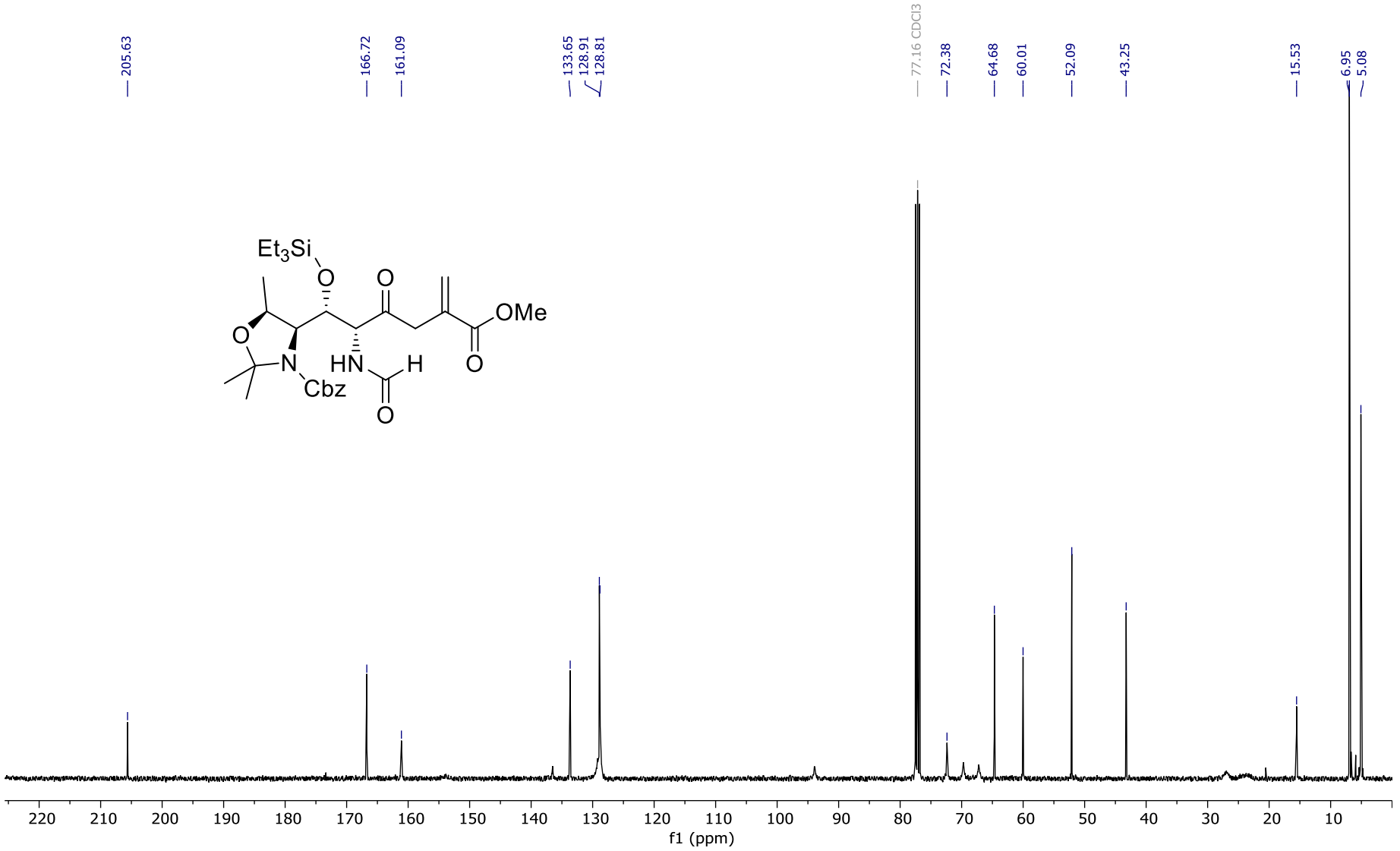
Compound **4.146 HMBC** (500/126 MHz, $CDCl_3$)



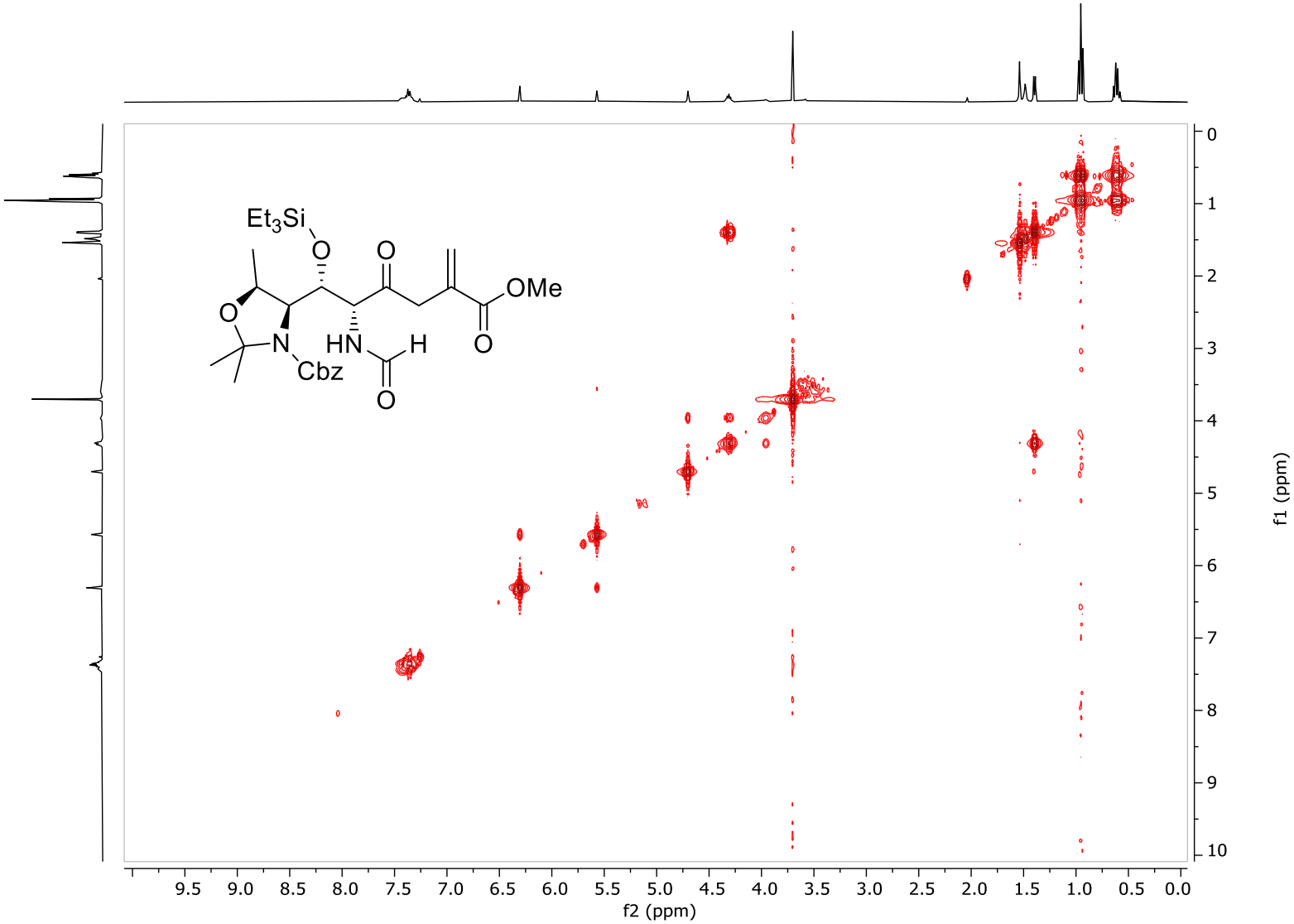
Compound **4.149** **^{1}H NMR** (400 MHz, $CDCl_3$)



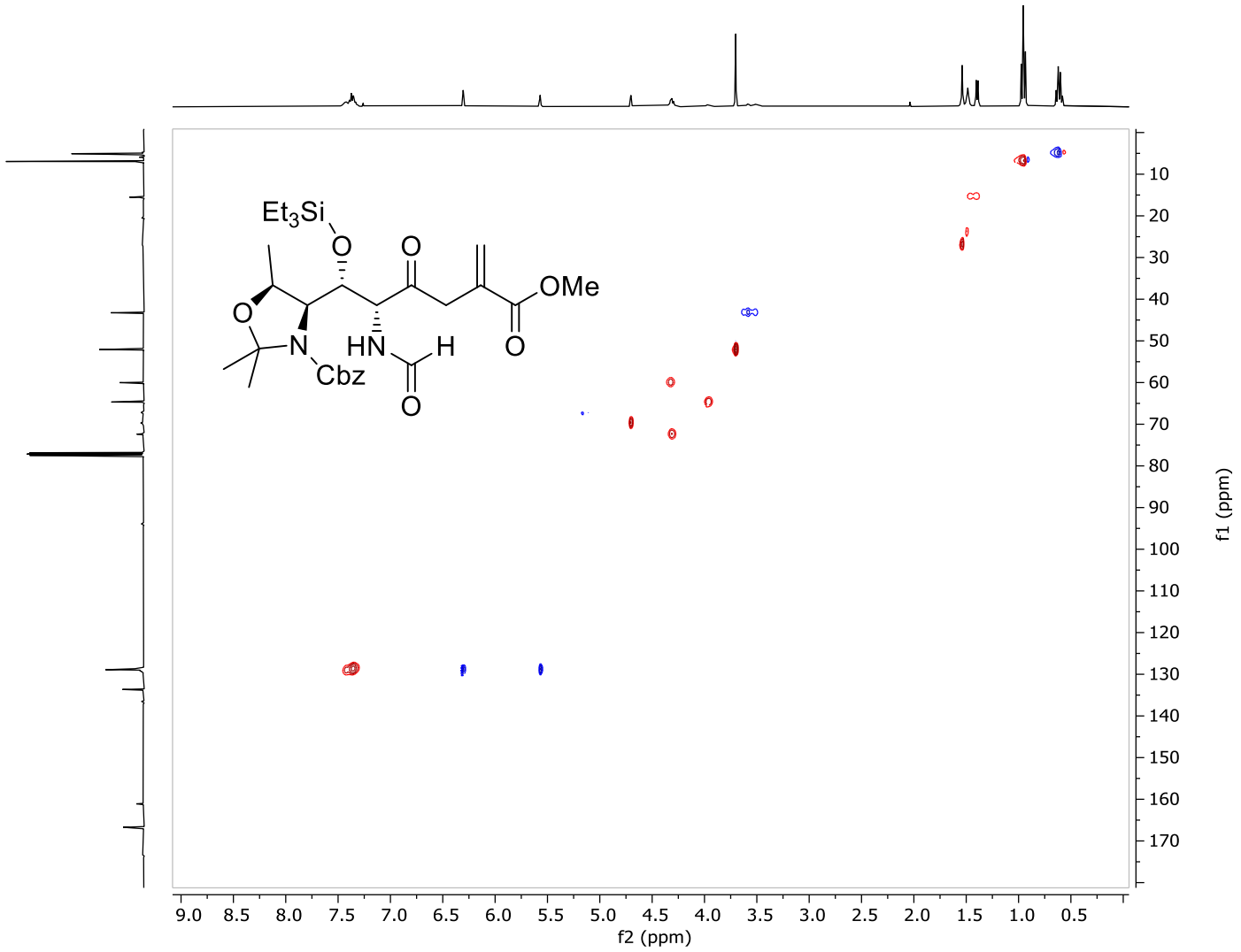
Compound **4.149** **^{13}C NMR** (101 MHz, $CDCl_3$)



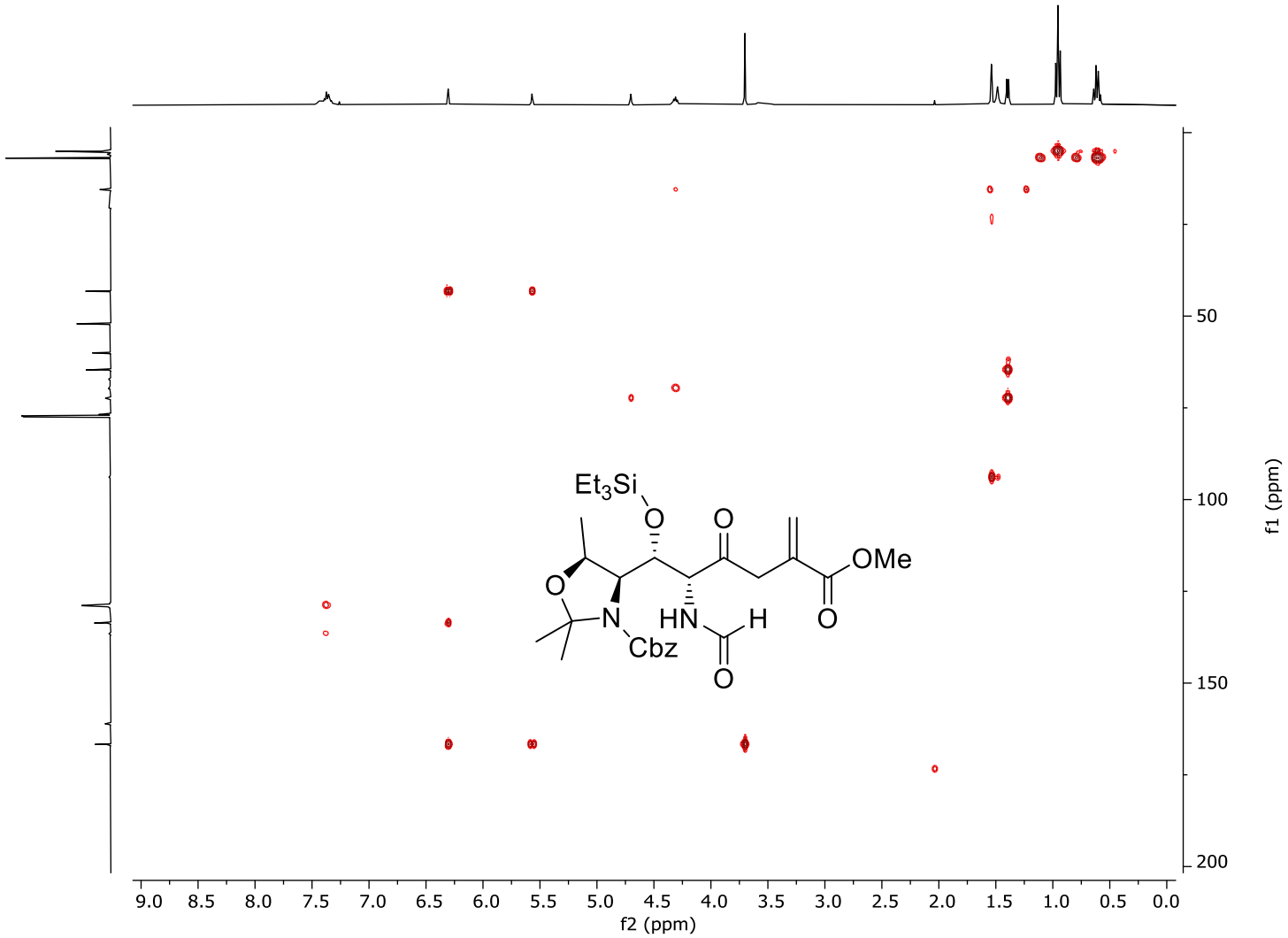
Compound **4.149 COSY** (400 MHz, $CDCl_3$)



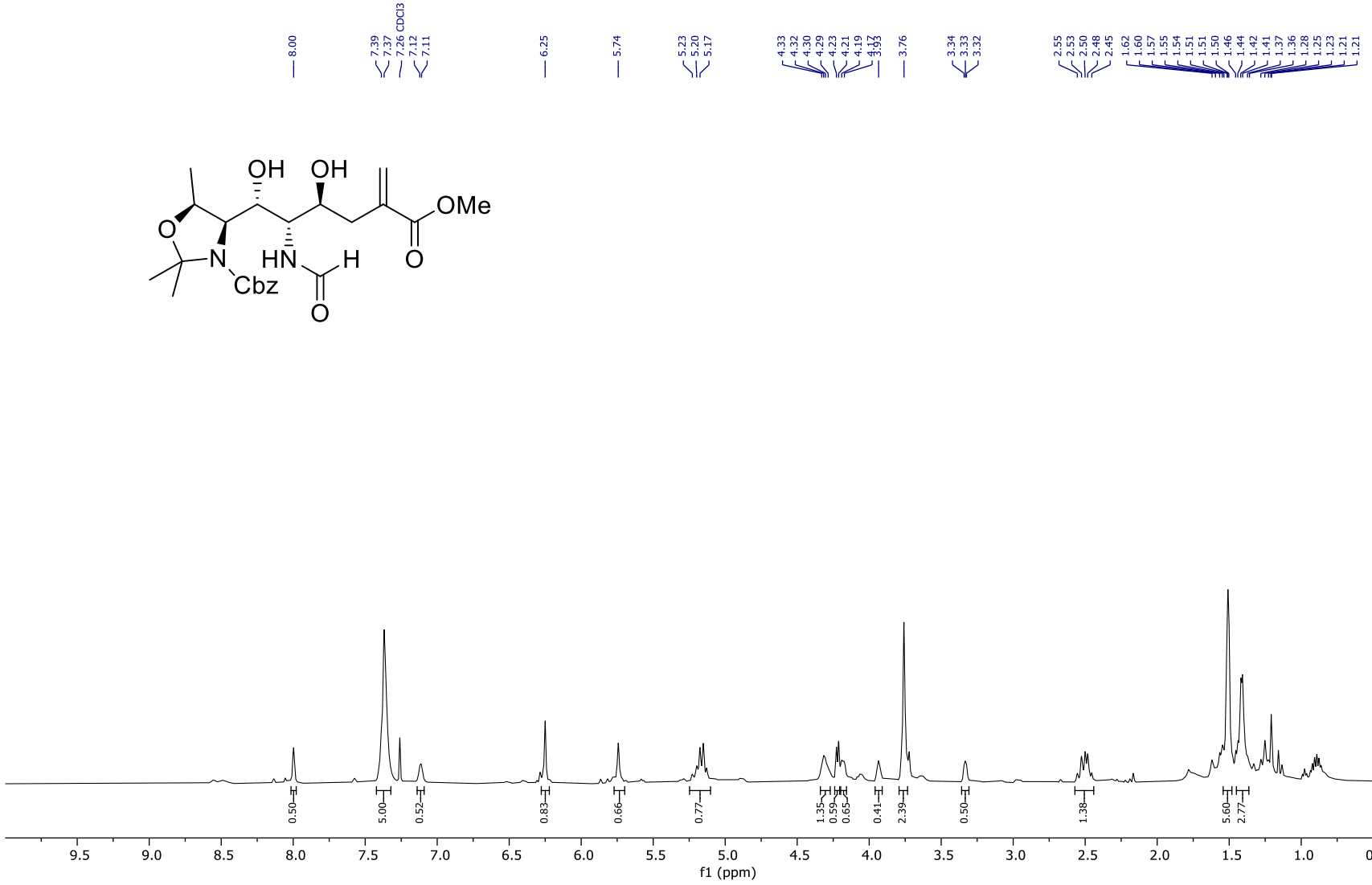
Compound **4.149 HSQC** (400/101 MHz, $CDCl_3$)



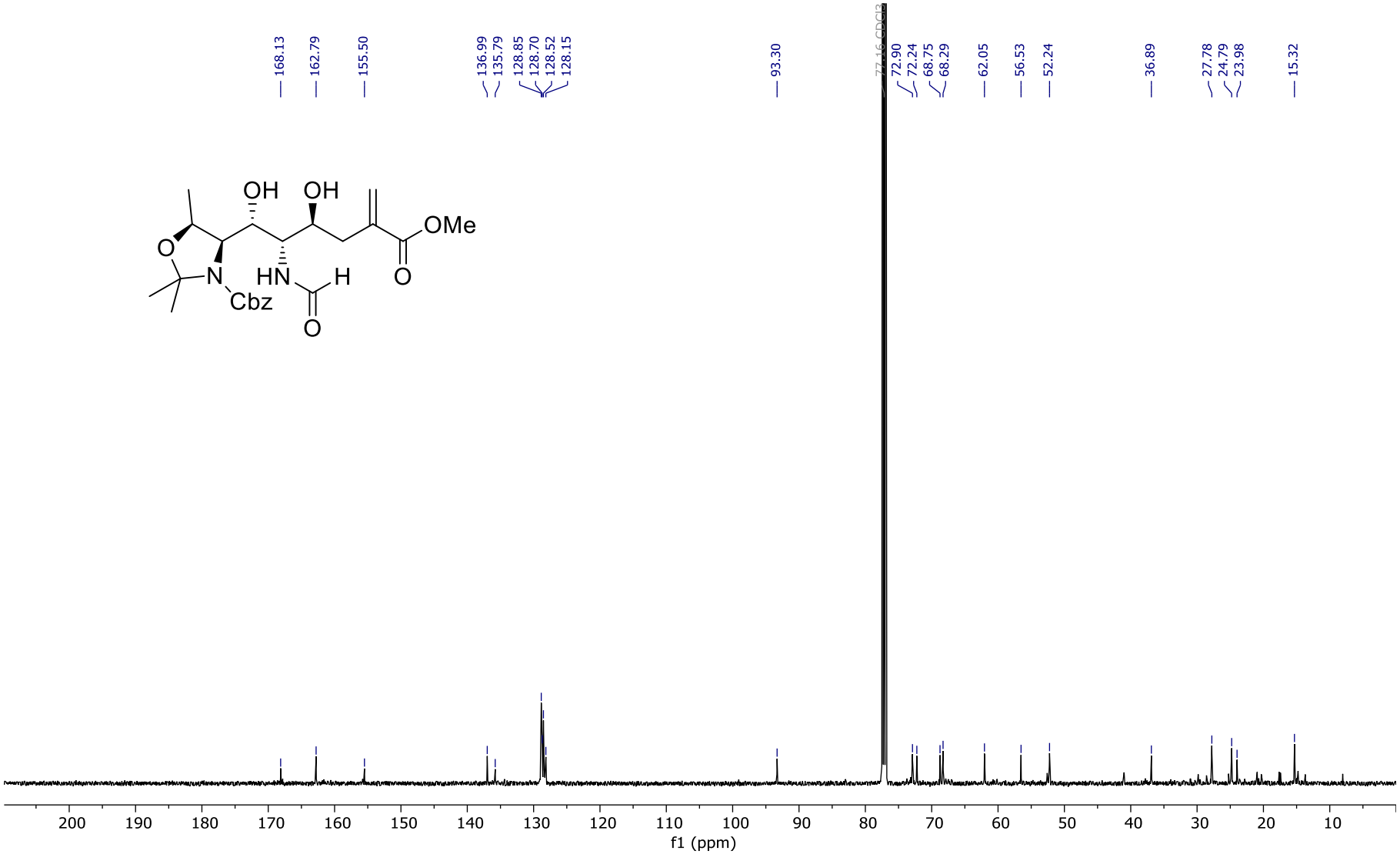
Compound **4.149 HMBC** (400/101 MHz, $CDCl_3$)



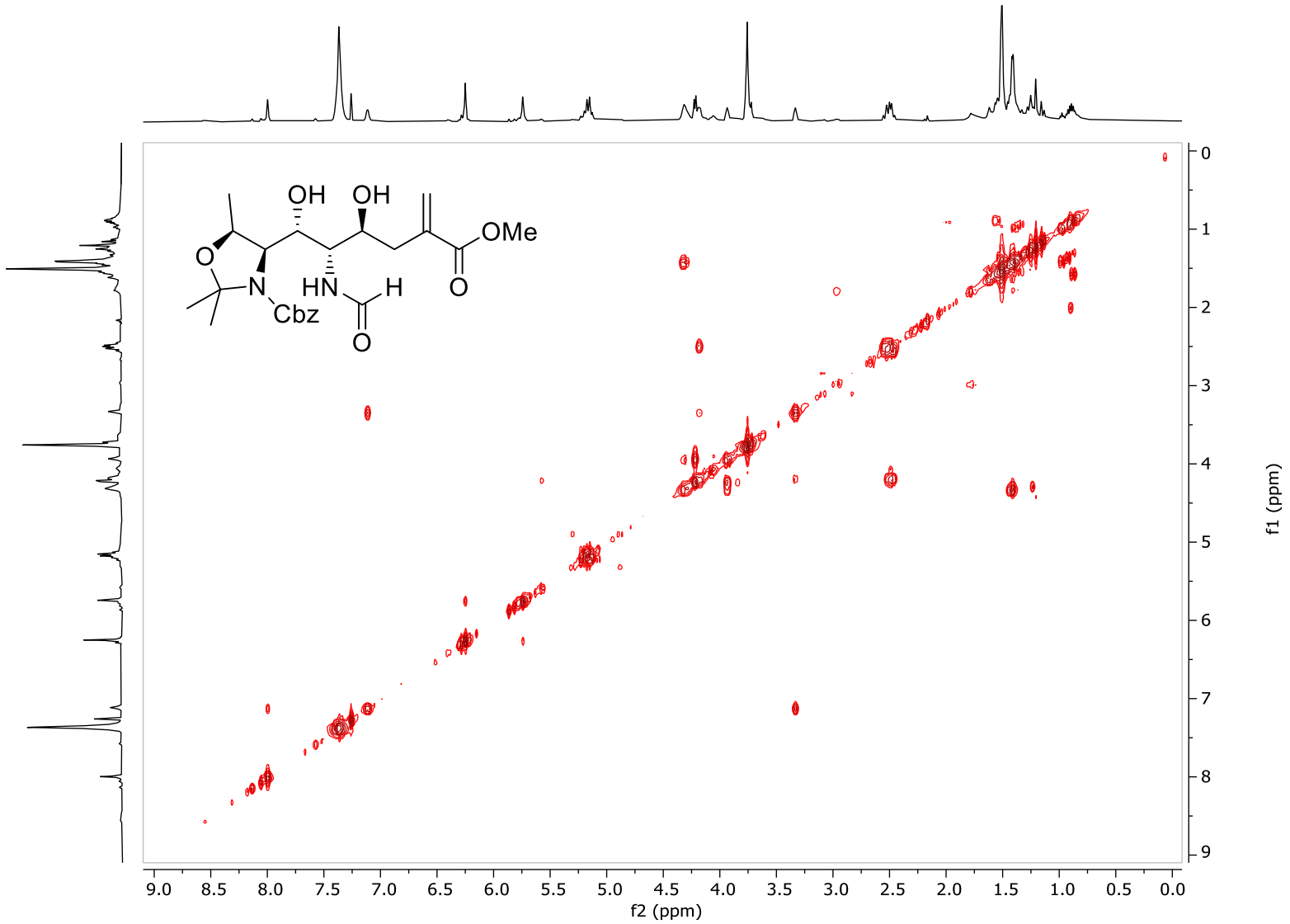
Compound **4.150** **^{1}H NMR** (500 MHz, $CDCl_3$)



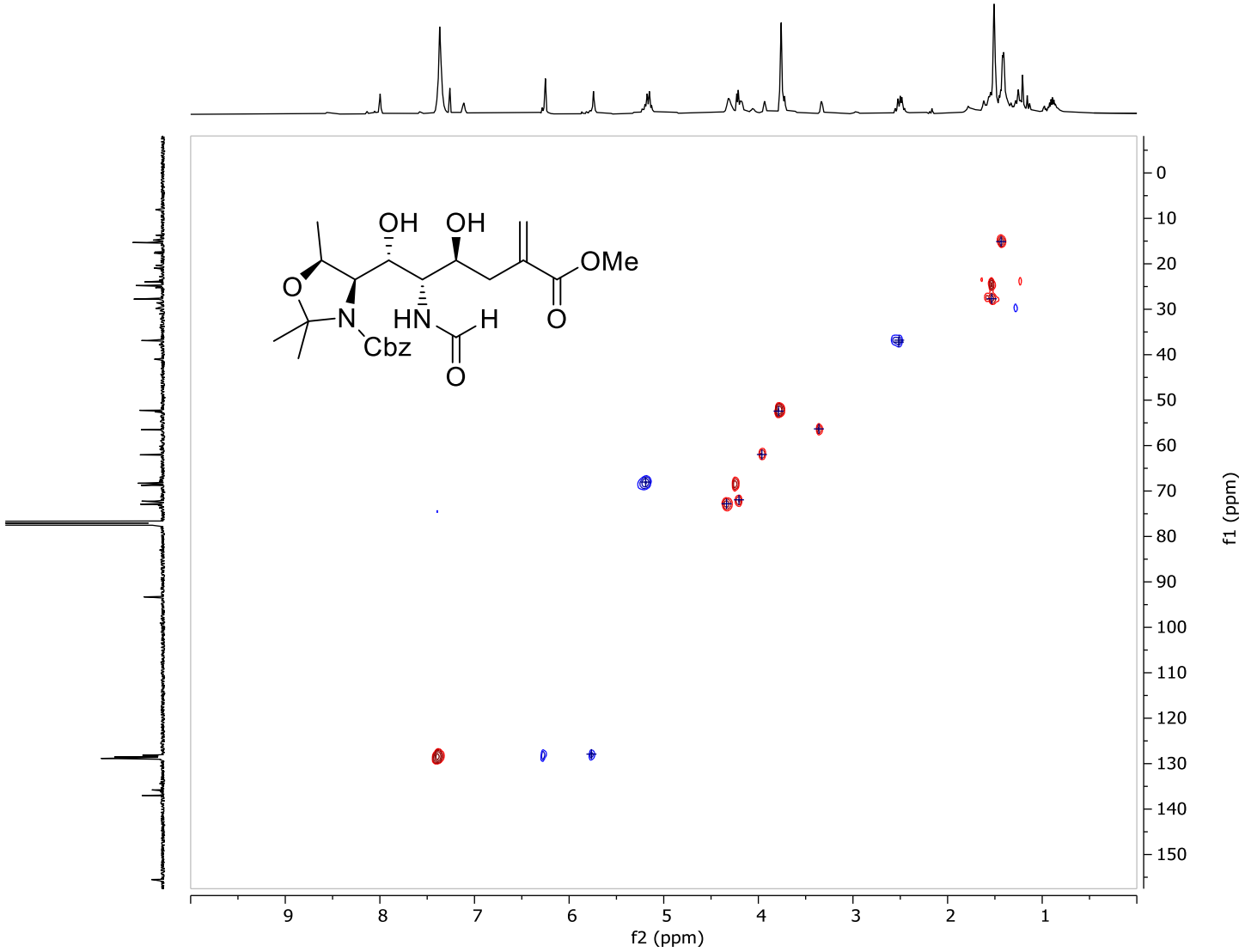
Compound **4.150** ^{13}**C NMR** (126 MHz, $CDCl_3$)



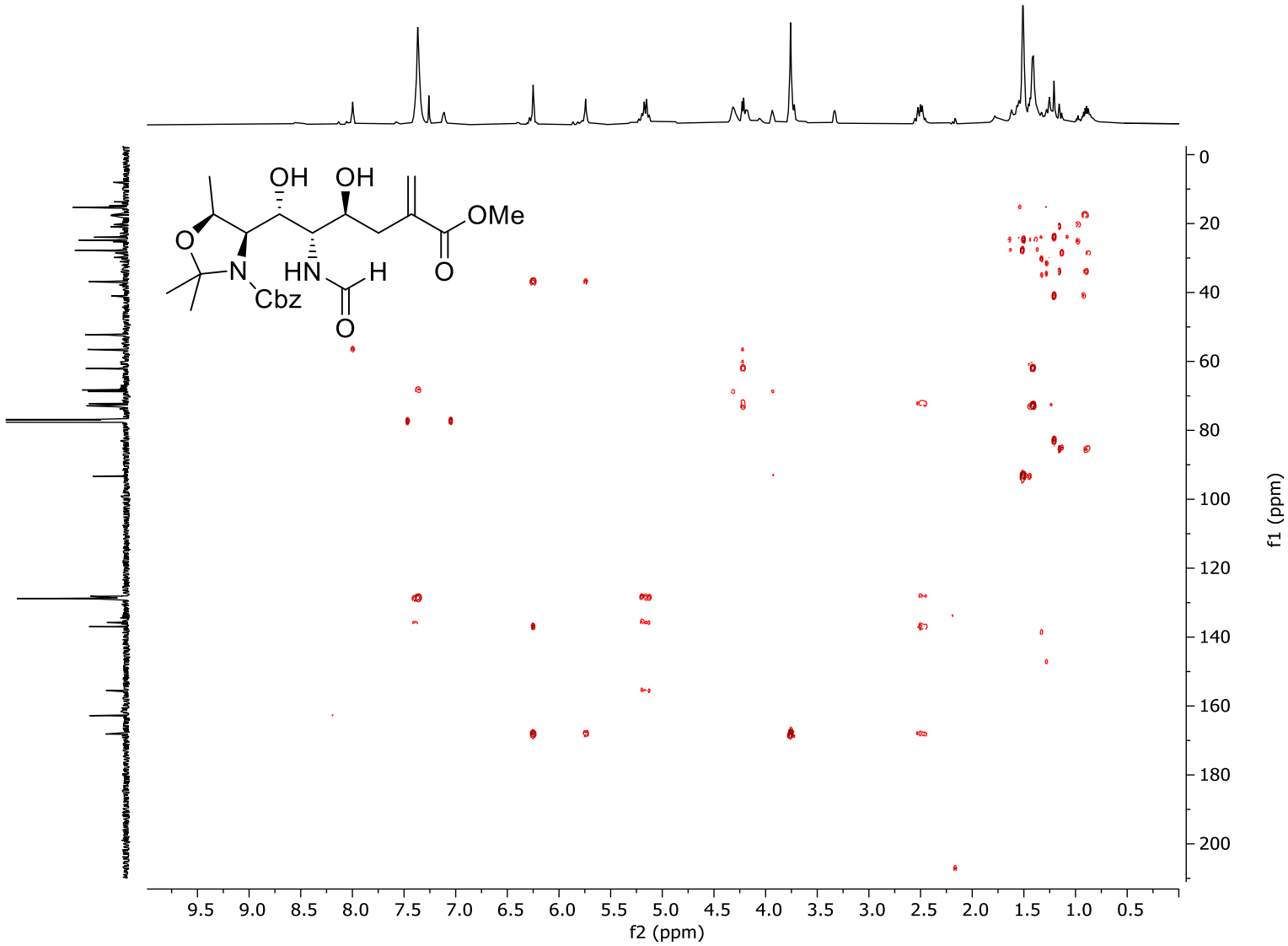
Compound **4.150 COSY** (500 MHz, $CDCl_3$)



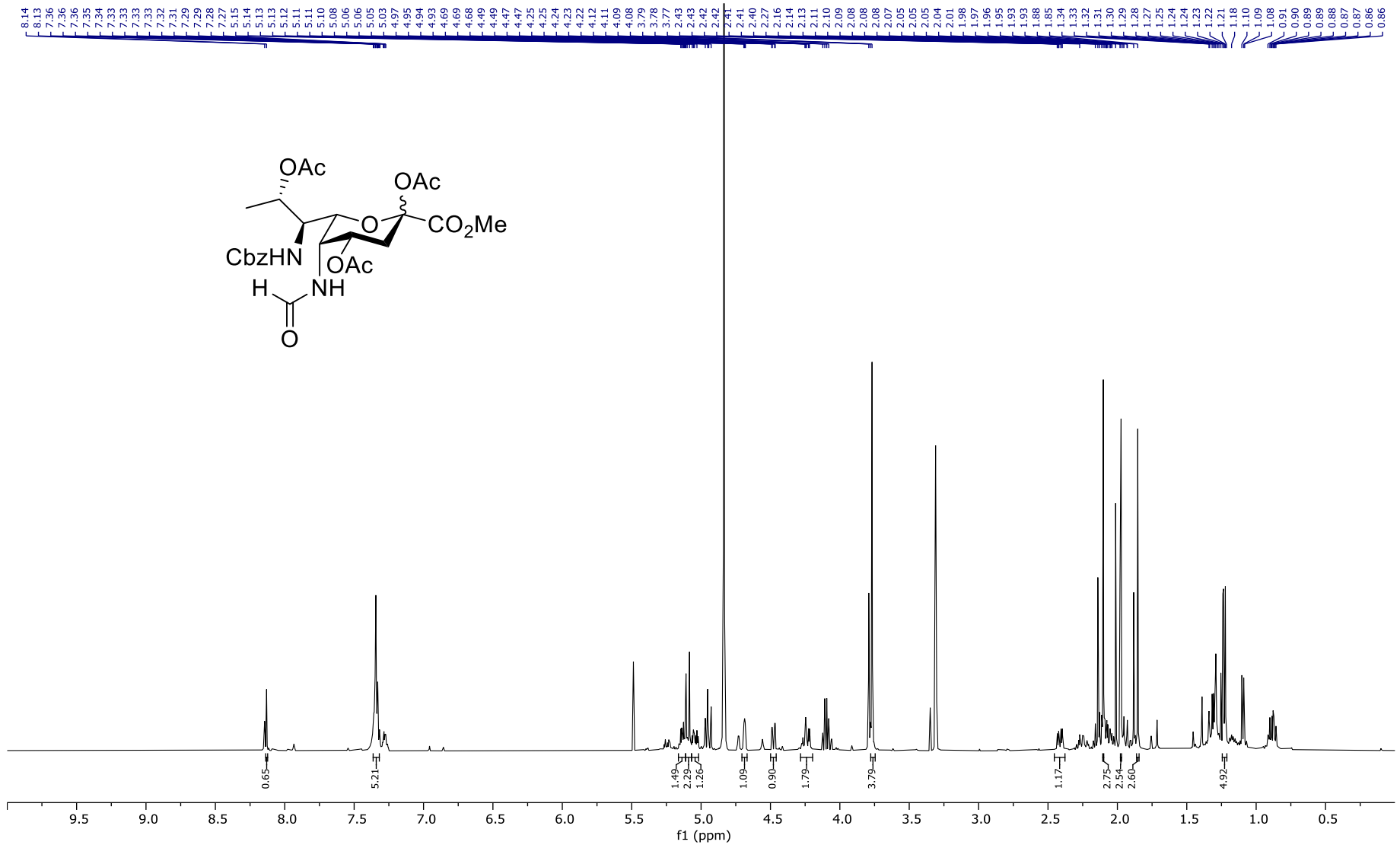
Compound **4.150 HSQC** (500/126 MHz, $CDCl_3$)



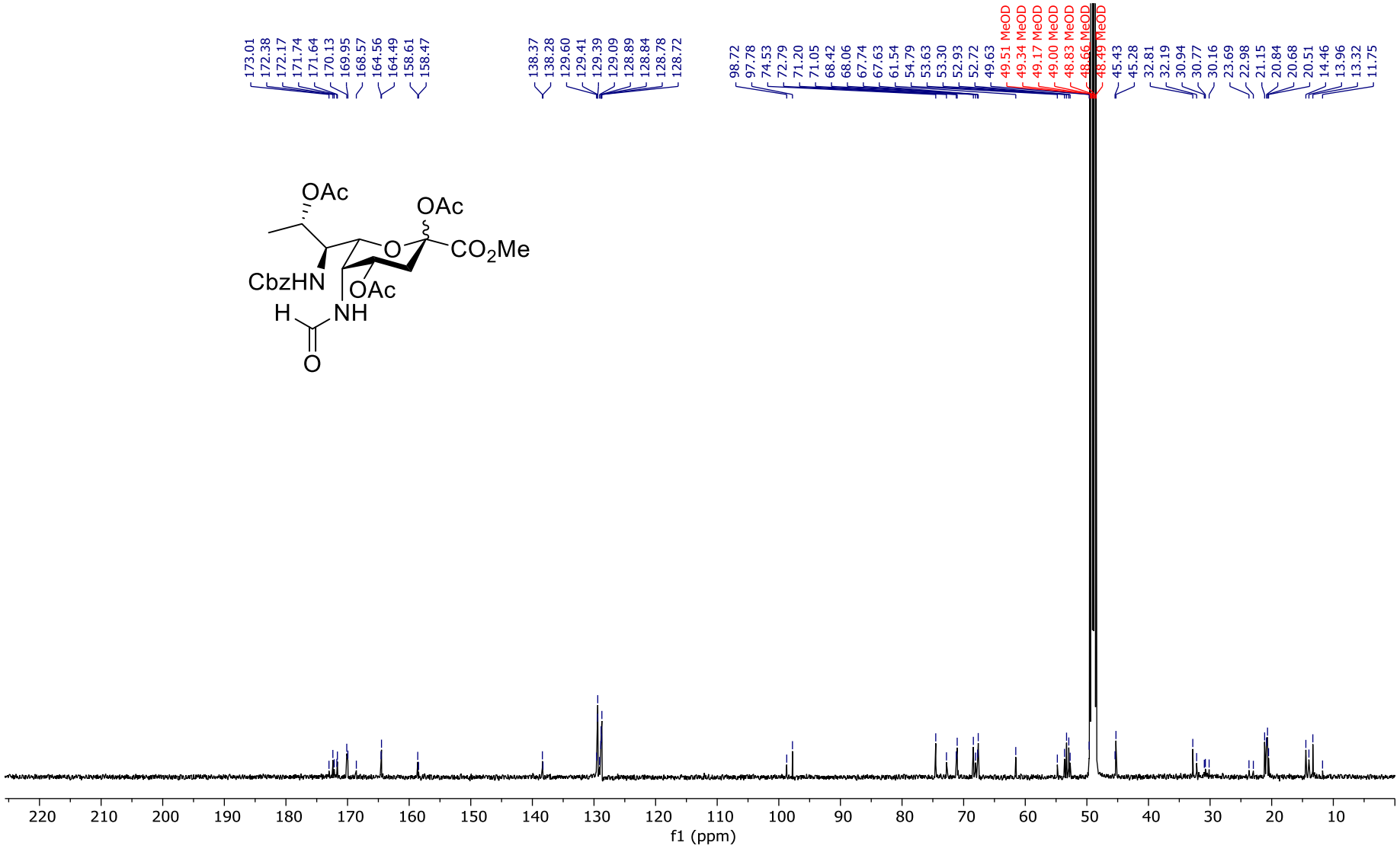
Compound **4.150 HMBC** (500/126 MHz, $CDCl_3$)



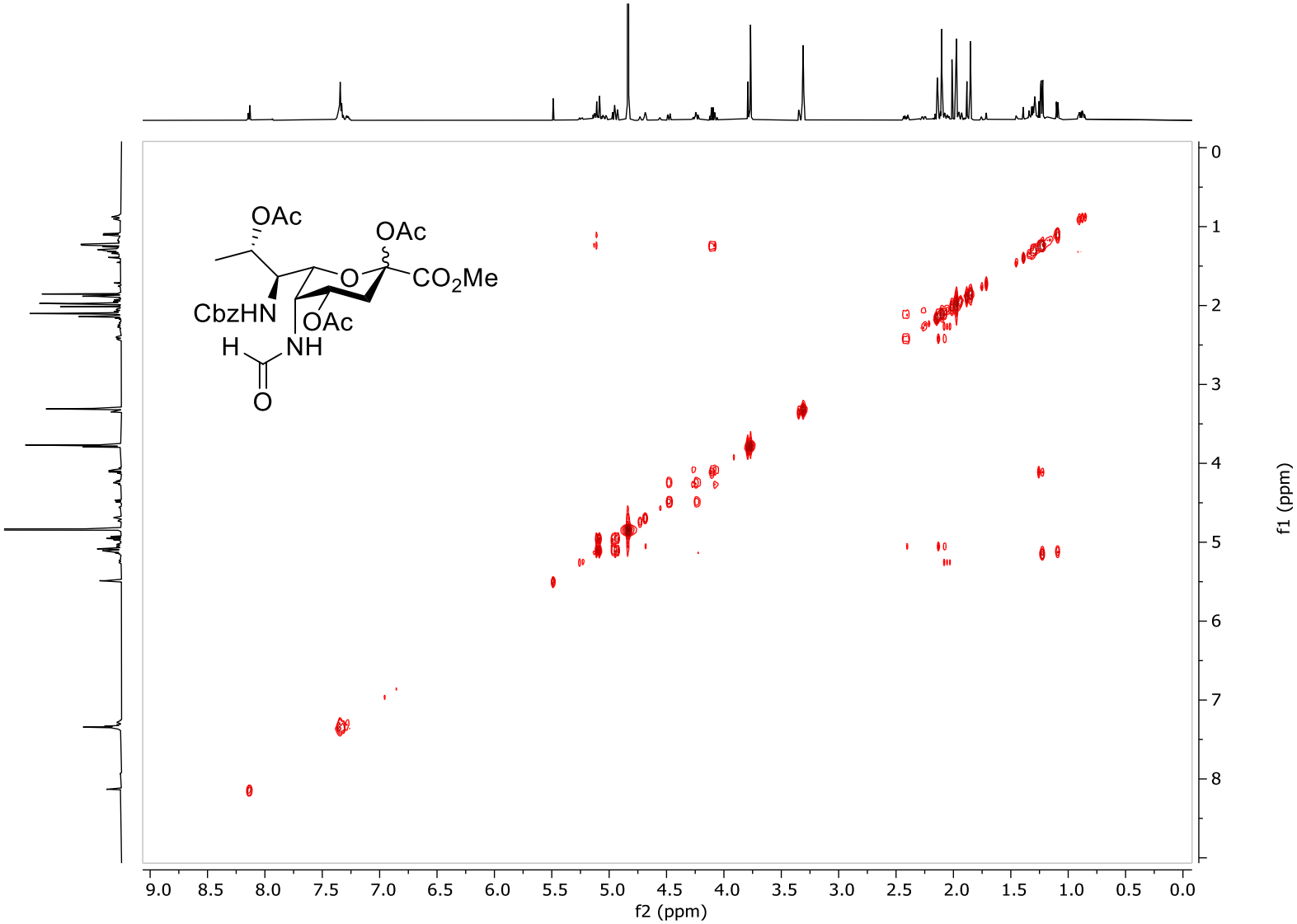
Compound **4.152** **^{1}H NMR** (500 MHz, MeOD)



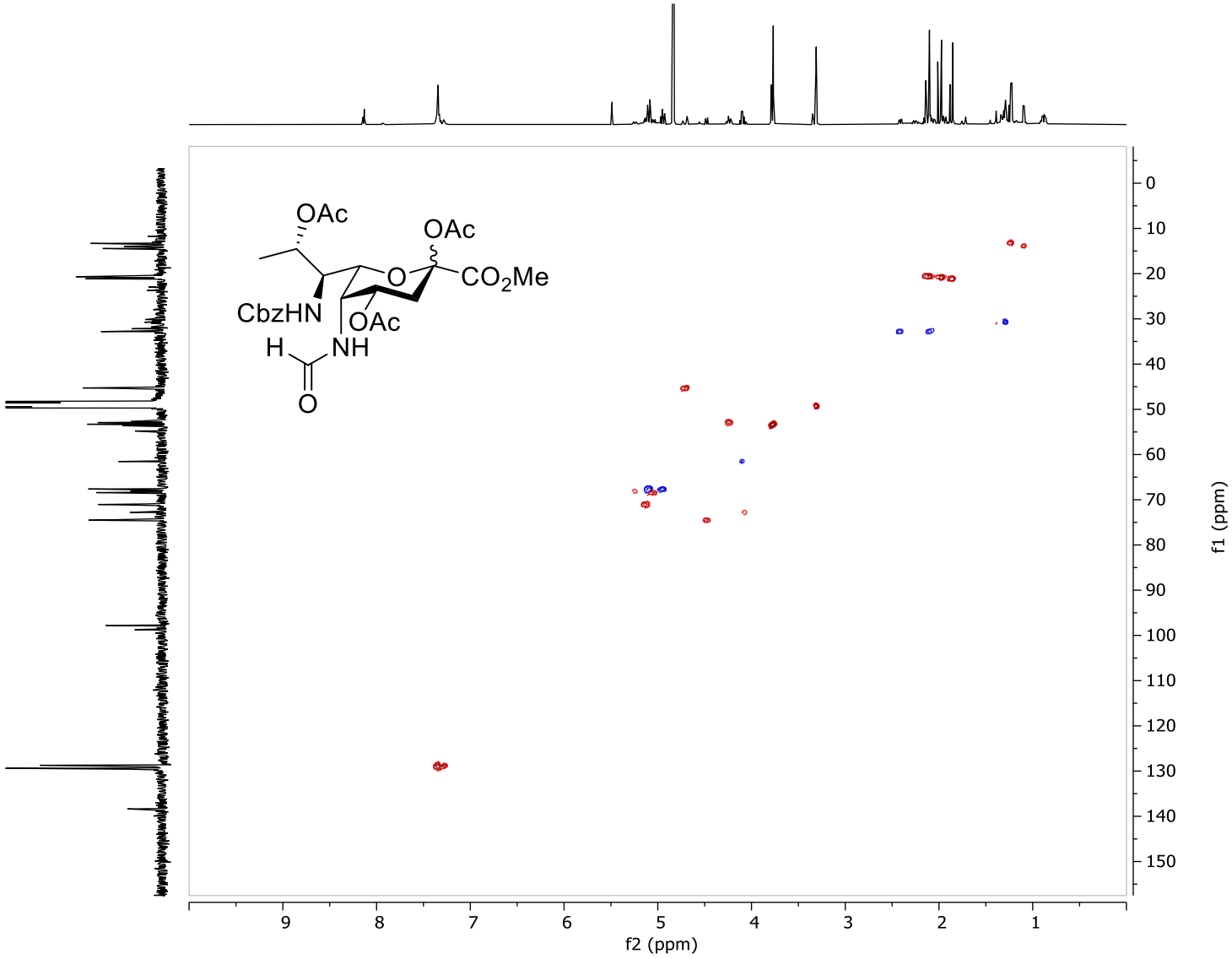
Compound **4.152** **^{13}C NMR** (126 MHz, MeOD)



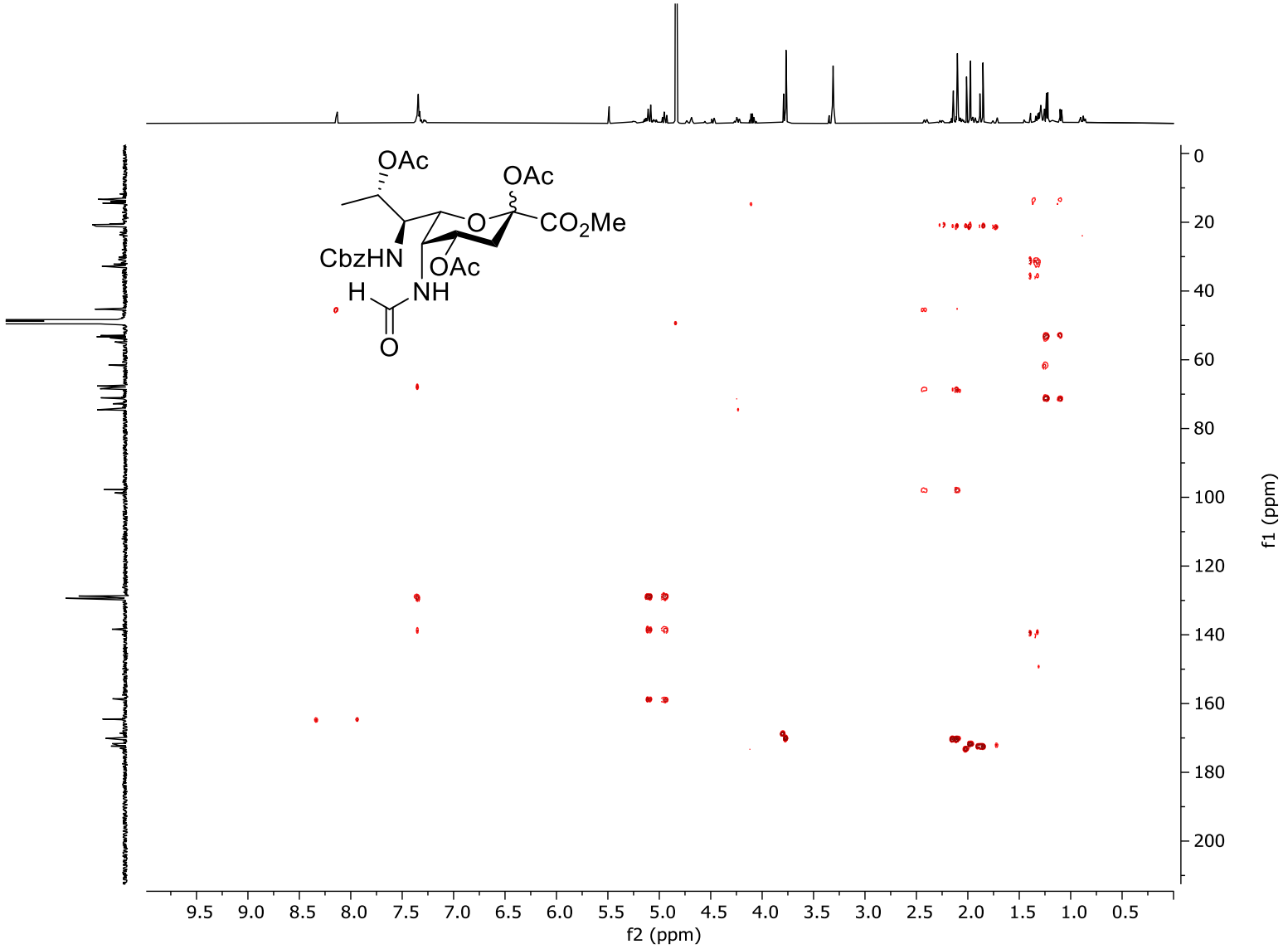
Compound **4.152 COSY** (500 MHz, MeOD)



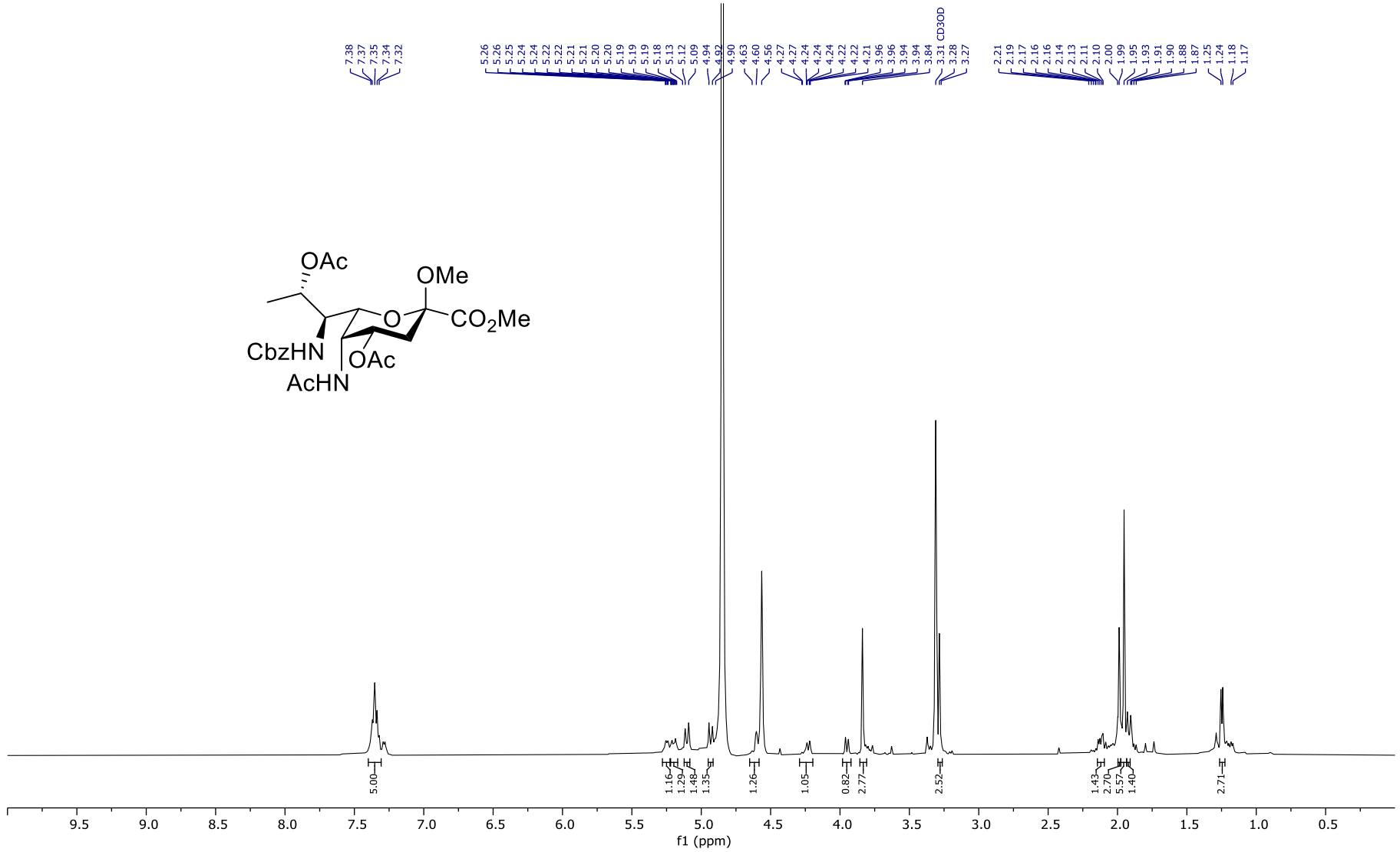
Compound **4.152 HSQC** (500/126 MHz, MeOD)



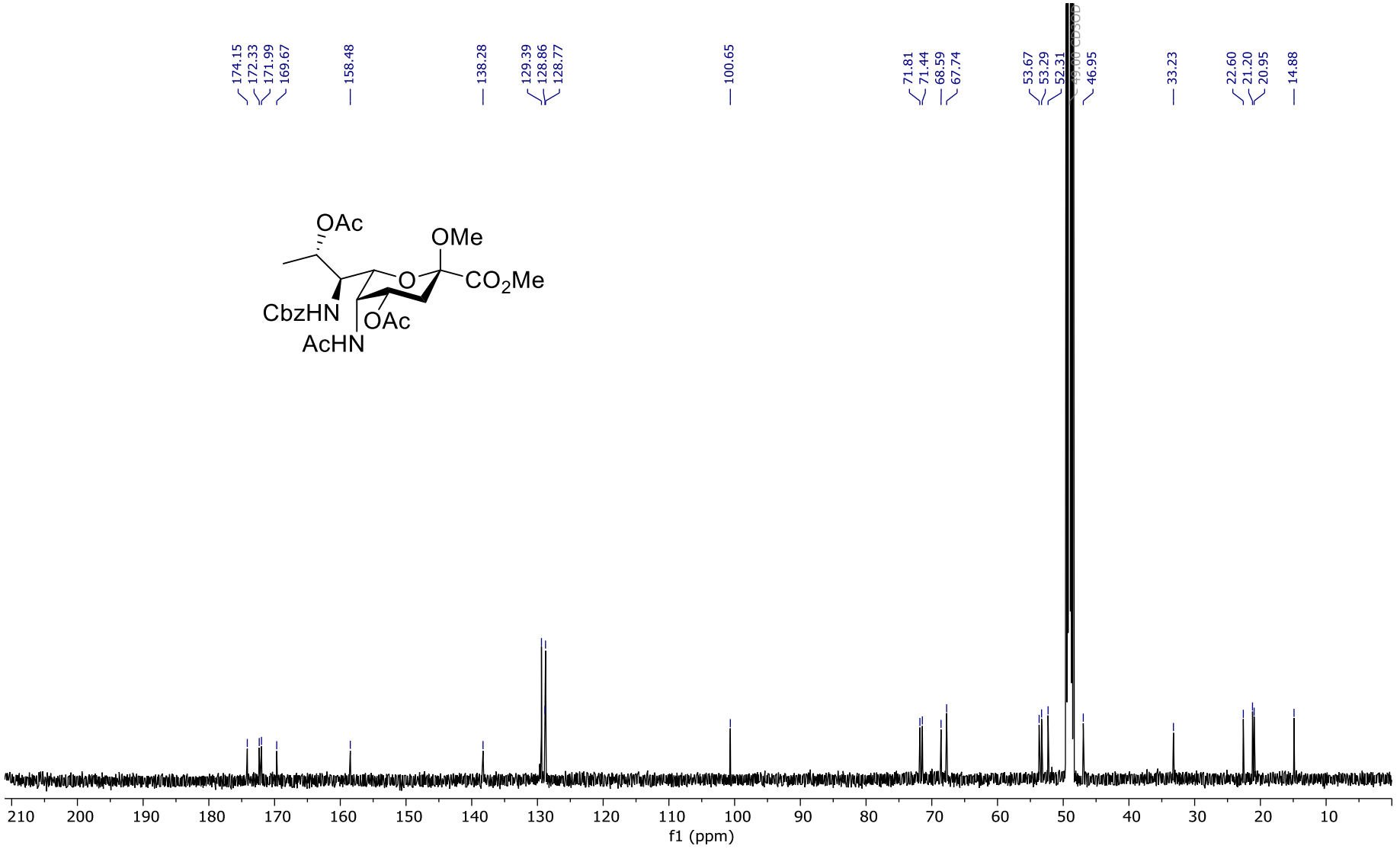
Compound **4.152 HMBC** (500/126 MHz, MeOD)



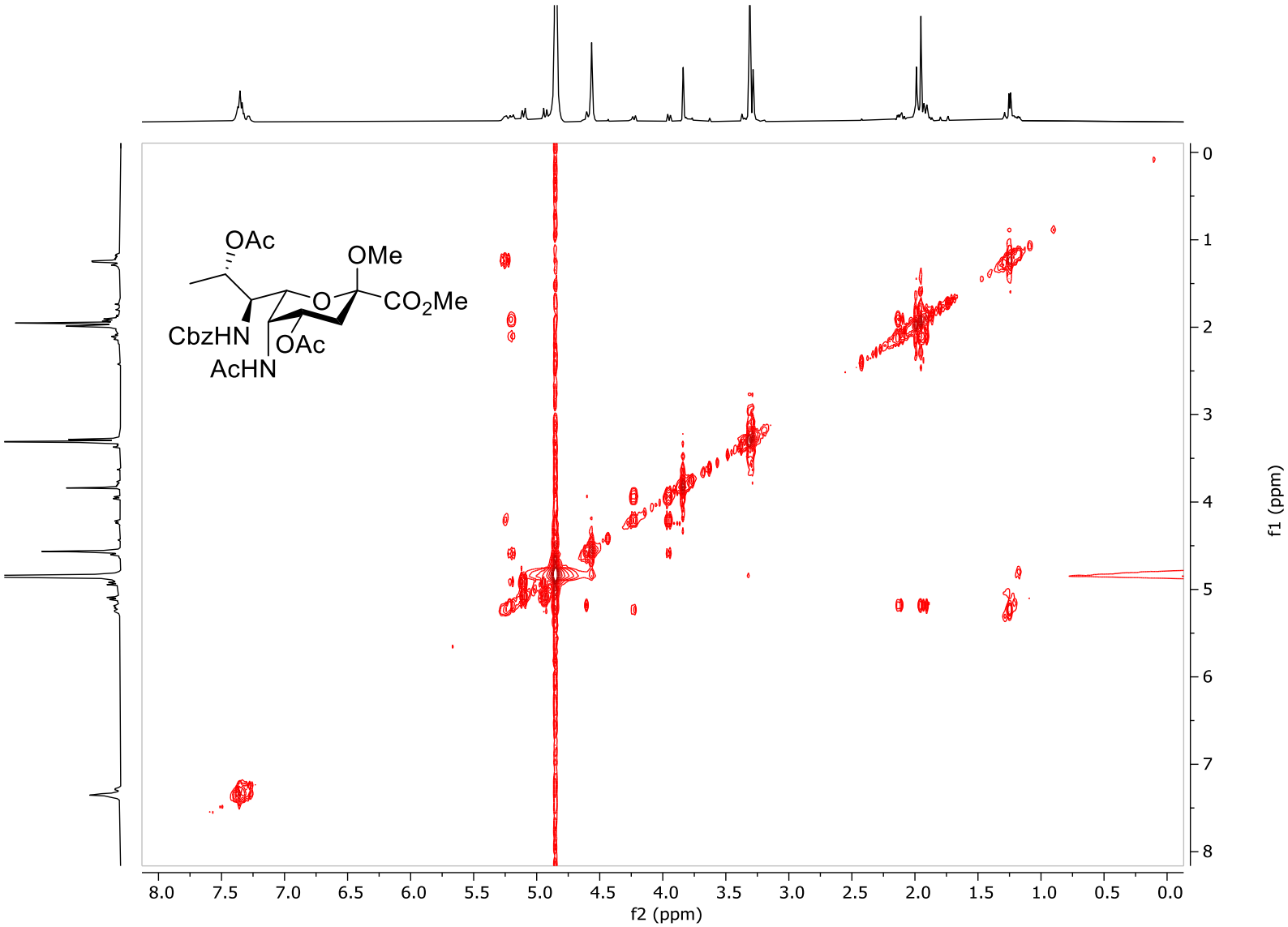
Compound **4.175** ^{1}**H NMR** (500 MHz, MeOD)



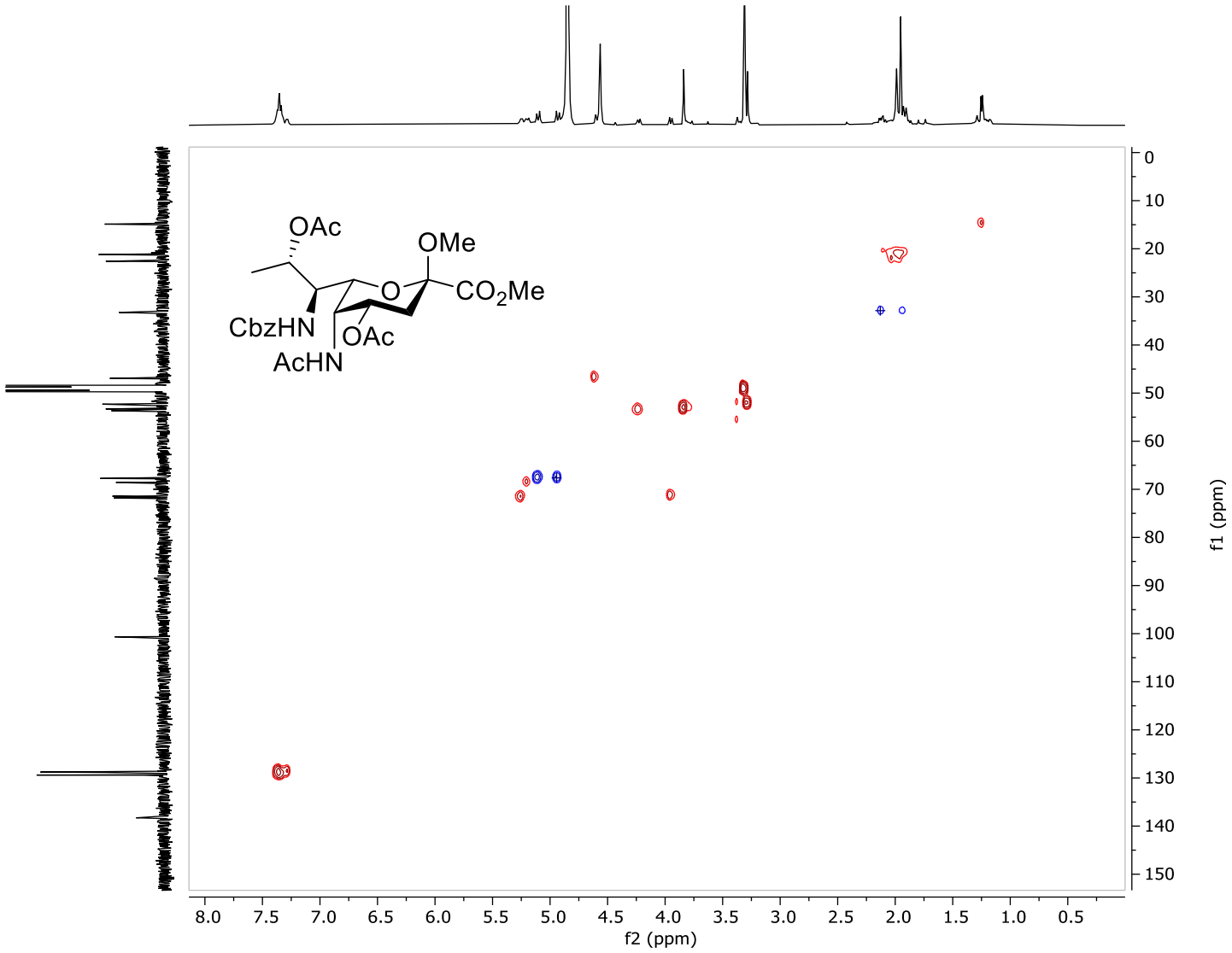
Compound **4.175** **^{13}C NMR** (126 MHz, MeOD)



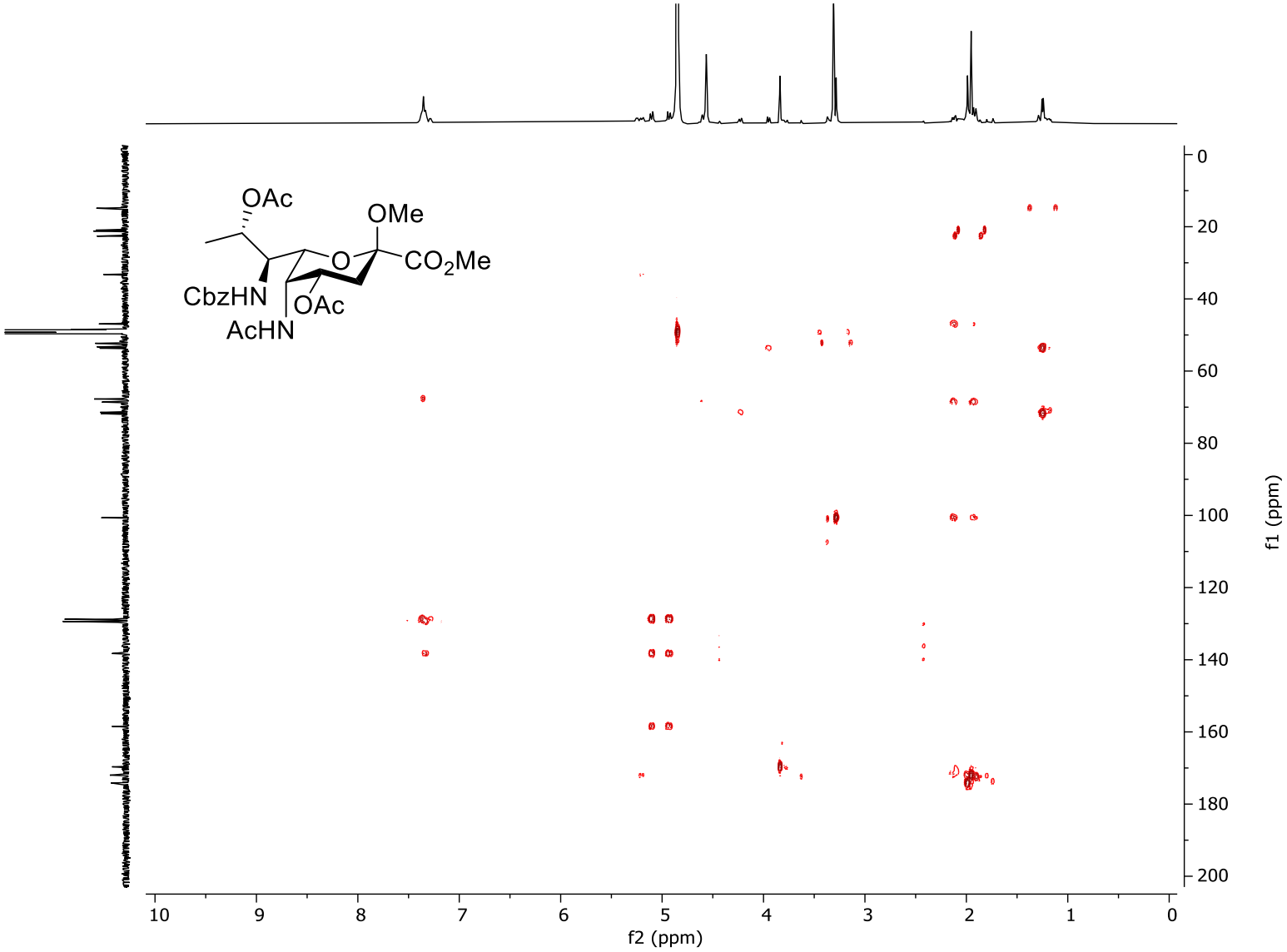
Compound **4.175 COSY** (500 MHz, MeOD)



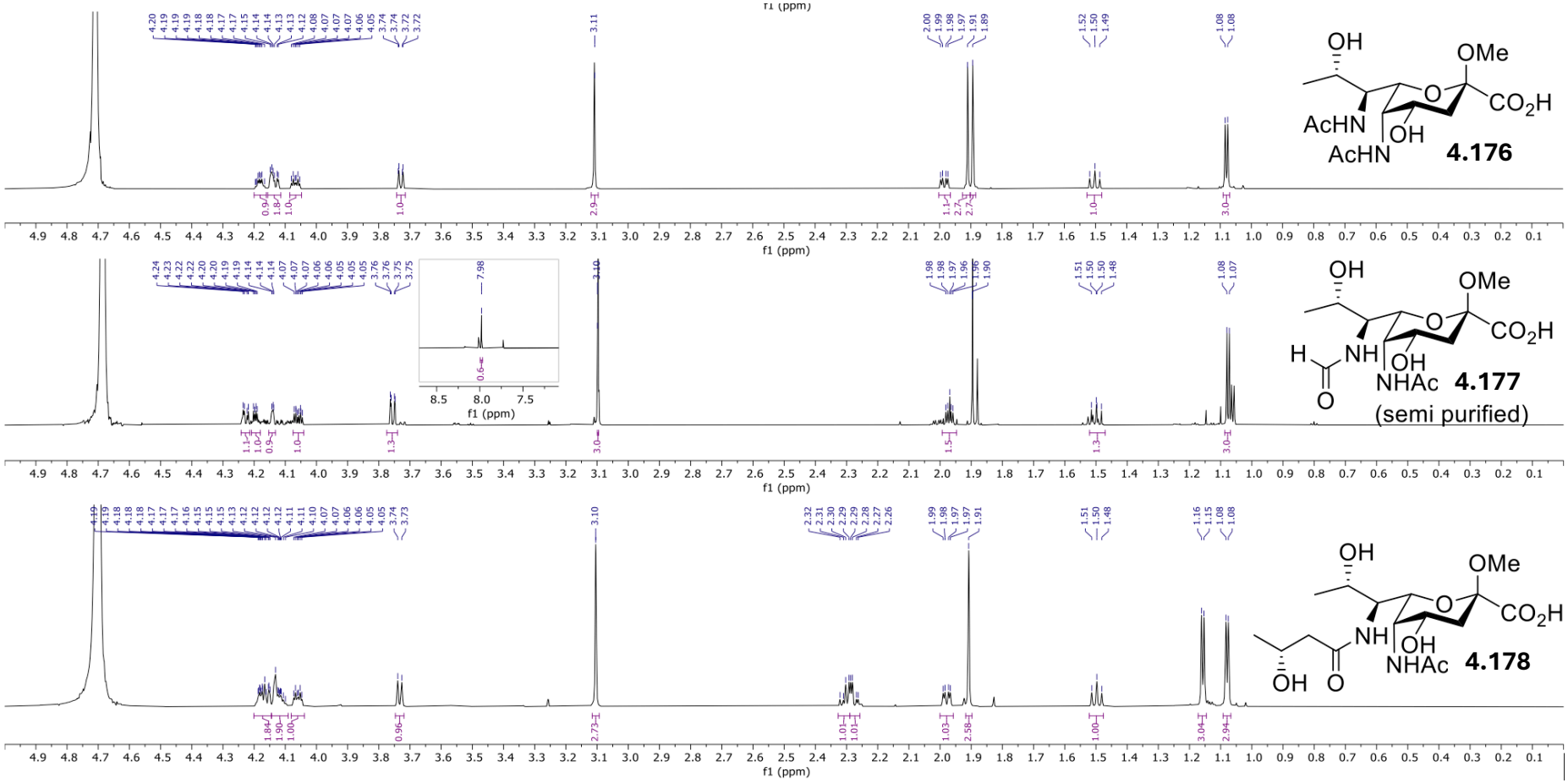
Compound **4.175 HSQC** (500/126 MHz, MeOD)



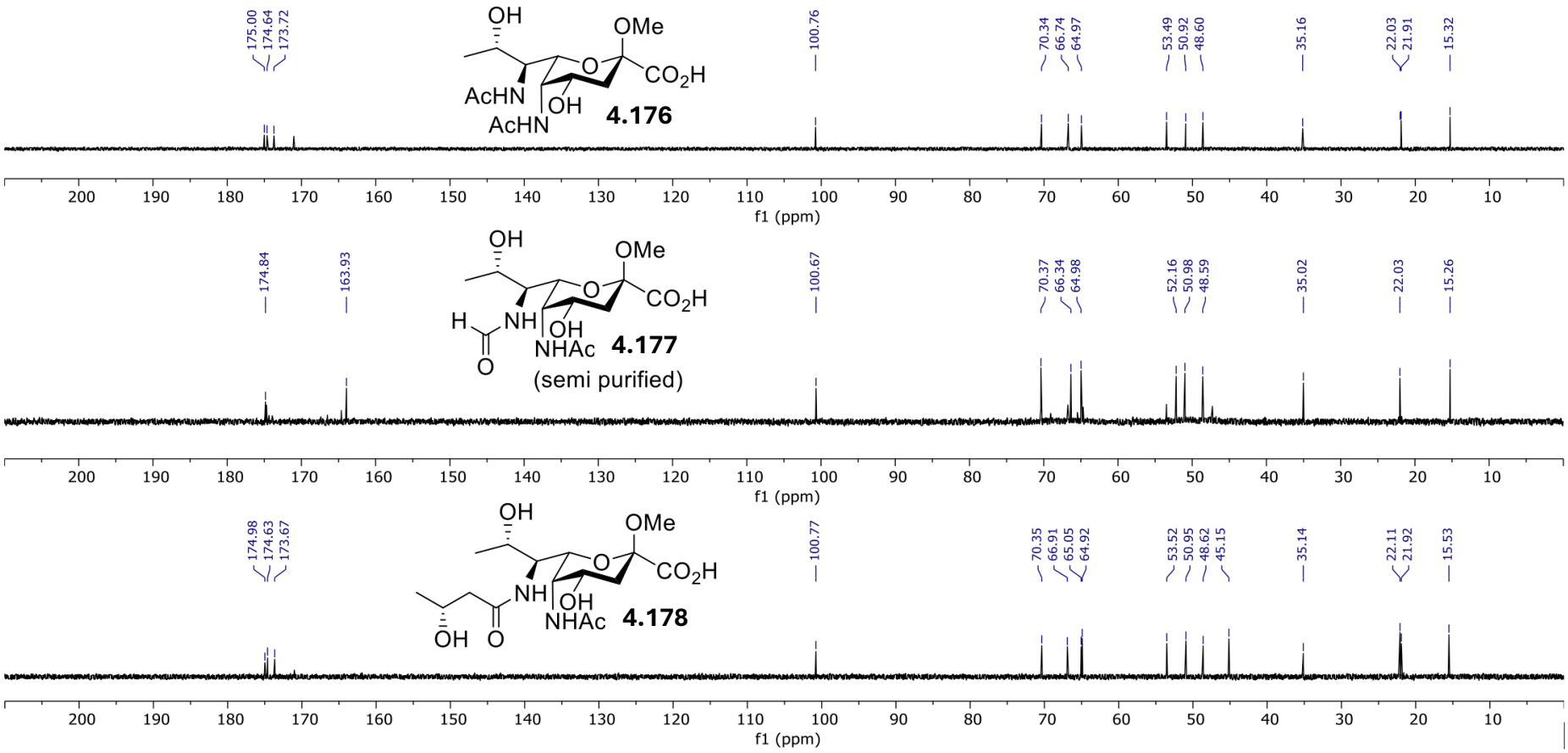
Compound **4.175 HMBC** (500/126 MHz, MeOD)



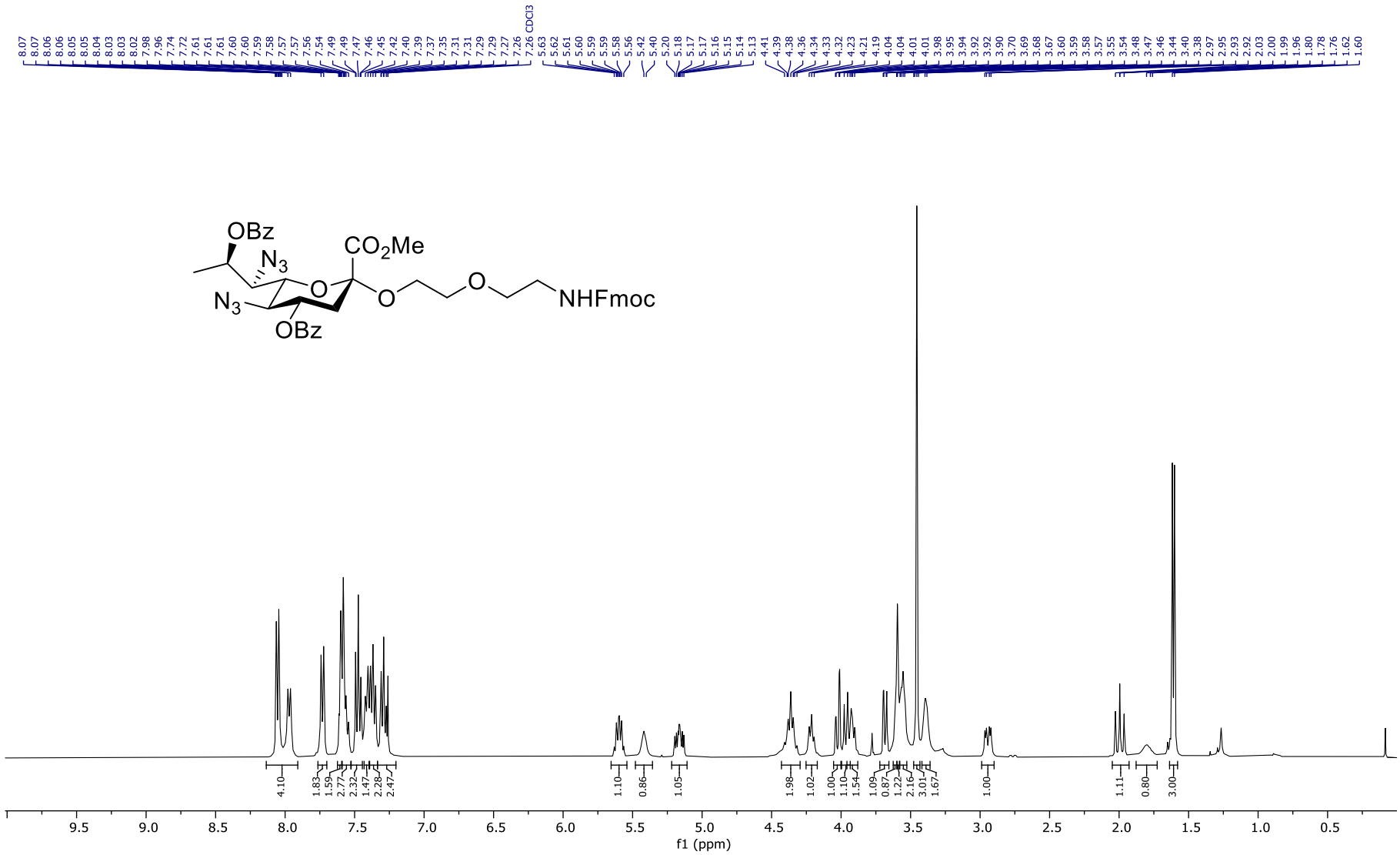
Pse5Ac7x methyl glycosides **4.176-4.178 ^{1}H NMRs** (800 MHz, D_2O)



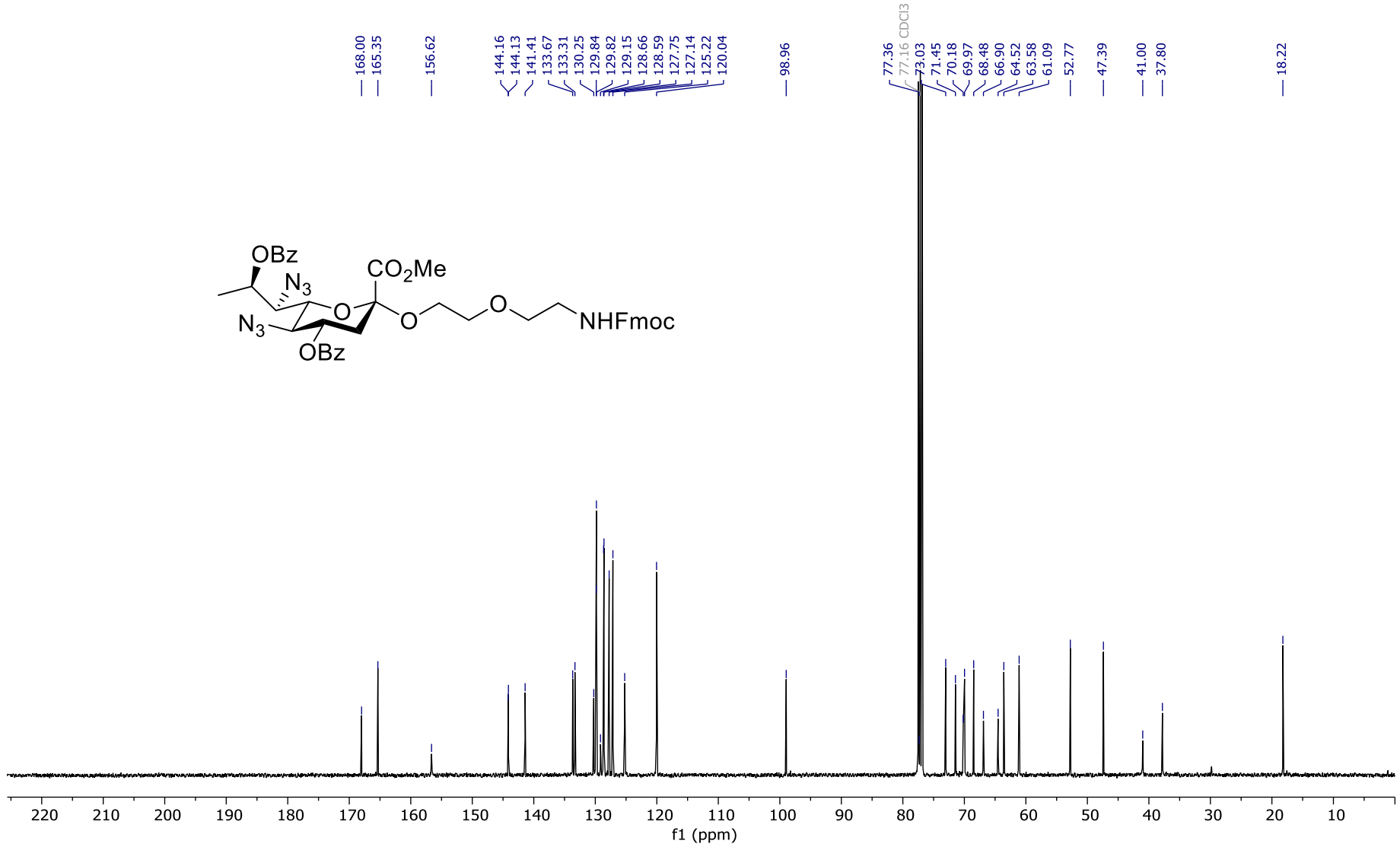
Pse5Ac7X methyl glycosides **4.176-4.178 ^{13}C NMRs** (200 MHz, D_2O)



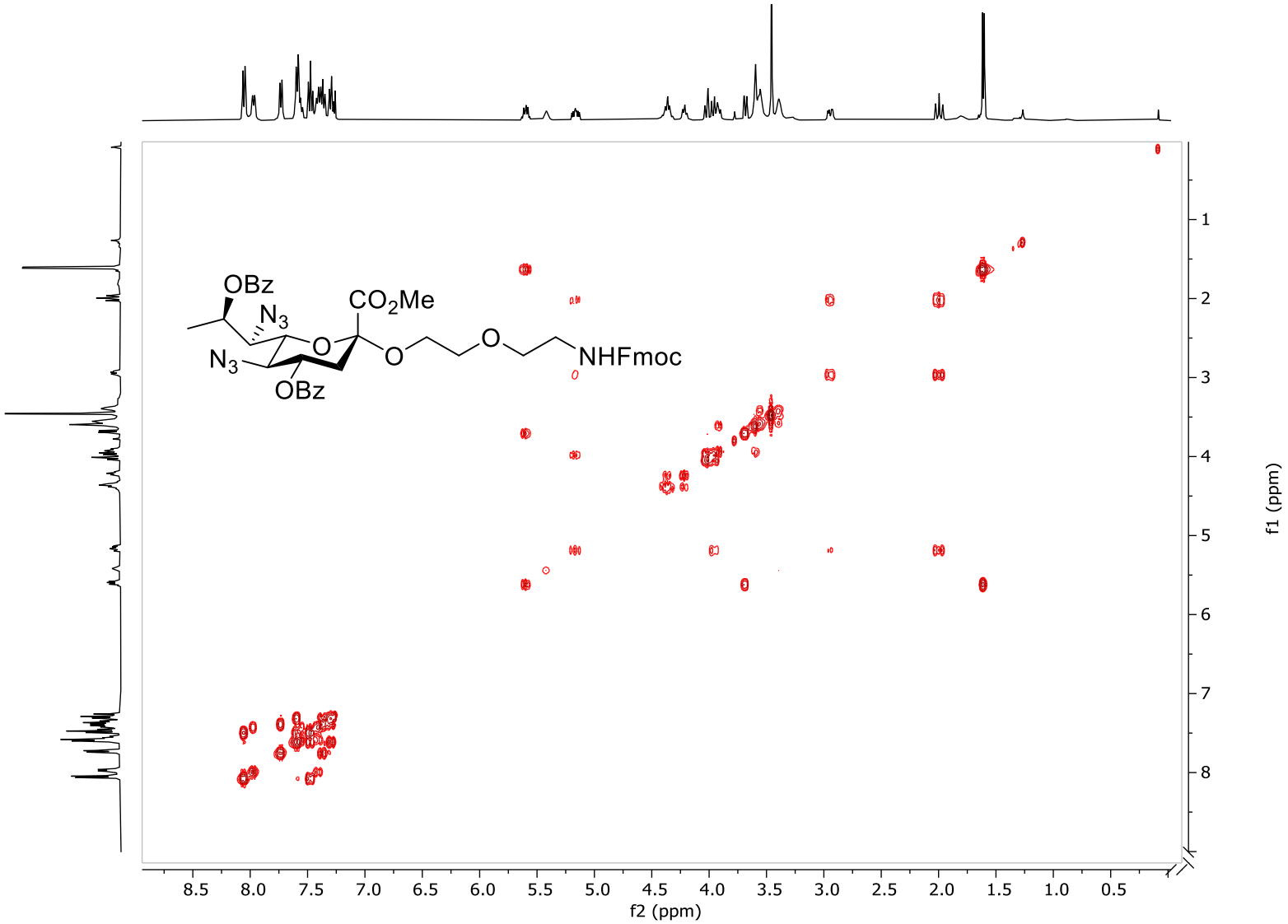
Compound **5.64 ^{1}H NMR** (400 MHz, $CDCl_3$)



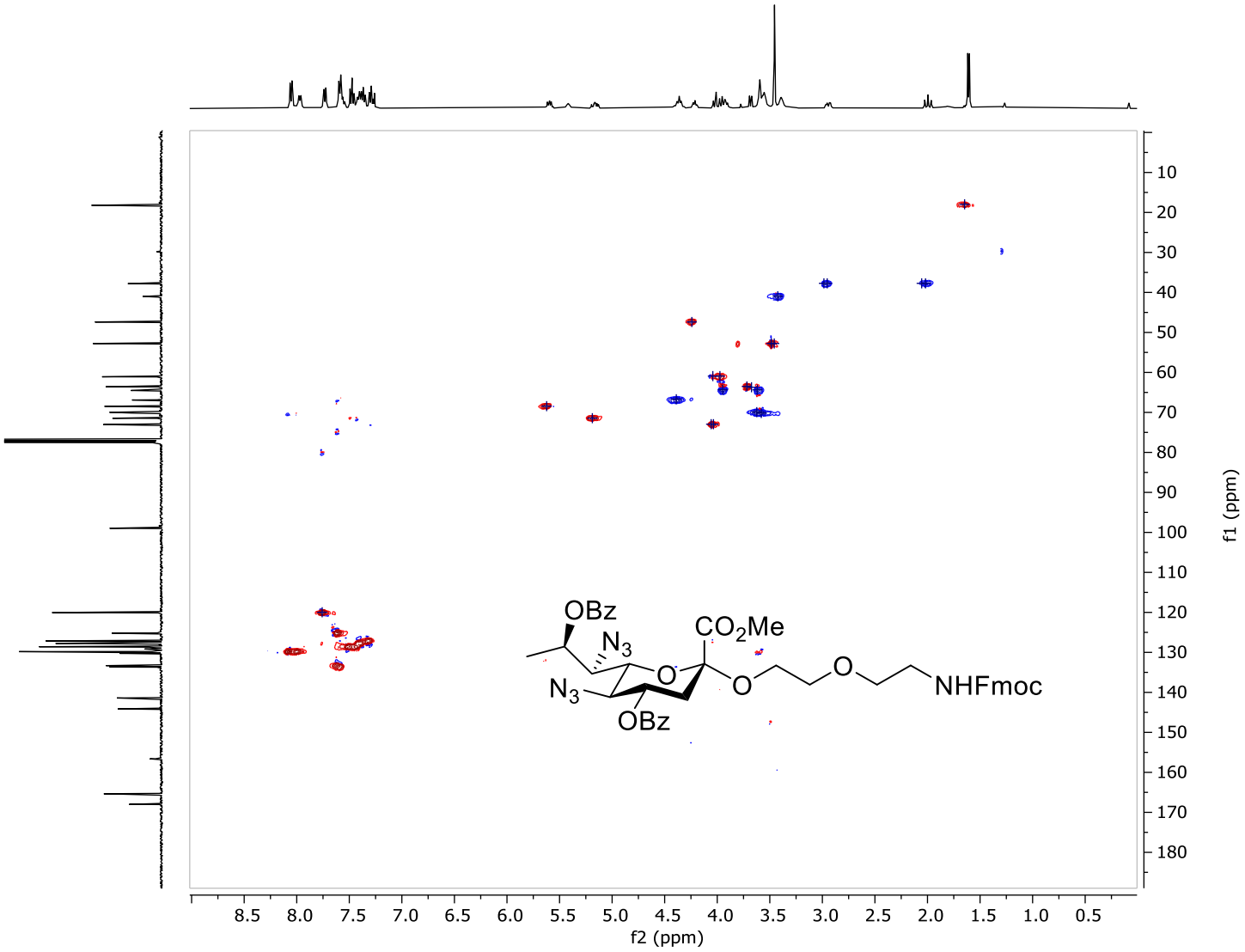
Compound **5.64** **^{13}C NMR** (101 MHz, $CDCl_3$)



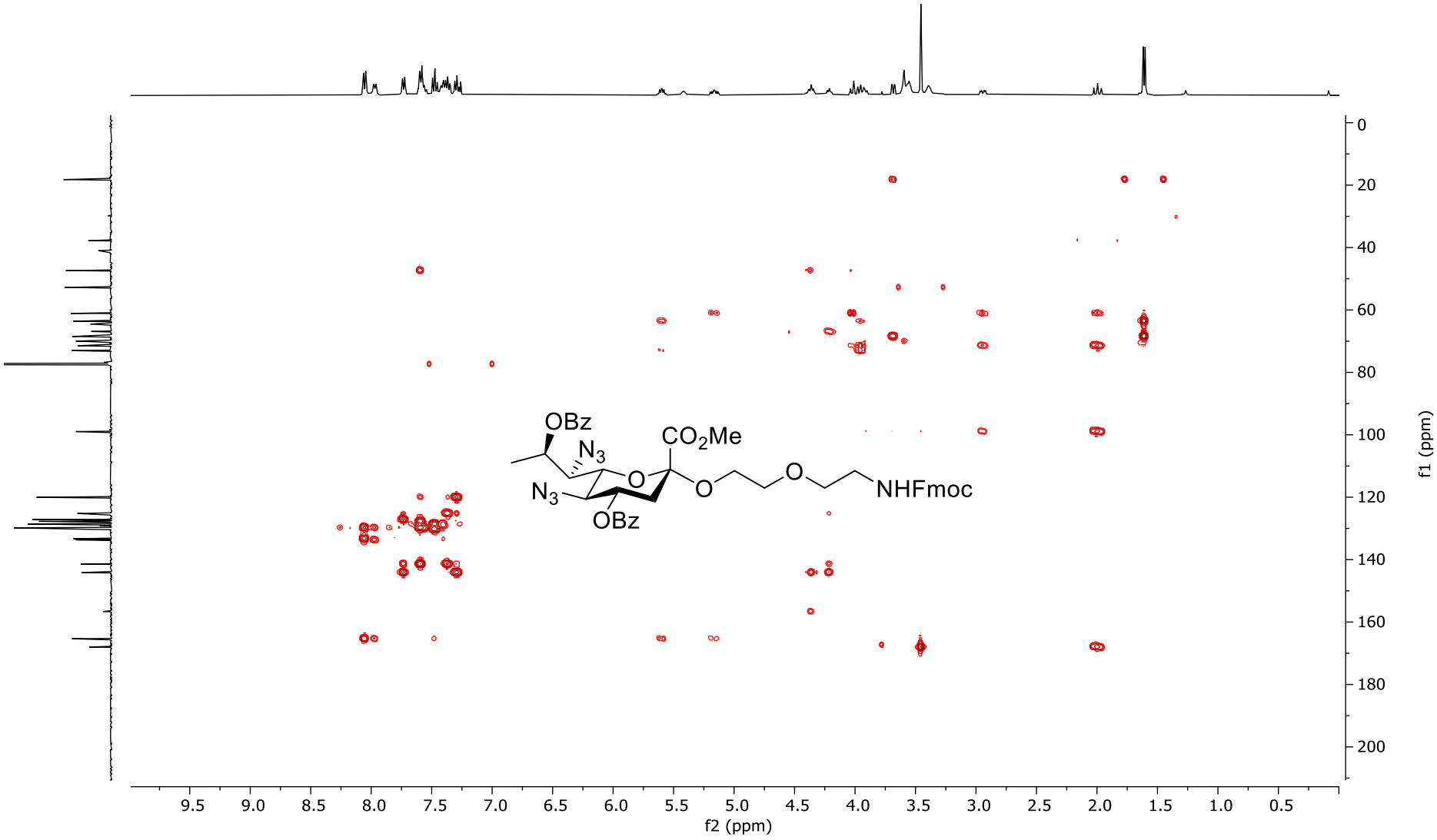
Compound **5.64 COSY** (400 MHz, $CDCl_3$)



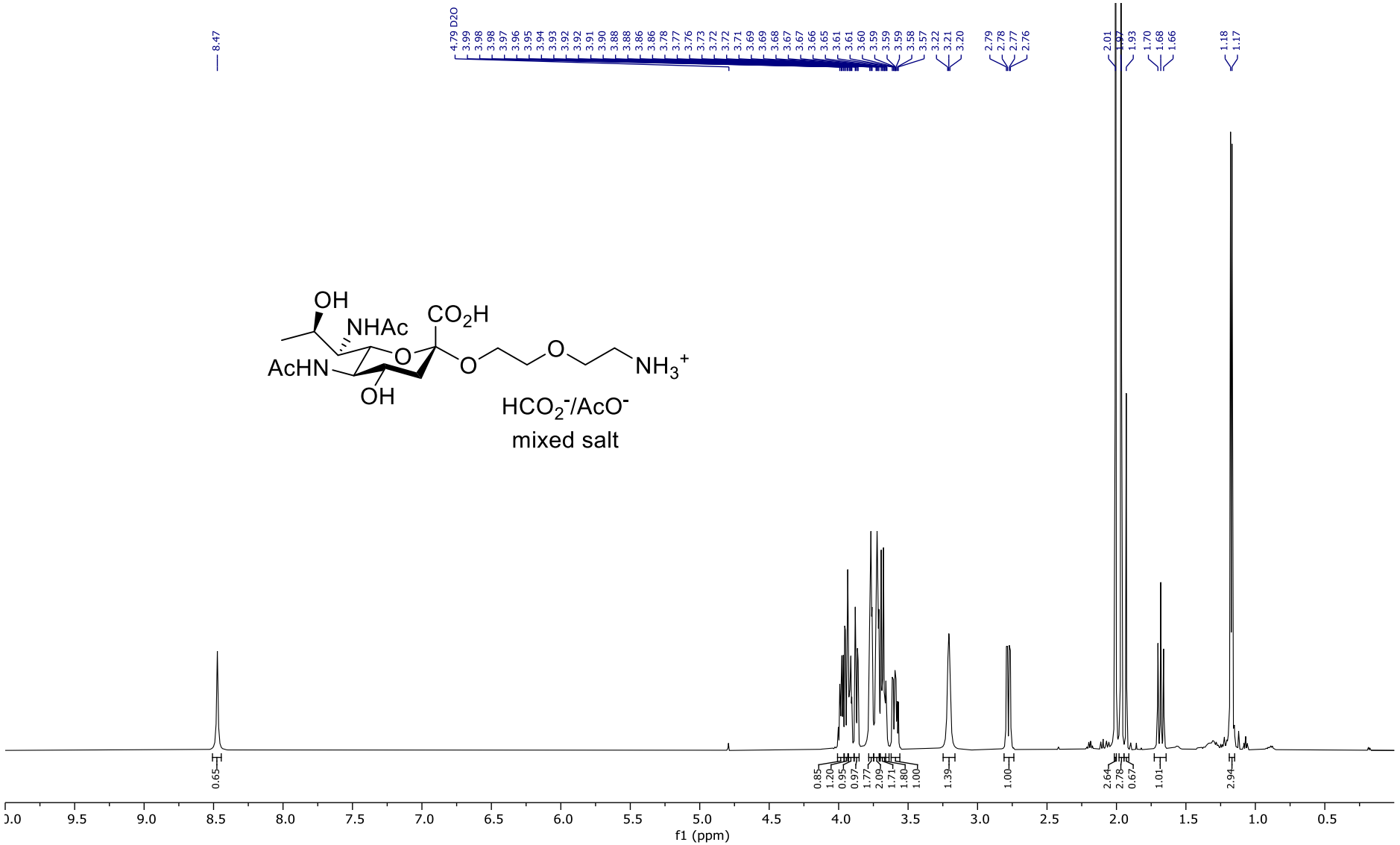
Compound **5.64 HSQC** (400/101 MHz, $CDCl_3$)



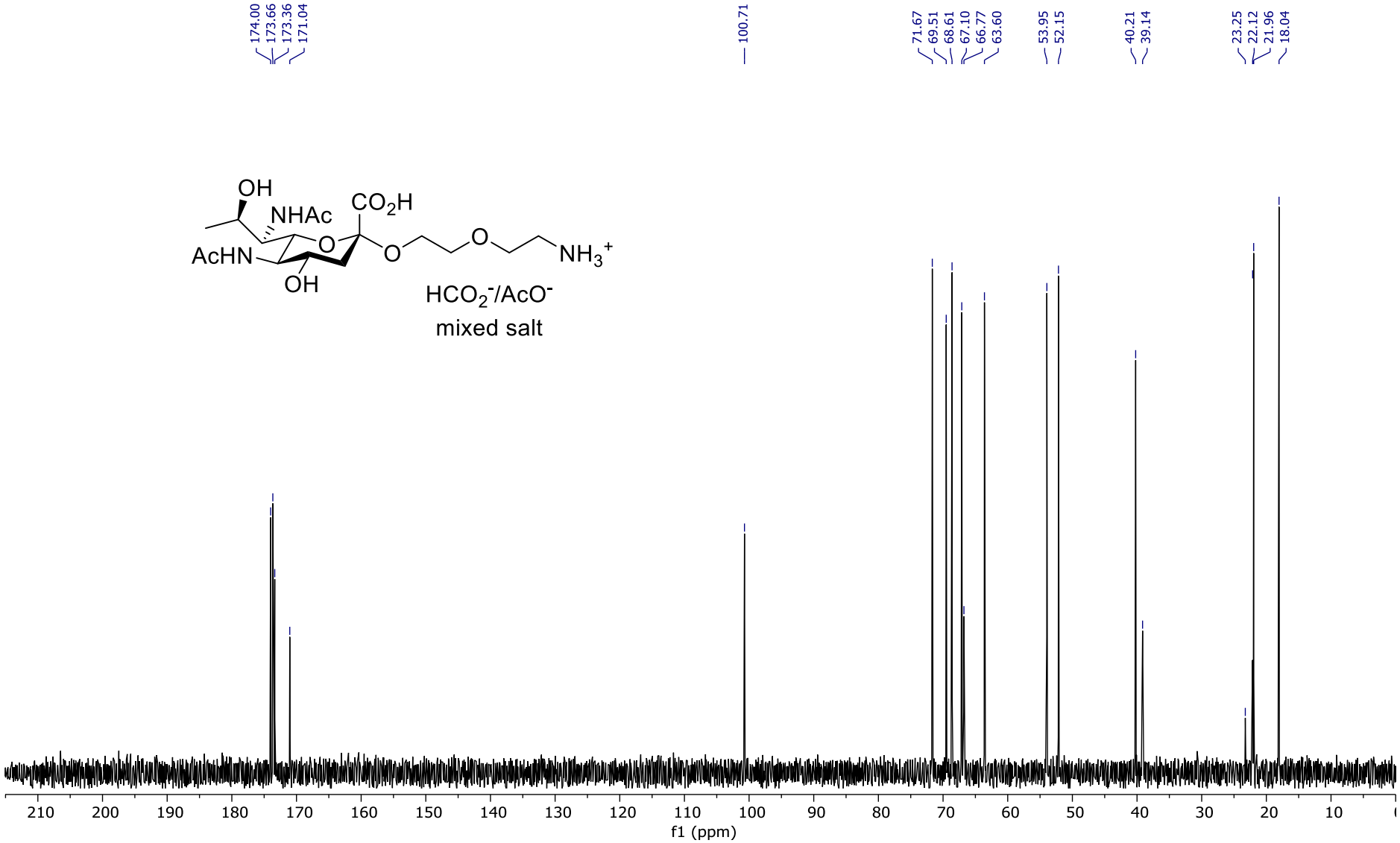
Compound **5.64 HMBC** (400/101 MHz, D_2O)



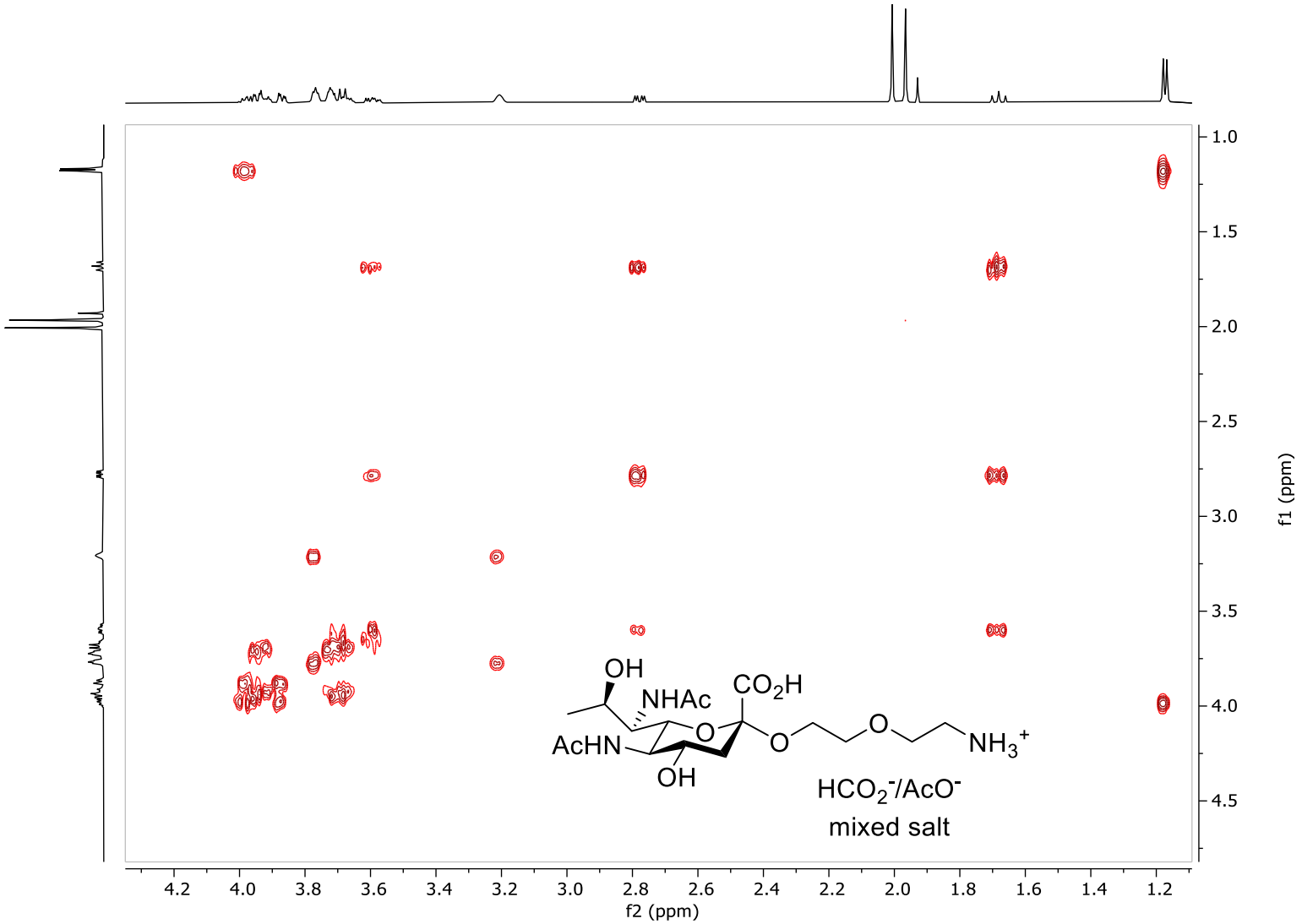
Compound **5.66** **^{1}H NMR** (600 MHz, D_2O)



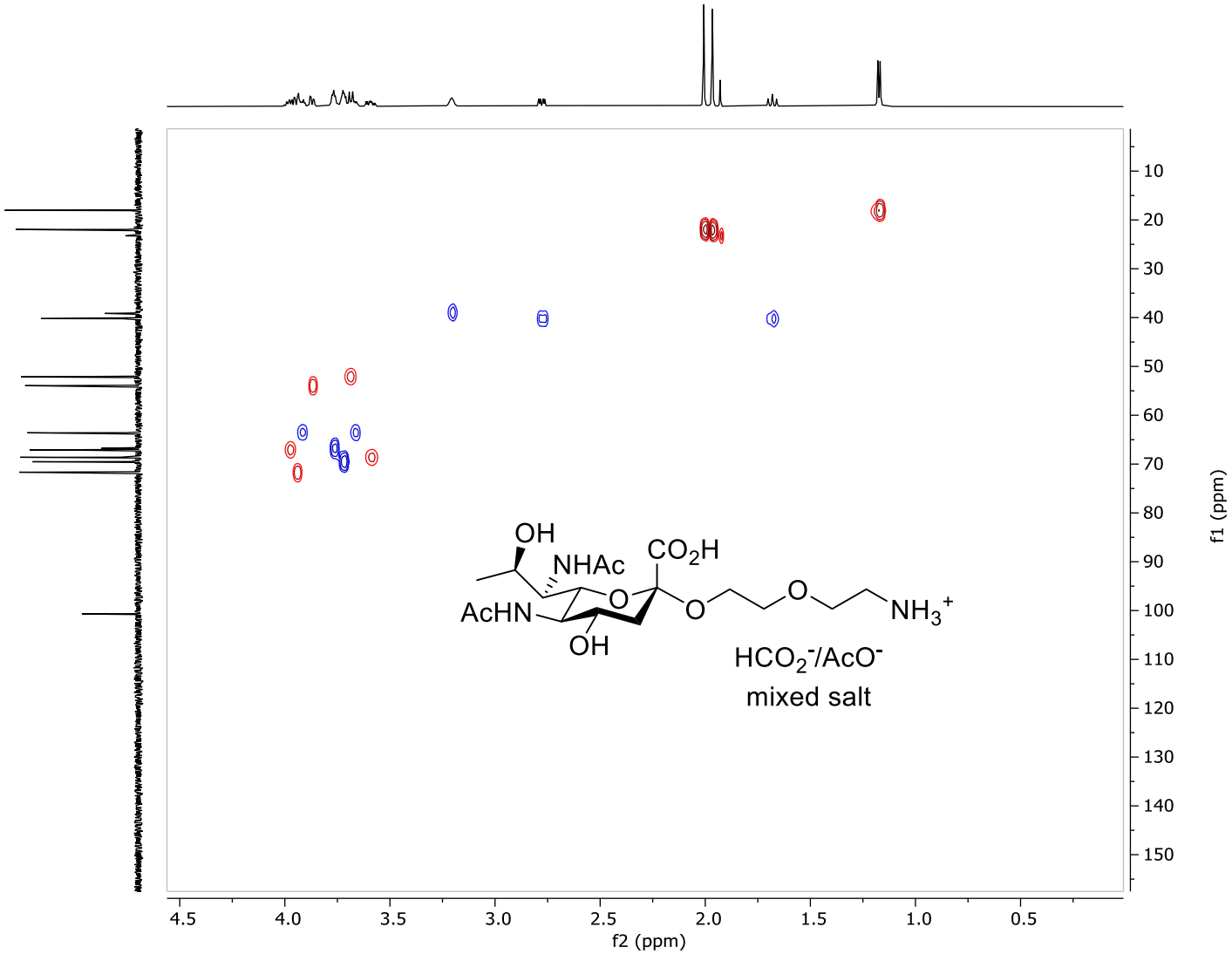
Compound **5.66** ^{13}**C NMR** (151 MHz, D_2O)



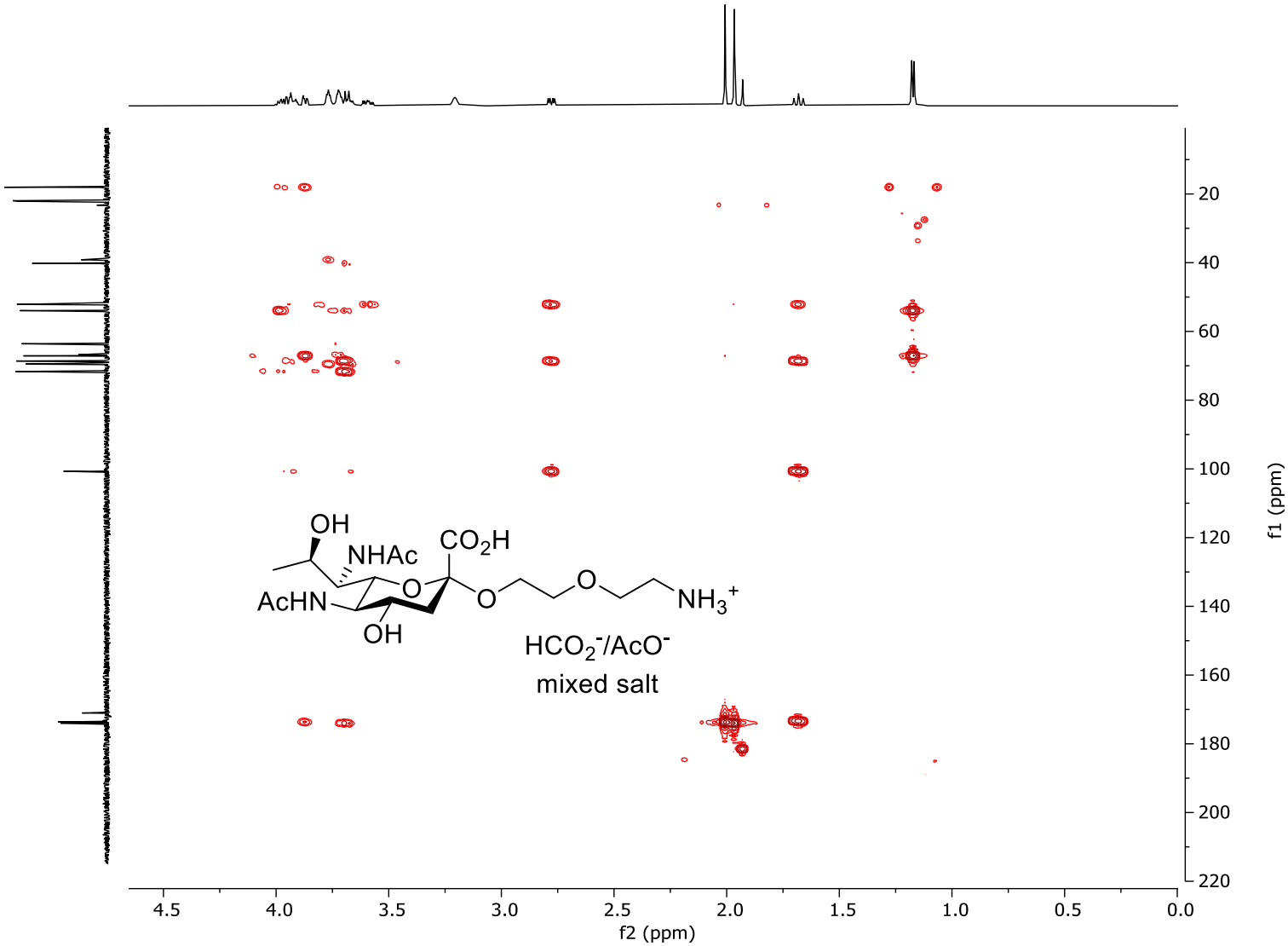
Compound **5.66 COSY** (600 MHz, D_2O)



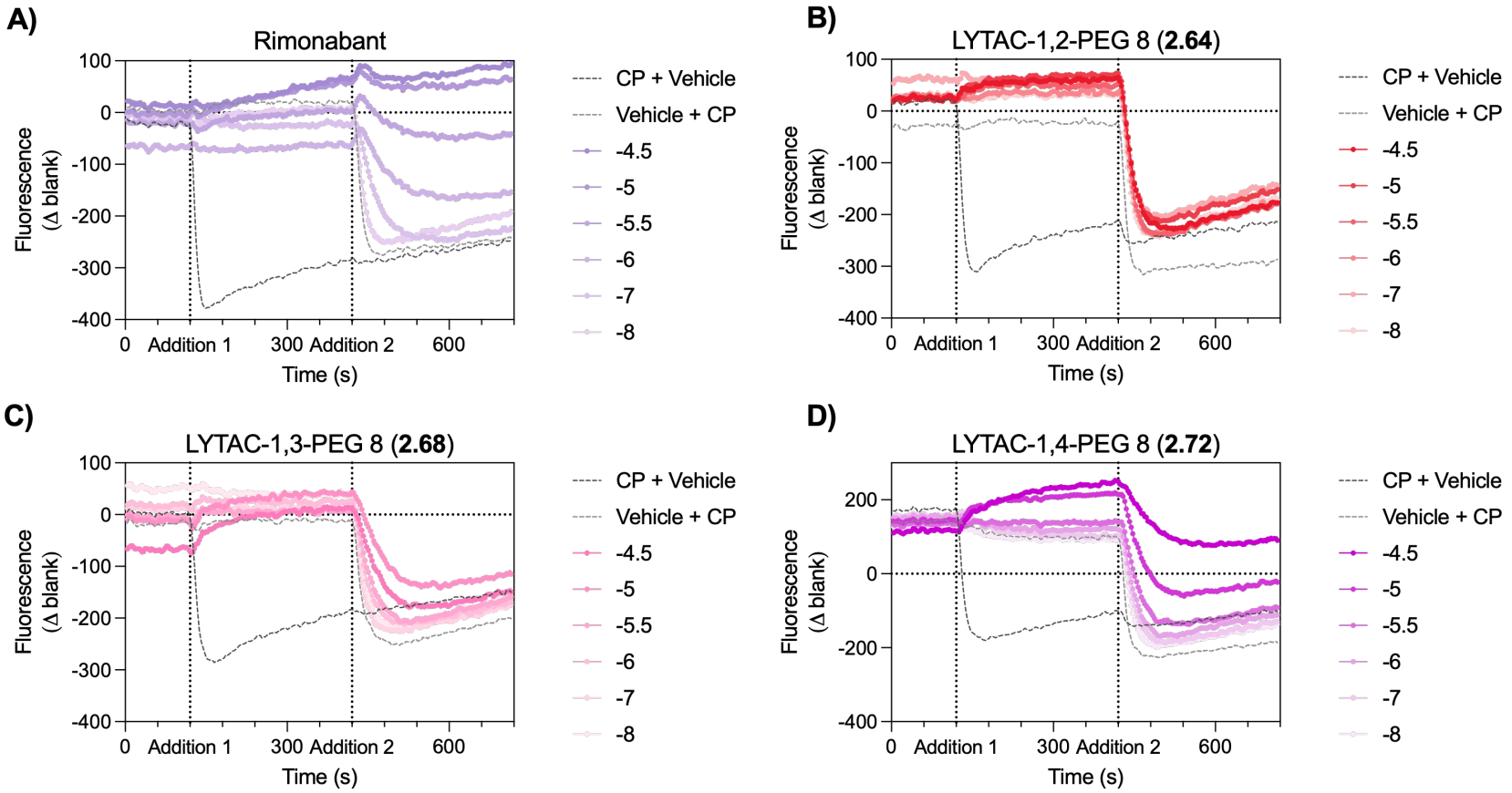
Compound **5.66 HSQC** (600/151 MHz, D_2O)



Compound **5.66 HMBC** (600/151 MHz, D_2O)



Appendix II: Raw data for CB_1 Activity Assays



dix 1. Raw FLIPR traces showing CB1-mediated K^+ flux following compound addition. Representative fluorescence LIPR membrane potential assays monitoring CB_1 activity in the presence of **A)** Rimonabant, **B)** LYTAC-1,2-PEG8 (**2.64**), **C)** G8 (**2.68**), and **D)** LYTAC-1,4-PEG8 (**2.72**). Compounds were tested across a concentration range (log M: -4.5 to -8), with esponses recorded over 600 s. Vertical dashed lines indicate the timing of compound additions.